



Viability of nanoporous films for nanofluidic applications

Davide Raffaele Ceratti

► To cite this version:

Davide Raffaele Ceratti. Viability of nanoporous films for nanofluidic applications. Chemical Physics [physics.chem-ph]. Université Pierre et Marie Curie - Paris VI, 2015. English. NNT : 2015PA066482 . tel-01316594

HAL Id: tel-01316594

<https://theses.hal.science/tel-01316594>

Submitted on 17 May 2016

HAL is a multi-disciplinary open access archive for the deposit and dissemination of scientific research documents, whether they are published or not. The documents may come from teaching and research institutions in France or abroad, or from public or private research centers.

L'archive ouverte pluridisciplinaire **HAL**, est destinée au dépôt et à la diffusion de documents scientifiques de niveau recherche, publiés ou non, émanant des établissements d'enseignement et de recherche français ou étrangers, des laboratoires publics ou privés.

Université Pierre et Marie Curie

ED 397 : Physique et Chimie des Matériaux

Laboratoire de Chimie de la Matière Condensée de Paris

Laboratoire de PHysicochimie des Electrolytes et Nanosystèmes Interfaciaux

Viability of nanoporous films for nanofluidic applications

Par Davide Raffaele Ceratti

Thèse de Doctorat de Chimie et Physico-Chimie des Matériaux

Dirigée par David Grosso

Soutenance prévue le 30 Septembre 2015

Devant un jury composé de :

Dr.	Cyril Aymonier	Directeur de recherche ICMCB	Rapporteur
Dr.	Jacques Leng	Chargé de recherche LOF	Rapporteur
Pr.	Giuseppe Foffi	LPS Orsay	Examineur
Pr.	Christophe Sinturel	Université d'Orléans	Examineur
Dr.	Vincent Dahirel	Université de Paris 6	Invité
Dr.	Marco Faustini	Univeristé de Paris 6	Invité
Pr.	David Grosso	Univeristé de Paris 6	Directeur de thèse

L'imagination gouverne le monde

N.

Per te Nonna.

Sarai sempre nei miei pensieri

Title : Viability of nanoporous films for nanofluidic applications

This thesis had a dual purpose: i) the development of nanofluidic devices through not lithographic, cheap and scalable bottom-up approach ii) the understanding of nanofluidic phenomena both through experiments and simulations. Mesoporous thin films, in particular Pillared Planar Nanochannels (PPNs), were prepared and utilized to study the capillary infiltration of liquids in nanostructures and have been tested for future nanofluidic applications like separations and nanoconfined reactions. Non organized mesoporous films have also been studied to determine the relationship between nanostructure characteristics and infiltration speed. It has been also demonstrated that in the case of porosities with reduced bottle-necks capillary penetration is performed through a vapor mediated mechanism.

The samples were prepared by dip-coating. A novel method of preparation based on the substitution of a large part of the depositing solution in dip-coating with an inert fluid has been developed in order to strongly reduce the fabrication costs and allow the preparation of larger samples. Moreover advancement in control of the dip-coating technique in “acceleration-mode” to produce thickness gradients has been developed and some potential application linked to fluidics shown.

Finally a part of the effort of this thesis has been placed in the modeling of the electro-osmotic phenomenon in nanostructures through a rather novel simulation method, Stochastic Rotational Dynamics, which takes into account the hydrodynamics and the other interactions inside a nanofluidic system. Validations of the method and further investigations in particular nanofluidic conditions have been performed.

Key words: Nanofluidic applications, dip-coating, bottom-up approach, capillary infiltration, nanoconfinement phenomena, hydrodynamic simulations, Stochastic Rotational Dynamics.

Titre : Couches minces nanoporeuses comme plateforme pour applications nanofluidiques.

Ces travaux de thèse ont eu deux objectifs: i) le développement de systèmes nanofluidique en utilisant une méthode non-lithographique, peu chère et facilement transposable à l'échelle industrielle ii) la compréhension des phénomènes nanofluidiques au travers des études expérimentales et de modélisation. Des couches minces mesoporeuses, en particulier des structures planaires avec des nanopiliers (Pillared Planar Nanochannel PPN en anglais), ont été utilisées pour des études sur l'infiltration capillaire des liquides dans espaces confinés au niveau nanométrique. En plus des premiers tests pour des applications plus complexes comme des séparations et réactions nanoconfinées. Des structures mesoporeuses non-organisées ont aussi été étudiées pour déterminer la relation entre la nanostructure et la vitesse de remplissage capillaire. A été aussi démontré que pour des porosités avec des forts rétrécissements le remplissage capillaire se produit par l'intermédiaire d'une phase vapeur. Les échantillons ont été préparés par dip-coating. Une nouvelle méthode de préparation basée sur une substitution de la plus grande partie de la solution à déposer par un fluide inerte a été développée. La méthode permet de réduire fortement le coût de procédé et, par conséquent, de faire des dépôts sur plus grande surface. En plus une étude fondamentale sur le dip-coating en accélération a été réalisée et application potentielle pour des applications de fluidique démontrée. Un effort dans la modélisation des phénomènes nanofluidiques a aussi été fait pendant cette thèse. Une méthode de simulation qui permet de décrire adéquatement les interactions hydrodynamiques dans un système nano a été utilisée pour simuler un flux électro-osmotique. La méthode, qui s'appelle Stochastic Rotational Dynamics, a été validée par confrontation avec des résultats connus et l'influence des certains paramètres de simulation évaluée dans le détail.

Mot-clé : applications de la nanofluidique, dip-coating, approche bottom-up, infiltration capillaire, effets de nanoconfinement, simulations hydrodynamiques, Stochastic Rotational Dynamics.

INTRODUCTION ----- 1

I : STATE OF THE ART ----- I-5

I.1 NANOFLUIDICS ----- I-7

I.1.a Nanofluidic applications ----- I-8

I.1.a.i Biomedical applications ----- I-9

I.1.a.ii Energy applications: nanofluidic batteries ----- I-12

I.1.a.iii Desalinization – particle separation ----- I-13

I.1.a.iv Fundamental studies. ----- I-14

I.1.a.v Nanofluidic studies for chemical and material sciences ----- I-14

I.1.b Fabrication of nanofluidic channels ----- I-15

I.1.b.i Top-down fabricated channels ----- I-16

I.1.b.ii Bottom-up techniques ----- I-20

I.1.b.iii Pillared Planar Nanochannels ----- I-21

I.2 OBJECTIVES AND CHALLENGES ----- I-23

I.3 BIBLIOGRAPHY ----- I-25

II : ADVANCES IN DIP-COATING ----- II-35

II.1 INTRODUCTION ----- II-37

II.1.a Withdrawal speed – thickness relation ----- II-39

II.1.a.i General considerations ----- II-40

II.1.a.ii Model for the capillarity regime ----- II-43

II.1.a.iii Model for the draining regime ----- II-44

I.1.a.i Combining models to describe simultaneous both regimes: ----- II-45

II.2 FILM HOMOGENEITY ----- II-46

II.2.a Draining and intermediate regime ----- II-46

II.2.a.i Starting meniscus effect ----- II-46

II.2.a.ii Evaporation time effects. ----- II-46

II.2.a.iii Marangoni effects ----- II-49

II.2.a.iv Physical boundaries contributions ----- II-50

II.2.b Capillary regime ----- II-52

II.3 RESULTS ----- II-54

II.3.a Bi-phasic dip-coating method ----- II-55

II.3.a.i The “biphasic” method ----- II-56

II.3.a.ii Droplet method for single-face dip-coating ----- II-61

II.3.a.iii Conclusion ----- II-63

II.3.b Dip-coating in acceleration mode ----- II-64

II.3.b.i	Dynamical variation of withdrawal speed	II-64
II.3.b.i.1	Effect of temperature, gradient intensity and concentration	II-65
II.3.b.ii	Thickness programming	II-70
II.3.b.iii	Applications	II-70
II.3.b.iii.1	Contact angle gradients	II-71
II.3.b.iii.2	Graded microfluidic channel	II-72
II.3.b.iv	Conclusion	II-73
II.4	CONCLUSION	II-74
II.5	APPENDIX	II-75
II.5.a.i	Draining regime (visco-capillary regime).	II-75
II.5.a.ii	Visco-inertial regime.	II-77
II.5.a.iii	Surfactant effect.	II-78
II.6	BIBLIOGRAPHY	II-82

III : MATERIALS SYNTHESIS ----- III-85

III.1	INTRODUCTION	III-87
III.1.a	<i>Sol-Gel chemistry</i>	III-89
III.1.b	<i>Hybrid mesostructured materials</i>	III-91
III.1.c	<i>Evaporation Induced Self Assembly</i>	III-93
III.1.d	<i>Block copolymers self assembly</i>	III-96
III.1.e	<i>Self-assembled block copolymer films</i>	III-101
III.2	SYNTHESIZED MATERIALS	III-105
III.2.a	<i>Environmental-Ellipsometric-Porosimetry</i>	III-106
III.2.b	<i>Non-organized porosities</i>	III-108
III.2.c	<i>Pillared Planar Nanochannels</i>	III-116
III.2.c.i	Preparation of the nanoporous Polystyrene films	III-116
III.2.c.ii	Sol-gel replica	III-119
III.2.c.iii	PPN from PS-b-PLA analysis	III-120
III.2.c.iv	PPN from PS-b-P2VP analysis	III-122
III.2.d	<i>Conclusion</i>	III-123
III.3	BIBLIOGRAPHY	III-124

IV : CAPILLARY INFILTRATION ----- IV-133

IV.1	INTRODUCTION	IV-135
IV.1.a	<i>The Lucas-Washburn equation</i>	IV-137
IV.1.b	<i>Capillary filling in a plane channel</i>	IV-138

IV.1.c	<i>Liquid properties at the nanoscale</i>	IV-141
IV.1.d	<i>Examples of nanoscopic effects</i>	IV-143
IV.1.d.i	Surface Tension and contact angle	IV-143
IV.1.d.ii	Viscosity	IV-146
IV.1.e	<i>Capillary infiltration experiments in nanochannels</i>	IV-149
IV.1.e.i	Experiments in nanosits	IV-149
IV.2	EXPERIMENTAL RESULTS	IV-153
IV.2.a	<i>Critical effect of pore characteristics</i>	IV-154
IV.2.a.i	Sample preparation and analysis	IV-154
IV.2.a.ii	Capillary ring experiment	IV-154
IV.2.a.ii.1	Capillary ring – solvent polarity influence	IV-155
IV.2.a.ii.2	Capillary ring – organic to inorganic precursor ration influence	IV-158
IV.2.a.iii	Dynamics of capillary infiltration	IV-161
IV.2.a.iii.1	Capillary infiltration speed and pore characteristics analysis	IV-161
IV.2.a.iii.2	Bottleneck – pore size dimensions influence on capillary filling speed.	IV-165
IV.2.a.iii.3	Size dependence of the transport mechanism.	IV-166
IV.2.a.iv	Conclusion	IV-170
IV.2.b	<i>Capillary infiltration in PPNs</i>	IV-171
IV.2.b.i	Description of the investigated PPNs structures.	IV-172
IV.2.b.ii	Dynamics of the capillary filling in PPN:	IV-173
IV.2.b.ii.1	The chemical nature of pillars has a strong influence on wicking	IV-174
IV.2.b.ii.2	The porosity of the pillars has a weak influence on wicking.	IV-174
IV.2.b.ii.3	The height of pillars matters only if it is small.	IV-175
IV.2.b.iii	Modeling the capillary filling in PPN:	IV-175
IV.2.b.iii.1	Computation of the hydrodynamic resistance of the PPN	IV-175
IV.2.b.iii.2	Evaluation of the pressure drop across the meniscus	IV-178
IV.2.b.iii.3	Computation of the Washburn transport coefficient	IV-178
IV.2.b.iii.4	Reproduction of the experimental results with a single fitting parameter	IV-180
IV.2.b.iii.5	The model helps understanding the influence of the PPN dimensions	IV-181
IV.2.b.iv	Conclusion	IV-182
IV.3	APPENDIX	IV-183
IV.4	BIBLIOGRAPHY	IV-185
V	SELF-DIFFUSION AND REACTIONS	V-191
V.1	EXPERIMENTAL RESULTS	V-193
V.1.a	<i>Patterning the PPN structure.</i>	V-194
V.1.b	<i>Coupling with microfluidics: self-diffusion</i>	V-196
V.1.b.i	Self diffusion of charged chromophores	V-197
V.1.c	<i>Coupling with microfluidics: reactions</i>	V-198

V.1.c.i	Metallic silver nanoparticles	V-198
V.1.c.ii	Multiple reactions: silver halides precipitation	V-205
V.1.d	Conclusions	V-207
V.2	BIBLIOGRAPHY	V-209

VI : HYDRODYNAMIC SIMULATIONS ----- VI-211

VI.1	INTRODUCTION	213
VI.1.a	Nanofluidic simulations	214
VI.1.b	Hydrodynamic interactions	215
VI.1.b.i	Navier-Stokes equations and hydrodynamic regimes	215
VI.1.b.ii	Hydrodynamics in presence of particles (moving boundary conditions)	218
VI.1.c	Electroosmotic flow – phenomenon	219
VI.2	STOCHASTIC ROTATIONAL DYNAMICS.	223
VI.2.a	The algorithm	224
VI.2.b	Adimensional numbers and time scales	227
VI.2.c	Walls, thermostat and Poiseuille flow	229
VI.2.c.i	Fluid-walls interaction	229
VI.2.c.ii	Thermostat	231
VI.2.c.iii	Poiseuille flow between two planes	232
VI.2.d	Solutes in SRD	235
VI.2.d.i	Fluid interaction with the solutes and force description	235
VI.2.d.ii	CC - Collisional Coupling	236
VI.2.d.iii	CFC – central force coupling	237
VI.2.d.iv	CFC-CC method comparisons	238
VI.2.d.v	Forces between solutes	239
VI.2.d.vi	Electrostatic interactions - Ewald summation	239
VI.2.d.vii	Ewald summation in slab geometry	241
VI.3	: SIMULATION RESULTS	243
VI.3.a	Validation of the SRD method	244
VI.3.a.i	Simulation box and boundary conditions	245
VI.3.a.ii	Validation	246
VI.3.a.iii	Effect of σ_w and d for low surface charge values	249
VI.3.b	Non-ideal case: beyond the PNP hypothesis	253
VI.3.c	From high to low surface charge	256
VI.3.c.i	PNP-“from p ⁺ ”-SRD flow confrontation and WCA interactions effect	258
VI.3.c.ii	Effect of σ_w	258
VI.3.c.iii	Effect of d	258
VI.3.d	Salt addition	261

VI.3.e	<i>Electro-osmosis in PPNs</i>	264
VI.3.e.i	Flow Charts	268
VI.3.f	<i>Conclusion</i>	271
VI.4	APPENDIX	273
I.1.a	<i>Adimensional numbers</i>	273
VI.4.a.i	Mach number	273
VI.4.a.ii	Reynolds number	274
VI.4.a.iii	Peclet Number	274
VI.4.a.iv	Schmidt number	275
VI.4.a.v	Knudsen number	275
VI.5	BIBLIOGRAPHY	276
CONCLUSION		281
RESUME EN FRANÇAIS		291
ACKNOWLEDGEMENTS		309

Introduction

The scientific field of nanotechnology is often perceived by the non-insider as a Wonderland World. In common conversations, if the word nanofluidics is pronounced, a reaction of astonishment and marvel seems to be the only alternative to an admission of complete ignorance of the subject. In the first hypothesis, if a self-praising approach is avoided and an honest one preferred, the researchers in the field have to somehow quench the expressed enthusiasm of the audience. This happens pointing out that the field is still under deep development and real applications are maybe expectable in the period of five to ten years. No free miracles for tomorrow.

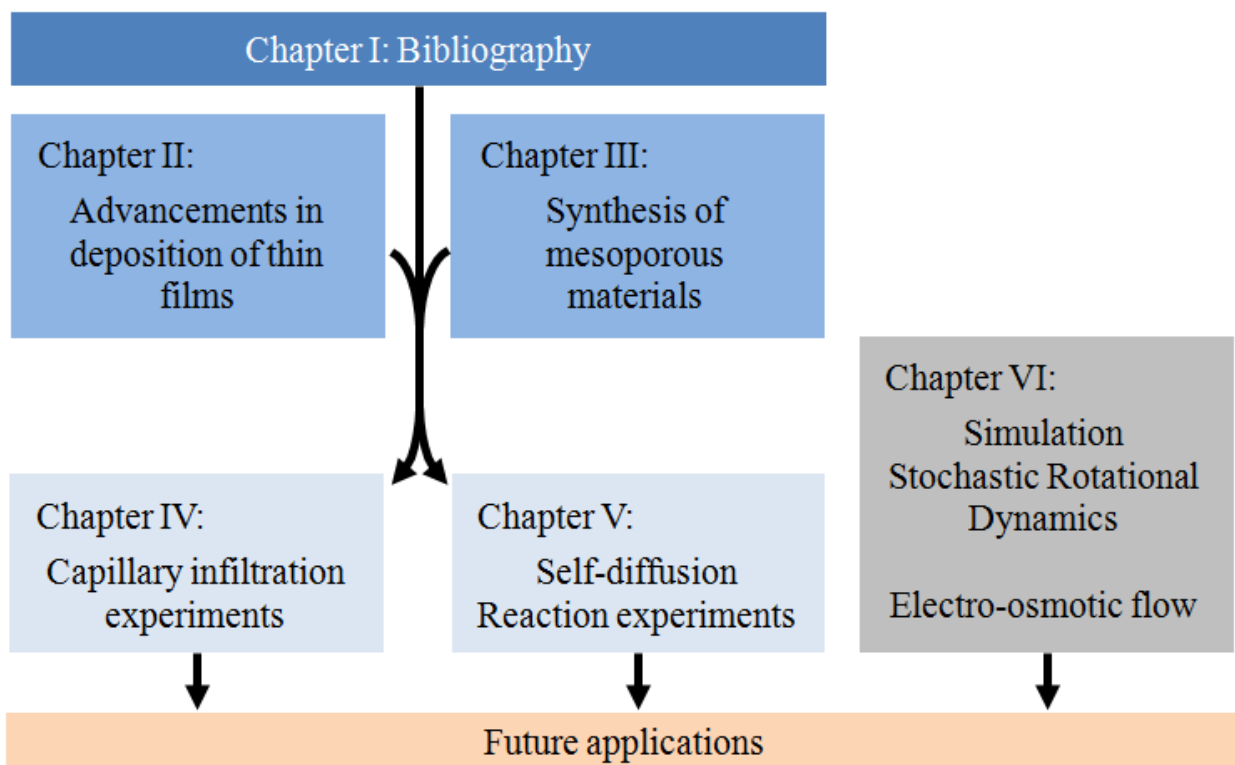
On the other hand, the challenges that arise in the nanofluidics field have strongly stimulated the researchers and nanofluidics is growing in importance in the scientific community. The study of the properties of fluids at the nanoscale and the exploitation of the known nanoscale effects to create new devices and applications constitute the principal efforts nowadays made in the field.

Nanofluidics promises to develop technologies allowing realizing, between the others, complex medical analysis and smart energy conversions on small scale devices called lab-on-a-chip. A race towards the development of real “chips”, once the complete control of the nanofluidic phenomena is established, is currently run by various groups in the world.

The fabrication of nanofluidic devices represents a key element of this run. Nanostructured and nanopatterned surfaces have to be created to access the potentiality of the nanoscale phenomena. The processing of these surfaces is usually accomplished by “top-down” techniques that consist in obtaining nanostructures by structural decomposition of a bulk solid. In this category the lithographic techniques offer flexibility in obtaining complex architectures and high control of the pattern regularity. However these methods are often time consuming, expensive and not suitable for large scale production.

In this thesis, a “bottom-up” approach based on the self-organization of molecules and materials is instead proposed. Disordered and ordered nanochannels are realized through liquid deposition techniques of block-copolymers and so-gel materials. In particular a structure called Pillared Planar Nanochannels (PPNs) showing a high degree of order and an extremely accessible nanostructure are evidenced as candidates for low-cost and scalable on large scale nanofluidic applications. Their applicability will be demonstrated and side support studies on nanoscale properties of liquids, fabrication methods of nanostructures and simulation of nanoconfined fluid flows presented in this thesis.

This thesis is organized in six chapters as showed in the following Figure.



Schematic guideline of the thesis

Chapter I consists of the scientific background about nanofluidics. It briefly presents the currently utilized fabrication techniques to produce nanofluidic devices and their already presented applications. Therefore the Pillared Planar Nanochannels (PPN) structure is briefly introduced and the scope and aims of this thesis stated. Chapter II, III, IV and VI are divided in a bibliographic and a results section.

In Chapter II, the dip-coating technique is presented with the present knowledge and control of the process. After a brief analysis of the critical parameters which have been identified as problematic

during deposition, the results concerning a dip-coating method that allows a serious reduction of the costs of the process and a second one allowing obtain graded thin films for fluidic applications are presented.

In Chapter III, after a bibliographic introduction of the materials utilized in this thesis and their assembly, the fabrication of the utilized nanostructures is presented. The characterization of the produced samples is also reported.

These samples are utilized in Chapter IV to study the capillary infiltration of liquids in the nanostructured thin-films. A relation to the structural parameters of the material and its chemical composition, in both case of disorganized structures and PPNs, is made. These studies follow a bibliographic introduction about the behavior of liquids and their properties at the nanoscale.

In Chapter V the PPN structures are integrated in microfluidic devices to perform preliminary tests of nanofluidic applications such as contemporary self-diffusion experiments (to test separation effects) and nanoconfined reactions.

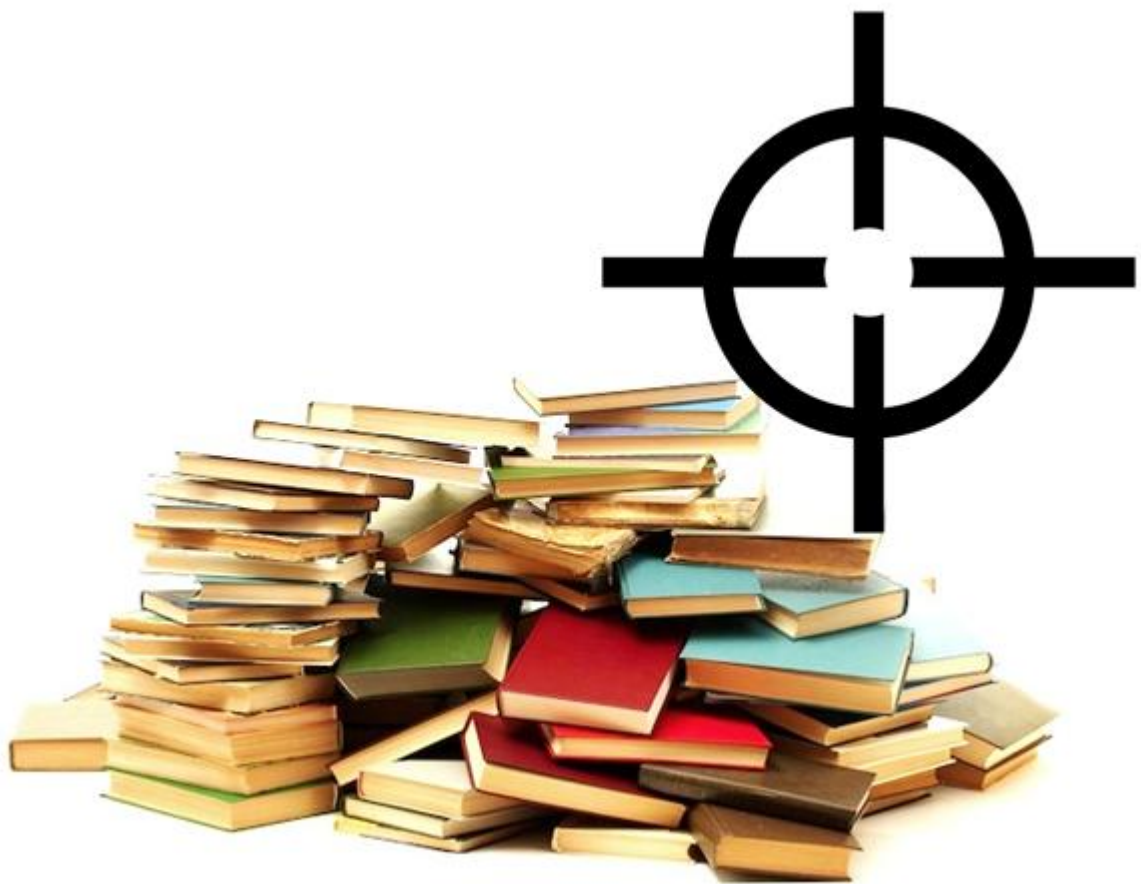
Finally Chapter VI changes point of view abandoning the experimental approach and acquiring a simulation one. The electro-osmotic flow, an important phenomenon reported in many nanofluidics applications, is studied by simulation through the Stochastic Rotational Dynamics (SRD) method. Results for planar nanochannels and preliminary results for the PPN geometry are reported for various values of the parameter simulations. A previous introduction of the electro-osmotic phenomenon and the SRD method accompanies the discussion. The simulation tool is presented as support to have a deeper understanding and microscopic point of view of nanofluidic phenomena.

Brief appendix are in some case added at the end of the chapters containing interesting information related to the main discussion but not directly necessary to understand it.

Some perspectives and conclusions are finally reported.

The articles published during this Ph.D. are given in the final annex.

I : State of the art



I	: STATE OF THE ART	I-5
I.1	NANOFLUIDICS	I-7
<i>I.1.a</i>	<i>Nanofluidic applications</i>	<i>I-8</i>
I.1.a.i	Biomedical applications	I-9
I.1.a.ii	Energy applications: nanofluidic batteries	I-12
I.1.a.iii	Desalinization – particle separation	I-13
I.1.a.iv	Fundamental studies.	I-14
I.1.a.v	Nanofluidic studies for chemical and material sciences	I-14
<i>I.1.b</i>	<i>Fabrication of nanofluidic channels</i>	<i>I-15</i>
I.1.b.i	Top-down fabricated channels	I-16
I.1.b.ii	Bottom-up techniques	I-20
I.1.b.iii	Pillared Planar Nanochannels	I-21
I.2	OBJECTIVES AND CHALLENGES	I-23
I.3	BIBLIOGRAPHY	I-25

I.1 Nanofluidics

Nanofluidics is the study and manipulation of fluids confined within nanostructures [1]. It is undoubtedly an emerging field of the recent scientific research with an increasing number of articles per year concerning fundamental studies and (some) possible applications.

However concepts and phenomena related to nanofluidics have been already studied in other research fields from colloidal chemistry to soil science, passing through the physics of fluids and physiology. It is sufficient to cite the nanosized cell or organelle membrane proteins pores [2]–[4], the fundamental aspect of nanosized hydrodynamic interactions in the aggregation of nanoparticles [5], [6] or phenomena related to infiltration and permeation of gases[7], [8], water or other liquids inside rocks or clays[9], [10], to understand how nanofluidic phenomena have already been somehow debated.

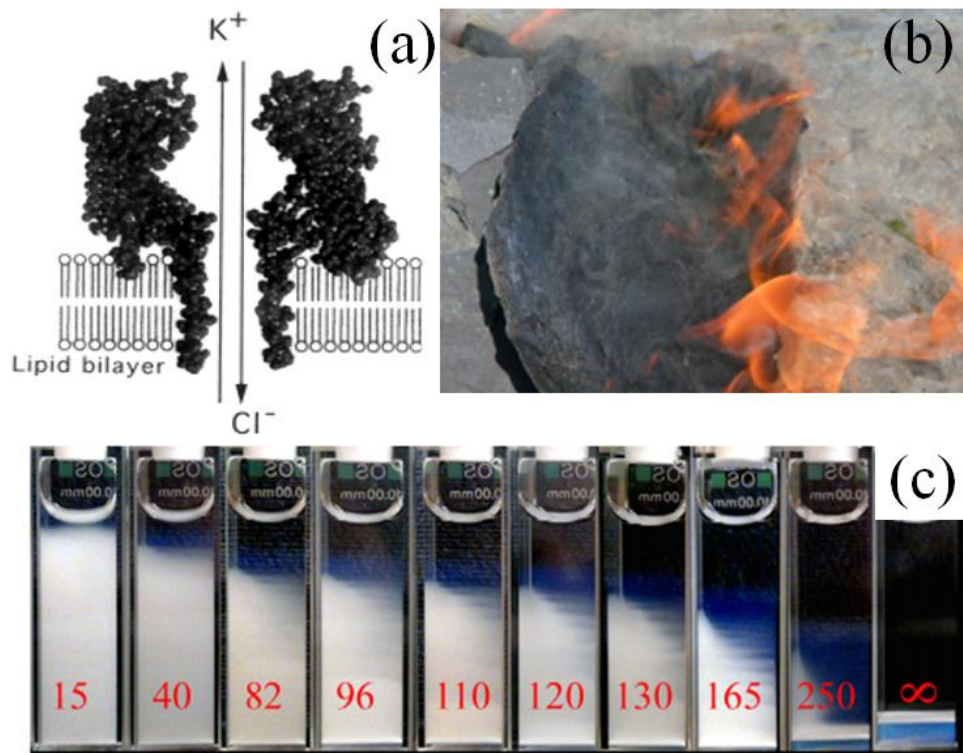


Figure. I-1. (a) [11] Biological nanopore in a cellular membrane interacting with ions in solutions. The knowledge of protein structure allows determining the size of nucleic acid chains if they are forced to pass through the pore blocking the ionic current. (b) Burning shale containing hydrocarbons in the nanoporosity. (c) [12] Clustering and sedimentation of a mixture of polymeric nanoparticles.

Nevertheless, even if the phenomena related to nanofluidics have been investigated, the handling and control of fluids at the nanoscale is a feature of the recent developments in science. New or improved methods of micro and nanofabrication indeed allow preparing nanofluidic devices with

controlled channel characteristics and sizes. Moreover, thanks to the large spreading of nanotechnology, more and more materials become available and can be used for nanofluidic applications or in-depth studies of the nanofluidic phenomena. A short overview of these applications is hereafter presented.

The fabrication of nanofluidic devices can be performed by two strategies: “top-down” and “bottom-up”. “Top-down” techniques consist of creating nanostructures by controlled cutting of supported bulk solids often achieved by selective local chemical etching through a mask (lithography) or using ultra thin particle single beams (FIB, EBL). Lithographic techniques offer the possibility to obtain complex architectures and high control over pattern regularity. A promising alternative is the “bottom-up” approach that consists of the controlled nanosegregation, and assembly of molecules or nano-objects, such as molecular precursors, block-copolymer micelles, nanoparticles or clusters, which form a wide range of nano and mesoscopic structures, with different chemical compositions, shapes and functionalities. In general can be defined “bottom-up” each approach that exploits an auto-organization property of a given material at the nanoscale. As will be shown the controlled nanoscale cracking of polymers under tensile stress constitute an example of this extended concept of bottom-up approach. Both techniques are presented in the second section of this chapter.

I.1.a Nanofluidic applications

While the literature about nanofluidic devices looks rather large, applied nanofluidics is still in its infancy. Generally artificial nanofluidic devices are built through different top-down techniques that will be illustrated in the next section. In some cases, bottom-up materials have also been utilized. These applications take advantage of the reduced size, high surface to volume ratio and other characteristics that allow the nanofluidic systems to perform tasks that are impossible to accomplish at the macroscopic scale. Biomedical and energy-related applications are the most studied but some others, such as desalinization or ion/molecules separations can be found. Moreover nanofluidic devices are used as customized platforms to perform fundamental studies in order to better understand phenomena occurring at the nanoscale and enlarge the number of potential applications. Some perspective nanofluidic applications are also reported at the end of this section based on known nanoscale phenomena that are still unexploited.

1.1.a.i Biomedical applications

The introduction of the biomedical applications of nanofluidic devices necessitates a previous explanation of the concept of lab-on-a-chip. A lab-on-a-chip is a device at the centimeter-millimeter scale that integrates many of a laboratory functions in a reduced space [13]. This device is meant to perform, on-site, all the analysis that could be realized in a laboratory, more efficiently and with a much lower quantity of analyzed liquid. Microfluidic lab-on-a-chip devices are already commercially available [14]–[20]. In the case of nanofluidic applications the idea is to realize a multi-scale device with some nanofluidic channels integrated in a microfluidic architecture. This design is similar to what happens for electronic cards where the operations are mainly realized in microchips. In the final device microchannels (connections) would then be used to feed the nanofluidic part (microchip) to perform the real experiment.

The uses of nanodevices for biomedical application can be divided in three main parts, concentration [21]–[26], [27], separation of biomolecules [26], [28]–[34] and DNA elongation [35]–[39], but other variegated devices such as protein transport transistors (channels in which the access of a protein can be controlled through an external potential) have been realized [40].

In the first case, the aim of the device is to create a local increase of the biomolecule concentration in a particular location within a microchannel/nanochannel device. This is obtained by exploiting the ion concentration polarization effect. The passage of ions is selective in nanochannels. Ions with the same charge (co-ions) of the walls are indeed inhibited from entering the channel due to strong electrostatic interactions. If, on the other hand, an external electric or pressure field is applied through the nanochannel, the ions of the contrary charge in respect of the walls (counter-ions) can pass through the channel and accumulate at its exit. As a result, the general ion concentration is increased due to the fact that electro-neutrality has to be maintained. On the other hand at the nanochannel entrance, the concentration of the counterions is reduced. The co-ions have then to leave the area to obtain electro-neutrality. This induces strong electric fields at the nanochannel entrance and exit. If further external forces are applied to the system (such as pressure or other electric fields in perpendicular direction) a perfect counterbalance of the (counter-) co-ions generated field and the external one can create in a certain location. In that position, the biomolecules (of the same charge of the co-ions) assume zero velocity and accumulate. This method has been applied in Figure. I-2a where electric fields in the vertical direction along the nanochannels and pressure gradients in the horizontal one have been used to concentrate fluorescent proteins in the microchannels for successive injection into an oil stream to form concentrated-in-protein droplets.

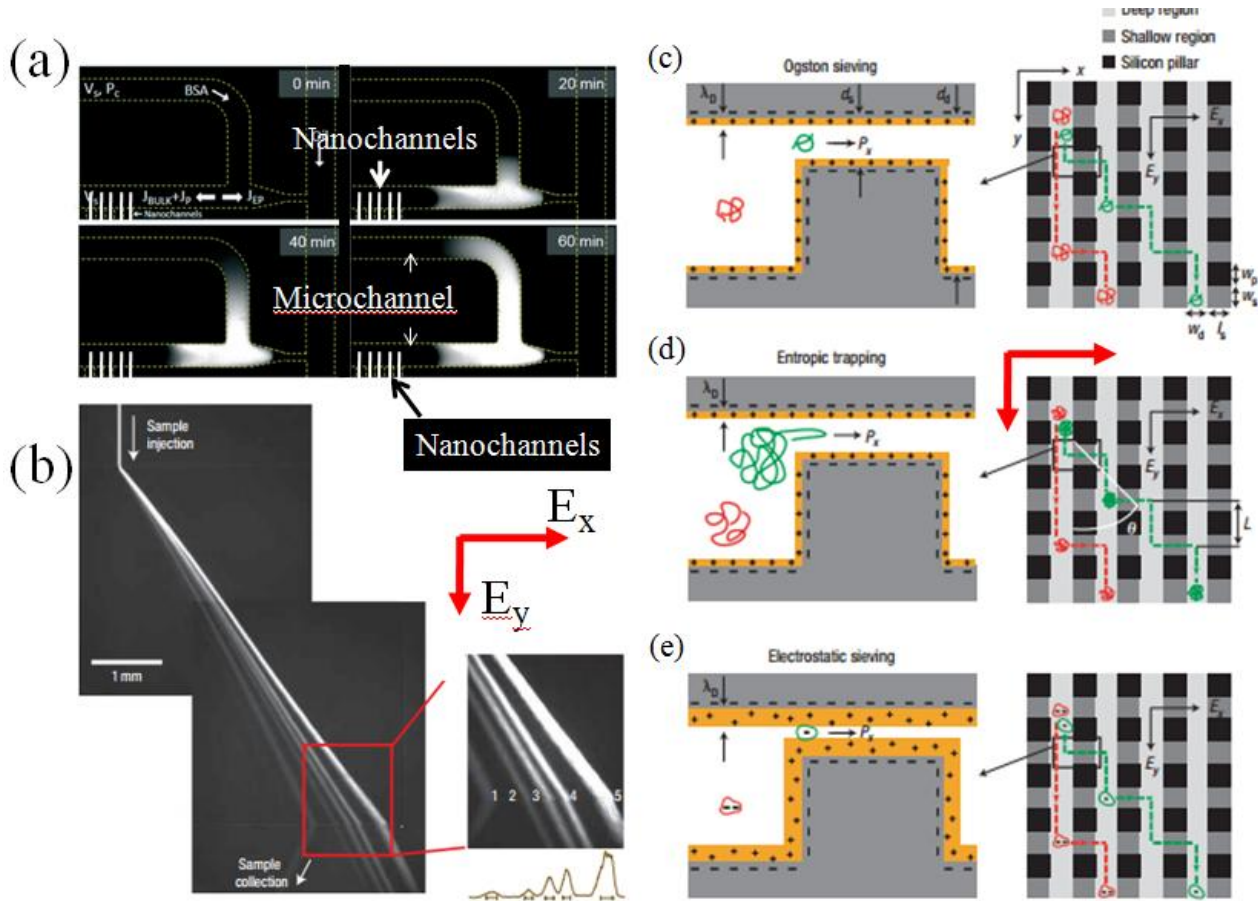


Figure. I-2. (a) [27] Protein concentration created in a microfluidic-nanofluidic device. The nanochannel is not shown but is just to the left of the (b)[33] Separation of DNA strands of e 2,322 bp (1), 4,361 bp (2), 6,557 bp (3), 9,416 bp (4), 23,130 bp (5) through the entropic trapping mechanism in (d). Other mechanism can separate DNA strands for other range of their (c) or channel dimension (e) sizes through an Ogston sieving or electrostatic sieving mechanism.

Separation of biomolecules is performed exploiting the similar dimension of the biomolecules and channel size. In Figure. I-2b DNA strands are electrically pushed into a complex architecture with deep channels in the y and thin ones in the x direction. Two perpendicular electric fields are applied to move the DNA strands in the y direction and eventually induce a passage in the x direction to another deep channel. The frequency of this passage determines the separation and depends of various parameters. In the case of DNA, three mechanisms can be identified. For short strands (hundreds of base pairs) the smaller molecules can pass through the channel while larger ones cannot because of the reduced channel size; this mechanism is called Ogston sieving (Figure. I-2c). Shorter strands have indeed a higher speed in the x direction. For longer strands (thousands of base pairs) direct passage is anyway impossible and the DNA has to deform in order to pass through the channel; in this case the entropic trapping phenomenon is exploited (Figure. I-2d). It is indeed more probable for longer strands to be completely pulled into the nanochannel because of the higher probability to have a section entering it and then dragging all the molecules thanks to the electrostatic force (DNA is charged). This causes longer strands to be collected further in the x direction. Finally, in the case of low ionic strength, the channel surface charge can operate as an

electrostatic screen (electrical double layer EDL of the same length of the channel) in respect to the charged molecules. Here, the selection mechanism based on the charge is called electrostatic sieving (Figure. I-2e).

To conclude this brief overview of the biomedical applications of nanofluidics, DNA elongation has to be mentioned. DNA molecules are dragged in the nanochannel by the electric field and, because entering in the nanochannel is impossible in a non-elongated conformation due to steric hindrance, elongation occurs. DNA elongation is relevant for pathogen detection or whole genome analysis allowing the detection of the exact position of a gene in a DNA strands. The ordering, orientation and distance between genes, the existence of genomic rearrangements (e.g. deletions) can thus be determined [41], [42]. An example is shown in Figure. I-3 DNA molecules, with different chain length were stretched and immobilized inside squared nanochannels.

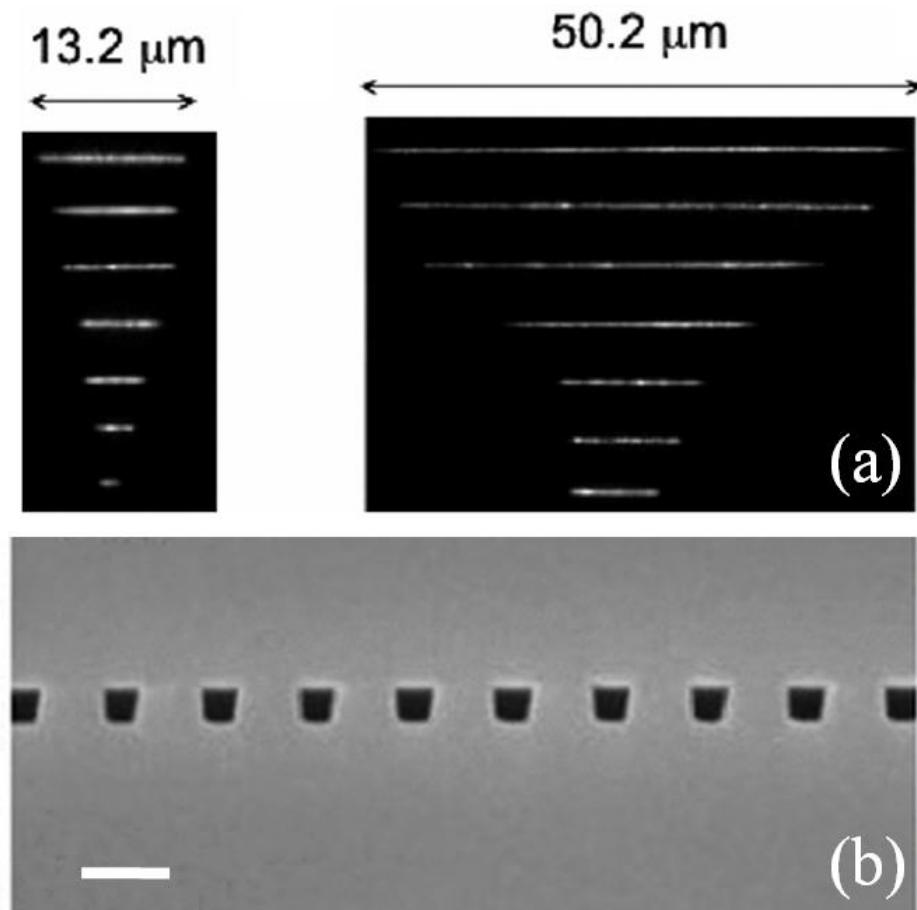


Figure. I-3. [42] (a) Elongated DNA molecules of different chain length inside squared nanochannels. A SEM image of the channels is reported in (b). The white bar corresponds to 200 nm.

1.1.a.ii Energy applications: nanofluidic batteries

Energy-related applications of nanofluidics mainly concern the extraction of electrical current from externally applied [43]–[47] pressure gradients to nanochannels. Some case of energy harvesting from osmotic pressure gradients to have also been reported [48].

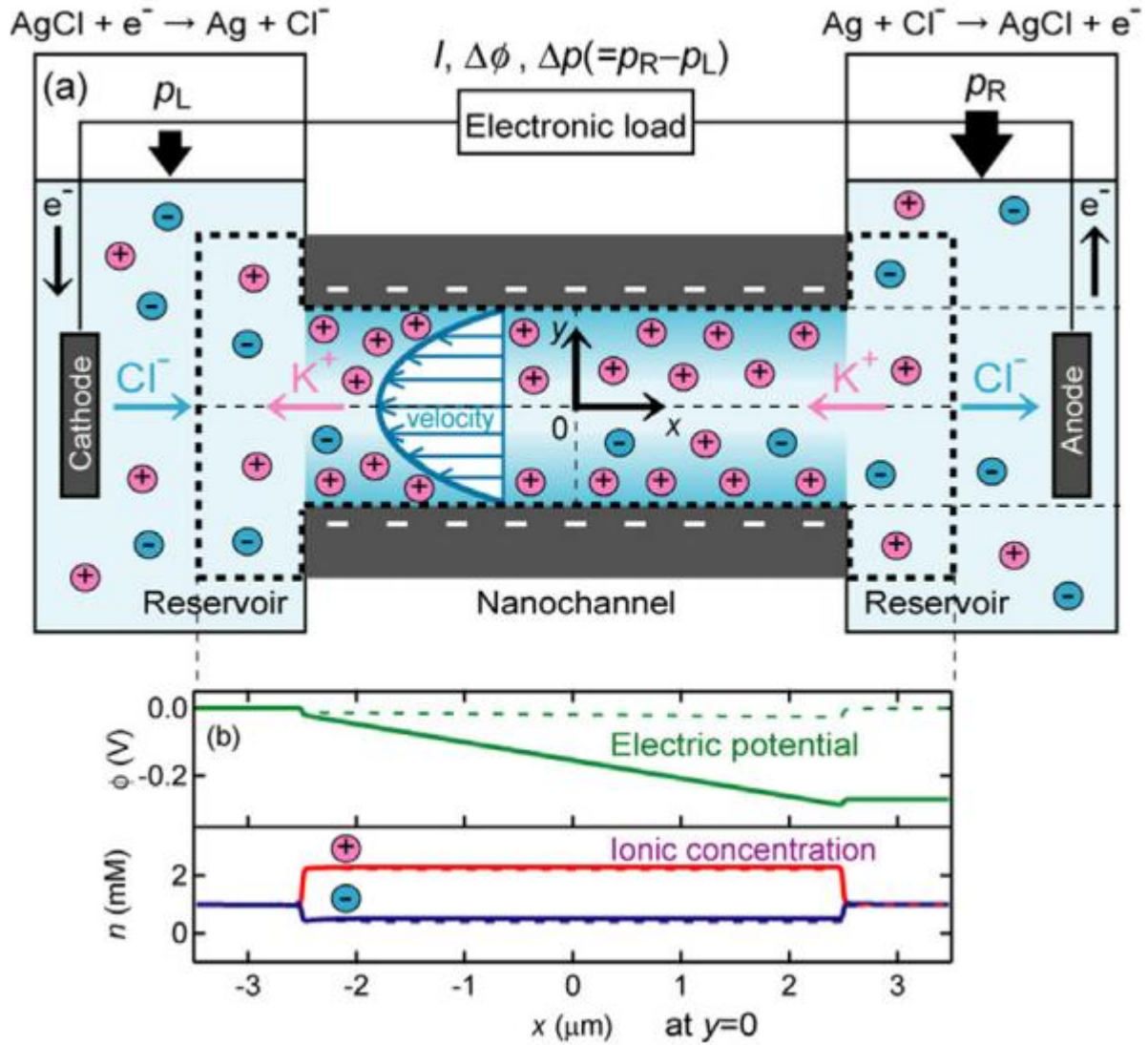


Figure. I-4. [45]. Scheme of a nanofluidic battery. In place of the salt bridge of a common battery a nanofluidic channel with negative surfaces is utilized. Being the EDL of the same size of the channel the population of positive charges is higher than the negative ones inside the channel. Upon application of a pressure gradient that causes a flow toward the left an electric potential is generated due to the accumulation of positive charges in the left reservoir.

In particular, the basic idea of “nanofluidic battery” is reported in Figure. I-4 and it exploits the concept of electrostatic sieving described in the previous section. In the nanofluidic channels, the surface is (totally or partially) screened by the electrical double layer (EDL) whose thickness is similar to the channel’s dimension. The channels result then to have a net charge in the liquid. Counterions (ions of the opposite charge with respect to the walls) are only allowed to pass. Co-ions (ion with the same charge of the channel walls) are not (or less) allowed to enter the channel. If an external pressure (or an osmotic difference [48]) induces a liquid flow in the channel, the counterions are displaced while the co-ions remain in their respective reservoirs. This creates a charge imbalance between the two reservoirs and electrons need to pass through the electrical circuit to maintain electro-neutrality. The electric current can then be exploited. Maximum

expected efficiencies of 50 % have been theoretically estimated [43] even if the currently reported maximum is only 5% [49].

1.1.a.iii Desalinization – particle separation

Similarly to nanofluidic batteries, applications of nanofluidics for desalinization mainly exploit the comparable dimension of the nanochannels and of the electrical double layer (EDL). In most cases, the “nanofluidic” system consist in separation membranes with pores in the nanoscale which separate two reservoirs, one of which with high salt content. Pressure, that has to be higher than the osmotic one that plays in the contrary direction, is applied and water filtered from ions. This well known process is called reverse osmosis [50]–[53]. Pressures of tenth or more bars are needed to obtain reasonable fluxes. On the other hand, some examples of desalinization device originally though for biomolecule preconcentration can be found in literature [54] which indicates the presence of new nanofluidic approaches to the problem. Energy in the form of electric fields [54] is applied and water separated from the salts exploiting the same fundamental phenomena used for concentration (creating a zero speed location just before of a fork blocking in this way one of the channels to the ions) (Figure. I-5a).

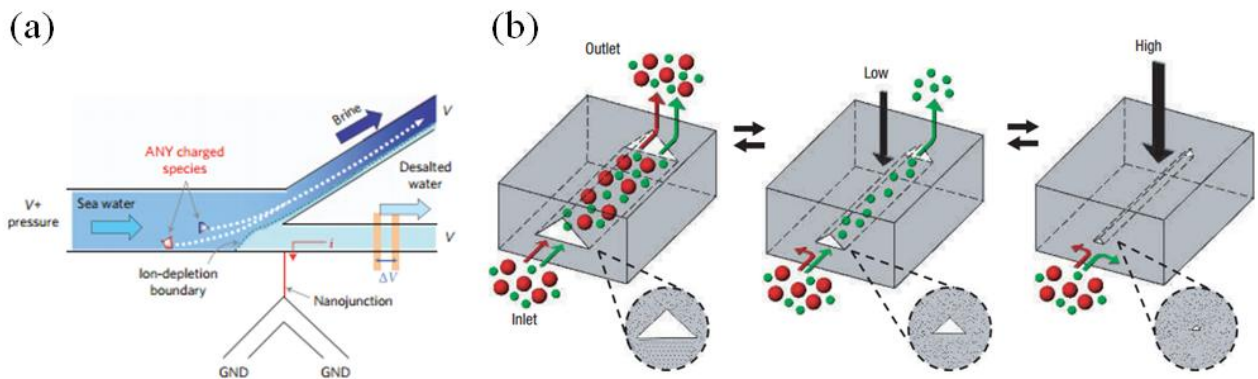


Figure. I-5. (a) [54] A desalinization nanofluidic device reconverted from a preconcentration one. The ions are concentrated before the fork preferentially in the uppermost channel. The pressure driven water in the lower channel is then ion free. (b) [55] Nanochannel with tunable height utilized to separate fluorophores of different dimensions.

Concerning particle and molecules separation, the strategies utilized are compatible with proteins separation too [56], [55], [57]. The only difference is that the entropic trapping phenomenon cannot be exploited for solid particles but the other separation methods based on steric or electrostatic interaction can be still exploited. For example in Figure. I-5b we report the scheme of a nanochannel utilized to separate fluorophores of different sizes due to the possibility of modifying dynamically the channel dimension and then maximum dimension of the penetration molecules. Methods coupling electro-osmotic and/or pressure driven flow have also been proposed and reported for the separation of ions [58]–[60].

1.1.a.iv Fundamental studies.

Various phenomena take place at the nanoscale due to the different properties of matter at these small dimensions. The study of these properties is then of general interest for the scientific community. Liquid structuration at the surface, increased viscosity, bubble formation, variation of contact angle are only some of the known differences found when working with nanofluidic devices. Understanding of these nanofluidics-related phenomena is then necessary to further explore these particular characteristics of the nanoscale that influence the macroscopic world too (as mentioned in the introduction). We will tackle these aspects in more detail on Chapter IV.

1.1.a.v Nanofluidic studies for chemical and material sciences

Nanofluidics can be used also as a useful tool for other studies in chemical reactivity or material science. Nanofluidic platforms could indeed be designed to study the effect of confinement for a wide range of relevant phenomena in the cited fields. For example, the use of nanofluidic channels could modify the reaction yield and, most importantly, the selectivity of organic reactions. Similarly the influence of the nucleation and growth dynamics of nanoparticles could be studied. Some examples exist but have not been exploited properly by the nanofluidic community. Reaction performed in zeolites (corresponding to very narrow nanofluidic channels) have shown a strongly increased selectivity of the nitration of toluene due to the steric hindrance due to the channel walls to the attack of the nitro group in meta and orto positions [61].

Effects on selectivity have been investigated for xylene isomerization [62], [63] or other organic reactions too [64]–[66].

For larger nanochannels, selective reaction on larger molecules such as polymer or protein could be performed thanks to the possible orientation and distortion effects obtainable during flow of these molecules in nanoconfined space. Moreover the formation/precipitation of nanoparticles and other crystals could be performed in nanoconfined space modifying their nucleation and growth kinetics. This would help to better understand various geological phenomena (whose explication has been imputed to nanoconfinement effects on solubility [67], [68]) or to obtain particular nanoparticle shapes and formations or crystal polymorphs [69], [70].

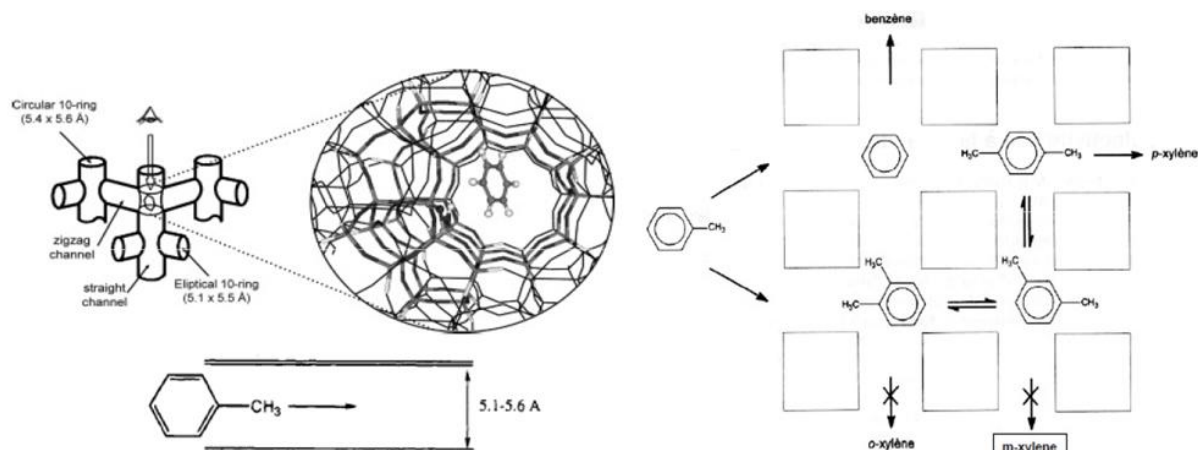


Figure. I-6. Simple scheme of the reaction selectivity due to confinement. Due to the steric hindrance isomerization of xylene to the para isomer is strongly favored over the other isomers.

Unfortunately, the application of nanofluidic devices for this kind of purposes is rather limited. This is principally due to the fact that the nanochannels' fabrication process is usually time-consuming and requires utilization of clean-room nanofabrication facilities (lithography, bonding...). This aspect is critical since a suitable amount of nanofluidic devices is necessary to perform systematic studies in which a large number of reactions should be performed to obtain adequate scientific results. Moreover, with the current technologies, the choice of nanochannel material composition is limited. Researchers are then discouraged from this kind of study and are more prone to valorize their device differently. A reduction of the production time and cost of nanochannels is then needed to allow these kinds of studies, such as the exploration of reactions, crystallizations and particle formations at the nanoscale.

The methods to produce nanofluidic devices by conventional techniques are reported in the next section and a brief analysis of each of them is given. The alternative method utilized in this thesis is then introduced.

I.1.b Fabrication of nanofluidic channels

Several techniques can be utilized to fabricate nanofluidic channels. As already mentioned, they can be separated in two main groups: top-down and bottom-up techniques. A better explanation and description of both the top-down and bottom up techniques are needed to understand the objectives of this thesis and a brief overview is here presented.

I.1.b.i Top-down fabricated channels

A brief list of the top-down techniques commonly utilized to obtain nanochannels is reported in Table. I-1.

Fabrication method	Minimum size of channel [nm]	Materials/substrate	Advantage/disadvantage
Conventional photolithography	40–100 in one dimension	Photoresist polymer/silicon(glass)	Easy and accessible, high throughput / simple patterning only, low resolution
Interference lithography	30 (with appropriate treatment)	Photoresist polymer/silicon(glass)	Fast, maskless, deep nanochannels / simple geometries only
Nanoimprint lithography	6–40	Photoresist polymer/silicon(glass)	High throughput/releasing issue, hard to form deep channels, mold fabrication
Electron beam lithography	<5	Photoresist polymer/silicon(glass)	freedom of patterns, small feature size / relatively slow process, high cost
Focused Ion Beam Lithography	10 nm	Si/glass/quartz/oxides	Freedom of patterns, small feature size /really slow process, high cost

Table. I-1. Top-down fabrication methods summary.

The easiest of the presented methods is conventional photolithography (CL) [33], [71]–[75]. A photosensitive organic layer (photoresist) is usually spun over a wafer. A mask (with patterns drawn by the researcher) is put between the light source and the wafer. The illuminated part of the photoresist reacts with the light and is then removed/maintained after a washing step. The light diffraction limit corresponds to the minimum size of the possible features. Then common semiconductor processing steps such as etching are used to transfer the pattern from the patterned photoresist to the wafer. An open channel structure is then formed which requires sealing with some bonding method, such as anodic bonding [76] or fusion bonding [77], that can be rather difficult (depending on the material). The dimension on the nanoscale is the one perpendicular to the wafer plane with a control of the channel depth depending of the etching time. A simple scheme of the method and some example of nanochannels are reported in Figure. I-8a and Figure. I-8c. The method is rather easy, cheap and accessible in most laboratories. On the other hand the architectural possibilities are limited, nanoconfinement can be easily attained in one direction only (if no other complex steps are added) and the bonding step can eventually fail and requires attentive operation and non-negligible times.

Interference Lithography, IL (based on the interference patterns of two incoming coherent laser beams) needs also to be mentioned [78]–[84]. It allows the production of periodic arrays of nanochannels. No complicated design is possible but simple linear channels with size down to 30

nm in diameter can be realized [79]. Large surfaces are easily patternable but, as in the previous case, bonding issues arise.

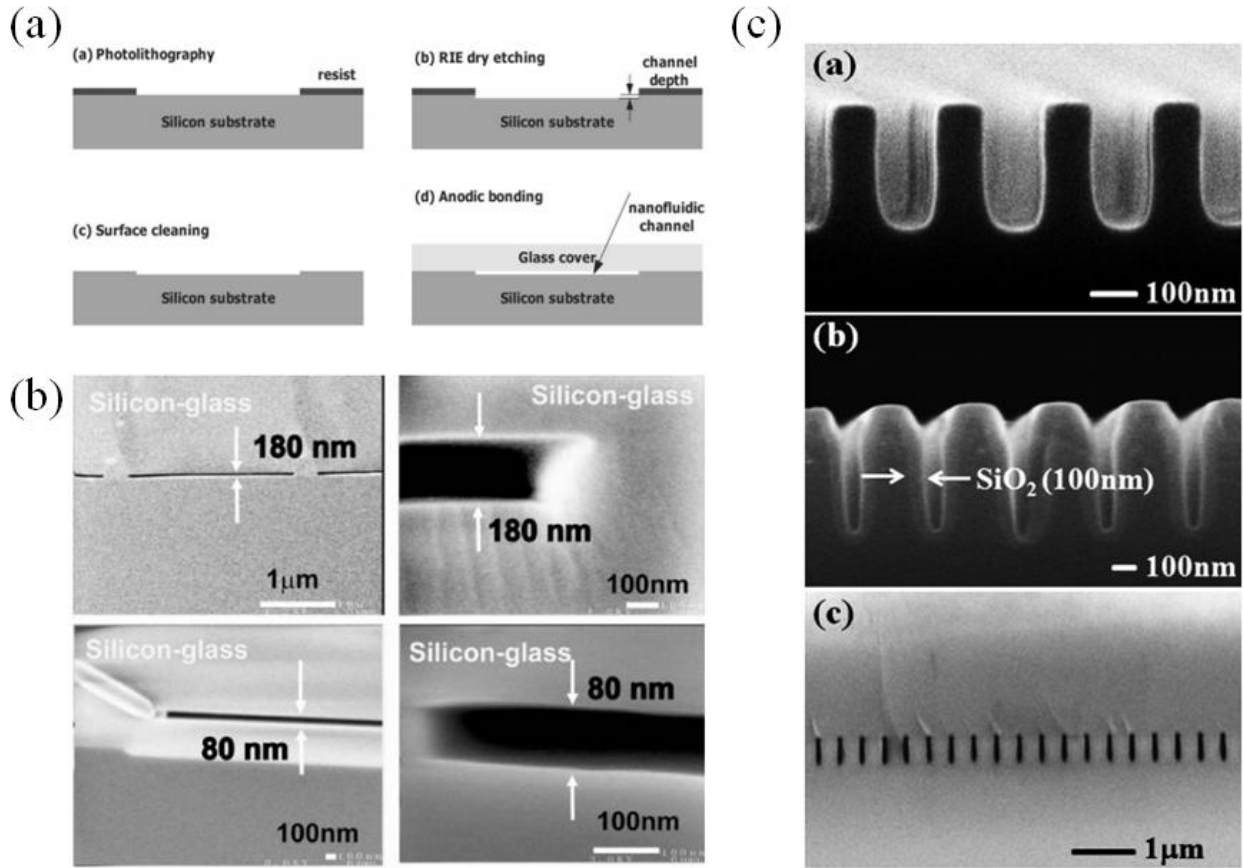


Figure. I-7. (a) [85] Scheme of the conventional photolithography process and (b) example of the obtained nanochannels. [86]. (c) [81] SEM images of nanochannels obtained after etching (b.a), oxidation (b.b) and bonding (b.c) with patterns defined with IL.

Nanoimprint lithography (NIL) [87]–[89] is also a good choice to fabricate nanopatterned surfaces that can then be utilized as nanochannels. It consists of mechanically pressing predefined molds into imprint resist which allows overcoming the light diffraction limit [90]. A layer of imprint polymer or resist is deposited onto the substrate. A hard mold with nanoscale patterns is then put in contact with the substrate and they pressed under certain load. The polymer/resist layer is cured/hardened and solidified by heat or UV light. Pressure and temperature during this imprinting (pressing and curing) have to be carefully controlled to have a good impression. The hard mold is removed, leaving the reverse nanostructures on the resist layer. The residual polymer can then be etched leaving open channels (Figure. I-8b). As in the previous case, bonding is required.

Actually, some alternative strategies can be used to avoid the bonding step taking advantage of the reduced dimensions of the patterns. A strategy consists in patterning a sacrificial polymer and

then using it as template for the deposition of a sol-gel material leaving, upon calcination, an empty channel [91]. A second strategy consists of the sealing of the structure by partial dissolution of the uppermost part of the channel. In case of polymer this can be obtained through organic vapor exposure. The dissolved chains merge closing the channel on the external part while the lower polymer structure remains stable Figure. I-8b.b [92]. A similar procedure can be used on silicon using a UV laser pulse (Figure. I-8b.d [93]). The technique involves various issues. The first one is the production of the initial mold that requires sophisticated, long-time and costly patterning techniques (which are also the ones described hereafter for nanochannels). Therefore channels of low depth can be produced only. If indeed the mold is too high, it becomes difficult to remove it without damaging the polymeric film or creating serious imperfections. The releasing of the mold is indeed a difficult aspect to handle and adequate operations should be performed to obtain proper results.

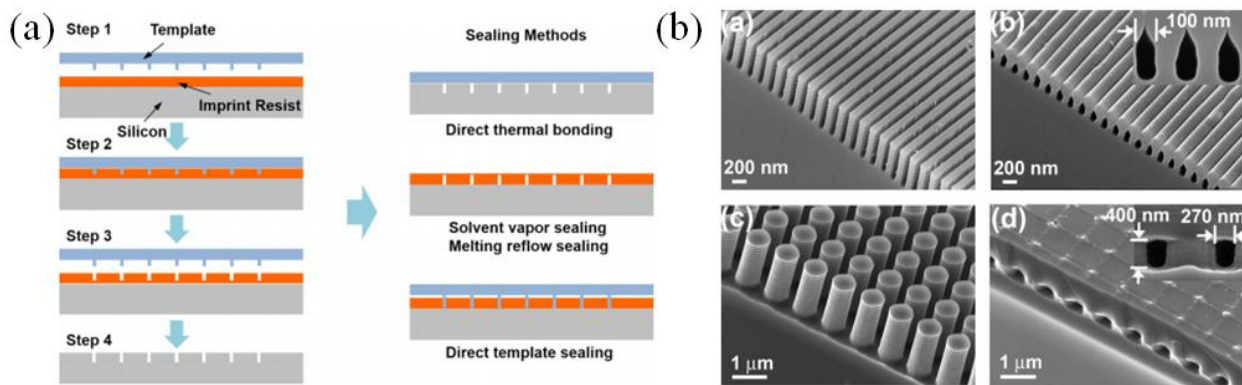


Figure. I-8 (a) Scheme of the nanoimprint lithography process and strategies to close the channels.[93] (b) Closing the open nanoimprinted structures with vapor exposure ((b.a) and (b.b)) and with UV laser pulses ((b.c) and (b.d)).

More advanced techniques in term of resolution are the electron beam lithography (EBL) and the focused ion beam lithography (FIB). The first one uses a focused electron beam to locally cure an electron sensitive resist. The process is similar to writing and no mask is utilized. The resolution is extremely high [94]. On the other hand the time needed to “write” large surfaces becomes extremely long too. The beam indeed cures surfaces of the order of one mm² in an hour (increase of an order of magnitude on this time depend on the resist and its thickness) which limits the application of the techniques to large surfaces. On the other hand the method allows designing extremely complex patterns being extremely free in the writing constraints. After the definition of the pattern, a step of etching is required. If no particular strategy is utilized [95] the formed channels need a bonding [96]–[101]. It has to be noticed that this method can be utilized to build the mold for NIL in “writing” the negative of the desired channels. The obtained mold can also be utilized as a template for casting PDMS nanofluidic channels [102]. The PDMS

(polydimethylsiloxane) in its liquid form is poured on the mold and then cured. Upon removal it can be easily bonded with a flat surface in order to seal the nanochannels.

In the same way focused ion beam lithography (FIB) is a sophisticated technique that utilizes a focused beam of ions to achieve site-specific fabrications, such as swelling, milling, implantation, ion-induced deposition, or etching, with nanometer resolution. Highly energetic ions can be utilized to locally etch the substrate without any mask directly creating the nanochannels without further etching step. The process is rather slow because similarly to EBL it is a scanning method but each spot has to be treated for a longer time to directly remove the material. A common strategy to create nanochannels is to drill circular nanometric holes [103]–[108] (down to 10 nm in diameter after adequate treatment of an originally 25 nm pore [104]) in thin membranes obtaining in this way nanochannels in the direction perpendicular to the membrane surface. Clearly nanochannels in the parallel direction of the substrate can be obtained too [109]–[111] with resolutions [110] down to 5 nm (Figure. I-9b). In this second case the bonding issue still persists and it is even more difficult to solve because of possible unwanted redeposition of milled material on the channel edges. The main advantage of FIB is the direct generation of nanoscale features. Unfortunately, this technique still requires costly equipment and the fabrication yield is even lower than EBL because of the direct milling/deposition mode.

In Figure. I-9 we report three examples of nanochannel fabricate with EBL and two with FIB respectively. As can be see both methods allow attaining an extremely high resolution.

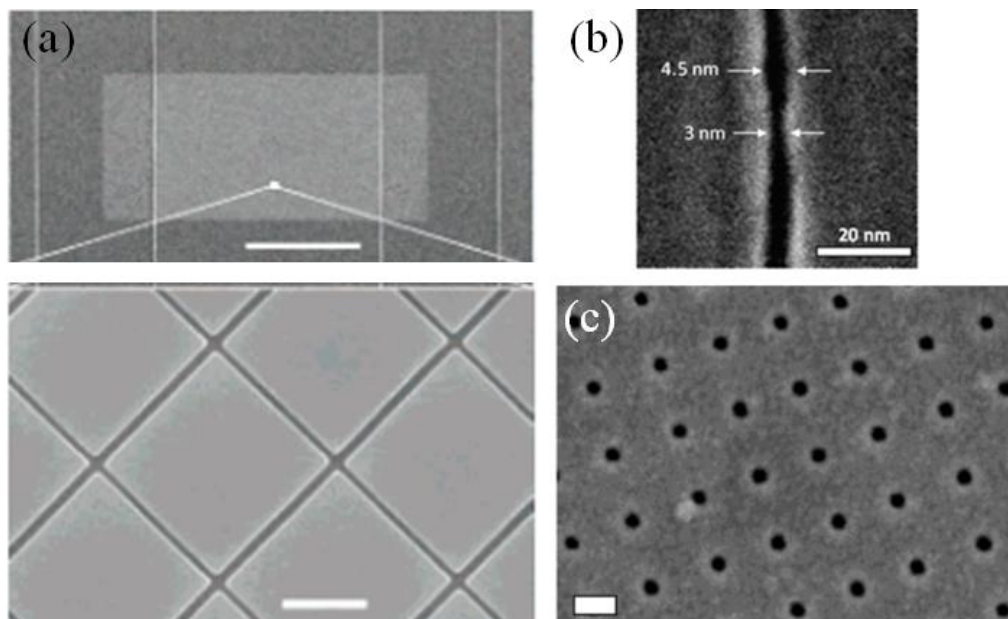


Figure. I-9. (a) EBL fabricated nanochannel. Scale bar of 1 μm in the lower image. (b) FIB fabricated nanochannel with a 5 nm resolution. (c) FIB fabricated nanoporous membrane. The nanochannels are in the perpendicular direction. Scale bar 50 nm.

I.1.b.ii Bottom-up techniques

Bottom-up techniques are much less wide spread compared to their top-down counterparts. Until now nanofluidics has indeed been dominated by a physical and engineering approach, which has induced to the almost exclusive use of micro-electronic technology to produce nanochannels. Wide possibilities arise when the world of porous material and self-assembly are considered to create nanofluidic devices, nevertheless much still needs to be done.

For example methods not requiring lithographic exploiting the natural cracking patterns of polymers upon tensile stresses (Figure. I-10a) have been utilized to produce nanofluidic channels [55], [112]–[114]. These cracks being in the nanoscale their direct use, or their PDMS replica has been utilized for DNA stretching [113], particles and biomolecules concentration [114], filtering [55] etc. Recent advancements allow building crack-based nanofluidic circuit with channels in different directions inducing cracks on the edge of photolithographically created micro-patterns (Figure. I-10b [112]).

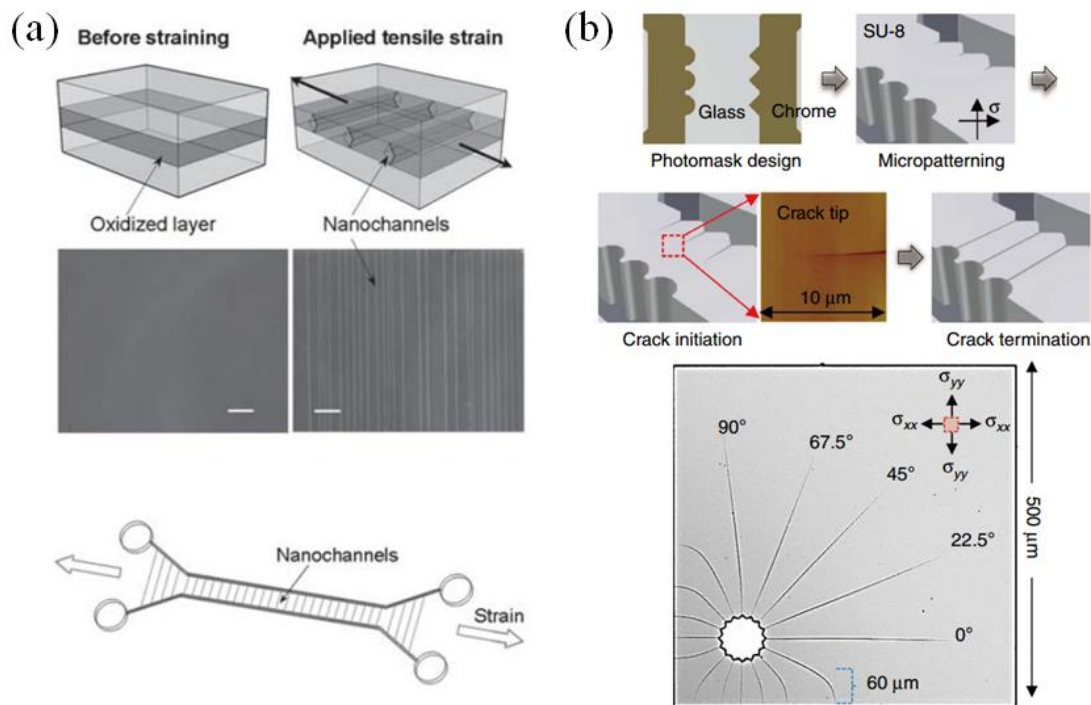


Figure. I-10.(a) [113] Scheme of the strategy, SEM images (scale bar 25 μm) and scheme of the final device for the tensile strength realized nanochannel in polymer. (b) [112] Scheme of the strategy and exemplum of different direction induced cracks in polymer for the realization of nanochannels.

Self-assembly of colloidal silica particles in a microchannel permitted to obtain a nanoporous membrane used for concentration purposes without performing lithography steps in nano-resolution [115], [116]. This is a generalizable strategy that has been used for this or similar

application substituting silica particles for example with a nafion membrane [117] or polystyrene nanoparticles [29].

Not many other strategies for the fabrication of nanochannels with bottom-up approach can be found in the literature even if many porous materials with pores at the nanoscale could be utilized for these aims.

In the next section an elegant bottom-up strategy reported by our group in 2010 is presented. It constituted the basis for the development of this thesis and has been amply utilized.

1.1.b.iii Pillared Planar Nanochannels

The method to create the Pillared Planar Nanochannels was introduced 5 years ago [118] and it is illustrated in Figure. I-11. It exploits the self-assembly properties of some block-copolymers to obtain organized solid replicated structures that can be used as nanochannels. The selected block-copolymers PS-b-PLA, composed of two blocks with different chemical and physical properties, forms hexagonally-organized cylindrical structures when deposited and adequately processed on silicon surfaces. The phase composing the vertical cylinder (PLA) can then be removed by chemical attack and the remaining PS structure utilized as template for a second material (Sol-Gel $\text{TiO}_2/\text{SiO}_2$ mixtures). Upon removal of the PS phase by calcination, a pillared structure in the nanoscale is generated which can be used as nanochannel.

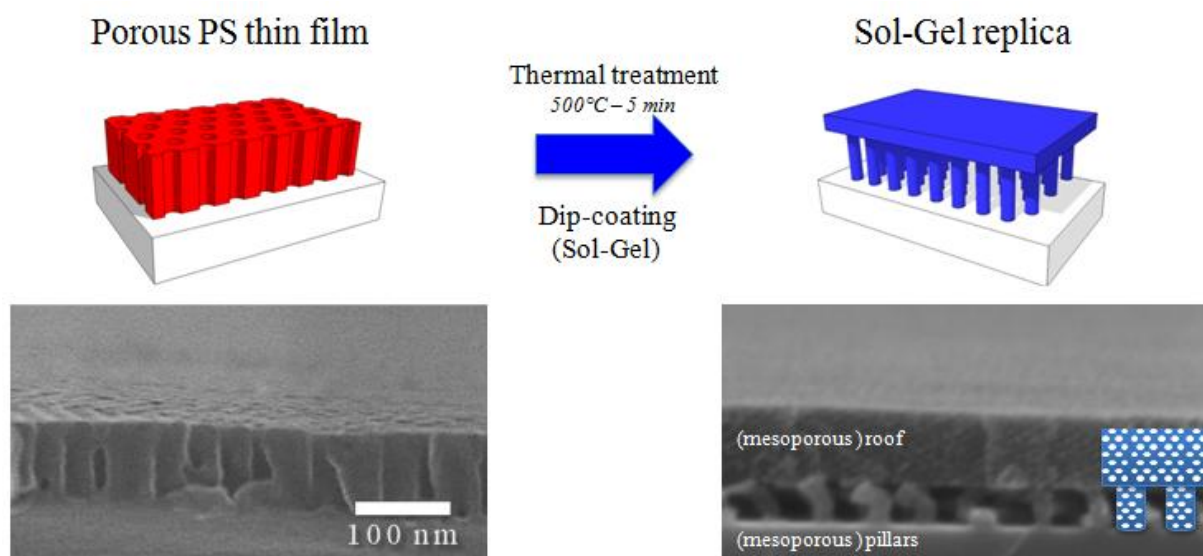


Figure. I-11. The polystyrene nanostructure derived by PS-b-PLA self-assembly is utilized as template for sol-gel deposition. The PPN structure is then formed showing pillars on the Si substrate and a roof covering them.

Applicability for nanofluidic applications has been demonstrated showing that the structure could be infiltrated with water by capillarity. The resolution of this kind of porous architecture is extremely high (pillar to pillar distance < 30 nm). Top-down methods such as EBL or FIB, could

potentially compete in term of resolution but they are indeed really expensive. Cheap ones, such as conventional lithography, don't allow fabrication of nanostructured systems at this size and with this degree of complexity. In any case, a bonding step would anyway be needed. In this system, instead, the presence of the roof allows avoiding the difficult bonding procedure and it protects the channel from any other material eventually deposited over the roof surface. This constitutes a second advantage of the system. Moreover, the richness of sol-gel chemistry permits to tune the Pillared Planar Nanochannels composition and to include an additional mesoporosity into the pillars. In sum, the production cost of a device fabricated through this bottom-up approach is extremely limited which constitute another serious positive element compared to other systems with the same resolution.

Starting from this brief overview on fabrication techniques and from the elements introduced in this last sub-section, the objectives of this thesis are then presented.

I.2 Objectives and challenges

As just shown, nanofluidic science was introduced together with various applications and fabrication methods. Nevertheless the field, even if growing, is not booming and, more importantly, real applications still remain remote. This is due to two principal factors:

- A technological limit due to the fabrication of nanofluidic devices that requires expensive equipment or, at least, many successive and time consuming steps (for CL, IL and NIL the bonding step remain difficult and time consuming because of needed manual operation)
- A still non-complete knowledge of nanofluidic phenomena that in some cases constitute effective obstacles to the further development of nanofluidics.

These two obstacles could be insuperable if the perspective is not shifted towards novel methods. This evidences the need to set two principal objectives for this Ph.D. thesis in nanofluidics. (i) The development of low-cost fabrication techniques that can be scale-up and develop in a conventional chemistry lab. (ii) The investigation of nanofluidic phenomena associated to original, sol-gel derived nanoporous materials.

In this thesis, then, the already presented PPNs have been identified as good candidates for these kinds of objectives thanks to their low cost, bonding-less fabrication, high nanostructuration (resolution) and tunability of the material composition.

The bottom-up approach permits a reduction of the costs and to seriously reduce the complexity of the fabrication. On the other side, their high structuration and tunability of the material permit to explore the nanofluidic phenomena at various dimensions and various surface properties. With a possibility to compare the obtained results with simulations too (that can be performed for system of reduced dimensions only).

Studies on PPNs were also coupled with other on more common sol-gel mesoporous materials that, with their nanoscale porosity, can be seen as disorganized nanochannels.

Four challenges have then been identified during this Ph.D.:

I: State of the art: Objectives and challenges

1. The setting-up of a method that permits to prepare nanochannels on large-scale production at a research level (and can be eventually exploited at an industrial one) which will be developed in Chapter II together with other fabrication techniques for eventual nanofluidic applications.
2. The creation of different kinds of nanostructures which can be utilized for nanofluidic experiments for fundamental and applicative purposes (Chapter III)
3. The study of nanoscopic effects on nanofluidic phenomena in nanoporous structures and PPNs such as capillary infiltration (Chapter IV)
4. The integration of bottom-up materials in nanofluidic devices for applications in nanoconfined separations and reaction (Chapter V)
5. The understanding of nanofluidic phenomena through adequate models and simulations. In particular the electro-osmotic flow (Chapter VI) that is a common phenomenon encountered in bio-medical application due to the presence of electric fields to drive the charged biomolecules movement.

Many other elements of interest have been identified but unfortunately the time for a Ph.D. is not unlimited. The thesis will conclude with still a lot of questions and ideas to develop.

I.3 Bibliography

- [1] “Nanofluidics : Latest content : nature.com.” [Online]. Available: <http://www.nature.com/subjects/nanofluidics>. [Accessed: 28-Jul-2015].
- [2] F. Bonardi, E. Halza, M. Walko, F. Du Plessis, N. Nouwen, B. L. Feringa, and A. J. M. Driessen, “Probing the SecYEG translocation pore size with preproteins conjugated with sizable rigid spherical molecules,” *Proc. Natl. Acad. Sci. U. S. A.*, vol. 108, no. 19, pp. 7775–80, May 2011.
- [3] S. C. Hinnah, R. Wagner, N. Sveshnikova, R. Harrer, and J. Soll, “The chloroplast protein import channel Toc75: pore properties and interaction with transit peptides,” *Biophys. J.*, vol. 83, no. 2, pp. 899–911, Aug. 2002.
- [4] M. P. Schwartz and A. Matouschek, “The dimensions of the protein import channels in the outer and inner mitochondrial membranes,” *Proc. Natl. Acad. Sci. U. S. A.*, vol. 96, no. 23, pp. 13086–90, Nov. 1999.
- [5] A. Furukawa and H. Tanaka, “Key Role of Hydrodynamic Interactions in Colloidal Gelation,” *Phys. Rev. Lett.*, vol. 104, no. 24, p. 245702, Jun. 2010.
- [6] J. K. Whitmer and E. Luijten, “Influence of hydrodynamics on cluster formation in colloid-polymer mixtures,” *J. Phys. Chem. B*, vol. 115, no. 22, pp. 7294–300, Jun. 2011.
- [7] F. Javadpour, D. Fisher, and M. Unsworth, “Nanoscale Gas Flow in Shale Gas Sediments,” *J. Can. Pet. Technol.*, vol. 46, no. 10, Apr. 2013.
- [8] A. S. Ziarani and R. Aguilera, “Knudsen’s Permeability Correction for Tight Porous Media,” *Transp. Porous Media*, vol. 91, no. 1, pp. 239–260, Sep. 2011.
- [9] H.-H. Liu and J. Birkholzer, “On the relationship between water flux and hydraulic gradient for unsaturated and saturated clay,” *J. Hydrol.*, vol. 475, pp. 242–247, Dec. 2012.
- [10] S. Hansbo, “Consolidation equation valid for both Darcian and non-Darcian flow,” *Géotechnique*, vol. 51, no. 1, pp. 51–54, Jan. 2001.
- [11] D. W. Deamer and D. Branton, “Characterization of Nucleic Acids by Nanopore Analysis,” *Acc. Chem. Res.*, vol. 35, no. 10, pp. 817–825, Oct. 2002.
- [12] R. Piazza, S. Buzzaccaro, and E. Secchi, “The unbearable heaviness of colloids: facts, surprises, and puzzles in sedimentation,” *J. Phys. Condens. Matter*, vol. 24, no. 28, p. 284109, Jul. 2012.
- [13] D. Mark, S. Haeberle, G. Roth, F. von Stetten, and R. Zengerle, “Microfluidic lab-on-a-chip platforms: requirements, characteristics and applications,” *Chem. Soc. Rev.*, vol. 39, no. 3, pp. 1153–82, Mar. 2010.

- [14] J. M. Hicks and M. Iosefsohn, "Reliability of home pregnancy-test kits in the hands of laypersons.," *N. Engl. J. Med.*, vol. 320, no. 5, pp. 320–1, Feb. 1989.
- [15] N. Kusano, K. Hirashima, M. Kuwahara, K. Narahara, T. Imamura, T. Mimori, K. Nakahira, and K. Torii, "Immunochromatographic assay for simple and rapid detection of Satsuma dwarf virus and related viruses using monoclonal antibodies," *J. Gen. Plant Pathol.*, vol. 73, no. 1, pp. 66–71, Feb. 2007.
- [16] G. A. Posthuma-Trumpie, J. Korf, and A. van Amerongen, "Lateral flow (immuno)assay: its strengths, weaknesses, opportunities and threats. A literature survey.," *Anal. Bioanal. Chem.*, vol. 393, no. 2, pp. 569–82, Jan. 2009.
- [17] R. Krska and A. Molinelli, "Rapid test strips for analysis of mycotoxins in food and feed.," *Anal. Bioanal. Chem.*, vol. 393, no. 1, pp. 67–71, Jan. 2009.
- [18] A. Heller and B. Feldman, "Electrochemical glucose sensors and their applications in diabetes management.," *Chem. Rev.*, vol. 108, no. 7, pp. 2482–505, Jul. 2008.
- [19] B. Cosmi, G. Palareti, M. Moia, M. Carpenedo, V. Pengo, A. Biasiolo, P. Rampazzo, G. Morstabilini, and S. Testa, "Accuracy of a Portable Prothrombin Time Monitor (Coagucheck) in Patients on Chronic Oral Anticoagulant Therapy," *Thromb. Res.*, vol. 100, no. 4, pp. 279–286, Nov. 2000.
- [20] "i-STAT Handheld Blood Analyzer | Abbott Point of Care." [Online]. Available: <https://www.abbottpointofcare.com/products-services/istat-handheld>. [Accessed: 21-Jul-2015].
- [21] S. H. Ko, Y.-A. Song, S. J. Kim, M. Kim, J. Han, and K. H. Kang, "Nanofluidic preconcentration device in a straight microchannel using ion concentration polarization.," *Lab Chip*, vol. 12, no. 21, pp. 4472–82, Nov. 2012.
- [22] D. Hlushkou, R. Dhopeswarkar, R. M. Crooks, and U. Tallarek, "The influence of membrane ion-permeability on electrokinetic concentration enrichment in membrane-based preconcentration units.," *Lab Chip*, vol. 8, no. 7, pp. 1153–62, Jul. 2008.
- [23] Y.-C. Wang, A. L. Stevens, and J. Han, "Million-fold preconcentration of proteins and peptides by nanofluidic filter.," *Anal. Chem.*, vol. 77, no. 14, pp. 4293–9, Jul. 2005.
- [24] Y.-C. Wang and J. Han, "Pre-binding dynamic range and sensitivity enhancement for immuno-sensors using nanofluidic preconcentrator.," *Lab Chip*, vol. 8, no. 3, pp. 392–4, Mar. 2008.
- [25] K.-D. Huang and R.-J. Yang, "A nanochannel-based concentrator utilizing the concentration polarization effect.," *Electrophoresis*, vol. 29, no. 24, pp. 4862–70, Dec. 2008.
- [26] D. W. Inglis, E. M. Goldys, and N. P. Calander, "Simultaneous concentration and separation of proteins in a nanochannel.," *Angew. Chem. Int. Ed. Engl.*, vol. 50, no. 33, pp. 7546–50, Aug. 2011.

- [27] M. Yu, Y. Hou, H. Zhou, and S. Yao, "An on-demand nanofluidic concentrator.," *Lab Chip*, vol. 15, no. 6, pp. 1524–32, Mar. 2015.
- [28] W.-L. Hsu, D. J. E. Harvie, M. R. Davidson, H. Jeong, E. M. Goldys, and D. W. Inglis, "Concentration gradient focusing and separation in a silica nanofluidic channel with a non-uniform electroosmotic flow.," *Lab Chip*, vol. 14, no. 18, pp. 3539–49, Sep. 2014.
- [29] Y. Zeng and D. J. Harrison, "Self-assembled colloidal arrays as three-dimensional nanofluidic sieves for separation of biomolecules on microchips.," *Anal. Chem.*, vol. 79, no. 6, pp. 2289–95, Mar. 2007.
- [30] T. Yamamoto and T. Fujii, "Nanofluidic single-molecule sorting of DNA: a new concept in separation and analysis of biomolecules towards ultimate level performance.," *Nanotechnology*, vol. 21, no. 39, p. 395502, Oct. 2010.
- [31] M. T. Blom, E. Chmela, R. E. Oosterbroek, R. Tijssen, and A. van den Berg, "On-chip hydrodynamic chromatography separation and detection of nanoparticles and biomolecules.," *Anal. Chem.*, vol. 75, no. 24, pp. 6761–8, Dec. 2003.
- [32] J. Han and J. Fu, "Biomolecule separation by steric hindrance using nanofluidic filters.," *Conf. Proc. ... Annu. Int. Conf. IEEE Eng. Med. Biol. Soc. IEEE Eng. Med. Biol. Soc. Annu. Conf.*, vol. 4, pp. 2611–4, Jan. 2004.
- [33] J. Fu, R. B. Schoch, A. L. Stevens, S. R. Tannenbaum, and J. Han, "A patterned anisotropic nanofluidic sieving structure for continuous-flow separation of DNA and proteins.," *Nat. Nanotechnol.*, vol. 2, no. 2, pp. 121–8, Feb. 2007.
- [34] J. Fu, P. Mao, and J. Han, "A Nanofilter Array Chip for Fast Gel-Free Biomolecule Separation.," *Appl. Phys. Lett.*, vol. 87, no. 26, p. 263902, Dec. 2005.
- [35] E. Abad, S. Merino, A. Retolaza, and A. Juarros, "Design and fabrication using nanoimprint lithography of a nanofluidic device for DNA stretching applications," *Microelectron. Eng.*, vol. 85, no. 5–6, pp. 818–821, May 2008.
- [36] L. J. Guo, X. Cheng, and C.-F. Chou, "Fabrication of Size-Controllable Nanofluidic Channels by Nanoimprinting and Its Application for DNA Stretching," *Nano Lett.*, vol. 4, no. 1, pp. 69–73, Jan. 2004.
- [37] W. Li, J. O. Tegenfeldt, L. Chen, R. H. Austin, S. Y. Chou, P. A. Kohl, J. Krotine, and J. C. Sturm, "Sacrificial polymers for nanofluidic channels in biological applications," *Nanotechnology*, vol. 14, no. 6, pp. 578–583, Jun. 2003.
- [38] N. Douville, D. Huh, and S. Takayama, "DNA linearization through confinement in nanofluidic channels.," *Anal. Bioanal. Chem.*, vol. 391, no. 7, pp. 2395–409, Aug. 2008.
- [39] W. Reisner, K. J. Morton, R. Riehn, Y. M. Wang, Z. Yu, M. Rosen, J. C. Sturm, S. Y. Chou, E. Frey, and R. H. Austin, "Statics and Dynamics of Single DNA Molecules Confined in Nanochannels," *Phys. Rev. Lett.*, vol. 94, no. 19, p. 196101, May 2005.

- [40] R. Karnik, K. Castelino, and A. Majumdar, "Field-effect control of protein transport in a nanofluidic transistor circuit," *Appl. Phys. Lett.*, vol. 88, no. 12, p. 123114, Mar. 2006.
- [41] H. U. Weier, M. Wang, J. C. Mullikin, Y. Zhu, J. F. Cheng, K. M. Greulich, A. Bensimon, and J. W. Gray, "Quantitative DNA fiber mapping," *Hum. Mol. Genet.*, vol. 4, no. 10, pp. 1903–10, Oct. 1995.
- [42] X. Michalet, "Dynamic Molecular Combing: Stretching the Whole Human Genome for High-Resolution Studies," *Science (80-.)*, vol. 277, no. 5331, pp. 1518–1523, Sep. 1997.
- [43] Y. Yan, Q. Sheng, C. Wang, J. Xue, and H.-C. Chang, "Energy Conversion Efficiency of Nanofluidic Batteries: Hydrodynamic Slip and Access Resistance," *J. Phys. Chem. C*, vol. 117, no. 16, pp. 8050–8061, Apr. 2013.
- [44] F. H. J. van der Heyden, D. J. Bonthuis, D. Stein, C. Meyer, and C. Dekker, "Power generation by pressure-driven transport of ions in nanofluidic channels," *Nano Lett.*, vol. 7, no. 4, pp. 1022–5, Apr. 2007.
- [45] H. Daiguji, Y. Oka, T. Adachi, and K. Shirono, "Theoretical study on the efficiency of nanofluidic batteries," *Electrochem. commun.*, vol. 8, no. 11, pp. 1796–1800, Nov. 2006.
- [46] H. Daiguji, P. Yang, A. J. Szeri, and A. Majumdar, "Electrochemomechanical Energy Conversion in Nanofluidic Channels," *Nano Lett.*, vol. 4, no. 12, pp. 2315–2321, Dec. 2004.
- [47] F. H. J. van der Heyden, D. J. Bonthuis, D. Stein, C. Meyer, and C. Dekker, "Electrokinetic energy conversion efficiency in nanofluidic channels," *Nano Lett.*, vol. 6, no. 10, pp. 2232–7, Oct. 2006.
- [48] A. Siria, P. Poncharal, A.-L. Biance, R. Fulcrand, X. Blase, S. T. Purcell, and L. Bocquet, "Giant osmotic energy conversion measured in a single transmembrane boron nitride nanotube," *Nature*, vol. 494, no. 7438, pp. 455–8, Feb. 2013.
- [49] Y. Xie, X. Wang, J. Xue, K. Jin, L. Chen, and Y. Wang, "Electric energy generation in single track-etched nanopores," *Appl. Phys. Lett.*, vol. 93, no. 16, p. 163116, Oct. 2008.
- [50] K. S. Spiegler and Y. M. El-Sayed, "The energetics of desalination processes," *Desalination*, vol. 134, no. 1–3, pp. 109–128, Apr. 2001.
- [51] D. PAUL, "Reformulation of the solution-diffusion theory of reverse osmosis," *J. Memb. Sci.*, vol. 241, no. 2, pp. 371–386, Oct. 2004.
- [52] J. G. Wijmans and R. W. Baker, "The solution-diffusion model: a review," *J. Memb. Sci.*, vol. 107, no. 1–2, pp. 1–21, Nov. 1995.
- [53] M. SOLTANIEH and W. N. GILL', "REVIEW OF REVERSE OSMOSIS MEMBRANES AND TRANSPORT MODELS," *Chem. Eng. Commun.*, vol. 12, no. 4–6, pp. 279–363, Apr. 2007.

- [54] S. J. Kim, S. H. Ko, K. H. Kang, and J. Han, "Direct seawater desalination by ion concentration polarization.," *Nat. Nanotechnol.*, vol. 5, no. 4, pp. 297–301, Apr. 2010.
- [55] D. Huh, K. L. Mills, X. Zhu, M. A. Burns, M. D. Thouless, and S. Takayama, "Tuneable elastomeric nanochannels for nanofluidic manipulation.," *Nat. Mater.*, vol. 6, no. 6, pp. 424–8, Jun. 2007.
- [56] L. R. Huang, E. C. Cox, R. H. Austin, and J. C. Sturm, "Continuous particle separation through deterministic lateral displacement.," *Science*, vol. 304, no. 5673, pp. 987–90, May 2004.
- [57] S. M. Stavis, J. Geist, and M. Gaitan, "Separation and metrology of nanoparticles by nanofluidic size exclusion.," *Lab Chip*, vol. 10, no. 19, pp. 2618–21, Oct. 2010.
- [58] D. Gillespie and S. Pennathur, "Separation of ions in nanofluidic channels with combined pressure-driven and electro-osmotic flow.," *Anal. Chem.*, vol. 85, no. 5, pp. 2991–8, Mar. 2013.
- [59] S. K. Griffiths and R. H. Nilson, "Charged species transport, separation, and dispersion in nanoscale channels: autogenous electric field-flow fractionation.," *Anal. Chem.*, vol. 78, no. 23, pp. 8134–41, Dec. 2006.
- [60] S. Pennathur and J. G. Santiago, "Electrokinetic transport in nanochannels. 2. Experiments.," *Anal. Chem.*, vol. 77, no. 21, pp. 6782–9, Nov. 2005.
- [61] T. J. Kwok, K. Jayasuriya, R. Damavarapu, and B. W. Brodman, "Application of H-ZSM-5 Zeolite for Regioselective Mononitration of Toluene," *J. Org. Chem.*, vol. 59, no. 17, pp. 4939–4942, Aug. 1994.
- [62] M. A. Uguina, J. L. Sotelo, and D. P. Serrano, "Roles of ZSM-5 modifier agents in selective toluene disproportionation," *Can. J. Chem. Eng.*, vol. 71, no. 4, pp. 558–563, Aug. 1993.
- [63] D. SEDDON, "Selectivity for para-xylene in the isomerization of xylenes catalyzed by zeolites with ten-ring windows," *J. Catal.*, vol. 98, no. 1, pp. 1–6, Mar. 1986.
- [64] M. Stratakis, R. Nencka, C. Rabalakos, W. Adam, and O. Krebs, "Thionin-sensitized intrazeolite photooxygenation of trisubstituted alkenes: substituent effects on the regioselectivity as probed through isotopic labeling," *J. Org. Chem.*, vol. 67, no. 25, pp. 8758–63, Dec. 2002.
- [65] M. Stratakis and G. Kosmas, "Enhanced diastereoselectivity of an ene hydroperoxidation reaction by confinement within zeolite Na-Y; a stereoisotopic study," *Tetrahedron Lett.*, vol. 42, no. 34, pp. 6007–6009, Aug. 2001.
- [66] N. J. Turro, "From Boiling Stones to Smart Crystals: Supramolecular and Magnetic Isotope Control of Radical–Radical Reactions in Zeolites," *Acc. Chem. Res.*, vol. 33, no. 9, pp. 637–646, Sep. 2000.

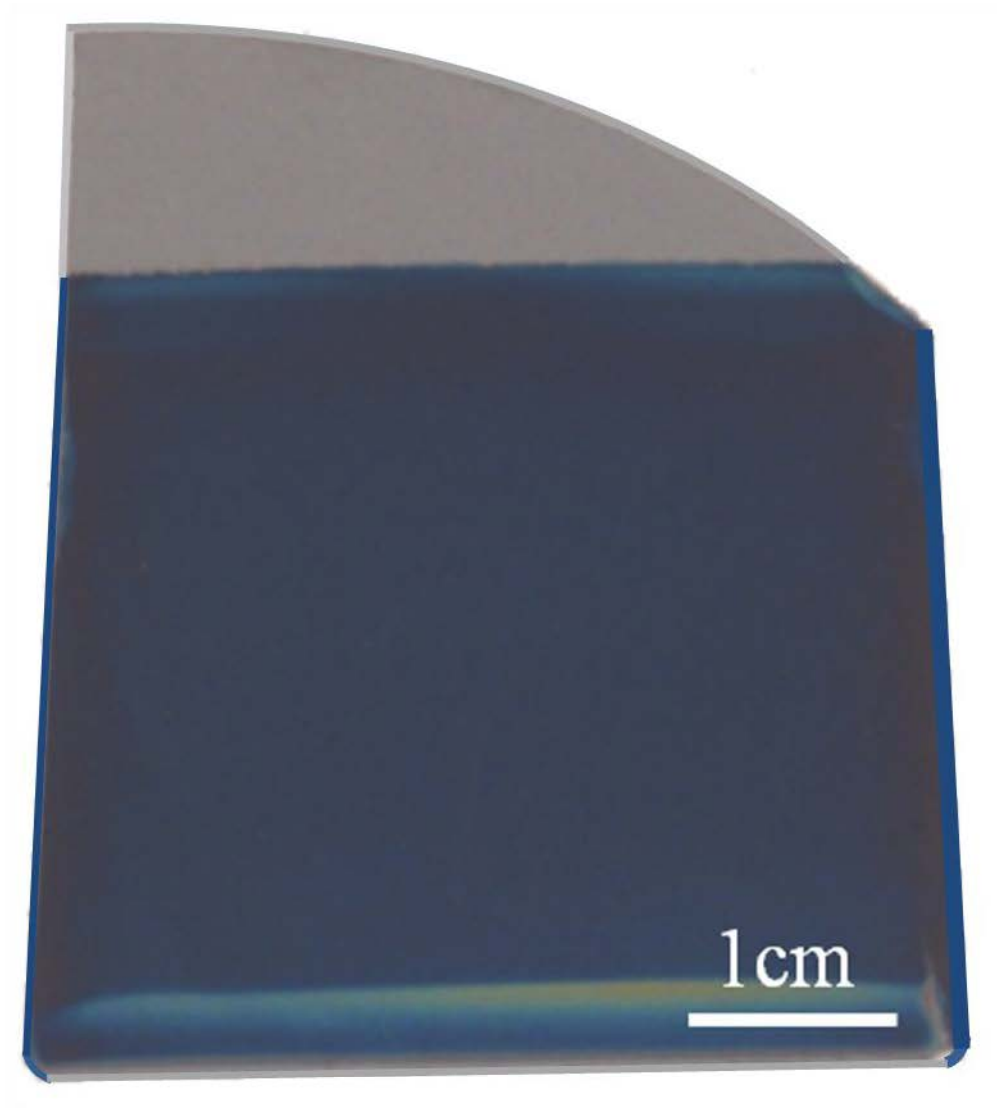
- [67] E. S. Ilton, A. Haiduc, C. O. Moses, S. M. Heald, D. C. Elbert, and D. R. Veblen, "Heterogeneous reduction of uranyl by micas: Crystal chemical and solution controls," *Geochim. Cosmochim. Acta*, vol. 68, no. 11, pp. 2417–2435, Jun. 2004.
- [68] M. Zilberbrand, "A Nonelectrical Mechanism of Ion Exclusion in Thin Water Films in Finely Dispersed Media," *J. Colloid Interface Sci.*, vol. 192, no. 2, pp. 471–4, Aug. 1997.
- [69] G. T. Rengarajan, D. Enke, M. Steinhart, and M. Beiner, "Size-dependent growth of polymorphs in nanopores and Ostwald's step rule of stages.," *Phys. Chem. Chem. Phys.*, vol. 13, no. 48, pp. 21367–74, Dec. 2011.
- [70] B. D. Hamilton, J.-M. Ha, M. A. Hillmyer, and M. D. Ward, "Manipulating crystal growth and polymorphism by confinement in nanoscale crystallization chambers.," *Acc. Chem. Res.*, vol. 45, no. 3, pp. 414–23, Mar. 2012.
- [71] V. R. S. S. Mokkapati, V. Di Virgilio, C. Shen, J. Mollinger, J. Bastemeijer, and A. Bossche, "DNA tracking within a nanochannel: device fabrication and experiments," *Lab Chip*, vol. 11, no. 16, p. 2711, Aug. 2011.
- [72] M. N. Hamblin, J. Xuan, D. Maynes, H. D. Tolley, D. M. Belnap, A. T. Woolley, M. L. Lee, and A. R. Hawkins, "Selective trapping and concentration of nanoparticles and viruses in dual-height nanofluidic channels.," *Lab Chip*, vol. 10, no. 2, pp. 173–8, Jan. 2010.
- [73] J. Fu, J. Yoo, and J. Han, "Molecular Sieving in Periodic Free-Energy Landscapes Created by Patterned Nanofilter Arrays," *Phys. Rev. Lett.*, vol. 97, no. 1, p. 018103, Jul. 2006.
- [74] J. Han, "Separation of Long DNA Molecules in a Microfabricated Entropic Trap Array," *Science (80-.)*, vol. 288, no. 5468, pp. 1026–1029, May 2000.
- [75] L. R. Huang, J. O. Tegenfeldt, J. J. Kraeft, J. C. Sturm, R. H. Austin, and E. C. Cox, "A DNA prism for high-speed continuous fractionation of large DNA molecules.," *Nat. Biotechnol.*, vol. 20, no. 10, pp. 1048–51, Oct. 2002.
- [76] G. Gerlach and W. Dotzel, "Introduction to Microsystem Technology: A Guide for Students (Wiley Microsystem and Nanotechnology)," May 2008.
- [77] G. U. Tong Q. Y., *SemiConductor Wafer Bonding: Science and Technology* -. Wiley, 1998.
- [78] D. Xia, T. C. Gamble, E. A. Mendoza, S. J. Koch, X. He, G. P. Lopez, and S. R. J. Brueck, "DNA transport in hierarchically-structured colloidal-nanoparticle porous-wall nanochannels.," *Nano Lett.*, vol. 8, no. 6, pp. 1610–8, Jun. 2008.
- [79] X. Chen, R. Ji, M. Steinhart, A. Milenin, K. Nielsch, and U. Gösele, "Aligned Horizontal Silica Nanochannels by Oxidative Self-Sealing of Patterned Silicon Wafers," *Chem. Mater.*, vol. 19, no. 1, pp. 3–5, Jan. 2007.
- [80] Y.-J. Oh, D. Bottenus, C. F. Ivory, and S. M. Han, "Impact of leakage current and electrolysis on FET flow control and pH changes in nanofluidic channels.," *Lab Chip*, vol. 9, no. 11, pp. 1609–17, Jun. 2009.

- [81] Y.-J. Oh, A. L. Garcia, D. N. Petsev, G. P. Lopez, S. R. J. Brueck, C. F. Ivory, and S. M. Han, "Effect of wall-molecule interactions on electrokinetic transport of charged molecules in nanofluidic channels during FET flow control.," *Lab Chip*, vol. 9, no. 11, pp. 1601–8, Jun. 2009.
- [82] Y.-J. Oh, T. C. Gamble, D. Leonhardt, C.-H. Chung, S. R. J. Brueck, C. F. Ivory, G. P. Lopez, D. N. Petsev, and S. M. Han, "Monitoring FET flow control and wall adsorption of charged fluorescent dye molecules in nanochannels integrated into a multiple internal reflection infrared waveguide.," *Lab Chip*, vol. 8, no. 2, pp. 251–8, Feb. 2008.
- [83] A. L. Garcia, L. K. Ista, D. N. Petsev, M. J. O'Brien, P. Bisong, A. A. Mammoli, S. R. J. Brueck, and G. P. López, "Electrokinetic molecular separation in nanoscale fluidic channels.," *Lab Chip*, vol. 5, no. 11, pp. 1271–6, Nov. 2005.
- [84] M. J. O'Brien, P. Bisong, L. K. Ista, E. M. Rabinovich, A. L. Garcia, S. S. Sibbett, G. P. Lopez, and S. R. J. Brueck, "Fabrication of an integrated nanofluidic chip using interferometric lithography," *J. Vac. Sci. Technol. B Microelectron. Nanom. Struct.*, vol. 21, no. 6, p. 2941, Dec. 2003.
- [85] P. Mao and J. Han, "Fabrication and characterization of 20 nm planar nanofluidic channels by glass-glass and glass-silicon bonding.," *Lab Chip*, vol. 5, no. 8, pp. 837–44, Aug. 2005.
- [86] C. Duan, W. Wang, and Q. Xie, "Review article: Fabrication of nanofluidic devices.," *Biomicrofluidics*, vol. 7, no. 2, p. 26501, Mar. 2013.
- [87] L. H. Thamdrup, A. Klukowska, and A. Kristensen, "Stretching DNA in polymer nanochannels fabricated by thermal imprint in PMMA.," *Nanotechnology*, vol. 19, no. 12, p. 125301, Mar. 2008.
- [88] B. Yang, V. R. Dukkupati, D. Li, B. L. Cardozo, and S. W. Pang, "Stretching and selective immobilization of DNA in SU-8 micro- and nanochannels," *J. Vac. Sci. Technol. B Microelectron. Nanom. Struct.*, vol. 25, no. 6, p. 2352, Dec. 2007.
- [89] X. Li, X. Wang, J. Jin, Q. Tang, Y. Tian, S. Fu, and Z. Cui, "Fabrication of micro/nano fluidic system combining hybrid mask-mould lithography with thermal bonding," *Microelectron. Eng.*, vol. 87, no. 5–8, pp. 722–725, May 2010.
- [90] L. J. Guo, "Nanoimprint Lithography: Methods and Material Requirements," *Adv. Mater.*, vol. 19, no. 4, pp. 495–513, Feb. 2007.
- [91] N. R. Hendricks, J. J. Watkins, and K. R. Carter, "Formation of hierarchical silica nanochannels through nanoimprint lithography," *J. Mater. Chem.*, vol. 21, no. 37, p. 14213, Sep. 2011.
- [92] Y. H. Cho, J. Park, H. Park, X. Cheng, B. J. Kim, and A. Han, "Fabrication of high-aspect-ratio polymer nanochannels using a novel Si nanoimprint mold and solvent-assisted sealing," *Microfluid. Nanofluidics*, vol. 9, no. 2–3, pp. 163–170, Nov. 2009.
- [93] Q. Xia, K. J. Morton, R. H. Austin, and S. Y. Chou, "Sub-10 nm self-enclosed self-limited nanofluidic channel arrays," *Nano Lett.*, vol. 8, no. 11, pp. 3830–3, Nov. 2008.

- [94] S.-W. Nam, M.-H. Lee, S.-H. Lee, D.-J. Lee, S. M. Rossmagel, and K.-B. Kim, "Sub-10-nm Nanochannels by Self-Sealing and Self-Limiting Atomic Layer Deposition," *Nano Lett.*, vol. 10, no. 9, pp. 3324–3329, Sep. 2010.
- [95] S. Choi, M. Yan, and I. Adesida, "Fabrication of triangular nanochannels using the collapse of hydrogen silsesquioxane resists," *Appl. Phys. Lett.*, vol. 93, no. 16, p. 163113, Oct. 2008.
- [96] R. Riehn, R. H. Austin, and J. C. Sturm, "A nanofluidic railroad switch for DNA.," *Nano Lett.*, vol. 6, no. 9, pp. 1973–6, Sep. 2006.
- [97] S. L. Levy, J. T. Mannion, J. Cheng, C. H. Reccius, and H. G. Craighead, "Entropic unfolding of DNA molecules in nanofluidic channels.," *Nano Lett.*, vol. 8, no. 11, pp. 3839–44, Nov. 2008.
- [98] Z. D. Harms, K. B. Mogensen, P. S. Nunes, K. Zhou, B. W. Hildenbrand, I. Mitra, Z. Tan, A. Zlotnick, J. P. Kutter, and S. C. Jacobson, "Nanofluidic devices with two pores in series for resistive-pulse sensing of single virus capsids.," *Anal. Chem.*, vol. 83, no. 24, pp. 9573–8, Dec. 2011.
- [99] E. Tamaki, A. Hibara, H.-B. Kim, M. Tokeshi, and T. Kitamori, "Pressure-driven flow control system for nanofluidic chemical process.," *J. Chromatogr. A*, vol. 1137, no. 2, pp. 256–62, Dec. 2006.
- [100] A. Hibara, T. Saito, H.-B. Kim, M. Tokeshi, T. Ooi, M. Nakao, and T. Kitamori, "Nanochannels on a Fused-Silica Microchip and Liquid Properties Investigation by Time-Resolved Fluorescence Measurements," *Anal. Chem.*, vol. 74, no. 24, pp. 6170–6176, Dec. 2002.
- [101] T. Yasui, N. Kaji, R. Ogawa, S. Hashioka, M. Tokeshi, Y. Horiike, and Y. Baba, "DNA separation in nanowall array chips.," *Anal. Chem.*, vol. 83, no. 17, pp. 6635–40, Sep. 2011.
- [102] R. Yokokawa, Y. Yoshida, S. Takeuchi, T. Kon, and H. Fujita, "Unidirectional transport of a bead on a single microtubule immobilized in a submicrometre channel," *Nanotechnology*, vol. 17, no. 1, pp. 289–294, Jan. 2006.
- [103] Z.-P. Tian, K. Lu, and B. Chen, "Unique nanopore pattern formation by focused ion beam guided anodization.," *Nanotechnology*, vol. 21, no. 40, p. 405301, Oct. 2010.
- [104] H. D. Tong, H. V. Jansen, V. J. Gadgil, C. G. Bostan, E. Berenschot, C. J. M. van Rijn, and M. Elwenspoek, "Silicon Nitride Nanosieve Membrane," *Nano Lett.*, vol. 4, no. 2, pp. 283–287, Feb. 2004.
- [105] V. Mussi, P. Fanzio, L. Repetto, G. Firpo, P. Scaruffi, S. Stigliani, G. P. Tonini, and U. Valbusa, "DNA-functionalized solid state nanopore for biosensing.," *Nanotechnology*, vol. 21, no. 14, p. 145102, Apr. 2010.
- [106] D. M. Cannon, B. R. Flachsbar, M. A. Shannon, J. V. Sweedler, and P. W. Bohn, "Fabrication of single nanofluidic channels in poly(methylmethacrylate) films via focused-ion beam milling for use as molecular gates," *Appl. Phys. Lett.*, vol. 85, no. 7, p. 1241, Aug. 2004.

- [107] V. Mussi, P. Fanzio, L. Repetto, G. Firpo, P. Scaruffi, S. Stigliani, G. P. Tonini, and U. Valbusa, "DNA-functionalized solid state nanopore for biosensing.," *Nanotechnology*, vol. 21, no. 14, p. 145102, Apr. 2010.
- [108] C. Danelon, C. Santschi, J. Brugger, and H. Vogel, "Fabrication and functionalization of nanochannels by electron-beam-induced silicon oxide deposition.," *Langmuir*, vol. 22, no. 25, pp. 10711–5, Dec. 2006.
- [109] Y. Xu and N. Matsumoto, "Flexible and in situ fabrication of nanochannels with high aspect ratios and nanopillar arrays in fused silica substrates utilizing focused ion beam.," *RSC Adv.*, vol. 5, no. 62, pp. 50638–50643, Jun. 2015.
- [110] L. D. Menard and J. M. Ramsey, "Fabrication of sub-5 nm nanochannels in insulating substrates using focused ion beam milling.," *Nano Lett.*, vol. 11, no. 2, pp. 512–7, Feb. 2011.
- [111] A. A. Tseng, "Recent Developments in Nanofabrication Using Focused Ion Beams," *Small*, vol. 1, no. 10, pp. 924–939, Oct. 2005.
- [112] M. Kim, D. Ha, and T. Kim, "Cracking-assisted photolithography for mixed-scale patterning and nanofluidic applications.," *Nat. Commun.*, vol. 6, p. 6247, Jan. 2015.
- [113] K. L. Mills, D. Huh, S. Takayama, and M. D. Thouless, "Instantaneous fabrication of arrays of normally closed, adjustable, and reversible nanochannels by tunnel cracking.," *Lab Chip*, vol. 10, no. 12, pp. 1627–30, Jun. 2010.
- [114] B.-Y. Xu, J.-J. Xu, X.-H. Xia, and H.-Y. Chen, "Large scale lithography-free nano channel array on polystyrene.," *Lab Chip*, vol. 10, no. 21, pp. 2894–901, Nov. 2010.
- [115] A. Syed, L. Mangano, P. Mao, J. Han, and Y.-A. Song, "Creating sub-50 nm nanofluidic junctions in a PDMS microchip via self-assembly process of colloidal silica beads for electrokinetic concentration of biomolecules.," *Lab Chip*, vol. 14, no. 23, pp. 4455–60, Dec. 2014.
- [116] K. Bell, M. Gomes, and N. Nazemifard, "Characterization of electroosmotic flow through nanoporous self-assembled arrays.," *Electrophoresis*, May 2015.
- [117] S. Wang, H. Yu, W. Wang, and Z. Li, "Nanofluidic device with self-assembled nafion membrane utilizing capillary valve," in *2012 7th IEEE International Conference on Nano/Micro Engineered and Molecular Systems (NEMS)*, 2012, pp. 657–660.
- [118] M. Faustini, M. Vayer, B. Marmioli, M. Hillmyer, H. Amenitsch, C. Sinturel, and D. Grosso, "Bottom-up Approach toward Titanosilicate Mesoporous Pillared Planar Nanochannels for Nanofluidic Applications," *Chem. Mater.*, vol. 22, no. 20, pp. 5687–5694, Oct. 2010.

II: Advances in Dip-coating



II : ADVANCES IN DIP-COATING ----- II-35

II.1 INTRODUCTION ----- II-37

II.1.a Withdrawal speed – thickness relation -----II-39

II.1.a.i General considerations ----- II-40

II.1.a.ii Model for the capillarity regime ----- II-43

II.1.a.iii Model for the draining regime ----- II-44

I.1.a.i Combining models to describe simultaneous both regimes: ----- II-45

II.2 FILM HOMOGENEITY----- II-46

II.2.a Draining and intermediate regime-----II-46

II.2.a.i Starting meniscus effect----- II-46

II.2.a.ii Evaporation time effects. ----- II-46

II.2.a.iii Marangoni effects----- II-49

II.2.a.iv Physical boundaries contributions ----- II-50

II.2.b Capillary regime-----II-52

II.3 RESULTS ----- II-54

II.3.a Bi-phasic dip-coating method-----II-55

II.3.a.i The “biphasic“ method----- II-56

II.3.a.ii Droplet method for single-face dip-coating ----- II-61

II.3.a.iii Conclusion----- II-63

II.3.b Dip-coating in acceleration mode -----II-64

II.3.b.i Dynamical variation of withdrawal speed----- II-64

I.1.a.i.1 Effect of temperature, gradient intensity and concentration----- II-65

II.3.b.ii Thickness programming ----- II-70

II.3.b.iii Applications ----- II-70

II.3.b.iii.1 Contact angle gradients ----- II-71

II.3.b.iii.2 Graded microfluidic channel ----- II-72

II.3.b.iv Conclusion----- II-73

II.4 CONCLUSION ----- II-74

II.5 APPENDIX ----- II-75

II.5.a.i Draining regime (visco-capillary regime). ----- II-75

II.5.a.ii Visco-inertial regime. ----- II-77

II.5.a.iii Surfactant effect. ----- II-78

II.6 BIBLIOGRAPHY ----- II-82

II.1 Introduction

Dip-coating is a well known technique. An object is immersed in a liquid or in a solution and withdrawn at constant speed (Figure. II-1). Then the solution dries or the liquid solidifies. With this procedure a thin film of solution is deposited over the front and rear surfaces forming a uniform coating.

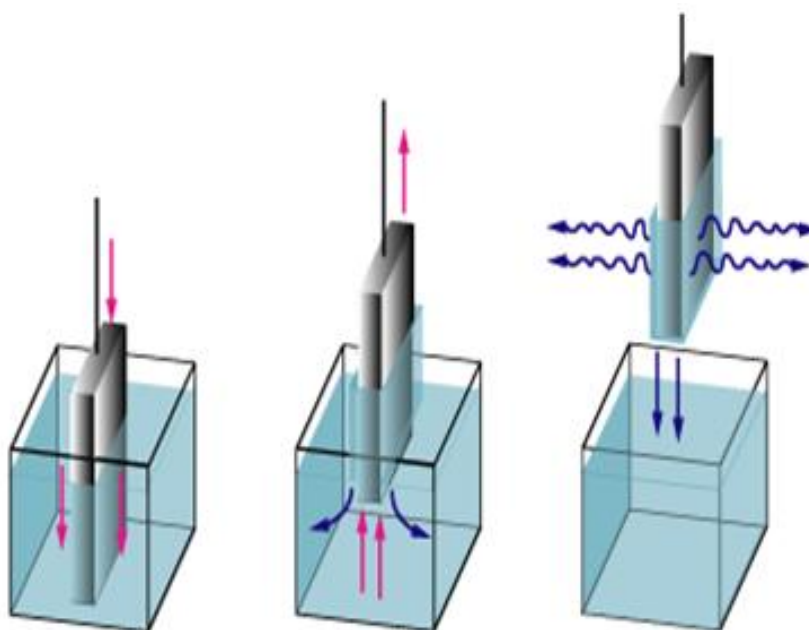


Figure. II-1. Scheme of the principle of dip-coating

Applications of dip-coating are widespread and commonly reported in industry. Protection against scratching and corrosive or other chemical attacks are common features of dip-coated objects. Other properties such as antireflective or antifogging effects are also commonly desired in coatings for glasses or other optical lenses (Figure. II-2a). Dip-coating is a fast and efficient method; due to its simplicity it lends to conveyors and automations (Figure. II-2b). Dip tanks are in all shapes and are sized to accommodate the largest object that has to be coated. It offers an excellent control on the final thickness and the processing conditions can also be adapted for the deposition of all types of material, including polymers, ceramics, hybrids, nanocomposites, biomolecules and all kind of nanoparticles, from many different solutions (even those containing poorly volatile solvents). The possibility to tune the evaporation conditions, during dip coating has proven to be necessary to control the nanostructure through Evaporation-Induced-Self-Assembled (EISA) process for example.



Figure. II-2 (a) Parallel dip-coating of several lenses with an antireflective-antifogging coating (image from North American Coating Laboratories® website) . (b) Conveyor-dip-coating system for continuous coating of leaf springs (image from Product Finishing website®)

However several drawbacks are associated to dip-coating deposition; film thickness non-homogeneities are often associated to edge effects; fire or explosion hazards can occur when organic based solutions are used; finally large quantities of depositing solution are needed to coat rather small surfaces which can lead to prohibitive cost in the case of high price or unstable solutions. All these aspects will be analyzed in the following pages.

In the first part of this chapter, the existing literature about dip-coating will be reported. Relevant experimental and theoretical studies and will be discussed in order to better introduce the experimental work performed during this thesis.

In the second part of this chapter original results and analysis about the dip-coating technique are reported. In this part we will focus mainly on the deposition technique. In particular two recent developments are described: the “bi-phasic” dip coating method and the dip-coating in acceleration mode. If no literature references are indicated, the materials preparation (sol-gel chemistry, self-assembly...) will be described extensively in the next chapter.

As it has been indicated in Chapter I, one of the aims of this thesis is to seriously diminish the cost per unit of nanofluidic devices. In this chapter we will describe a novel dip-coating method called “biphasic dip-coating” that was developed to seriously reduce costs of dip-coating for research and production applications. The method is based on the substitution of part of the solution used to perform dip-coating with an inert fluid. In the context of this thesis, this new method allowed us to seriously multiply the number of samples that could be prepared from a given quantity of chemical precursors. This is an important improvement since one of the main chemical precursor (PS-P2VP block copolymer) for preparing nanofluidic channels was quite expensive (300 euro/g) and available in small quantities.

In the last part of the chapter we will describe how functionality gradient on thin films can be obtained by dip-coating in “acceleration mode”. Applications linked to nanofluidics, microfluidics and behaviors of liquids in contact with nanoporous materials will be presented. This method could be used to produce sophisticated devices for complex nanofluidics or wetting applications.

II.1.a Withdrawal speed – thickness relation

As mentioned before, changing the withdrawal speed is the simplest way to control the thickness of a coating. In this part, the dependence of speed on film thickness will be analyzed.

A normal dip-coating process is usually performed at speeds ranging from $1\mu\text{m/s}$ to $10\text{--}15\text{ mm/s}$ even if for some industrial application much higher speeds can also be attained. Phenomena occurring in this range of speed (from $1\mu\text{m/s}$ to $10\text{--}15\text{ mm/s}$) will be discussed in the following sections since they have been extensively exploited during this thesis. Phenomena taking place at higher speeds will be briefly discussed in the appendix.

In the considered range of speeds, two opposite regime of deposition are identified as function of the withdrawal speed. The analysis of the mechanisms has been reported in a semi-fundamental work by our group and illustrated in Figure. II-3. This work precedes of some years the beginning of this thesis [1].

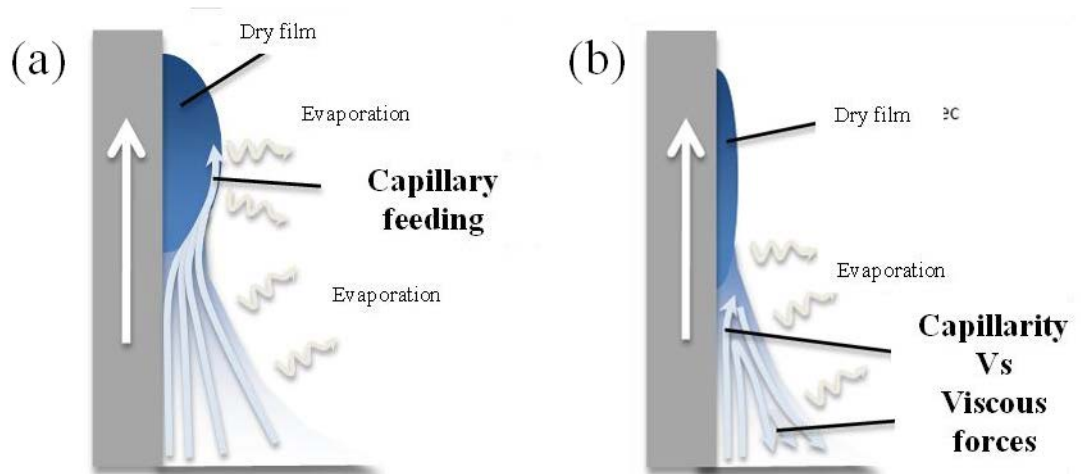


Figure. II-3 (a) Scheme of the phenomena taking place in the capillary regime and (b) the corresponding scheme for the draining one.

At low speeds (< 0.1 mm/s), the films are deposited in the so-called “capillary” regime. In this range of speeds, viscous forces can be neglected and gravity gives no contribution with the exception of determining the shape of the static meniscus between the liquid and the substrate. At low withdrawal speeds, solvent evaporation becomes faster than the motion of the drying line (three-phases-frontier), which leads to the continuous feeding of the upper part of the meniscus by the solution through capillarity raise.

For higher speeds (>1 mm/s), viscous forces become dominant and the films are obtained in the so-called “draining” regime. In this configuration, solvent evaporation is slower than the motion of the drying line which leads to the deposition of a liquid thin film of solution. In case of volatile solutions the liquid films dries in contact with the atmosphere leaving a solid film. The liquid film thickness is related to the equilibrium between viscous drag, gravity and wetting property of the fluid with the substrate surface.

For even higher speeds (more than 100 mm/s) the liquid film can become so thick that viscous forces are counterbalanced by gravity becoming the capillary forces effect negligible. At even higher speed inertial forces at the interface (generated by the viscous forces in the immersed part of the substrate) can further add complexity to the system and influence the final thickness too.

As mentioned we proceed here to the description of the “capillary” and “draining” regimes. The regimes at higher speeds are briefly described in appendix. Other effects such as the influence of surfactant in solution or the derivation of the laws given here are also reported in appendix.

II.1.a.i General considerations

Some models have been proposed to describe the formation of a homogeneous fluid layers by dip-coating. The most referred one is the Landau-Levich model for which the thickness of a Newtonian and non-evaporating fluid on the surface of the substrate is described by the equilibrium between the adhesion of the fluid on the substrate and gravity induced viscous drag. It predicts that the equilibrium thickness depends on the density, the surface tension, and the viscosity of the fluid and is proportional to the withdrawal speed at the power of $2/3$. Some works were then conducted to improve this model [2]–[5], but only a few describe the influence of evaporation using simplified systems [6], [7]. However, most of the solutions used in dip-coating are non-Newtonian fluids and especially the sol-gel solutions for which the solvent evaporates, simultaneously inducing a modification of the viscosity, the density, and the surface tension, but also often triggers polycondensation of the inorganic species through pH change and spatial gathering of the precursors. Kinetics of evaporation of solute/solvent systems at the meniscus has

been modelled [8] and the various phenomena taking place during dip-coating have been accurately described and explained by Brinker et al more that 20 years ago [9]. In this process, the thickness is tuned not only through the adjustment of the withdrawal speed but also by the concentration of the solution, knowing that increasing the speed or the solution concentration, or both, leads to thicker films. In most cases, the deposition is performed with solutions loaded with around 5 to 10% in weight of the non-volatile species and at speeds ranging from 1 to 10 mm.s⁻¹. Thickness typically stands between 50 and 500 nm. Appropriate solvents are alcohols because they have low surface tension, so as to prevent dewetting, and are fairly volatile to promote relatively fast evaporation. Both properties are necessary to obtain highly homogeneous films. In sol-gel, the basic chemistry involves hydrolysis of the inorganic molecular precursor and polycondensation into extended solids. The first reaction needs to be initiated for the second one to start. Both reactions start thus in the solution, run during deposition along the evaporation process, and are generally completed on the dry film during a final thermal treatment. It is therefore important to tune the kinetic of both reactions since it governs the degree of condensation, the density and the structure of the species assembling to form the final film upon evaporation. It is not unusual to end up with porous films where the porosity is controlled by the latter chemical and processing conditions.

The Landau-Levich model is thus barely verified with these complex systems [10], especially in extreme conditions (ultra low or fast speeds, high evaporation rate, high solution concentration, highly reactive species...) at which additional phenomena can take place. Indeed, at ultra low speed, the capillary raise of the solution at the substrate surface is strongly opposing the draining, while at high temperatures the rapid evaporation of the solvent creates a fast increases in viscosity. The capillary raise of the solution is analogous to the “pinning” phenomena known as the coffee-ring effect [8]. It has been recently demonstrated that, for the “coffee-ring” effect, the evaporation rate is linear. The study was performed by in situ FTIR analysis during evaporation of an aqueous / methylene-blue sessile droplet deposited onto a surface [11]. The so-called “convective deposition” has been used to deposit and self-arrange colloids [12] or non-volatile molecules on surfaces. The description of this capillary-driven convective deposition process was made and compared to Landau-Levich regime of deposition for phospholipidic solutions on horizontal substrates [13] and for complex reactive sol-gel solutions on vertical substrates [1]. In the latter work, thicknesses evolution of films dip-coated at extreme withdrawal speed conditions (from 0.01 to 20 mm.s⁻¹) were studied and showed that several distinct regimes of deposition exist for different ranges of speed. The draining/evaporation regime, described by the Landau-Levich

model and for which the thickness increases with the speed, is verified for higher speeds (disregarding all evaporation dependent quantitative parameters and examining only the slope). In addition, a second regime of film formation that is governed by capillarity feeding and for which thickness decreases with speed, was evidenced at lower speeds. The latter regime was called the capillary/evaporation regime for which the thickness was found to be inversely proportional to the speed. For intermediate speeds, a mixed draining/capillary/evaporation regime was found, for which the thickness was perfectly described by the sum of the contribution of both previous regimes. These regimes have been illustrated in Figure. II-3. The resulting dependence from the withdrawal speed is reported in Figure. II-4 showing that thicker films can be build up at lower speeds (in the capillary/evaporation regime) than at higher speeds with equivalent optical quality, which is useful when species to deposit can be stabilized only in highly diluted solutions.

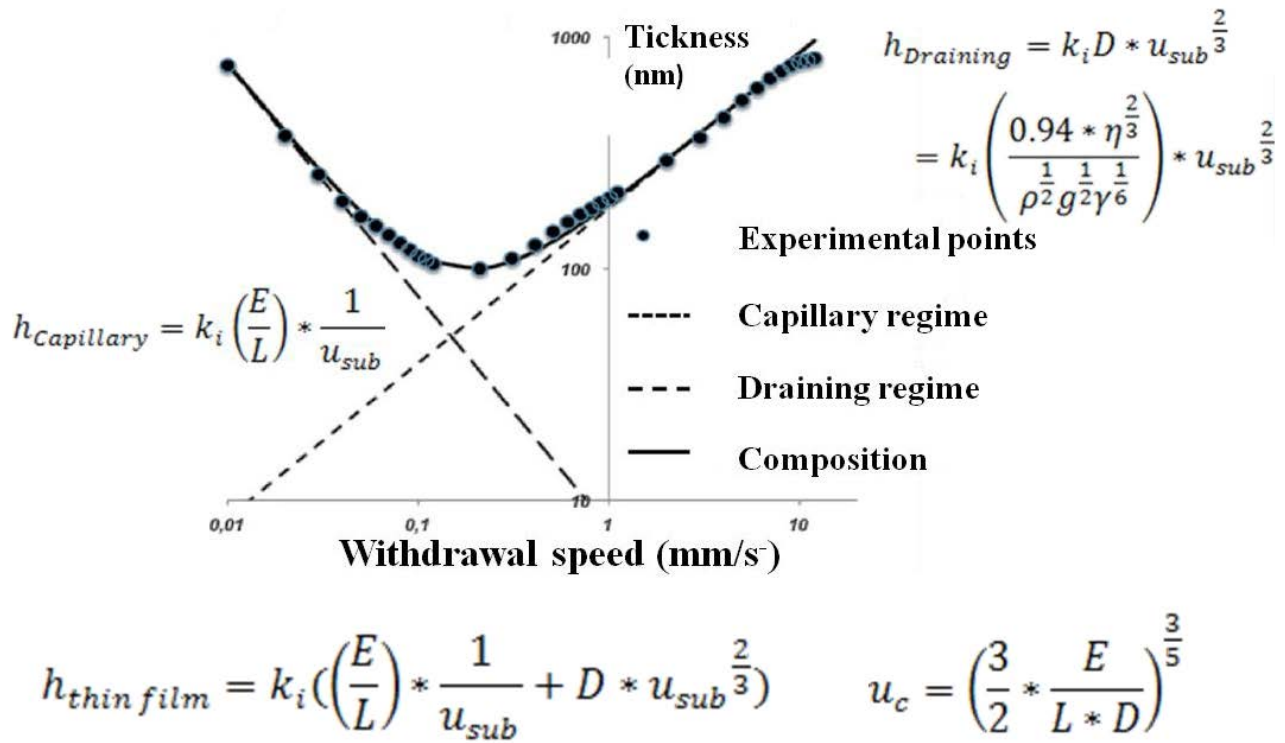


Figure. II-4. Equations and corresponding typical plot of the evolution of thickness versus withdrawal speed in both capillary and draining regimes.

Interestingly, when both regimes perfectly counterbalance each other, a minimum of thickness is experimentally found, which corresponds to the critical speed u_c . Semi experimental equations linking the expected thickness versus the solution composition and the speed of withdrawal were established without having to take into account involved important phenomena that are difficult to assess, such as viscosity variation, evaporation cooling, and thermal Marangoni flow. The involved fundamental hydrodynamic required indeed simplifications and assumptions.

II.1.a.ii Model for the capillarity regime

At low withdrawal speeds, solvent evaporation becomes faster than the motion of the drying line (three-phases-frontier), which leads to the continuous feeding of the upper part of the meniscus by the solution through capillarity raise. In what follows, it is assumed that the evaporation rate is constant and the mass conservation law tells that the rate of film volume formation (F) can be related to the rate of solution feeding the upper zone of the drying line, which is directly related to the rate of solution undergoing evaporation (E). If c_i is the solution inorganic molar concentration and α_i the volume fraction of inorganic material in the final film, that can be deduced from the refractive index [1], one can write:

$$F = \frac{c_i M_i}{\alpha_i \rho_i} E = k_i E \quad (1)$$

F and E are in $\text{m}^3 \cdot \text{s}^{-1}$, while M_i and ρ_i are the molar weight and the density of the thermally stabilized inorganic material respectively. These chemical solution characteristics can be replaced by k_i that is the material proportion constant for each solution. The rate of film formation F corresponds to the variation of film volume with time, which leads to

$$\frac{dV_f}{dt} = \frac{c_i M_i}{\alpha_i \rho_i} E = h_{\text{capillary}} L * \frac{dl}{dt} \quad (2)$$

With V_f , $h_{\text{capillary}}$, l and L being the volume, the thickness, the height and the width of the considered final film respectively. Since L is constant and l varies with the withdrawal speed $u_{\text{sub}} = dl/dt$, which transforms the last equation into

$$h_{\text{capillary}} = \frac{c_i M_i E}{\alpha_i \rho_i L} * \frac{1}{u} = k_i \frac{E}{L} * \frac{1}{u} \quad (3)$$

The $h_{\text{capillary}}/k_i$ versus $1/u$ plot gives a straight line when the capillarity/evaporation regime is dominating the formation of the film, for which the slope corresponds to the rate of solution consuming E/L (in $\text{m}^2 \cdot \text{s}^{-1}$). The latter value is thus deduced experimentally, and can then be reintroduced in equation the last equation to predict the thickness with respect to withdrawal rate in the capillarity regime. The latter tendency confirms that the thickness proportionally varies with u at the power -1 in these dip-coating conditions, while Le Berre et al. found a power of -1.1 with their horizontal set-up [13].

II.1.a.iii Model for the draining regime

For higher speed values, the formation of film is usually described by the following Landau-Levich equation that allows to predict the thickness (h_s) of a non evaporating Newtonian fluid (the solution here) deposited by dip-coating with respect to the fluid physical-chemical properties and the deposition processing conditions such as speed and temperature [10]. This equation was established considering that the fluid thickness is homogeneous all over the substrate surface if the speed is constant, which is due to a delicate balance between the viscous drag and the wetting property of the fluid with the substrate surface.

$$h_{Landau-Levich} = \left(\frac{0.94 * \eta^{\frac{2}{3}}}{\rho^{\frac{1}{2}} g^{\frac{1}{2}} \gamma_{LV}^{\frac{1}{6}}} \right) * u_{sub}^{\frac{2}{3}} \quad (4)$$

η , γ_{LV} and ρ are the viscosity, the surface tension, and the density of the fluid respectively, while g is the standard gravity. In the present case the fluid is the initial solution. For the modelling one considers that the solution behaves as a Newtonian fluid (which is an approximation since the viscosity and surface tension change with evaporation that simultaneously induces concentration increase and condensation). The evaporation is taken into account by introducing the material proportion constant k_i in the equation while the physic-chemical constants of the solution are gathered into a global constant D such that the last equation, describing the fluid equilibrium thickness, becomes

$$h_{Draining} = k_i D * u_{sub}^{\frac{2}{3}} \quad (5)$$

describing the final film thickness, disregarding the evaporation-dependent parameters.

For the Landau-Levich-based model to be verified, D must be constant whatever the value of u . D can be calculated from experimental data since one know k_i and $h_{Draining}$ for each speed. D values are reported for various sol-gel solutions [1]. It was observed that the evolution of D with u is roughly constant for high value of u , where the draining regime dominates, as expected. However, a slight decrease of D is noticed for the highest values of u . Such deviation is attributed to the fact that in these extreme conditions, the thickness of the deposited solution is too high introducing new contributions in the equilibrium of forces that describe the draining regime. Further information about other contributions can be found in the appendix. D can be extracted from experimental points, in a range of u where D is rather constant, and can then be reintroduced in

the last equation to predict the thickness with respect to the withdrawal rate in the draining regime.

1.1.a.i Combining models to describe simultaneous both regimes:

At intermediate u values, both regime of film formation are overlapping and must be taken into account. Summing both Draining and Capillary contributions allows a fairly well description of the final thickness with respect to the speed, suggesting that each regime does not influence significantly the other one when overlapping.

$$h_{thin\ film} = k_i \left(\left(\frac{E}{L} \right) * \frac{1}{u_{sub}} + D * u_{sub}^{\frac{2}{3}} \right) \quad (6)$$

The global evolution of the thickness described by this equation perfectly matches the experimental points, especially at intermediate u values. Since the thickness reaches a minimum value h_{min} at intermediate critical speed u_c , the derivative of the last equation must be equalled to zero for $u = u_c$. u_c can thus be calculated for which $(dh_0/du) = 0$.

$$u_c = \left(\frac{3}{2} \frac{E}{DL} \right)^{\frac{3}{5}} \quad (7)$$

Adjusting final thickness by dip-coating may also be achieved by playing on the dilution that changes the parameter k_i . Viscosity values do not vary excessively when changing the concentration in a reasonable range for typical sol-gel solution. The thickness is then quasi proportional to the initial sol-gel concentration in both capillary and draining regimes. It is thus easy to adjust the thickness if the processing conditions are fixed. On the other hand, increasing evaporation rate can be tuned by lowering partial vapor pressure of the component to evaporate in the drying chamber or by simply increasing atmospheric temperature. While increasing evaporation rate has no significant effect in the draining regime, it is a critical parameter in the capillary regime. Experimental investigations confirmed that final film thickness is proportional to evaporation rate at low withdrawal speed as revealed by equation. It was also demonstrated that optical quality sol-gel films can be processed from pure aqueous solutions at temperatures above 40°C since surface tension of water drops down with increasing temperature, speeding up evaporation and improving the wetting properties of the solution [14].

II.2 Film Homogeneity

As just showed the dip-coating technique allows a precise control of film thickness as function of withdrawal speed. It is clear that if homogeneous films are desired, a constant withdrawal speed needs to be used. Depending on the solution composition (concentration and solvent), thin films with thickness from a few molecular layers up to 1 or two micrometers can be obtained. However, inhomogeneities are often encountered after deposition.

In following part, we will discuss some aspects that influence the homogeneity of the coatings that have been identified during this thesis and are usually not reported or discussed in literature. Depending on the deposition regime, different phenomena can be identified as responsible of the formation of non-homogeneous coatings. The following discussion will constitute a useful starting point for the next sections and chapters.

II.2.a Draining and intermediate regime

The “draining regime” produces in many cases uniform films but some elements can worsen it. A brief overview of the effects that produce non-homogeneities is here reported.

II.2.a.i Starting meniscus effect

Even if it is a small effect it has to be mentioned that at the beginning of the dip-coating the meniscus shape is not the same as it is in the stationary regime. This produces a variation in film thickness in the first millimeter of samples due to a variation of the position of the stationary point during the stabilization of the liquid flows. This, with the fact that a some hundred micrometers zone is coated capillary (and non uniformly) at the triple point at time zero, force to eliminate the first few millimeters of every sample if real uniformity is needed (see Figure. II-9).

II.2.a.ii Evaporation time effects.

A brief list of evaporation related effects is presented here and resumed in Figure. II-5.

A major contribution to non-homogeneities founded in some systems is due to the fact that the liquid layer deposited during operation, which is rather tick in respect of the final film, has to dry over the sample substrate. During this time, two main phenomena can occur: 1) the liquid can

strain due to gravity if the evaporation is not fast enough creating a variation of thickness from the upper part (thinner) of the sample to the bottom (thicker). 2) The solution remains in the liquid form enough time to allow dewetting, atmosphere adsorption and non-uniform evaporation effect to take place. If the substrates could be indefinitely long, these elements (in exception of dewetting) would not create serious problems in uniformity because the condition would be the same for all the substrate length.

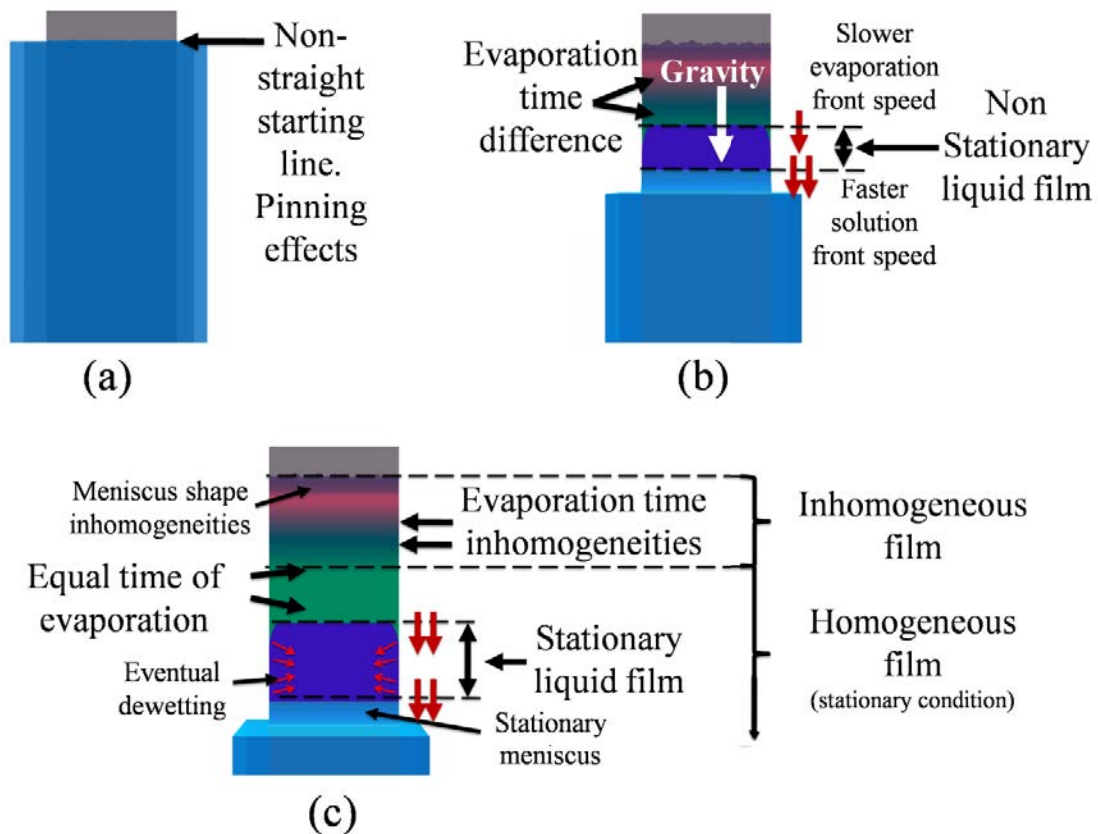


Figure. II-5. Scheme of some cause of inhomogeneities in the draining regime: (a) Pinning effect causing inhomogeneities in the first microns. (b) The meniscus had to reach the stationary shape at the start of the deposition. A zone of inhomogeneity at the top of the sample is due to this effect. This zone is about one millimeter large. A second cause of inhomogeneity is the non uniform evaporation time from spot to spot due to the fact that the liquid film has not yet reached the stationary regime. The evaporation front line is indeed slower than the solution one due to the proximity of the solution itself. Because of this the time needed for the upper part of the film to evaporate is longer in respect of the lower part. Because of gravity the liquid can descend along the substrate for different times from spot to spot modifying the final thickness. (c) The final film is formed. In the stationary regime the evaporation and liquid front have the same speed. Even if gravity effects are present they have the same contribution everywhere not causing any inhomogeneity. If dewetting is avoided using adequate samples and the atmosphere is controlled (no flows are present in the deposition chambers) the final film should be uniform. A distance of the order of two centimeters is usually needed to arrive to the stationary regime (for high speeds a longer run could be needed).

The problem arises for finite length samples. The upper “part” of the sample experiences indeed different conditions from the bottom one. During the dip-coating process two moving lines exist over the sample, the triple contact line (between atmosphere, solution and substrate) and the dried front line (that separates the film still in solution and the dried one). If the two lines move at the same speed with a certain (increasing with the withdrawal speed) “equilibrium distance” between

them, the drying conditions are equal and thus the formed film. On the contrary if the two speeds are different, as in example in the “upper part”, is different a different drying time is found from spot to spot. This is because there the drying line has to move more slowly due to the presence of the solution at a lower distance than the previously defined equilibrium distance. In this case film uniformity is not granted in this zone. Because of this, slowly evaporating solvents or very viscous ones (that form very thick liquid films) are bad choices if a uniform dried film is aimed. This is why hydroalcoholic solutions (with water as a minority part needed to induce hydrolysis) are commonly used for deposition of sol-gel solutions by dip-coating. The “upper part” size is indeed extremely reduced and, in any case, the drying time is of the same order even in this zone which produces negligible inhomogeneities. Anyway temperature increase in the drying chamber could help to fasten evaporation, reduce the equilibrium distance, and decrease in this way the “upper part” size.

These aspects will be further analyzed in the result section of this chapter when dip-coating in acceleration mode is discussed. In that case, the speed is varied during dip-coating and the mentioned effects of different drying time become an important issue to deal with to obtain the desired features. The fundamental role of heating is stressed.

Heating is also a good method to avoid dewetting not allowing the solution to form droplets on the substrate surface but instantaneously drying the liquid film just extracted from the solution.

As can be easily seen, reducing the withdrawal speed reduces the source of non-uniformity during deposition for the “draining regime”. The “intermediate regime” as lower limit of the “draining regime” forms indeed the most uniform coatings. Speed is limited and the “equilibrium distance” corresponds usually to few millimeters. On the other hand, inhomogeneities due to the fluctuation of evaporation or stick-and-slip phenomena (due to the “capillary regime” contribution explained rather) are not remarkable. In general for small samples the “intermediate regime” has to be utilized if uniform coatings are needed.

Two photographic images of some of the mentioned phenomena are reported in Figure. II-6 to permit a better comprehension of the issues mentioned.

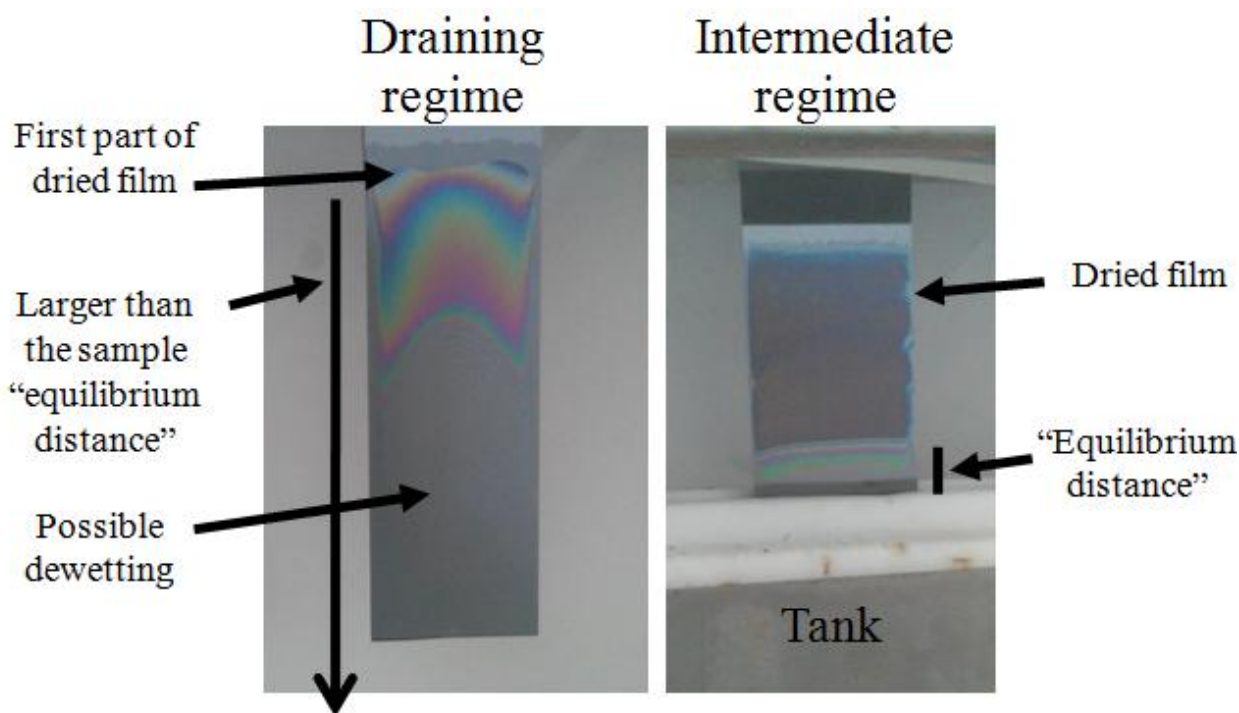


Figure. II-6. Draining and intermediate regime image of dip-coating during deposition. In the case of draining regime the tank has already abandoned the substrate when the film dries in the uppermost part. This means that in no position the evaporation time is equal. The large liquid layer deposited with this method can therefore de-wet if the substrate affinity is low (this is not the case). In the case of the intermediate regime this issues are resolved. The homogeneous liquid film length is in the scale of the millimeters and it dries.

It has to be noticed that similarly to what happens in the “upper zone” the “bottom zone” (near the end of the sample) experiences different drying condition in respect of the film in the middle. This is because after the ending of the sample no more liquid film is present below the drying film thus lowering the vapor pressure of the drying solvent. Moreover air flow is changed too with a further modification of the drying.

II.2.a.iii Marangoni effects

The Marangoni effect is defined as a mass transfer due to a gradient of surface tension. A thin film, during evaporation, can have fluctuation of the solutes concentration. This causes the surface tension to increase/diminish which then generates a modification of the surface that loses its planarity. Hills and valleys can then form creating important inhomogeneities in the hundredths of micron scale. This effect is particularly important in presence of surfactants or polymers. Fast evaporating solvent enhance the effect. Differences of hundreds of nanometers can be generated for thick samples. Variation of the 20% of the thickness can indeed be inspected in some occasions. In Figure. II-7 is reported a scheme of the phenomenon and in Figure. II-9c the result of this effect on a polystyrene film deposited from a THF solution.

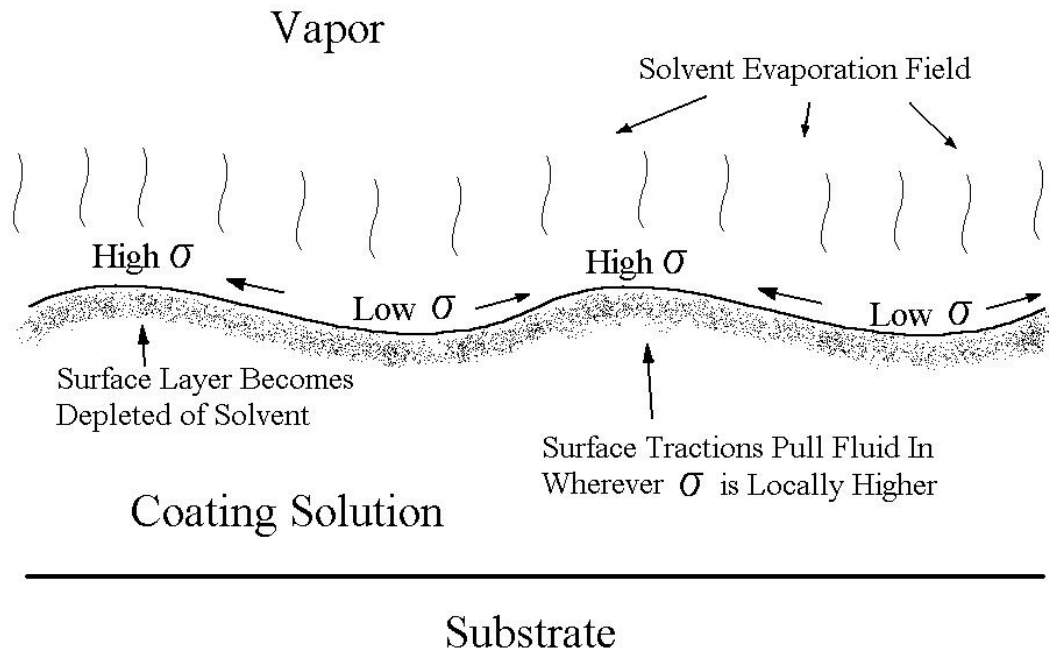


Figure. II-7. [15] Scheme of the elements governing the Marangoni effects.

II.2.a.iv Physical boundaries contributions

Substrate and container dependent inhomogeneity effects have also to be mentioned. Wedge effects, container wall proximity and varying liquid level upon deposition constitute the elements of this subsection.

Wedge effects are produced by inhomogeneities in fluid flow boundary conditions in correspondence of the sides and the bottom of the substrate surfaces (Figure. II-9a and Figure. II-9b). This last contribution, in particular, forms a droplet at the end of the deposition which completely modifies the film thickness in the final lower area of the sample.

Because fluid flow is determined by shear forces, increasing them by increasing the viscosity or the withdrawal speed causes larger edge effects. This is particularly important for the drop that forms at the bottom of the sample during dip-coating. Fast speeds indeed do not allow coating small samples because the size of this drop can become comparable to the sample size (that would be then completely inhomogeneous). In this case, as well, the intermediate regime is preferable over the draining one.

The effect of wall proximity is also an element to consider. It has to be said that the variation of liquid flow or meniscus shape can induce variations in thickness. If the container wall is near the substrate, convective flows can be created inside the solution causing modifications of the film thickness during operation. In the same way the meniscus can be deformed thus modifying the final film thickness. This is simply showed in Figure. II-8 [16].

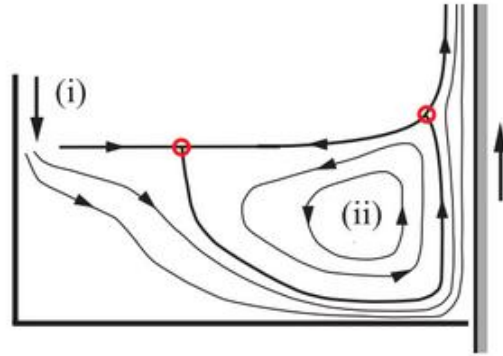


Figure. II-8.[16],[17] Qualitative sketch of streamlines for the withdrawal of a flat plate from a small container. A feed flux (i) is used to maintain the liquid level uniform. Note the location of two surface stagnation points (circles) and the vortex (ii). The stagnation point is displaced by the finite effect of the container deforming the meniscus and then modifying the final film thickness. This scheme is part of a theoretical study. The flow line can be modified solving equations for other values of viscosity, surface tension etc.

To conclude the effect of solution level has also to be considered. It has been stressed how the formation of a stationary regime is necessary to have uniform films. If the level of liquid decreases during the dip-coating (for instance because a very voluminous sample has to be coated) the shape of the meniscus can be changed thus modifying the final thickness of the film (Figure. II-9d). This effect has still to be adequately described. For common sol-gel solutions in ethanol this contribute is not often evidence. Nevertheless its importance is not negligible for solutions of polymers as illustrated in Figure. II-9c.

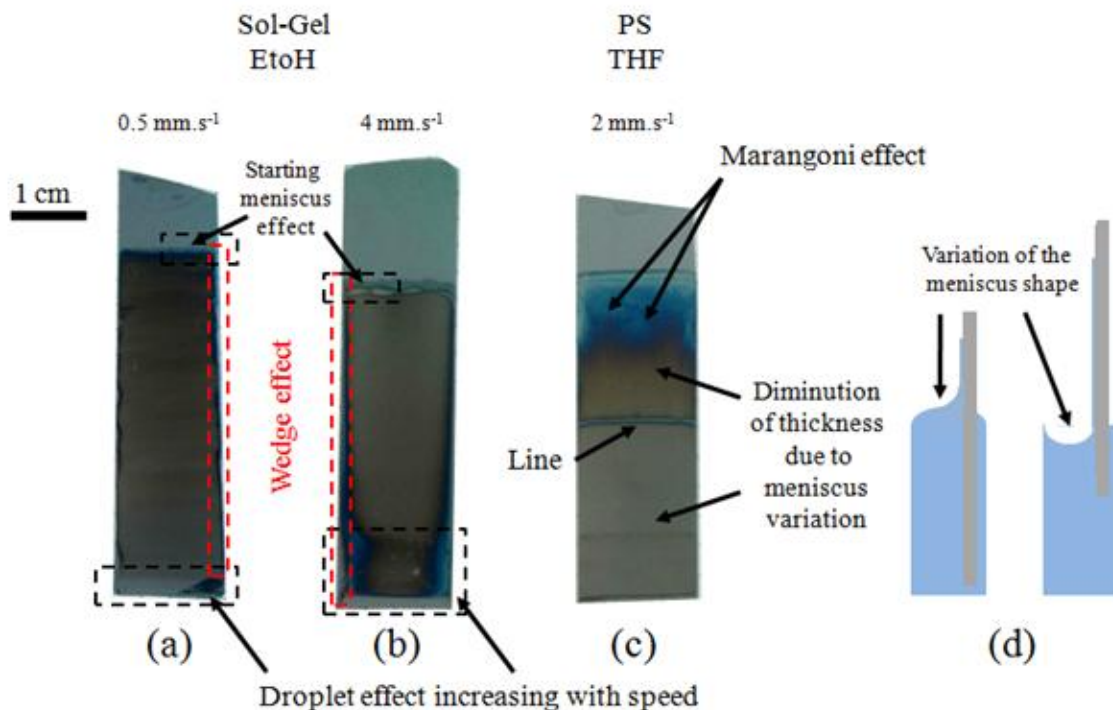


Figure. II-9. (a) and (b) Classical Si sample dip-coated with a mesoporous sol-gel $\text{SiO}_2\text{-TiO}_2$ solution in the intermediate and draining regime respectively. Increasing with speed wedge and droplet effects are evidenced. (c) Classical Si sample dip-coated with polystyrene in fast evaporating THF. The Marangoni effect creates dishomogeneities in the horizontal direction. The variation of the meniscus shape (d) has critical effects for polymeric solutions reducing to one fourth of the film thickness from top to bottom. This effect is evidenced by the line that has been created by a shock on the tank and then local deformation of the meniscus.

II.2.b Capillary regime

The “Capillary regime” is, as mentioned, the regime at low speeds. Because of the low speeds it is a slow method. It is indeed generally used to coat small samples. On the other hand, this method can be used to generate very thick samples ([14]). In general, in such a regime, a lower degree of homogeneity has been found with respect to the others. This regime, indeed, is based on the convective transport of species to the slowly moving triple point. This mechanism itself is based on inhomogeneities of the chemical potential. It is not astonishing then, if in many cases it generates local thickness variation ($\pm 5\text{-}20\%$). A mechanism of stick-and-slip of the liquid meniscus modifies its shape dynamically during the deposition with consequent local variation of the deposition rate through the coffee-ring phenomenon. The pinning of the meniscus causes indeed a local increase of the film thickness in respect of other parts. It has to be noticed that this effect can be used to create linear patterns at the micrometer scale [18].

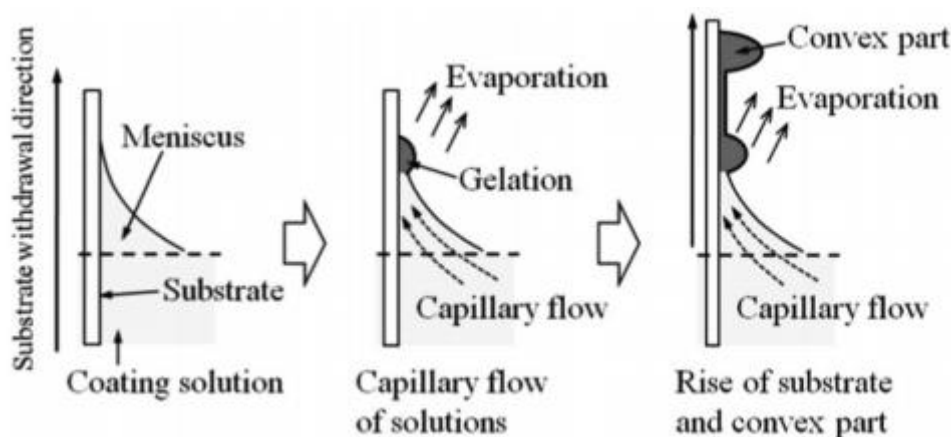


Figure. II-10. [18]. The stick-and-slip phenomenon in capillary regime. The capillary flow brings material to the solid-liquid-gas triple point. The meniscus remains pinned to the formed solid breeding more the already deposited solid. After a while the meniscus, being too elongated, moves to another place where it is pinned again. This causes the final film to be inhomogeneous.

This can be thought as the main effect causing inhomogeneities. Furthermore the arrival of non-evaporating species on the meniscus is determined by the evaporation of the solvent at the substrate liquid interface (Figure. II-11b). Therefore, fluctuations of atmosphere composition and temperature cause further variations in thickness from spot to spot of the final film (Figure. II-11c). It has to be said that these kinds of non-homogeneities are found for extremely low speeds or high desired thicknesses (that normally cannot be reached in the draining regime). A sampled obtained in the near capillary regime is reported in Figure. II-12. The withdrawal speed (0.05 mm.s^{-1}) is rather fast in order not to have an exaggerated number of stick-and-slip lines and have

an easy visualization of thickness variations thank to interference created colors (for slower speeds and thicker film this is more difficult to visualize).

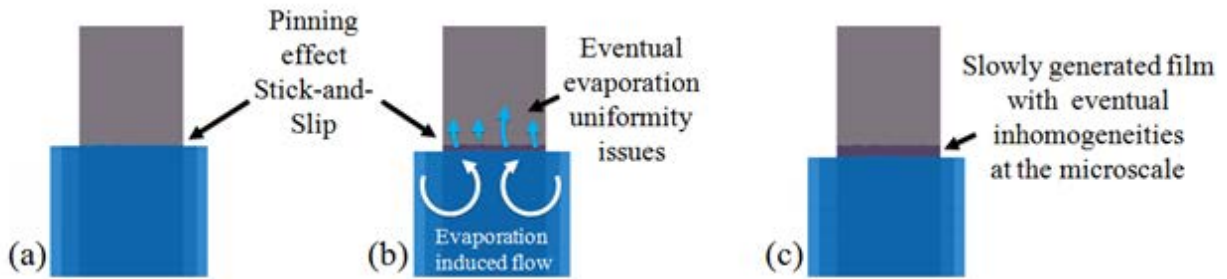


Figure. II-11 The elements causing film inhomogeneities in the capillary regime are highlighted. (a) In all cases the very beginning (firsts micrometers) of the deposition is not uniform due to the different wetting of the solution over the substrate. (b) the arrival of non-volatile species to the meniscus is driven by evaporation. The evaporation can be non-uniform due to Marangoni effects. (c) The evaporation inhomogeneities are transformed in film thickness ones.

Finally effects of liquid level have to be mentioned in the capillary regime too. Depending on the liquid level in the tank the velocity at which the solvent vapors are evacuated change. In particular the evaporation rate diminishes in lowering the liquid level causing a diminution of the final film thickness as the substrate is gradually extracted (Figure. II-12). This effect is currently under study in the laboratory.

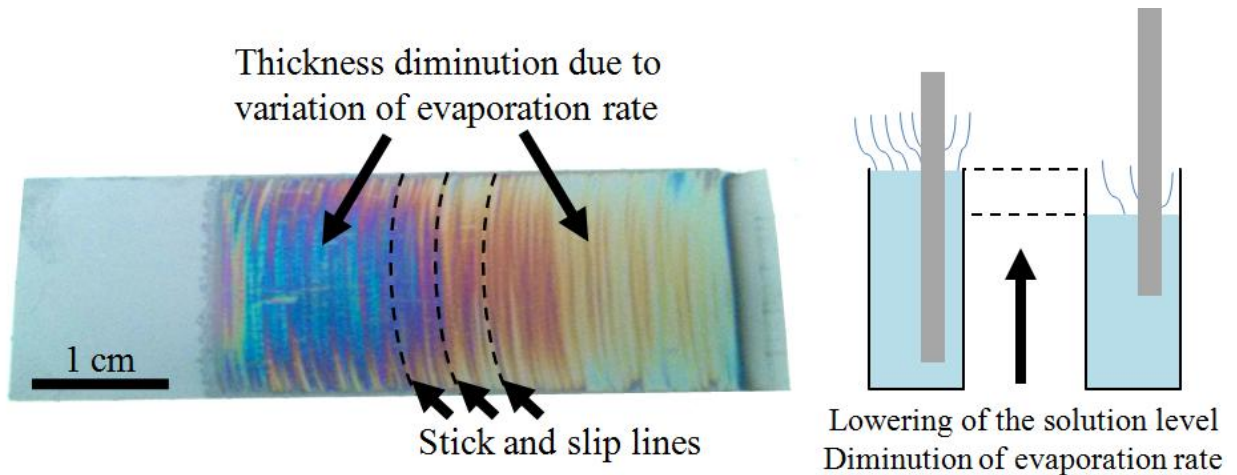


Figure. II-12. Classical Si sample dip-coated with a mesoporous sol-gel $\text{SiO}_2\text{-TiO}_2$ solution in the near capillary regime (0.05 mm.s^{-1}) before calcination. The lines due to stick and slip are present over the entire sample. The variation of thickness (the thickness is more than halved) due to the diminution of the evaporation rate is evidenced from the variation of color due to optical interferences. The diminution of the evaporation rate is due to the lowering of the solution during the extraction of the substrate.

II.3 Results

The following part of the chapter reports some of the main results obtained in this thesis regarding the dip-coating deposition technique.

In the first part, we will report the results of a new “biphasic” dip-coating method that allow deposition of large surface coating with low amount of solution. In the context of this thesis, the development of this method has allowed to overcome one of the main limitations on the fabrication of block-copolymers derived nanofluidic devices.

Finally, in the second section, we will show how dip coating process can be performed in acceleration mode in order to fabricate thickness and functional gradients. The effect of acceleration and other process parameters on the final thickness profile versus acceleration effects are discussed. Some applications of graded functional devices (fluidics and wettability) will be shown.

II.3.a Bi-phasic dip-coating method

As previously mentioned the dip-coating technique needs to operate a minimum amount of solution that is usually larger in respect of its spin-coating counterpart. In particular if large surfaces (because speed has to vary slowly over a large surface) have to be coated great quantities of the depositing solution have to be used.

This aspect becomes a critical issue in many practical cases: (i) when the precursor solution is not stable in time such as in the case of condensation or precipitation of the solute or fast evaporation of the solvent; (ii) if the solution is particularly toxic, flammable or explosive; (iii) for high added value systems where the precursor /solvent amount is limited because of its price or its availability such as in the case of lab-synthesized materials.

During this thesis, high-price or lab-synthesized block copolymers had to be deposited on the substrate in order to fabricate the desired nanofluidic channels. Being the disposable quantities limited, only few milliliters of solution could be prepared. Unfortunately, such low volume of solution allowed preparation by dip-coating 2-3 square centimeters samples only. Due to the limited size, thickness uniformity (and organization) could not be obtained and the method had to be abandoned. This issue forced us to move to spin-coating deposition to obtain adequate self-assembled polymeric films. The number of samples produced by this technique was still unsatisfying. A great amount of solution was indeed wasted during spin-coating and small samples only can be produced.

This main technical issue motivated us to develop a method to coat extremely large areas with only few drops of solution without any waste and with good control of depositing conditions and uniformity. This method was called “biphasic” dip-coating method and it is simple adaptation of the conventional dip coating process. We will also show that this method could be adapted to allow single-side coating, another common limitation of conventional dip-coating process. The effect of the process conditions is discussed and the feasibility of the deposition method is demonstrated on high value, expensive systems such as RuO₂-based optical absorber, P3HT conductive polymers and of course block-copolymer derived nanofluidic channels.

II.3.a.i The “biphasic” method

Hereafter, we will refer to the “monophasic” and “biphasic” method to describe the conventional and the new dip-coating approaches respectively. The very simple idea is presented in Figure II-13. In the conventional “monophasic” method (scheme in the left), the entire reservoir is filled with the precursor chemical solution (in blue). In the “biphasic” method (scheme in the right), the majority of the tank’s volume is replaced by an immiscible, inert liquid (in yellow), non-affine with the substrate such a perfluoroalcanes or liquid metal (both liquids being not flammable [19]). Because perfluoroalcanes and all the metals are commonly heavier than most of the organic and inorganic solvents, they will remain at the bottom of the reservoir while a low volume of depositing chemical solution is placed on the top. The dip-coating process is then performed as usual: the sample is immersed in both phases and withdrawal at constant speed. In this configuration, only the top phase will form a meniscus and act as “active” solution in order to coat a much larger surface as compared to the monophasic dip-coating method with the same solution volume. Dip-coating in two phase system composed by water and organic solvent have been recently used to prepare aligned micro-stripes of semiconductor [20]. However homogenous coatings can’t be obtained by dip-coating from simple polar/non-polar couple as water and an organic solvent because they normally exhibit good affinity/adhesion with the substrate (in opposition to perfluoroalcanes and metals). This means that during dip-coating both the water and the organic solvents would remain on the sample surface leading to non-homogenous coating due to phase separation.

Inexpensive perfluorohexane was mainly used for the presented results. Other perfluoroalcanes, such as perfluorodecaline and other liquid metals such as gallium and mercury have been tested in order to validate the concept. In particular, mercury was chosen instead of the more environmentally friendly gallium (even if some tests were performed obtaining equivalent results), due to the common larger availability in laboratories. A minimal amount of depositing solution is needed at the top in order to ensure the stability of top liquid phase and avoid the formation of discrete droplets. In general, 0.5 cm height of the chemical depositing solution is sufficient for any amount of the underneath “inert” phase.

Monophasic method

Biphasic method

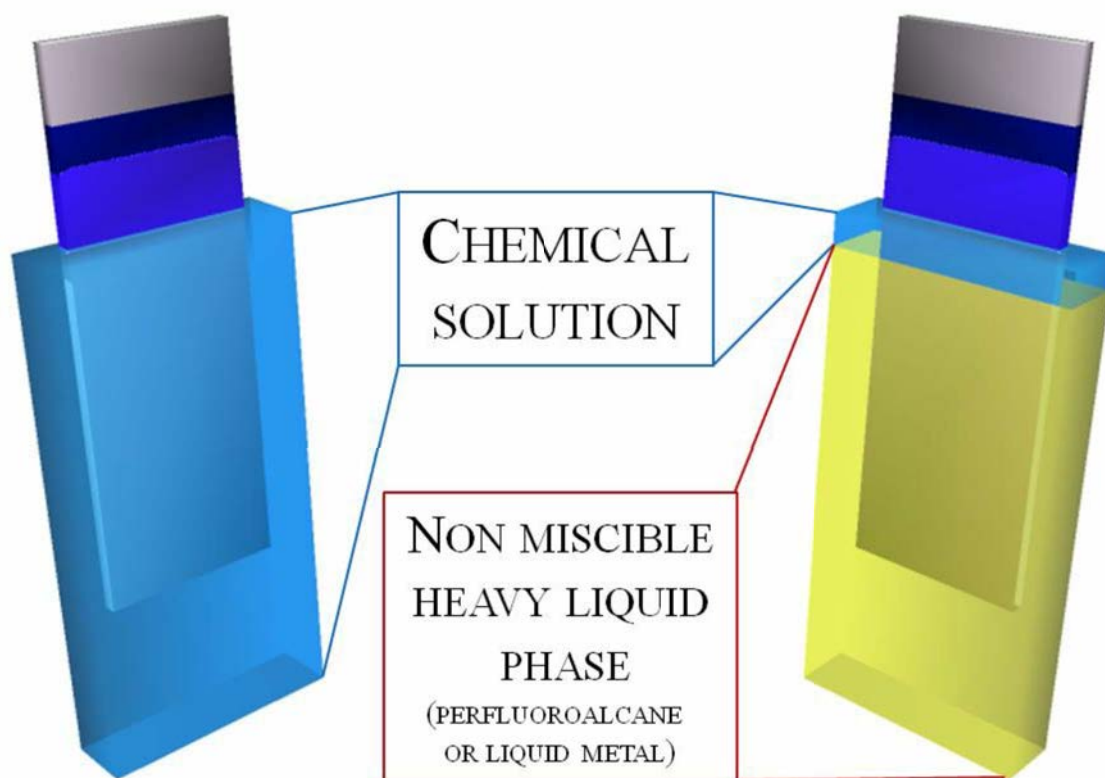


Figure. II-13 Simple scheme of the dip-coating biphasic and monophasic methods.

In order to validate the concept, the effect of the processing conditions on the final thickness and structure of the layers was investigated by spectroscopic ellipsometry on two model systems composed by sol-gel derived mesoporous SiO_2 and TiO_2 . In Figure. II-14 we report the evolution of the thickness and refractive index of the two model layers as function of the withdrawal speed in monophasic and biphasic dip-coating. The composition of the “inert” phase was varied in the case of the silica-based solution (Figure. II-14a). In particular we report the evolution of the thickness and refractive index for the monophasic and biphasic method by using perfluorohexane and liquid mercury) and the quantity of the depositing one increased in two steps for the TiO_2 -based one. As reported previously the two dip-coating regimes are clearly identifiable in Figure. II-14a and Figure. II-14b. In all cases the samples obtained by the “biphasic” method exhibit similar thicknesses and optical quality with respect to the “monophasic” method.

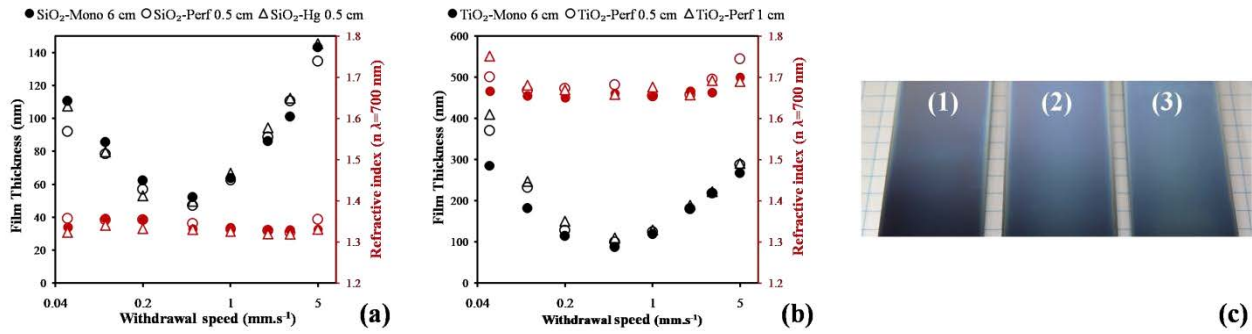


Figure. II-14. The equivalence of the monophasic and biphasic method is here shown. (a) Thin film thickness (black) and refractive index solution (red) of a SiO₂ based solution as function of withdrawal speed for different inert phases. (b) Thin film thickness (black) and refractive index solution (red) of a TiO₂ based solution as function of withdrawal speed for different chemical solution height. (c) Photograph of the three SiO₂ based samples obtained at 5 mm/s of withdrawal speed. Sample (1) and (3) are realized by the biphasic method using perfluorohexane and mercury respectively and sample (2) is realized by the monophasic method.

An image of the three silica-based films obtained with the withdrawal speed of 5 mm/s is shown in Figure. II-14c. Films uniformity and appearance are equivalent in the three cases.

In the case of the TiO₂-based solution (Figure. II-14b), the influence of the amount of chemical solution was investigated. In particular we report the results for the monophasic method and for biphasic methods with the chemical solution height of 0.5 cm and 1 cm. Here again, no significant differences in thickness and refractive index were observed.

The nanostructure of the mesoporous SiO₂ materials was accessed by Environmental Ellipsometric Porosimetry (EEP) and GI-SAXS measurement (Figure. II-15) confirming that film properties are not modified by the use of the biphasic method over the various speeds. A slight variation of the film thickness is found for low speeds for TiO₂-based systems. It has to be taken into account that for low speeds, where evaporation drives the deposition, a little change in the air flows at the meniscus and liquid level in the tank can influence the deposition even in monophasic dip-coating. These inhomogeneities in classical dip-coating are of the same order of the inhomogeneities in the various methods reported here; therefore we are prone to say that even at low speeds the biphasic method is equivalent to the monophasic one.

After validation of the biphasic method over model materials, we demonstrate the effectiveness of the “biphasic” method for the deposition of high-cost functional materials.

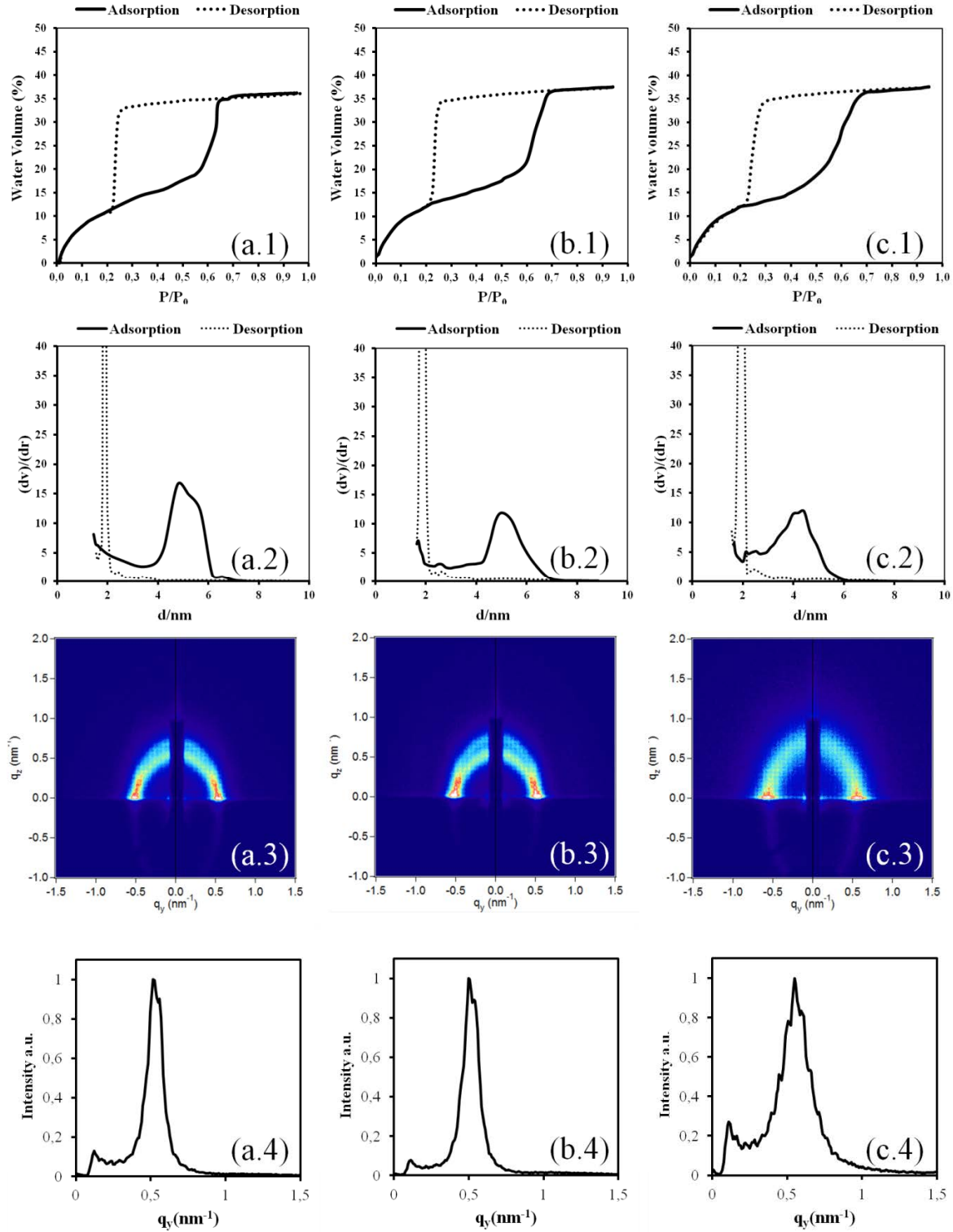


Figure. II-15 (.1) EEP-cycles, (.2) Pore size distributions, (.3) GI-SAXS patterns and (.4) diffused intensity of the thin films in Figure. II-14c of the main text realized by (a) monophasic dip-coating, (b) biphasic dip-coating using perfluorohexane as inert phase and (c) biphasic dip-coating using liquid mercury as inert phase. All the extracted data are within the limit of reproducibility for sol-gel/surfactant depositions of monophasic dip-coating. Calculated pore size in adsorption and desorption are 4.8 nm, 5.0 nm, 4.6 nm and 1.8 nm, 1.8 nm, 1.9 nm for monophasic, biphasic-perfluorohexane and biphasic-mercury deposited films respectively; calculated center to center distance obtained by GI-SAXS data are 12.1 nm, 12.5 and 11.5 nm respectively.

The first example concerns the large fabrication of an efficient $\text{SiO}_2/\text{RuO}_2$ optical absorber coating for solar energy conversion exhibiting outstanding thermal stability [21]. The coating is prepared from solutions containing very expensive Ru precursors with limited stability in time (due to silica condensation). In Figure. II-16a we show two $\text{SiO}_2\text{-RuO}_2$ films realized with the same amount of chemical solution (5.5 ml) with monophasic and biphasic methods (63 ml of perfluorohexane were used under the 5.5 ml of chemical solution). The utilization of the “biphasic” method allows the coating of a surface 15 times larger than in the case of classical dip-coating with the same precursor solution volume. The optical effectiveness of the large-surface coating is preserved after “biphasic” dip-coating as demonstrated by the reflectance measurements of two $\text{SiO}_2/\text{RuO}_2$ films of 159 nm and 150 nm from monophasic and biphasic dip-coating respectively are shown in Figure. II-16b.

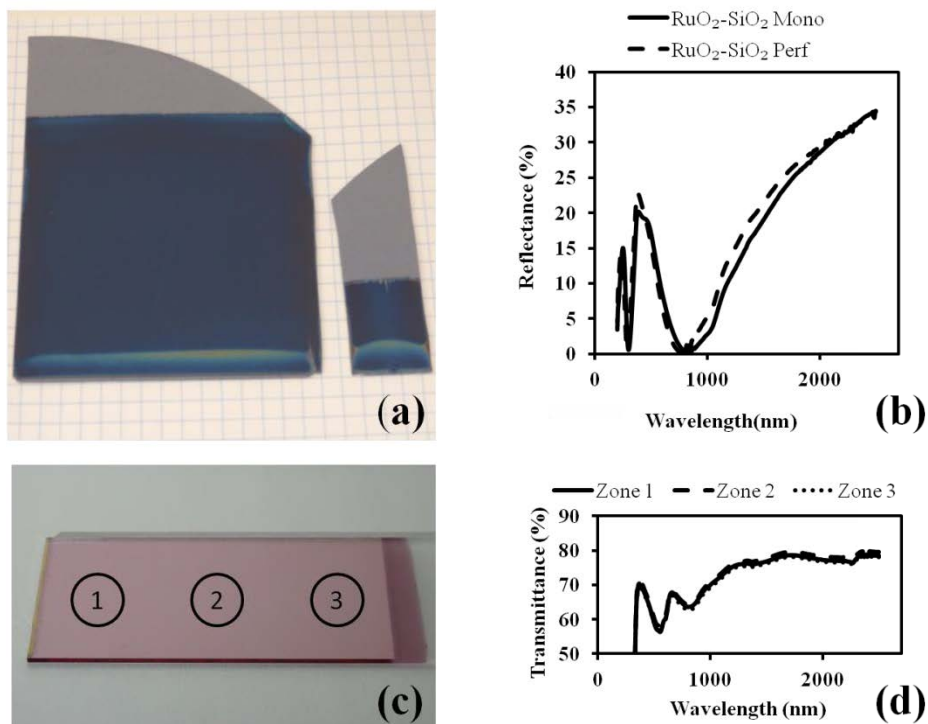


Figure. II-16 (a) $\text{SiO}_2\text{-RuO}_2$ films obtained with the same amount of chemical solution (5.5 ml) with monophasic (right) and biphasic (left) methods. A fifteen fold increase of the covered surface is obtained (using 63 ml of perfluorohexane) with the biphasic method with respect to the monophasic one. (b) Reflection spectrum of the two films in (a) having a thickness of 159 nm and 150 nm for monophasic and biphasic method respectively. (c) P3HT thin film on a glass slide obtained by biphasic dip-coating. Three zones are evidenced. The film uniformity is checked in figure (d) by the transmission spectra of the three zones.

In the second example, P3HT thin films are fabricated. In Figure. II-16c, an image of a sample prepared from a solution containing 6.2 mg of P3HT and 0.75ml of chlorobenzene over 11.25 ml of perfluorohexane is shown. Compared to the conventional method, only the 6% of the solution is required with the “biphasic” method in order to coat the same surface. The film uniformity and optical quality are verified by transmission measurements reported in Figure. II-16d over the three

spots indicated in Figure. II-16c. It has to be noticed that, either for monophasic and biphasic dip-coating, proper film uniformity and quality is possible only in the “intermediate regime”.

These examples demonstrate the potentiality of the biphasic method in saving large amounts of depositing solution. The procedure that has to be adapted, the law governing the thickness, the final properties of the film and the previously mentioned issues about film uniformity remain exactly the same as in the monophasic one. Already optimized procedures developed for conventional dip-coating process can then be utilized without changing any parameter except the quantity of solution. This is particularly important for the industrial applications that rely on well-known and completely controlled procedures where a new optimization study would be undesired. The only added element that has to be considered is the evaporation of the solvent upon operation: being the solvent quantity reduced the effect of concentration of the solution due to evaporation are more important. Adequate refilling of solution/solvent has to be considered for repeated or long depositions.

This method, as described, is very simple. Unfortunately, even if reducing the quantity of needed solution, it still conserves a main disadvantage with respect to other deposition techniques (such as spin coating) that allow deposition only on a single face of the substrate (which can be important in optical applications such as anti-reflective coatings).

In the following section an approach based, on biphasic method and allowing single-side coating is presented.

II.3.a.ii Droplet method for single-face dip-coating

This last method called “droplet” method only few drops of solutions are needed to coat the substrate over a single-face which represents a further improvement of the exposed biphasic method. The process is illustrated in (Figure. II-17). The substrate is first immersed in the inert phase (without chemical solution). Once immersed, some droplets of the depositing solution are deposited on the front side of the substrate. Because of capillary forces and discontinuity in shape at the corner of the sample, the chemical solution remains confined to the front side and no wetting of the solution is observed over back faces of the substrate. The confined liquid, if not in excess, consists in a uniform stripe around the wetted surface. Dip-coating proceeds then normally, leading to deposition on the front face of the substrate only. Upon complete extraction of the substrate, the solution can pass to the other side of it. Care has to be taken (for example recovering the solution droplet with a syringe) to avoid this phenomenon. In this configuration,

the relationship between withdrawal speed and film thickness is not always following the same trend as in the case of monophasic dip-coating.

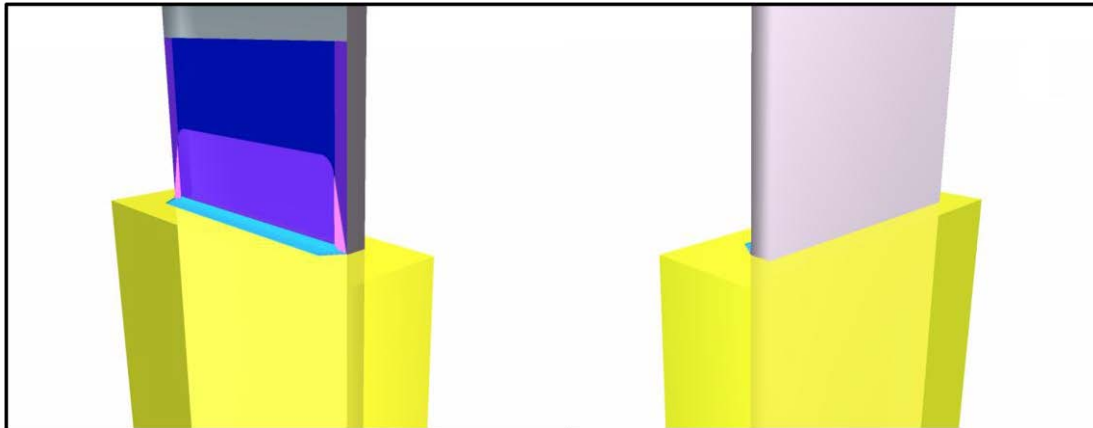


Figure. II-17. Face and back scheme of the droplet method tested to obtain monoface dip-coating.

Effect of confinement of the solution can indeed influence the fluid flow inside it during deposition [16], [17]. This is particularly true with fast-evaporating solutions, such as polymers in dichloromethane or chloroform, where a much higher thickness is found using the same solution with this method in respect of the classic monophasic one. An example of the droplet method is reported in

Figure. II-18. Two photos of the front and back-sides of a sample that was coated by biphasic method using only three drops (0.1 ml) of the previously mentioned $\text{SiO}_2\text{-RuO}_2$ solution.

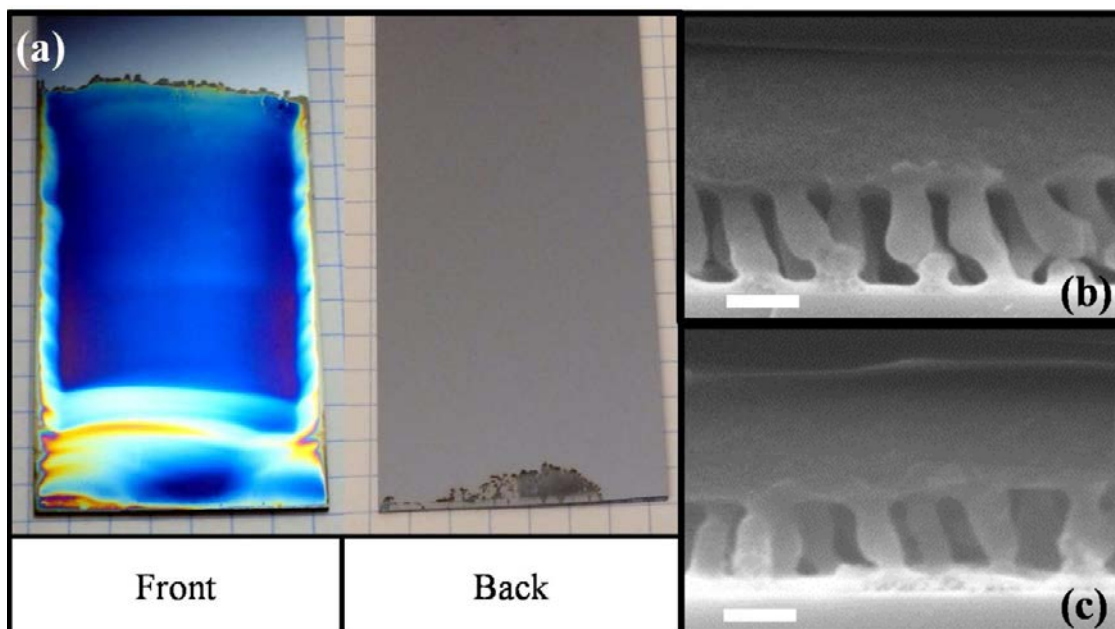


Figure. II-18 (a) Photograph of the front and back side of the sample coated with $\text{SiO}_2/\text{RuO}_2$ film obtained by droplet method. Silica Pillared Planar Nanochannels replicas obtained from two self-assembled block-copolymer obtained by (b) monophasic and (c) biphasic-droplet method dip-coating.

After dip-coating, no material is deposited on the back side of the sample except in the bottom part where the drop could finally pass to the back side of the sample by capillary forces causing a little deposition. As mentioned in other samples this effect could be avoided recovering the depositing chemical solution before extraction of the lower border of the sample.

The droplet deposition method is also applied for the fabrication of the previously mentioned (Chapter I) "Pillar Planar Nanochannels" (PPN) layers. In this case PS-b-P2VP was used as template for the sol-gel replica. A detailed preparation protocol is reported in the next chapter of this thesis (Chapter III). Deposition PS-b-P2VP was performed by monophasic and biphasic-droplet method to coat only the front side.

Figure. II-18b and Figure. II-18c displays two SEM-FEG images representing the SiO₂ PPNs obtained from self-assembled block copolymer. The polymer layer was prepared by the monophasic method (Figure. II-18b) and by single-drop-biphasic method (Figure. II-18c). Good quality PPN channels were obtained by biphasic method as confirmed by the SEM-FEG images. The single-droplet biphasic method has then demonstrated not to modify the self assembly of block-copolymers and thus it is suitable for the fabrication of nanofluidic channels.

II.3.a.iii Conclusion

It has to be stressed here that the development of this method substantially improved the possibility to reach the desired nanofluidic channels with low cost techniques and materials substantially reducing the price or/and increasing the quantity of disposable sample during this thesis.

In particular, the droplet method has been extensively used to create the PS-b-P2VP derived PPNs samples that will be shown in the next Chapters. Unfortunately, this method has been developed at the end of the second year of the thesis, so, experiences regarding other block copolymers (such as PS-b-PLA, available only in the beginning of this project) could be performed only on small sample and on limited amount; in general the preparation of PPNs was much less affordable in the first part of the thesis.

II.3.b Dip-coating in acceleration mode

In the next section, we will present a work realized during this thesis, in collaboration with other group members, concerning the effect of the dynamic variation of withdrawal speed during dip-coating process in acceleration mode. The parameters that have to be controlled and the relation with the final thickness are exposed in the beginning; then some examples of application of thin films with thickness and functionality gradient obtained by this technique are also shown.

II.3.b.i Dynamical variation of withdrawal speed

Conventional (and industrial) dip-coating is usually performed in the draining regime at moderate speeds (1-10 mm/s). As mentioned, this allows having good uniformity and reasonable process time. In the previous sections, the dependence of the final thickness of withdrawal speed on thickness has been often explained. Intuitively, one would expect to be able to tune the thickness into preprogrammed gradients, or into more complex thickness profiles, by just playing on the withdrawal speed modulation. We decided to fabricate thickness gradients achieved through controlled acceleration modes. Different speed variation profiles can be settled in order to obtain graded thin films as illustrated in Figure II-19. The dip-coating process is performed by dynamically varying speed as function of the position (in a controlled way). Two zones in the time/space domain can be identified in the scheme in Figure II-19. First, a graded liquid layer is formed between the triple-phase line and the drying line in zone I, where evaporation of the volatile species is active. Zone II is located above the drying line and represents the graded solid thin film composed of the non-volatile species.

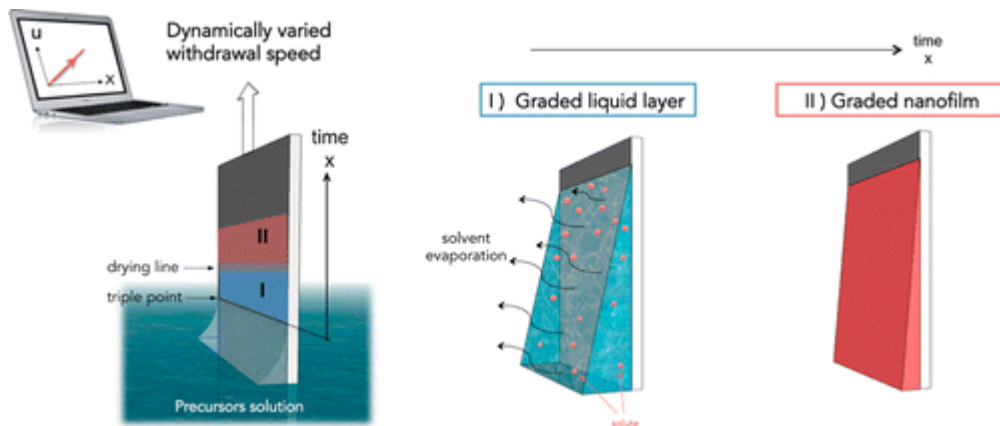


Figure II-19 Scheme of the dip-coating process with gradient of speed

To obtain velocity gradients with a spatial resolution of 0.01 mm and a speed resolution of 0.0005 mm/s, an extremely accurate and precise dip-coater “ACEdip” from the Sol-Gel-Way society has been used (Figure. II-20). Such characteristics are important so as to be able to decouple the fluid inertia from the mechanical motion inertia. The latter dip-coater is also equipped with an atmosphere and temperature controlled environmental chamber to insure controlled evaporation and reproducibility.

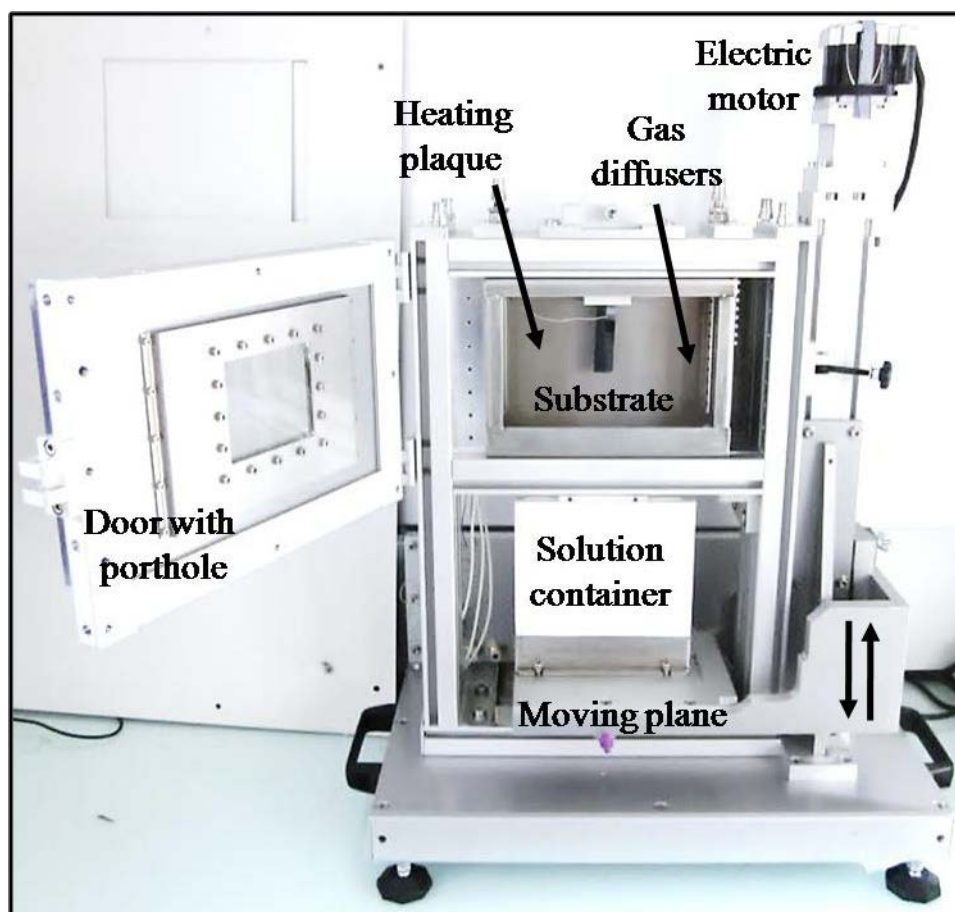


Figure. II-20 . Photo of the « ACEdip » dip-coater from Sol-gel-way. Atmosphere composition and temperature can be controlled in the deposition chamber. The substrate is fixed and the solution is moving.

II.1.b.i.1 Effect of temperature, gradient intensity and concentration

In order to evaluate the influence of the speed variation and the degree of control in the formation of such graded layers, a parametric study was performed. In this work, we focused the study of acceleration only in the draining regime. Sol-gel mesoporous titania was chosen as model material to study the influence of speed gradients and their control because it is a well-known material in our laboratory. As usual ellipsometry was used to check the final thickness after stabilization at 500 °C for 5 minutes. Plots of the film thickness measured after stabilization versus withdrawal

speed (constant regime) for three different temperatures are reported in Figure II-21. As expected, in the capillarity regime, higher temperature in the chamber causes an increase in evaporation rate and thus on thickness. Nevertheless, in the range of speeds considered in this study (1-6 mm/s) the same thicknesses are obtained for all the considered atmosphere temperatures. The first experiment in acceleration mode consisted in a three steps profile dip-coating speed conditions, as shown in Figure. II-22. The first step, consisting in a constant speed at 1 mm.s⁻¹, is followed by a second step where speed is linearly increased from 1 and 6 mm.s⁻¹ on 1 mm distance. Finally, a constant speed of 6 mm.s⁻¹ is maintained as the third step. In these range of speeds, where the capillary contribution can be neglected.

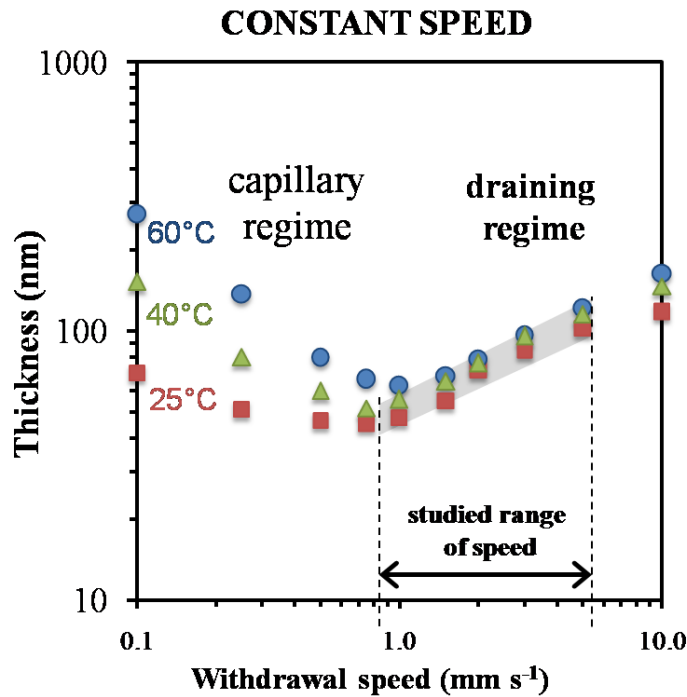


Figure. II-21 final film thickness if function of withdrawal speed for the considered titania solution. The range of speeds utilized in this study is reported.

The expected final film thickness $h(x)$ as function of withdrawal speed $U(x)$ can be calculated as

$$h(x) = k_i D [U(x)]^{\frac{2}{3}} = k_i D \left[U_0 + \frac{dU(x)}{dx} x \right]^{\frac{2}{3}} \quad (8)$$

where u_0 is the initial withdrawal speed, k_i is the material proportional constant, D is the Landau-Levich physicochemical constant, and $dU(x)/dx$ is the position dependent speed variation. This predicted thickness values are indicated by the grey band of Figure II-21.

As already described in the first part of the chapter, the global constant « D » and k_i could be determined semi-empirically from some thickness measurements of films obtained in the draining

regime. The two constants were obtained from the results of thickness versus withdrawal speed reported in Figure. II-21. Figure. II-22 first shows that the experimental thicknesses obtained between 25 and 60°C deviated from the theoretical values, especially in the later part of the acceleration zone.

As can be easily seen, increasing the temperature, in any case, allows reducing the deviation between theory and experiments. The deviation from the theoretical value is larger for slower evaporation. The expected thickness is reached after a larger zone where thickness is not finely controlled. The deviation from prediction is due to a draining-induced-thickness-shift effect that is present in all dip-coated systems. In Figure. II-23 a scheme with the effects of different drying times, gravity and surface tension is shown. As already mentioned, the graded liquid layer (zone I) is simultaneously subjected to draining and to evaporation, both effects tending to decrease the solution layer thickness. The length of zone I depends thus on the time required to dry the layer and it tends to decrease when the speed is low (thinner liquid layer) and when the evaporation rate is high. Indeed, a faster evaporation rate allows a faster increase of the viscosity and thus a much lower draining contribution, which results in a much lower deviation as experimentally observed. This draining distance was found to be 8mm, 5mm and 2mm long for 25 °C, 40 °C and 60 °C respectively.

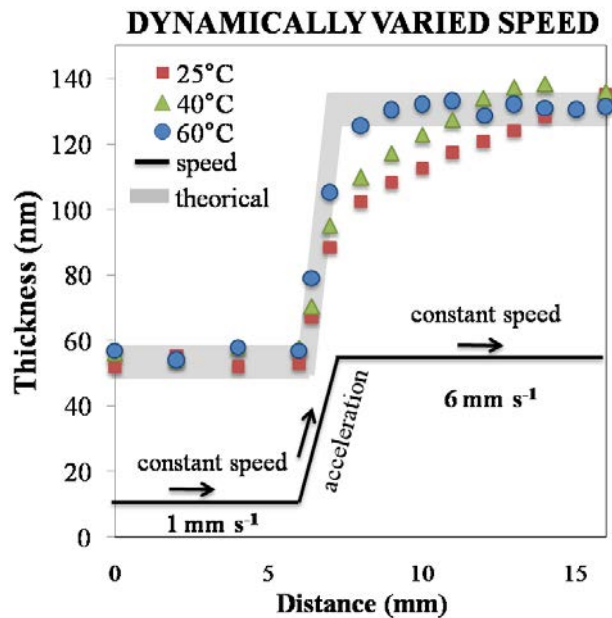


Figure. II-22 effect of temperature. Thickness of mesoporous TiO₂ thin films in function of the position for three values of the temperature (25 °C, 40 °C, 60 °C). Experimental and expected thickness values for a « step » in speed. Increasing the temperature the actual thickness approaches to the expected value faster than at low temperature. Solution concentration (0.39 mM).

Increasing the temperature allows the liquid film to evaporate faster which shortens the time in which the liquid can be displaced by gravity. The role of temperature and evaporation rate in increasing the ability of the system to follow the expected values. Unfortunately, a further increase in temperature is not possible due to the boiling point of ethanol. If indeed higher temperatures are reached (even if the solution remains cold) non uniform film are often obtained.

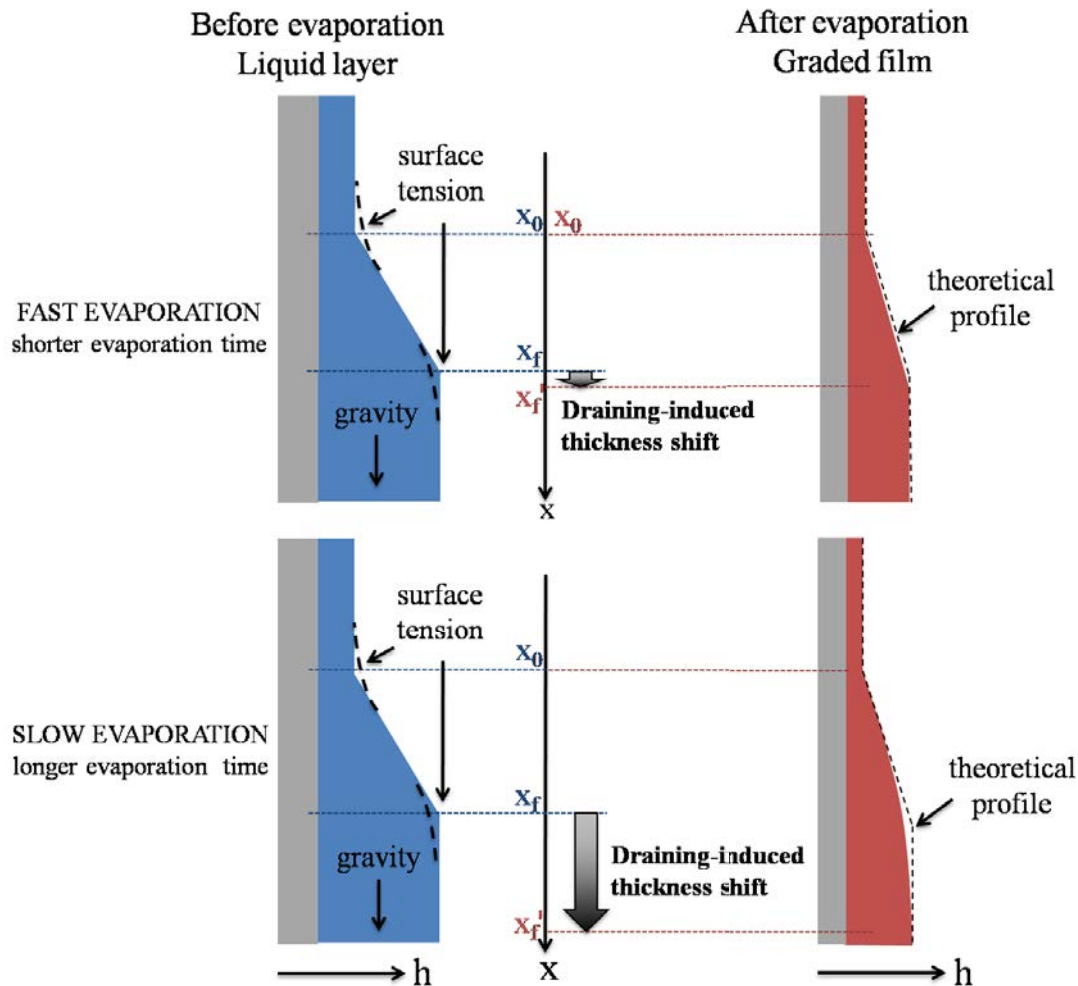


Figure. II-23 Film final thickness modification in function of the temperature. Increasing the evaporation rate the film has less time to reorganize and is not modified by gravity or surface tension.

A similar 3 steps experiment was performed to study another parameter, the effect speed variation ($dU(x)/dx$). In Figure. II-24 data obtained at 60 °C for three different values of $dU(x)/dx$ (10, 2 and, 0.2 s^{-1}) are reported. While a fairly good correspondence is found at 0.2 s^{-1} , the deviation in thickness profiles from prediction is observed for increasing speed variation values. This is in agreement with the previous investigation since a faster increase of speed would create a greater difference in draining distance, and therefore a higher deviation from the theoretical thickness. Few lines will be dedicated here to the influence of solution concentration too. We have analyzed how evaporation rate plays a key role to fabricate the good thickness profile. In general increase

of the concentration of a solution is accompanied by an increase of its viscosity. Consequently the deposited liquid layer will be thicker and then more time is needed to evaporate. It follows, then, that in the experimental results shown in Figure. II-25 a dilute a solution (0.26 mM) can follow a step gradient while a more concentrate one cannot (1.03 mM). In general, it is then possible to obtain sharp low thickness gradients or smooth high thickness gradients.

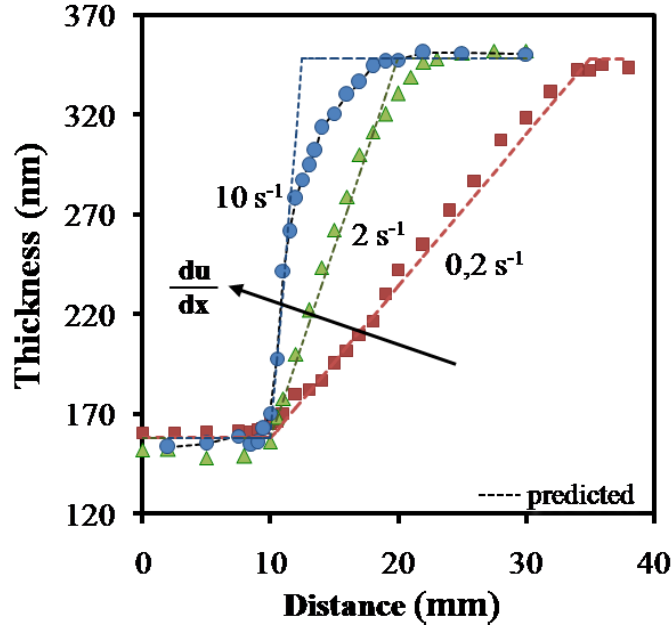


Figure. II-24 effect of gradient intensity. Thickness of mesoporous TiO₂ thin films in function of the position for three values of $dU(x)/dx$ (between $U = 1$ mm/s and $U = 6$ mm/s). Blue points correspond to 10 s⁻¹, orange ones to 2 s⁻¹ and light blue ones to s⁻¹. In lowering the intensity of the gradient the actual deposited thickness respects in a better way the point expected values of thickness. Solution concentration (0.39 mM).

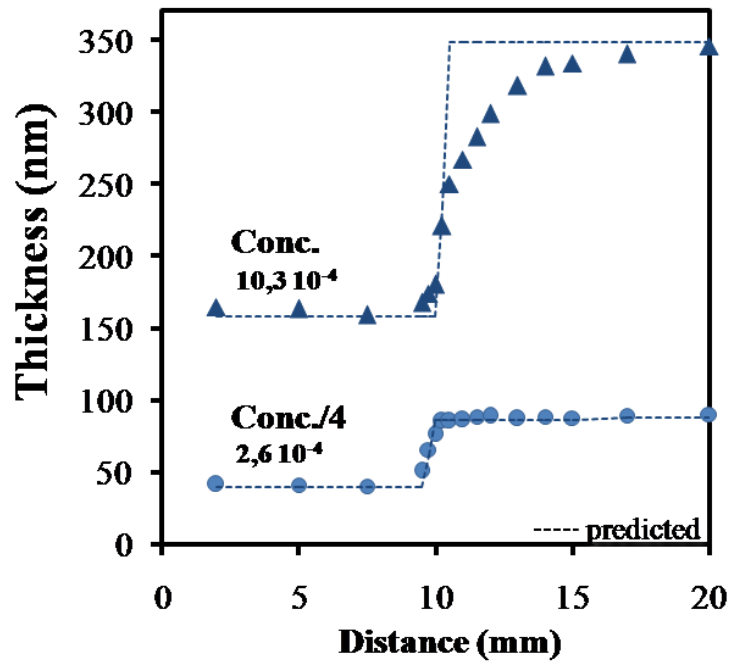


Figure. II-25. Effect of solution concentration. Thickness of mesoporous TiO₂ thin films as function of the position for two concentration values (0.26 mM and 1.03 mM) with a gradient of $dU(x)/dx = 10$ s⁻¹ between $U = 1$ mm/s and $U = 6$ mm/s. The temperature is set at 60 °C.

II.3.b.ii Thickness programming

By taking into account the critical parameters that influence the preparation of graded layers, it is now possible to create almost perfect thickness profiles. The dip-coater can easily be programmed, acceleration profile can be applied inverting the previously shown Equation. 4 into:

$$U(x) = \left[\frac{h(x)}{k_i D} \right]^{\frac{3}{2}} \quad (9)$$

Experimental and theoretical values are reported in Figure. II-26a for logarithmic, linear and parabolic profiles with a perfect matching. The reported analyses can be extended to other materials. In Figure. II-26b thin films with linear gradients of thickness are realized on dense silica, ZIF-8 (synthesized through well known procedures [22]) and PS-b-PEO block copolymer. Some examples of application of these graded systems will be shown in the next section.

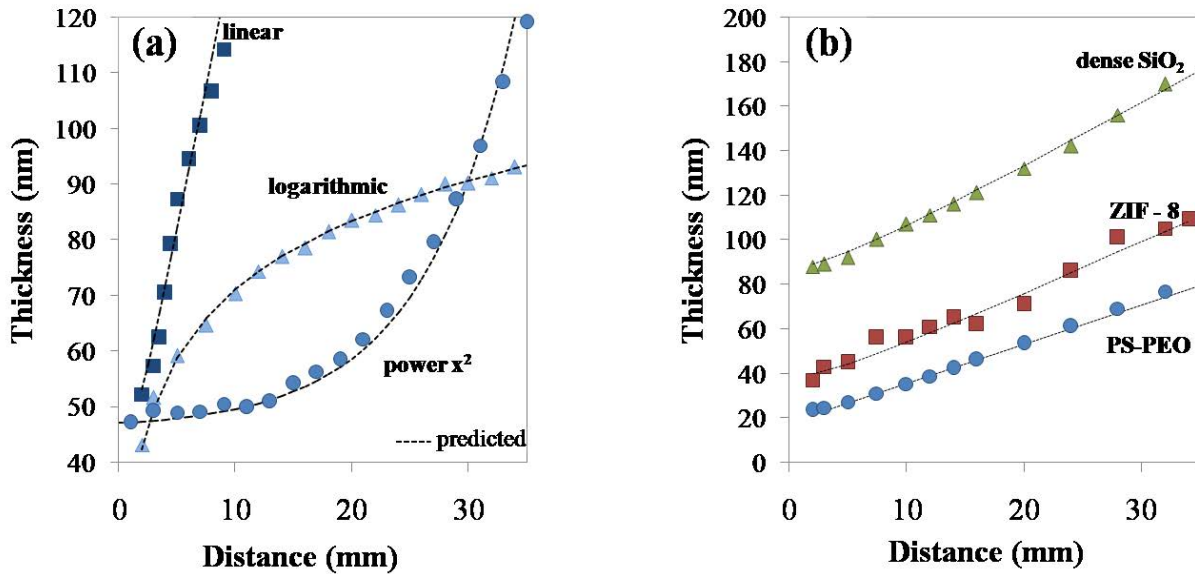


Figure. II-26 (a) . Thickness of mesoporous TiO_2 thin films as function of the position for various acceleration profiles: linear, parabolic and logarithmic. (b) Thickness of dense SiO_2 , ZIF-8 and PS-b-PEO thin films in function of the position (linear gradients). Temperature set at 60 °C.

II.3.b.iii Applications

Gradients of thickness can become, upon the application of a good fabrication strategy, gradients of properties. In this section, potentiality of the method will be demonstrated by two examples. In the first one a gradient of chemical properties and thus contact angle is realized; applications connected with wetting can then be aimed. The second one is connected with microfluidics. A channel with gradient in height is here realized.

II.3.b.iii.1 Contact angle gradients

Gradients in contact angle upon various surfaces have been realized by various techniques in the last years (vapor diffusion limited functionalization [23], differentiated anodic oxidation [24] or plasma treatment [25] etc.). Interest in this kind of feature has grown since motion of droplets has been reported [26] in the uphill direction. With the present method the gradient of wettability is obtained through a new strategy reported in Figure. II-27a. A hydrophilic mesoporous TiO_2 thin film with gradient of thickness (42 to 83 nm) was prepared over a silicon wafer. The gradient of thickness corresponds to a gradient of pore volumes and internal surface. A second deposition of hydrophobic methylated silica species (m-SiO_2) at constant withdrawal speed is then performed on the mentioned sample. The liquid film formed during the dip-coating process (of uniform thickness) is then capillary adsorbed in the porosity of the graded mesoporous layer that acts as reservoir. Due to the gradient of porous volume and surface of the TiO_2 underlayer, the same amount of hydrophobic species is less or more diluted over the porous surface/volume. After thermal treatment and stabilization following known procedures [27] the thicker part of the film is less hydrophobic with respect to the thinner one because of the lower concentration of hydrophobic species. This concentration gradient generates a gradient in contact angle as can be seen in Figure. II-27b (1 μl droplets). The actual values of contact angle as function of the position are reported in Figure. II-27d with a linear variation from 35° to 98° .

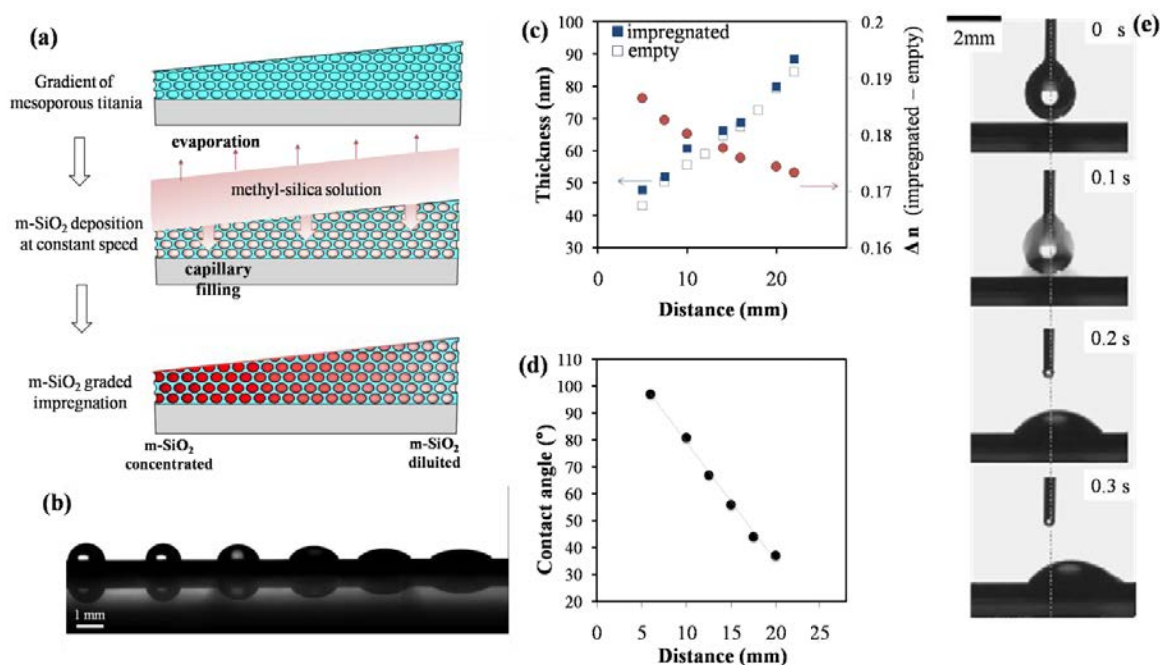


Figure. II-27 (a) Scheme of the preparation of the thin film with a contact angle gradient. (b) Photo of droplets deposited in different spots of the surface with decreasing contact angle. (c) Thickness of the TiO_2 film before and after impregnation as function of the position and difference of refractive index between the state before and after impregnation in function of the position. This value can be related to the concentration of the hydrophobic m-SiO_2 inside the porosity. (d) Contact angle values as function of the position. (e) Displacement of the droplet due to the contact angle gradient shows through a photo sequence

Ellipsometry was used to check that no excess of hydrophobic solution has been deposited on the top of the surface: the same film thickness is indeed found for the empty and impregnated film (Figure. II-27c). The optical density (and then the hydrophobic species concentration) expressed in Figure. II-27c as Δn , the difference of refractive index between the empty film and the impregnated one, varies as expected as function of the position. Droplet motion was also demonstrated on this graded surface. After deposition on the surface, a 4 μ L droplet moves towards the more hydrophilic part of the surface as shown in Figure. II-27e. The difference in contact angle at both sides of the droplet is also clearly visible. The procedure involving gradient of thickness presents several advantages with respect of previously reported ones. First of all a complete control over the contact angle profiles is possible that could be used for particular applications such as bio-inspired water harvesting [28]. Finally the obtained films are transparent, mechanically stable and easily regenerable by heating at 400° for some minute (to remove eventual organic pollutants).

II.3.b.iii.2 Graded microfluidic channel

A second application of the process in acceleration mode is the creation of microfluidic channels with graded height. With the classical dip-coating or spin-coating procedure is indeed impossible to create films with gradients of thickness. The most utilized procedure to obtain microchannels consists in making a PDMS (Polydimethylsiloxane) replica of a patterned master obtained by UV lithography of photosensitive resist through UV exposure in presence of a mask (to define the pattern).

These resists are currently mainly deposited as mentioned through dip-coating or spin-coating with constant thickness. The use of the dip-coating in acceleration mode adds a degree of freedom to the structures obtainable. The film thickness (and then channel height) becomes indeed a variable of the project of the final microfluidic devices. This can opens a great number of possibilities for size dependent experiments or parallel testing. The experimental protocol is reported in Figure. II-29a. Varying the dipping speed from 1 to 3 mm/s it has been possible to create a linear gradient of film thickness of negative photoresist (AZ photoresist) on a silicon wafer (experimental values of thickness as function of the position are reported in Figure. II-28d). The graded resists was then exposed for 1 min to UV light through a mask and developed in 0.15M KOH solution. The PDSM molding has been then prepared as usual by pouring the liquid PDMS on this wafer and cross-linking it for 12h through heating at 70 °C. The prepared PDMS has then been demolded and bonded to another silicon wafer. A microfluidic channel with height channel gradient ranging from 1.5 to 2.8 μ m and a width of 150 μ m was obtained. The channel (Figure. II-28b) was then

infiltrated with a fluorescent solution whose intensity as function of the position was investigated through a fluorescence microscope (Figure. II-28c). The fluorescent profile is in agreement with the measured film thickness profile of the initial photoresist. This simple proof of concept demonstrates the effectiveness of the dip-coating acceleration mode approach for the creation of microfluidic devices containing complex profiles of height.

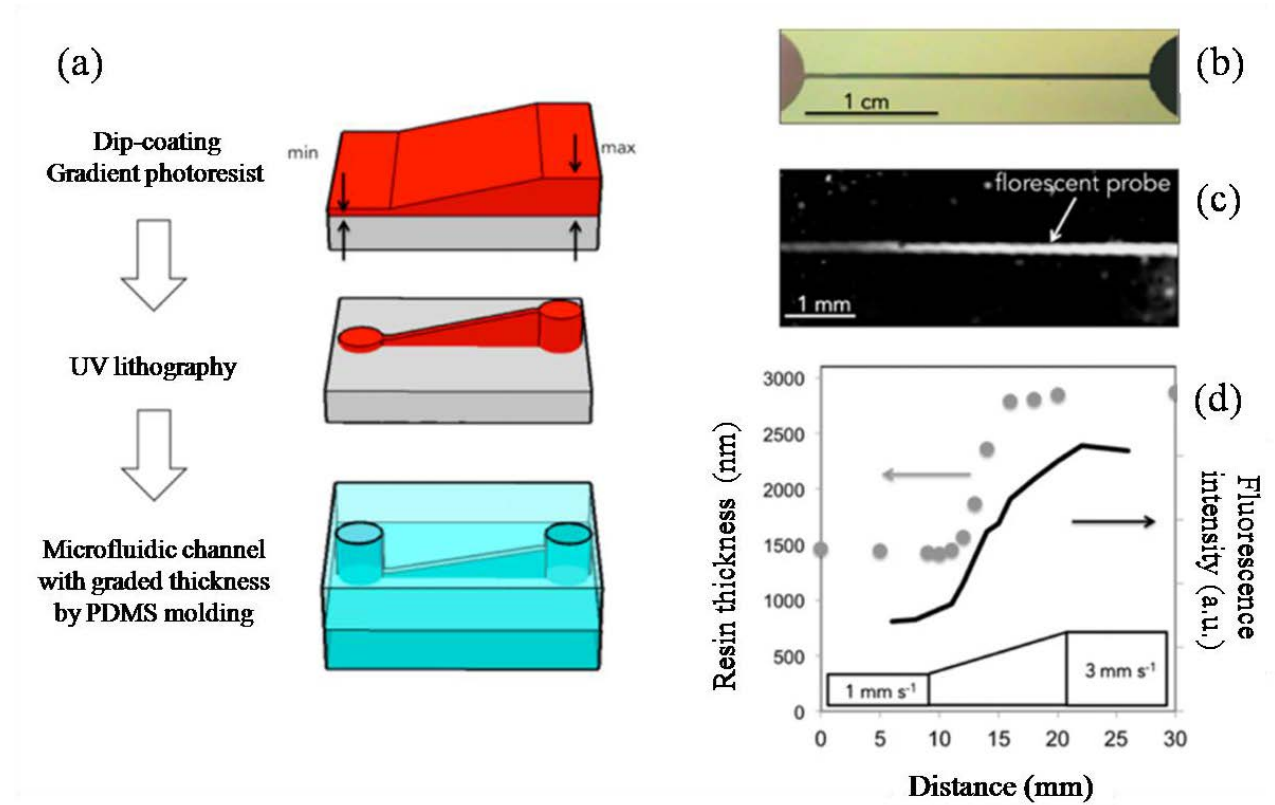


Figure. II-28. (a) Fabrication of the graded microfluidic device. (b) Optical microscope photograph of the graded patterned photoresist template. (c) Fluorescence microscopy image of the graded microfluidic channel filled with a fluorescent probe. (d) Comparison between the thickness of the photoresist layer and the fluorescent intensity as a function of the distance.

II.3.b.iv Conclusion

Dip coating in acceleration mode has proved to be a simple and general strategy to create thin film with gradients of thickness. The evaporation speed of the solvent has been identified as a key parameter to obtain proper films. Some applications regarding wettability and microfluidics have been shown as example to demonstrate the potentialities of this method. Other applications such in photonics can also be aimed to and are presented in the published article [29].

II.4 Conclusion

This chapter concerned the dip-coating technique the main liquid deposition technique that was used during this thesis to create bottom-up thin films.

In the first part of this chapter, the technique was introduced together with the basic principles. In particular the film thickness as function of the withdrawal speed of the substrate was discussed.

In the second part of this chapter, new results about dip-coating were exposed. In a first section the issues arising for film uniformity for the used materials have been examined.

In the second section a new dip-coating method called “biphasic dip-coating” has been introduced. It allowed reducing substantially the quantity of solution needed to perform coatings. It has been show that the thin films obtained through this technique conserve their properties with respect to the one realized in the classical way. The method therefore allows covering a single face of a substrate, which could be particularly important for some high-tech applications.

Finally, a step forward in the knowledge of the physical law governing the film thickness-speed relationship has been accomplished. In this case the withdrawal speed has been varied during the dip-coating obtaining gradients of thickness and properties. Some applications linked to the microfluidics and wettability have been presented in order to express the potential of the so-called “acceleration mode”.

II.5 Appendix

In this appendix a work of review about the laws that govern dip-coating is reported. The Landau-Levich equation is obtained and some laws for particularly fast withdrawal speed (more than 20 mm.s⁻¹) are presented. Furthermore, the effects of other contributions, such as the effect of surfactants, are reported. A chemical physic approach is used. No drying is considered thus the film that is mentioned in the appendix refers to the liquid one. The dependence of the liquid film thickness from withdrawal speed is obtained starting from the balance of forces in the dip-coating.

II.5.a.i Draining regime (visco-capillary regime).

If the withdrawal speed is instead high enough, viscous forces become relevant. Viscous stresses try to drain the solution in the positive vertical direction, a drop in pressure due to the concave meniscus (the pressure is lower than far from the film due to Laplace pressure) pushes the liquid films that forms downwards. A further element downwards directing is gravity but, as will be exposed, it is negligible in this regime. Due to the viscous forces a thin film of liquid solution is dragged outside the solution. Its speed changes from point to point with a profile depending on y , the direction perpendicular to the movement (that is x).

The balance of forces can be written as [30]

$$\eta u_{yy} = -\gamma h_{xxx} + \rho g \quad (10)$$

with η the solution viscosity, γ the surface tension, ρ solution density, g constant of gravity, u_{yy} the second derivative of the fluid speed in the direction perpendicular to the speed, h_{xxx} the third derivative of the thin liquid film height in the parallel direction corresponding to the variation of the curvature (second derivative) of the liquid surface. The speed depend on the distance from the surface in the liquid film; integrating two times imposing the no-slipping condition at the solid surface ($u_{h=0} = u_{sub}$) and no strain at the liquid air surface ($u_{hfinal} = 0$) can be used to determine the liquid flow

$$u(y) = \frac{-\gamma h_{xxx} + \rho g}{\eta} * \left(\frac{y^2}{2} - y * h \right) + u_{sub} \quad (11)$$

and the flux per unit of width is

$$Q = \int_0^h u(y) dy = \frac{+\gamma h_{xxx} - \rho g}{3\eta} * h^3 + u_{sub} * h \quad (12)$$

with h the local film height. This is the quantity of solution that is actually extracted per unit of time by the withdrawn substrate. It is clear that this quantity is independent on the position even if local film thickness can vary (from near the meniscus to far away from it). This flow has to match to the flow in the flat film ($h=h_{final}$, $h'=h''=0$, $u= u_{sub}$)

$$Q = -\frac{\rho g}{3\eta} * h_{final}^3 + h_{final} * u_{sub} \quad (13)$$

these two equations can then be combined in

$$h_{xxx} = \frac{\rho g}{\gamma} * \frac{(h^3 - h_{final}^3)}{h^3} + \frac{h_{final} - h}{h^3} * \frac{3\eta u_{sub}}{\gamma} \quad (14)$$

that expressing the variables adimensionally $h = h_{final} * H$ and $x = h_{final} * Ca^{1/3} X$ with Ca the capillary number $Ca = \eta u_{sub} / \gamma$ and $\kappa^{-1} = (\gamma / \rho g)^{1/2}$ the capillary length, becomes.

$$H_{XXX} = \frac{h_{final}^2 \kappa^2}{Ca} * \frac{H^3 - 1^3}{H^3} + 3 * \frac{1 - H}{H^3} \quad (15)$$

This equation describes the liquid profile in the whole range. If the middle term of the equation (the gravity term) is neglected the equation becomes

$$H_{XXX} = 3 * \frac{1 - H}{H^3} \quad (16)$$

which can be integrated numerically. The boundary condition to impose to determine the value of e the final film thickness is that the static and dynamic meniscus has the same curvature. To obtain this they can be matched asymptotically.

$$\left(\frac{d^2 h_{dyn}}{dx^2} \right)_{h \rightarrow \infty} = \left(\frac{d^2 h_{static}}{dx^2} \right)_{h \rightarrow 0} \quad (17)$$

that becomes

$$\left(\frac{d^2 H_{dyn}}{dX^2} \right)_{H \rightarrow \infty} * \frac{Ca^{\frac{2}{3}}}{h_{final}^2} = 1.34 * \frac{Ca^{\frac{2}{3}}}{h_{final}^2} = \sqrt{2} \kappa \quad (18)$$

which gives the well known result from Landau-Levich and Derjaguin

$$h_{final} = 0.94 * \kappa^{-1} Ca^{\frac{2}{3}} = 0.94 * \frac{\eta^{\frac{2}{3}}}{\rho^{\frac{1}{2}} g^{\frac{1}{2}} \gamma^{1/6}} * u_{sub}^{\frac{2}{3}} \quad (19)$$

with a 2/3 dependence from the withdrawal speed. This result has been obtained by neglecting the contribution given by the gravity. This is possible for low capillary numbers $Ca \ll 1$ and starts to become not adequate for values of $Ca > 10^{-2}$ (for ethanol at 10 mm.s⁻¹ $Ca = 0.5 * 10^{-3}$). Further effects like meniscus deformation due to strain can also further modify the film thickness at these high velocities. The analysis of this phenomenon is anyway too long and complex to be reported in this thesis.

II.5.a.ii Visco-inertial regime.

In these final notes some elements that are considered interesting will be briefly cited. In any case a deep analysis of the considered one will not be performed but some clues just introduced.

As can be seen in Figure. II-4 for fast speeds the presented model starts to predict thicker films in respect of experimental reality. This is due to the influence of multiple factors.

First of all the contribution of gravity can no more be neglected because for thick liquid films the amount of liquid becomes big enough that the force exerted by gravity become comparable and even bigger than the capillary force. For extremely high speeds (more than 10 cm/s) a different dependence on the speed is expected and reported in respect of the previously discussed one. This can be understood if equation

$$H_{xxx} = \frac{h_{final}^2 \kappa^2}{Ca} * \frac{H^3 - 1^3}{H^3} + 3 * \frac{1 - H}{H^3} \quad (20)$$

is reconsidered neglecting the term H_{xxx} (neglecting capillary forces) and linearising it (considering the film thickness far from the meniscus), $H = 1 + \varepsilon$, obtaining

$$0 = 3 * \varepsilon * \left(\frac{h_{final}^2 \kappa^2}{Ca} - 1 \right) \quad (21)$$

that gives

$$h_{final} = \sqrt{\frac{Ca}{\kappa^2}} = \sqrt{\frac{\eta}{\rho g}} * \sqrt{u_{sub}} \quad (22)$$

with a 0.5 power dependence from the withdrawal speed. Unfortunately this regime cannot so simply be linked to the previous ones because various effects have to be considered in a large range to obtain adequate description of the final film formation.

In example film thinning due to the falling of the liquid lead by gravity generates a parabolic height profile from the top of the deposition with a “diffusion” kinetics that is linear with the time [31]. Furthermore the curvature of the meniscus can no more be considered as $-h_{xx}$ but needs to be described by the exact expression $-h_{xx}/(1+h_x)^{1.5}$ that adds complexity to the differential equation. Both the capillary and gravitational terms have to be considered in the equation describing the liquid profile too. Adequate boundary conditions have also to be set and proven. The investigation on this and the linking with the other regimes has been tried theoretically [30] and experimentally [32], [33]. Rather good agreement has anyway been found with more complex theories trying to cover the regime where capillarity, viscosity and gravity are both important [2], [3] but a proper and complete description of the phenomena in this regime without approximations has still to be done.

Moreover at such high speeds an inertial contribution to the deposition becomes important. The substrate immersed in the solution causes indeed a flow inside the bulk liquid. This flow, if strong enough, can reach and modify the surface shape and project the liquid in the vertical direction helping the building of the liquid film. Inertial forces (expressed through the Reynolds number (ratio of inertial forces to viscous forces)) have then to be considered and studied for high [34], [35],[36] or low [30],[36] capillary numbers (in dependence of the liquid properties for a given speed and in any case not describing the intermediate capillary number range) giving results rather satisfying. As said these issues have not been reported during the Ph.D. but it was useful to justify why very high speeds are never used during experimental operation. Control on the film thickness is indeed lost. A long study would indeed be needed to know which thickness is obtained for every speed. Further issues regarding low homogeneity for fast withdrawal speeds not reported in the literature will also be described in the beginning of the experimental results section.

II.5.a.iii Surfactant effect.

This section will be concluded introducing to the discussed problems about film thickness the effect of particular solutes: the surfactants. It is clear that the addition of solutes in a liquid can modify its properties such as viscosity, surface tension and density. In the case of surfactants a film thickening phenomena has been reported for fast regimes even considering these influences

directly measuring the cited properties of the solution. It seems that some other phenomena take place even increasing the film thickness.

A multiplicative factor should indeed be added (in our experimental procedure by fitting the terms no correction has actually to be considered being this correction contained into the fit) to properly forecast the film thickness in function of the solution properties [37], [38].

$$h_{surfactant} = \alpha * h_{final} \quad (23)$$

Because the surfactant is preferentially distributed at the liquid-air interface (if it not in extremely large excess in the bulk) the surface stretching induces a variation of surface concentration of surfactant and then a Marangoni flow in the direction of the substrate causing a film thickening. A scheme of this phenomenon is reported in Figure. II-29a. It has to be considered that, on the other hand, if withdrawal speed is too high, the Marangoni flow, even if at its maximum value, becomes negligible and spreads over large surfaces (with high speeds the Marangoni flow in a given period of time thickens in a less extent a larger surface). At high speeds then the final thicknesses will not be seriously influenced by this phenomenon [37]. This means that after an initial thickening due to this phenomenon the final thickness recovers the values expected not considering the Marangoni flow. This could then be seen as a thinning effect if experimental values of thickness in the thickened part only have been previously obtained. To conclude this theoretical introduction to the problem it has to be then stressed that the multiplicative factor α ranges between 1 and $4^{2/3}$ in function of the experimental condition varying its value in function of the filling speed (in Figure. II-29b the value of the prefactor is reported for various values of the Marangoni number (expressed as

$$M = \frac{\Gamma_0}{\gamma} * \left(\frac{d\gamma}{d\Gamma} \right)_{\Gamma_0} \quad (24)$$

which express how surface tension γ varies with surface concentration Γ).

The Marangoni flow has been visualized experimentally (Figure. II-29c confronted with the free-surfactant case Figure. II-29d) and, as can be seen, changes radically the flow of solution during dip-coating. This could eventually have effects on the structuration of the species at the nanoscale for particular chemical compounds but these kinds of studies have not been performed yet.

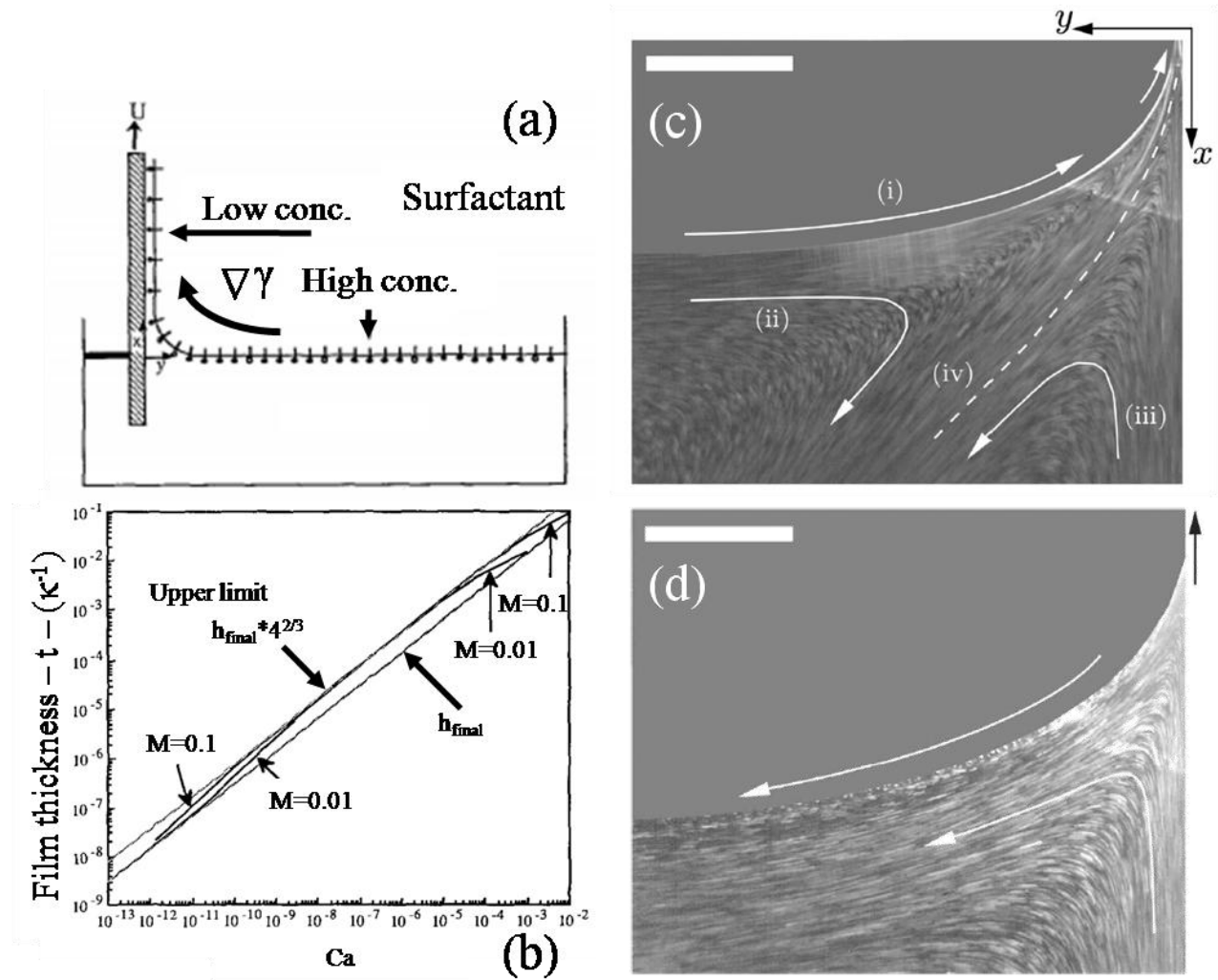


Figure. II-29 (a) scheme showing the formation of the gradient of surface tension. The surfactant at high surface concentration for the plane surface is stretched in the meniscus. A lower surface concentration is then reported on the film surface causing a net surface tension gradient. (b) film thickness expressed in capillary length units (κ^{-1}) in function of the capillary number considering the surfactant effect for two Marangoni numbers for non evaporating liquids. As can be seen a lower Marangoni number reduces the effect of the surfactant (in many cases low Marangoni number corresponds to low surfactant concentrations). The difference between the curved lines and the lower line (indicated by h_{final}) is due to the multiplication with the prefactor α . At a certain low threshold the surfactant effect starts to become important thanks to the higher viscous stresses. A second threshold is found at higher capillary numbers when the Marangoni contribution becomes negligible in respect of the viscous one. (c) and (d) flow profiles detected through addition of traceable microparticles in presence and absence of surfactant during dip-coating at 12.7 mm/s. As can be easily seen in figure (d) an outward flow is present only. On the contrary for the dip with surfactants a Marangoni flow is present on the liquid surface: part of it contributes to the final film thickness (i) and part reenters the solution (ii) meeting on the separation line (iv) the normal flow expected due to the substrate movement (iii).

In the case of the hydroalcolic solution used in this thesis containing surfactants the use of surfactants did not cause serious problems: the experimental procedure to forecast final thickness is indeed based on the fitting of the experimental values (in order to avoid the viscosity and surface tension of the solution) which means that the cited prefactor could be included in the fitted parameters if its values remain constant. From the literature [37] (considering non volatile liquid solutions

Figure. II-29b) it is possible to inspect that the speed regime in which the Marangoni flow influences the thickness covers all the speeds in the draining regime utilized in this thesis (for hydroalcolic solutions $Ca=10^{-4}$ corresponds to speeds of 2 mm/s). It indeed become relevant for the draining regime contribution when the capillary regime is still dominant (not modifying then the film thickness) and starts to lose in importance in correspondence of the upper limits of the used speeds. This phenomenon then can also contribute to the deviation from the expected values at the upper limit of the draining regime in Figure. II-4.

The actual effect of this contribution on the production of thin film is a even serious increase of film thickness upon addition of surfactants in sol-gels solutions that cannot be explained by the sample variation of viscosity an surface tension. Films with differences up to two hundred nanometers can indeed be produced from an initial sol-gel solution with different quantities of added surfactant.

It has to be noticed that in the case of organic solutions containing block-copolymers the influence of this effect has not been studied. Inhomogeneities have been reported that can be due to Marangoni flow. As will be exposed in the next section polymeric solutions are particularly difficult to deposit uniformly. This is why the effects of the just mentioned Marangoni flows cannot be adequately studied and isolated from other undesired effects.

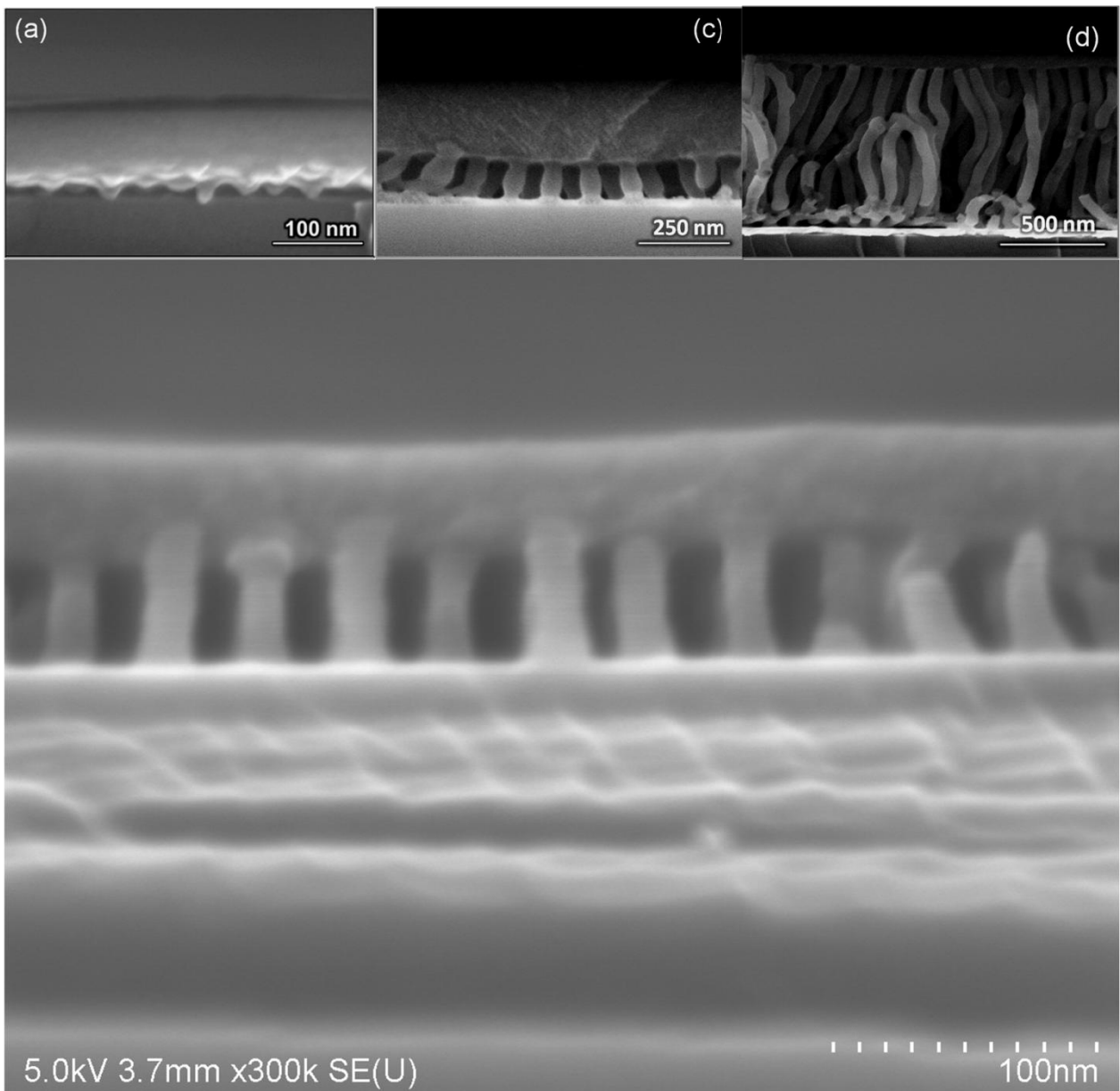
II.6 Bibliography

- [1] M. Faustini, B. Louis, P. A. Albouy, M. Kuemmel, and D. Grosso, "Preparation of Sol–Gel Films by Dip-Coating in Extreme Conditions," *J. Phys. Chem. C*, vol. 114, no. 17, pp. 7637–7645, May 2010.
- [2] D. A. White and J. A. Tallmadge, "Theory of drag out of liquids on flat plates," *Chem. Eng. Sci.*, vol. 20, no. 1, pp. 33–37, Jan. 1965.
- [3] R. P. Spiers, C. V. Subbaraman, and W. L. Wilkinson, "Free coating of non-newtonian liquids onto a vertical surface," *Chem. Eng. Sci.*, vol. 30, no. 4, pp. 379–395, Apr. 1975.
- [4] C. Y. Lee and J. A. Tallmadge, "Meniscus Shapes in Withdrawal of Flat Sheets. 3. A Quasi-One-Dimensional Flow Model Using a Stretch Boundary Condition," *Ind. Eng. Chem. Fundam.*, vol. 15, no. 4, pp. 258–266, Nov. 1976.
- [5] B. G. Higgins, W. J. Silliman, R. A. Brown, and L. E. Scriven, "Theory of Meniscus Shape in Film Flows. A Synthesis," *Ind. Eng. Chem. Fundam.*, vol. 16, no. 4, pp. 393–401, Nov. 1977.
- [6] S. Kistler S, "Free-Meniscus Coating Processes.," in *Liquid Film Coating*, S. F. Kistler and P. M. Schweizer, Eds. Dordrecht: Springer Netherlands, 1997, pp. 673–708.
- [7] A. V. Kuznetsov and M. Xiong, "Effect of evaporation on thin film deposition in dip coating process," *Int. Commun. Heat Mass Transf.*, vol. 29, no. 1, pp. 35–44, Jan. 2002.
- [8] R. D. Deegan, O. Bakajin, T. F. Dupont, G. Huber, S. R. Nagel, and T. A. Witten, "Capillary flow as the cause of ring stains from dried liquid drops," vol. 389, no. 6653, pp. 827–829, Oct. 1997.
- [9] C. J. Brinker, G. C. Frye, A. J. Hurd, and C. S. Ashley, "Fundamentals of sol-gel dip coating," *Thin Solid Films*, vol. 201, no. 1, pp. 97–108, Jun. 1991.
- [10] L. B. Landau L, "Dragging of a liquid by a moving plate," *Acta Physicochim. Urss*, vol. 17, pp. 42–54, 1942.
- [11] P. Innocenzi, L. Malfatti, T. Kidchob, S. Costacurta, P. Falcaro, M. Piccinini, A. Marcelli, P. Morini, D. Sali, and H. Amenitsch, "Time-Resolved Simultaneous Detection of Structural and Chemical Changes during Self-Assembly of Mesostructured Films," *J. Phys. Chem. C*, vol. 111, no. 14, pp. 5345–5350, Apr. 2007.
- [12] L. Malaquin, T. Kraus, H. Schmid, E. Delamarche, and H. Wolf, "Controlled particle placement through convective and capillary assembly.," *Langmuir*, vol. 23, no. 23, pp. 11513–21, Nov. 2007.

- [13] M. Le Berre, Y. Chen, and D. Baigl, "From convective assembly to Landau-Levich deposition of multilayered phospholipid films of controlled thickness.," *Langmuir*, vol. 25, no. 5, pp. 2554–7, Mar. 2009.
- [14] N. Krins, M. Faustini, B. Louis, and D. Grosso, "Thick and Crack-Free Nanocrystalline Mesoporous TiO₂ Films Obtained by Capillary Coating from Aqueous Solutions," *Chem. Mater.*, vol. 22, no. 23, pp. 6218–6220, Dec. 2010.
- [15] "Coating Defects." [Online]. Available: <http://www.coatings.rutgers.edu/Defects.htm>. [Accessed: 23-Jul-2015].
- [16] C. Y. Lee and J. A. Tallmadge, "Meniscus vortexing in free coating," *AIChE J.*, vol. 18, no. 4, pp. 858–860, Jul. 1972.
- [17] H. C. Mayer and R. Krechetnikov, "Landau-Levich flow visualization: Revealing the flow topology responsible for the film thickening phenomena," *Phys. Fluids*, vol. 24, no. 5, p. 052103, May 2012.
- [18] H. Uchiyama, M. Hayashi, and H. Kozuka, "Spontaneous pattern formation on silica and titania dip-coating films prepared at extremely low substrate withdrawal speeds," *RSC Adv.*, vol. 2, no. 2, pp. 467–473, Dec. 2012.
- [19] C. Huggett, "Habitable atmospheres which do not support combustion," *Combust. Flame*, vol. 20, no. 1, pp. 140–142, Feb. 1973.
- [20] M. Li, C. An, W. Pisula, and K. Müllen, "Alignment of organic semiconductor microstripes by two-phase dip-coating.," *Small*, vol. 10, no. 10, pp. 1926–31, May 2014.
- [21] X. Paquez, G. Amiard, G. de Combarieu, C. Boissière, and D. Grosso, "Resistant RuO₂/SiO₂ Absorbing Sol–Gel Coatings for Solar Energy Conversion at High Temperature," *Chem. Mater.*, vol. 27, no. 7, pp. 2711–2717, Apr. 2015.
- [22] A. Demessence, C. Boissière, D. Grosso, P. Horcajada, C. Serre, G. Férey, G. J. A. A. Soler-Illia, and C. Sanchez, "Adsorption properties in high optical quality nanoZIF-8 thin films with tunable thickness," *J. Mater. Chem.*, vol. 20, no. 36, p. 7676, Aug. 2010.
- [23] N. Moumen, R. S. Subramanian, and J. B. McLaughlin, "Experiments on the motion of drops on a horizontal solid surface due to a wettability gradient.," *Langmuir*, vol. 22, no. 6, pp. 2682–90, Mar. 2006.
- [24] S. Feng, S. Wang, Y. Tao, W. Shang, S. Deng, Y. Zheng, and Y. Hou, "Radial wettable gradient of hot surface to control droplets movement in directions.," *Sci. Rep.*, vol. 5, p. 10067, Jan. 2015.
- [25] F. M. Mancio Reis, P. Lavieille, and M. Miscevic, "Toward enhancement of water vapour condensation using wettability gradient surface," *Exp. Therm. Fluid Sci.*, Nov. 2014.
- [26] M. K. Chaudhury and G. M. Whitesides, "How to make water run uphill.," *Science*, vol. 256, no. 5063, pp. 1539–41, Jun. 1992.

- [27] M. Faustini, L. Nicole, C. Boissière, P. Innocenzi, C. Sanchez, and D. Grosso, “Hydrophobic, Antireflective, Self-Cleaning, and Antifogging Sol–Gel Coatings: An Example of Multifunctional Nanostructured Materials for Photovoltaic Cells,” *Chem. Mater.*, vol. 22, no. 15, pp. 4406–4413, Aug. 2010.
- [28] J. Ju, H. Bai, Y. Zheng, T. Zhao, R. Fang, and L. Jiang, “A multi-structural and multi-functional integrated fog collection system in cactus,” *Nat. Commun.*, vol. 3, p. 1247, Jan. 2012.
- [29] M. Faustini, D. R. Ceratti, B. Louis, M. Boudot, P.-A. Albouy, C. Boissière, and D. Grosso, “Engineering functionality gradients by dip coating process in acceleration mode,” *ACS Appl. Mater. Interfaces*, vol. 6, no. 19, pp. 17102–10, Oct. 2014.
- [30] de Ryck A and D. Quéré, “Gravity and Inertia Effects in Plate Coating,” *J. Colloid Interface Sci.*, vol. 203, no. 2, pp. 278–85, Jul. 1998.
- [31] H. Jeffreys, “The Draining of a Vertical Plate,” *Math. Proc. Cambridge Philos. Soc.*, vol. 26, no. 02, p. 204, Oct. 2008.
- [32] D. Quéré, “FLUID COATING ON A FIBER,” *Annu. Rev. Fluid Mech.*, vol. 31, no. 1, pp. 347–384, Jan. 1999.
- [33] M. Maleki, M. Reyssat, F. Restagno, D. Quéré, and C. Clanet, “Landau-Levich menisci,” *J. Colloid Interface Sci.*, vol. 354, no. 1, pp. 359–63, Feb. 2011.
- [34] A. J. Soroka and J. A. Tallmadge, “A test of the inertial theory for plate withdrawal,” *AIChE J.*, vol. 17, no. 2, pp. 505–508, Mar. 1971.
- [35] M. N. Esmail and R. L. Hummel, “Nonlinear theory of free coating onto a vertical surface,” *AIChE J.*, vol. 21, no. 5, pp. 958–965, Sep. 1975.
- [36] P. Groenveld, “Laminar withdrawal with appreciable inertial forces,” *Chem. Eng. Sci.*, vol. 25, no. 8, pp. 1267–1273, Aug. 1970.
- [37] C.-W. Park, “Effects of insoluble surfactants on dip coating,” *J. Colloid Interface Sci.*, vol. 146, no. 2, pp. 382–394, Oct. 1991.
- [38] O. Ou Ramdane and D. Quéré, “Thickening Factor in Marangoni Coating,” *Langmuir*, vol. 13, no. 11, pp. 2911–2916, May 1997.

III : Materials synthesis



III : MATERIALS SYNTHESIS ----- III-85

III.1 INTRODUCTION ----- III-87

III.1.a Sol-Gel chemistry-----III-89

III.1.b Hybrid mesostructured materials -----III-91

III.1.c Evaporation Induced Self Assembly -----III-93

III.1.d Block copolymers self assembly -----III-96

III.1.e Self-assembled block copolymer films ----- III-101

III.2 SYNTHESIZED MATERIALS ----- III-105

III.2.a Environmental-Ellipsometric-Porosimetry ----- III-106

III.2.b Non-organized porosities----- III-108

III.2.c Pillared Planar Nanochannels ----- III-116

III.2.c.i Preparation of the nanoporous Polystyrene films -----III-116

III.2.c.ii Sol-gel replica -----III-119

III.2.c.iii PPN from PS-b-PLA analysis-----III-120

III.2.c.iv PPN from PS-b-P2VP analysis -----III-122

III.2.d Conclusion----- III-123

III.3 BIBLIOGRAPHY ----- III-124

III.1 Introduction

In this chapter we will describe the synthetic strategies utilized to produce the nanoporous films suitable for nanofluidic applications. As discussed in the previous chapter, dip coating was exploited as main deposition technique. From a material point of view, samples were mainly prepared by sol-gel chemistry rationally coupled with self-assembly of amphiphilic molecules, such as block-copolymers.

In the first part of this chapter, some elements of sol-gel chemistry are then introduced. Pure inorganic or hybrid organic-inorganic materials can indeed be realized through this method. The concept of “Evaporation Induced Self-Assembly” (EISA) during dip-coating of the presented hybrid materials is also discussed. This section will be followed by a brief overview on block-copolymers and their self-assembly in the bulk and, more important, film configuration. Block-copolymers can be used to produce materials with highly organized porosity but the handling of their organization is critical. It depends on various parameters that will be introduced and analyzed. This will constitute a basis for the results of the second part of the chapter.

In the second part of the chapter, we report the results concerning the preparation and characterization of nanoporous thin films after a brief introduction of the main technique utilized to determine the porosity characteristics in this thesis: Environmental-Ellipsometric-Porosimetry.

A first series of samples has been realized through the EISA mechanism using a combination of sol-gel and block-copolymers or surfactants. Mastering both the chemical parameters and the deposition process allowed preparation of films with various kinds of porosities with various characteristic dimensions. The possibility to create such a variegated pool of porous networks has been extremely useful to understand infiltration mechanism at the nanoscale as it will be shown in the next chapter.

A second series of samples, constituted by the PPNs (pillared planar nanochannels), is then introduced. They are constituted by a forest of nanopillars hexagonally organized covered by a roof. They will constitute a reference material for the final part of this thesis being studied for infiltration, nanoconfined reactions and diffusion experiments. Their architecture has also been modeled in the VI chapter of this thesis simulating the electro-osmotic flow.

As it will be shown they are realized through two-step replication process of a self-assembled polymeric template with a sol-gel material. A deeper explanation of their synthesis is reported in the last section of this chapter.

III.1.a Sol-Gel chemistry

Sol-gel chemistry allows the preparation of inorganic materials (mainly oxides) through inorganic polymerization of molecular precursors in solution. These precursors have, in general, a chemical formula of the kind MX_n ($M = \text{Si, Ti, Zr, Al, ...}$) with n the charge of the metal M and X a easily hydrolysable group. Usually X corresponds to a chlorine atom (eventually another halides) or an alkoxide group ($-\text{OR}$).

Sol-gel synthesis is usually performed in hydroalcoholic or aqueous medium at room temperature or in hydrothermal conditions. In order to obtain sol-gel materials, two fundamental steps, hydrolysis and condensation, have to take place as is shown in Figure.III-1.

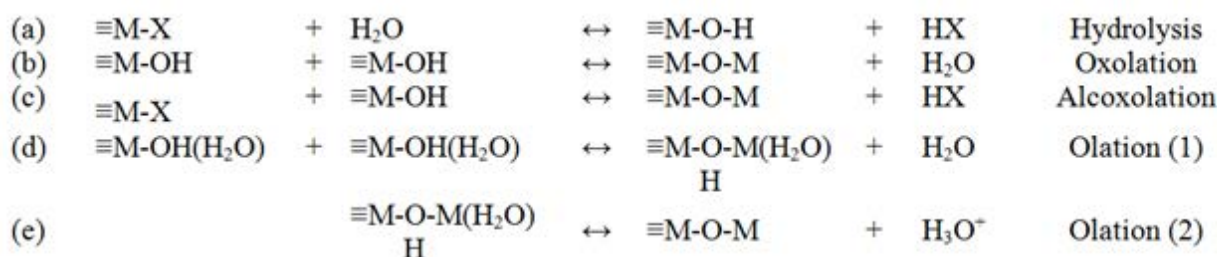


Figure.III-1.Sol-gel chemistry reactions: (a) hydrolysis. (b) Condensation through the oxolation mechanism. (c) Condensation through the alcoxolation mechanism. (d) and (e) condensation through the olation mechanism.

First of all, the X group is substituted by a hydroxyl group during hydrolysis (Figure.III-1(a)). This group can then reacts again through three pathways with another molecule containing a metallic center. In the first pathway, oxolation (Figure.III-1(b)), the oxygen of the hydroxyl group attacks ahydrolyzed metal center (nucleophilic attack S_N), its proton is transferred to the other hydroxo-ligand within the transition state and a water molecule is eliminated. In the second one, alcoxolation (Figure.III-1(c)),that same attack is performed over a non-hydrolyzed metal center with the transfer of the proton to the alkoxide/halide group of the attacked metal and elimination of an alcohol or a hydrogen halide. In the last one, olation (Figure.III-1(d-e)), for which hydroxo-aquo precursors are needed, the S_N mechanism is not directly followed by a proton transfer but just by the removal of one of the metal-coordinated water molecules. The elimination of the proton from the bridging hydroxyl group happens in a second time (the group becomes more acidic in this form). In the three cases the two metal centers are finally bound to an oxygen atom. The kinetics of the three different mechanisms depend on many factors such as pH, temperature, solvent, ionic force, concentration, stirring and determine the exact shape of the of the molecular structures (linear or branched and polymeric length) [1], [2].

To make an example the kinetics of reactions of Tetra Ethyl OrthoSilicate TEOS (the most used silicon-based precursor) have been studied as function of the pH (in the mechanism species such as Si-OH_2^+ or Si-O^- appear in different conditions). Acid or basic catalysis is possible and the slowest kinetics are found at $\text{pH}=7$ for the hydrolysis reaction and $\text{pH}=2$ for the condensation one (silica zero point charge). In Figure.III-2 is reported the dependence of the hydrolysis (H), condensation (C) and silicate re-dissolution (D) rate from pH in an alcoholic $r=1.5$ ($\text{H}_2\text{O}:\text{TEOS}$) solution [3].

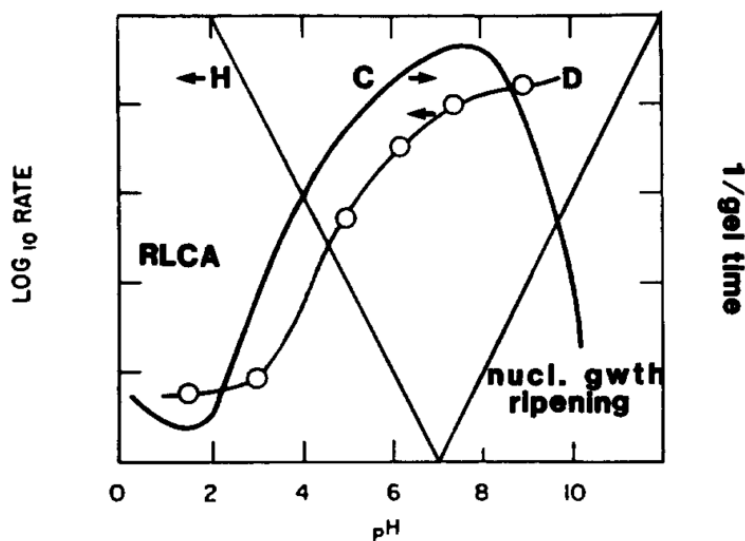


Figure.III-2.[3]Hydrolysis (H), condensation (C) and silicate re-dissolution (D) rate in function of pH for a alcoholic $r=1.5$ ($\text{H}_2\text{O}:\text{TEOS}$) solution.

In general it is found that at acidic pH, being the re-dissolution of the silicate slower (and thus the formed clusters more stable), more linear oligomers are formed with a lower degree of condensation. Increasing the pH, weakly branched sited re-dissolve thus more branched structures are formed, condensation is faster and gelation takes place at shorter times. For high pH this phenomenon is so fast that nanoparticles are formed and electrostatically stabilized as illustrated by Stöber[4].

Acidic conditions have been used during this thesis for TEOS and TiCl_4 solutions in order to have the most stable solution with the longest gelation time and the simplest structure.

Upon full condensation due to time, pH or temperature variation or solvent drying an inorganic solid gel is formed. As function of the particular procedure utilized this gel-material can be produced in form of particles, fibers, monoliths or thin films [5], [6]. As mentioned plenty of precursors are available thus a great number of metallic oxides (and all their blends) can be realized (SiO_2 , TiO_2 , ZrO_2 , SnO_2 , *etc...*) either in amorphous or crystalline form. It has to be

pointed out that sol-gel chemistry allows preparing inorganic metal oxide at mild conditions and doesn't need high energy consumption processes in order to obtain the desired materials.

Because ceramic materials can be realized by sol-gel process without using high temperatures, organic entities can be added (such as molecular functional groups, surfactant or block-copolymers) in order to obtain organic/inorganic hybrid materials. This kind of materials will be presented in the next section.

III.1.b Hybrid mesostructured materials

Hybrid materials can be classified based on the possible interactions connecting the inorganic and organic species. Class I hybrid materials are those that show weak interactions between the two phases, such as Van der Waals, hydrogen bonding or weak electrostatic interactions. Class II hybrid materials are those that show strong chemical interactions between the components such as covalent bonds[5]. Here we will focus of Class I hybrid materials; in particular we will describe those forming periodically-organized organic/inorganic mesophases, the transition system toward mesoporous materials (pore size between 2 and 50 nm).

When a surfactant or a block-copolymer is added to a sol-gel solution, it can form self-assembled structures as function of its concentration in the solution. In particular a threshold concentration, called critical micelle concentration (CMC), can be identified, that corresponds to the first formation of self-assembled supramolecular structures (micelles assemblies in most cases) in solution (Figure.III-3). Increase of the concentration can cause formation of other liquid crystal phases that depend on the particular organic molecule, temperature and other parameters.

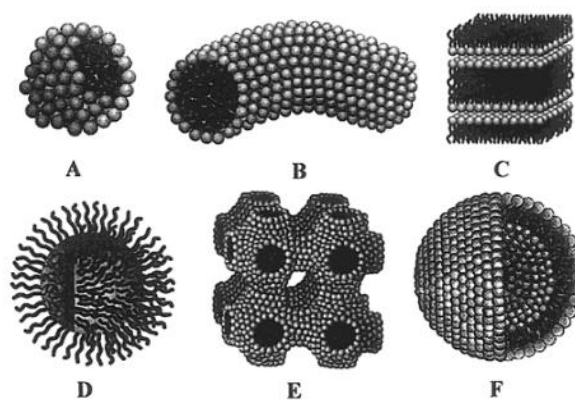


Figure.III-3.[7]Micellestructures: A = Sphere, B = Cylinder, C = Plane bilayer, D = Inverse Micelle, E = Bicontinuous phase, F = Liposome.

Increase in concentration can be also driven by the evaporation of the solvent as it will be discussed later.

Some examples of these dependences for a particular surfactant and block-copolymer, Pluronic F127 can be found in the literature [8]–[13]. In presence of these liquid crystal phases, the inorganic precursors and oligomers are mostly found in the hydrophilic phase leading to the formation of inorganic/organic mesostructured hybrid materials. The formation of the inorganic structure occurs by sol-gel polycondensation in the confined space surrounding the hydrophobic core. This templating process can take place after the formation of the organic mesophase or can happen at the same time through a cooperative mechanism (Figure.III-4). If, after gelation, the material is heated at a sufficient temperature, the organic part can burn away leaving a porous structure; if the size of the pores goes from 2 to 50 nm they are called mesopores. Similar templating approaches have been proposed with preformed nanoparticles and biomolecules (such as proteins or viruses) to form nanoporous materials [14]–[17].

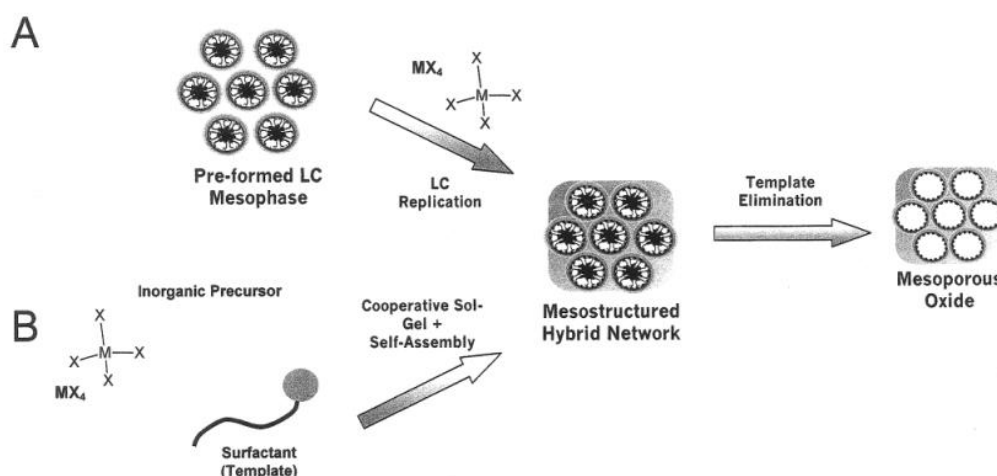


Figure.III-4.[7]Two ways to obtain a mesoporous metal oxide material: a) the mesophase is formed in solution and b) the sol-gel process and organic self- assembly take place at the same time.

Two main families of organic structuring agents can be identified:

The first one consists in all the ionic surfactants. In this thesis, ionic surfactants with quaternary ammonium ions were used: an alkyl chain, hydrophobic, is bound to an ammonium ion that constitutes the hydrophilic part. It is interesting to notice that the first example of metal oxide organized porosities was obtained using these molecules in 1992 by the researchers of Mobil Oil Corp [18] CTAB (Cetyltrimethylammonium bromide - $CH_3(CH_2)_{15}N(CH_3)_3Br$) [19]–[21] and DTAB (Dodecyltrimethylammonium bromide - $CH_3(CH_2)_{11}N(CH_3)_3Br$) [22], [23]. Their limited industrial application is due to the chemical hazards of the quaternary ammonium molecules (irritating and dangerous for the environment).

The second class is constituted by non-ionic amphiphilic molecules. Non-ionic porogens such as block-copolymers are constituted at least by 2 blocks of different polarity. Many examples of these molecules can be found from 1995 in literature [24]. In example F127 has already been mentioned and has been broadly used during this thesis. Its structure ($[\text{PEO}]_{106}-[\text{PO}]_{70}-[\text{PEO}]_{106}$) contains two hydrophilic parts, the polyethylene oxide chains, and an hydrophobic part, the polypropylene oxide chain. In general it allows obtaining larger pores [25] with respect to CTAB or DTAB with thicker walls [26]–[28]. Other block-copolymers have been used as templating agent during this thesis; in particular a series of Polystyrene – Poly ethylene oxide block copolymers (PS-*b*-PEO) with different block chain length was used to modify the pore size and organization.

III.1.c Evaporation Induced Self Assembly

The concept of « Evaporation Induced Self Assembly » (EISA) has been introduced for the first time by J. Brinker and coworkers at the end of the '90s [29]–[31]. In this approach, the inorganic precursors (sol-gel) and the structuring agents (surfactants or block-copolymers) are mixed in the same solution in adequate quantities and condition in order to obtain a homogeneous solution. The solution is then deposited through a liquid deposition method such as spin-coating, spray-coating, flow-coating or, in the case of this thesis, dip-coating.

The self-assembly of amphiphilic molecules usually takes place during the evaporation step. The evaporation of the solvent induces an increase the concentration of the species. During evaporation indeed the concentration of the surfactant molecules rises to a level higher than the critical micelle concentration (CMC) creating, in this way, surfactant micelles constituted by a hydrophobic core and a hydrophilic corona surrounded by the sol-gel precursors.

The EISA mechanism was further studied by our group (among others) in the past years in the case of dip-coating [32]. It consists of 3 successive steps as schematized in Figure.III-5 for CTAB/silica systems:

1. Fast evaporation of the solvents (most of the solvent is removed but a certain amount is retained by the concentrated species of the film).
2. Formation and stabilization of the hybrid mesophases (Tunable steady state)
3. Condensation of the inorganic sol-gel network.

The fast evaporation of step-1 has the effect, as mentioned, to concentrate the species in solution, and generate the micelles. A fast evaporation is advisable in order to quench the system and avoid eventual chemical modifications and separations induced by the incompatibility of the solutes.

The second step, step-2, is particularly important to determine the final morphology of the thin film. This is called « Modulable Steady State » (MSS) or « Tunable Steady State » (TSS) and it is usually depending on the atmospheric relative humidity. A variation of water concentration in the thin film just after drying can indeed substantially modify the mobility of the species and thus the final organization of the film [33]. After equilibration with the atmosphere, the system is still flexible and the structuration evolves. It is clear that the time of evolution seriously influences the final structure permitting either to arrive to the thermodynamic equilibrium or blocking the structure kinetically. Atmosphere composition is again determinant. As function of the film composition and of the process, the film can attain a more or less stable equilibrium. If it is exposed to particularly strong modifications in atmosphere it is possible to make it evolve again. It is then necessary to stabilize its morphology in order to avoid any uncontrolled modification.

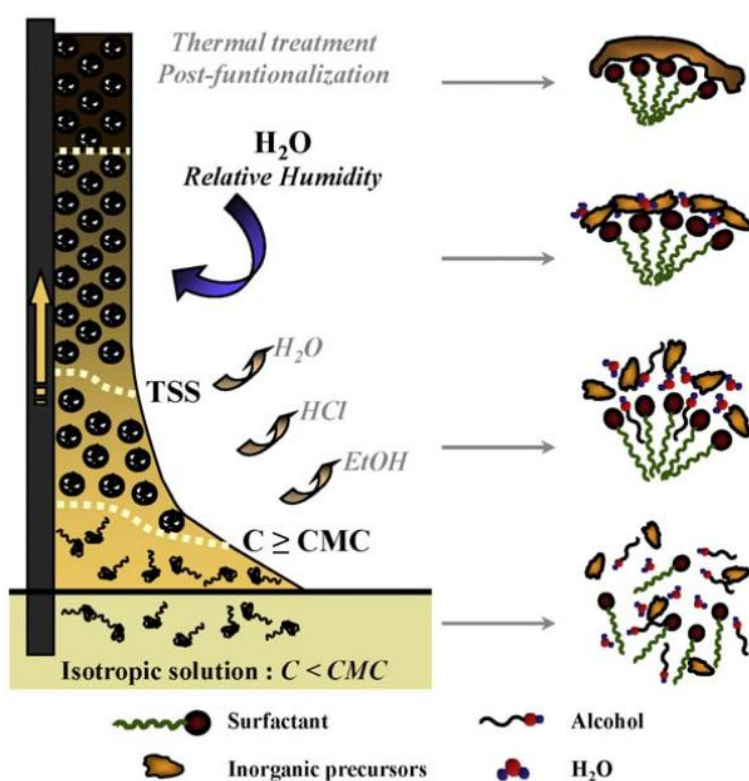


Figure.III-5 Mesostructured thin film formation mechanism through EISA [34].

In the last step (step-3) the structure is stabilized irreversibly by condensation of the sol-gel network. In addition the inorganic structure can be consolidated through thermal treatment or, as recently shown, through chemical treatment at low temperatures [35].

The elements introduced are sufficient to discuss the results reported in this thesis. The EISA mechanism is particularly complex and various investigations have been performed for the formation of mesostructured sol-gel films[36]·[37]·[38]·[39].

In the case of block copolymers with high hydrophobic/hydrophilic contrast and high molecular weight micelles already exists in the starting solution. In this category PBH-b-PEO (Hydrogenated Poly(Butadiene) – block – Poly(Ethylene Oxide)), PIB-PEO(Poly(IsoButene)-block-Poly(Ethylene Oxide)), PS-PEO (Poly(Styrene)-block-Poly(Ethylene Oxide)) or PB-PEO (Poly(Butadiene)-block-Poly(Ethylene Oxide)) are included. In this case the self-assembly mechanism is called Evaporation Induced Micellar Packing (EIMP)[40]or Evaporation Induced Micellar Assembly (EIMA) [41] and an assembly of rigid spheres, surrounded by the inorganic precursor takes place: in reality EIMP can be conceptually considered as a particular case of Evaporation Induced Self-Assembly. Starting from block-copolymer micelles it is particularly useful to create mesoporous layer with difficult systems (such as RuO₂ and multicationic oxides)[41], [42]. Depending on the processing conditions (i.e. water and solvent relative pressures, temperature), the micelles could self-organize on a large scale leading to a liquid-crystalline phase before the extended condensation of inorganic species locks the system. Another important advantage is their high thermal stability: the high decomposition temperature of the hydrophobic core of the micelle (i.e., 250-300 °C) allows the completely dehydration and stabilization of the amorphous inorganic network before total decomposition of the organic template, preventing mesoporosity collapsing (Figure.III-6a and Figure.III-6b).

To conclude it has to be mentioned a further assembly mechanism that can take place during dip-coating evaporation. It is called spinodal phase separation (SPS) [43], [44]. It doesn't necessarily require surfactants or block copolymers to create a porosity but just a sudden condition of immiscibility between two phases. If a solvent can dissolve two incompatible materials upon its evaporation the two materials tend to phase separate. If the utilized solvent is very volatile and the evaporation extremely fast, the phases could not have the time to reorganize to a phase separated low-energy structure before quenching and solidification. A rather disorganized structure is then found that, for opportune conditions, can have the scale of tenths or hundredths of nanometers. If, on the other hand the phases have more time to reorganize the typical dimensions of the porosity increases (Figure.III-6c and Figure.III-6d).

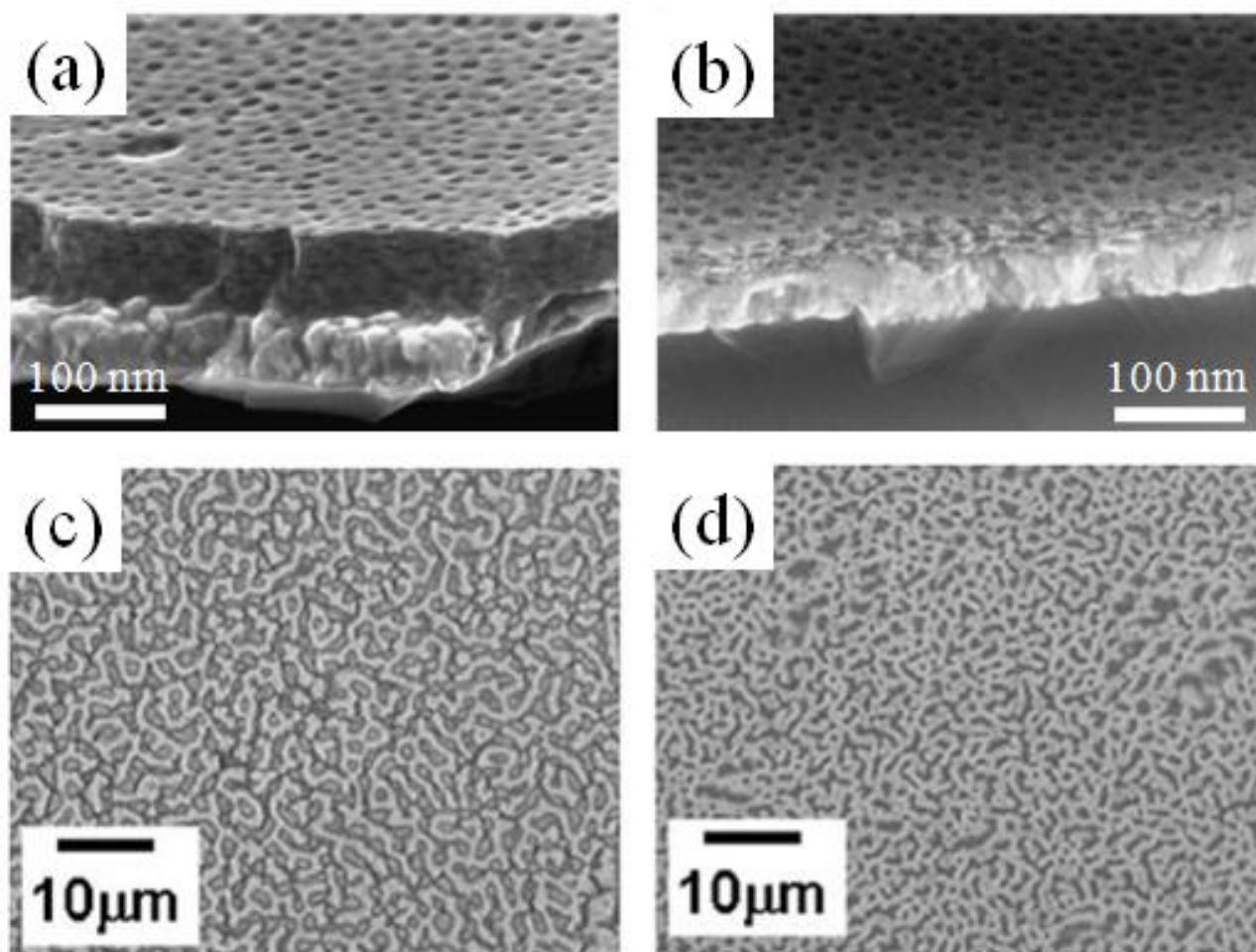


Figure.III-6. Typical EIMP formed film of $\text{RuO}_2 \cdot x\text{H}_2\text{O}$ at different annealing temperature (200 °C (a) and 330°C (b)) giving different morphologies. In any case a structure with thick walls and spherical distant pores is obtained. Different spinodal phase separated TiO_2 films obtained for different evaporation time of a solution containing titanium tetraisopropoxide and polyoxyethylene (20) nonylphenyl ether which are strongly incompatible for longer (c) and shorter (d) evaporation time.

III.1.d Block copolymers self assembly

Another way to obtain template nanoporous materials consists in obtaining an inorganic replica of preformed organic templates by infiltration of the sol-gel precursors. A particular case of this method, which has been extensively used in this thesis, is the deposition of a sol-gel solution inside the porosity of a nano-organized polymeric film. It is thus convenient to introduce here some elements of the self-assembly of block-copolymers. It is indeed through the use of block-copolymers and their organization at the nanoscale that such structures can be realized.

Block-copolymer can be composed, as mentioned, by two, three or even more blocks [45]. Only the case of diblock-copolymer will be analyzed here because no polymers containing three or more blocks were used for this purpose during this thesis.

If we consider a mixture of two or more immiscible homo-polymers, upon drying phase separation takes place accompanied by formation of distinct macroscopic domains each one constituted by a single polymeric phase. The characteristics of this heterogeneous material (size of the grains, reciprocal surface etc.) depend on the drying conditions and on the polymers compatibility [46]. Typical domains size exceed the hundreds of nanometers [47], [48] and can even self-organize in ordered structures [49]. Nevertheless these sizes are difficult to control. Upon annealing (thermal or solvent) the structure evolves and the size of domains increases radically through coalescence or Oswald ripening processes.

If we consider now block-copolymers with immiscible blocks, upon drying a phase separated structure is equally occurring. Unlike the blend case, the domains have typical dimensions of the chain lengths of each block. Upon further (solvent or thermal) annealing, the morphology can evolve but the typical dimensions of the phase domains remain unchanged. The covalent bond linking the block, indeed, prevents the macroscopic phase separation of binary mixtures of homopolymers. Even if kinetic and other conditions such as temperature, solvent, substrate etc., remain important, the process of phase separation of block-copolymers is more controllable and can generate highly organized structures (Figure.III-7).

To have a better understanding of the system some elements of polymer theory have to be introduced.

The final structure of a two block copolymer material is mainly determined by the volume fraction, the incompatibility of the two blocks and the total length of the block-copolymer. The degree of the incompatibility can be defined through the Flory-Huggins parameter χ_{AB} that considers the variation in energy from the formation of an interface between the two phases [50], [51] (equation.1).

$$\chi_{AB} = (\epsilon_{AB} - \frac{\epsilon_{AA} + \epsilon_{BB}}{2})/KT \quad (1)$$

with ϵ_{XY} energy of interaction between the monomer X and Y.

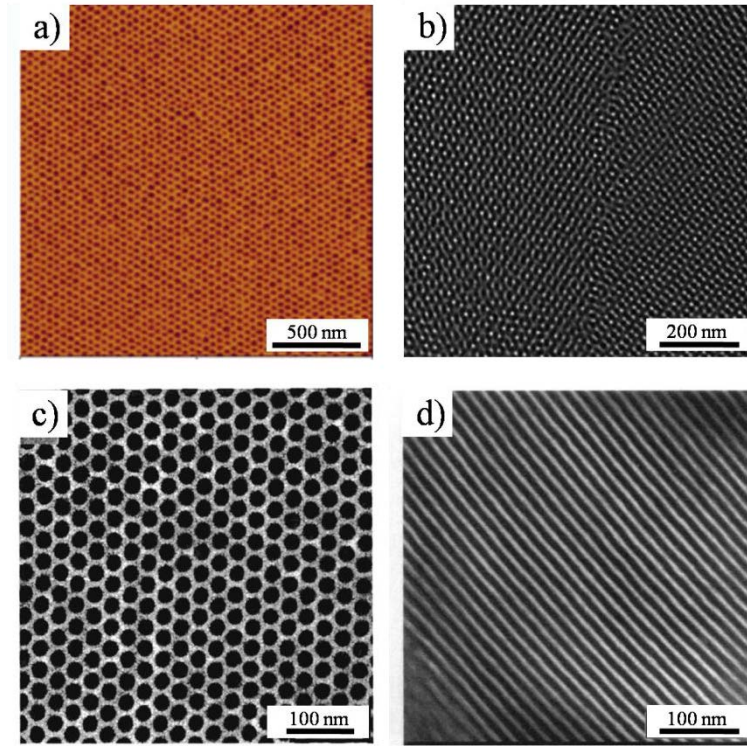


Figure.III-7. Strongly organized block-copolymer self assembled structures. These large-scale ordered structures have been reproduced from citation: (a) [52] (PS-b-PEO 19k-6.3k annealed 4 hours in toluene) periodic - cylindrical structure. (b) [53] (PBd-b-PDMS weight fraction 0.6-0.4 thermal annealed and cross-linked at 140 °C for 2h under nitrogen) gyroid structure. (c) [54](PI-b-PEO 12.4k-1.8k in presence of aluminum sec-butoxide(that increases the volume of the PEO phase) periodic – cylindrical/honeycomb structure of the calcined sample. (d) (PI-b-PEO 8.4k-1.5k in presence of (3-glycidyloxypropyl)-trimethoxysilane and aluminum sec-butoxide (that increase the volume of the PEO phase) periodic – lamellar structure of the calcined sample.(c) and (d) are bulk structures. (a) is a thin film on silicon and (b) a free standing membrane.

In general, polymers are incompatible if $\chi_{AB} > 0$, meaning that mixing of the blocks is endothermic. In some cases however (if for example the two blocks have interacting polar groups) $\chi_{AB} < 0$, mixing is exothermic and the blocks are compatible.

Phase separation takes place if ΔG_m , defined as:

$$\Delta G_m = k_B T * \left(\frac{\varphi_A}{N_A} * \ln(\varphi_A) + \frac{\varphi_B}{N_B} * \ln(\varphi_B) \right) + \varphi_A \varphi_B \chi_{AB} \quad (2)$$

is greater than zero (with N_A and N_B degree of polymerization, φ_A and φ_B the volume fractions of the monomers of each block). The first two terms take into account the entropy of mixing while the last one corresponds to the enthalpy. With immiscible blocks the last term is greater than zero; in the case of short chains, the entropic contribution (smaller than zero due to the fact that φ_1 and φ_2 are smaller than one) can compensate it and a mixed phases can be obtained. On the other hand, increasing the number of monomers in each macromolecule their contribute tends to zero. This means that, in general, longer block-copolymers are more prone to phase separate.

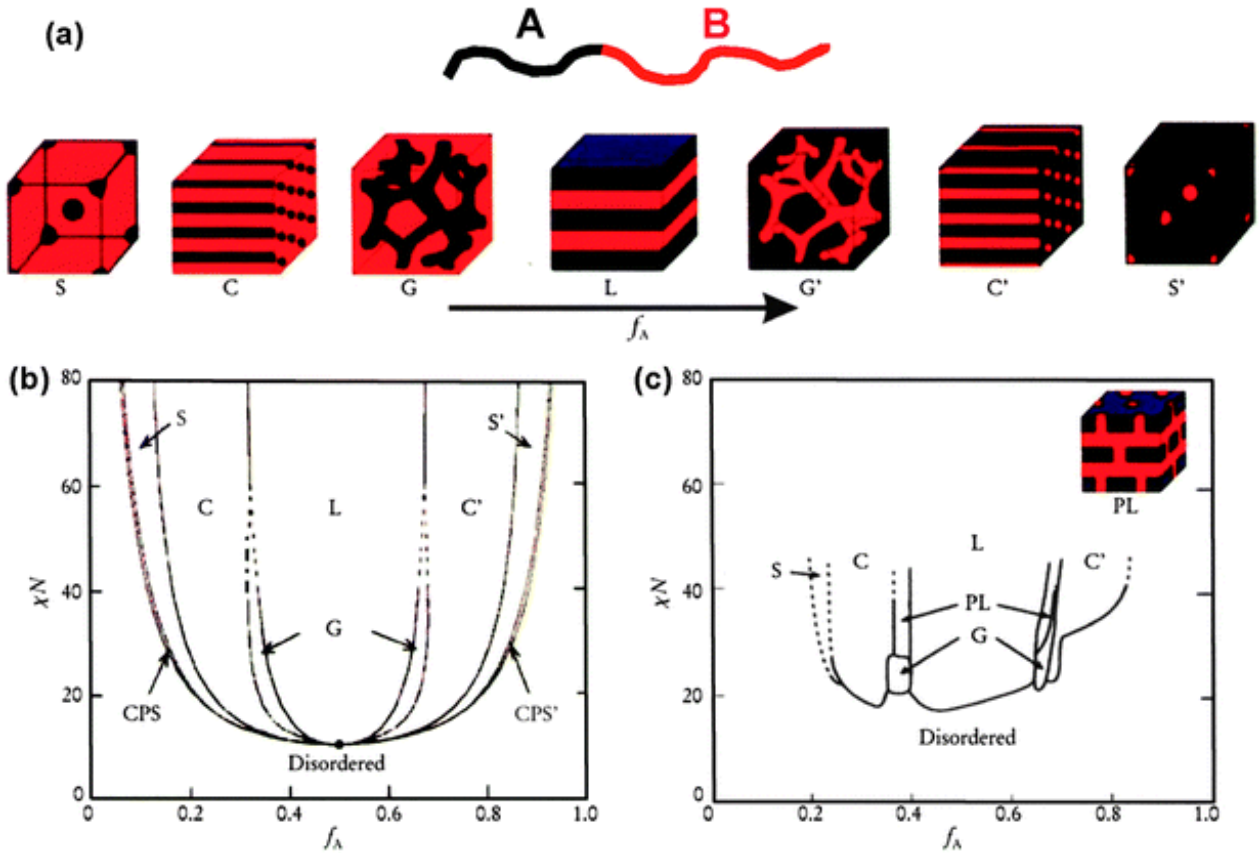


Figure.III-8. Image taken from [55]. a) equilibrium morphologies of diblock copolymers in the bulk: S-S' body-centered cubic spheres phase, C-C' hexagonally packed cylinders phase, G-G' bicontinuous gyroid phase and L lamellar phase. b) Theoretical phase diagram of a diblock copolymer predicted by the mean-field theory. far corresponds to ϕ_A in our discussion and χN to $\chi_{AB}N$. CPS and CPS0 = closely packed spheres, two not shown phases. c) experimental phase diagram from [56]. The PL (perforated layers phase) is not theoretically predicted.

Through equation (2) it is possible, for immiscible blocks, to create a phase diagram as function of N ($N=N_A+N_B$), χ_{AB} and ϕ_A ($\phi_A = 1 - \phi_B$) that distinguishes the phase-separated from the mixed-zone. For short chains (little $N=N_A+N_B$) miscibility is favored through entropy but increasing the product $\chi_{AB}N$ entropy is no more sufficient to contrast enthalpy and the blocks demix. The exact $\chi_{AB}N$ at which this happens depends from the volume fractions of the block with a minimum for the half/half chains.

As shown in Figure.III-8.b the phase diagram is much more complex [55]. In the phase-separation zone, multiple phases can be identified. The illustration of these phases is reported in Figure.III-8a. In the scheme “disordered” stands for the mixed phase.

Given a certain $\chi_{AB}N$ increasing the volume fraction ϕ_B of the second block it is possible to pass through (thus drawing a horizontal line in the scheme of Figure.III-8b) : a mixed state, B-block body-centered cubic spheres phase, B-block hexagonally packed cylinders phase, B-block bicontinuous gyroid phase and lamellar phase once arrived at the half/half chains. Then the scheme proceeds in the inverse order with the block A composing the minority phase. It has to be taken

into account that the phase diagram reported in Figure.III-8.b is a computationally calculated one and some approximations have been taken (coarse-grained segments, local interaction, uniform density, equal volume monomers etc.) but “retains the three most important ingredients: entropic chain stretching, incompressibility, and immiscibility between unlike segments” [57]. An experimental phase diagram [56] (Figure.III-8.c polyisoprene-b-polystyrene) can be compared to the theoretical one. As we can see the boundaries of the various phases do not follow quantitatively the theory even if qualitatively the same patterns can be recognized. The most evident differences are the presence of a new phase (PL – perforated lamellar phase) and the disappearance of the spherical phase for high volume fractions of polystyrene. Even considering fluctuations in chain length effects (the polydispersity generally decrease the compatibility (phase transition for shorter chains)) [58], [59] and conformational asymmetry (asymmetry of monomers), [60] in more complex models, the real phase diagram cannot be reproduced exactly. More effects such as temperature gradients, stresses in the formation of the polymeric material etc. should be indeed considered and are extremely dependent on the particular method utilized to create the sample. In any case, a qualitative idea of the parameters governing the morphology of diblock-copolymers has been identified and the concepts introduced will be used in the experimental part of this chapter.

Furthermore it has to be taken into account that in the case of thin films, the film thickness, the interaction with the substrate and the air interface are among other additional parameters that play a role on self-assembly. The next section is devoted to the particular case of self-assembly of thin films block copolymers and such effects will be evaluated.

As a final note, it has to be stressed that the phase diagrams presented here show the morphology of block copolymers in the bulk at a temperature that is higher than the glass transition temperature. If this temperature is not attained, indeed, the polymer chains cannot move due to the extremely high viscosity of the material. Over this temperature, instead, chains can move and equilibrium can be reached in reasonable times. It is thus normally needed to heat the block-copolymers to attain the equilibrium morphology. This treatment is called thermal annealing and is a really common step in self-assembly procedures. This and other ones will also be analyzed in the next section.

III.1.e Self-assembled block copolymer films

As mentioned in the previous section the morphology of block copolymers deposited as thin film over a substrate is strongly dependent on the film thickness and the interaction of the copolymer with it. It has been demonstrated that its properties (as the glass transition temperature) can be modified by size interaction with the substrate effects with respect to bulk ones even for large thicknesses [61], [62]. In general, for what concerns morphology, the stronger effects are evidenced when the substrate is affine to one of the two blocks only. In the equilibrium configuration this block “wets” the substrate leaving the non affine inside the film [63]. A similar reasoning can be done considering the film-air interface with a more favorable presence in the surface of the lower surface tension block.

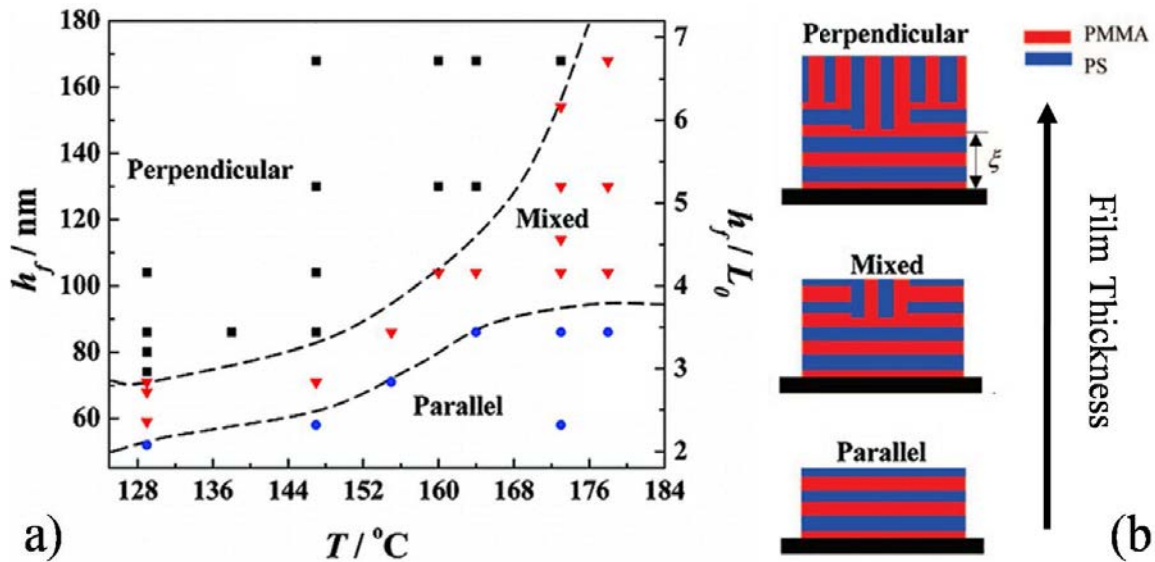


Figure. III-9. [64] a) surface phase diagram of PS-b-PMMA 36k-12k deposited by flow coating on plasma threaded silicon in function of film thickness and annealing temperature. b) Scheme of the three phases introduced in the face diagram. It has to be noticed that even if some samples present perpendicular alignment (upper scheme) the substrate induce a parallel orientation of the block copolymer over the first layers (represented by ξ).

This can lead to important consequences regarding the film morphology such as the formation of (a periodicity high) “steps” at the interface with the air (due to the strongly horizontal lamellar phase induced by the substrate) [65] or the modification of the symmetry of lamellar phases from parallel to perpendicular to the substrate surface [66]. It is interesting here to analyze an experimental example of this effect [64]. In Figure. III-9 we report the morphological phase diagram of a PS-b-PMMA block copolymer as function of the annealing temperature and the film thickness (the volume morphology was determined by neutron reflectance measurement on PS deuterated samples).

The film thickness strongly influences the morphology at the surface of the film and the substrate induces a parallel alignment even if the perpendicular one would be preferred for substrates equally compatible with the two blocks. It is clear that if perpendicular orientation has to be created, neutral substrate surfaces have to be prepared [67]. Alternatively, other stronger forces should be applied to induce vertical orientation. Graphoepitaxy (self-assembly directed by preformed patterns), electric fields [68], mechanical forces [69], temperature gradients [70] and fast solvent evaporation gradients [71] are examples of forces/methods used to obtain vertically aligned block copolymer self-assembly.

As mentioned, in order to reach the equilibrium morphology, block-copolymers need energy to allow chain movement. In the previous discussion, thermal annealing has been mentioned as a method to increase chain reorganization to an equilibrium configuration. Unfortunately this method often needs hours or even days to obtain the desired organization. Further efforts have then been made in order to reduce the time necessary to produced well organized samples.

Solvent annealing has been demonstrated as a valid alternative and a valuable method to overcome long-time annealing times [72].

The idea of solvent annealing is to expose the thin film to a controlled atmosphere of vapors of a certain solvent that can enter the structure and partially dissolve the chain. Upon solvent adsorption by the film, the film itself increases its volume. This creates “space” for the chains to move in an environment that is much less viscous than in the non swollen film but that can still be considered as solid-like. If too much solvent is adsorbed in the polymer, the chains can become too mobiles and dewetting can take place [73] eventually destroying the film. In normal procedures, the thin films are suspended in a closed chamber in presence of the liquid solvent that creates a saturated atmosphere following the Antoine equation [74] or exposed to known quantities of solvent vapors through continuous flow systems [75]. Clearly the control of all the process parameters is critical. Solvent choice, annealing temperature and time and vapor pressure gradients need to be controlled. A particular aspect that has to be taken into account is that the presence of the solvent in the swollen film can modify the value of the Flory-Huggins parameter thus modifying the compatibility of the two blocks and then the film morphology [76].

$$\chi_{AB} \sim \varphi(\chi_{AB} + \Delta\chi) = \varphi(\chi_{AB} + |\chi_{SA} - \chi_{SB}|) \quad (3)$$

with φ the volume fraction of the polymer in the swollen state and $\Delta\chi$ the difference between the block A and block B parameters of interaction with the solvent. In many cases solvents have no or

reduced selectivity towards each block of the copolymer ($\Delta\chi = 0$). This aspect allows the chains of both type to reorganize and causes a reduction of the Flory-Huggins parameter inducing, for example, a transition from an ordered to a disordered morphology. In some cases, preferential swelling of one part is desired. In Figure.III-10a a phase diagram reporting the effect of both kinds of solvents is shown.

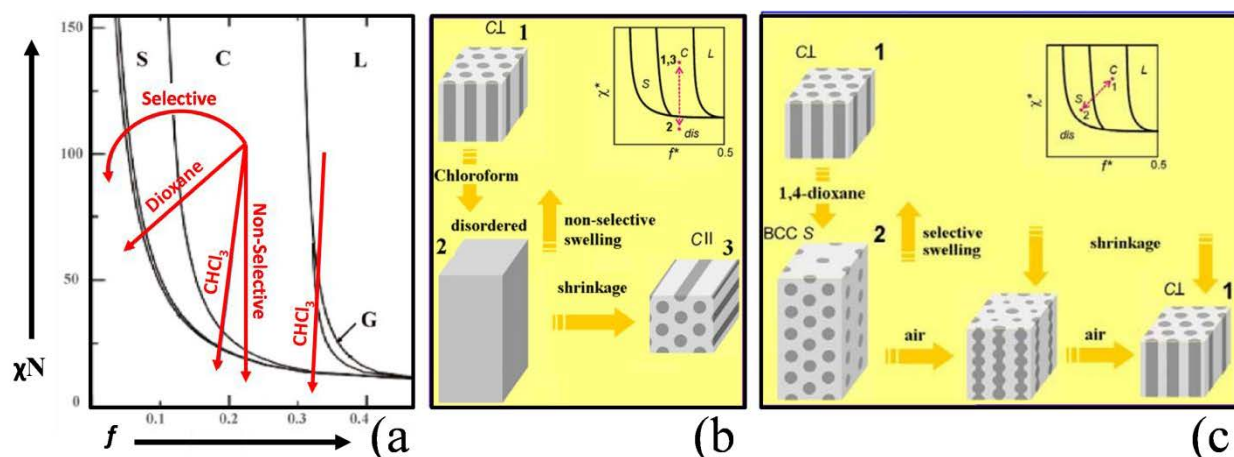


Figure.III-10 (a) [77] Trajectory of a block-copolymer in the previously introduced phase diagram upon swelling. (b) and (c) [78] Final effect on morphology exposing a PS-*b*-P4VP 32.9k-8k block copolymer to non selective chloroform vapors and selective dioxane vapors respectively.

Non selective solvents reduce the effective value of χ and “move” the phase in the vertical direction of the phase diagram. Selective solvents instead can modify the volume fraction of the space occupied by a block selectively causing a displacement in the horizontal direction (and a possible phase transition) too. This can cause formation of different morphologies as presented in the caption of Figure.III-10b and Figure.III-10c. It is clear that the dynamics of solvent penetration and extraction from the film influences the final organization. The film, indeed, needs enough time to “move” through the phase diagram and, as function of the drying time, it can stay in a configuration similar at the swollen one (that in some case can be lamellar, cylindrical, spherical etc. even in solution [79]) or return to the original state. Kinetics studies relating swelling time and final morphology are then necessary to have proper annealing. A common case of time dependent reorganization is the perpendicular to parallel change in orientation for cylindrical phases over too long annealing [80], [81]. Moreover, during drying, the gradient of solvent concentration that forms inside the thin film can create a strong orientating field [82]. In reducing the drying rate, this field is reduced which means that the final morphology is also drying rate dependent.

As mentioned, solvent annealing is now a key method to obtain well organized block-copolymer well organized thin film. Nevertheless the complexity and the number operation parameters still

represent an issue. Particular care has to be taken to obtain reproducible results and in general, inter-laboratory reproducibility is rather low due to the fact that the exact experimental condition cannot be really reproduced. The chamber shape and volume, the exact position of the sample, the dimension of the sample etc. are parameters that usually are not carefully reported in the experimental section of the articles.

Two other aspects deserve to be mentioned here even if not analyzed. The “residual solvent effect” that consists in the trapping of solvent molecules in the glassy structure of block-copolymers. It can cause irreproducible results or deposition method dependence on the final morphology [64] modifying, without control, the Flory-Huggins parameter in the film. The second element is the use of block copolymer/homopolymers mixtures in order to obtain morphologies with tunable spacing upon certain conditions. The homopolymer (of the same kind of one of the blocks), at low concentrations, do not demix macroscopically but can be considered as an increase in volume fraction of the corresponding block. This can cause a change in morphology, but, in certain cases, it can simply change the spacing between the periodical structures [83]. If instead an heterogeneous polymer is used, potential changes in the Flory-Huggins parameter are possible to cause phase separation in previously mixed copolymer phases [84].

The aspects discussed in this section will be recalled for explaining the block copolymers self-assembly results in this thesis. In the second part of this chapter, the experimental procedures performed to obtain self-assembled (vertical) cylindrical block copolymer patterns will be presented.

III.2 Synthesized materials

In this section the synthesis of the materials utilized in Chapter IV and V is reported. Two main families of materials have been realized.

The first is obtained through the EISA, EIMP and spinodal phase separation mechanisms utilizing various block-copolymers in sol-gel solutions. Non-organized porosities are then obtained with different structure and size characteristics. These series of samples were used to perform a systematic study of capillary filling in Chapter IV.

The second family is constituted by the mentioned PPNs. They have been produced in different height, periodic size and material. Their preparation is reported in the second section of this chapter part.

Before proceeding to the exposition of the synthesized films it is necessary to give a brief description of the Environmental-Ellipsometric-Porosimetry technique that has been largely utilized during this thesis to characterize the film porosities. Because of its importance in the next discussion it has not been reported in appendix but it is the subject of the next section.

III.2.a Environmental-Ellipsometric-Porosimetry

Environmental-Ellipsometric-Porosimetry (EEP) is a fundamental technique to characterize the porosity of thin films. The ellipsometer is an instrument capable to simply establish the thickness and refractive index of transparent thin films measuring the changes in the polarization state of light upon reflection.

Because the porosity of mesostructured thin films is consistently smaller than the wavelength of light the ellipsometer sees a layer whose refractive index is between the one of the composing material and the refractive index of the air. The volumetric fractions of the material and air determine directly the averaged refractive index through the Bruggemann effective medium approximation (BEMA) model [85]

$$f_A * \frac{(n_A^2 - n_{measured}^2)}{n_A^2 + 2n_{measured}^2} + f_B * \frac{(n_B^2 - n_{measured}^2)}{n_B^2 + 2n_{measured}^2} = 0 \quad (4)$$

with f_A and f_B volume fraction, n_A and n_B refractive index of the film material and air (or any other porosity filler) respectively and $n_{measured}$ the measured refractive index.

Porous thin films present concave surfaces. Because of this water, or other solvents, can more easily condensate in the porosity in respect than in free volumes (for hydrophilic surfaces). This is described by the Kelvin equation. For spherical pores the condensation takes place when the vapor pressure P satisfy the relation

$$RT \ln \left(\frac{P}{P_0} \right) = \frac{\gamma V_L \cos(\theta)}{R} \quad (5)$$

with R the gas constant, T the temperature, P_0 the saturation vapor pressure, γ the surface tension, θ the contact angle, V_L the molar volume of the condensing liquid and R the pore radius. For non-spherical pores more complex but not substantially different conditions have to be satisfied [85]. Because of this, identifying the critical humidity corresponding to the condensation, it is possible to determine the radius of the pores of a thin film. Upon condensation, indeed, the refractive index of the film changes and the ellipsometer detects this modification. In the same way, when the liquid evaporates from the porosity, the ellipsometry can detect the return of the refractive index to the original value. If a closed chamber is built around the sample (Figure.III-11a) the relative

humidity can be varied continuously and the refractive index measured at various humidity values. It is then possible to detect the exact humidity for which condensation takes place.

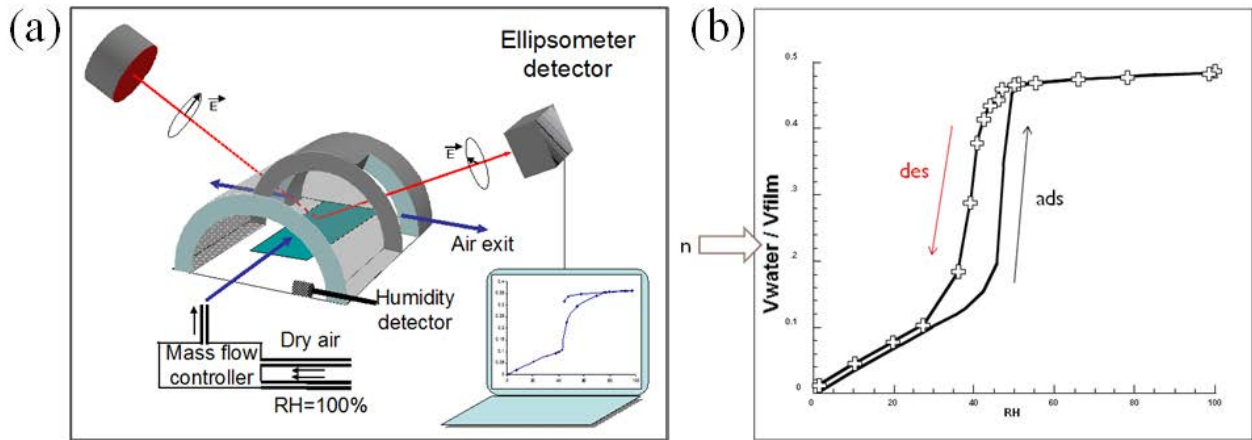


Figure.III-11.(a) scheme of the Environmental-Ellipsometer. A mass flow controller is used to mix humid and dry air controlling in this way the humidity inside a closed chamber. The refractive index of the film contained in the chamber is measured in real time by ellipsometry. **(b)** typical EEP profile of a porous thin film. The adsorption of water takes place at higher humidity than desorption. The explanation of this effect is reported in the main text.

In Figure.III-11b it is reported a typical EEP profile of a porous thin film. The adsorption of water (in this case) and then condensation takes place at a higher humidity value in respect of the desorption (evaporation). This should correspond, in first instance, to two different radius of the pores which seems to be inconsistent. Actually this phenomenon can be understood if it is considered that the pores have connection between them whose diameter is smaller than the pore one. In Figure.III-12 it is reported a scheme linking the state of the porosity with the already reported EEP cycle. In dry air the porosity is completely empty (Figure.III-12 point A). When some water in the vapor phase is added a layer of condensed water is formed inside the porosity leaving empty the center of the pores. This increase slightly the refractive index that augment linearly with the relative humidity. When the critical humidity is attained the pores fill suddenly and the refractive index has a vertical step. Then a plateau is reached corresponding to the filled pores (Figure.III-12point B). When the humidity is decreased the pores are already filled. The interface with the air consists of the pore interconnections thus the filled configuration is maintained till the critical humidity corresponding to the connections (and not the pore itself) diameter is reached. The diameter of the interconnection can then be determined too. When the water starts to evaporate from the interconnections all the pores suddenly empty because liquid water is unstable at this humidity. Then the porosity remains with some liquid layer in the porosity that decreases till an empty configuration. The profile forms a hysteresis. The wider it is the larger is, in general, the difference between the pore and the pore interconnection radius (also called bottle-neck). This particular importance of this will be explained in Chapter IV. As a final

notice it has to be said that if more than a single layer composes a thin film the two layers can be modeled independently and the pore sizes of each one determined.

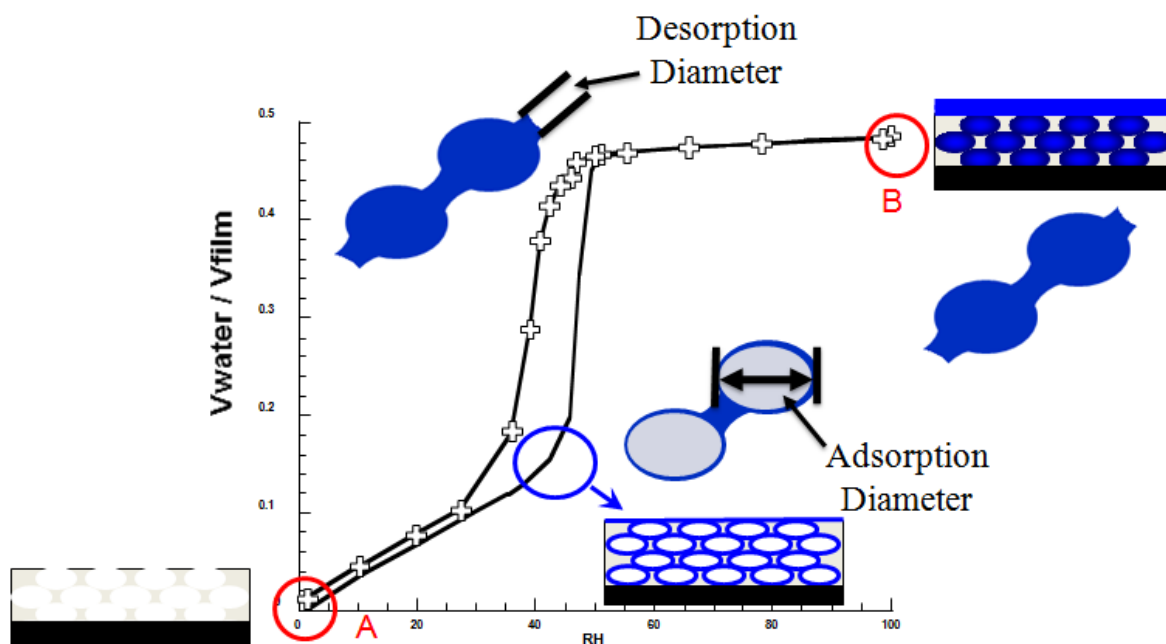


Figure.III-12.Scheme linking the state of the porosity with the refractive index reported in an EEP cycle

In this chapter EEP profiles have been utilized to determine the pore size and pore interconnection sizes of all the samples that are hereafter presented.

III.2.b Non-organized porosities

The non-organized samples utilized in the next chapter have all been realized in the following way. The same solution composed 2.26 g of TEOS(TetraEthylOrthoSilicate – Aldrich), 1.1g of HCl 0.5M, and 60 g THF was utilized to dissolve the various block-copolymers. Different times of stirring for this solution before and after mixing with the block copolymers were utilized and are reported in Table.III-1. Samples with one or more * need further experimental details. SEM-FEG and EEP measurement were utilized as main instruments of investigation to determine the pore structure. The solutions have been used for dip-coating at a withdrawal speed of 10 mm.s⁻¹. The deposition has then been followed by calcination under IR lamps (450 °C for 10 min). The surface energy can be considered constant in first approximation.

Films were labeled XN with X corresponding to the block copolymer responsible of the porosity in the sample followed by the label N corresponding to the order of appearance in the Figures of

the next sections. The main information for the synthesis of the film utilized in this section (component amounts, block copolymer types, and stirring times are reported in Table.III-1.

Sample PS2 indicated by a * has been prepared utilizing a mixture of THF (75%) and Acetone (25%) in the initial sol-gel solution. This modifies the final porosity as will be illustrated in the following figures. Sample PS6 has been prepared normally but upon addition of the block-copolymer 1g of THF has been added too. Sample F1 has been prepared without using the mentioned sol-gel solution in THF. An ethanol based sol-gel solution has been used instead. The TEOS and HCl are indicated in Table.III-1 but 17.5g of ethanol have been used as solvent.

Sample	TEOS (g)	HCl 0.5 M (g)	THF (g)	Initial stirring	BCP type	BCP (g)	Final stirring
PS1	0.113	0,055	3,000	-	PS(80k)-b-PEO(52k)	0.04	12 hours
PS2*	0.113	0,055	3,000	-	PS(80k)-b-PEO(52k)	0.04	12 hours
PS3	0.358	0,174	3,168	4 days	PS(80k)-b-PEO(52k)	0.042	3 days
PS4	0.290	0,141	2,566	4 days	PS(80k)-b-PEO(52k)	0.068	3 days
PS5	0.295	0,144	2,611	4 days	PS(80k)-b-PEO(52k)	0.105	3 days
PS6**	0.290	0,141	2,566	4 days	PS(80k)-b-PEO(52k)	0.102	6 hours
Bj1	0.358	0,174	3,168	4 days	Brij C10	0.187	2 days
Bj2	0.290	0,141	2,566	4 days	Brij C10	0.102	1 day
Bj3	0.557	0,271	4,929	4 days	Brij C10	0.392	2 days
F1***	1.940	1,04**	17,5**	-	F127	0.52	12 hours
F2	0.290	0,141	2,566	4 days	F127	0.102	1 day
PBd1	0.374	0,182	3,310	2 days	Pbd(11.8k)-b-PEO-(61k)	0.130	1 day
PBd2	0.474	0,231	4,195	15 days	Pbd(6k)-b-PEO(12k)	0.166	2days
PS7	0.290	0,141	2,566	1 day	PS(16.4k)-b-PEO(36.4k)	0.102	1 day
PBd3	0.340	0,165	3,009	2 days	Pbd(40k)-b-PEO(60k)	0.117	1 day
PBd4	0.347	0,169	3,071	1 day	Pbd(32k)-b-PEO(43.5k)	0.130	1day
Bj4	0.450	0,219	3,982	4 days	Brij C10	0.052	2 days
Bj5	0.368	0,179	3,257	4 days	Brij C10	0.086	2 days
PS8	0.350	0,170	3,097	4 days	PS(40k)-b-PEO(38k)	0.122	3 days

Table.III-1 Amount of inorganic solution, block copolymer and stirring time for the solutions used for the preparation of all the samples. See description in the text for *, ** and *.**

In Table.III-2 are reported the characteristics of the porosity of the various samples. The samples are ordered in function of the water filling speed that will be introduced in the next Chapter. Its role here is just to illustrate the wide range of pore sizes and porous volumes that have been realized in this thesis. In general because EEP is not appropriated to determine pore size above 50

nm [85], estimation from SEM images was used when capillary condensation occurred above 95% RH. Thus, in this case, pore diameter is determined evaluating SEM-FEG images of the samples.

The symbol * is used in Table.III-2 when the corresponding value has not been determined. In all cases the inorganic material of the films is composed by SiO₂ and with the exception of samples PS3, PS4, Bj4 and Bj5 the organic/inorganic ratio of the solution used for the deposition step has the same value for all samples (see Table.III-1).

The pore structure of all these samples is formed through the EISA mechanism. Due to the high humidity needed to achieve condensation pore size has been evaluated by SEM.

Sample	Ads. RH(%)	Des. RH(%)	SEM diam. (nm)	Ad. Diam. (nm)	Des. Diam. (nm)	Δ RH(%)	Por. Vol. (%)
PS6	99.4	97	180±40	*	*	2.4	59
PS5	97.9	97.5	75±20	*	*	0.4	54
PS1	96.8	96.5	60±10	*	*	0.3	64
PPN	93.4	91.5	20±4	17.1 ^s	15.2 ^s	1.9	86
Bj1	63.5	52.4	*	5.2	3.8	11.1	58
Bj2	59.3	48.0	*	4.6	3.4	11.3	59
Bj3	69.3	57.8	*	6.3	4.4	11.5	61
F1	68.9	48.0	*	6.2	3.4	20.9	55
F2	75.0	49.2	*	7.8	3.5	25.8	55
PBd1	83.5	33.0	*	12.0	2.3	50.5	50
PBd2	80.6	27.0	*	10.2	2.0	53.6	50
PS7	88.5	42.9	*	17.5	3.0	45.6	55
PBd3	91.8	55.4	*	24.3	4.1	36.4	53
PBd4	93.0	60.9	*	27.5	4.8	32.1	53
PS2	96.0	55.4	60±5	*	4.1	40.6	63
PS3	93.3	50.5	*	29.9	3.6	42.8	33
PS4	95.8	69.4	50±10	*	6.3	26.4	47
Bj4	37.0	22.8	*	2.6	1.8	14.2	32
Bj5	43.0	39.2	*	3.0	2.7	3.8	46
PS8	95.2	71.4	55±15	*	6.8	23.8	47

Table.III-2. Structural and capillary filling properties and of the different films used in this study. Sample names are coded in function of the block-copolymer used for the film synthesis. Humidity of adsorption and desorption in EEP cycles are reported. The pore diameters have been determined either with SEM (for samples with Ads. RH and Des. RH higher than 95 (%)) or though the method reported in [85] from EEP isotherms. The SEM diameter like the adsorption diameter corresponds to the actual diameter, the desorption diameter is instead an evaluation of the pore bottle-necks. Δ RH is reported in order to evaluate the hysteresis width. The porous volume is expressed in % of the whole film volume.

Films with large and open porosities are reported in Figure.III-13. This kind of porosity can be mainly attributed to phase separation. It is characterized by a low difference in pore size determined by the adsorption and desorption branch of the EEP isotherms. As it will be illustrated in the next chapter this has important consequence on the infiltration of liquids in the porosity.

In Figure.III-14 and Figure.III-15 we show various films whose porosity is smaller. The size of the pores determined by the two branches is different as it can be inspected in EEP cycles. These porosities are characterized by a micellar structure as it can be seen in SEM images.

To conclude in Figure.III-16 and Figure.III-17 we report films with a particularly large difference between the pore dimensions determined by the two branches or with a low porous volume. In the next chapter these elements will be identified as key ones to determine or avoid capillary infiltration. In particular the role of the desorption pore size, which can be seen as a bottle-neck size, will be illustrated.

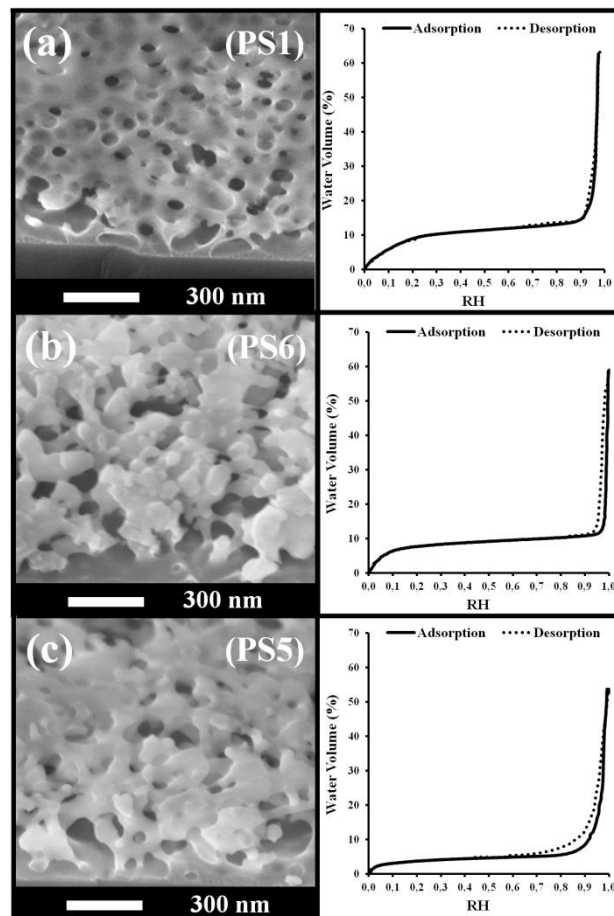


Figure.III-13. SEM images and corresponding EEP adsorption/desorption isotherms (water volume versus relative humidity) of the PS1, PS5 and PS6 samples (top section of Table.III-2).

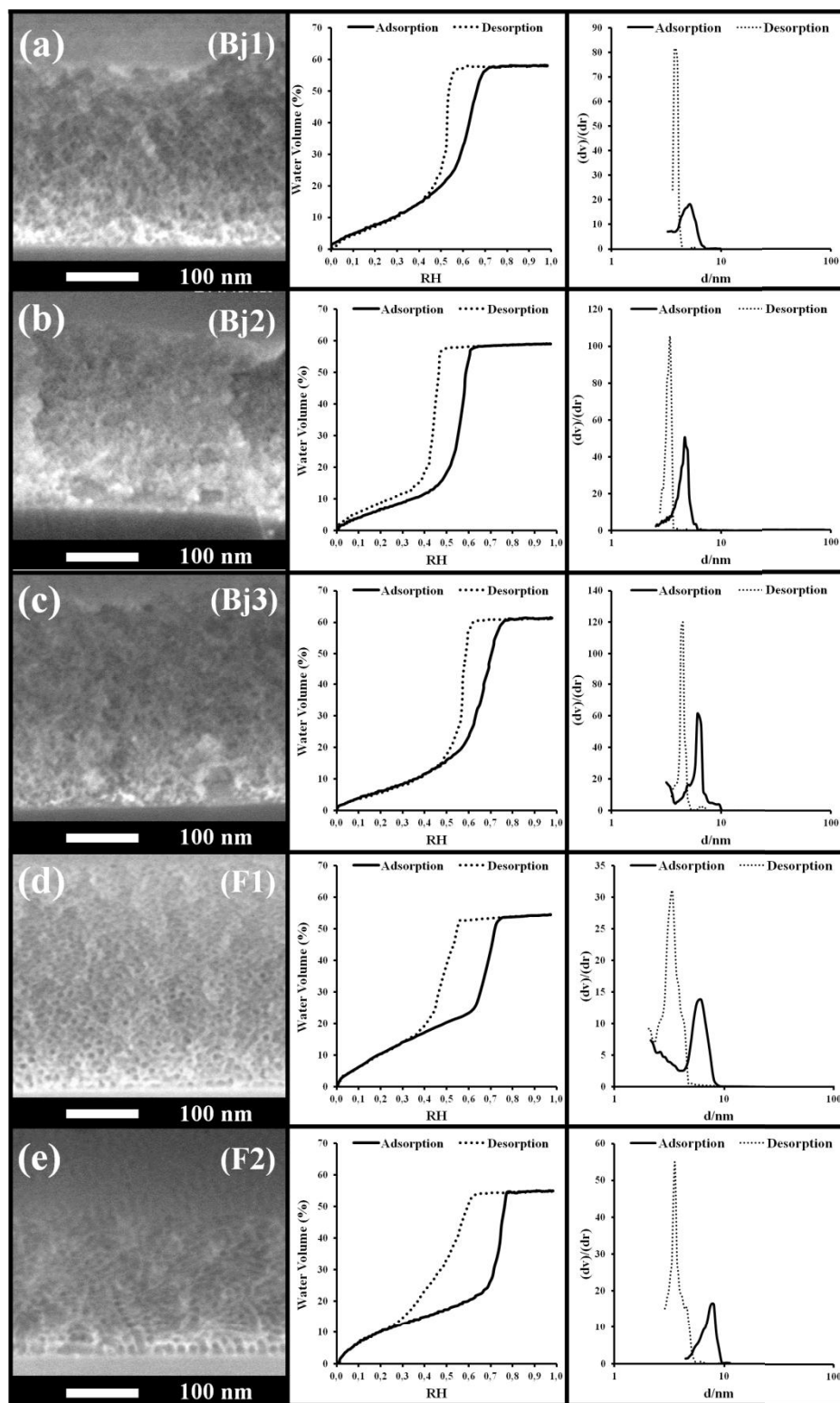


Figure.III-14. left) SEM images, center) EEP adsorption/desorption isotherms (water volume versus relative humidity) and right) pore size distribution of the Bj1, Bj2, Bj3, F1 and F2 samples of the intermediate section of Table.III-2.

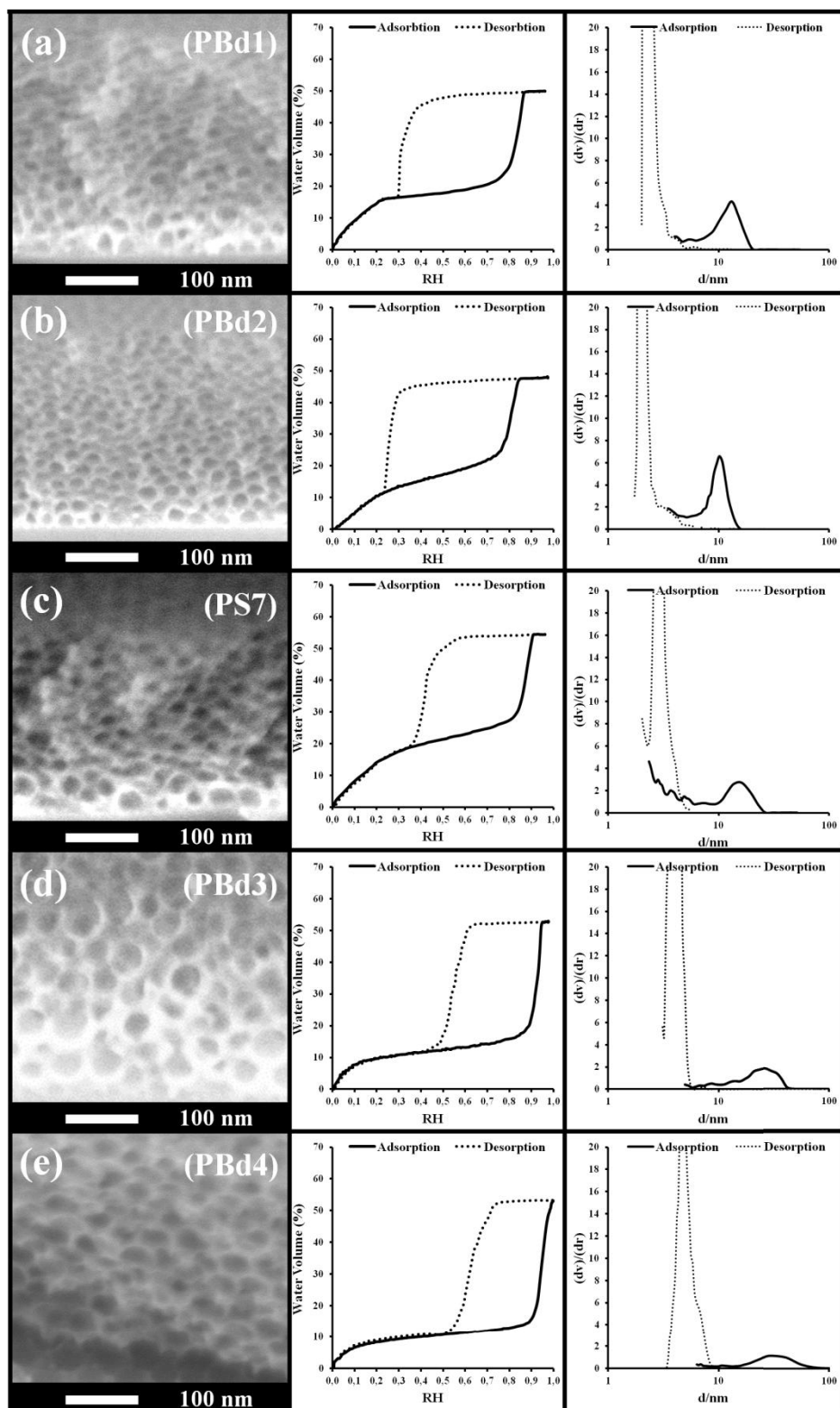


Figure.III-15. left) SEM images, center) EEP adsorption/desorption isotherms (water volume versus relative humidity) and right) pore size distribution of the PBd1, PBd2, PS7, PBd3 and PBd4 samples of the intermediate section of Table.III-2.

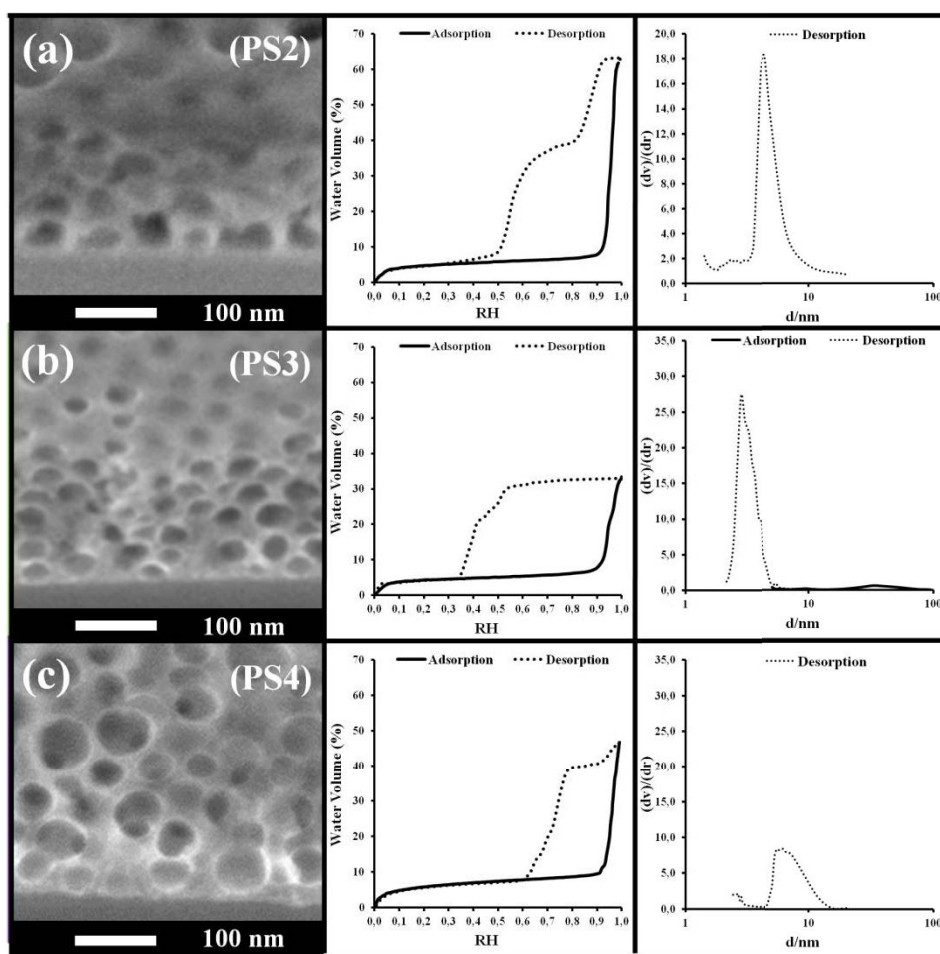


Figure.III-16. left) SEM images, center) EEP adsorption/desorption isotherms (water volume versus relative humidity) and right) pore size distribution of the PS2, PS3, PS4 samples of the third section of Table.III-2.

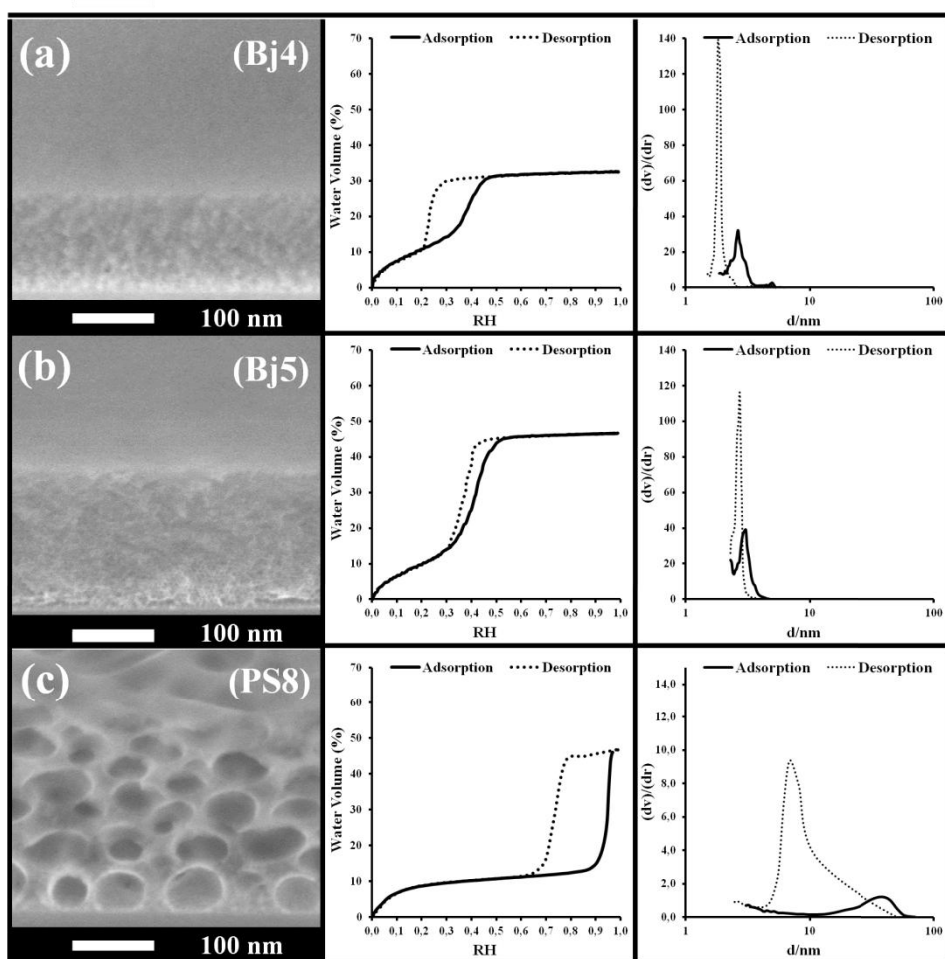


Figure.III-17 left) SEM images, center) EEP adsorption/desorption isotherms (water volume versus relative humidity) and right) pore size distribution of the Bj4, Bj5, PS8 samples of the third section of Table.III-2.

III.2.c Pillared Planar Nanochannels

In this section the fabrication of the pillared planar nanochannels (PPN) already introduced in Chapter I is discussed [86]. As it will be shown, PPNs is particularly adapted for nanofluidic applications and it is easily modelisable at a theoretical and simulation level. These aspects are particularly important because this structure can be studied and analyzed in order to understand the phenomena taking place at the nanoscale. PPN samples have been utilized for studies about capillary infiltration that are reported in the next chapter. They are also the main material used for nanofluidic experiments involving the diffusion and reaction of species in nanoconfined environment as shown in Chapter V.

Their preparation is composed of two steps :(i) the self-assembly of a block copolymer in order to obtain nanoporous polystyrene film templates and (ii) inorganic replica by sol-gel deposition and calcination.

III.2.c.i Preparation of the nanoporous Polystyrene films

As mentioned, the first step is based on the self-assembly of a block-copolymer in order to obtain PS films bearing vertical cylindrical pores. The choice of the block-copolymer determines the final morphology of the nanostructure being the size of the periodical patterns determined by the chains chemistry and length as exposed in the previous chapter. The two block-copolymer used in this thesis are poly(styrene)-block-poly(lactide) (PS(55k)-b-PLA(35k)) and poly(styrene)-block-poly(2vinylpyridine) (PS(290k)-b-P2VP(72k)). They have been selected from previous publications, the first due to its extremely high level of organization over large surfaces [87] and the second due to its commercial availability[88].

Two slightly different procedures have been utilized to produce PPNs from different block-copolymers with different structure characteristics. The two processes are resumed in Figure.III-18.

In the case of (PS-b-PLA) a solution in chlorobenzene (concentrations of the order of 20 mg/mL) is spin coated on a silicon wafer treated with HMDS (if the surface is not treated the final morphology is completely different) and then exposed to THF vapor for 4-5 minutes to orient the cylindrical PLA domains vertically to the surface and into a 2D-hexagonal structure as shown in Figure.III-18 (left side).

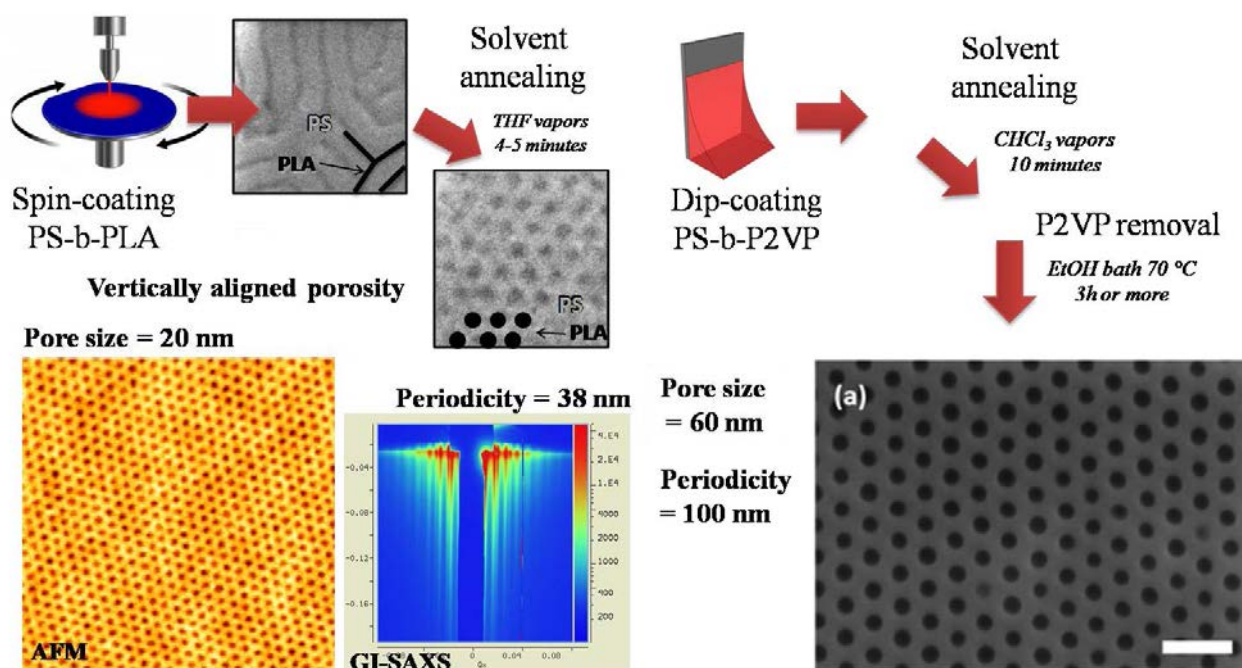


Figure.III-18.(Left) deposition and analysis of the PS-b-PLA thin film. After spin-coating the film is annealed in THF for 4-5 minutes. The organization is checked by AFM (1 μ m border size) and GI-SAXS. Pore size is found to be 20 nm and the center to center distance 38 nm. (Right) [88] in the case of PS-b-P2VP the dip-coating deposited film is annealed in chloroform for 10 min. After removal of the P2VP part pore size is found to be 60 nm and the periodicity 100 nm (scale bar 200 nm). The P2VP removal influences the pore size as reported in the text.

The spin-coating step requires an acceleration/spreading step with 15s at 300 rpm followed by 40s at a speed varying from 1000 to 3000 rpm as function of the desired final thickness (this has been the only use of spin-coating in this thesis, if more information are needed about the technique and the dependence on the operation parameters [89] and [90] are signaled). After solvent annealing, PLA domains can be easily removed by hydrolysis in a NaOH solution for 30 min. Treatment time is important. For shorter times not all the PLA is removed causing structure failures in the next step of the synthesis while for longer ones the Si substrate can be attacked and dissolved causing the detachment of the PS layer.

In the case of the PS-b-P2VP block copolymer, the deposition has been performed by dip-coating in particular with the droplet-biphasic dip-coating method with solutions in the same concentration range (Figure.III-18, right side). Chlorobenzene, dichloromethane and chloroform were tested as deposition solvents. Chlorobenzene is proved to be the best solvent to obtain uniform film thickness due to its lower volatility. Unfortunately the films obtained using this solvent does not reach the desired level of organization. Films obtained from dichloromethane and chloroform are much better organized at the end of treatment. In particular dichloromethane was identified as the best solvent. Annealing is then performed for 10 min in chloroform vapors in

order to orient the cylindrical P2VP domains vertically to the surface and into a 2D-hexagonal structure.

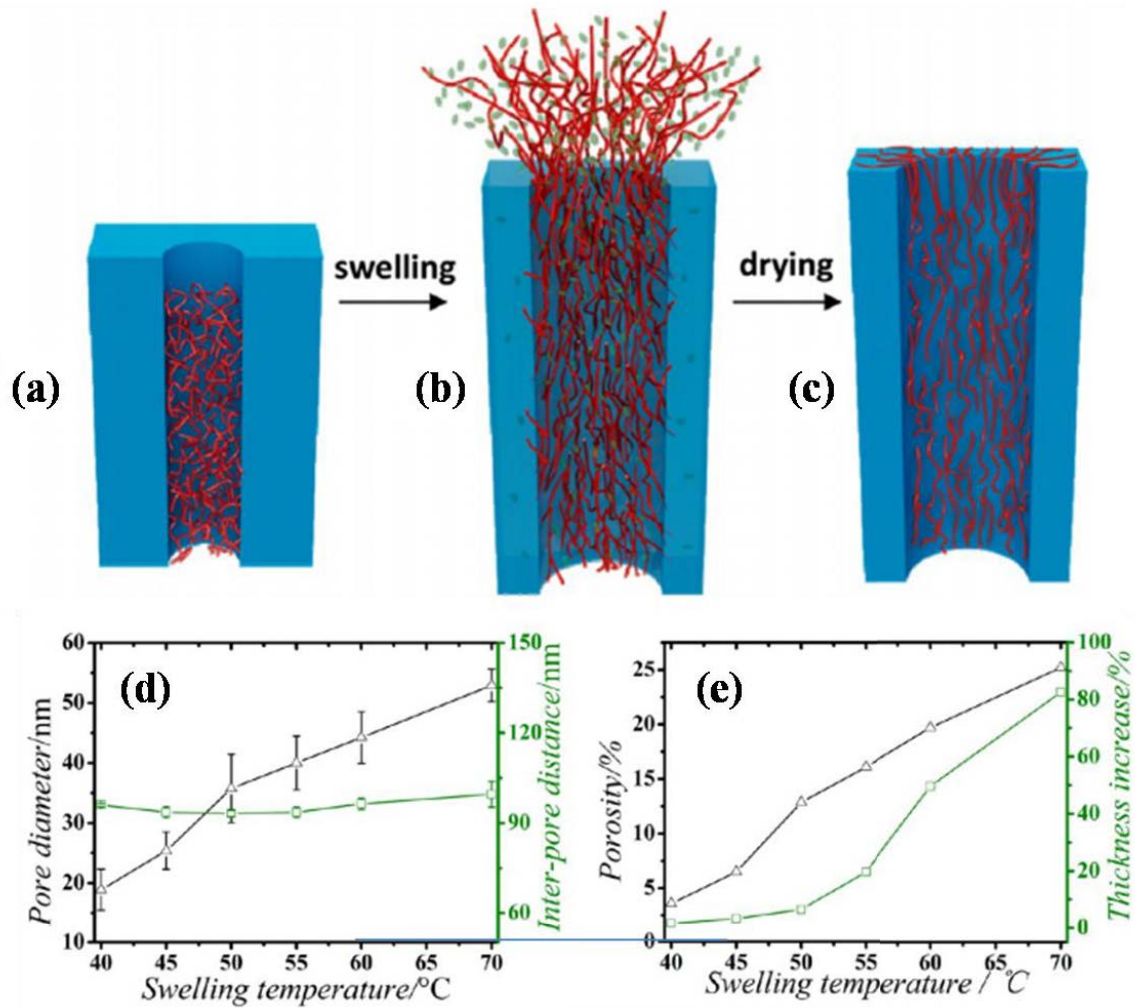


Figure. III-19. [88] (a-c) mechanism of pore opening / P2VP removal in the PS-b-P2VP thin films in presence of hot ethanol. The ethanol swells selectively the P2VP block that is partially extracted by the PS matrix. (d) increase in pore diameter (conserving the inter-pre distance and then periodicity) in function of ethanol swelling temperature obtained by GI-SAXS. (e) Increase in thickness and film porosity due to the deformation of the PS matrix caused by the P2VP swelling.

In the case of the P2VP part the block is not really removed or dissolved. The thin film is indeed plunged in hot ethanol for at least two and a half hours. The P2VP part, being soluble in ethanol, selectively swells and due to its higher volume is partially extracted (Figure. III-19b) from the pore (causing a deformation of the PS matrix too; the thickness increase due to this effect is reported in Figure. III-19e). Upon drying the chains remain at the exterior of the pore (Figure. III-19c) leading pores with size varying from 20 to 50 nm in function of the ethanol temperature (Figure. III-19d).

III.2.c.ii Sol-gel replica

For both block-copolymers then the resulting nanoporous PS film is infiltrated with a sol-gel solution containing the inorganic precursors and structuring agents by dip-coating. After calcination, the structure obtained consists of nanopillars covered by a roof of the same composition.

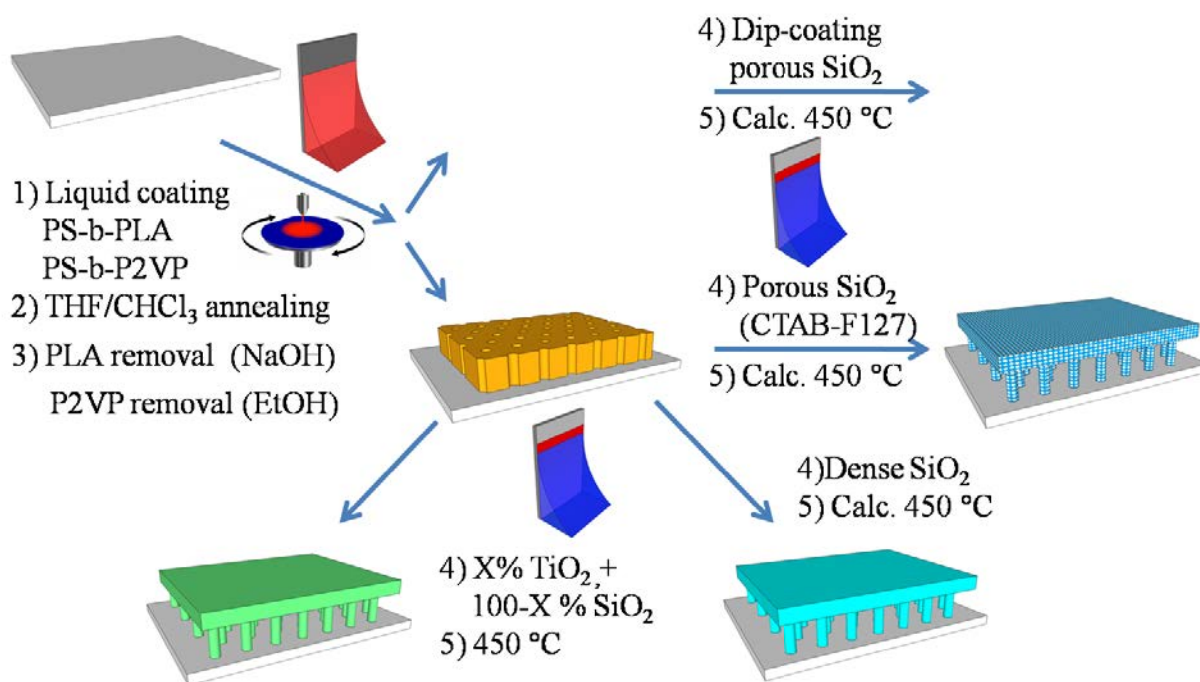


Figure.III-20.Preparation procedure of the PPN: PS-b-PLA or PS-b-P2VP layer is first deposited on a Si substrate with a controlled thickness. After annealing in THF or CHCl₃ vapor respectively and PLA/P2VP removal with NaOH or hot ethanol, an ordered PS porous film is obtained that is then used as hard template. A sol-gel replication process is then applied to obtained PPN with different SiO₂-TiO₂ compositions, mesoporosity and pillar height.

The thickness of the roof can be adjusted by deposition of excess of sol-gel precursors. Mesoporosity has been introduced in the some of the silica pillars using CTAB as a template. The whole procedure is reported in Figure.III-20 in a simple scheme. The sol-gel material used to form the final structure can have various compositions. This can allow studying the influence of the material composition on various nanofluidic phenomena. It has anyway to be noticed that as function of the sol-gel material utilized, different thermal treatment are necessary in order to avoid cracks in the structures. In general soft ramps are preferable. The temperature of 300 °C is sufficient to burn the most part of the PS matrix but some carbonates are conserved (modifying the surface properties) which need temperatures higher than 400 °C (usually 450 °) to be completely eliminated.

III.2.c.iii PPN from PS-b-PLA analysis

Figure.III-18(left) of the previous section shows an AFM image of the initial PS-b-PLA film and a GI-SAXS of the porous PS film. In

Figure.III-21a the GI-SAXS pattern obtained from the final ceramic SiO₂film are shown. In the intensity profile plot, the q -value of the diffraction was found at 0.192 nm^{-1} , which corresponds to a periodicity of $d_{(10)} = 33 \text{ nm}$ and a center-to-center distance of 38 nm , in agreement with the AFM data.

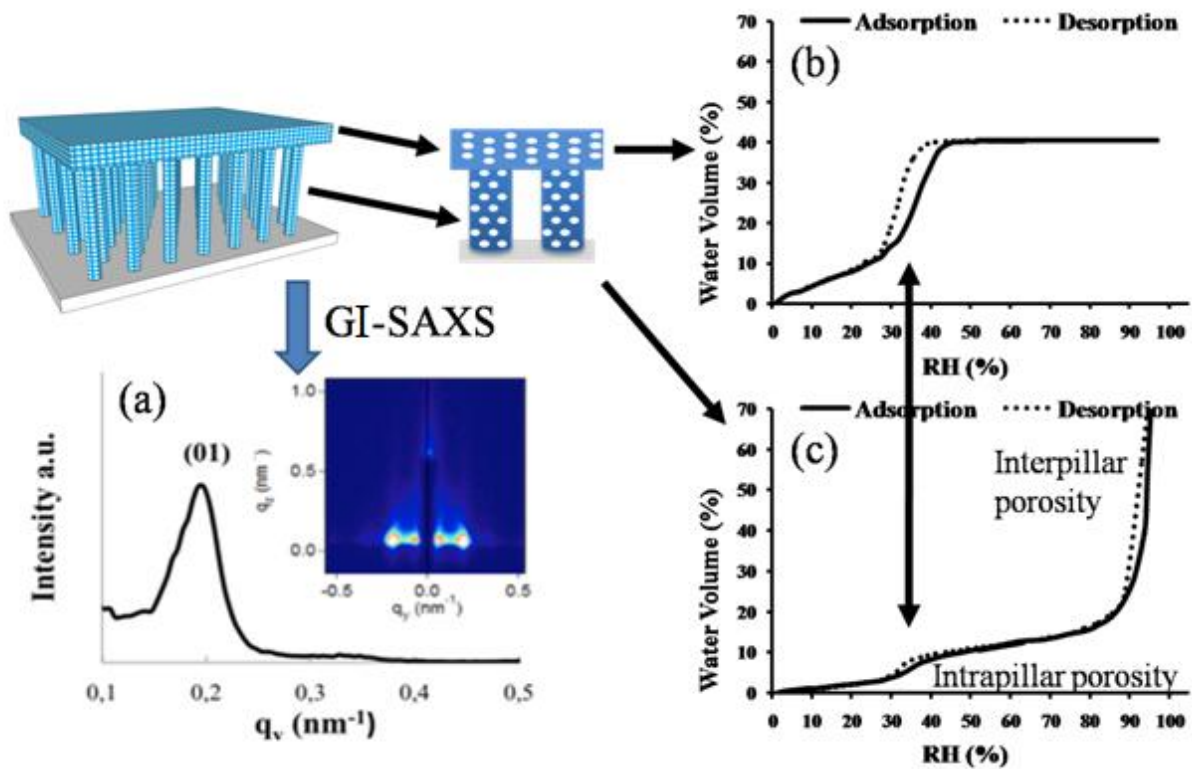


Figure.III-21. (a) GI-SAXS pattern and lateral intensity profile a typical dense SiO₂ PPN sample.(b)and (c) Adsorption/desorption isotherm of the roof and pillared layer respectively of a typical mesoporous SiO₂ PPN (in that case the pillars are composed of mesoporous silica template with CTAB).

The interpretation of EEP investigation requires modeling PPN using a two “layer” model consisting of the roof and the pillar arrays. The adsorption/desorption isotherm of the bottom layer only of a typical mesoporous silica PPN film is shown in

Figure.III-21c. The low pressure increase in refractive index is attributed to the pillar inner mesoporosity created by the CTAB template, and the high pressure increase in refractive index is attributed to the inter-pillar porosity taking place above 90% RH. In the range of humidity > 90%, determination of the interpillar pore size is difficult since a slight shift of the critical humidity of capillary condensation (sensor nominal error: $\pm 2\%$) induces a significant change in the estimated pore dimension. In any case the interpillar pore sizes is evaluated being around 17 and 15 nm for

adsorption and desorption using a cylindrical model [85]. A narrow hysteresis loop is present on the main large porosity. As will be shown in the next chapter this is clue of a fully interconnected network, ideal for capillary-driven flow. The porosity of the roof was also evaluated as shown in EEP analysis of (Figure.III-21b).that evidences the presence of typical mesoporosity obtained by CTAB templating (as into the pillars).

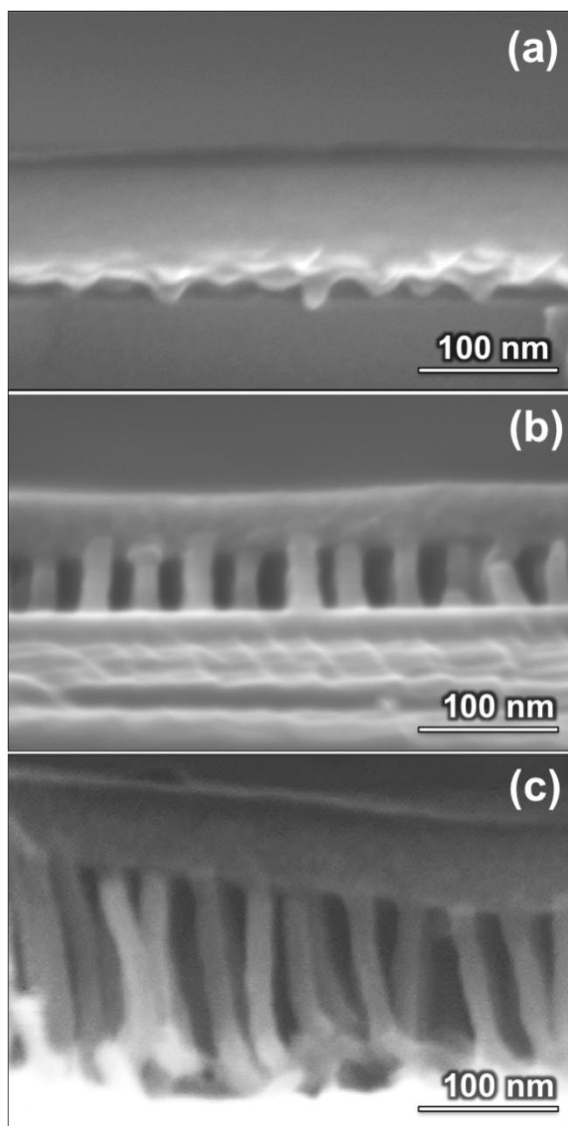


Figure.III-22.SEM-FEG images of 3 different SiO₂ PPN samples obtained from PS-b-PLA: the pillar height can be tuned by changing the initial PS-b-PLA layer thickness. (a) 12nm dense SiO₂, (b) 60 nm dense SiO₂ and (c) 202 porous SiO₂.

Adjusting the PS-b-PLA initial thickness allows tuning the final pillar height. In the same way the thickness of the roof can be adjusted by deposition of excess of sol-gel precursors.

Figure.III-22 displays cross sectional SEM images of three samples, all exhibiting the characteristic PPN pillar/roof morphology with a constant pillar diameter of 20 ± 1 nm but differing by their thicknesses. The thicker sample was made of mesoporous silica while the two

thinner ones were composed of dense silica. The fact that the taller pillars are less ordered was attributed to the higher aspect ratio that render the whole structure more fragile during cutting for observation and to thickness dependent effects. Ordered films, indeed, were never obtained for thickness larger than 220 nm probably because for large film thickness the kinetics of organization or the equilibrium structure are different from the thinner case.

III.2.c.iv PPN from PS-b-P2VP analysis

The structure obtained from PS-b-P2VP just after removal of the P2VP has been analyzed in literature [88]. In that case the thin polymeric film has been deposited by spin-coating while during this thesis dip-coating (biphasic droplet method) has been preferred for the already mentioned motivations of waste reduction. The domain's organization after annealing is a bit less perfect with respect to the literature samples. This can be due to the different deposition technique (that develops different strains on the block-copolymer) or to a variation of the annealing dynamics due to the use of a different annealing chamber (that is not reported).

Due to the increased periodicity size, GI-SAXS patterns cannot be obtained on the GI-SAXS instruments available in our laboratory being the maximum distance of the detector limited. The scattering angle corresponding to a periodicity of around 100 nm is indeed at around 0.062 nm^{-1} which is not large enough to create clearly distinguishable and isolated spots. In the same way, for large porosity, the water adsorption in EEP takes place at a value of humidity next to 100%. For these values, the 2% error due to the sensor produces a too large incertitude to really evaluate the pore size. For the roof layer results similar to the ones exposed for the PS-b-PLA samples are obtained.

SEM-FEG is then the only technique that allows to check the porous structure of the pillared layer and verify the size reported in literature and Figure. III-19. Various tests have been realized varying the film thickness and substrate material. Thicknesses up to 2 μm have been produced with a reasonable level of organization. Decreasing degree of ordering was obtained by performing self-assembly on silicon, gold, glass and steel substrates (in this order). The fact that gold is suitable as substrate for this block-copolymer is extremely important. It is indeed possible, in this way, to easily realize electrodes in direct contact with the solution (on the ground of the channel). In Figure. III-23 are reported various PPN samples with different heights and substrates. Images both at 90° and 45° are reported as function of the sample. In particular PPNs created on glass and steel cannot be analyzed at 90° because of the impossibility to have a neat cut that does not destroy the structure. Finally as a test, using a PS porous film deposited on gold, copper PPNs

have been produced by electrodeposition. The PS matrix was removed after formation of the copper pillars by dissolution in chloroform in order to avoid the oxidation of the metal (as can be seen in Figure.III-23f).The procedure was not optimized (in particular the electrodeposition step requires a good control of electric intensity and deposition time) but this example demonstrates the possibility to extend the range of materials that can be shaped by this approach.

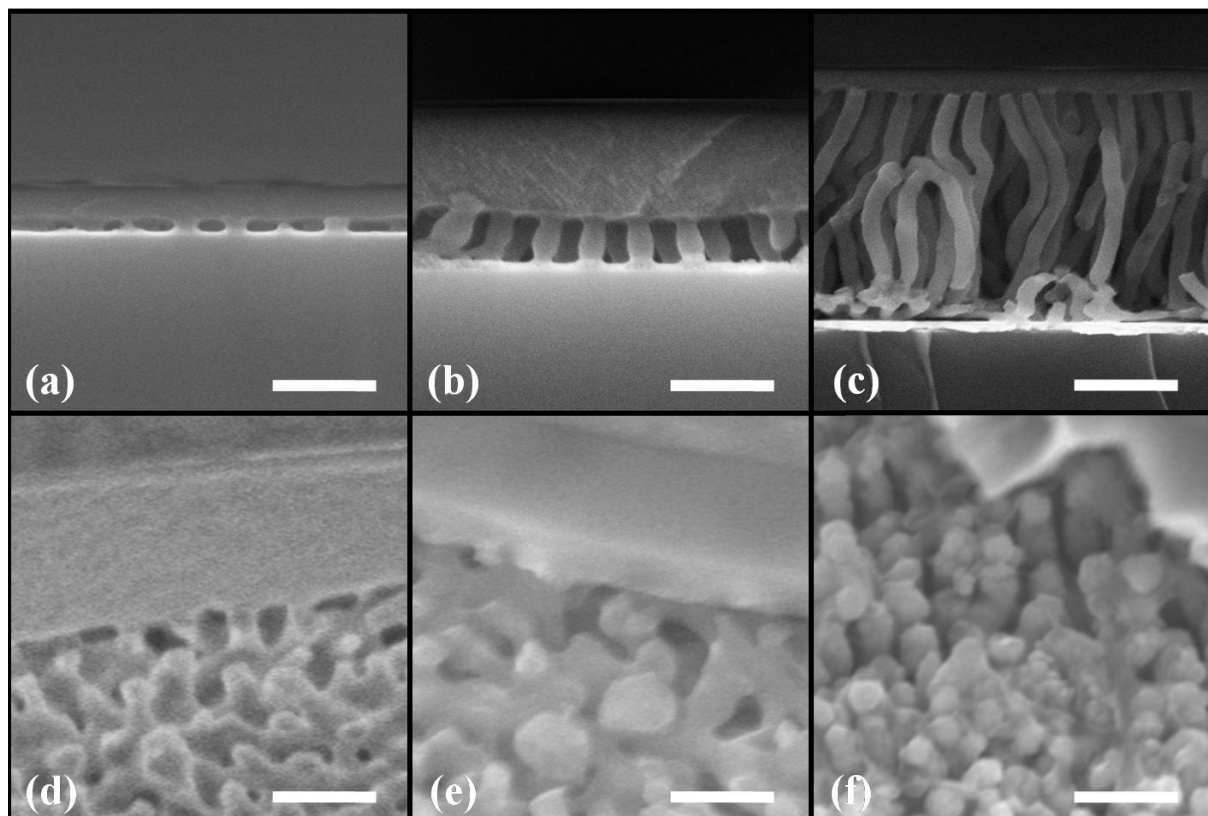


Figure.III-23 SEM-FEG images of various PPN samples obtained from PS-*b*-P2VP block copolymer. (a-b): the pillar height can be tuned by changing the initial PS-*b*-P2VP layer thickness. (a) 50nm porous SiO₂ on Si, (b) 140 nm porous SiO₂ on Si,(c) 800 nm porous SiO₂ on gold,(d) 45° image porous SiO₂-TiO₂-9-1 on glass, (e) 45° image porous SiO₂-TiO₂-9-1 on steel, (f) 45° image metallic Cu on gold with traces of PS; in this case the roof is not plane (not shown). Scale bars (a) 100 nm, (b) 250 nm, (c) 500 nm, (d) 200 nm, (e) 200 nm, (f) 200 nm.

III.2.d Conclusion

The synthetic strategies to obtain the nanoporous materials exploited in this thesis have been presented in this chapter. The main concepts of sol-gel, block-copolymer self-assembly and Evaporation Induced Self Assembly have also been introduced. These elements constitute a useful tool for further discussions. Particular attention has to be paid on the particularity of the PPN structure. As it will be shown in the next chapters, it is extremely adapted to allow fast penetration of liquids and solutes. It also permits the modeling thanks to its periodical organization which can help to have a deeper understanding on nanofluidic phenomena.

III.3 Bibliography

- [1] C. J. B. and G. W. Scherer, *Sol-gel science, the physics and chemistry of sol-gel processing*, vol. 3, no. 10. Boston: Academic Press, 1990.
- [2] L. J., *Sol-Gel Technologies for Glass Producers and Users*. Springer, 2004.
- [3] C. J. Brinker, "Hydrolysis and condensation of silicates: Effects on structure," *J. Non. Cryst. Solids*, vol. 100, no. 1–3, pp. 31–50, Mar. 1988.
- [4] W. Stöber, A. Fink, and E. Bohn, "Controlled growth of monodisperse silica spheres in the micron size range," *J. Colloid Interface Sci.*, vol. 26, no. 1, pp. 62–69, Jan. 1968.
- [5] C. Sanchez, C. Boissiere, S. Cassaignon, C. Chaneac, O. Durupthy, M. Faustini, D. Grosso, C. Laberty-Robert, L. Nicole, D. Portehault, F. Ribot, L. Rozes, and C. Sasse, "Molecular Engineering of Functional Inorganic and Hybrid Materials," *Chem. Mater.*, vol. 26, no. 1, pp. 221–238, Jan. 2014.
- [6] M. Faustini, C. Boissière, L. Nicole, and D. Grosso, "From Chemical Solutions to Inorganic Nanostructured Materials: A Journey into Evaporation-Driven Processes," *Chem. Mater.*, vol. 26, no. 1, pp. 709–723, Jan. 2014.
- [7] G. J. de A. A. Soler-Illia, C. Sanchez, B. Lebeau, and J. Patarin, "Chemical Strategies To Design Textured Materials: from Microporous and Mesoporous Oxides to Nanonetworks and Hierarchical Structures," *Chem. Rev.*, vol. 102, no. 11, pp. 4093–4138, Nov. 2002.
- [8] Lin Yang and Paschalis Alexandridis, *Controlled Drug Delivery*, vol. 752. Washington, DC: American Chemical Society, 2000.
- [9] J. Zipfel, P. Lindner, M. Tsianou, P. Alexandridis, and W. Richtering, "Shear-Induced Formation of Multilamellar Vesicles ('Onions') in Block Copolymers," *Langmuir*, vol. 15, no. 8, pp. 2599–2602, Apr. 1999.
- [10] R. Ivanova, B. Lindman, and P. Alexandridis, "Effect of pharmaceutically acceptable glycols on the stability of the liquid crystalline gels formed by Poloxamer 407 in water," *J. Colloid Interface Sci.*, vol. 252, no. 1, pp. 226–35, Aug. 2002.
- [11] R. Ivanova, B. Lindman, and P. Alexandridis, "Evolution in Structural Polymorphism of Pluronic F127 Poly(ethylene oxide)–Poly(propylene oxide) Block Copolymer in Ternary Systems with Water and Pharmaceutically Acceptable Organic Solvents: From 'Glycols' to 'Oils' †," *Langmuir*, vol. 16, no. 23, pp. 9058–9069, Nov. 2000.
- [12] P. Holmqvist, P. Alexandridis, and B. Lindman, "Modification of the Microstructure in Poloxamer Block Copolymer–Water–'Oil' Systems by Varying the 'Oil' Type," *Macromolecules*, vol. 30, no. 22, pp. 6788–6797, Nov. 1997.

- [13] R. Ivanova, P. Alexandridis, and B. Lindman, "Interaction of poloxamer block copolymers with cosolvents and surfactants," *Colloids Surfaces A Physicochem. Eng. Asp.*, vol. 183–185, pp. 41–53, Jul. 2001.
- [14] Z. Niu, S. Kabisatpathy, J. He, L. A. Lee, J. Rong, L. Yang, G. Sikha, B. N. Popov, T. S. Emrick, T. P. Russell, and Q. Wang, "Synthesis and characterization of bionanoparticle—Silica composites and mesoporous silica with large pores," *Nano Res.*, vol. 2, no. 6, pp. 474–483, Mar. 2010.
- [15] B. Hatton, L. Mishchenko, S. Davis, K. H. Sandhage, and J. Aizenberg, "Assembly of large-area, highly ordered, crack-free inverse opal films," *Proc. Natl. Acad. Sci. U. S. A.*, vol. 107, no. 23, pp. 10354–9, Jun. 2010.
- [16] T. Coradin, A. Coupé, and J. Livage, "Interactions of bovine serum albumin and lysozyme with sodium silicate solutions," *Colloids Surfaces B Biointerfaces*, vol. 29, no. 2–3, pp. 189–196, Jun. 2003.
- [17] F. Fernandes, T. Coradin, and C. Aimé, "Self-Assembly in Biosilicification and Biotemplated Silica Materials," *Nanomaterials*, vol. 4, no. 3, pp. 792–812, Sep. 2014.
- [18] J. S. Beck, J. C. Vartuli, W. J. Roth, M. E. Leonowicz, C. T. Kresge, K. D. Schmitt, C. T. W. Chu, D. H. Olson, and E. W. Sheppard, "A new family of mesoporous molecular sieves prepared with liquid crystal templates," *J. Am. Chem. Soc.*, vol. 114, no. 27, pp. 10834–10843, Dec. 1992.
- [19] T. Peng, D. Zhao, K. Dai, W. Shi, and K. Hirao, "Synthesis of Titanium Dioxide Nanoparticles with Mesoporous Anatase Wall and High Photocatalytic Activity," *J. Phys. Chem. B*, vol. 109, no. 11, pp. 4947–4952, Mar. 2005.
- [20] Z. Wen, Q. Wang, Q. Zhang, and J. Li, "In Situ Growth of Mesoporous SnO₂ on Multiwalled Carbon Nanotubes: A Novel Composite with Porous-Tube Structure as Anode for Lithium Batteries," *Adv. Funct. Mater.*, vol. 17, no. 15, pp. 2772–2778, Oct. 2007.
- [21] M. Klotz, P.-A. Albouy, A. Ayral, C. Ménager, D. Grosso, A. Van der Lee, V. Cabuil, F. Babonneau, and C. Guizard, "The True Structure of Hexagonal Mesophase-Templated Silica Films As Revealed by X-ray Scattering: Effects of Thermal Treatments and of Nanoparticle Seeding," *Chem. Mater.*, vol. 12, no. 6, pp. 1721–1728, Jun. 2000.
- [22] E. Y. Trofimova, D. A. Kurdyukov, S. A. Yakovlev, D. A. Kirilenko, Y. A. Kukushkina, A. V. Nashchekin, A. A. Sitnikova, M. A. Yagovkina, and V. G. Golubev, "Monodisperse spherical mesoporous silica particles: fast synthesis procedure and fabrication of photonic-crystal films," *Nanotechnology*, vol. 24, no. 15, p. 155601, Apr. 2013.
- [23] L. P. Singh, S. K. Bhattacharyya, G. Mishra, and S. Ahalawat, "Functional role of cationic surfactant to control the nano size of silica powder," *Appl. Nanosci.*, vol. 1, no. 3, pp. 117–122, Jul. 2011.
- [24] P. T. Tanev and T. J. Pinnavaia, "A neutral templating route to mesoporous molecular sieves," *Science*, vol. 267, no. 5199, pp. 865–7, Feb. 1995.

- [25] D. R. Ceratti, M. Faustini, C. Sinturel, M. Vayer, V. Dahirel, M. Jardat, and D. Grosso, "Critical effect of pore characteristics on capillary infiltration in mesoporous films.," *Nanoscale*, vol. 7, no. 12, pp. 5371–82, Mar. 2015.
- [26] D. Zhao, Q. Huo, J. Feng, B. F. Chmelka, and G. D. Stucky, "Nonionic Triblock and Star Diblock Copolymer and Oligomeric Surfactant Syntheses of Highly Ordered, Hydrothermally Stable, Mesoporous Silica Structures," *J. Am. Chem. Soc.*, vol. 120, no. 24, pp. 6024–6036, Jun. 1998.
- [27] M. Faustini, L. Nicole, C. Boissière, P. Innocenzi, C. Sanchez, and D. Grosso, "Hydrophobic, Antireflective, Self-Cleaning, and Antifogging Sol–Gel Coatings: An Example of Multifunctional Nanostructured Materials for Photovoltaic Cells," *Chem. Mater.*, vol. 22, no. 15, pp. 4406–4413, Aug. 2010.
- [28] A. Galarneau, H. Cambon, F. Di Renzo, R. Ryoo, M. Choi, and F. Fajula, "Microporosity and connections between pores in SBA-15 mesostructured silicas as a function of the temperature of synthesis," *New J. Chem.*, vol. 27, no. 1, pp. 73–79, Jan. 2003.
- [29] M. Ogawa, "Formation of Novel Oriented Transparent Films of Layered Silica-Surfactant Nanocomposites," *J. Am. Chem. Soc.*, vol. 116, no. 17, pp. 7941–7942, Aug. 1994.
- [30] C. J. Brinker, Y. Lu, A. Sellinger, and H. Fan, "Evaporation-Induced Self-Assembly: Nanostructures Made Easy," *Adv. Mater.*, vol. 11, no. 7, pp. 579–585, May 1999.
- [31] M. Ogawa, "Preparation of Layered Silica–Dialkyldimethylammonium Bromide Nanocomposites," *Langmuir*, vol. 13, no. 6, pp. 1853–1855, Mar. 1997.
- [32] D. Grosso, F. Cagnol, G. J. de A. A. Soler-Illia, E. L. Crepaldi, H. Amenitsch, a. Brunet-Bruneau, a. Bourgeois, and C. Sanchez, "Fundamentals of Mesostructuring Through Evaporation-Induced Self-Assembly," *Adv. Funct. Mater.*, vol. 14, no. 4, pp. 309–322, Apr. 2004.
- [33] F. Cagnol, D. Grosso, G. J. d. A. A. Soler-Illia, E. L. Crepaldi, F. Babonneau, H. Amenitsch, and C. Sanchez, "Humidity-controlled mesostructuration in CTAB-templated silica thin film processing. The existence of a modulable steady state," *J. Mater. Chem.*, vol. 13, no. 1, pp. 61–66, Dec. 2003.
- [34] C. Sanchez, L. Rozes, F. Ribot, C. Laberty-Robert, D. Grosso, C. Sasse, C. Boissiere, and L. Nicole, "'Chimie douce': A land of opportunities for the designed construction of functional inorganic and hybrid organic-inorganic nanomaterials," *Comptes Rendus Chim.*, vol. 13, no. 1–2, pp. 3–39, Jan. 2010.
- [35] M. Boudot, V. Gaud, M. Louarn, M. Selmane, and D. Grosso, "Sol–Gel Based Hydrophobic Antireflective Coatings on Organic Substrates: A Detailed Investigation of Ammonia Vapor Treatment (AVT)," *Chem. Mater.*, vol. 26, no. 5, pp. 1822–1833, Mar. 2014.
- [36] D. Grosso, F. Babonneau, P.-A. Albouy, H. Amenitsch, A. R. Balkenende, A. Brunet-Bruneau, and J. Rivory, "An in Situ Study of Mesostructured CTAB–Silica Film Formation

- during Dip Coating Using Time-Resolved SAXS and Interferometry Measurements,” *Chem. Mater.*, vol. 14, no. 2, pp. 931–939, Feb. 2002.
- [37] D. Grosso, F. Babonneau, G. J. D. a a Soler-Illia, P.-A. Albouy, and H. Amenitsch, “Phase transformation during cubic mesostructured silica film formation,” *Chem. Commun.*, no. 7, pp. 748–749, Mar. 2002.
- [38] D. Grosso, a. R. Balkenende, P. a. Albouy, A. Ayrat, H. Amenitsch, and F. Babonneau, “Two-Dimensional Hexagonal Mesoporous Silica Thin Films Prepared from Block Copolymers: Detailed Characterization and Formation Mechanism,” *Chem. Mater.*, vol. 13, no. 5, pp. 1848–1856, May 2001.
- [39] P. Innocenzi, L. Malfatti, T. Kidchob, S. Costacurta, P. Falcaro, M. Piccinini, A. Marcelli, P. Morini, D. Sali, and H. Amenitsch, “Time-Resolved Simultaneous Detection of Structural and Chemical Changes during Self-Assembly of Mesostructured Films,” *J. Phys. Chem. C*, vol. 111, no. 14, pp. 5345–5350, Apr. 2007.
- [40] N. Krins, J. D. Bass, D. Grosso, C. Henrist, R. Delaigle, E. M. Gaigneaux, R. Cloots, B. Vertruyen, and C. Sanchez, “NbVO₅ Mesoporous Thin Films by Evaporation Induced Micelles Packing: Pore Size Dependence of the Mechanical Stability upon Thermal Treatment and Li Insertion/Extraction,” *Chem. Mater.*, vol. 23, no. 18, pp. 4124–4131, Sep. 2011.
- [41] C. Sassoey, C. Laberty, H. Le Khanh, S. Cassaignon, C. Boissière, M. Antonietti, and C. Sanchez, “Block-Copolymer-Templated Synthesis of Electroactive RuO₂-Based Mesoporous Thin Films,” *Adv. Funct. Mater.*, vol. 19, no. 12, pp. 1922–1929, Jun. 2009.
- [42] D. Grosso, C. Boissière, B. Smarsly, T. Brezesinski, N. Pinna, P. A. Albouy, H. Amenitsch, M. Antonietti, and C. Sanchez, “Periodically ordered nanoscale islands and mesoporous films composed of nanocrystalline multimetallic oxides,” *Nat. Mater.*, vol. 3, no. 11, pp. 787–92, Nov. 2004.
- [43] R. Mori, M. Takahashi, and T. Yoko, “2D spinodal phase-separated TiO₂ films prepared by sol–gel process and photocatalytic activity,” *Mater. Res. Bull.*, vol. 39, no. 13, pp. 2137–2143, Nov. 2004.
- [44] R. Mori, M. Takahashi, and T. Yoko, “Domain size change of spinodal phase separation structure in the sol-gel derived TiO₂ thin film,” *J. Mater. Res.*, vol. 21, no. 01, pp. 270–275, Jan. 2006.
- [45] F. S. Bates and G. H. Fredrickson, “Block Copolymers—Designer Soft Materials,” *Phys. Today*, vol. 52, no. 2, p. 32, Jan. 1999.
- [46] L. Xue, J. Zhang, and Y. Han, “Phase separation induced ordered patterns in thin polymer blend films,” *Prog. Polym. Sci.*, vol. 37, no. 4, pp. 564–594, Apr. 2012.
- [47] D. Slep, J. Asselta, M. H. Rafailovich, J. Sokolov, D. A. Winesett, A. P. Smith, H. Ade, Y. Strzhemechny, S. A. Schwarz, and B. B. Sauer, “Phase Separation of Polystyrene and Bromo-Polystyrene Mixtures in Equilibrium Structures in Thin Films,” *Langmuir*, vol. 14, no. 17, pp. 4860–4864, Aug. 1998.

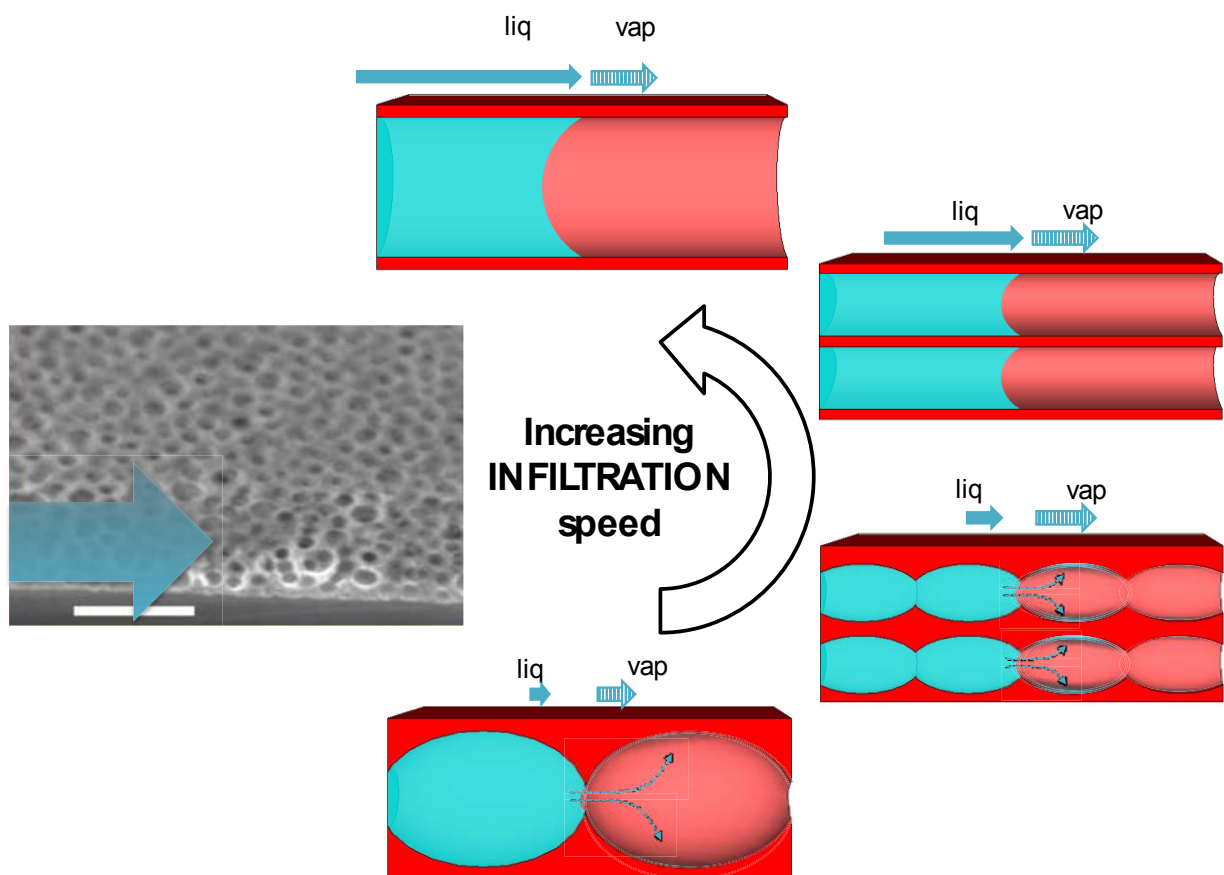
- [48] S. Affrossman and M. Stamm, "Topography and Surface Composition of Thin Films of Blends of Polystyrene with Brominated Polystyrenes: Effects of Varying the Degree of Bromination and Annealing," *Macromolecules*, vol. 31, no. 18, pp. 6280–6288, Sep. 1998.
- [49] Z. Mitov and E. Kumacheva, "Convection-Induced Patterns in Phase-Separating Polymeric Fluids," *Phys. Rev. Lett.*, vol. 81, no. 16, pp. 3427–3430, Oct. 1998.
- [50] M. L. Huggins, "Solutions of Long Chain Compounds," *J. Chem. Phys.*, vol. 9, no. 5, p. 440, Dec. 1941.
- [51] P. J. Flory, "Thermodynamics of High Polymer Solutions," *J. Chem. Phys.*, vol. 10, no. 1, p. 51, Dec. 1942.
- [52] J. Masuda, A. Takano, Y. Nagata, A. Noro, and Y. Matsushita, "Nanophase-Separated Synchronizing Structure with Parallel Double Periodicity from an Undecablock Terpolymer," *Phys. Rev. Lett.*, vol. 97, no. 9, p. 098301, Aug. 2006.
- [53] L. Li, L. Schulte, L. D. Clausen, K. M. Hansen, G. E. Jonsson, and S. Ndoni, "Gyroid nanoporous membranes with tunable permeability," *ACS Nano*, vol. 5, no. 10, pp. 7754–66, Oct. 2011.
- [54] P. F. W. Simon, R. Ulrich, H. W. Spiess, and U. Wiesner, "Block Copolymer–Ceramic Hybrid Materials from Organically Modified Ceramic Precursors," *Chem. Mater.*, vol. 13, no. 10, pp. 3464–3486, Oct. 2001.
- [55] Y. Mai and A. Eisenberg, "Self-assembly of block copolymers," *Chem. Soc. Rev.*, vol. 41, no. 18, pp. 5969–85, Sep. 2012.
- [56] A. K. Khandpur, S. Foerster, F. S. Bates, I. W. Hamley, A. J. Ryan, W. Bras, K. Almdal, and K. Mortensen, "Polyisoprene-Polystyrene Diblock Copolymer Phase Diagram near the Order-Disorder Transition," *Macromolecules*, vol. 28, no. 26, pp. 8796–8806, Dec. 1995.
- [57] M. W. Matsen and F. S. Bates, "Unifying Weak- and Strong-Segregation Block Copolymer Theories," *Macromolecules*, vol. 29, no. 4, pp. 1091–1098, Jan. 1996.
- [58] C. Burger, W. Ruland, and A. N. Semenov, "Polydispersity effects on the microphase-separation transition in block copolymers," *Macromolecules*, vol. 23, no. 13, pp. 3339–3346, Jun. 1990.
- [59] G. H. Fredrickson and E. Helfand, "Fluctuation effects in the theory of microphase separation in block copolymers," *J. Chem. Phys.*, vol. 87, no. 1, p. 697, Jul. 1987.
- [60] F. S. Bates and G. H. Fredrickson, "Conformational Asymmetry and Polymer-Polymer Thermodynamics," *Macromolecules*, vol. 27, no. 4, pp. 1065–1067, Jul. 1994.
- [61] H. Ahn, Y. Lee, H. Lee, Y. Kim, D. Y. Ryu, and B. Lee, "Substrate interaction effects on order to disorder transition behavior in block copolymer films," *J. Polym. Sci. Part B Polym. Phys.*, vol. 51, no. 7, pp. 567–573, Apr. 2013.

- [62] C. Shin, H. Ahn, E. Kim, D. Y. Ryu, J. Huh, K.-W. Kim, and T. P. Russell, "Transition Behavior of Block Copolymer Thin Films on Preferential Surfaces," *Macromolecules*, vol. 41, no. 23, pp. 9140–9145, Dec. 2008.
- [63] T. P. Russell, G. Coulon, V. R. Deline, and D. C. Miller, "Characteristics of the surface-induced orientation for symmetric diblock PS/PMMA copolymers," *Macromolecules*, vol. 22, no. 12, pp. 4600–4606, Dec. 1989.
- [64] X. Zhang, B. C. Berry, K. G. Yager, S. Kim, R. L. Jones, S. Satija, D. L. Pickel, J. F. Douglas, and A. Karim, "Surface morphology diagram for cylinder-forming block copolymer thin films," *ACS Nano*, vol. 2, no. 11, pp. 2331–41, Nov. 2008.
- [65] G. Coulon, T. P. Russell, V. R. Deline, and P. F. Green, "Surface-induced orientation of symmetric, diblock copolymers: a secondary ion mass-spectrometry study," *Macromolecules*, vol. 22, no. 6, pp. 2581–2589, Nov. 1989.
- [66] Q. Wang, Q. Yan, P. F. Nealey, and J. J. de Pablo, "Monte Carlo simulations of diblock copolymer thin films confined between two homogeneous surfaces," *J. Chem. Phys.*, vol. 112, no. 1, p. 450, Jan. 2000.
- [67] E. Huang, S. Pruzinsky, T. P. Russell, J. Mays, and C. J. Hawker, "Neutrality Conditions for Block Copolymer Systems on Random Copolymer Brush Surfaces," *Macromolecules*, vol. 32, no. 16, pp. 5299–5303, Aug. 1999.
- [68] T. Thurn-Albrecht, J. Schotter, G. A. Kastle, N. Emley, T. Shibauchi, L. Krusin-Elbaum, K. Guarini, C. T. Black, M. T. Tuominen, and T. P. Russell, "Ultrahigh-Density Nanowire Arrays Grown in Self-Assembled Diblock Copolymer Templates," *Science (80-.)*, vol. 290, no. 5499, pp. 2126–2129, Dec. 2000.
- [69] M. A. Villar, D. R. Rueda, F. Ania, and E. L. Thomas, "Study of oriented block copolymers films obtained by roll-casting," *Polymer (Guildf)*, vol. 43, no. 19, pp. 5139–5145, Sep. 2002.
- [70] J. Bodycomb, Y. Funaki, K. Kimishima, and T. Hashimoto, "Single-Grain Lamellar Microdomain from a Diblock Copolymer," *Macromolecules*, vol. 32, no. 6, pp. 2075–2077, Mar. 1999.
- [71] S. H. Kim, M. J. Misner, T. Xu, M. Kimura, and T. P. Russell, "Highly Oriented and Ordered Arrays from Block Copolymers via Solvent Evaporation," *Adv. Mater.*, vol. 16, no. 3, pp. 226–231, Feb. 2004.
- [72] C. Sinturel, M. Vayer, M. Morris, and M. A. Hillmyer, "Solvent Vapor Annealing of Block Polymer Thin Films," *Macromolecules*, vol. 46, no. 14, pp. 5399–5415, Jul. 2013.
- [73] E. O. Ningrum, W.-T. Lin, and C.-T. Lo, "The nanostructure and dewetting of block copolymer thin films annealed in different neutral solvents," *Polym. Eng. Sci.*, vol. 51, no. 7, pp. 1339–1346, Jul. 2011.

- [74] C. Antoine, "Tensions des vapeurs; nouvelle relation entre les tensions et les températures," *Comptes Rendus des Séances l'Académie des Sci.*, vol. 107, pp. 681–684, 778–780, 836–837, 1888.
- [75] K. W. Gotrik, A. F. Hannon, J. G. Son, B. Keller, A. Alexander-Katz, and C. A. Ross, "Morphology control in block copolymer films using mixed solvent vapors.," *ACS Nano*, vol. 6, no. 9, pp. 8052–9, Sep. 2012.
- [76] Y. Li, X. Wang, I. C. Sanchez, K. P. Johnston, and P. F. Green, "Ordering in asymmetric block copolymer films by a compressible fluid.," *J. Phys. Chem. B*, vol. 111, no. 1, pp. 16–25, Jan. 2007.
- [77] B. Nandan, M. K. Vyas, M. Böhme, and M. Stamm, "Composition-Dependent Morphological Transitions and Pathways in Switching of Fine Structure in Thin Films of Block Copolymer Supramolecular Assemblies," *Macromolecules*, vol. 43, no. 5, pp. 2463–2473, Mar. 2010.
- [78] E. B. Gowd, M. Böhme, and M. Stamm, "In Situ GISAXS Study on Solvent Vapour Induced Orientation Switching in PS- b -P4VP Block Copolymer Thin Films," *IOP Conf. Ser. Mater. Sci. Eng.*, vol. 14, no. 1, p. 012015, Nov. 2010.
- [79] T. P. Lodge, B. Pudil, and K. J. Hanley, "The Full Phase Behavior for Block Copolymers in Solvents of Varying Selectivity," *Macromolecules*, vol. 35, no. 12, pp. 4707–4717, Jun. 2002.
- [80] J. G. Son, K. W. Gotrik, and C. A. Ross, "High-Aspect-Ratio Perpendicular Orientation of PS- b -PDMS Thin Films under Solvent Annealing," *ACS Macro Lett.*, vol. 1, no. 11, pp. 1279–1284, Nov. 2012.
- [81] E. M. Freer, L. E. Krupp, W. D. Hinsberg, P. M. Rice, J. L. Hedrick, J. N. Cha, R. D. Miller, and H.-C. Kim, "Oriented mesoporous organosilicate thin films.," *Nano Lett.*, vol. 5, no. 10, pp. 2014–8, Oct. 2005.
- [82] J. Rzayev and M. A. Hillmyer, "Nanochannel array plastics with tailored surface chemistry.," *J. Am. Chem. Soc.*, vol. 127, no. 38, pp. 13373–9, Sep. 2005.
- [83] S. H. Kim, M. J. Misner, and T. P. Russell, "Solvent-Induced Ordering in Thin Film Diblock Copolymer/Homopolymer Mixtures," *Adv. Mater.*, vol. 16, no. 23–24, pp. 2119–2123, Dec. 2004.
- [84] C. G. Gamys, A. Vlad, O. Bertrand, and J.-F. Gohy, "Functionalized Nanoporous Thin Films From Blends of Block Copolymers and Homopolymers Interacting via Hydrogen Bonding," *Macromol. Chem. Phys.*, vol. 213, no. 19, pp. 2075–2080, Oct. 2012.
- [85] C. Boissiere, D. Grosso, S. Lepoutre, L. Nicole, A. B. Bruneau, and C. Sanchez, "Porosity and mechanical properties of mesoporous thin films assessed by environmental ellipsometric porosimetry.," *Langmuir*, vol. 21, no. 26, pp. 12362–71, Dec. 2005.
- [86] M. Faustini, M. Vayer, B. Marmiroli, M. Hillmyer, H. Amenitsch, C. Sinturel, and D. Grosso, "Bottom-up Approach toward Titanosilicate Mesoporous Pillared Planar

- Nanochannels for Nanofluidic Applications,” *Chem. Mater.*, vol. 22, no. 20, pp. 5687–5694, Oct. 2010.
- [87] M. Vayer, M. A. Hillmyer, M. Dirany, G. Thevenin, R. Erre, and C. Sinturel, “Perpendicular orientation of cylindrical domains upon solvent annealing thin films of polystyrene-*b*-polylactide,” *Thin Solid Films*, vol. 518, no. 14, pp. 3710–3715, May 2010.
 - [88] J. Yin, X. Yao, J.-Y. Liou, W. Sun, Y.-S. Sun, and Y. Wang, “Membranes with highly ordered straight nanopores by selective swelling of fast perpendicularly aligned block copolymers,” *ACS Nano*, vol. 7, no. 11, pp. 9961–74, Nov. 2013.
 - [89] B. D. Washo, “Rheology and Modeling of the Spin Coating Process,” *IBM J. Res. Dev.*, vol. 21, no. 2, pp. 190–198, Mar. 1977.
 - [90] D. B. Hall, P. Underhill, and J. M. Torkelson, “Spin coating of thin and ultrathin polymer films,” *Polym. Eng. Sci.*, vol. 38, no. 12, pp. 2039–2045, Dec. 1998.

IV : Capillary infiltration



IV : CAPILLARY INFILTRATION -----IV-133

IV.1 INTRODUCTION -----IV-135

IV.1.a The Lucas-Washburn equation ----- IV-137

IV.1.b Capillary filling in a plane channel----- IV-138

IV.1.c Liquid properties at the nanoscale----- IV-141

IV.1.d Examples of nanoscopic effects----- IV-143

IV.1.d.i Surface Tension and contact angle ----- IV-143

IV.1.d.ii Viscosity ----- IV-146

IV.1.e Capillary infiltration experiments in nanochannels ----- IV-149

IV.1.e.i Experiments in nanosits----- IV-149

IV.2 EXPERIMENTAL RESULTS -----IV-153

IV.2.a Critical effect of pore characteristics----- IV-154

IV.2.a.i Sample preparation and analysis----- IV-154

IV.2.a.ii Capillary ring experiment----- IV-154

IV.2.a.ii.1 Capillary ring – solvent polarity influence -----IV-155

IV.2.a.ii.2 Capillary ring – organic to inorganic precursor ration influence -----IV-158

IV.2.a.iii Dynamics of capillary infiltration ----- IV-161

IV.2.a.iii.1 Capillary infiltration speed and pore characteristics analysis-----IV-161

IV.2.a.iii.2 Bottleneck – pore size dimensions influence on capillary filling speed.-----IV-165

IV.2.a.iii.3 Size dependence of the transport mechanism. -----IV-166

IV.2.a.iv Conclusion----- IV-170

IV.2.b Capillary infiltration in PPNs ----- IV-171

IV.2.b.i Description of the investigated PPNs structures. ----- IV-172

IV.2.b.ii Dynamics of the capillary filling in PPN: ----- IV-173

IV.2.b.ii.1 The chemical nature of pillars has a strong influence on wicking-----IV-174

IV.2.b.ii.2 The porosity of the pillars has a weak influence on wicking. -----IV-174

IV.2.b.ii.3 The height of pillars matters only if it is small. -----IV-175

IV.2.b.iii Modeling the capillary filling in PPN: ----- IV-175

IV.2.b.iii.1 Computation of the hydrodynamic resistance of the PPN-----IV-175

IV.2.b.iii.2 Evaluation of the pressure drop across the meniscus -----IV-178

IV.2.b.iii.3 Computation of the Washburn transport coefficient-----IV-178

IV.2.b.iii.4 Reproduction of the experimental results with a single fitting parameter -----IV-180

IV.2.b.iii.5 The model helps understanding the influence of the PPN dimensions-----IV-181

IV.2.b.iv Conclusion----- IV-182

IV.3 APPENDIX -----IV-183

IV.4 BIBLIOGRAPHY -----IV-185

IV.1 Introduction

In this chapter the phenomenon of capillary infiltration in nanostructures will be examined. Understanding capillary filling at the nanoscale is still an open problem. The macroscopic laws, which will be briefly reported in the first part of this chapter, are indeed still inaccurate to describe quantitatively the capillary infiltration in nanopores or nanochannels. As it will be shown, variations of the macroscopic values of parameters such as surface tension and viscosity have been reported in nanoconfinement with consequent modification of the filling dynamics.

The understanding of liquids infiltration at this scale has practical applications that can be of particular interest. Even if this thesis is oriented towards nanofluidic applications, it has to be mentioned that understanding the capillarity and flow of water in nanoporous rocks would greatly help to manage hydro-geological phenomena (it is sufficient to think about clays) and, most importantly, to increase substantially the recovery of hydrocarbons contained in the oil or gas rich rocks [1]. The recovery of oil in these days can be performed for example by infiltrating water (eventually adding surfactants) in them [2]. Water having more affinities with the rocks than oil, it penetrates, displacing and freeing the oil that would remain otherwise trapped. The current technology normally allows recovering the 30-40% of the oil contained in the rocks due to the fact that the portion contained in the mesoporosity is still inaccessible (in shale oil rocks the inaccessible oil is even more [1]). As mentioned, advances in knowledge [3] and technology could permit a better extraction of oil resources and are currently being financed [4].

Coming back to the nanofluidic and lab-on-a-chip point of view, capillary infiltration is an efficient way to provoke flows at the nanoscale. Pressure driven flows require extremely high pressure due to the reduced dimensions of the channels. Producing such high pressures is both expensive, due to instrumentation, and difficult. The system has indeed to be pressure resistant (the bonding between channel and cover can fail due to the high pressure). That is why electro-osmotic flow, which will be examined in the next chapter, is commonly used for such applications. Capillary infiltration represents anyway a valid alternative. The pressure needed to create the flow is, indeed, automatically created by the advancing meniscus without any problem of pressure handling.

At the end of this chapter two studies regarding capillary infiltration in both disorganized porosities and strongly symmetrical ones are reported. We investigated the influences of the

porosity characteristics on the dynamics of the filling, and we tried to build up a model to describe it.

In order to have the necessary knowledge and facilitate the discussion, the concept and the laws governing the capillary filling at the nanoscale will be introduced.

A short discussion about the results obtained by other groups concerning the variation of macroscopic properties of liquids at the nanoscale and capillary infiltration is also reported in order to give a clearer vision of the problem and of the related difficulties.

IV.1.a The Lucas-Washburn equation

The Lucas-Washburn equation, normally referred as the Washburn equation, has been introduced in 1921 by Washburn [5]. It determines the position of a liquid front entering a capillary as function of the time and of the other physical quantities such as liquid viscosity and surface tension. The front advancement is found to be proportional to the square root of time with a dynamics that is similar to 1D-diffusion phenomena. This kind of dynamics is determined by the balance between a constant force, the capillary pressure due to the liquid-solid affinity, and the viscous drag of the flow inside the porosity that dissipates the energy gained by wetting. The equation can be easily written as

$$l^2 = D * t \quad (1)$$

with l the distance between the capillary entering and the liquid front position, t the time, and D the “coefficient of penetrance” or “penetrability” (as defined by Washburn). Actually, during this thesis, the coefficient is simply called the Washburn coefficient for clarity.

The Washburn equation is obtained considering the walls of the channels as completely smooth and affine with the liquid. The boundary condition at the walls is the no-slip condition, which means that the liquid is imposed to have speed equal to zero at the walls. The smooth hypothesis and the no-slip condition have both to be considered with care at the nanoscale where the roughness of the walls can become comparable with the channel width and some slip can be found for specific couples of solid and liquid. Moreover the properties of the liquid (and the solid) could be modified by the strong interaction between the solid and the liquid. Structuration of water, effect of counterions, modified contact angle shapes and values are just some examples. The Washburn equation will be obtained and analyzed in the next section that will discuss the dependences with the liquid properties in macroscopic experiments. This description will then be followed by a fast study of the variation of liquid properties at the nanoscale and their effect in capillary filling experiments performed by other groups.

IV.1.b Capillary filling in a plane channel

The Washburn law of capillary filling has just been introduced. It is here useful to (extremely briefly) show how the same equation can be obtained from basic laws in the case of a plane channel. Infiltration is directed in the x direction and walls are at $Z = \pm h/2$. The same procedure will be used in more complex cases at the end of this chapter. The text that follows will have then to be considered as a tutorial. Figure. IV-1. Scheme of a planar channel infiltrated by a liquid. Figure. IV-1 represents the examined system.

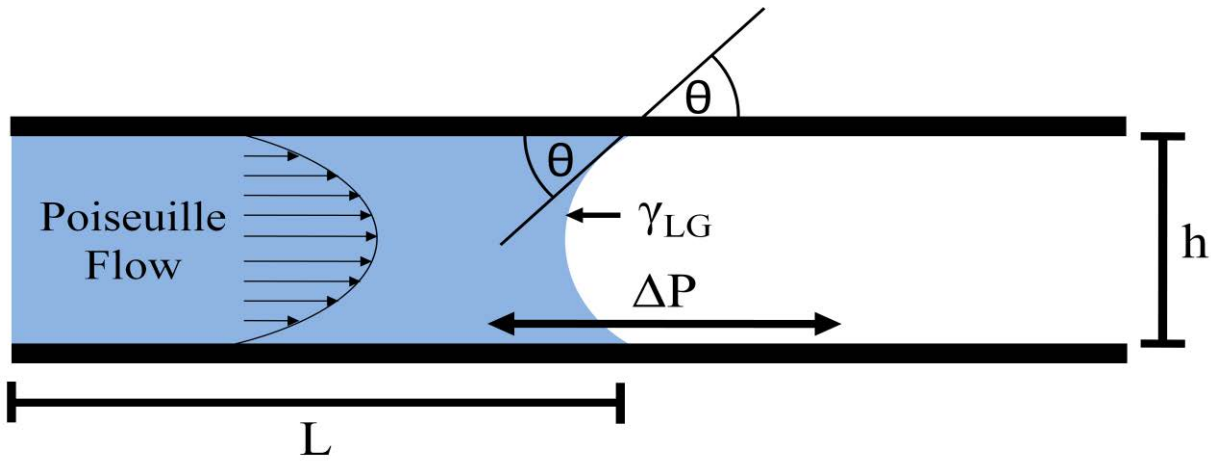


Figure. IV-1. Scheme of a planar channel infiltrated by a liquid.

In the case of capillary infiltration inside a plane channel, the pressure difference ΔP existing at the interface of the curved meniscus is constant. The meniscus, once that the movement has started, should maintain the same shape as function of the time. There is indeed no serious difference in the meniscus conditions between short or long times of infiltration. ΔP can be defined by the Laplace equation:

$$\Delta P = \gamma_{lg} \left(\frac{1}{R_1} + \frac{1}{R_2} \right) \quad (2)$$

With R_1 the meniscus curvature radius in the Z direction and R_2 in the Y direction (show Z and Y in Figure 1). Neglecting R_2 (that is much larger than R_1) with θ the contact angle, the equation can be re written as (with h the channel height and γ_{LG} the surface tension):

$$\Delta P = \gamma_{lg} * \frac{2 * \cos(\theta)}{h} \quad (3)$$

It is here important to stress that this result can be also obtained by applying the principle of the virtual work. The forces acting on the meniscus are respectively the adhesion force between the liquid and the solid, and the capillary force. One can thus write:

$$\delta W = -\Delta P_{menisc}(h) dV(h, L(t)) + \Delta\gamma dS(h, L(t)) \quad (4)$$

Where δW is the elementary work, L the length between the liquid front position at the start and the current time of infiltration t , $S(h, L(t))$ is the surface of the corresponding wetted solid, and $\Delta\gamma = \gamma_{sg} - \gamma_{sl} = \gamma_{lg} * \cos(\theta)$ is the difference of the surface tensions of solid-gas and solid-liquid interfaces, with γ_{lg} surface tension of the liquid-gas interface and θ the contact angle. From the quasi-equilibrium, $\delta W = 0$ and then

$$\Delta P_{menisc}(h) = \Delta\gamma \frac{dS(h, L(t))}{dV(h, L(t))} = \Delta\gamma * \frac{2 * W * dL}{W * H * dL} \quad (5)$$

That upon simplification and substitution becomes again the Laplace pressure. Energy (virtual work) reasoning has to be used to obtain the actual capillary pressure. This formula can be considered general and easily applicable for planar structures. The application of the known Laplace pressure expression (equation 2) is instead more difficult because it is not easy to identify meniscus curvature radius for complex structures.

Once having established the value of the pressure that drives the flow, it is needed to determine the other forces that act on the flow. In the case of a horizontal channels open to the atmosphere at both sides, the only force easily identified is the viscous stress induced by the flow itself. The flow $Q(L, t)$ of liquid induced by the Laplace pressure depends on the front position, because the resistance force due to the dragging, whose physical origin is the interaction with the pore walls, is proportional to the distance traveled by the water front. The Darcy's law can be used to quantify this effect:

$$-\Delta P = R_h(l) * Q(L, t) \quad (6)$$

with R_h the hydrodynamic resistance and L the travelled distance. If the hydrodynamic resistivity is denoted by ρ , with $R_h(L) = \rho * L / (H * W)$ and $Q(L, t)$ rewritten as $dV/dt = W * H * dL/dt$ the Washburn's law can be obtained [5]:

$$-\Delta P = \rho * \frac{L}{H * W} * (H * W) \frac{dL}{dt} \Rightarrow \frac{-2 * \Delta P}{\rho} * t = L^2 = D * t \quad (7)$$

where D can be seen as a diffusion coefficient. In the case of a plane channel the value of resistivity is easy to obtain. Considering the Poiseuille law for the pressure driven flow inside it:

$$v(\nabla P, h, H) = -\frac{\nabla P}{\eta} \left(\frac{h^2}{2} - \frac{H^2}{8} \right) = U \left(\frac{6 * h^2}{H^2} - \frac{3}{2} \right) \quad (8)$$

with η the liquid viscosity, ∇P the gradient of pressure in the X direction and U the average velocity (that for capillary filling experiments corresponds to the front speed). The average velocity is

$$U = -\frac{\nabla P}{\eta} \left(\frac{H^2}{12} \right) \quad (9)$$

that, expressed as a flow rate gives:

$$Q = U * W * H \quad (10)$$

In a channel of defined length, the mentioned Darcy law could be obtained again (considering $\nabla P = \Delta P / L$ due to the planarity of the channel).

$$Q(L, t) = -\frac{\nabla P}{\eta} \left(\frac{H^2}{12} \right) * W * H \Rightarrow -\Delta P = Q(L, t) * \frac{12 * \eta}{H^2} * \frac{L}{W * H} \quad (11)$$

then the hydrodynamic resistance can be written as:

$$R_h(L) = \rho * \frac{L}{W * H} = \frac{12 * \eta}{H^2} * \frac{L}{W * H} \Rightarrow \rho = \frac{12 * \eta}{H^2} \quad (12)$$

which can be inserted in Washburn equation parameter to obtain

$$D = \frac{2 * \Delta P}{\rho} = \frac{4 * \gamma_{lg} * \cos(\theta)}{H} * \frac{H^2}{12 * \eta} = \frac{\gamma_{lg} * \cos(\theta)}{3 * \eta} * H \quad (13)$$

With the Washburn coefficient depending linearly from the channel height. A totally similar result could be obtained for a cylindrical channel with its radius as governing factor and a slightly different constant.

This brief derivation of the Washburn law from the Darcy law and the simple case of a flat channel will be useful for the discussion in the experimental part of this chapter: the infiltration speed / channel dimension linearity will be indeed verified for nanoporous networks and a model for capillary infiltration in the PPN structures attempted.

In the next section a brief analysis of the physical parameters appearing in the last equation are reported, pointing out the variation of their value observed at the nanoscale (which influences the infiltration speed). Then the effects of this variation will be discussed in light of some experiments of capillary infiltration performed by other groups.

IV.1.c Liquid properties at the nanoscale

In bulk fluids, the properties that are normally identified at a macroscopic level are function of the fluid itself, temperature, pressure and other macroscopic variables. If a solute is added the liquid properties change as function of the solute and its concentration. Solute molecules create discontinuities in the fluid but, if their number is low enough, the fluid can anyway be considered homogenous and, by considering averages over large volumes (much larger than the molecular scale) its properties too. When a nanochannel or nanopore is used, more parameters have to be taken into account. Shape, charge and chemical composition constitute new important factors that have to be considered. Unfortunately, except in very fortunate cases, symmetry at the nanoscale cannot be found: atoms and molecules stay at the surfaces and are oriented, local stresses modifying local properties at atomic level and atomic roughness destroys geometrical planes and axes.

For a nanofluidic system, the number of variables that have to be considered is too high and the properties have compulsorily to be considered locally. Because the mentioned macroscopic properties are defined statistically they have a statistical and average signification too. It has to be kept in mind that this signification subsists only if this statistic or average can be done. It would be indeed pointless to identify the phase transition temperature of a few molecules or identify it in strong non-equilibrium conditions (the average could not be defined in that case). For example considering the temperature, it is true that even in non-equilibrium conditions, a local thermal equilibrium can be identified and a local temperature somehow defined (this is why it is possible to define a temperature along a bar that is asymmetrically heated at one side (Figure.IV-2a)).

Every macroscopic point is indeed composed of billions of molecules. The process of averaging is made by the macroscopic thermometer that is put in contact and interacts with billions of metal atoms even if localized (at a macroscopic level). An instantaneous temperature is then definable. On the other hand this approximation ceases to be acceptable when the typical considered dimension become of the order of the thermal fluctuations length and the term “local” stands for only a few molecules or atoms. In Figure.IV-2b, we report the results of a computational study of a similar heating experiment but applied for carbon nanotube [6.]The authors showed the trend of calculated temperature versus position of the atoms composing the unit cell of a carbon nanotube heated from one side (the difference between the imposed temperature and the temperature at the extremes is due to a mismatch due to the technique with the structure phonon density distribution as stated in [7]). Differently from the macroscopic case, the nominal temperature of the carbon nanotube is strongly fluctuating over the space do to the nanometric size of the system.

Indeed, even with an equivalent gradient, it is impossible to define a temperature in a system composed of a few molecules or atoms at a given time. Clearly an average over the time can be taken and, through the ergodic theorems, a temperature defined over a repeated set of the considered system. Nevertheless a defined value of temperature at certain and sufficient reduced time and space is something that virtually doesn't exist being the considered ensemble too little to define a statistics.

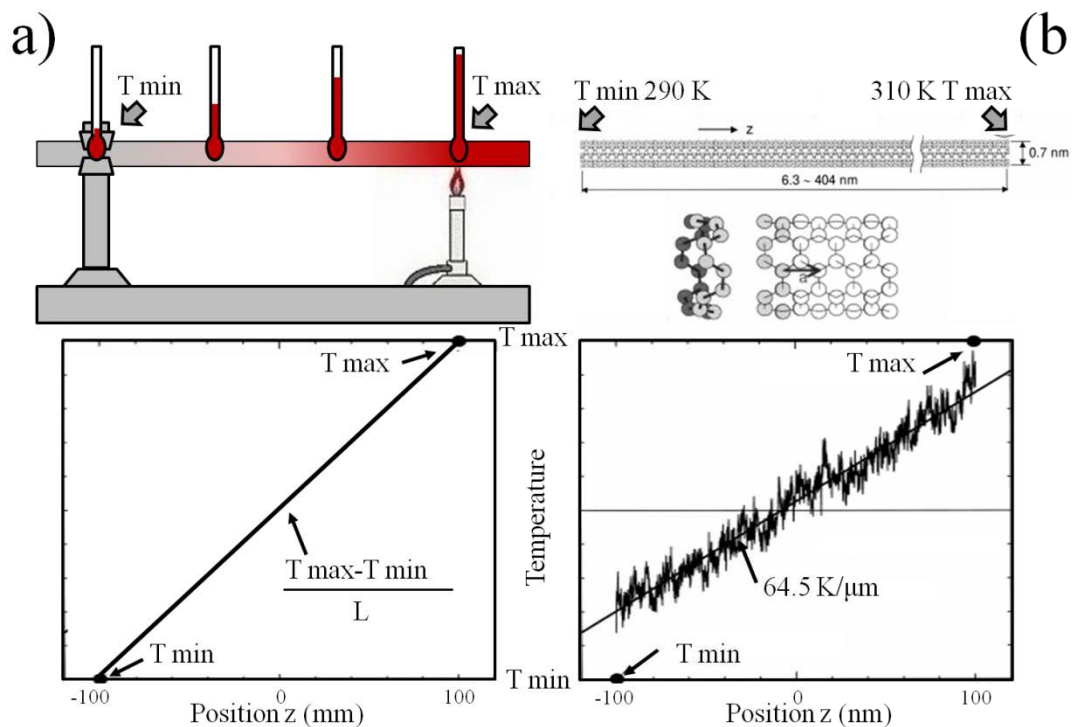


Figure.IV-2(a) Temperature (bottom) in every point of a metal bar heated from one side (up). **(b)** Calculated time averaged (slowly convergent) temperature [6] (bottom) of the atoms composing the unit cell (in the middle) of a carbon nanotube (up) heated from one side.

The same state of a system at a particular time and space can indeed be generated at different temperatures and only a statistical analysis over time or repeated systems can allow defining univocally a temperature. Local fluctuations of the macroscopic variables have important consequences even in the bulk (for example for nucleation phenomena) and are therefore considered and studied. Assumptions on their statistical distributions have been made and verified in order to explain a wide range of phenomena (nucleation, turbulences, crystallization, diffusion etc.). Particular attention has then to be used when utilizing macroscopic names and values of properties such as viscosity, contact angle, freezing and ebullition point, critical point, surface charge, surface tension, internal pressure, temperature and many others for nanoscopic systems such as nanoconfined fluids. It is thus not surprising that a great number of contradictory results are found in the literature, depending if the nanoscopic phenomena are considered or not.

IV.1.d Examples of nanoscopic effects

As has just been exposed, macroscopic fluid properties can significantly vary due to nanoconfinement. Surface tension, contact angle and viscosity will be analyzed here and some recent experimental results will be reported in order to understand the difficulty in determining their value. A broad range of other properties could be influenced by the nanoconfinement or other nanoscale effects. Addressing them in details is out of the aim of this thesis and would probably require hundredths of pages. These parameters, entering the Washburn equation, influence the capillary filling speed at the nanoscale. In the following section the difference between the macroscopic and actual “nanoscopic” values of filling speed in nanochannels will be investigated.

IV.1.d.i Surface Tension and contact angle

The surface tension of a material is defined macroscopically as the derivative of the Gibbs free energy G (the equation valid in the isothermal-isobaric ensemble: Number of particles, Temperature, Pressure are constant) with respect to its surface area A [8]. Equilibrium between the liquid and the vapor phase can be defined:

$$\gamma_{lg} = \left(\frac{\partial G}{\partial A} \right)_{N,T,P} \quad (14)$$

It is clear that all the quantities defined in this equation are statistically defined. It is known from more than a century (Eötvös rule – following equation) that its value for most of liquids is temperature dependent (with V molar volume, T_c critical temperature and k Eötvös constant with a value of $2.1 \times 10^{-7} \text{ J}/(\text{K} \cdot \text{mol}^{2/3})$)

$$\gamma_{lg} V^{2/3} = k(T_c - T - 6^\circ \text{C}) \quad (15)$$

which means, following the reasoning of the previous section, that its value should, in a first approximation, fluctuate at the nanoscale. Similar dependences over pressure and atmosphere composition [9] can be found in the literature. The local, molecular scale, surface tension value should then be influenced by fluctuations of these two variables too. Therefore, if the atmosphere composition modifies the surface tension of water, it is clear that local fluctuations of the atmosphere composition can again modify the local spatiotemporal value of surface tension. The same reasoning could be made for local fluctuations of the pressure. The level of complexity of the system is then extremely high and the evaluation of all the connected fluctuations extremely difficult.

The contact angle value can be simply defined as:

$$\cos(\theta) = \frac{\gamma_{sg} - \gamma_{sl}}{\gamma_{lg}} \quad (16)$$

If the previous discussion about surface tension fluctuation is valid, the contact angle is also supposed to fluctuate with the fluctuating values of surface tension between solid - gas (γ_{sg}) and solid – liquid (γ_{sl}).

Moreover additional contributions influence the value of contact angle at the nanoscale. For example it has to be mentioned the critical contribution of line tension for nanodroplets. It consists in the excess free energy per unit length at the gas-solid-liquid interface that arises when the line contribution to free energy $dF = PdV + \sum_i \gamma_i dA_i + \tau dL$ (with τ not necessarily positive)[10] is considered. It modifies the expression of the contact angle in the case of nanoscopic sessile drops to:

$$\cos(\theta) = \frac{\gamma_{sg} - \gamma_{sl}}{\gamma_{lg}} - \frac{\tau}{\gamma_{lg} R} \quad (17)$$

with R the droplet radius (at the triple phase point) and τ the line tension (whose values have range over six order of magnitude in function of the measurement technique up to 10^{-5} J/m). The line

tension contribution is anyway extremely difficult to quantify because multiple and precise measures are needed. It is not straightforward, indeed, to attribute the variation of contact angle to this contribution only. Even considering it, it is in some cases impossible to explain the dimension dependence of contact angle [11] and more complex models have to be introduced [12], with non directly measurable nanoscopic parameters (as the Lennard-Jones parameters values[13]–[15]), to give good results and a good descriptions.

Experimental effects of nanoscale confinement on surface tension and contact angle values have been often investigated. A few examples are here reported.

As an example [16] the value of surface tension of water in porous silica glass and highly ordered mesoporous silica (MCM-41) was found to progressively become half of the bulk value for pores down to 1 nm. This information was obtained by comparison of the pore size determined from nitrogen and water desorption isotherms. The pore size determined by Nitrogen -sorption was assumed to be the “real” one while the pore size determined though the water isotherm didn’t gave the same results. The surface tension value was then assumed to be different from the bulk one with a correcting factor as high as 0.5 in order to obtain the same pore size value from the isotherms of nitrogen and water. While this assumption could look a bit arbitrary, the fact that a phenomenon in which surface tension plays a key role gives unexpected results indicates that surface tension varies in this dimension range. In this study, surface chemistry and packing effects were also found to influence the adsorption and desorption of water and other molecules.

In another study, capillary filling experiments were conducted with a low viscosity prepolymer that could be rapidly photo cross-linked during infiltration in order to “freeze” the system. In this way, the meniscus shape could be visualized ex-situ by electron microscopy in a nanochannel, The contact angle and the meniscus shape itself, were found extremely different from their macroscopic equivalents causing, together with the other effects, a slow-down of capillary penetration [17].

In a last example, contact angle measurement of sessile nanodroplets of water [18], [19] and short alkanes [11] using an AFM in AC-non contact mode over various metallic and oxide surfaces systematically showed lower contact angle values with respect to their macroscopic counterpart. Which is in contrast of what previously described. It is clear that the techniques and the assumptions used to extract data from instruments and observations seriously affect the estimated value of contact angle. On the other hand, it is also evident that confinement effects at the nanoscale.

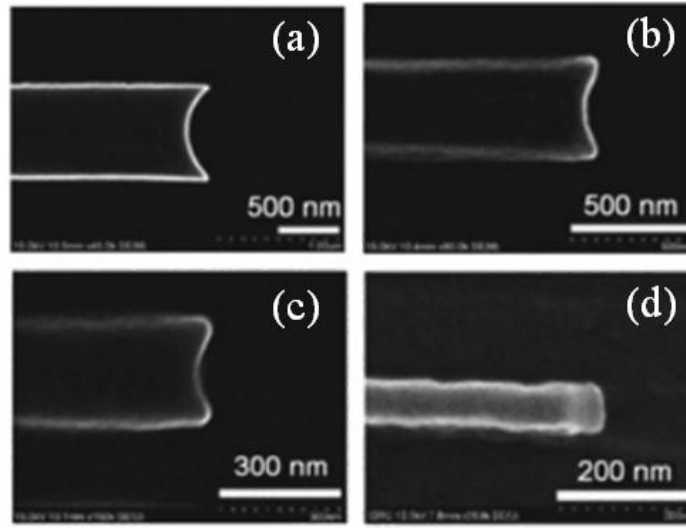


Figure.IV-3. [17] Meniscus shape of a capillary infiltrating low-viscosity polymer. The meniscus shape strongly depends from the channels dimensions showing unusual multi-curvature profiles in the smallest cases. The dimensions of the channel are 800nm (a), 400 nm (b), 250 nm (c), 50 nm (d) of width and 200 nm of height.

To conclude the evaluation of the surface tension and contact angle at the nanoscale is extremely difficult because a large amount of linked and interfering phenomena occur at the same time. Moreover, due to the small dimensions, indirect techniques are always needed even with several assumptions. Therefore even the most complex models need unknown parameters that have to be determined experimentally. Computer simulations [20]–[23] are continuously performed to improve the description of these quantities but more precise models and necessary comparison with the experiments still need to be done.

IV.1.d.ii Viscosity

Viscosity (η) is defined macroscopically as the ratio between the shear stress (exerted upon) and the shear rate of a liquid between two imaginary surfaces.

$$\eta = \frac{\tau}{\left(\frac{\partial v_x}{\partial y}\right)} \quad (18)$$

with τ the shear stress (the force exerted perpendicularly to the planes divided by the surface of application) and $\partial v_x / \partial y$ the derivative of the speed parallel to the planes in the direction perpendicular to them (the share rate). In general the viscosity of a liquid can be seen as the fluid resistance to flow or alternatively as the ability (and speed) to transfer momentum inside it. At a microscopic level it has been demonstrated that the viscosity is related to the fluctuation of the pressure and can be expressed integrating the autocorrelation function of the pressure over the

time [24], [25]; it can also be related to the decay in amplitude of velocity waves which is found to be frequency dependent (the commonly considered viscosity is extrapolated at frequency 0) [26]. Viscosity can also be interpreted at a molecular level: in a gas, it can be equaled to the product of the mean molecular velocity \bar{u} , the mean free path λ and the density ρ divided by two [27].

$$\eta = \frac{\rho \lambda \bar{u}}{2} \quad (19)$$

To understand this expression each element should be considered alone. It is clear that increasing the density, increases the number of molecules encountered per unit of time which means that the momentum is more frequently transferred. In the same way if the mean velocity is increased the momentum is passed more readily due to the higher number of impacts per unit of time. Increasing the mean free path increases the viscosity in a different way. Given a mean velocity if the mean free path is higher the momentum transported by a molecule goes farther in less time. This means that the gas “feels” the stress in a shorter time and counterbalances it with more fluid, which is, by definition, the effect of viscosity. Obviously the mean free path is difficult to define and, most importantly, not measurable. The mean free path depends also from the geometrical boundaries of the region of movement of the gas particles. In the same way the molecular velocity has an average that can vary from place to place at the nanoscale and can also be influenced by the shape of the confined space or other boundary conditions. Density has already been discussed to be size dependent for extremely low dimensions. Therefore fluctuations effects similar to the ones discussed for surface tension should be considered.

The transition from the gas to the liquid phase is readily done in substituting the mean free path with a sort of structuration distance that can be intended as the maximum distance where the position (and orientation) of a molecule is correlated to another one (the larger this distance the shorter is the time the momentum needs to diffuse). The structuration of the molecules can be modified at the nanoscale and can again fluctuate. This means that viscosity has non-uniform values in space and time even in liquids.

Many experimental results about the modification of the viscosity at the nanoscale have been reported. Because its microscopic definition of viscosity cannot be used, experiments considering its macroscopic one have to be performed. The problem arises because the experimental set-ups normally utilized to measure viscosity cannot be easily miniaturized. Particular techniques have then to be used and, in this case too, assumption made. It is then clear that it is still hard to have

definitive conclusions about its value for most liquids and conditions. When these modifications are reported the concept of apparent viscosity is often introduced. The apparent viscosity is used in equations involving the classic viscosity modifying (usually increasing) its value due to nanoscopic effects.

AFM is a common technique used to estimate the viscosity values of water over hydrophilic surfaces. The tip “feels” different forces as function of the experimental conditions that are then related to the viscosity value through complex models. In some cases the tip makes steps gradually approaching the surface evacuating the water [28] that resists, in others piezoelectric induced lateral movements are viscously slowed down by condensed [29] or deposited[30]water at the interface between the tip and a hydrophilic surface.

Values of viscosity have generally been found to increase at the nanoscale. Despite this, the amount of this increase seriously depends from the experiment settings and the group performing it. Values ranging from the bulk value [28] to seven order of magnitudes more [29],[31] have indeed been found. The fact that the nanoscopic effects are completely attributed to the viscosity, (keeping bulk values for the other parameters), can be the reason why the values obtained in these experiments are not in accordance. Moreover, additional effects as deformations, local surface affinities (the same that produce pinning when displacing droplets) were not considered. Only recently slip effects have been taken into account which helped understanding the surface material dependence of measured forces in this kind of measurements [32].

In any case, more efforts are still needed to exactly determine the viscosity value of liquids at the nanoscale. Even at a theoretical level the definition of viscosity should be adapted in the case of nanoconfined fluids. It is then not surprising that the values determined experimentally depend on the experimental settings because the molecular organization, orientation, bond strengths and other effects (not considered or just considered as averaged in the description of continuous fluid) start to play a role at the nanoscale.

In the following section some examples of capillary infiltration experiments performed by other groups are illustrated.

As will be shown, the experimental values of capillary filling speed never match with the expected ones in small nanochannels. The mentioned effects on surface tension, contact angle and viscosity surely play a fundamental role in causing these differences. Actually other effects too have been identified as influencing the capillary filling at the nanoscale but, again, agreement has not yet been found on their reciprocal contribution.

IV.1.e Capillary infiltration experiments in nanochannels

In this section, a short review of the infiltration experiments in nanochannels fabricated by top-down approaches is reported. As will be evidenced, no agreement is found between the values obtained for similar setups. In general, anyway, a slower than macroscopically expected infiltration speed is shown. Various effects have been evoked as the cause of this slowing down but no agreement has been found. No proper and repeatable procedure has indeed been identified which allow separating the various nanoscopic influences on the infiltration experiment. Furthermore in every experience the channel structures and materials are different which do not allow performing real comparison of the filling speed rates.

The infiltration of various liquids has been performed showing the influence of polarity, ionic charge and other parameters. Various causes have then been summoned to explain the different infiltration dynamics and will be briefly mentioned. Anyway, no complete model has yet been proposed and the infiltration experiments at the nanoscale always gave unexpected results.

IV.1.e.i Experiments in nanosits

A large amount of capillary infiltration experiments in nanochannels have been performed. Usually channels with rectangular sections were fabricated by microfabrication techniques using hard materials. Liquid such as water, ethanol, silicone oil have been introduced in the channels. Beneath the experimental values, some simulations have also been attempted. In most cases the filling speed was found to be slower than expected with few exceptions. In Figure.IV-4a, we show a common analysis of the filling speed (plotting the square of the infiltrated length as function of the time). The slope of the line corresponds to the D parameter from the Washburn law and indicates the filling speed. A scheme resuming some of the main results found in the literature is reported in Figure.IV-4b. In particular, the ratio between the experimental and theoretical value of Washburn coefficient is plotted as function of the channel dimension for different liquids. As can be seen, the results are heterogeneous but the nanoscopic effects becomes more and more intense when reducing the channel size with results approaching the bulk values for channel higher than 100 nm. It is interesting to notice that, in some cases, experimental D values (filling speed) were similar to the bulk value, while they were even found to be greater than the expected one for

certain liquids [33] or mixtures [34], introducing even more doubts about the phenomena contributing to the filling at the nanoscale.

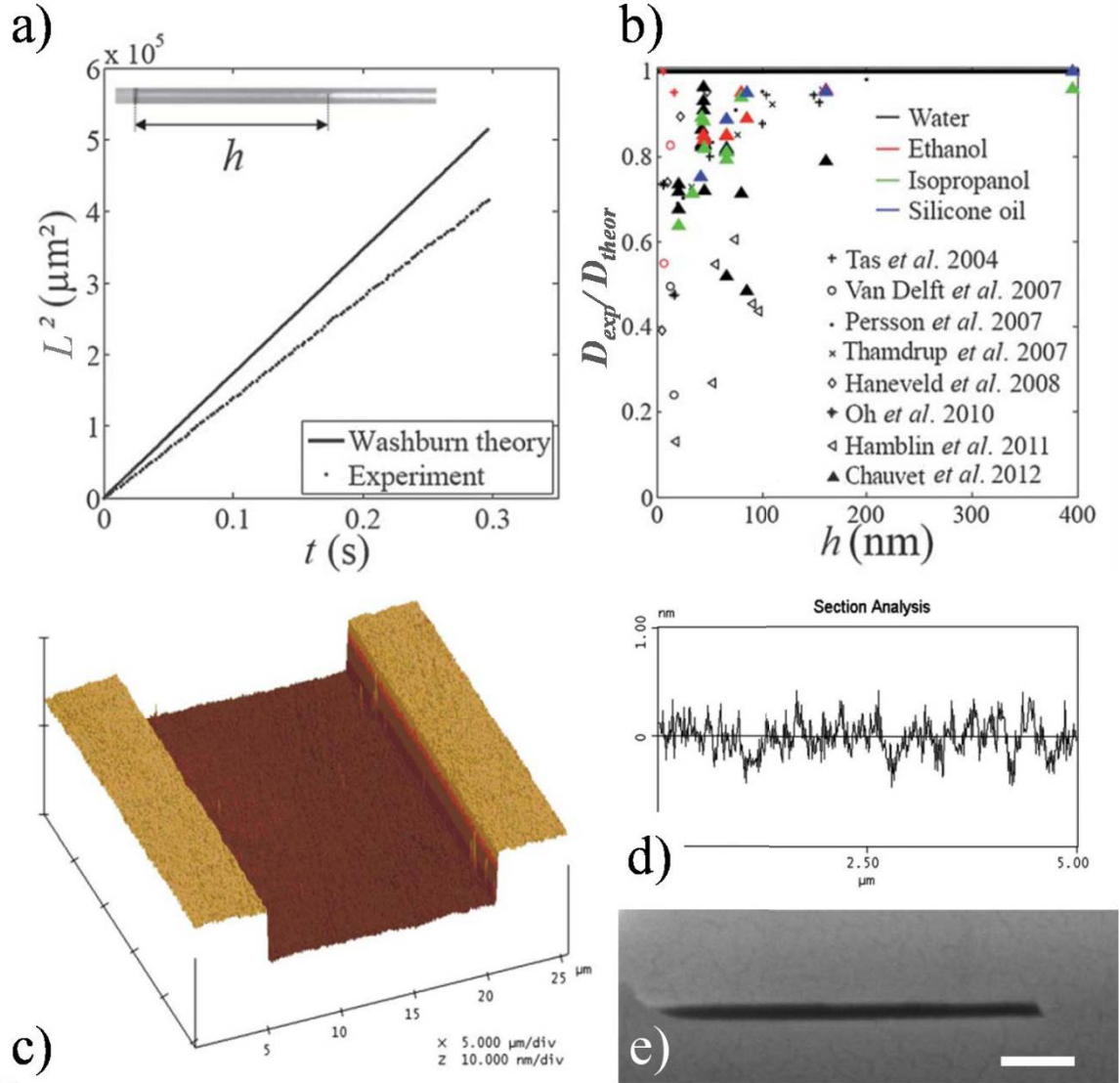


Figure IV-4. a) Common analysis used to determine the Washburn constant parameter [35]. The square of the length is reported as function of time. The slope corresponds to the D parameter in the Washburn law. b) List of the results obtained in some literature works, comparing the experimental to theoretic ratio of the D parameter with respect to the planar channel height [33], [35]–[41]. c) AFM analysis of a nanochannels to check the internal roughness of the surface that could cause pinning effects. d) Plot of a single line scan of the previous image [41]. e) SEM image of a nanochannel created with microfabrication techniques; the white bar has a length of 200 nm [34].

Channel internal morphology is often inspected in order to avoid pinning or other roughness related phenomena (Figure IV-4c and Figure IV-4d). The material of the channel walls can be either homogeneous or not as function of the procedure used to produce the channel (channels with different materials at the upper and lower surface are often used due to the bonding step of

certain channel productions). The channel filling rate is usually determined through observation of optical interferences inside the channel (Figure.IV-4e),

As mentioned, the filling kinetics is usually slower than expected and various causes have been identified and controversially discussed to explain this behavior. Nanoscopic effects over surface tension, contact angle and viscosity at the nanoscale have already been discussed. Researchers often attribute this variation at the nanoscale to contact angle increases [17], [34], [36], [42] or liquid structuration on the wall surface that increases the viscosity [41]. Other effects are actually introduced for the special case of the capillary filling such as bubble formation [39], [43] (Figure.IV-5a), increase of the viscosity due to the electroviscous effect [37], [38] (Figure.IV-5b) or effects due to the evacuating gas phase [35] (Figure.IV-5c). Again the respective value of these effects is controversial or not adequately explored. Bubbles, for example, are identified to increase the viscous drag reducing the actual channel size but proper calculation demonstrates an opposite trend [35]. The electroviscous effect is caused by an accumulation of ions at the meniscus surface (because upon wetting the surface release some charge) creating an electric field (Figure.IV-5b). The streaming current (to the left caused by negative ions) and the conductive current (positive ions going to the right) do not balance the charge formation at the meniscus. At the end, the electric field creates a force in the direction opposed to the liquid flow, reducing its intensity (the liquid column contains more negative than positive ions)[44]. Anyway this effect is found to be not strong enough to induce the observed slowing down [45]. Eventual channel deformation [46] has also been sometimes evoked too as a possible cause of the slowing down of the filling speed but proper studies demonstrate that it has, in fact, an opposite effect for adequate channel conformations (large channel width) [47] (Figure.IV-5c).

In the end, the capillary infiltration in nanochannels remains an unsolved problem with the contribution of various effects to analyze separately. Computer simulations have also been performed stressing, for example, the importance of the channel surface roughness [48] or wall-fluid (Lennard-Jones parameters value) interaction [49] but more still has to be done.

In the last part of this chapter a study about the capillary infiltration in the PPN structure is presented. The structure geometry is relatively less “exact” with respect to planar nanochannels but the possibility to modify the composing pillar and roof material without influencing the geometry opens new prospective in the understanding of the material contributions to the filling dynamics (due to surface charge, contact angle etc.).

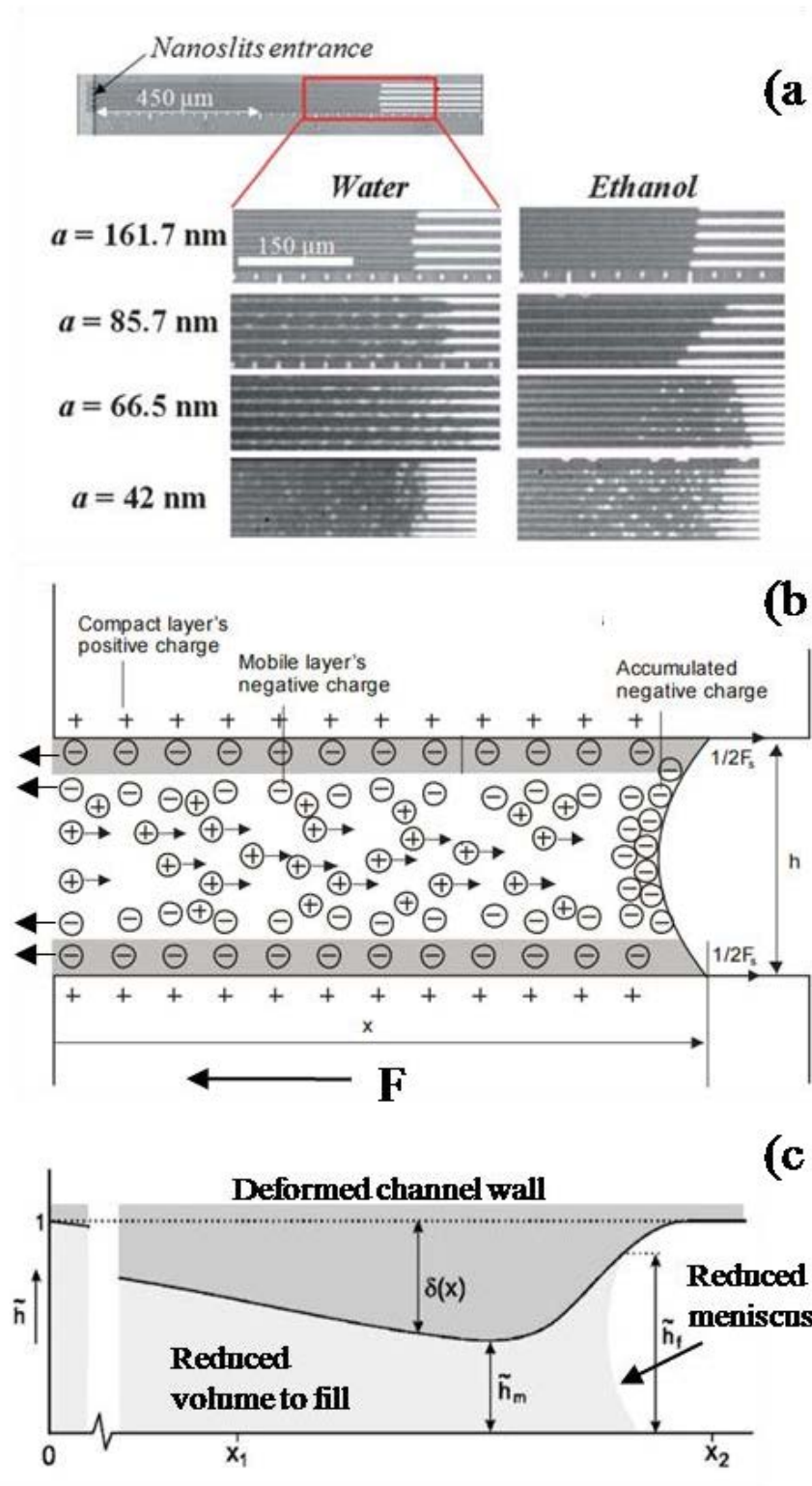


Figure.IV-5 (a) Example of bubble formation during the filling of nanochannels. The quantity of bubble is dependent to the liquid infiltrating the nanochannels and to its height[35]. (b) Scheme of the electroviscous effect. (c) Effect of channel wall deformation.

IV.2 Experimental Results

The following part of the chapter reports some of the results and progresses obtained in this thesis regarding the infiltration of liquids in nanoporous structure. In the first section the infiltration of water and ionic liquid is related to the porosity characteristics of thin films. The concept of “capillary ring” is introduced and proposed as easy method to verify if a porous thin film allows capillary infiltration. The infiltration speed is then related to the porosity characteristics obtained by Environmental Ellipsometric Porosimetry which involves condensation/evaporation of water in the porosity. This technique permits to determine the pore and bottle-neck size which are determined as critical parameters for capillary infiltration speed. If bottle-neck size is of the same dimension of pore size, indeed the filling speed increases linearly with the pore size. Conversely for a given bottle-neck size, increasing the pore dimension seems to slow down exponentially the filling speed. To understand this, a mechanism involving successive and repeated evaporation and condensation is proposed for the filling of small porosities.

In the second section, an experimental and theoretical study of capillary infiltration in the PPN nanostructures is reported. Differently from non-organized porous networks, the PPNs periodic structure can be modeled and computer simulation used to determine some parameters as the hydrodynamic resistance of the structure (solving the Navier-Stokes equations with COMSOL). Moreover the internal surface per unit of length of infiltration can be estimated and used to evaluate the capillary pressure that causes the infiltration.

The results obtained about capillary infiltration are of particular importance for nanofluidic applications. At these dimensions, indeed, the hydrodynamic resistance is usually so elevated that maximum imposed pressures with common instruments do not allow fluid flows of adequate intensities for many applications. Capillarity, conversely, provides extremely high pressures that can be utilized as driving force in adequately conceived systems in the same way as it is now attempted in paper-based microfluidic devices [50]–[52].

IV.2.a Critical effect of pore characteristics

In this section, a study relating pore structure and capillary filling speed is exposed. Various self-assembled porous structures obtained by the mentioned sol-gel and EISA (Chapter III) mechanism are presented. The porous structure was tuned by varying the porogens type, the solution composition or deposition conditions. Liquids have been capillary infiltrated inside these structures and their dynamics studied.

The critical role of bottle-necks has been established. Open porosities, showing no, or reduced, bottle-neck allows a better and faster liquid infiltration while porosities with restrictions seems to significantly reduce the wicking speed. A large number of samples were produced to confirm this hypothesis. A simple experiment involving the deposition of a sessile drop on the film surface is proposed to test qualitatively the infiltrability of thin films. Conclusion can be obtained by simple eye inspection. Furthermore a systematic relationship between pore size and bottle-neck size of thin film porosities and capillary infiltration speed is established.

IV.2.a.i Sample preparation and analysis

SEM-FEG and EEP measurement were utilized as main instruments of investigation to determine the pore structure as mentioned in the previous chapter. The capillary filling dynamics was determined by analyzing microscope videos: the advancing front is indeed easily detectable from the change in color and light intensity induced by the variation of refractive index in the film (which causes a variation of the light interferences).

The syntheses of the films utilized for this investigation have been already presented in Chapter III.

IV.2.a.ii Capillary ring experiment

In the first part of this section the so-called “capillary ring” is utilized to inspect in a fast and easy way if a thin film allows capillary infiltration. If this is the case, the considered porosity could be a candidate for nanofluidic application or for other process involving high solid-liquid interaction such as heterogeneous catalysis. The capillary ring experiment consists simply in depositing a sessile drop over a surface and inspecting by eye if a colored ring forms around it. If it is the case it means that water can penetrate the porosity and then change locally the refractive index and thus the interferential color. If, instead, the film doesn't allow capillary infiltration no change in color

can be seen at the triple line (solid-gas-liquid). This test can be performed in few seconds on every prepared film. It has been extensively utilized during this Ph.D. to check if the synthesis process utilized for various films for nanofluidic applications worked correctly. Two examples of the use of this test are reported to check the influence of solvent polarity and surfactant/block-copolymer to inorganic precursor ratio on the final structure and water infiltration behavior of thin films.

IV.2.a.ii.1 Capillary ring – solvent polarity influence

In the first part of the study concerns, we report the experiment on two mesoporous silica films, called PS1 and PS2 as in the previous Chapter. They were prepared to have similar thickness ($\approx 150\text{nm}$), pore size ($\approx 60\text{nm}$) and pore volume ($\approx 65\%$), but different pore interconnectivity.

Indeed, SEM-FEG images of both samples exhibit the same apparent porosity with pores size of around 60nm (see Figure.IV-6b and Figure.IV-6e). A very accurate description of the film porosity (volume, size distribution, and interconnection) can be deduced from the water adsorption/desorption isotherms obtained by Environmental Ellipsometric Porosimetry (EEP) and plotted in Figure.IV-6c and Figure.IV-6f [53]. Refractive indices measured by EEP at 0% RH are 1.15 for both films, which suggests a similar pore volume of 65% (estimated by the Bruggemann Effective Approximation Model). Both adsorption curves show a sudden increase of refractive index above 95% of relative humidity attributed to the capillary condensation of water in the pores. In this range of humidity, deducing the corresponding pore size is not relevant since a slight shift of the critical humidity of capillary condensation (sensor nominal error: $\pm 2\%$) induces a significant change in the estimated pore dimension. As a result, it can be concluded only that the main population of the pores stands above 50nm in diameter in both films, in agreement with the SEM images.

For PS1, desorption curve follows perfectly the adsorption one, suggesting a good interconnectivity between the pores due to the small difference between the bottle-neck and pore diameters). Inversely for PS2 the desorption is centered at 55% RH which corresponds to the presence of “bottle-necks” with size centered at 4.1 nm , as calculated using a spherical model in the adapted Kelvin’s equation.[14] As a result, PS2 bearing 4.1 nm “bottlenecks” has a much less pore interconnectivity than PS1 due to the presence of constrictions.

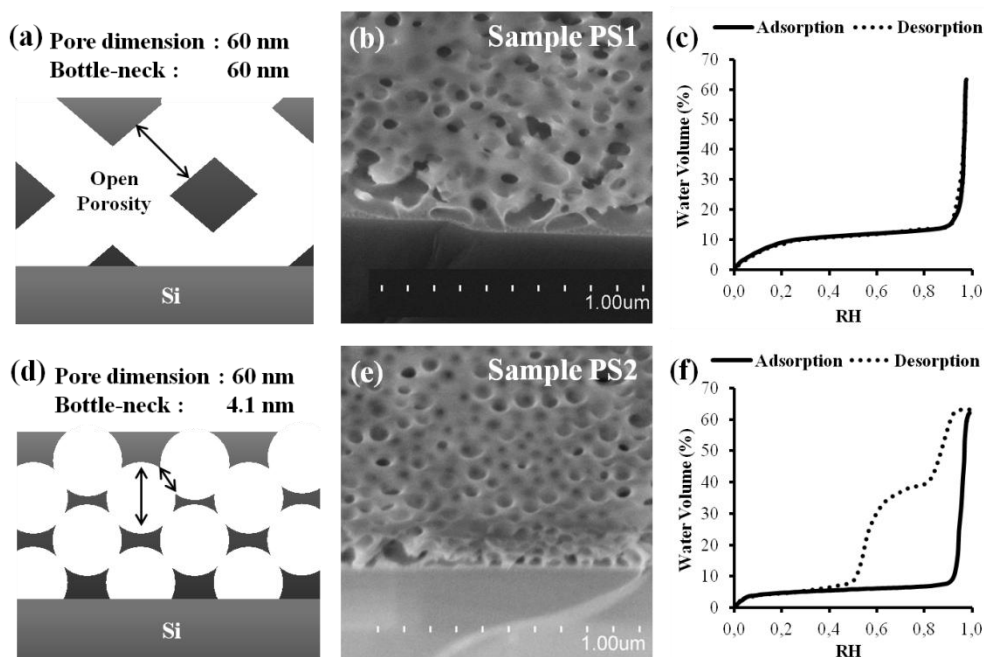


Figure.IV-6. (a,d) Simplified scheme b,e) SEM images c,f) EEP adsorption/desorption isotherms (water volume versus relative humidity) of the PS1,PS2 samples. The lack of hysteresis in (c) allows supposing an internal structure of the thin film with no bottlenecks.

The desorption occurring at around $P/P_0 = 90\%$ (corresponding to the 25% of the total porous volume - Figure.IV-6f), corresponds to the fraction of pores standing at the coating surface, that are more or less open to the atmosphere and can more easily desorb water than the inner porosity.

The difference in interconnectivity between both samples was obtained by varying solubility of the block-copolymer template using different solvents during film synthesis. The highly interconnected film (PS1) was obtained from an initial solution prepared with 100% THF (Figure.IV-6a-Figure.IV-6c), as opposed to the low-interconnected film (PS2), for which the solvent was a mixture of 75% acetone and 25% THF (Figure.IV-6d-Figure.IV-6f). As described in one of the previous chapters the solvent higher polarity of the acetone-rich solution modifies the solubility of the PS chains (without inducing precipitation in the present conditions) decreasing it. PS-*b*-PEO is amphiphilic, it forms then discrete spherical micelles in the acetone-rich medium, while it remains not aggregated in the THF one. During liquid deposition by dip-coating, evaporation takes place inducing the simultaneous concentration of silica precursors and polymers as the silica cross-links rigidifying thus the coating onto the substrate. Upon deposition, the described Evaporation Induced Self-Assembly takes place. In the acetone case the micelles co-assemble into a percolated 3D-array of spheres with a minimal degree of coalescence. On the other hand, for the acetone-free system, the fast evaporation of THF drives the polymer to aggregate into a continuous 3D network, following a spinodal-type phase separation with the inorganic phase. After the block-copolymer removal through thermal decomposition, both

approaches yield coatings bearing a porosity network that corresponds to the inverse of the intermediate polymer network. Similar pore volume and pore size were obtained in both samples. The precursor to template ratio being is indeed identical in both systems, and the organic domain dimension is fixed by the length of the polymer blocks. On the other hand, a much more interconnected network is formed in pure THF (PS1) system than in presence of acetone (PS2).

Figure.IV-7 illustrates what can be observed when a drop of water is deposited at the surface of the porous PS2 and PS1 films. After a few second of equilibration, the sessile drop on the PS1 film is accompanied by a millimeter wide lighter ring formed at its periphery. Zooming on the drop triple-phase line as in Figure.IV-7b reveals that the latter ring is homogeneous all around the drop, and is stable as long as evaporation is hindered. This ring is caused by the variation of optical interferences due to a local increase of the film refractive index induced by the presence of water into the porosity at the vicinity of the drop. This ring will be named from now onwards “capillary ring”. The mechanism responsible for the establishment of its formation is schemed in Figure.IV-7a. The water from the droplet penetrates by capillary infiltration inside the thin film porosity and builds a radial flow outward of the triple contact line by capillarity [54].

At a certain critical distance (d_c) from the triple line, a stationary water-front is established (Figure.IV-7a), where capillarity filling balances evaporation. Evaporation occurs indeed at the drop surface and all over the surface of the capillary ring. A gradient of Relative Humidity (RH) is then established going from saturation ($RH = 100\%$) at the drop surface to the ambient atmosphere at a distance from the drop that depends on the diffusion of vapor H_2O in air. Evaporation rate increases then getting away from the drop. The capillary ring can be observed only if the atmospheric relative humidity of the surrounding ambient atmosphere is inferior to the relative humidity of capillary condensation, which is above 95% in the present case, as deduced from the EEP investigations in Figure.IV-6c and Figure.IV-6f. Interestingly, the capillary ring is not observed for the PS2 sample (see Figure.IV-7d) in the same conditions. The poor interconnectivity of the PS2 structure, being the only structural difference with PS1, is then considered responsible for the non-formation of the ring by capillary-driven out-flow from the drop. A direct relation might exist then between the absence or the low amplitude of a hysteresis loop on the water adsorption/desorption isotherm (EEP) and an efficient capillary-driven filling.

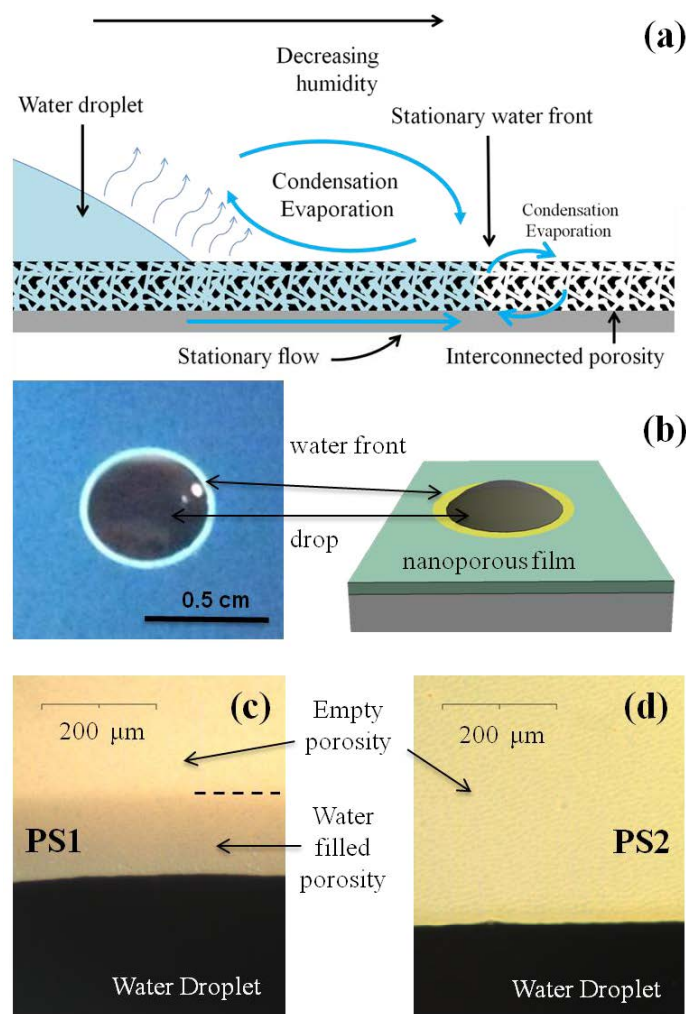


Figure.IV-7. (a) Scheme of the phenomena taking place when a water drop stands free on a thin film that allows wicking; (b) picture and corresponding scheme representing a sessile water drop deposited onto the surface of PS1 and surrounded by its capillary ring. (c) and (d) zoomed optical images of the triple line showing the presence of the capillary ring in PS1 and no capillary ring in PS2.

IV.2.a.ii.2 Capillary ring – organic to inorganic precursor ration influence

In Figure.IV-8a set of silica thin films prepared using the same block copolymer of samples PS1 and PS2 is reported. PS3, PS4 and PS5 samples are prepared from the same starting inorganic solution adding different increasing of block-copolymer (see Table. 1 of CHAPTER III) in order to have films with different porous volume (33%, 47% and 54% respectively evaluated by EEP). The sessile drop experiment is then performed. Figure displays the SEM images of the porous structure, the corresponding EEP isotherms, and the optical image of the sessile drop. The photographs of the droplets in Figure.IV-8a reveal that no capillary ring is formed for samples PS3 and PS4 (porosity 33% and 47% vol respectively) while PS5 (porosity 54% vol) does exhibit a capillary ring. As expected, the porous volume is one of the critical parameters influencing the filling properties of these thin films.

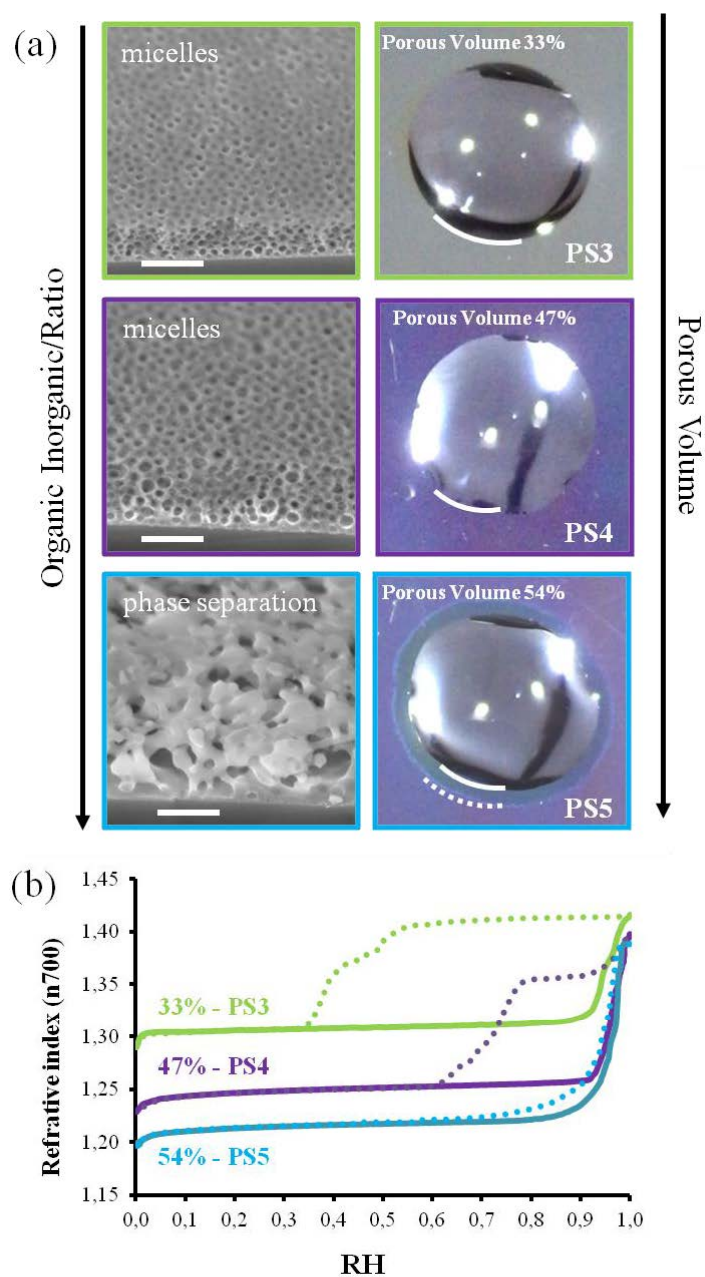


Figure.IV-8. (a) SEM images (scale bar 300 nm) and corresponding images of a water drop deposited onto the surface of PS3, PS4 and PS5 films. Only sample PS5, which has a higher porosity vol%, shows a capillary ring. (b)EEP adsorption/desorption isotherms (film refractive index at wavelength 700nm versus relative humidity) of PS3, PS4 and PS5 samples.

The water adsorption/desorption isotherms obtained by Environmental Ellipsometric Porosimetry (EEP) are plotted in Figure.IV-8b (in this case the refractive index at the wavelength of 700nm is reported as function of the relative humidity RH %). Capillary condensation occurs above 92% RH, suggesting that pores have dimension larger than 30 nm in all considered films. As can be seen on the SEM images (Figure.IV-8a), PS3 and PS4 samples show characteristic micellar pore structure. On the other hand, PS5 shows large open porosity characteristic of spinodal phase

separation. Looking at the hysteresis loops that are reported in Figure.IV-8b we can observe different -sorption behaviors related to the porous network morphology: PS3 shows a large hysteresis with two desorption steps likely attributed to pore blocking (two populations) or pore blocking followed by cavitation; PS4 shows a narrower hysteresis attributed to pore blocking; while for PS5, desorption and adsorption curves are almost overlapping revealing limited pore blocking. From these, one can conclude that the bottlenecks are much smaller in PS3 than in PS4, while PS5 has the larger constrictions in its porosity. The increase of block-copolymer quantity during synthesis induces an increase in porous volume % and also a progressive morphological transformation, reducing the bottle-neck number and size, giving a structure that finally allows wicking in the PS5 sample (see the capillary rings in Figure.IV-8a).

This study confirms that a more “open” or homogeneous porosity favors capillary filling. This conclusion can be generalized to smaller pore network. The same experience was repeated using another block-copolymer that generates smaller pores, Brij c10, varying the organic/inorganic ratio in the solutions (samples Bj1 to Bj5, in Table .2 of Chapter III, see Figure.III-14 and Figure .III-17 of Chapter III for SEM images and EEP cycles). In the same way droplets deposited on films with low values of porous volume do not generate a capillary ring (photos not shown) reporting the same tendency of the PS3 to PS5 samples. In general it was observed that porosities higher than 50% are needed for wicking to take place (independently from the pore size). This statement has to be considered with attention: it is obvious that a set of separated parallel open linear channels in a dense matrix would allow wicking even for low values of the porous volume for the corresponding material; this implies that porous volume could not represent a direct and critical parameter by itself. On the other hand in bottom-up fabrication of nanoporous materials the porous volume is the result of many processes that determine the whole pore structure.

As can be seen in Figure.IV-8, porous volume and pore shape are difficult to adjust independently: thus the study of porous volume as a critical parameter for wicking is not straightforward due to the difficulties in performing a synthesis of thin films with similar porous structure and shape but different porous volume.

Anyway it seems that the formation of a high porosity by the present templating approach, promotes the formation of networks with less pore-blocking effect, which then seems to be the critical parameter for efficient capillary filling.

It can then be concluded that the defined 50 % of porous volume is the limit for wicking/non-wicking behavior, and has to be considered as statistical. Indeed it is not allowed to completely

exclude that bottom-up fabricated mesoporous materials could allow wicking even for lower values of the porous volume in particular if porogens different for the ones used in this article are utilized.

IV.2.a.iii *Dynamics of capillary infiltration*

In this section the dependence of capillary from the film porosity characteristics is analyzed. In particular, we report the dynamics of filling in a configuration where evaporation is hindered. The pore structure will be related to the actual filling speed and we will analyze the mechanism of the advancement of the visible liquid front. The fundamental importance of evaporation/condensation equilibrium is stressed for porosities with small bottle-neck and we will propose a law relating the capillary filling speed and the pore dimensions.

The importance of this study for nanofluidic application is broad. Wicking / capillarity infiltration can be indeed utilized as driving forces to induce the liquid flow in the nanochannels. Pressure driven flows in nanochannels need indeed extremely high-pressure gradients to attain reasonable speed. Capillarity (due to the dependence on the reciprocal of pore size) induces extremely high pressures in the liquid not reachable through external application. Capillarity can then be seen as a precious phenomenon to induce a (stationary) nanoconfined flow useful for application such as separations.

IV.2.a.iii.1 **Capillary infiltration speed and pore characteristics analysis**

In what follows, the dynamics of capillary filling was investigated by recording the advancement of the liquid front in the film porosity using a configuration where the direct transversal evaporation in the atmosphere is significantly hindered. This is achieved by applying a PDMS stamp onto the top of the films (see Figure.IV-9a). This configuration was chosen because it permits a good and uniform covering of the film surface, and because its transparency allows *in situ* visualization of the fluid front propagation with the help of an optical microscope.

A drop of water is then applied at the edge of the stamp and the water front progression underneath the stamp, where exchanges with atmosphere are minimized, was recorded. In the case of the PS2 film, no capillary filling was observed underneath the stamp, which is consistent with the absence of a capillary ring. In PS1 film, rapid capillary filling was observed. The plots of the square of the fluid-front travelled distance L with respect to time t for water (black-squares) and for the poorly volatile 1-Ethyl-3-methylimidazolium dicyanamide ionic liquid (red-triangles), are shown in Figure.IV-9b.

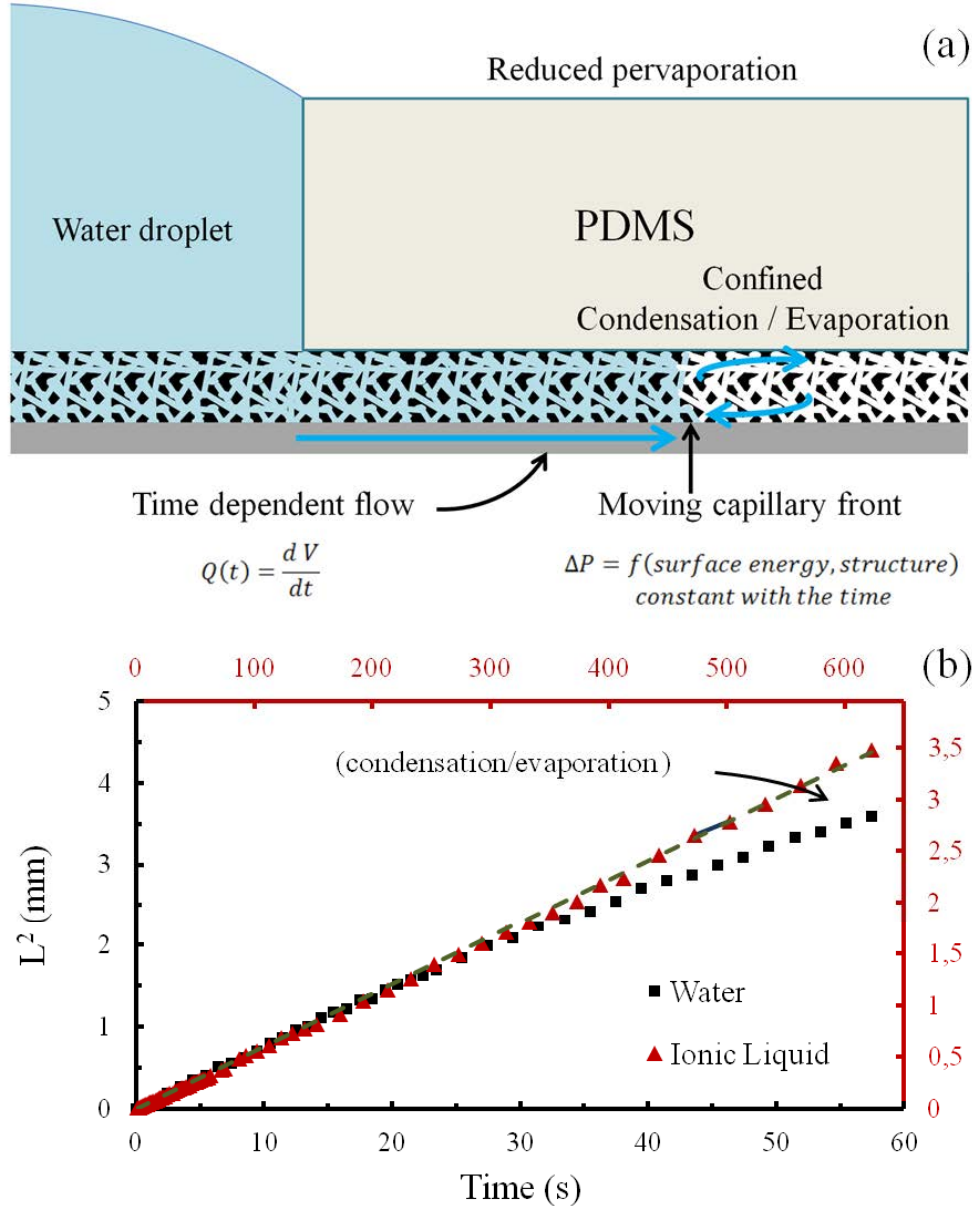


Figure.IV-9. (a) Scheme of the phenomena taking place when a water drop stands at the edge of PDMS top cover (stamp) on a thin film that allows wicking. (b) Graphic displaying the diffusion limited capillary filling in the highly interconnected S-60/60 porous film with water and with an ionic liquid fluid (1-Ethyl-3-methylimidazolium dicyanamide), as observed by optical microscopy in the configuration illustrated in a). Black (points and axes) corresponds to water, while red (points and axes) correspond to the ionic liquid. The graphic is plotted with the distance of the fluid front from the original position being the edge of the PDMS stamp, in the porous film versus time. Dots are experimental points and plain lines are linear fits of the first 20 points of both curves.

The experimental points corresponding to the early stage of the capillary filling with either water or ionic liquid, shows that the square of the traveled distance is linear with time, which suggests a diffusion limited transport that perfectly fits the Washburn theory of capillary filling [5]. It can be observed that the filling with the ionic liquid (red axes) is much slower than the filling for water due to its higher viscosity [55]. For long times of experiment, the water front tends to slow down more than predicted by the Washburn law, whereas the ionic liquid front stills follow the linear regime. This is related to the much higher volatility of water compared to that of the ionic liquid,

which involves water evaporation at the advancing front (and through the PDMS porosity) that cannot be neglected after a certain distance. Indeed, evaporation rate at the front is limited by the evacuation of the gaseous water outside of the porous network and is thus assumed to be constant during the experiment time frame. On the other hand, the liquid front speed progressively slows down with the covered distance. Evaporation of water becomes thus more and more dominant with the front slowing down, a phenomena not accounted for in the classical Washburn prediction, but which was reported for single slit nanochannels of less than 20nm [56]. This aspect will be also addressed in the next section when the theoretical model of capillary filling is built up. It has to be noticed that even if no PDMS is applied, the ionic liquid fills the porous structure with the same law. Because the ionic liquid has a very low vapor pressure, no PDMS stamp is necessary, and filling the thin film porosity by capillarity can anyway be completed over time. Capillary filling under PDMS was repeated for all films with water and in some cases with ionic liquid and studied dynamically. The corresponding filling speed are expressed as the D parameter of the equation from Washburn theory of capillary filling [5].

$$L^2 = D * t \quad (20)$$

In Table.III-1 D values are then correlated to the porosity characteristics (pore diameter and porosity) of the corresponding film, deduced from SEM images and/or EEP isotherms shown in Chapter IV. The code for the samples is conserved. The already presented values of pore and bottle-neck size are here reported for simplicity. As mentioned earlier it has to be stressed that because EEP is not appropriated to determine pore size above 50 nm [53], estimation from SEM images was used when capillary condensation occurred above 95% RH. Thus, in this case, pore diameter is determined from SEM-FEG images. As in the already presented Table the symbol “*” is used in Table.III-1 when the corresponding value has not been determined. In the last two columns the values of the filling speed for water and ionic liquid are expressed as D of equation (1); in the case where no filling was reported the symbol X was used. It is remembered here that in all cases the inorganic material of the films is composed by SiO₂. In exception of samples PS3, PS4, Bj4 and Bj5 the organic/inorganic ratio of the solution used for the deposition step has the same value for all samples (see Table.III-1 of Chapter III).

The samples are listed in decreasing values of water capillary filling speed and, in exception of the PPN samples whose synthesis is reported in the previous chapter, their pore structure is obtained through EISA templating approach.

Table.IV-1 is divided in 3 sections. The top section gathers films exhibiting larger pores and rather homogeneous porosity as evidenced by the quasi overlapping of the adsorption and desorption

curves at high water relative pressure as shown in the isotherms of Figure.III-13 of the previous chapter. Limited bottle-neck effect is observed and the porosity is (in exception of the PPN sample) generated through a spinodal phase separation templating mechanism. The second section reports a set of samples with a more micellar-like porous structure (SEM images in Figure.III-14 and Figure.III-15 of Chapter III). These samples show different values of pore diameter calculated by the adsorption branch but rather similar values of the bottle-neck size calculated by the desorption branch of the EEP isotherms. These samples have indeed values of pore diameter between 4.6 and 27.5nm from adsorption, and values between 2.0 and 4.8 nm from desorption. In the third section are reported the characteristics of the films that do not allow infiltration and do not show the capillary ring around a sessile drop. The SEM images, EEP hysteresis cycles, and pore size distributions of these samples have been reported in Figure.III-16 of Chapter III.

Sample	Ads. RH(%)	Des. RH(%)	SEM diam. (nm)	Ad. Diam. (nm)	Des. Diam. (nm)	$\Delta RH(\%)$	Por. Vol. (%)	D_{water} * 10^{-2} (mm ² /s)	D_{IL} * 10^{-2} (mm ² /s)
<i>PS6</i>	99.4	97	180±40	*	*	2.4	59	21	4.8
<i>PS5</i>	97.9	97.5	75±20	*	*	0.4	54	7.9	3.8
<i>PS1</i>	96.8	96.5	60±10	*	*	0.3	64	7.6	0.55
<i>PPN</i>	93.4	91.5	20±4	17.1 ^s	15.2 ^s	1.9	86	7.0	1.2
<i>Bj1</i>	63.5	52.4	*	5.2	3.8	11.1	58	2.8	0.18
<i>Bj2</i>	59.3	48.0	*	4.6	3.4	11.3	59	2.1	0.020
<i>Bj3</i>	69.3	57.8	*	6.3	4.4	11.5	61	1.9	0.028
<i>F1</i>	68.9	48.0	*	6.2	3.4	20.9	55	1.4	*
<i>F2</i>	75.0	49.2	*	7.8	3.5	25.8	55	0.64	0.013
<i>PBd1</i>	83.5	33.0	*	12.0	2.3	50.5	50	0.21	*
<i>PBd2</i>	80.6	27.0	*	10.2	2.0	53.6	50	0.060	0.00017
<i>PS7</i>	88.5	42.9	*	17.5	3.0	45.6	55	0.044	*
<i>PBd3</i>	91.8	55.4	*	24.3	4.1	36.4	53	0.015	*
<i>PBd4</i>	93.0	60.9	*	27.5	4.8	32.1	53	0.0070	*
<i>PS2</i>	96.0	55.4	60±5	*	4.1	40.6	63	-	-
<i>PS3</i>	93.3	50.5	*	29.9	3.6	42.8	33	-	-
<i>PS4</i>	95.8	69.4	50±10	*	6.3	26.4	47	-	-
<i>Bj4</i>	37.0	22.8	*	2.6	1.8	14.2	32	-	-
<i>Bj5</i>	43.0	39.2	*	3.0	2.7	3.8	46	-	-
<i>PS8</i>	95.2	71.4	55±15	*	6.8	23.8	47	-	-

Table.IV-1: Structural and capillary filling properties and of the different films used in this study. The table has already been reported in the previous chapter but here the values of capillary infiltration speed, expressed as the Washburn coefficient D are reported too. The D values for capillary filling for water and ionic liquid respectively are reported in the last two columns.

IV.2.a.iii.2 Bottleneck – pore size dimensions influence on capillary filling speed.

Here we analyze the quantitative data contained in Table.IV-1, regarding the capillary filling speed.

To do so, in Figure.IV-10a, D values for water are plotted with respect to pore size and bottleneck size. Presence and diameter of bottlenecks were evaluated from EEP desorption experiments as reported in Table. IV-1 (Des. Diam.). In the case of larger pores, where EEP could not be used to determine their dimension, a continuous bar is used that represents the approximated dimensions measured on the SEM images. In Figure.IV-10a, the samples from the first section (larger pores) are clearly distinguishable as faster than the samples of the second one. As was said, increasing the pore diameter (supposing no bottle-necks and a uniform nanochannel) leads to an increase of the filling speed as expected from the Washburn theory. In particular a roughly linear increase is found as expected from Washburn theory for samples PS1, PS5, PS6 and Bj1 that show a very thin hysteresis. It has to be pointed out that the “tortuosity” of the porous structure is not taken into account by Washburn law. However, to the similar porous morphology of the cited PS1, PS5, PS6 and Bj1 samples, this D vs pore size linear trend can be plausible. The D value of the PPN sample is positioned above the tendency line, which is attributed to the lowest tortuosity associated to the uniformly standing periodical pillar array conformation. This is another example of why PPNs structure is considered as ideal for fluid transportation. It also is important to underline that the pillar inner porosity composed of 2 nm pores does not govern the filling. If it was the case, the D value would be located below the tendency line.

A different trend is observed for the sample with lower pore sizes. In order to be able to better inspect the data for the samples of the intermediate section, Figure.IV-10b expands the bottom-left corner of Figure.IV-10a. A logarithmical scale in the vertical direction is used in order to have a clearer view of water filling speeds that range over three orders of magnitude. As can be easily seen, for the samples of the second section, the bottle-neck size can be considered uniform with values ranging from 2 nm to 4.8 nm. The pore diameter, instead, varies ranging from 4.6 nm to 27.5 nm. Figure.IV-10b shows a clear and unexpected tendency: considering an almost constant bottle-neck size, larger the pore size leads to the slower filling speed of water in the porous network. This decrease is counterintuitive with respect to the known laws for liquid capillarity because an increase of pore size should lead to a higher (or at least constant) filling speed even in presence of smaller constrictions.

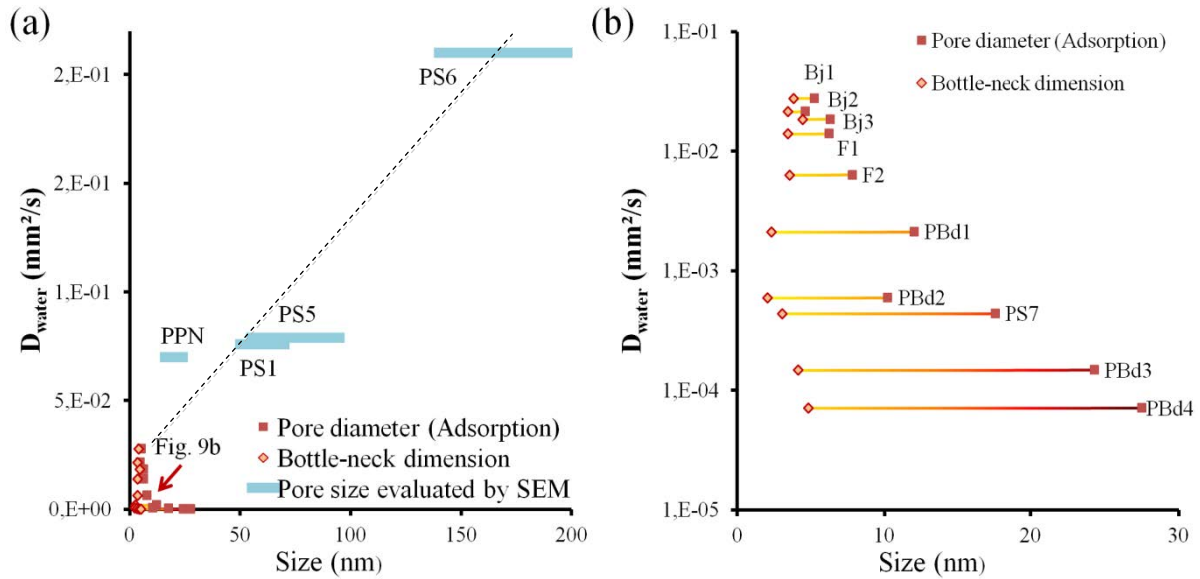


Figure.IV-10. (a) D values versus pore and constriction size. The blue bars correspond to the samples of the top section of Table.III-1 while the yellow and red points correspond to the mesoporous samples of the intermediate section (dashed line represents the global tendency and a guide for the eyes). (b) zoom of (a) between 0 and 40 nm.

The most convenient way to describe this tendency is to consider the hysteresis width. It is interesting to notice that for samples with small bottle-necks, a large hysteresis means a slower water filling while for samples with larger bottle-necks (PS2, PS4, PS8, PS9) a large hysteresis totally block the filling of the porosity. Thus, a general rule can anyway be obtained from these results: narrower EEP hysteresis leads to the faster and efficient the capillary filling. This effect might be due to other phenomena characteristic of the mesoscale such capillary condensation and evaporation.

IV.2.a.iii.3 Size dependence of the transport mechanism.

These discrepancies in the filling behavior between the samples with large bottle-necks and small bottle-necks have to be investigated. In order to evaluate the effect of water evaporation / condensation / filling, some of the experiments were repeated with a non-volatile ionic liquid in order to avoid any condensation/evaporation effect. The experiments for the ionic liquid were conducted in exactly the same conditions than the ones for the water filling.

As can be seen from Table.IV-1 the filling with the ionic liquid always proceeds slower than water one due to its higher viscosity. From Table.IV-1 it is possible to see that the D value versus pore size with the ionic liquid follows the similar tendencies that have been found for water. However, from the comparison of the D values of water and the ionic liquid, a new feature appears. In Figure.IV-11 the $D_{\text{water}}/D_{\text{Ionic-Liquid}}$ ratio as function of the pores and bottleneck size for some of the samples, is reported in Figure.IV-10.

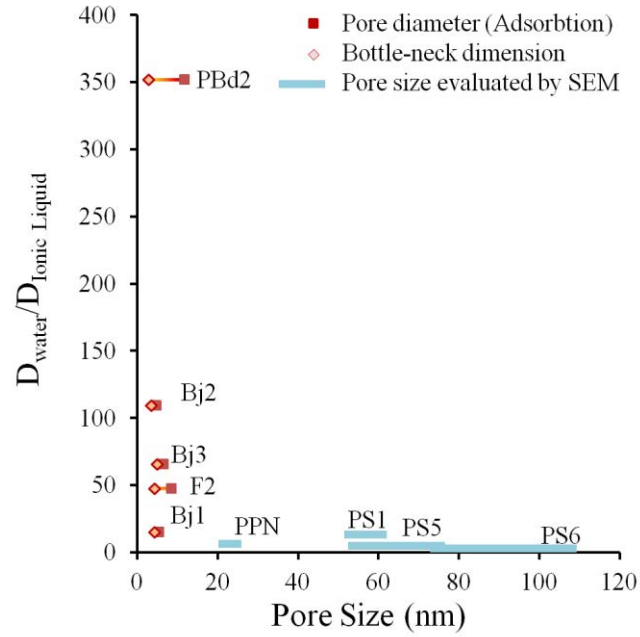


Figure.IV-11. $D_{\text{water}}/D_{\text{IL}}$ values for samples reported in Table.III-1. The same code of Figure.IV-10 has been used to express the pore and constriction sizes.

As can be easily seen, this ratio is rather low for the samples of the first section with values ranging from 2 to 14 while for the samples of the second section this ratio assumes higher values ranging from 15 to 350. For the samples of the first section (larger pores) the water and ionic liquid difference in the $D_{\text{water}}/D_{\text{IL}}$ values is attributed to the porosity structural characteristics and to the relative variation of viscosity of fluids in nanoconfinement (as discussed previously). For samples of the second section, increasing the difference between the pore size (adsorption) and the bottle-neck size seems to slow down the filling of the ionic liquid much more than in the case of water (even if water itself is slowed down) which cannot be explained through tortuosity reasoning. Due to its low vapor pressure the ionic liquid has to penetrate in the porosity in a pure liquid way contrary to what could happen with water. In order to explain this unexpected behavior the evaporation/condensation equilibrium that establishes at the liquid front within the porous network has to be considered. A global picture of the possible mechanisms is illustrated in Figure.IV-12 and is explained as follows. As already mentioned, evaporation at the liquid front within the porous network depends on the evacuation of the vapor phase and thus on the pore structure. It is therefore assumed to be constant in the same film during the capillary filling, and one may conclude that a decreasing gradient of vapor pressure exists from the liquid front. Knowing that, capillary condensation occurs at vapor pressures below saturation in nanopores due to confinement, it is consistent to expect that evaporated water molecules may recondense in empty pores before the liquid front reaches it. The smaller the pores are, the lower is the critical vapor pressure for capillary condensation. It is then possible to imagine a mechanism of the water

filling where the main part of the water molecules that contribute to the advancement of the water front evaporate from it and condense again one pore away cyclically moving, in this way, the front forward. In the case of the ionic liquid, clearly, this mechanism is not possible. Being the filling driven by the diffusion of water in the vapor phase, in a mono-dimensional channel, the filling dynamics would anyway follow the same mathematical laws of the Washburn theory (with the squared length of the filled channel proportional to the time through a constant D) but with values of the speed and of the D constant that depends, in a different way, from the porosity characteristics. Supposing this kind of mechanism the tendency revealed in Figure 9b could be easily explained: because for larger pores, the relative humidity needed to fill them by capillary condensation is much higher than the humidity needed for smaller ones; the time needed to the system to reach the adequate humidity in the next pores is much longer for larger pores than for smaller ones and then the speed of the advancing front is lower. This interpretation seem also consistent if the actual and quantitative tendency shown in Figure.IV-10b (with a filling speed that decreases exponentially with the pore diameter (adsorption) (notice that the vertical axe is in the logarithmic scale)) is compared with the exponential characteristics of the Kelvin equation for pore condensation with respect to vapor pressure.

The mechanism of water filling in such small porosities is thus cooperative between capillary filling and capillary condensation as seen in Figure.IV-12. D includes thus two driving forces for filling that are depending, in a different way, on the porosity characteristics. An adequate mathematical model could be derived but proper knowledge of the exact porosity shape would be needed. Otherwise computer simulation (MD) could provide a useful tool to modeled porous structures.

It has to be noticed that in the case of porosities with larger bottle-neck and larger pore sizes, the dynamic of the evaporation/condensation mechanism could be so slow for water that no filling is observed. In the cases where neither capillary ring or capillary infiltration was observed (samples in the third section of Table.IV-1), the critical vapor pressure for water capillary condensation in the front close-by porosity is never reached due to a too slow liquid progression (tortuosity and presence of solid dead-ends) compared to the vapor phase evacuation (diffusion away from the front). Similarly to solid dead-ends in the porous network, water flow blockage could also be related to air-trapping in the pores due to water condensation at the smaller pore intersections between larger pores. This can explain why the PS2 sample doesn't show any filling.

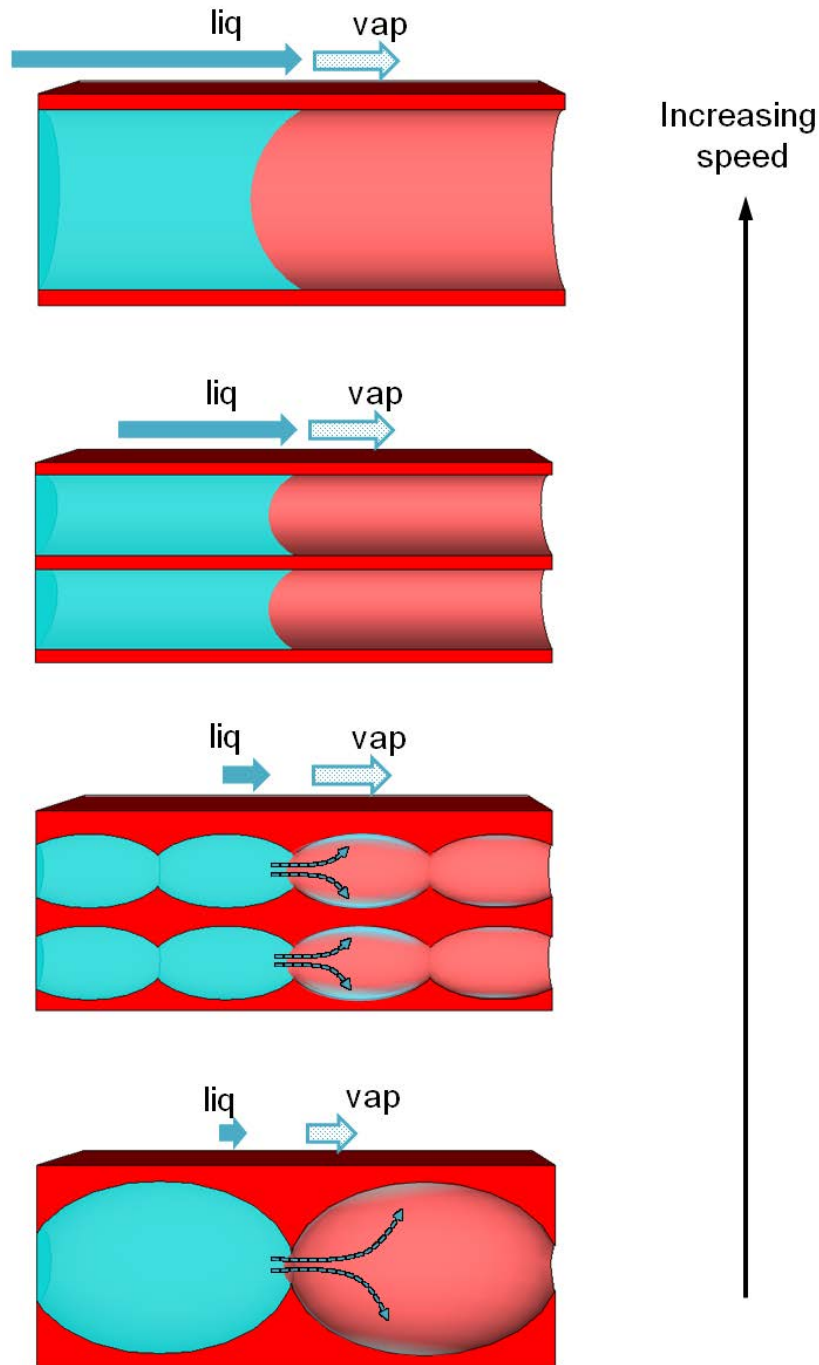


Figure.IV-12. Illustration of the capillary infiltration mechanism in the various porosities, taken into account the pore relative dimension and the presence of constrictions (bottlenecks), and the two driving forces related to liquid capillary transport and vapor capillary condensation. Liquid front progression proceeds faster from the bottom to the top.

As a final remark, it has to be said that evaporation depends on temperature and relative humidity and that the present experiment were performed at $25 \pm 2^\circ\text{C}$ and $30 \pm 10\%$ RH. However, the influence of external humidity has been investigated for the sample Bj1 for which the transport through cooperative evaporation/condensation at the front prevails. No significant difference in front advancement rate was observed for three different relative humidity values (8, 30 and 55% RH) applied in a close chamber. This suggests that the time scale of the water vapor exchange

between the atmosphere and porosity to reach equilibrium is much longer than that of the evaporation/co-condensation occurring at the advancing front. In other words, when humidity in the atmosphere is below critical humidity for capillary condensation, the phenomena taking place at the front are not significantly influenced by the external humidity. On the other hand, when the experiment is performed above critical humidity for capillary condensation (at 100% RH), an additionally condensation of water at the edge of the PDMS stamp has been observed with the propagation of the front underneath the PDMS as expected.

IV.2.a.iv Conclusion

In conclusion this study allowed understanding that:

- The capillary ring experiment can be utilized to simply inspect if a thin film allows capillary infiltration.
- A higher porous volume is often associated to a lower tortuosity and to a faster capillary infiltration for thin films prepared by EISA.
- For large pores samples (>50 nm) with similar bottle-neck- pore dimensions (open porosity) the infiltration rate increases with the pore sizes.
- Porosities with small bottle-neck dimensions allow faster infiltration for smaller pore size (reducing the pore size to values similar to the bottle-neck size the filling speeds up).
- Liquid natural infiltration in nanoporous materials is governed by a cooperative mechanism, involving liquid transport by capillarity and vapor transport.
- For large pores (more than ≈ 50 nm), the liquid transport by capillarity dominates.
- In the mesoporous range, the evaporation at the liquid front can no more be neglected, and the capillary condensation dominates the filling.

The results obtained have importance for nanofluidic applications. The transport mechanism for thin films involving the evaporation/condensation could indeed modify the transport of solutes if solutions (instead of pure liquids) are infiltrated. In the case of the evaporation/condensation mechanism indeed the solutes “feels” a different flow from the totally liquid case. Solutes are not transported through the gas phase thus their migration should be limited to the liquid contribution of the advancement. Alternatively, evaporation of the solvent could cause solute re-precipitation into the pores. Further investigations could clarify what happens to solutes in separation experiments. Due to the multiple nanoscopic effects a forecast is not attempted but the condensation/evaporation mechanism in small pore structures could play a key role among the other nanoscopic phenomena.

IV.2.b Capillary infiltration in PPNs

As described earlier, a precise description of the pore structure is needed in order to allow the modeling of capillary filling keeping into account tortuosity consideration. An accurate description can be obtained locally, for example from high-resolution tomography TEM techniques. Nevertheless the information gathered through electron microscopy are referred to a limited area and then the extracted structure would be no representative of the system. Moreover, in order to perform simulations, it is necessary to create simulation boxes with periodic boundary conditions (that is not the case of most of EISA systems). It is then necessary to create structures that are themselves periodical in order to be able to simulate the various phenomena that take place inside them and further investigate the influences of the structure characteristics.

The perfect candidate for this kind of study is then the Pillared Planar Nanochannel structure introduced in the previous Chapter. With its hexagonal periodicity it is indeed adapted to be modeled in an easy way. Moreover, the deep control over its structure allows to study each element separately which could help to better understand the various contributions to the filling.

The PPN chosen for this study were realized with the PS-b-PLA block copolymer since they allows fabrication of very ordered periodical structures. The samples obtained through the PS-b-P2VP block copolymer are indeed not perfect enough to be really modeled computationally. Quality of pillar verticality and long-range order of samples obtained from PS-b-P2VP are indeed not at the same level of the PS-b-PLA based one.

Unfortunately the samples that could be studied were produced by spin-coating (before the introduction of the biphasic dip-coating deposition method). So only few 1cm^2 samples were produced and could be utilized for this study.

The influence of the larger and smaller dimensions will be analyzed by both experimental and modeling approaches. Moreover the effect of a smaller porosity in coexistence of a larger one (PPN structures realized with a mesoporous SiO_2 (CTAB)) and the influence of the material composition will be analyzed.

In order to perform modeling, we will reuse and adapt the equations described for the case of a plane channel described in the first part of this chapter (section IV.1.b) with the PPNs geometry.

IV.2.b.i Description of the investigated PPNs structures.

In order to perform the infiltration experiments in the PPN structure some samples have been prepared. Pillar height was varied between 12 and 202 nm by adjusting the PS-b-PLA initial thickness. The thickness of the roof was adjusted by deposition of excess of sol-gel precursors.

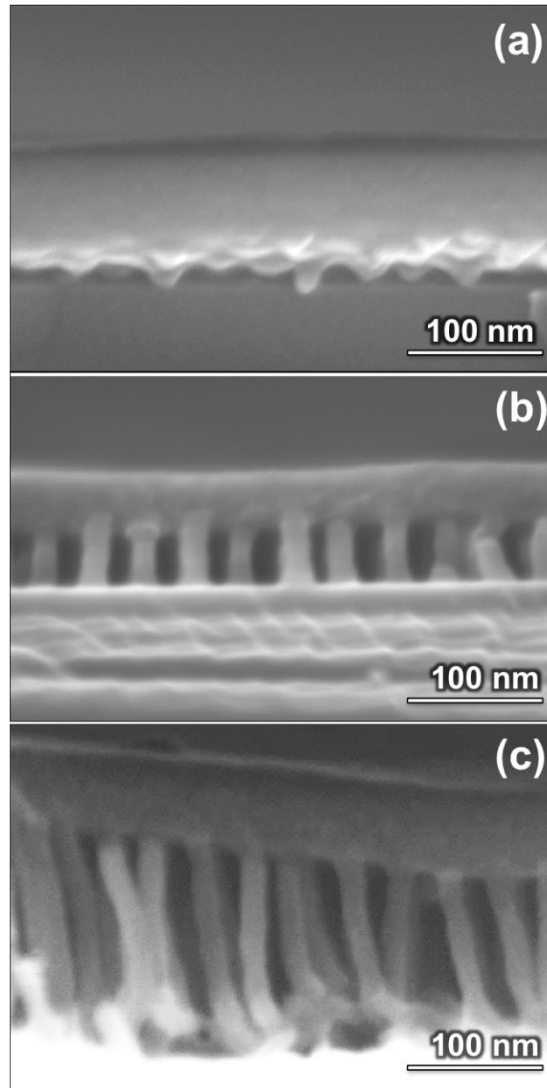


Figure IV-13. SEM-FEG images of 3 different SiO₂ PPN samples: the pillar height can be tuned by changing the initial PS-B-PLA layer thickness. a) SD 12, b) SD 60 and c) SP 202.

The pillar composition was either pure SiO₂ or a solid solution of 70% SiO₂ + 30% TiO₂. As mentioned mesoporosity was introduced in the silica pillars using CTAB as a template. Figure IV-13 displays the cross sectional SEM images of three samples, all exhibiting the characteristic PPN pillar/roof morphology with a constant pillar diameter of 20 ± 1 nm but different pillar height of 12, 51 and 202 nm (accessed by ellipsometry). In order to avoid cracks, the thicker sample was made of mesoporous silica while the two thinner ones were composed of dense silica. As already described, PPNs built using PS-b-PLA have the center-to-center distance

equal to 38 nm. Taking into account the average pillar diameter of 20 nm from SEM, the mean pillar surface-to-surface distance ($ds-s$) is 18 nm; this is smallest dimension of the interconnections for PPN when pillar heights are greater than $ds-s$.

As seen before, no sorption hysteresis is observed in EEP experiment on PPNs confirming a fully interconnected network, ideal for capillary-driven flow. In the experiments of capillary infiltration, no effect of the roof thickness was evidenced on the filling behaviour. This parameter is thus not reported. Final samples characteristics are listed in Table.IV-2.

<i>Sample</i>	<i>Composition</i>	<i>Pillar height</i>	<i>Pillar porosity</i>	<i>d s-s</i>	<i>D (mm²/s)</i>
SD 12	SiO ₂	12 nm	none	18 nm	4.42 *10 ⁻²
SP 51	SiO ₂	51 nm	CTAB (2.5nm)	18 nm	7.45 *10 ⁻²
SD 60	SiO ₂	60 nm	none	18 nm	7.18 *10 ⁻²
SP 202	SiO ₂	202 nm	CTAB (2.5nm)	18 nm	7.17 *10 ⁻²
TSD 56	SiO ₂ (70%) TiO ₂ (30%)	56 nm	none	18 nm	12.92 *10 ⁻²

Table.IV-2. Composition, pillar height, pillar porosity, minimal pillar surface to surface distance, and Washburn's coefficient of samples considered in the present discussion.

IV.2.b.ii Dynamics of the capillary filling in PPN:

In Figure.IV-14 we show the time dependence of the square of the distance of the water-front from the PDMS stamp edge during the first seconds of capillary filling in PPN samples (with the configuration already described in Figureb). In Figure.IV-14b, a reconstruction of the filling with the orthogonal view tool of ImageJ for stacks is shown. The image is obtained from a video showing the infiltration in the vertical direction. A single line of pixels is selected and its appearance reproduced for increasing times moving it rightward. The filling can then be followed in the time in a single image having the time in the abscissa direction. In the five different samples, a linear dependence of L^2 with respect to time allowed extraction of a diffusion coefficient (D) (Table.IV-2).

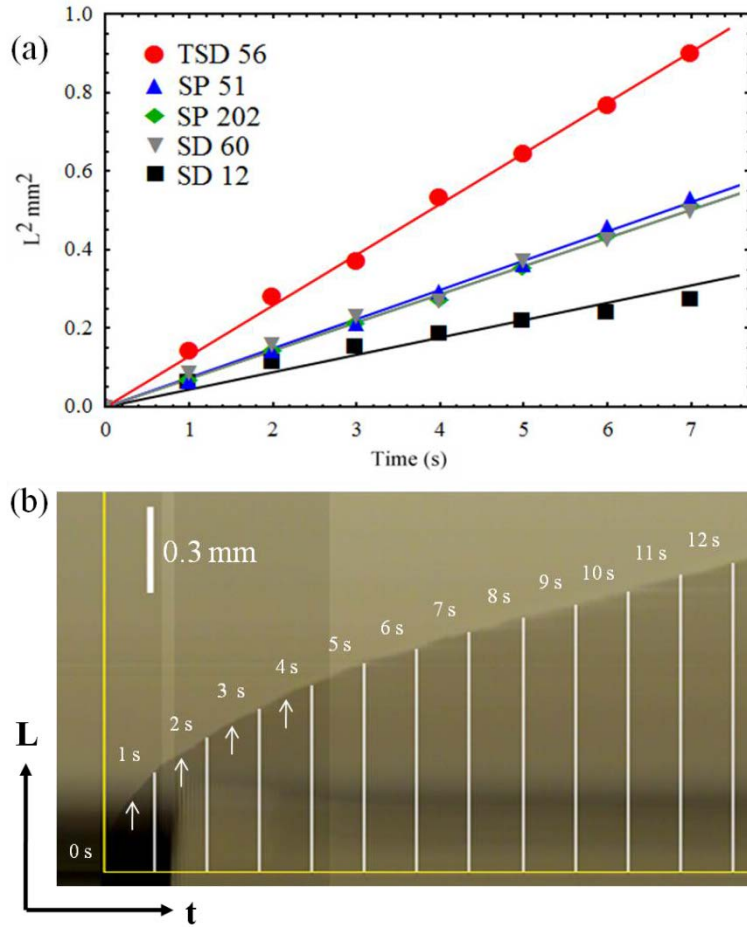


Figure.IV-14. (a) Square of the travelled distances of the water front by capillary as a function of time in PPNs (SD 12 : 12 nm tall dense silica pillars; SP 51, 51nm tall mesoporous silica pillars; SD 60, 60 nm tall dense silica pillars; SP 202, 202 nm tall mesoporous silica pillars; TSD 56, 56nm tall dense silica-titania (30%) pillars. In the range of mechanical stability associated to the system no effect of the roof thickness was evidenced on the filling behaviour (data not shown). (b) Reconstruction of the filling in the time domain.

IV.2.b.ii.1 The chemical nature of pillars has a strong influence on wicking

The first most important observation that can be made concerns the effect of the chemical nature of the pillars (and roof). The more hydrophilic pillars containing 30% of TiO_2 in TSD56[57] give a diffusion coefficient of $12.92 \cdot 10^{-2} \text{ mm}^2/\text{s}$ compared to 7.45 in the pure dense silica PPN with the same pillar height (SP51). The contact angles of water on both these materials are close ($<25^\circ$), so that the strong discrepancy between the filling dynamics is not only due to a different wettability but mainly to other effects occurring at the nanoscale.

IV.2.b.ii.2 The porosity of the pillars has a weak influence on wicking.

The dense SP 51 sample and the mesoporous SD 60 samples have similar D values of $7.45 \cdot 10^{-2} \text{ mm}^2/\text{s}$ and $7.41 \cdot 10^{-2} \text{ mm}^2/\text{s}$, respectively. This result is at first glance unexpected: the average size of CTAB-based pores is around 2.5 nm, which is small enough for the pores to be filled up with water for humidity above 40%. Since the measurement was performed at $\text{RH} > 50\%$, pillars were

already full of water, leaving only the inter-pillar porosity empty before the wicking, which could have induced an increase of the real wetting efficiency. Nevertheless, no notable influence of the mesoporosity was observed. This suggests that surface area could be increased through the introduction of an inner-pillar porosity without perturbing the infiltration mechanism, which is extremely useful for certain applications, such as heterogeneous catalysis, separation or sensing.

IV.2.b.ii.3 The height of pillars matters only if it is small.

In this section it will be demonstrated that the hydrodynamic capillary filling is governed at the nanoscale by the open porosity being composed of the largest pores and interconnections, as in the macroscale [58]. The influence of the pore anisotropy can indeed be studied by varying the pillar height: the dimension of the restriction varies only in the transversal direction, leaving the lateral dimension constant and equal to the pillar surface-to-surface distance ($d_{s-s} = 18$ nm here). The limitations of the used approach did not allow realizing both dense and porous SiO₂ for all pillar heights: 12 nm pillars were realized only with dense SiO₂, while 202nm pillars required more flexible porous SiO₂, because a dense silica structure cannot stand the mechanic stresses created during the calcination. Interestingly, plots in Figure.IV-14a reveals that there was no significant evolution of the diffusion coefficient between the 51 nm and 202 nm samples, while it drops of around 60% for the 12 nm thin samples, passing from $7.45 \cdot 10^{-2} \text{ mm}^2/\text{s}$ to $4.42 \cdot 10^{-2} \text{ mm}^2/\text{s}$. It seems thus that the filling speed is influenced by the pillar height only at low values of the height. It will be shown in the next modeling section that this behavior is related to the actual aspect ratio of the restrictions, interconnecting the larger cavities of the porosity.

IV.2.b.iii Modeling the capillary filling in PPN:

In order to interpret quantitatively the experimental results, and to extract more information from the measurement of the Washburn coefficient D , it is necessary to model the fluid dynamics within the PPN. As will be shown, the proposed model predicts surprisingly well the influence of the pore dimensions on the filling speed, considering only basic macroscopic fluid laws.

IV.2.b.iii.1 Computation of the hydrodynamic resistance of the PPN

As already mentioned, the fluid flux results from a balance between the capillary driving and the viscous dragging forces, which can be classically written as the Darcy's law: $\Delta P_{menisc}(h) = R(h, L(t), t) * Q(h, L(t), t)$ with $R(h, L(t), t)$ the hydrodynamic resistance of the structure, $Q(h, L(t), t)$ the flux, and $\Delta P_{menisc}(h)$ the pressure drop across the meniscus.

The Washburn's coefficient D is related to the flux Q . For a complex structure such as the PPN, there is no analytical solution of hydrodynamic equations that leads to a value of the hydrodynamic resistance. Numerical routes can be used to solve this difficulty, i.e. by numerically solving the Navier-Stokes equation. This equation cannot be solved with the full PPN structure, but, as mentioned, advantage of the hexagonal symmetry of the structure can be taken, and the equation only solved within a unit cell represented in Figure.IV-15a. The hydrodynamic resistance of the whole system can be seen as the sum of the hydrodynamic resistances of all the unit cells crossed by the flow. The expression of the resistance can be rewritten as

$$R(h, L(t), t) = R_{cell}(h) * n(t) \quad (21)$$

with $n(t)$ the number of cells crossed by the water front. In this case, $n(t)$ can be considered as a continuous function of time. Expressions of the hydrodynamic resistance have already been derived for forests of pillars without considering any symmetry[59], or in the case of squared symmetry, and have been applied to describe wicking[60]. Here the calculation concerns the hydrodynamic resistance in a structure with hexagonal symmetry as illustrated in Figure.IV-15. The value of $R_{cell}(h)$ can be obtained by solving the equation based on Darcy's law

$$R_{cell}(h) = \Delta P_{cell} / Q_{cell} \quad (22)$$

Here, Q_{cell} is the calculated flux through a cell for an imposed pressure drop (ΔP_{cell}) between the cells boundaries over the indicated flow direction (see arrow in Figure.IV-15a). The finite element program COMSOL has been used as a Navier-Stokes solver, with no slip conditions on the walls (fluid speed at the wall interface is zero), imposing periodic boundary conditions on the flow in the x and y directions. The viscosity η of the fluid was set equal to $\eta_{wat} = 0.001$ Pa.s, which is the viscosity of bulk water at the temperature of the performed experiments (20.2°C [61]), and ΔP was arbitrarily chosen equal to 1 Pa. In these conditions the resulting flow is laminar as expected by the typical nano-dimension of the real system for any value of the pillar height (h). The COMSOL method was previously validated with typical Poiseuille flow between two planes at the same height scale. In this investigation, various directions of the flow through a forest of 2D-hexagonal 50 nm pillars have also been tested and deviations of less than 5% of the nominal flow were found. This can be related to computation artifacts (imposed mesh), but these deviations are not significant enough for all flow directions to be considered in this simulation.

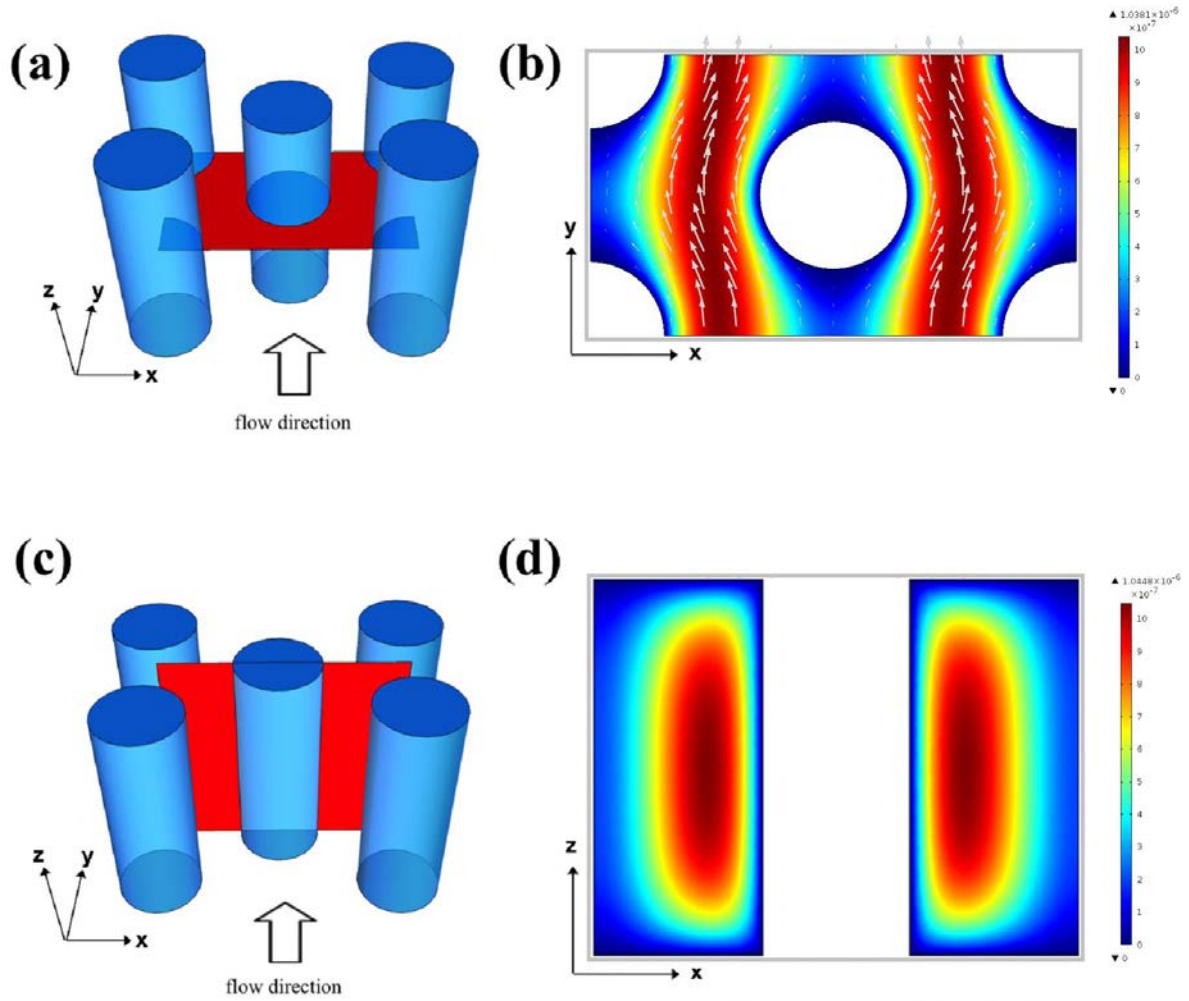


Figure IV-15. The unit cell of the Navier-Stokes COMSOL simulations is composed of 4 pillars at the corners of the cell and a pillar in the middle organized into a 2D-hexagonal structure. (a) Horizontal plane of plotting (xy plane). (b) Flow velocity field in the y direction, in the plane described in (a). (c) vertical plane of plotting (zx plane); and (d) flow velocity field in the plane described in (c) (in the y direction with the imposed constraints (the flow is imposed in the y direction; the arrows indicate the real flow direction and intensity in every points).

As expected, calculated flows Q_{cell} in the PPN for our choice of parameters decrease with the height h of the pillars: for example, $Q_{cell}(h=12 \text{ nm}) = 8.91 \times 10^{-2} \text{ nm}^3/\text{ns}$; $Q_{cell}(h=51 \text{ nm}) = 1.18 \times 10^{-2} \text{ nm}^3/\text{ns}$ and $Q_{cell}(h=202 \text{ nm}) = 5.72 \times 10^{-2} \text{ nm}^3/\text{ns}$. Using the Darcy's law derived equation, this yields values of the hydrodynamic resistance of the cell. In order to obtain the hydrodynamic resistance for another fluid viscosity η , advantage is taken of the linearity of the Navier-Stokes equation in the laminar regime: $R_{cell}(h, \eta) = \beta * R_{cell}(h, \eta_{wat})$ with $\beta = \frac{\eta}{\eta_{wat}}$. It has to be noticed that also the value of the viscosity in nanostructures cannot be straightforward considered equal to the value in bulk [32], [56], [38, 39] and that therefore the value of β could be different from 1 even for water in the nanostructure.

Representations of the fluid velocity fields are shown in Figure.IV-15b for the selected unit cell. As expected for no slip conditions, the flow is higher in regions that are far from the pillar surface. The no-slip condition is responsible for the building up of the resistance with increasing surface to volume ratio. More interestingly, the flow seems to settle mainly under quasi-straight pathways (red zones on Figure.IV-15b). The fluid that is located between two pillars aligned parallel to the flow direction is almost immobile (blue zones in Figure.IV-15b). These regions can be seen as hydrodynamic traps for separation of elongated biomolecules blobs such as DNA.[62]

IV.2.b.iii.2 Evaluation of the pressure drop across the meniscus

As already described it is possible to obtain the value of capillary pressure from virtual work reasoning (with $\Delta\gamma = \gamma_{sg} - \gamma_{sl} = \gamma_{lg} * \cos(\theta)$)

$$\Delta P_{menisc}(h) = \Delta\gamma \frac{dS(h, L(t))}{dV(h, L(t))} \quad (23)$$

A discretization can be performed in this case to obtaining

$$\Delta P_{menisc}(h) = \alpha * \Delta\gamma \frac{S_{cell}(h, L(t))}{V_{cell}(h, L(t))} \quad (24)$$

where the dimensionless parameter α is added to address the discretization approximation. Inside a cell, the geometry of the meniscus varies indeed with the time during the propagation. The last Equation accounts for a spatial average of the capillary force at the cell scale, so that the parameter α actually accounts for the difference between the spatial average and the accurate temporal average. Just to give an idea of the pressures that are taken into account, considering the unit cell described in Figure.IV-15 with a height of 50 nm, pressure of the order of $70 * 10^5 \text{ Pa}$ are found.

IV.2.b.iii.3 Computation of the Washburn transport coefficient

Once the hydrodynamic resistance is computed using the Navier-Stokes solver, and once the pressure drop across the meniscus is evaluated, the Washburn diffusion coefficient can be deduced using the following strategy.

The flow $Q(h, l, t)$ in the Darcy's law can be written as

$$Q(h, L, t) = A_{lateral}(h) * dL/dt \quad (25)$$

that can be rewritten by discretization

$$Q(h, L, t) = A_{lateral}(h) * l_0 \frac{dn}{dt} = V_{cell}(h) * \frac{dn}{dt} \quad (26)$$

where $A_{lateral}(h)$ is the section of the unit cell perpendicular to the liquid flow direction and l_0 the dimension of the cell parallel in the same direction. Introducing this in the Darcy's law equation it can be obtained:

$$\Delta P_{menisc}(h) = R_{cell}(h, \eta) * n(t) * V_{cell}(h) * dn(t)/dt \quad (27)$$

which leads to

$$\Delta P_{menisc}(h) * \frac{1}{V_{cell}(h)} * \frac{1}{\beta * R_{cell}(h, \eta)} = n(t) \frac{dn(t)}{dt} \quad (28)$$

In term of the Washburn's law, the last equation can be integrated over time and number of unit cell into

$$n(t)^2 = \frac{2}{V_{cell}(h)} * \frac{\Delta P_{menisc}(h)}{R_{cell}(h, \eta)} * t = D_n * t \quad (29)$$

with $D_n = D/l_0^2$.

$$L(t)^2 = \frac{2}{V_{cell}(h)} * \frac{\Delta P_{menisc}(h)}{R_{cell}(h, \eta)} * l_0^2 * t = D * t \quad (30)$$

Using the expression of $\Delta P_{menisc}(h)$, we finally obtain

$$L(t)^2 = \frac{2 * \alpha}{\beta} * \frac{\Delta \gamma}{R_{cell}(h, \eta_{wat})} * \frac{S_{cell}(h, L(t))}{V_{cell}(h, L(t))^2} * l_0^2 * t = D * t \quad (31)$$

Within the expression, there are two unknown parameters α and β . A priori, the ratio α/β depends on the material chemical nature and dimensions, and on the fluid viscosity.

IV.2.b.iii.4 Reproduction of the experimental results with a single fitting parameter

In order to test the predictive power of our modeling procedure, for our silica PPN/water systems, the value of the ratio α/β is assumed as a constant. A reference value is extracted from the diffusion coefficient D measured in a single experiment, with the sample SP 51. In this reference case, the contact angle θ was measured to be below or equal to 10° (average value measured on sol-gel silica surfaces). $(\alpha/\beta)_{SP51} = 1/3.54 = 0.28$ is obtained. This value is then introduced in the last equation (24) to calculate D values for heights ranging from 2 to 250 nm, with a step δh of 2 nm. The resulted plot is displayed in Figure.IV-16 for a pillar center-to-center distance of 38 nm, corresponding to a pillar surface-to-surface distance of 18 nm. The model is remarkably predictive: the experimental D values for the other pure silica samples (*i.e.* SD 12, SP 51, SD 60) are remarkably close to the simulated plot.

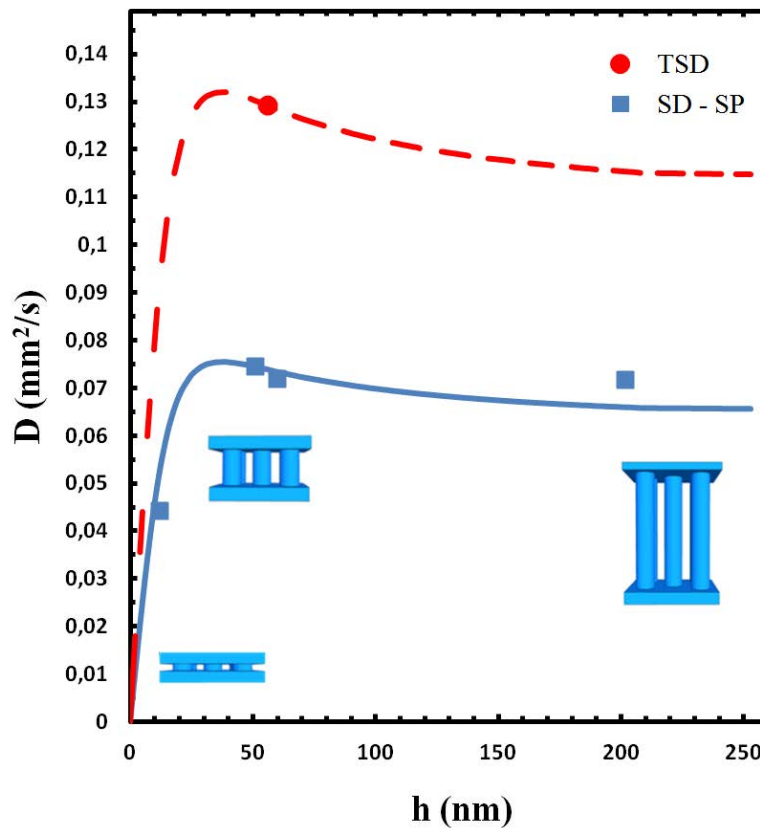


Figure.IV-16. Blue Continuous line : simulated values of D for various values of the pillar height (the α/β parameter used was 0.28 and was deduced from the experimental data for the SP 51 sample). Blue Square points: real values of D deduced from experimental investigation on silica based PPN samples. Red dashed line : simulated values of D for various values of the pillar height (the α/β parameter used was 0.49 and was deduced from the experimental data for the TSD 56 sample). Red round point: real values of D of the TSD 56 sample.

The experimental value of D is almost two times greater for the TSD 56 TiO_2 containing sample than for silica ones. Extracting the correcting factor α/β from this experimental value leads to

$\alpha/\beta = 0.49$, assuming the contact angle of $\theta = 5^\circ$. Indeed, this contact angle must be smaller for TiO_2 than for SiO_2 because TiO_2 has a higher surface energy than SiO_2 , one can take the contact angle to be closer to 0° [63].

IV.2.b.iii.5 The model helps understanding the influence of the PPN dimensions

Once a model is validated, it can be used to have a better idea of the different phenomena occurring. It is clear from the plot that two main regimes of fluid transport exist in the PPN. When the height h is smaller than the surface-surface distance between neighboring pillars (denoted by $ds-s$), the wicking is governed by h . Conversely, when the height h is greater than $ds-s$, this role is attributed to $ds-s$ independently of h . In summary the smallest dimension of the restriction composing a porous network governs the capillary filling. Actually, the maximal diffusion coefficient is found for $h \approx 30$ nm, which is almost twice the value of $ds-s$, suggesting that the optimal combination between capillary forces against viscous drag is not for the height exactly equal to the distance between pillars, as it would be intuitively thought. The pillar height is thus an additional lever to adjust fluids and solute relative transport in PPN in addition to the pillar-pillar distance, to the pillar porosity and to the surface properties that control the surface tension.

The model also helps understanding the role of the PPN dimension in another way. Indeed, the low values of α/β indicate that the front speed is significantly slower than in the macroscopic case where α/β would be equal to one. Indeed, the fluid is water, so in a macroscopic context, β should be equal to one. Moreover, if the fluid dynamics was a macroscopic Poiseuille flow, the value of α would also be equal to one. Therefore, the value of α/β is a measure of the deviation from macroscopic laws, deviations that are due to specific nanoscale effects that slow down the waterfront. Similar deviations from the macroscopic capillary filling law, attributed to the same effects, have been reported for experiments in nanochannels by other groups [56],[33]–[35], [40], [64], [65]. At this stage, it is not possible to go further and explore more in detail the nature of these nanoscale effects, but a few ideas can be given. It has been reported that the viscosity of the structured water attached to the surface [29]–[32] is higher than in the bulk, and contributes to the substantial increase of the apparent viscosity, and thus of β . In our case, this effect is not relevant due to the thinness of the quasi-static layer compared to the minimum channel width ($ds-s = 18$ nm). Because silica is known to be charged in water at neutral pH, [66] surface induced electroviscous effect occurred and is taken into account in β . This latter is expected to be one of the main reasons for the deviation. Finally, the PPN network synthesized using the low-cost and rapid sol-gel approach is not defect-free, so that considering a perfectly periodic system is an

approximation. These local defects could influence both α (driving pressure) and β (integrated hydrodynamic resistance).

These results show that measuring only one value of the Washburn coefficient D per material allows extrapolating the fluid behavior to other dimensions without any further experiments, thanks to a Navier-Stokes solver. As a future prospective, it would be interesting to map the values of α/β for various PPN compositions.

IV.2.b.iv Conclusion

Water capillary filling has been investigated in nanoporous materials, from poorly interconnected random porous films to highly interconnected pillar planar nanochannels, using both complementary experimental approaches and simulation. The simulation has proven to be a useful tool to assess the overall effect of the dimension and structure on the fluid transport. However, contrary to simulation, experimental approaches take all side phenomena in account but cannot cover all region of interest due to technical limitations. The critical dimension of the porous network governs the fluid transport is the smallest dimension of the larger pores interconnecting the network, which corresponds to the pillar surface-to-surface distance in most of the PPNs. Despite the fact that PPNs have the ideal porosity interconnectivity, the pillar composition, inner porosity and height can be individually tuned to adjust transport of solvent and solute. This allows also identifying and separating the contribution of the material composition from effects of confinement that would remain invariant with every composition. In addition, it is possible to combine inner pillar mesoporosity with PPN network so as to increase the specific surface area without changing the fluid hydrodynamics for many nanofluidic applications including analysis, separation, and heterogeneous catalysis.

IV.3 Appendix

It has been mentioned in the previous discussion that the evaporation could influence the filling dynamics for long infiltration times. This has already been taken into account when considering only the firsts points of the filling in order to extrapolate the value of D .

At a mathematical level it is possible to consider the effect of evaporation at the front by adding to the previously described flux $Q(h, L, t) = A_{lateral}(h) * dL/dt$ a constant term in time and space obtaining the composed flux (capillary flux flow plus evaporation)

$$Q_{f+e}(h, L, t) = A_{lateral}(h) * \left(\frac{dL}{dt} + \phi \right) \quad (32)$$

with $A_{lateral}(h) * \phi$ equivalent to the volume of liquid water that evaporates per second and thus ϕ equivalent to a speed. Writing $\rho(h)$ (see equation 1) as $R_{cell}(h)/X_0$, starting again from the Darcy's law

$$\Delta P_{menisc}(h) = \rho(h) * L * A_{lateral}(h) * \left(\frac{dL}{dt} + \phi \right) \quad (33)$$

whose solution

$$\int_0^t dt = \int_0^{L_{front}} \frac{L dL}{\frac{\Delta P_{menisc}(h)}{\rho(h) * A_{lateral}(h)} - L * \phi} \quad (34)$$

can be used to describe the advancement of a liquid flow with an evaporation contribution at the meniscus.

If the effect of pervaporation (evaporation through de PDMS) has to be taken into account a further term has to be added to the flux. Because over the top of the PDMS the humidity can be considered constant, we could consider the rate of pervaporation equal over the surface between the wetted porous film and the PDMS. Denoting as σ the local pervaporation speed (similarly to ϕ) and as l the distance between the channel entrance and the considered position the differential flux from a differential surface between PPNs and PDMS is

$$d Q_{perv}(l) = \sigma * W * d l \quad (35)$$

where $W = \frac{A_{lateral}(h)}{h}$. Because of the delocalized flux all over the top surface of the porous film the pressure drop for every value of l is not equal. At $l = 0$ the flow is the sum of the flux that causes the advancement of the front, of the evaporation at the front and of the pervaporation from all the upper surface of the porous film. At $l = L_{front}$ the last contribution is zero. It is easy to understand that the flow in every point is a linear interpolation between the two values and so

$$Q_{perv}(l) = \sigma * W * (L - l) \quad (36)$$

then, writing $\Delta P_{menisc}(h) = \int_0^L dp(h, l)$ with $dp(h, l) = \rho(h) * Q_{f+e+p}(h, l, L, t) dl$

(where $Q_{f+e+p}(h, l, L, t) = Q_{f+e}(h, L, t) + Q_{perv}(l)$, l dependent) the differential equation

$$\Delta P_{menisc}(h) = \rho(h) * (L * A_{lateral}(h) * \left(\frac{dL}{dt} + \phi\right) + \sigma * W * \frac{L^2}{2}) \quad (37)$$

is obtained whose solution (inverted or calculated numerically through a numerical solver)

$$\int_0^t dt = \int_0^{L_{front}} \frac{A_{lateral}(h) * L * dL}{\frac{\Delta P_{menisc}(h)}{\rho(h)} - L * A_{lateral}(h) * \phi - \sigma * W * \frac{L^2}{2}} \quad (38)$$

can again be used to analyze data of capillary infiltration with slowing down of the liquid front at large times. Because the effect on the function shape of both the contribution is similar and the values of ϕ and σ cannot be easily known independently it is hard to distinguish which is stronger between the two effects. Fitting of the capillary infiltration data have been performed and good agreement obtained between the simulated law and the experimental one. Unfortunately a whole combination of values for the two parameters give reasonably good fits of the experimental curves not allowing identifying the exact values.

Further studies should be accomplished in order to determine the values of ϕ and σ on PPN samples independently. Repeating the experiments for various values of humidity and at different temperatures would indeed allow identifying the evaporation speed of the two mechanisms exactly. This information would provide a further inspect in nanoscopic phenomena probably being evaporation influenced by nanoconfinement and strong surface interaction effects too.

IV.4 Bibliography

- [1] R. Aguilera, “Flow Units: From Conventional to Tight-Gas to Shale-Gas to Tight-Oil to Shale-Oil Reservoirs,” *SPE Reserv. Eval. Eng.*, vol. 17, no. 02, pp. 190–208, May 2014.
- [2] M. Latil, “Water Injection,” in *Enhanced Oil Recovery*, Editions OPHRYS, pp. 35–43.
- [3] S. Wang, Q. Feng, F. Javadpour, T. Xia, and Z. Li, “Oil adsorption in shale nanopores and its effect on recoverable oil-in-place,” *Int. J. Coal Geol.*, vol. 147–148, pp. 9–24, Aug. 2015.
- [4] “More efficient oil extraction using nanofluidics.” [Online]. Available: <http://www.alphagalileo.org/ViewItem.aspx?ItemId=61369&CultureCode=en>. [Accessed: 18-Jul-2015].
- [5] E. W. Washburn, “The Dynamics of Capillary Flow,” *Phys. Rev.*, vol. 17, no. 3, pp. 273–283, Mar. 1921.
- [6] S. Maruyama, “A MOLECULAR DYNAMICS SIMULATION OF HEAT CONDUCTION OF A FINITE LENGTH SINGLE-WALLED CARBON NANOTUBE,” *Microscale Thermophys. Eng.*, vol. 7, no. 1, pp. 41–50, Jan. 2003.
- [7] S. Maruyama, *Molecular Dynamics Method for Microscale Heat Transfer*. 2000.
- [8] P.-G. de Gennes, F. Brochard-Wyart, and D. Quere, *Capillarity and Wetting Phenomena: Drops, Bubbles, Pearls, Waves*. 2004.
- [9] R. Massoudi and A. D. King, “Effect of pressure on the surface tension of water. Adsorption of low molecular weight gases on water at 25.deg.,” *J. Phys. Chem.*, vol. 78, no. 22, pp. 2262–2266, Oct. 1974.
- [10] J. H. Weijs, A. Marchand, B. Andreotti, D. Lohse, and J. H. Snoeijer, “Origin of line tension for a Lennard-Jones nanodroplet,” *Phys. Fluids*, vol. 23, no. 2, p. 022001, Feb. 2011.
- [11] A. Checco, P. Guenoun, and J. Daillant, “Nonlinear Dependence of the Contact Angle of Nanodroplets on Contact Line Curvature,” *Phys. Rev. Lett.*, vol. 91, no. 18, p. 186101, Oct. 2003.
- [12] T. Getta and S. Dietrich, “Line tension between fluid phases and a substrate,” *Phys. Rev. E*, vol. 57, no. 1, pp. 655–671, Jan. 1998.
- [13] N. M. Putintsev and D. N. Putintsev, “Method for Determining the Parameters of the Lennard-Jones Potential,” *Dokl. Phys. Chem.*, vol. 399, no. 1–3, pp. 278–282, Nov. 2004.

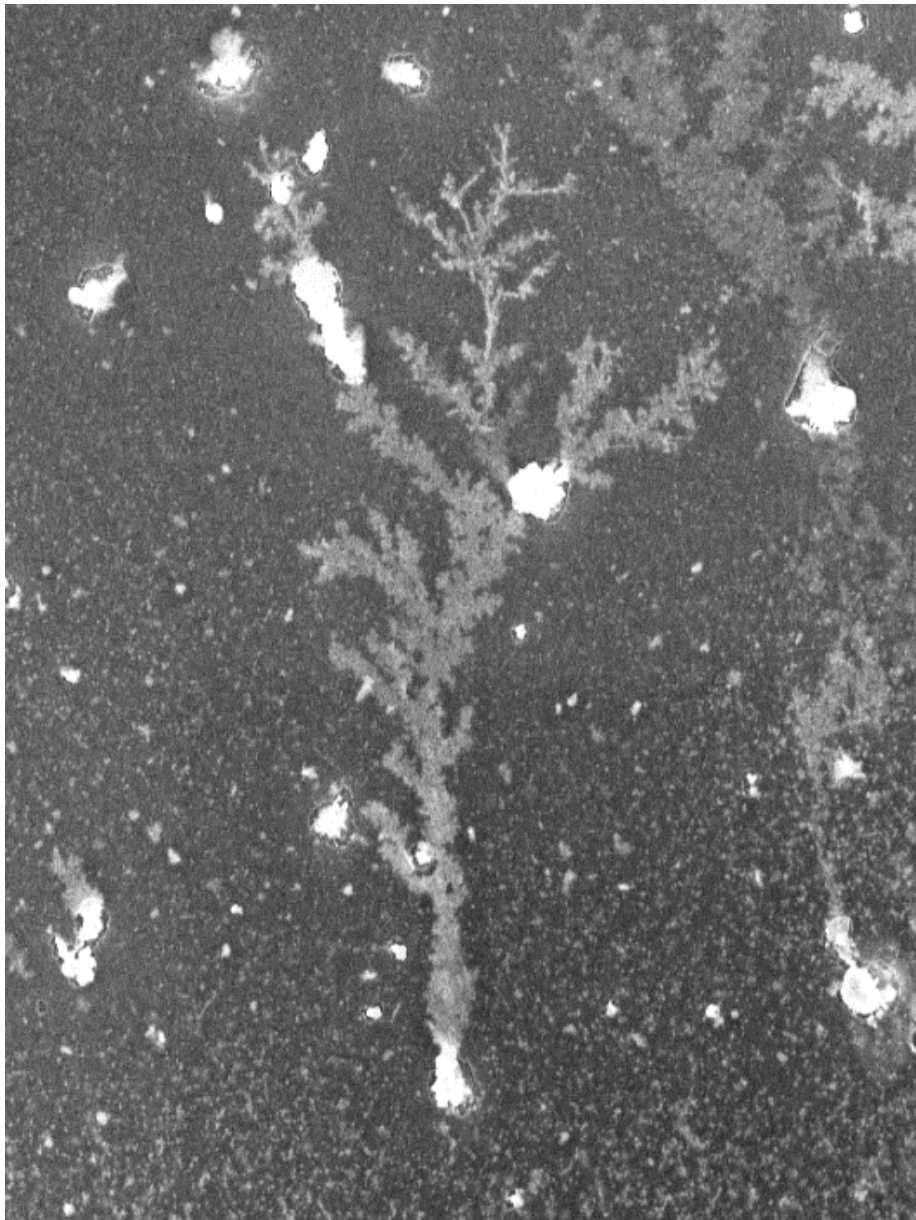
- [14] J. E. Jones, "On the Determination of Molecular Fields. I. From the Variation of the Viscosity of a Gas with Temperature," *Proc. R. Soc. A Math. Phys. Eng. Sci.*, vol. 106, no. 738, pp. 441–462, Oct. 1924.
- [15] J. E. Jones, "On the Determination of Molecular Fields. II. From the Equation of State of a Gas," *Proc. R. Soc. A Math. Phys. Eng. Sci.*, vol. 106, no. 738, pp. 463–477, Oct. 1924.
- [16] T. Takei, K. Mukasa, M. Kofuji, M. Fuji, T. Watanabe, M. Chikazawa, and T. Kanazawa, "Changes in density and surface tension of water in silica pores," *Colloid Polym. Sci.*, vol. 278, no. 5, pp. 475–480, May 2000.
- [17] P. Kim, H.-Y. Kim, J. K. Kim, G. Reiter, and K. Y. Suh, "Multi-curvature liquid meniscus in a nanochannel: evidence of interplay between intermolecular and surface forces," *Lab Chip*, vol. 9, no. 22, pp. 3255–60, Nov. 2009.
- [18] R. Wang, L. Cong, and M. Kido, "Evaluation of the wettability of metal surfaces by micro-pure water by means of atomic force microscopy," *Appl. Surf. Sci.*, vol. 191, no. 1–4, pp. 74–84, May 2002.
- [19] R. Wang, M. Takeda, and M. Kido, "Micro pure water wettability evaluation with an AC no-contact mode of atomic force microscope," *Mater. Lett.*, vol. 54, no. 2–3, pp. 140–144, May 2002.
- [20] S. K. Singh, A. Sinha, G. Deo, and J. K. Singh, "Vapor–Liquid Phase Coexistence, Critical Properties, and Surface Tension of Confined Alkanes," *J. Phys. Chem. C*, vol. 113, no. 17, pp. 7170–7180, Apr. 2009.
- [21] W. Stroberg, S. Ketten, and W. K. Liu, "Hydrodynamics of capillary imbibition under nanoconfinement," *Langmuir*, vol. 28, no. 40, pp. 14488–95, Oct. 2012.
- [22] B. Shi and V. K. Dhir, "Molecular dynamics simulation of the contact angle of liquids on solid surfaces," *J. Chem. Phys.*, vol. 130, no. 3, p. 034705, Jan. 2009.
- [23] K. Bui and I. Y. Akkutlu, "Nanopore wall effect on surface tension of methane," *Mol. Phys.*, pp. 1–8, Apr. 2015.
- [24] B. Hess, "Determining the shear viscosity of model liquids from molecular dynamics simulations," *J. Chem. Phys.*, vol. 116, no. 1, p. 209, Jan. 2002.
- [25] R. Zwanzig, "Time-Correlation Functions and Transport Coefficients in Statistical Mechanics," *Annu. Rev. Phys. Chem.*, vol. 16, no. 1, pp. 67–102, Oct. 1965.
- [26] B. J. Palmer, "Transverse-current autocorrelation-function calculations of the shear viscosity for molecular liquids," *Phys. Rev. E*, vol. 49, no. 1, pp. 359–366, Jan. 1994.
- [27] P. B. Rhines, "Lectures on geophysical fluid dynamics," *Fluid Dyn. Astrophys. Geophys.*, vol. 20, 1983.
- [28] U. Raviv, P. Laurat, and J. Klein, "Fluidity of water confined to subnanometre films," *Nature*, vol. 413, no. 6851, pp. 51–4, Sep. 2001.

- [29] R. C. Major, J. E. Houston, M. J. McGrath, J. I. Siepmann, and X.-Y. Zhu, “Viscous Water Meniscus under Nanoconfinement,” *Phys. Rev. Lett.*, vol. 96, no. 17, p. 177803, May 2006.
- [30] T.-D. Li, J. Gao, R. Szożkiewicz, U. Landman, and E. Riedo, “Structured and viscous water in subnanometer gaps,” *Phys. Rev. B*, vol. 75, no. 11, p. 115415, Mar. 2007.
- [31] M. P. Goertz, J. E. Houston, and X.-Y. Zhu, “Hydrophilicity and the viscosity of interfacial water,” *Langmuir*, vol. 23, no. 10, pp. 5491–7, May 2007.
- [32] D. Ortiz-Young, H.-C. Chiu, S. Kim, K. Voitchovsky, and E. Riedo, “The interplay between apparent viscosity and wettability in nanoconfined water,” *Nat. Commun.*, vol. 4, Sep. 2013.
- [33] K. M. van Delft, J. C. T. Eijkel, D. Mijatovic, T. S. Druzhinina, H. Rathgen, N. R. Tas, A. van den Berg, and F. Mugele, “Micromachined Fabry-Pérot interferometer with embedded nanochannels for nanoscale fluid dynamics,” *Nano Lett.*, vol. 7, no. 2, pp. 345–50, Feb. 2007.
- [34] A. Han, G. Mondin, N. G. Hegelbach, N. F. de Rooij, and U. Staufer, “Filling kinetics of liquids in nanochannels as narrow as 27 nm by capillary force,” *J. Colloid Interface Sci.*, vol. 293, no. 1, pp. 151–7, Jan. 2006.
- [35] F. Chauvet, S. Geoffroy, A. Hamoumi, M. Prat, and P. Joseph, “Roles of gas in capillary filling of nanoslits,” *Soft Matter*, vol. 8, no. 41, p. 10738, Oct. 2012.
- [36] M. N. Hamblin, A. R. Hawkins, D. Murray, D. Maynes, M. L. Lee, A. T. Woolley, and H. D. Tolley, “Capillary flow in sacrificially etched nanochannels,” *Biomicrofluidics*, vol. 5, no. 2, p. 21103, Jun. 2011.
- [37] F. Persson, L. H. Thamdrup, M. B. L. Mikkelsen, S. E. Jaarlgard, P. Skafte-Pedersen, H. Bruus, and A. Kristensen, “Double thermal oxidation scheme for the fabrication of SiO₂ nanochannels,” *Nanotechnology*, vol. 18, no. 24, p. 245301, Jun. 2007.
- [38] N. R. Tas, J. Haneveld, H. V. Jansen, M. Elwenspoek, and A. van den Berg, “Capillary filling speed of water in nanochannels,” *Appl. Phys. Lett.*, vol. 85, no. 15, p. 3274, Oct. 2004.
- [39] L. H. Thamdrup, F. Persson, H. Bruus, A. Kristensen, and H. Flyvbjerg, “Experimental investigation of bubble formation during capillary filling of SiO₂ nanoslits,” *Appl. Phys. Lett.*, vol. 91, no. 16, p. 163505, Oct. 2007.
- [40] J. M. Oh, T. Faez, S. Beer, and F. Mugele, “Capillarity-driven dynamics of water–alcohol mixtures in nanofluidic channels,” *Microfluid. Nanofluidics*, vol. 9, no. 1, pp. 123–129, Nov. 2009.
- [41] nm nanochannels,” J. Haneveld, N. R. Tas, N. Brunets, H. V. Jansen, and M. Elwenspoek, “Capillary filling of sub-10 J. *Appl. Phys.*, vol. 104, no. 1, p. 014309, Jul. 2008.
- [42] J.-N. Kuo and Y.-K. Lin, “Capillary-Driven Dynamics of Water in Hydrophilic Microscope Coverslip Nanochannels,” *Jpn. J. Appl. Phys.*, vol. 51, no. 10R, p. 105201, Sep. 2012.

- [43] S. Kelly, M. T. Balhoff, and C. Torres-Verdín, “Quantification of bulk solution limits for liquid and interfacial transport in nanoconfinements,” *Langmuir*, vol. 31, no. 7, pp. 2167–79, Feb. 2015.
- [44] V. N. Phan, N.-T. Nguyen, C. Yang, P. Joseph, L. Djeghlaf, D. Bourrier, and A.-M. Gue, “Capillary filling in closed end nanochannels,” *Langmuir*, vol. 26, no. 16, pp. 13251–5, Aug. 2010.
- [45] V.-N. Phan, C. Yang, and N.-T. Nguyen, “Analysis of capillary filling in nanochannels with electroviscous effects,” *Microfluid. Nanofluidics*, vol. 7, no. 4, pp. 519–530, Jan. 2009.
- [46] N. R. Tas, P. Mela, T. Kramer, J. W. Berenschot, and A. van den Berg, “Capillarity Induced Negative Pressure of Water Plugs in Nanochannels,” *Nano Lett.*, vol. 3, no. 11, pp. 1537–1540, Nov. 2003.
- [47] J. W. van Honschoten, M. Escalante, N. R. Tas, H. V. Jansen, and M. Elwenspoek, “Elastocapillary filling of deformable nanochannels,” *J. Appl. Phys.*, vol. 101, no. 9, p. 094310, May 2007.
- [48] M. R. Stukan, P. Ligneul, J. P. Crawshaw, and E. S. Boek, “Spontaneous imbibition in nanopores of different roughness and wettability,” *Langmuir*, vol. 26, no. 16, pp. 13342–52, Aug. 2010.
- [49] S. Ahadian, H. Mizuseki, and Y. Kawazoe, “On the kinetics of the capillary imbibition of a simple fluid through a designed nanochannel using the molecular dynamics simulation approach,” *J. Colloid Interface Sci.*, vol. 352, no. 2, pp. 566–72, Dec. 2010.
- [50] A. W. Martinez, S. T. Phillips, M. J. Butte, and G. M. Whitesides, “Patterned paper as a platform for inexpensive, low-volume, portable bioassays,” *Angew. Chem. Int. Ed. Engl.*, vol. 46, no. 8, pp. 1318–20, Jan. 2007.
- [51] A. W. Martinez, S. T. Phillips, E. Carrilho, S. W. Thomas, H. Sindi, and G. M. Whitesides, “Simple telemedicine for developing regions: camera phones and paper-based microfluidic devices for real-time, off-site diagnosis,” *Anal. Chem.*, vol. 80, no. 10, pp. 3699–707, May 2008.
- [52] A. W. Martinez, S. T. Phillips, G. M. Whitesides, and E. Carrilho, “Diagnostics for the developing world: microfluidic paper-based analytical devices,” *Anal. Chem.*, vol. 82, no. 1, pp. 3–10, Jan. 2010.
- [53] C. Boissiere, D. Grosso, S. Lepoutre, L. Nicole, A. B. Bruneau, and C. Sanchez, “Porosity and mechanical properties of mesoporous thin films assessed by environmental ellipsometric porosimetry,” *Langmuir*, vol. 21, no. 26, pp. 12362–71, Dec. 2005.
- [54] J. Bico, U. Thiele, and D. Quéré, “Wetting of textured surfaces,” *Colloids Surfaces A Physicochem. Eng. Asp.*, vol. 206, no. 1–3, pp. 41–46, Jul. 2002.
- [55] E. Quijada-Maldonado, S. van der Boogaart, J. H. Lijbers, G. W. Meindersma, and A. B. de Haan, “Experimental densities, dynamic viscosities and surface tensions of the ionic liquids

- series 1-ethyl-3-methylimidazolium acetate and dicyanamide and their binary and ternary mixtures with water and ethanol at $T=(298.15 \text{ to } 343.15\text{K})$,” *J. Chem. Thermodyn.*, vol. 51, pp. 51–58, Aug. 2012.
- [56] J. Haneveld, N. R. Tas, N. Brunets, H. V. Jansen, and M. Elwenspoek, “Capillary filling of sub-10 nm nanochannels,” *J. Appl. Phys.*, vol. 104, no. 1, p. 014309, 2008.
 - [57] M. Järn, F. J. Brieler, M. Kuemmel, D. Grosso, and M. Lindén, “Wetting of Heterogeneous Nanopatterned Inorganic Surfaces,” *Chem. Mater.*, vol. 20, no. 4, pp. 1476–1483, Feb. 2008.
 - [58] P. D. Sofien Benltoufa, P. D. Faten Fayala, and P. D. Sassi BenNasrallah, “Capillary Rise in Macro and Micro Pores of Jersey Knitting Structure,” *J. Eng. Fiber. Fabr.*, vol. 3, no. 3, pp. 47–54, 2008.
 - [59] C. Ishino, M. Reyssat, E. Reyssat, K. Okumura, and D. Quéré, “Wicking within forests of micropillars,” *Europhys. Lett.*, vol. 79, no. 5, p. 56005, Sep. 2007.
 - [60] T. T. Mai, C. Q. Lai, H. Zheng, K. Balasubramanian, K. C. Leong, P. S. Lee, C. Lee, and W. K. Choi, “Dynamics of Wicking in Silicon Nanopillars Fabricated with Interference Lithography and Metal-Assisted Chemical Etching,” *Langmuir*, vol. 28, no. 31, pp. 11465–11471, Jul. 2012.
 - [61] D. R. Lide, *CRC Handbook of Chemistry and Physics*, 85th Editi. Boca Raton: Taylor & Francis, 2004.
 - [62] D. Nykypanchuk, H. H. Strey, and D. A. Hoagland, “Brownian motion of DNA confined within a two-dimensional array,” *Science*, vol. 297, no. 5583, pp. 987–90, Aug. 2002.
 - [63] M. Järn, F. J. Brieler, M. Kuemmel, D. Grosso, and M. Lindén, “Wetting of Heterogeneous Nanopatterned Inorganic Surfaces,” *Chem. Mater.*, vol. 20, no. 4, pp. 1476–1483, Feb. 2008.
 - [64] N. R. Tas, J. Haneveld, H. V. Jansen, M. Elwenspoek, and A. van den Berg, “Capillary filling speed of water in nanochannels,” *Appl. Phys. Lett.*, vol. 85, no. 15, p. 3274, Oct. 2004.
 - [65] J. C. T. Eijkel, J. Bomer, N. R. Tas, and A. van den Berg, “Filling kinetics of liquids in nanochannels as narrow as 27 nm by capillary force,” *Lab Chip*, vol. 4, no. 3, pp. 161–3, Jun. 2004.
 - [66] S. H. Behrens and D. G. Grier, “The charge of glass and silica surfaces,” *J. Chem. Phys.*, vol. 115, no. 14, p. 6716, Oct. 2001.

V: Self-diffusion and reactions



V : SELF-DIFFUSION AND REACTIONS ----- V-191

V.1 EXPERIMENTAL RESULTS ----- V-193

V.1.a Patterning the PPN structure. ----- V-194

V.1.b Coupling with microfluidics: self-diffusion ----- V-196

V.1.b.i Self diffusion of charged chromophores----- V-197

V.1.c Coupling with microfluidics: reactions ----- V-198

V.1.c.i Metallic silver nanoparticles ----- V-198

V.1.c.ii Multiple reactions: silver halides precipitation ----- V-205

V.1.d Conclusions ----- V-207

V.2 BIBLIOGRAPHY ----- V-209

V.1 Experimental Results

In this chapter the previously described PPN structures will be coupled to some basic microfluidic device to demonstrate the easy integration of bottom-up fabricated nanoporous sol-gel materials within microfluidic channels.

Simple applications of the system will be presented and some preliminary results on self-diffusion of species and reactions in nano-confinement will also be exposed.

Some patterning techniques will be showed. They permit to add complexity to the nanofluidic architecture permitting to develop hybrid microfluidic-nanofluidic device potentially performing more than an operation at a time.

The necessary information to understand the work presented in this chapter have already been presented previously and in particular in Chapter I. Results are then immediately presented.

V.1.a Patterning the PPN structure.

The PPN structure is periodic in 2 dimensions. In the previous chapter the infiltration was tested in 1 dimension by utilizing a PDMS stamp in the direction perpendicular to the water infiltration lowering in this way the system symmetry. In some cases, however, it could be useful to have a nanofluidic circuitry that does not show any symmetry. Patterning of the PPN film is then a strategy to have microchannels with PPNs that can be variously utilized in a lab-on-a-chip device. For example, if two liquids with two different infiltrating speed, have to merge in a particular time and spot two different channels with different lengths could be utilized to match their infiltration time. The reaction product can be mixed with a third liquid and so on (Figure.V-1a) which also needs to have correct timing. Two different strategies have been utilized to pattern the PPN structure (Figure.V-2).

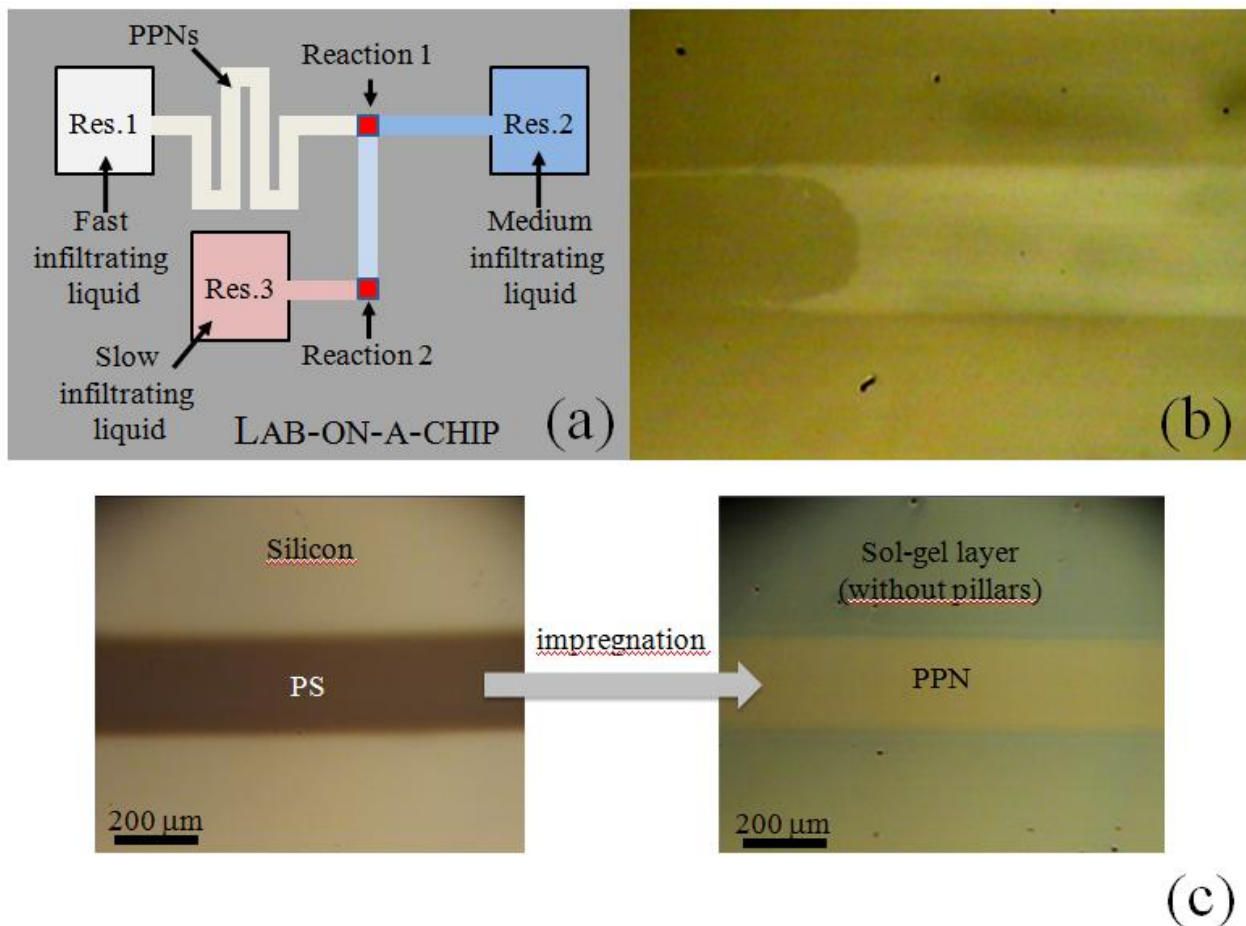


Figure.V-1.(a) Example of a PPN Lab-on-a-chip system based on PPNs in which patterning could be useful: being the infiltration rate of 3 liquids different the length ran by the three is modified in order to make them reach the reaction point at the same time. (b) Example of patterned PPN channels infiltrated by water. (c) Patterned PS and the final PPN patterned channel. See text for explanation.

The first strategy is the exposure of the porous PS hard template layer to UV light (254 nm) through a fused silica patterned mask (the exposure time depends on the lamp power). The UV light photo-degrades the polymer (Figure.V-1c), and a porous PS micro-pattern is obtained. The PPN fabrication process then proceeds normally and PPN structure with micrometric width is realized. The edges of the channel are in this case closed with the sol-gel material (Figure.V-2b). Figure.V-1b shows an optical microscope image of a hybrid nano-in-microfluidic channel realized with this technique and infiltrated with water. The front advancement is not uniform along the width, and the origin of this edge effects yet not understood.

In the second strategy, the lithography step is applied after sol-gel deposition, before the final calcination. It can be utilized only if a titania containing solution is used ($\text{TiO}_x(\text{OR})_y$ absorbs UV light even in the amorphous form). The exposure to 254 nm irradiation increases indeed the reticulation rate of the sol-gel in the semi-definitive form. If the process is performed properly, a pattern, which is the negative of the mask remains after washing with water. In this case the edges of the channel remain open (Figure.V-2c).

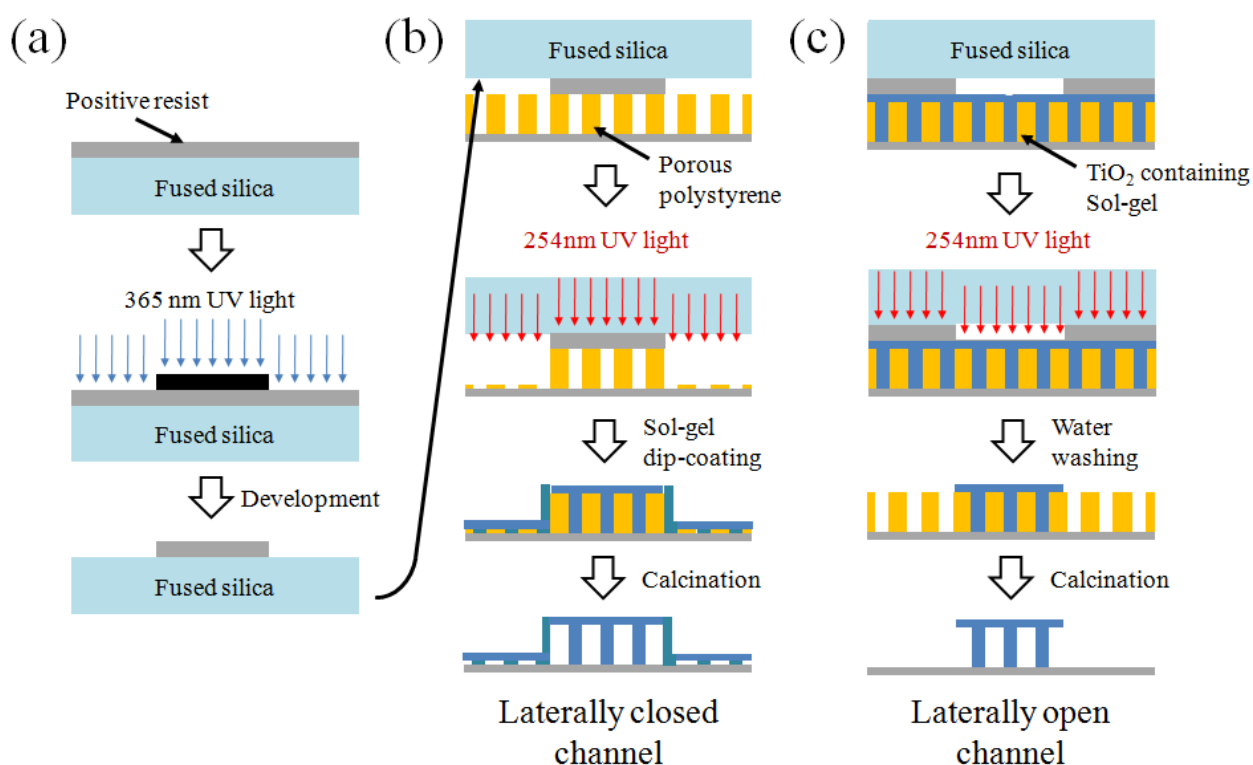


Figure.V-2. Strategy to obtain patterned PPNs. (a) Being the needed mask non transparent to 254 UV light on a transparent support, common plastic masks cannot be utilized (plastics absorbs UV at this wavelength). Another cheap strategy is possible. A common photoresist is patterned on fused silica with 365 nm UV light with plastic masks. The patterned photoresist then constitutes the mask for the next steps. (b) First strategy to obtain patterned PPNs.

In both methods a fused silica mask has to be used. Normally fused silica masks are patterned with metals. This allows having a high resolution during the photolithography. Anyway, if

resolution is not a principal concern, another strategy could be adopted which allows the reusing of the fused silica sample. This strategy consists in coating the fused silica with a commercial photoresist (MC Dip – Coating resist from Microchemicals has been utilized) and patterning it with near UV light (365 nm which allows the use of plastic mask). The photoresist pattern can then be used as a mask being non-transparent to the UV light (254nm) for polystyrene degradation or titania condensation (Figure.V-2a).

V.1.b Coupling with microfluidics: self-diffusion

As already mentioned, it is possible to couple the PPN structure with common microfluidics circuitry. Microfluidic channels are often realized with PDMS, which has already been shown to be compatible with the PPN structure. A PDMS stamp with a microfluidic channel at its surface can be simply applied over the (patterned) PPNs. Simple devices as the ones showed in Figure.V-3 have been realized. The yellow square between the two micro-channels is composed of PPNs. Electrodes can be easily integrated by sputtering gold on the sample before or after the PPN structure fabrication. Electrodes will then be located at the ground or over the roof of the pillared structure.

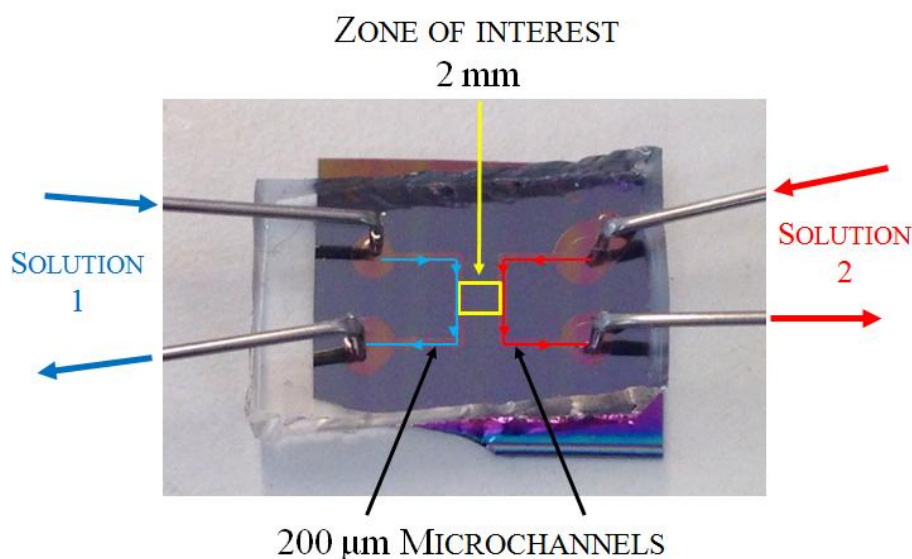
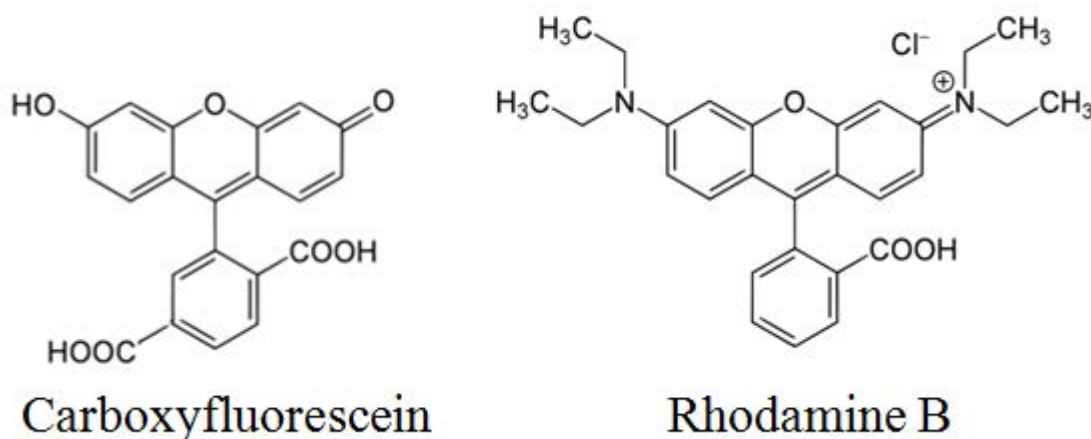


Figure.V-3. Simple example of PDMS microchannel integrated PPNs device. PPN are in the yellow BOX.

V.1.b.i Self diffusion of charged chromophores

A simple experiment of self-diffusion was performed by injecting solutions of Carboxyfluorescein (0.3 mg.ml^{-1} , $8 \times 10^{-7} \text{ mol/L}$) or Rhodamine B (0.7 mg.ml^{-1} , $1.5 \times 10^{-6} \text{ mol/L}$) in phosphate buffer water (0.01 Mol , $\text{pH} \sim 7.0$) in the 120 nm high PPN zone of the device shown in Figure.V-3 (Solution 1, left microchannel).



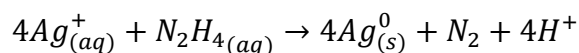
A slow flow in the left micro-channel has been imposed to assure constant concentration at the left edge of the PPN zone. A flow of water in the second channel (Solution 2 in Figure.V-3) assured that no evaporation induced flow could modify the self-diffusion. The diffusion coefficient in one dimension has been determined for both molecules, by following the kinetic of advancement of Carboxyfluorescein and Rhodamine B using fluorescence microscopy exciting at 488 and 555 nm respectively. Diffusion coefficients of the order of $1.8 \times 10^{-12} \text{ m}^2 \cdot \text{s}^{-1}$ and $2.5 \times 10^{-12} \text{ m}^2 \cdot \text{s}^{-1}$ for Carboxyfluorescein and Rhodamine B respectively were found. These values are much lower than in bulk water ($4.9 \times 10^{-10} \text{ m}^2 \cdot \text{s}^{-1}$ and $4.2 \times 10^{-10} \text{ m}^2 \cdot \text{s}^{-1}$ for Carboxyfluorescein and Rhodamine B, respectively [1], [2]). An inverse order is even observed. This demonstrates that the interaction with the walls and their surface charge can influence both diffusion kinetics at this scale, as expected from the Debye theory. A whole range of similar experiments performed changing the solute, ionic force, pH, PPN composing material, PPN height or pillar to pillar distance would give a broader vision of how the material composition and other parameters influence the self-diffusion in these kind of structures. But this could not be performed in the time scale of the project. The variation of both molecule diffusion coefficient gives the idea of how much the PPN structure influence molecular movement inside the nanofluidic channels. This could then be exploited for separation purposes.

V.1.c Coupling with microfluidics: reactions

The presented simple device can also be utilized to perform nano-confined reactions. Two simple examples will be reported here. The precipitation of nanoparticles has been selected as the most representative and interesting reaction because of its simplicity of detection giving high contrast in optical images.

V.1.c.i *Metallic silver nanoparticles*

The already presented device has been utilized to perform reduction reactions of silver nitrate with hydrazine in the PPN structure. The used PPNs for the presented reaction were 200 nm high composed of mesoporous silica. A solution of silver nitrate in water (0.05 M) was injected from one side, while hydrazine (0.05 M) in water was injected from the other side, after previous infiltration with deionized water (Figure.V-4). Again slow flows in the micro-channels have been imposed to assure a constant concentration at the PPN zone edges. The reduction of silver nitrate into silver nanoparticles by hydrazine takes place when the molecules from both sides diffuse and meet in the center of the PPN zone [3].



The hydrazine, being a base, can be protonated, thus the reaction kinetics are influenced from the values of pH. Actually the mechanism involves a first complexation of the silver ion by the protonated hydrazine molecule. Successive reaction with an hydroxide ion gives a neutral silver atom and an unstable radical that reacts readily with a second silver ion. Another silver atom and a diimide intermediate are then created. The diimide finally reacts rapidly with two other silver ions [4]. A first order kinetics with respect of hydrazine, silver ion and hydroxide ion concentration is then expected and actually observed for low hydrazine concentration (the equilibrium between the basic and acid forms modifies indeed the kinetics for higher concentrations). It has to be noticed that neutral silver atoms can bound to silver ions and form various species of colloidal silver. These clusters can then increase in size by feeding of other atoms or merge with other clusters forming the nanoparticles [5].

Even if hydrazine is a basic compound (pKa = 8.10 [6]) no local dissolution of the PPN was evidenced by SEM. Only the micro-channel parts where the hydrazine solution flow was imposed suffered from dissolution due to evacuation of the solubilized silica.

For the reaction three different schemes have been utilized: (i) the simultaneous diffusion of both compounds, (ii) diffusion of one reactant previous to the second one (hydrazine first or silver nitrate first tested, and the first reactant diffusing freely for 6 hours).

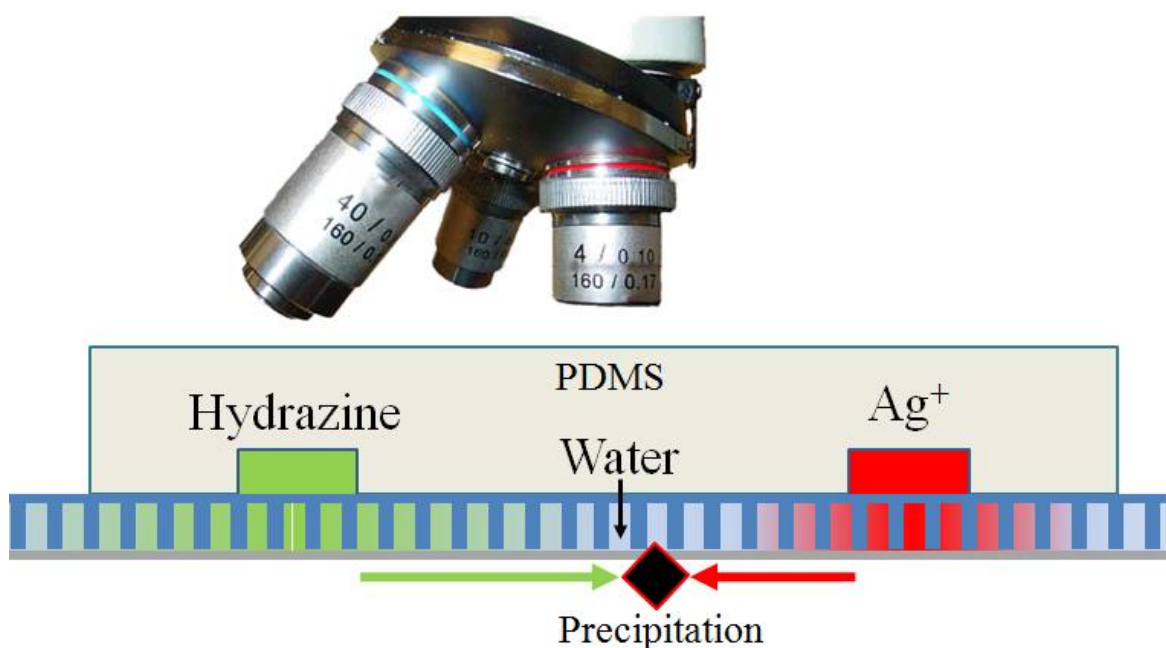


Figure.V-4.Configuration of the microchannels/PPNs for the precipitation of silver nitrate nanoparticles experiments.

Figure.V-5 reports a series of optical images of the zone of interest taken at various times. A line of silver nanoparticles is first formed close to one edge and displaces progressively towards the center, being continuously alimented. This constant feeding of the moving line is evidenced by slight increase in optical contrast and is likely attributed to the sparse precipitation of silver nanoparticles (see later discussion). Eventually, the line stops at a specific position (L_{\max}). This is characteristic due to the nanoscale size of the PPNs. Indeed, repeating a similar experiment in a micro-channel, the formation of such a line did not show because the nanoparticles could move away by diffusion. It has also to be noticed that diffusion speeds of the silver ions and hydrazine are expected to be slower in PPN than in the macroscopic case. Indeed, the 2 mm distance between the micro-channels, should be filled at half of the imposed concentration in the order of an hour for the bulk values (the coefficient of diffusion for silver ions is $1.5 \cdot 10^{-9} \text{ m}^2 \cdot \text{s}^{-1}$ [7] and for hydrazine $2.4 \cdot 10^{-9} \text{ m}^2 \cdot \text{s}^{-1}$ [8]) but, as the precipitation reaction starts for longer times (and the needed concentration is much lower) it can be concluded that the diffusion of the two species is slower than in the bulk.

As can be seen in Figure.V-5 the zone in which the line forms, depends on the order of the reactant injection. In first approximation, the line can indeed be identified as the place where the concentrations (chemical potential) of the reactants are high enough that the reaction can occur.

Taking the case where hydrazine is first injected for 6h before injection of silver nitrate, the line forms first close to the silver nitrate reservoir edge. The inverse is observed when silver nitrate is injected first. In both cases the line progressively displaces towards the centre of the zone, suggesting that both products and second reactant diffuse away from the second reactant reservoir. In the mean time, the reaction proceeds at the line by consumption of the second reactant, creating a local depletion that induces further diffusion of the first reactant towards the line. The line displacement is thus dependent on the diffusion of both reactants and of the silver nanoparticle product, not forgetting that for the last one, the mobility depends on the size with respect to the inter-pillar distance. One expects the line to stop when the particles could no more diffuse into the nanoporosity due to their size and the diffusion of species is balanced creating a steady state. The two reactant have indeed to arrive in stoichiometric quantity at the line. The incoming and reacting quantity of reactants has indeed to match. Otherwise the line would displace further.

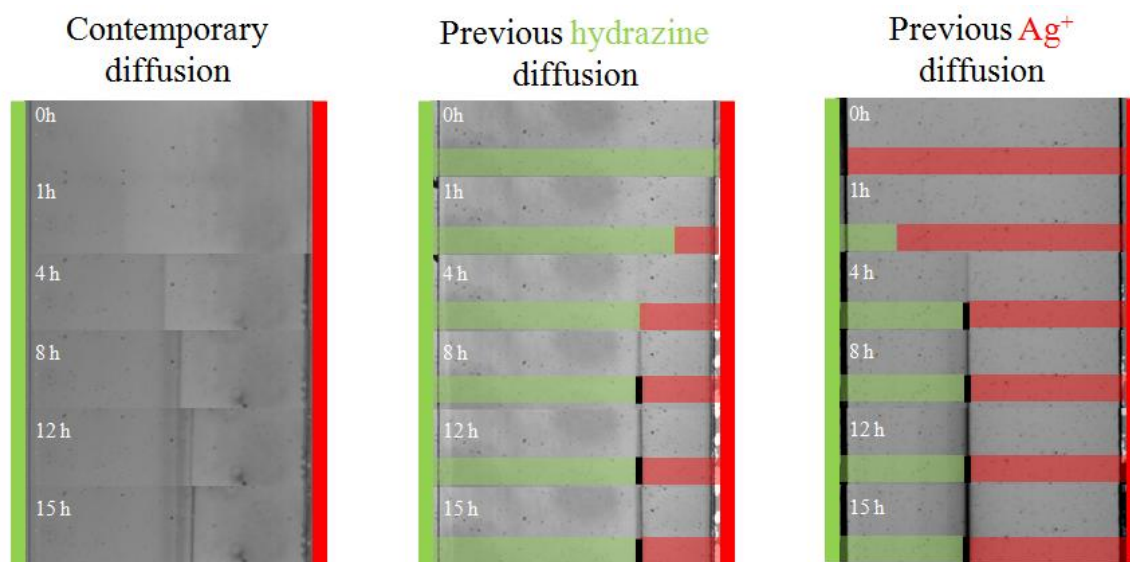


Figure.V-5.Optical images of the zone of interest between the two microchannels as a function of time. In the first case both hydrazine and silver diffuse at the same time. In the second case the channel is initially filled with hydrazine, while the silver nitrate is injected in a second time. In the third one the silver nitrate initially occupies the PPNs and the hydrazine is injected in a second time.

Effectively, the ions/hydrazine can modify the surface chemistry of the PPNs, which modifies the diffusion of the incoming molecular and particular species that continuously feeds the line site. The quantity of reactants incoming from both sides by diffusion depends on the surface properties and on the distances from the respective reservoirs.

Actually, for the latter experiments (Figure V.5) a little amount of nanoparticles is formed at the edge of the second added reactant reservoir as evidenced by a slight diminution of luminosity in the optical images. With time the second reactant diffuses inside the PPN zone; the condition of reaction is displaced to the line position as previously described. The kinetics of the precipitation

reaction displacement can be followed and is reported in Figure.V-6. Calling the distance between the line and the reservoir of the secondly added reactant L_{\max} and $L(t)$ the place where the precipitation is taking place at each moment, it is possible to define the distance between the front of the instantaneous precipitation and the steady state precipitation site as $L_{\max}-L(t)$. As can be seen, this distance is in both cases decaying almost exponentially. Anyway an adequate model taking into account all the phenomena (diffusion, reactions, interactions) together with the various steps involved in the reduction reaction [4] should be built up to better interpret the present results.

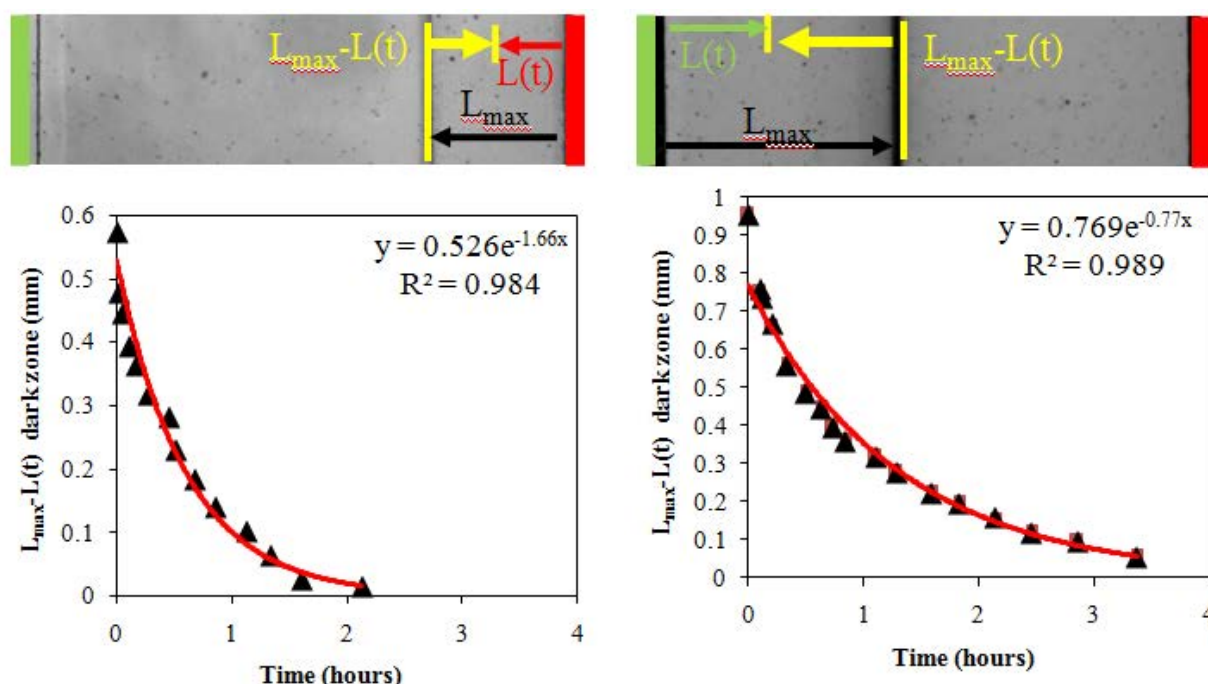


Figure.V-6.Position of the precipitation front for the experiment with previous introduction of hydrazine (left) and silver nitrate (right). The zero is the position of the steady-state lane.

Looking at the case where both solutions are injected simultaneously, one observes the formation of several lines at different positions and at various times from $t(0)$, confirming the complexity of the reaction. In such systems both kinetics and thermodynamics effects have to be studied and understood. More experimental tests have thus to be performed to have an idea of the relative importance of each event contributing to the observed precipitation reaction displacement.

The investigation of the zone of interest by SEM is also reported and shows remarkable features. In the next discussion the sample with contemporary separation is excluded. In Figure.V-7 a list of SEM images of both samples is showed. They both show disperse particles formed on the edge of the second reactant reservoir and nothing on the other side, as expected from the previous interpretation. However, the size of the particles is different.

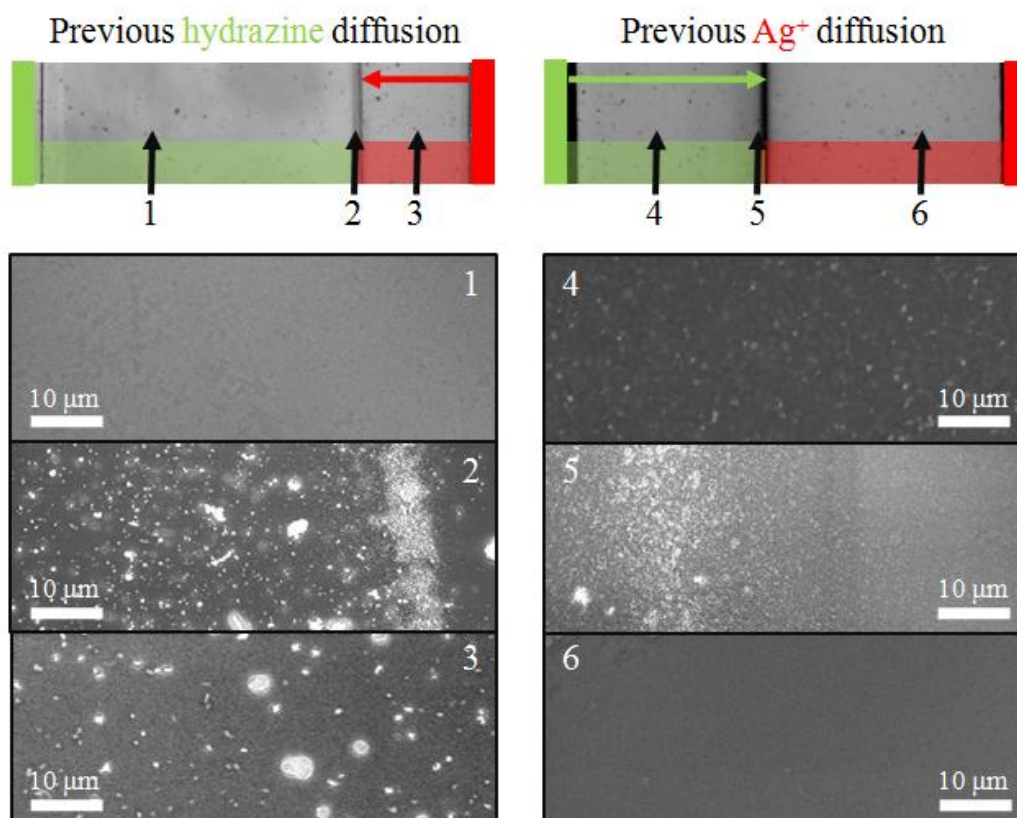


Figure.V-7.SEM images of the indicated spots for the two experiments discussed in the main text.

When silver nitrate has been first injected, particles are of smaller size (maximum diameter of 100 nm) in respect to the particles obtained in condition of previous hydrazine diffusion (maximum diameter of 300 nm). This can be seen by confrontation of Figure.V-8a and Figure.V-8b In the case of previous hydrazine diffusion the growth of particles actually destroyed the PPN structure. In Figure.V-8a it is indeed possible to identify the broken edges of the roof that are indicated by red arrows. Evidently the energy gain of increasing the particle size has been higher than that of the PPNs roof.

As already mentioned the steady state line position depends by the reciprocal distance and diffusion rate of species in the PPN structure. The quantity of silver atoms produced per unit of time then changes in the two configurations and the probability to encounter free silver ions to form charged silver cluster too. Evidently in the configuration with previous hydrazine injection the mechanism of already present nanoparticle growth is favored over nucleation of new particles even against the mechanical resistance of the nanostructure. In the case of silver injection the probable stabilization of silver atoms by more readily incoming silver ions (the line is nearer to the silver nitrate reservoir) probably favors a nucleation mechanism of new particles once the formed one occupy all the space between the nanopillars.

Another interesting feature is the tree-like deposit formed in the experiment with previous hydrazine diffusion (Figure.V-8c). Its position is slightly more in the silver side in respect of the steady-state line. The growth of the structure is originated on the surface of a large nanoparticle (that has destroyed the roof) but is then continued in the PPN structure. As can be seen, it ramifies. On the silver side of the line the concentration of hydrazine is extremely low. So low that the silver ion reduction is not statistically favorable and only happens at the line. Nevertheless the structure developed over various microns from the starting point. The reaction between the silver ion and the poorly concentrated hydrazine has then to be favored by the presence of the silver through growth mechanism. However, a full understanding of the mechanism would require once more to consider the different steps involved in the reaction and to perform additional experiments in different pH and concentration conditions.

Nevertheless, these few preliminary investigations revealed that kinetic and thermodynamic aspects related to chemical reaction in nano-confinement can be studied using our PPN based nano-in-microfluidic device. Moreover, many nanoscopic effects associated to diffusion-nucleation-growth have been reported demonstrating the richness of studying reactions in nano-confinement. One can clearly understand the potential in transferring the latter approaches to studying heterogeneous catalysis reactions.

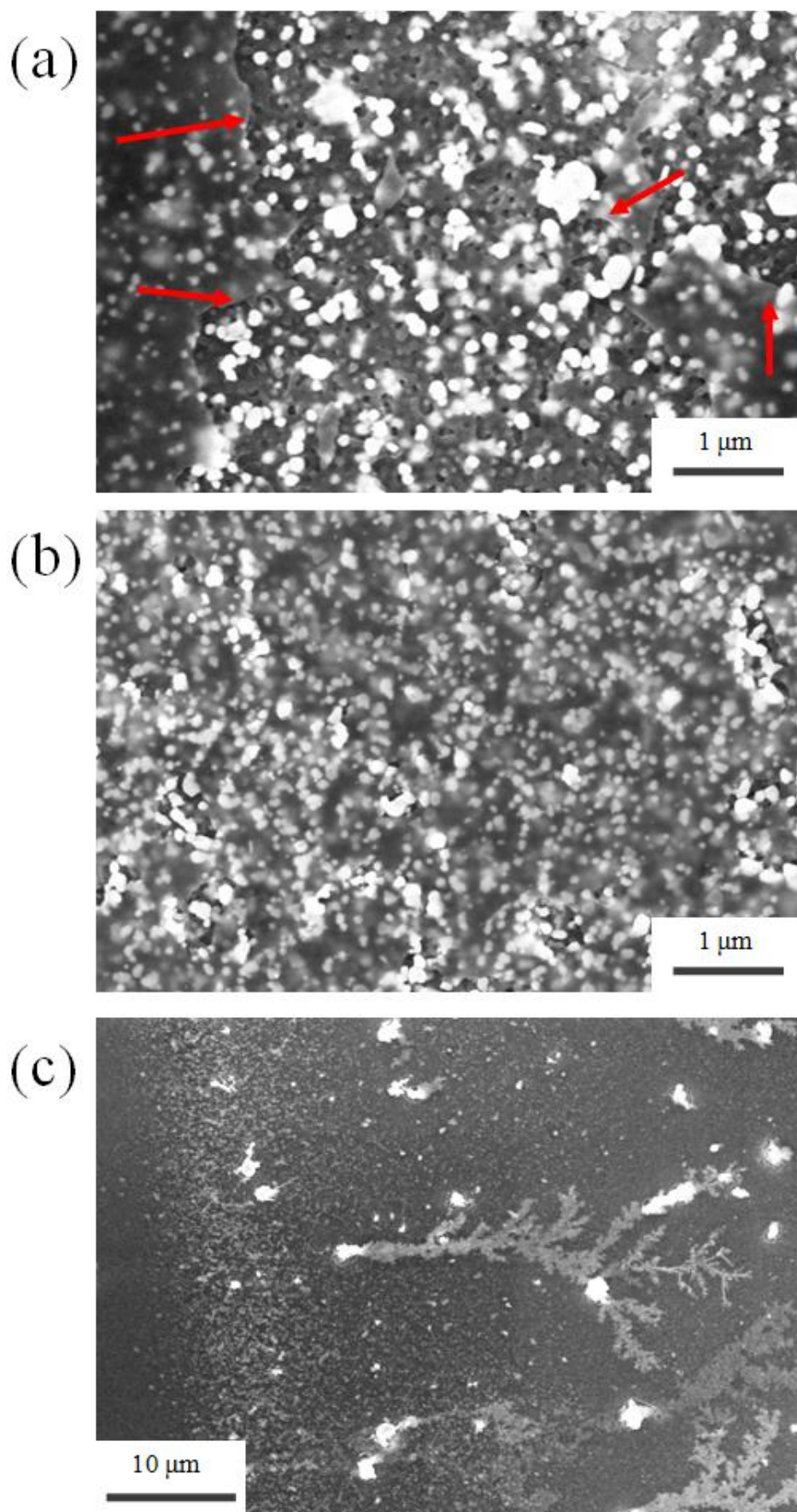


Figure.V-8. Zoom of the site of the steady state line for (a) the previous hydrazine diffusion and (b) previous silver nitrate diffusion. (c) Reports a tree-like structure formed on the silver reservoir side of the steady state line.

V.1.c.ii Multiple reactions: silver halides precipitation

In the previous experiment two reactants were introduced from both reservoirs and a single product was formed in line. In the following experiment, more simple reactions of precipitation are used but three different competitive reactants will be introduced on one side. The same settings of the previous experiment has been utilized but the hydrazine solution has been substituted by a mixed KCl-KBr-KI one (same concentration for the three components for a summed concentration in salt of 0.05 M). Precipitates of AgCl, AgBr and AgI are then expected to form in the PPNs due to their low solubility (K_{ps} 1.7×10^{-10} , 5.3×10^{-13} and 8.5×10^{-17} , respectively [9]). In an experience where both solutions are introduced simultaneously, the silver ions diffuse again from the right, while the chloride, bromide and iodide ones diffused from the left. In bulk the three anions have respective coefficient of diffusion 2.03×10^{-9} , 2.08×10^{-9} and 2.05×10^{-5} [10], but, as in the previous case, a modification of these values is expected due to the nano-confinement effects. Results are presented in Figure.V-9. Figure.V-9a displays an optical image of the PPNs in the zone of interest.

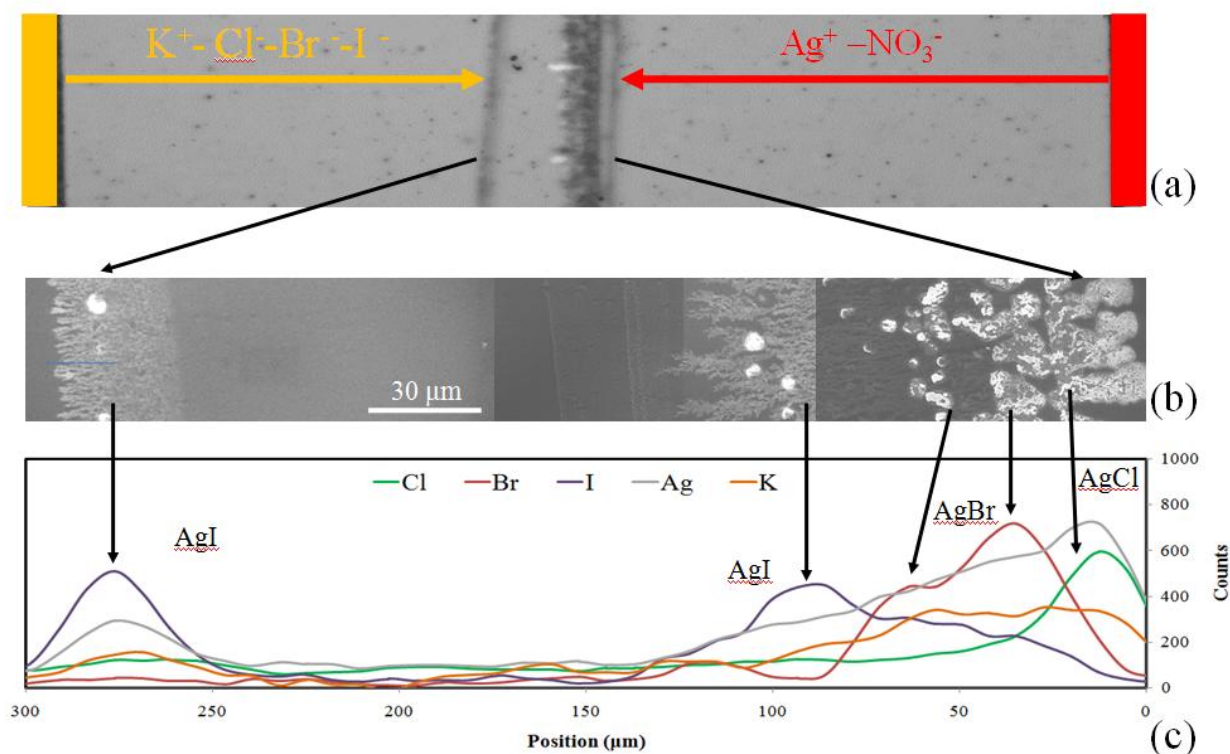


Figure.V-9. (a) Optical image of the zone of interest for the reaction. The distance between the two microchannels at left and right is 2 mm. (b) SEM image of the zones where precipitation took place. The various crystals reported are related to an EDX map (c) that localizes the various crystal composition.

The distance between the micro-channels indicated in orange and red is 2 mm. Again the particle and other structure formations take place in times of the order of hours. In Figure.V-9b a SEM image of the zone where multiple lines were formed is showed (in Figure.V-10 a zoom of some specific area is reported) and in Figure.V-9c is reported a map describing the ionic distribution obtained by EDX for the same area. This is just a qualitative analysis since EDX profiles have not been normalized. The first silver salt that precipitated was silver chloride close to the halide reservoir. It was then followed by the successive precipitations of silver bromide and iodide farer towards the silver nitrate reservoir. The time of diffusion and reaction lasted more than 10 hours but the system was still evolving. The fact that silver chloride has been the first to precipitate is anti-intuitive. Its product of solubility is indeed higher than that of silver bromide and iodide, the diffusion coefficient being almost equal. In our PPN, the silver iodide was thus the last to precipitate, suggesting that in PPNs the diffusion of Cl^- is faster than that of Br^- and of I^- .

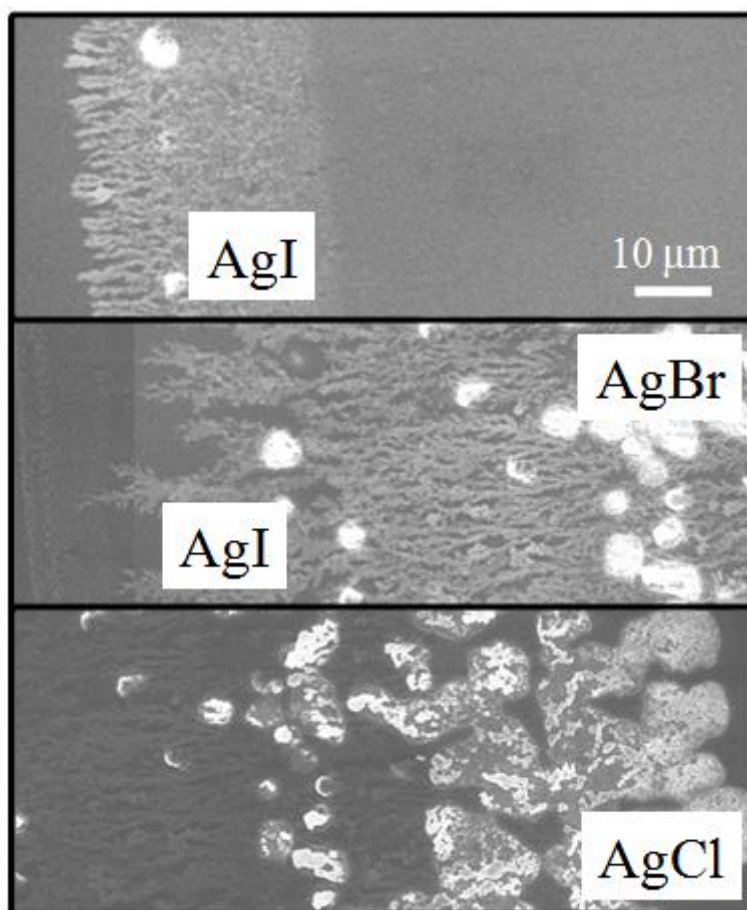


Figure.V-10. Zoom of the SEM image of Figure.V-9b.

This unexpected behavior has again to be attributed to the nano-confinement effect that can both change the reaction constants and kinetics values and the diffusion coefficients of the different halides. It is interesting to notice, therefore, that the three salts generated different kinds of

structures. Silver chloride forms rather big crystals that actually destroy the roof while silver bromine forms littler ones (some of them eventually breaks the roof too) and starts some tree-like structures. Silver iodine forms tree-like dendrites only (Figure.V-10). All this might again be attributed to the delicate balance among diffusion, nucleation and growth, but would require additional investigation to conclude on a fully understood mechanism.

The modeling of this kind of systems would be rather complex even in the bulk (where the coefficient of diffusion and reaction constants values are known) with the presence of 6 different diffusion dynamics (potassium and silver cations and nitrate, chloride, bromide and iodide anions), and 3 contemporary reactions. In nano-confinement, the said values change, so to model the system is at this level still impossible.

Nevertheless this experiment, that can be somehow seen as an equivalent of mineral formation in water filled rocks, shows again how these nano-in-micro systems could be useful to study the behavior of fluids, reactions and diffusion at the nanoscale for, mostly, fundamental study and applications.

V.1.d Conclusions

This chapter showed some preliminary experiments realized inside PPNs through coupling them with a microfluidic device. The coupling is useful at this level to avoid problem of evaporation and to demonstrate the possibility to integrate the PPN in a more complex lab-on-a-chip device without particular effort.

The studied reactions and self-diffusion tests showed interesting effects related to the confinement at the nanoscale (steric and double layer effects related to the chemical nature of the PPN materials) that modifies the values of the diffusion, kinetic and thermodynamic constants of reactions, as already known in the scientific communities working with nanoporous materials.

This latter effort constitutes the first investigation of nano-in-micro fluidic systems and more effort, both at the experimental and theoretical level, is needed to better understand the involved phenomena. The objective to demonstrate the applicability of the devices realized in this thesis for nanofluidic applications has anyway been accomplished and PPN materials have really shown to be the ideal system for such purposes.

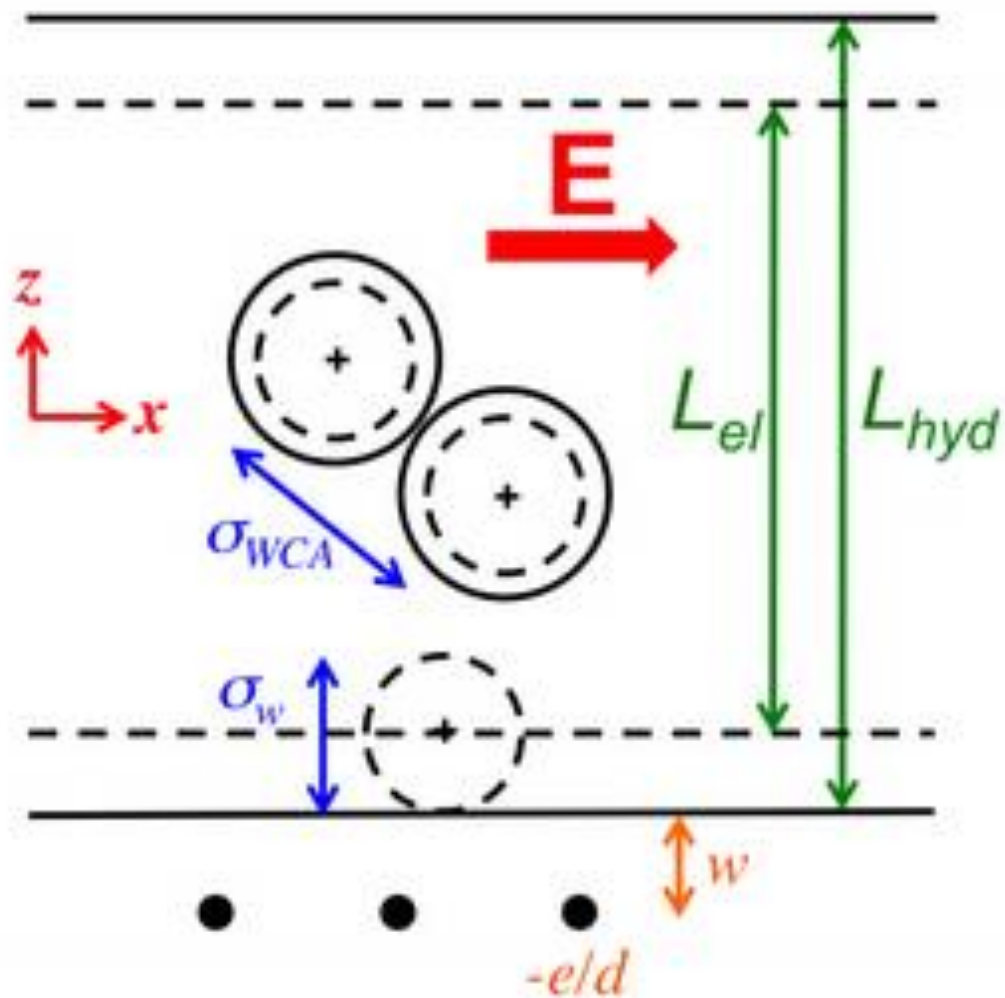
Because of the “enormous” complexity of the system a modeling approach would also be recommended to, at least, have an idea of the variation of the diffusion coefficients and other effects at the nanoscale. In the next chapter a first effort in this direction has been made.

Unfortunately the time of a Ph.D. is limited and the desire to continue this work is high. It is indeed highly frustrating to be obliged to abandon the studies now that the complicated fabrication parts have been solved. I hope however to have transmitted to the reader curiosity about this kind of system, which is now easy to fabricate, low-cost, and has enormous potentialities thanks to the possibility to vary the composing materials and structure.

V.2 Bibliography

- [1] E. M. Kramer, N. L. Frazer, and T. I. Baskin, "Measurement of diffusion within the cell wall in living roots of *Arabidopsis thaliana*," *J. Exp. Bot.*, vol. 58, no. 11, pp. 3005–15, Jan. 2007.
- [2] C. Culbertson, "Diffusion coefficient measurements in microfluidic devices," *Talanta*, vol. 56, no. 2, pp. 365–373, Feb. 2002.
- [3] U. Nickel, A. zu Castell, K. Pöpl, and S. Schneider, "A Silver Colloid Produced by Reduction with Hydrazine as Support for Highly Sensitive Surface-Enhanced Raman Spectroscopy †," *Langmuir*, vol. 16, no. 23, pp. 9087–9091, Nov. 2000.
- [4] Z. Khan, S. A. Al-Thabaiti, E. H. El-Mossalamy, and A. Y. Obaid, "Studies on the kinetics of growth of silver nanoparticles in different surfactant solutions," *Colloids Surf. B. Biointerfaces*, vol. 73, no. 2, pp. 284–8, Oct. 2009.
- [5] B. G. Ershov, E. Janata, A. Henglein, and A. Fojtik, "Silver atoms and clusters in aqueous solution: absorption spectra and the particle growth in the absence of stabilizing Ag⁺ ions," *J. Phys. Chem.*, vol. 97, no. 18, pp. 4589–4594, May 1993.
- [6] H. K. Hall, "Correlation of the Base Strengths of Amines 1," *J. Am. Chem. Soc.*, vol. 79, no. 20, pp. 5441–5444, Oct. 1957.
- [7] R. R. M. Johnston and M. Spiro, "Diffusion coefficients of the silver ion and the disulfite-silver (I) ion by the rotating disk method," *J. Phys. Chem.*, vol. 71, no. 12, pp. 3784–3790, Nov. 1967.
- [8] M. M. Ardakani, M. A. Karimi, M. M. Zare, and S. M. Mirdehghan, "Investigation of Electrochemical Behavior of Hydrazine with Alizarin as a Mediator on Glassy Carbon Electrode," *Int. J. Electrochem. Sci.*, no. 3, pp. 246–258, 2008.
- [9] "K_{sp} solubility product constants of many popular salts at SolubilityOfthings." [Online]. Available: http://www.solubilityofthings.com/water/ions_solubility/ksp_chart.php. [Accessed: 27-Jul-2015].
- [10] E. L. Cussler, *Diffusion: Mass Transfer in Fluid Systems*. 1997.

VI : Hydrodynamic simulations



VI : HYDRODYNAMIC SIMULATIONS ----- VI-211

VI.1	INTRODUCTION -----	213
VI.1.a	<i>Nanofluidic simulations</i> -----	214
VI.1.b	<i>Hydrodynamic interactions</i> -----	215
VI.1.b.i	Navier-Stokes equations and hydrodynamic regimes-----	215
VI.1.b.ii	Hydrodynamics in presence of particles (moving boundary conditions)-----	218
VI.1.c	<i>Electroosmotic flow – phenomenon</i> -----	219
VI.2	STOCHASTIC ROTATIONAL DYNAMICS. -----	223
VI.2.a	<i>The algorithm</i> -----	224
VI.2.b	<i>Adimensional numbers and time scales</i> -----	227
VI.2.c	<i>Walls, thermostat and Poiseuille flow</i> -----	229
VI.2.c.i	Fluid-walls interaction -----	229
VI.2.c.ii	Thermostat-----	231
VI.2.c.iii	Poiseuille flow between two planes -----	232
VI.2.d	<i>Solutes in SRD</i> -----	235
VI.2.d.i	Fluid interaction with the solutes and force description -----	235
VI.2.d.ii	CC - Collisional Coupling -----	236
VI.2.d.iii	CFC – central force coupling-----	237
VI.2.d.iv	CFC-CC method comparisons -----	238
VI.2.d.v	Forces between solutes-----	239
VI.2.d.vi	Electrostatic interactions - Ewald summation-----	239
VI.2.d.vii	Ewald summation in slab geometry -----	241
VI.3	: SIMULATION RESULTS-----	243
VI.3.a	<i>Validation of the SRD method</i> -----	244
VI.3.a.i	Simulation box and boundary conditions-----	245
VI.3.a.ii	Validation-----	246
VI.3.a.iii	Effect of σ_w and d for low surface charge values -----	249
VI.3.b	<i>Non-ideal case: beyond the PNP hypothesis</i> -----	253
VI.3.c	<i>From high to low surface charge</i> -----	256
VI.3.c.i	PNP-“from p ⁺ ”-SRD flow confrontation and WCA interactions effect -----	258
VI.3.c.ii	Effect of σ_w -----	258
VI.3.c.iii	Effect of d -----	258
VI.3.d	<i>Salt addition</i> -----	261
VI.3.e	<i>Electro-osmosis in PPNs</i> -----	264
VI.3.f	<i>Conclusion</i> -----	271
VI.4	APPENDIX -----	273
VI.5	BIBLIOGRAPHY -----	276

VI.1 Introduction

In the previous chapters of this thesis results regarding the fabrication, infiltration and reactions inside nanoporous thin films have been exposed. The phenomena described have been analyzed in function of their macroscopic optically detectable effects. It has been showed that the behavior of fluids and solutions at the nanoscale is different from the bulk value and interest has been arisen towards the nanoscopic description of the observed phenomena.

In this final chapter the scale of the observations is then shifted to the nanoscale. No real experiment is performed but simulations of the behavior of ions in nanochannels are analyzed. The aim is to have a better understanding of their behavior in charged nanochannels, a situation that, as it will be illustrated, is the normality. To do so a hydrodynamic simulation method (Stochastic Rotational Dynamics - SRD) has been used. It successfully succeeds in describing the hydrodynamic interactions and describes their influences on solutes diffusion, streaming and other phenomena. Moreover it allows to consider the phenomena taking place at different time scales without needing excessively and impossibly long simulation times (in contrast to classical Molecular Dynamics simulations for which simulating nanochannels would take enormous amounts of computer time). Its features and advantages will be presented accurately in the second part of the chapter. The first part consists in a necessary and brief introduction about simulation methods and concepts. It is indeed needed to introduce the general ideas that are at the basis of this kind of simulations and of their interpretations. A brief description of the electro-osmotic flow is also introduced in order to allow the reader to have a better comprehension of the result obtained though simulations during this thesis (that describe the electro-osmotic flow through the SRD method).

The second part of this chapter describes the simulation method actually utilized during this thesis: the already mentioned Stochastic Rotational Dynamics (SRD). Its algorithm and setting up are briefly discussed. Moreover few previously reported examples are shown.

The results obtained in this thesis with the SRD technique are instead presented in the third and final part. The phenomenon analyzed is the electro-osmotic flow in planar nanochannels and then in PPNs. Once again the symmetric aspect of the PPN is fundamental. The high degree of

symmetry allows indeed using periodic boundary conditions which are absolutely necessary for such kind of simulations.

Finally a short appendix describing the meaning of adimensional numbers is reported. They univocally determine the fluid flow inside a system independently of the length, time and other scales. The ones cited in the discussion are briefly explained in the final part of this chapter.

VI.1.a Nanofluidic simulations

The simulation of microfluidic or nanofluidic systems is extremely complex. An adequate model to describe separations, electrophoresis or other phenomena needs to take into account a wide range of effects, and needs to describe adequately all the elements that contribute to the studied phenomenon. The transport, interaction dynamics, reactivity or the hydrodynamics inside the systems have all to be taken into account in different situations if different experiences have to be reproduced through simulations. Moreover the time scale of all the interactions, effects and phenomena that take place in the real system could be extremely different. In example attractive-repulsive interactions between molecules of a liquid are effective at the millionth of nanosecond while the collective transport of liquid due to a pressure gradient acquires importance at the macroscopic time scale of seconds. Thermal fluctuations, particle self diffusion and compression waves are just some other phenomena that have different characteristic time scales.

A simulation that adequately describes a fast phenomenon should be run for enough time to describe a longer one. This, obviously, needs the simulation to significantly extend the calculation time. If the slower phenomenon has a time scale sufficiently different from the one of the original simulation it can even become impossible to describe it due to technical limitations. Methods and models that do not consider the faster phenomena or, more probably, that treat it as an average effect, have then to be utilized. In this way an adequate description of the slower phenomena could be in some case performed. To cite an example, in Brownian Dynamics the thermal fluctuations of the solvent, that influence the positions of colloids in solutions, are averaged. The solvent is not explicitly described but its effect is modeled through a succession of random steps of the colloid. The colloids in solution then interact with each other and different phenomena linked to their diffusion can be described [1].

Nevertheless, in some case, this operation is impossible and long calculation times are needed to obtain reasonable results. This is the case, as another example, of protein folding. The process of

folding, indeed, last for times of the order of the millisecond; on the other hand the fundamental steps to describe it (integration of the Newton's second law between the atoms and protein parts) need to be in the femtosecond scale in order to adequately describe the system [2] and no averaging operation can be performed.

Moreover the models can be valid in certain limits only. Their description could indeed be no more valid if certain conditions are not satisfied. To cite again Brownian Dynamics, its algorithms adequately describe diluted suspensions only (less than 10% in volume fraction [3]) or the behavior of colloids in free or simple confined spaces[4], [5]not allowing to obtain good results for more complex geometries.

It is then clear that the choice of the simulation method has to be adequately done. An adequate description of the considered interactions and proper formulation of the algorithm to extract physical quantities need, in the same way, appropriate care.

VI.1.b Hydrodynamic interactions

In the case of this thesis the study of the transport of species inside nanochannels has been identified as an objective. To do so it is necessary to adequately describe the hydrodynamic interactions, electrostatic forces and thermal fluctuations (to take into account the diffusion) inside the system. If the last two can be easily implemented in the already cited Brownian Dynamics this is not the case for the hydrodynamics. The transport of momentum in a fluid due to diffusion, convection or externally induced flows is indeed a key element to predict the behavior of the fluid itself and of solutes or colloids suspended in it. The fluid speed inside a channel is indeed entirely determined from hydrodynamics when external forces are added to the system and this speed seriously influences the position of solutes and colloids. Moreover colloids or solutes in solutions influence each other through hydrodynamic interactions too. When a colloid moves, its displacement pushes all the liquid around it. This then influences the movement of a second colloid and so on. This means that keeping into account these kinds of interactions (that decay as $1/r$ [6]) is important even for system at equilibrium. In particular in concentrated ones the contribution cannot be neglected without qualitative errors.

VI.1.b.i Navier-Stokes equations and hydrodynamic regimes

Actually hydrodynamics can already be adequately described for systems that can be considered stationary. The laws of conservation of momentum, energy and matter can be coupled to obtain

the well known Navier-Stokes equations. Solving these differential equations permits to obtain the desired hydrodynamics interactions. This, in example, has been done in Chapter IV to obtain the hydrodynamic resistance of the PPN structure to model the capillary infiltration speed in that kind of structures. An important role is played by the boundary conditions. Solids surfaces usually constitute boundary conditions: if these surfaces are immobile, such as the case of walls, simple solutions can be found. In the same way an autonomous (not influenced by the flows) movement of the solid surfaces can be integrated in the Navier-Stokes calculations.

The solution of these equations in such kind of systems can be indeed rather easily obtained with finite elements software (such as COMSOL used in Chapter IV). It has to be mentioned here that the fluid flow is completely defined from what are called adimensional numbers. They are obtained rewriting the Navier-Stokes equations with adimensional variables. The various elements of the equations are then preceded by these numbers that determine their reciprocal importance. Systems having different physical dimensions, viscosity or other variables values behave in the same way if the values of the adimensional numbers are matched. Some adimensional numbers are cited in the following part of this chapter. These are then better explained in the appendix where their expression and meaning are explained. It has finally to be said that these numbers define different “regimes”. If their values are inside certain intervals the system presents the same features and only quantitative differences are found. If, on the contrary, a different regime is reached, qualitative differences are generated. This is due to the fact that in certain intervals of the adimensional number values some components of the Navier-Stokes equation can be neglected while for others this is not possible. In example if a flow around a fixed cylinder of diameter L is considered (with velocity U_∞ far away from the body), rewriting the Navier-Stokes equation for incompressible flow (with ρ and η the fluid density and viscosity, \mathbf{u} the velocity vector, P the pressure)

$$\rho \frac{\partial \mathbf{u}}{\partial t} + (\mathbf{u} \cdot \nabla) \mathbf{u} = -\nabla P + \eta \nabla^2 \mathbf{u} \quad (1)$$

in adimensional form (applying the substitution $P' = P/\rho U_\infty^2$, $\mathbf{u}' = \mathbf{u}/U_\infty$, $\mathbf{x}' = \mathbf{x}/L$ and $t' = tU_\infty/L$ with \mathbf{x} the position vector)

$$\frac{\partial \mathbf{u}'}{\partial t'} + (\mathbf{u}' \cdot \nabla) \mathbf{u}' = -\nabla P' + \frac{1}{Re} \nabla'^2 \mathbf{u}' \quad (2)$$

the so called Reynolds number ($Re = \rho U_\infty L / \eta$) appears. In the stationary state ($\partial \mathbf{u}' / \partial t' = 0$) if the Reynolds number is little the last term ($\nabla'^2 \mathbf{u}'$) which corresponds to viscosity forces is dominant while the term $(\mathbf{u}' \cdot \nabla) \mathbf{u}'$ can be neglected. On the contrary if the Reynolds number is big the inertial term becomes dominant. In function of the Reynolds number, then, a viscous or inertial dominated regime appears in fluid flow which is called laminar and turbulent respectively. An intermediate regime where both contributions have to be considered is also present. In are reported three examples of fluid flow in laminar (Figure.VI-1a), intermediate (Figure.VI-1b) and turbulent (Figure.VI-1c) regimes. The values that are normally considered as separators for the Reynolds number in this configuration are 5 and 40 for the simplest solutions. A family of other behaviors has to be considered for higher values.

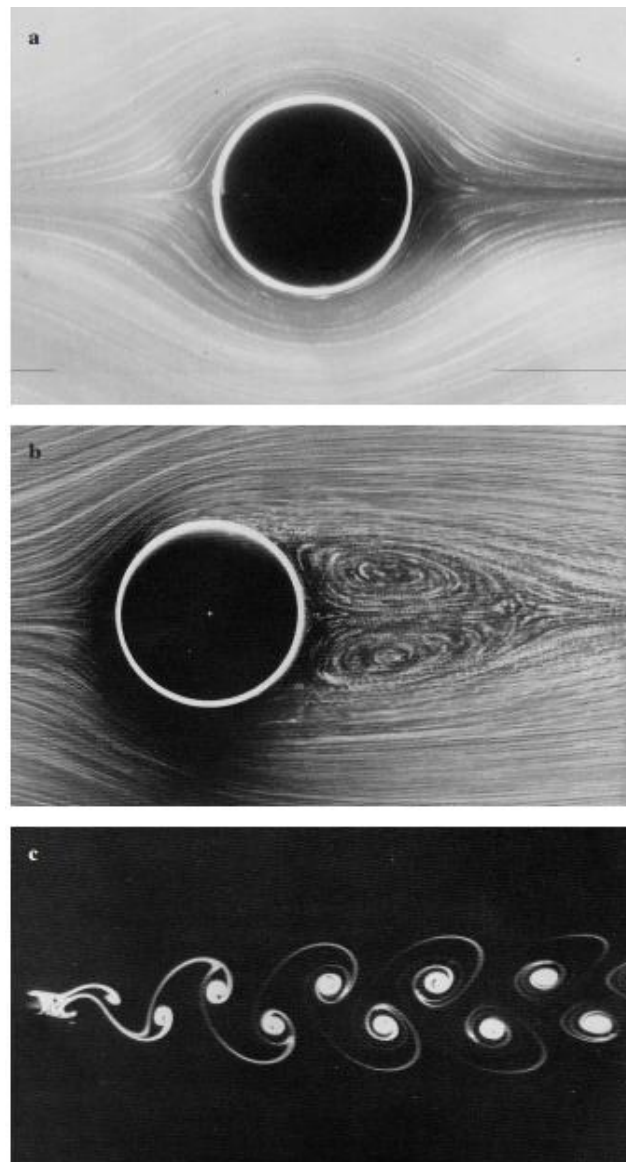


Figure.VI-1. [7]. Photographs of streamlines (the lines are tangent to the fluid velocity) (a, b) or streak lines (lines are generated by a single point in the front of the cylinder) (c) for steady flow past a circular cylinder at different values of the Reynolds number: (a) $Re \ll 1$ (b) $Re=26$ (c) $Re=105$.

This means that doubling the speed, fluid density or cylinder dimension (which doubles the Reynolds number) doesn't change the qualitative aspect of the flow but has just a quantitative effect (in displaced mass, fluid speed and position respectively). The calculation performed for a given Reynolds number can then be reused just rescaling the real values at condition that the new value of the Reynolds number is still in the good interval. If it is not the case a new solution of the Navier-Stokes equation has to be found.

This consideration is particularly important for the actual simulation method used in this thesis. The actual fluid used has indeed different properties to the one that could really be used in experiments. The adimensional number can then assume values that do not correspond to reality but, if the right regimes are considered, real values can be easily calculated.

Other adimensional numbers have in certain occasion to be considered to take into account compressibility (Mach number), diffusion (Schmidt number), heat transfer (Peclet number) or confinement (Knudsen number). The definition of the corresponding adimensional numbers is reported in the appendix.

VI.1.b.ii Hydrodynamics in presence of particles (moving boundary conditions)

Coming back to complex simulations with mobile bodies immersed in a fluid, if the flow influences and determines the position of solid surfaces, as it is in the case of colloidal particles, everything becomes more complex. An iterative procedure has indeed to be set-up with the hydrodynamic force that has to be calculated for each position assumed step by step by the moving surface/colloid. Moreover if interactions are present in the fluid that are not inserted in the Navier-Stokes equations (such as electrostatic interactions between ions or short excluded volume ones) they have to be somehow added to the system. The same is valid for thermal fluctuations. The Navier-Stokes equation cannot then be easily resolved and other methods have to be introduced to consider both the hydrodynamic and the other interactions present in the system.

The Stochastic Rotational Dynamics (SRD) method, as previously said, simulates the hydrodynamics. Therefore electrostatics and excluded volume effects can be and are implemented in the algorithm. This is more deeply discussed in the second section of this chapter.

It has here to be mentioned the presence in the literature of two other methods that can be utilized to obtain similar results over different hypothesis. Dissipative Particle Dynamics (DPD) and Lattice Boltzmann (LB). In DPD the simulation particles iteratively exchange momentum with other particles inside a certain radius of interaction and then propagate. The momentum exchange is performed through an algorithm that assures the final correct Maxwell-Boltzmann distribution

of speeds [8], [9]. The method has been broadly developed and the discussion about its actual applications are reported elsewhere [10], [11]. In the case of LB, instead, the simulation space is partitioned and a lattice created. The simulation particles can move only on this lattice and iteratively propagate and collide. A discrete Boltzmann equation is solved in place of the Navier-Stokes ones [12], [13]. The method has large diffusion in the literature. It has been utilized and validated for phenomena such as the ones that will be considered in the third part of this chapter [14]–[17].

VI.1.c Electro-osmotic flow – phenomenon

The electro-osmotic flow phenomenon is here illustrated extremely briefly in order to allow the reader to understand the discussion of the results part of this chapter.

The surface of most materials becomes charged when put in contact with polar solvents. In example silica [18] and titania [19] showed to have a surface charge of the order of tenths of mC/m^2 when put in contact with water at neutral pH. This charge is formed by the loss of an equivalent opposite charge in the solvent. The counterions stay then in the proximity of the surface charge forming a sort of screen. The liquid results anyway to be charged due to the presence of the counterions. This remains true even if salts are initially present in the liquid. Added salts modify the screening of the surface charge. Nanoscopic effects on the value of the surface charge in function of the size have been reported. For example in case of alumina particles either lower or higher values of surface charge in respect of larger samples have been found [20], [21]; however the discussion about this variation is not in the aim of this thesis. If an electric field is applied on the system the liquid experiences a neat force localized on the dissolved ions inducing a flow. The intensity, profile and characteristic of this flow are determined by the geometry and other characteristics of the system. The simple case of a plane channel with uniform surface charge is here presented.

The first element to analyze is the charge distribution. As has been mentioned the liquid is charged. This charge is not distributed uniformly in the channel but is mainly placed near the walls. This can be intuitively explained following this reasoning illustrated in Figure.VI-2.

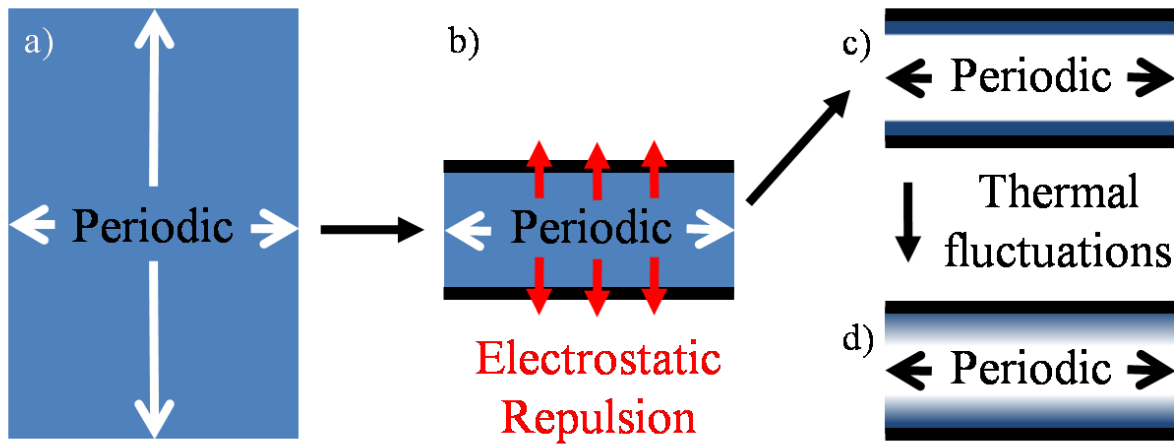


Figure.VI-2. (a) If a uniform charge with density equal to the ratio between the charged released by the surfaces and the channel volume is not confined it is uniformly distributed. (b) Upon removal of the charge outside the channel the remaining one experience electrostatic repulsion from inside the channel not compensated by the charge that was outside it. (c) two layers of charge are then formed that relax (d) to the equilibrium distribution determined by thermal fluctuations.

If a charge can occupy all the space (both inside and outside the channel-wall interface) it will be distributed uniformly in it; upon removal of the charge outside the channel the electrostatic contribution given by it vanishes. Because the removed charge was outside the channel the electrostatic force of repulsion coming from “outside” is no more there. This causes the remaining charge to move towards the wall-channel interface because of the unbalanced repulsion force from inside the channel. An accumulation of charged at the channel walls is then formed. At equilibrium the charges are distributed by thermal fluctuations. The charges are then accelerated by the electric field.

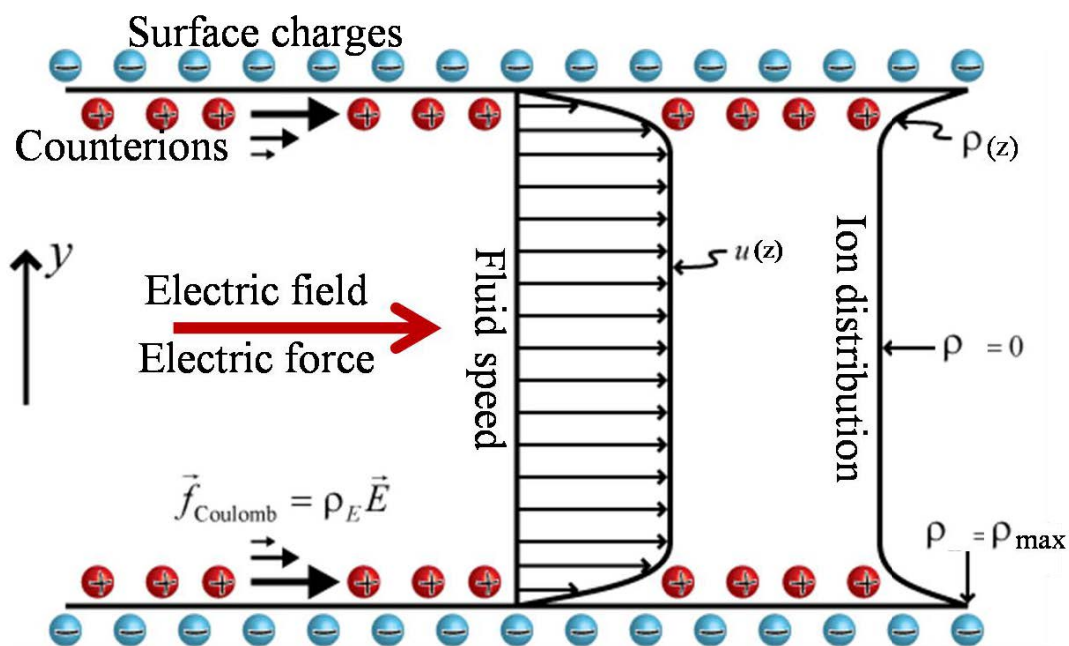


Figure.VI-3. Simple scheme of the electro-osmotic flow phenomenon.

The charged ions acquire momentum that, through viscous hydrodynamics interactions, is transmitted to the fluid. Because the charges are mostly at the wall-channel interface the largest part of the momentum is transmitted at the wall-channel interface. In the middle of the channel no more momentum is added. This means that the fluid velocity too changes mostly at the interface and has a constant value in the middle of the channel. This is simply illustrated in Figure.VI-3 where the fluid speed profile and the ion distribution are reported.

Ion distribution has evidently an extremely important role in determining the final fluid profile. It has to be noticed that the net charge of the liquid does not determine the profile alone. The salt concentration in the liquid (or the ionic strength) modifies it changing the length of the screening as is commonly described in the Debye-Huckel theory. Salt concentration in the liquid is therefore a fundamental parameter and its influence will also be analyzed. Finally it is worth saying that the distribution of charges on the solid surface can influence the flow, since it creates potential wells in which the ions remain trapped. These aspects will be analyzed too.

Analytical solutions for the electro osmotic flow can be found in the literature. In particular the Nernst-Planck equation describing the motion of charges in fluid under electrical field can be integrated with the adequate boundary conditions to obtain

$$u_x(z) = u_x\left(\frac{L_{ch}}{2}\right) - \frac{e^-E}{\eta} \int_{\frac{L_{ch}}{2}}^z \int_0^{z'} \rho_+(z'') dz'' dz' \quad (3)$$

with L_{ch} the channel height and ρ_+ the ion density distribution. This distribution can be determined either by molecular simulation (such as MD or SRD in this case) or by analytical theories such as the Poisson-Boltzmann theory. In this latter case the analytical solution, the charge density gives [22]

$$\rho_+(y) = \frac{\alpha^2}{2\pi l_B} * \frac{1}{\cos^2(\alpha z)} \quad (4)$$

and the fluid flow is

$$u_x(z) = \frac{e^-E}{2\pi\eta * l_B} \ln\left(\frac{\cos(\alpha z)}{\cos\left(\frac{\alpha L_{ch}}{2}\right)}\right) \quad (5)$$

with α defined by

$$\frac{\alpha L_{ion}}{2} \tan\left(\frac{\alpha L_{ion}}{2}\right) = \pi \sigma L_{ion} l_B \quad (6)$$

with σ the surface charge and $l_B = e^{-2}/4\pi\epsilon_0\epsilon_r k_B T$ the Bjerrum length and L_{ion} the width of the canne that the ion can effectively experience (if it is a large complex it cannot approach effectively the channel wall so L_{ion} is littler than L_{ch}).

The characteristic speed of the system is defined by $u_0 = \frac{e^{-E}}{2\pi\eta * l_B}$ and can be used to calculate the Reynolds number or the other adimensional numbers.

It is important to say that for the Nernst-Plank equation to be valid the ions are considered point charges. The hypothesis for the Poisson distribution to be valid is that the charges have to be monovalent and the potential value low (which corresponds to low surface charge values).

VI.2 Stochastic Rotational Dynamics.

In the second part of this chapter, a simulation method named Stochastic Rotational Dynamics (SRD) is presented. As it will be exposed, the method takes into account the hydrodynamics interactions inside the system which allows describing phenomena such as pressure driven flows or electro-osmosis. The solvent is not described at a molecular level but a particle-like description is maintained. Ions (or colloids) are described explicitly and their interactions are described by laws that will be later discussed.

The fluid in the simulation cannot be considered as real. It has no internal structure, no interaction between pairs of fluid particles such as chemical or hydrogen bonds, no dielectric constant etc. The fluid transports the momentum in the simulation box and its role is limited to this objective.

In order to perform simulations it is needed to create a model environment (the simulation box) that represents the real equivalent. In many cases the model box has a high level of symmetry that allows the use of periodic boundary conditions and virtually represents an infinite space. The simulation of the hydrodynamics in a nanoporous material can then be performed only taking into account periodical porosities. As already said, the PPNs, thanks to their hexagonal symmetry, represents an optimum candidate for simulations. This has been another of the motivations that induced to use this kind of material. Disorganized porosities cannot, indeed, be easily replicated in simulations due to their low level of symmetry.

Being a rather new method, SRD needs to be validated and calibrated for the various systems. In this section, results obtained before this thesis are presented. They allow identifying SRD as suitable to adequately describe hydrodynamic interactions between particles and pressure driven flow. The algorithm at the basis of the method is initially introduced. Then the expressions of some important simulation parameters are reported and a brief description of the different time scales in the simulation discussed. Finally the case of pressure driven flow and the measure to obtain an adequate flow profile are described.

VI.2.a The algorithm

Stochastic Rotational Dynamics is a rather new technique (1999). It has been developed by Malevanets and Kapral[23]. They verified the equivalence of SRD results to well known hydrodynamic problems whose solution can be obtained using the Navier-Stokes equations. In particular they demonstrated that energy, momentum are conserved locally demonstrating in this way that Navier-Stokes hydrodynamics is generated correctly.

This method allows the scaling up of fluid simulations avoiding describing the huge amount of molecules (and their interaction). The molecules are substituted by “particles” whose positions and velocities are treated as continuous variables. The simulation box is divided in cells and there is no restriction in the number of particles that may reside in a cell. Discrete time steps are used. The particles can ballistically move or “collide” with other particles. The ballistic evolution is described by

$$R_j(t + \delta t) = R_j(t) * V_j(t) * \delta t \quad (7)$$

with δt the time step, and the collision of the particles in a cell by

$$V_j(t + \delta t) = V^{cell} + R^\alpha(V_j(t) - V^{cell}) \quad (8)$$

with V^{cell} the average speed of fluid particle in the cell and R^α an operation of rotation around a random axis by an angle α . It has to be noticed that the collision step doesn't change the momentum direction and energy intensity in each cell but redistribute them between the particles inside the cell. Conservation of momentum and energy is true for the streaming step too. Schematically the algorithm can be summarized in Figure.VI-4. The method displaces periodically by a random distance ranging from minus a half to half of the cell size in the three directions the position of the cells in which the average is done. Without this operation indeed the Galilean invariance would be broken. Furthermore, at low particle speed, the collision-interaction between nearby particles would be repeated many times creating a false correlation between them. This is again avoided through the mentioned random displacement even at extremely low particle speeds [24], [25]. Thanks to the collision step the momentum is spread between these particles in the same way it is distributed by the molecules in a real solvent. This means that the hydrodynamic interactions are correctly described if the typical dimensionless numbers stay in the good intervals

describing the right regimes. The meaning of the fluid flow adimensional numbers is exposed in the appendix. Analytical formulas can be obtained for the viscosity and transport coefficients in function of the simulation parameters used. The simulation is indeed set-up defining some independent variables such as the rotation angle α , the time step between collisions δt , the box and the simulation cell sizes.

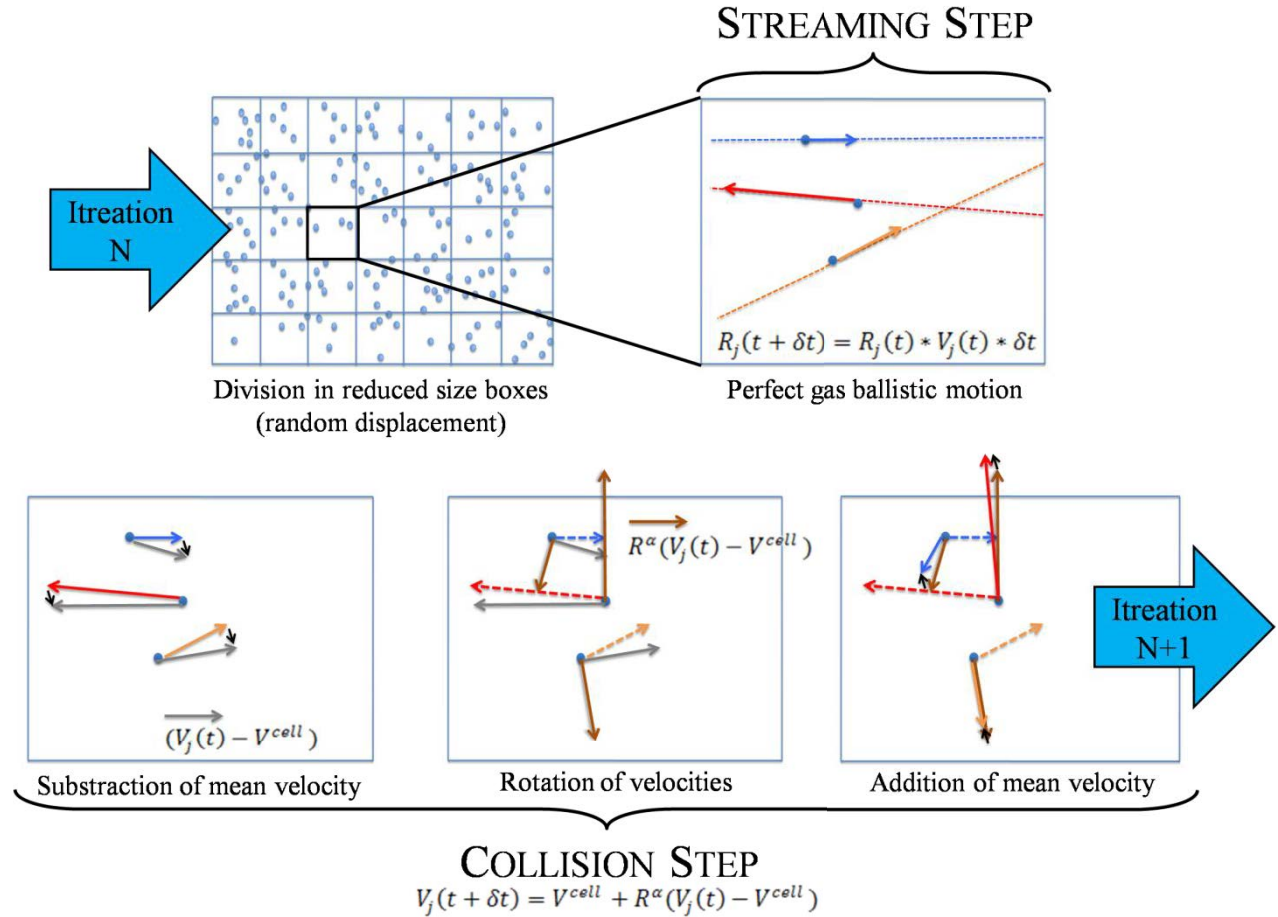


Figure.VI-4. Simple scheme of the SRD algorithm: in each step the simulation box is divided in multiple sub boxes using a random displacement to conserve Galilean invariance. The particles are then moved to their new position determined by their speed vector in the streaming step. In the collision step they interact with each other through three sub-steps. In the first to the velocity is subtracted the average speed of the box. Then the speed of each particle is rotated around a random axis by a defined angle. The average speed is then added again. The momentum of the cell (given by the speed average) is conserved but the particles have exchanged their speed through this procedure. The whole procedure is then repeated in the now iteration.

Other independent variables could be defined and the given one obtained from them. All depends on which variables are considered fundamental. Here it is reported the most common and effectively choice of independent variables. As reported in the introduction, SRD has been used to determine the electro osmotic flow between two charged plates. The typical distance between the plates H_{box} represents then an independent variable of the system. The same is true for the number of cells in the height direction that determines the cell side. The cell side is then used as length

unity $a_0 = H_{box}/N_{box}(Zdir)$. Then the number of fluid particles per cell γ and their mass m_f has to be defined and, in the second case, used as mass unity. If charged particles are added to the simulation too the charge of the electron e^- is used as unit of charge.

Once having defined the independent variables all the other ones can be obtained. In example the time unit becomes

$$t_0 = a_0 \sqrt{\frac{m_f}{k_b T}} \quad (9)$$

and the mean free path, the distance traveled by a particle between two collisions

$$\lambda = \frac{\delta t}{t_0} \quad (10)$$

More complex expression can be found for the kinematic viscosity (shear viscosity η can be easily obtained multiplying for γ)

$$\nu = \nu_{kin} + \nu_{col} \quad (11)$$

composed of the composition of the viscosity due to the kinetic and collision contribution respectively (the formulas have been proved by dedicated simulations[6], [26], [27])

$$\nu_{kin} = \frac{a_0^2}{t_0} * \frac{\lambda}{3} * \frac{15 \gamma}{(\gamma - 1 + e^{-\gamma})(4 - 2 * \cos(\alpha) - 2 * \cos(2\alpha))} \quad (12)$$

$$\nu_{col} = \frac{a_0^2}{t_0} * \frac{\gamma}{18 \lambda} * \left(1 - \cos(\alpha)\right) \left(1 - \frac{1}{\gamma} + \frac{e^{-\gamma}}{\gamma}\right) \quad (13)$$

or for the fluid (kinematic) diffusion coefficient (exact to a 25% error for short free paths) [6], [28], [29]

$$D_f = \frac{a_0^2}{t_0} * \lambda * \left(\frac{3}{2(1 - \cos(\alpha))} \left(\frac{\gamma}{\gamma - 1} \right) - \frac{1}{2} \right) \quad (14)$$

among the others. Particular conditions have been applied in these studies (some of these results could then not be valid in different simulation schemes). It has to be mentioned here that the value

of the adimensional numbers in an SRD simulation is not conserved. This aspect is analyzed in the next section.

VI.2.b Adimensional numbers and time scales

As previously mentioned adimensional numbers determine the hydrodynamics of the systems. The concept of different regimes has also been introduced. In a certain regime the behavior of the fluid is modified only quantitatively by a variation of the simulation or real variables. This means that it is possible to perform simulation with higher or lower values of these variables and then rescale them to the real ones. This could be useful, in example if this has the effect to reduce the time needed to obtain simulation results.

For example, when the pressure driven flow is considered inside a planar channel, it is possible to perform calculations (at it has been done in Chapter IV) considering a given pressure. If the value of the real pressure is five times higher than the one imposed in the simulation, then, obtained values of fluid speed or flow have to be multiplied of the same factor at the condition that the fluid regimes remain the same. In the particular case of pressure driven flow the condition is that the Reynolds number, describing the reciprocal intensity of inertial and viscous forces, has to be, in example, lower than 0.1 if the so called “laminar regime” is the considered one.

The SRD fluid has not the same properties as the real fluid that it should represent (it has no chemical interactions, no dielectric constant, it is much less dense etc.) and, as just described, the values of viscosity, the fluid particle diffusion coefficient etc. can have extremely different values from their real counterparts. Nevertheless if the adimensional numbers define the right regimes real values can be extracted easily.

Due to its characteristics the SRD flow allows to reduce the time of calculation remaining in any case in the right regimes. The timescales that have to be considered in real system span over 15 orders of magnitudes from the fluid collision time scale (of the order of femptoseconds) to the colloid diffusion one (of the order of seconds). The SRD simulation technique allows to sensibly reduce this difference between the time scales (keeping the different phenomena over different timescales) thus reducing the calculation time without loss of generality [6].

Because the systems that have to be simulated are nanofluidic ones the regimes corresponding to this kind of systems are the chosen one. An expression of the values of the adimensional number in function of the SRD parameters is then needed.

For example (see the appendix of this chapter for definitions) the Reynolds number (which can be defined only in presence of solid surfaces and whose definition should be slightly modified in function of the real system) is defined as (with v_s the flow velocity)

$$Re = \frac{N_{box(Zdir)} * v_s}{\nu} \quad (15)$$

the Mach number

$$Ma = \frac{v_s}{v_{sound}} = \frac{v_s}{\sqrt{\frac{5}{3} * \frac{k_b T}{m_f}}} \quad (16)$$

the Knudsen number

$$Kn = \frac{\lambda}{N_{box(Zdir)}} \quad (17)$$

the Schmidt number

$$Sc = \frac{v_s}{D_f} \quad (18)$$

and the Peclet number (with a_{col} and D_{col} radius and diffusion coefficient of an eventual colloid)

$$Pe = \frac{v_s a_{col}}{D_{col}} \quad (17)$$

whose meaning and definition is expressed in the appendix.

For example the Mach number has no serious influence on the flow patterns below the value of 0.3. So if the fluid speed is low enough the Mach number in the simulation can even be different from the one in the real systems. This means that under this limit the speed of the fluid can be increased without changing qualitatively the obtained results (the rescaling is of course needed). In the same way the Reynolds number, that has to be kept below 0.1 for a “laminar regime”, can be freely modified inside this limit. Moreover changing the fluid viscosity increasing in example the particle numbers can allow a further increase of the speed without loss of validity.

All these manipulations can be performed in the limit that the modifications of some parameters do not change too much the value of other dimensionless numbers provoking non physical behavior of the system.

After having introduced these concepts concerning the solvent it is now time to introduce the three other objects that can be included in the simulations: fix walls, solutes and colloids. These three objects have different interactions with the fluid and with each other. A brief list of these interactions is here reported and discussed in the light of the simulations performed in the past.

To do so the concept of thermostat is also presented. It has a particularly important role to produce physical results. If indeed an external force field is added to the system, energy is added too and has to be evacuated from it. Temperature would otherwise increase indefinitely. Temperature/molecular agitation effects could also be caused by the description of the boundary conditions. The role of the thermostat in this case is described in the next section.

VI.2.c Walls, thermostat and Poiseuille flow

In this section various schemes to describe the boundary conditions for the fluid flow in SRD simulations are introduced and discussed. The zero-speed condition on solid surface is not, indeed, straightforwardly implemented in the simulation method and some analysis is needed. The Poiseuille flow between two planes will then be analyzed in function of the different methods after having introduced the concept of thermostat which is necessary to obtain a physical result for the flow avoiding divergences of the energy in the simulation box.

VI.2.c.i Fluid-walls interaction

The walls constitute usually a boundary condition in the resolution of normal fluid dynamic problems. A common condition set is the no-slip condition that imposes a speed equal to zero for the fluid at the interface of the fluid with the wall. This condition is in general verified for water on hydrophilic surfaces in the macroscopic limit. It is usually considered true in the nanoscopic one also (even if the wall cannot be really described as a geometric surface when molecules are considered). Exceptions can be observed when the surface is hydrophobic. In this case water has a non affine interaction with the walls and can actually slip on the surface with a speed different from zero. In this thesis, we are interested in aqueous liquids interacting with hydrophilic pores, and therefore the desired boundary condition is the no-slip condition. The analytic condition has then to be transformed to an interaction of fluid particles with the walls that gives actually the

same results. When a particle encounters the wall, it cannot continue its trajectory because it would exit the box. A possibility is to specular reflect it in the simulation volume conserving the momentum in the direction parallel to the wall and reflecting the momentum orthogonal to it. It is clear that in this case the wall doesn't "stop" the particles at all and a slipping condition is set [30]. Another method called "bounce back" [23] has then been proposed to handle the interactions between the fluid and the wall. In this case the whole particle momentum is reflected in the opposite direction upon interaction. In practical terms if a particle should encounter a wall during the streaming step its velocity is inverted and its position calculated as the symmetrical point of the non-modified ending position (inside the wall) in respect of the particle trajectory – wall intersection point. This causes that at the end of the streaming step the average speed on the first layer adjacent to the wall is set to zero.

Similar result can be obtained by the so called "stochastic" condition. In this case the particles entering the walls are put at the surface, and assume a tangential speed v_t that is randomly selected in a half-space Maxwell-Boltzmann distribution. Practically their speed is chosen from a Gaussian distribution with zero mean and standard deviation $v_0 = \sqrt{k_B T / m_f}$. This sets the average speed near the wall to zero. The normal direction speed v_n is drawn from a degree-2 Weibull distribution with mean v_0 and standard deviation v_0 [31].

$$P(v_n) \sim v_n * e^{-\frac{m_f v_n^2}{2 k_B T}} \quad (19)$$

$$P(v_t) \sim e^{-\frac{m_f v_t^2}{2 k_B T}} \quad (20)$$

In this way a part of the momentum and energy of the particles interacting with the walls is destroyed. This affects the total energy of the system and then its temperature that is imposed on the walls.

Simulations of pressure induced flow between parallel walls are extremely useful to understand how these conditions apply. As mentioned, the pressure adds energy to the system at any step. The regulation of the temperature of the system is then necessary not only for the stochastic method but also for the bounce-back one. It is then here introduced the concept of thermostat without which further discussion is impossible.

VI.2.c.ii Thermostat

If an external force is applied to the liquid (as could be the force induced by pressure gradient or to the coupling of an electric field and charged particles) the fluid energy increases with time due to the work by this force. This is true in the real systems too that can heat up if the energy dissipation is not fast enough. In the real word microchannel and nanochannels dissipate heat readily due to high volume to surface ratio and low heat capacity due to the low quantity of contained fluids. Their typical dimension allows releasing the heat generated promptly and constant temperature can be assumed in the system. To simulate such kind of systems, it is then necessary to keep the temperature constant in the simulations too. Since thermal conduction is not naturally described in the fluid-dynamic algorithm of SRD, an additional element that allows maintaining the temperature controlled in the simulation is needed. Without it the fluid particle speeds would promptly increase due to the accumulation of energy in the box.

The most common method to control temperature in particle simulations (such as Molecular dynamics) is the Andersen thermostat [32]. It is a valuable tool to describe equilibrium properties but for time-dependent or stationary states, it cannot be applied because of its loss-of-memory effect (simply after each collision the velocities in the systems are reinitialized obeying the temperature constraint). Another strategy has then to be used to thermostat the SRD fluid [6], [33].

In the discussion that follows the following method has been used: the temperature of the simulation is measured from particle speeds (from the equipartition theorem the 3D kinetic energy contribution is $\frac{1}{2}m_f v^2$ is equal to $\frac{3}{2}k_b T$)

$$k_B T_{measured} = \frac{m_f}{3 * N_{free}} \sum_{cell=1}^{N_{cell}} \sum_{i=1 \in cell}^{N_{part \in cell}} (V_i(T_{mes}) - V^{cell})^2 \quad (21)$$

with $N_{part \in cell}$ the particles in the considered cell and N_{cell} the total number of cells. Practically the component of the kinetic energy due to thermal fluctuations (this is why the average speed of the cell is subtracted in order to be able to conserve collective fluid flow speed) of every particle in every cell is summed and divided for the total number of particles that stays in cells with two or more particles. N_{free} is indeed defined as

$$N_{free} = \sum_{cell=1}^{N_{cell}} (N_{part \in cell} - 1) \quad (22)$$

(this means that cells with only one particle do not contribute to the calculation).

The particle thermal velocity is then renormalized to set the temperature

$$V_i(T_{set}) = V^{cell} + \sqrt{\frac{T_{set}}{T_{measured}}} * (V_i(T_{mes}) - V^{cell}) \quad (23)$$

which for simulations with an adequate number of particles gives physical results [6].

As will be presented in the next section the temperature can also be calculated in each cell and each cell thermostated independently. This is the method actually used in the performed simulations during this thesis.

VI.2.c.iii Poiseuille flow between two planes

As it has been announced it is interesting to analyze the effect of the different boundary conditions on the fluid flow. In Figure.VI-5, we report the results from the work of Lujten et al. [34]. The calculated values of fluid speed for bounce-back (BB) and stochastic boundary conditions are reported in green squares and blue triangles respectively. As can be easily seen, the obtained fluid speeds using these methods do not match with the theoretical values obtained by the solution of Navier-Stokes equations. Some errors or inaccuracies are indeed present in the simple description performed with the two methods. Some elements have to be added to the simulation algorithms to obtain the desired values of fluid flow. In Figure.VI-5 various methods are presented to solve these inaccuracies. These methods are coupled with the bounce-back technique. A very brief discussion is here presented.

When performing the simulation with the random displacements to conserve Galilean invariance a problem arises when the collision step is performed. As previously discussed a moving frame is used which can cause the cell to be occupied mostly by free-of-particles space or mostly by the particle-filled space. In the case that the box volume is mostly inside the wall the number of particles inside the box is usually lower than the average number. This means that the particle number dependent viscosity is reduced in proximity of the wall during the collision step. This is probably one of the causes of the faster than expected speed for the simple bounce-back simulations.

The average number of particles in the wall-filled boxes has then to be set equal to the general one. To do this it is possible to add virtual particles in the wall that participate to the collision step. In order to have proper no-slip results the average speed of these particles should be zero. It

is possible to put zero speed particles in the wall in order to reach the average particle density and make them interact with the others. Unfortunately this is equivalent to have a wall at 0 K. Fluid particles then accumulate at the wall interface from the middle of the channel and can be somehow thought as frozen [35].

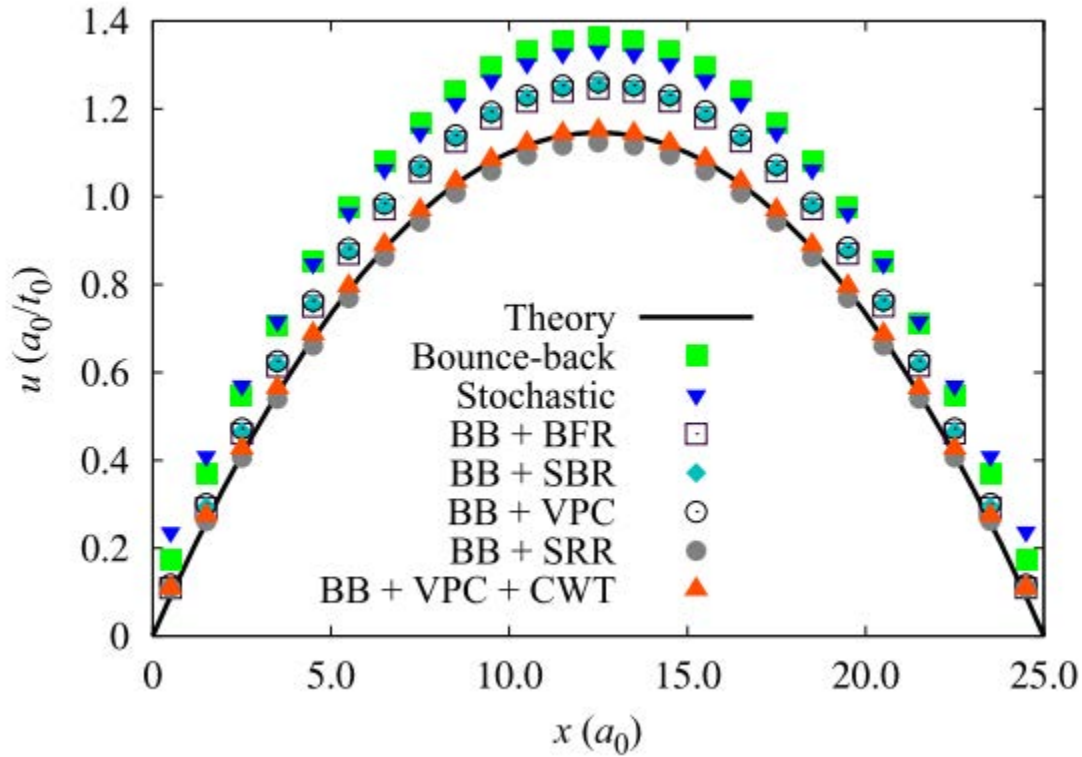


Figure.VI-5. [34] Fluid flow in function of the position for different boundary conditions utilized during SRD simulation. The Black line is the analytical value from Navier-Stokes equations. The various conditions are discussed in the main text.

Virtual particles have then to have a speed distribution whose average is zero but that obeys the Boltzmann (temperature dependent) distribution [35]. This correction reduces the differences between the simple bounce-back simulated values and the analytical ones but still overestimates the fluid speed (Figure.VI-5. BB+BFR (bounce-back bulk-filling-rule) white squares). Different modifications of this scheme have been introduced trying to remove this difference. In example, with the above-mentioned virtual particle method, the density in the cells at the wall can fluctuate only in the positive direction (if a particle is missing it is added but if a particle in excess is present it is not removed); a method to avoid this has then been created that calculates the whole number of particles to add and adds them randomly in the wall-present boxes. This correction does not have serious effects (probably because the positive fluctuations are not so frequent) as can be seen in Figure.VI-5 BB+VPC (bounce-back virtual-particle-condition) method. Equivalently in the case of the BB+SBR (bounce-back symmetrized-bulk-filling-rule) and BB+SRR (bounce-back simple-rescaling-rule) methods the same reasoning induces to modify the

algorithm by imposing a variation of the average speed of the box used in the collision step. For the BB+SBR method in the case of positive particle number fluctuations the average speed is set to [34]

$$V_{corrected}^{cell} = \frac{1}{\gamma} (N_{part} V^{cell} - (N_{part} - \gamma) v_{Maxwell-Boltzmann}) \quad (24)$$

subtracting a Maxwell-Boltzmann distributed speed to the cell average. Again in Figure.VI-5 it is possible to see that this correction doesn't allow the BB+SBR method to fit with the analytical value. In the case of the BB+SRR method a better agreement is instead obtained. The method doesn't uses virtual particles but simply rescales the average velocity of the cell by a factor $\frac{N_{part}}{\gamma}$

$$V_{corrected}^{cell} = \frac{N_{part}}{\gamma} V_{cell} \quad (25)$$

which, if N_{part} is smaller then γ is actually equivalent to the virtual particle method. Unfortunately the sometimes inspected accordance is not stable and for other parameter choices it gives non valid results [34].

All these methods suffer for a common inaccuracy that has been identified as due to the thermostat. Because virtual particles (or their equivalent algorithmic description) acquire energy and momentum from real particles during the collision step, real particles are in general cooler at the wall surface than far away from them. Because of this the calculated average temperature is cooler than the real one. Because its effect is general, it heats up the center of the channel in order to have the correct general energy distribution (the particles at the wall have then the good temperature) which signifies that the velocity of the particles at the center of the channel are higher than it should be. This causes the whole parabolic profile of the Poiseuille flow to grow in intensity giving the showed results. If a local (box size) thermostat is used, this effect is removed and the right profile found as shown in Figure.VI-5 for the BB+VPC+CWT method (bounce-back virtual-particle-condition cell-wise-thermostat method) [34]. To do that the temperature in each cell is calculated (removing the summation over all the cells)

$$k_B T_{measured_{cell}} = \frac{m_f}{3 * N_{free}} \sum_{i=1}^{N_{part} \in cell} (V_i(T_{mes}) - V^{cell})^2 \quad (26)$$

And the new speed renormalized with the already presented equation

$$V_i(T_{set}) = V^{cell} + \sqrt{\frac{T_{set}}{T_{measured_{cell}}}} * (V_i(T_{mes}) - V^{cell}) \quad (27)$$

During this thesis the cell wise thermostat method has been used coupled with the bounce-back bulk-filling-rule (BB+CWT). No need to utilize the VPC method has indeed been identified with tests precedent to this thesis.

VI.2.d Solutes in SRD

Stochastic Rotational Dynamics has been proven to be a stable and usable method to describe fluid flow. On the other hand its use would be not necessary if simple hydrodynamic calculations with fluid only are needed. Other more classical methods could be used in that case. SRD is actually needed if solute particles are added to the fluid (and the system is too big to be described with MD calculations). The elements that it is needed to add are the solute-fluid interactions and the solute-solute ones. Two main schemes can be implemented in the SRD algorithm to describe the solute-fluid interactions that are called “collisional coupling”, CC, scheme and “central force coupling”, CFC, scheme. They will be introduced in the next section. Interactions between solute particles are described with potentials similar to the MD ones. In this part of the chapter, the two schemes of interaction between fluid and solutes will be introduced. A brief description of the potential between solutes is also reported.

VI.2.d.i Fluid interaction with the solutes and force description

In order to feel hydrodynamic effects, solute particles have to interact with the solvent ones. To do so they can enter the collision step (this scheme is called collisional coupling “CC”) and exchange there their momentum and energy or can interact explicitly with the solute through a central force coupling (this scheme as then the “CFC” acronym). In this case, momentum, energy etc. are communicated during the streaming step from and to solute particles. The central forces are exerted indeed on both solute and fluid particles. This interaction is calculated and added to the streaming step. The streaming step has then to be modified and it can be described through the standard Verlet algorithm for Molecular Dynamics [36]

$$R_j(t + \delta t_{MD}) = R_j(t) * V_j(t) * \delta t_{MD} + \frac{F_j(t)}{2M} \delta t_{MD}^2 \quad (28)$$

$$V_j(t + \delta t_{MD}) = V_j(t) + \frac{F_j(t) + F_j(t + \delta t_{MD})}{2M} \delta t_{MD} \quad (29)$$

where a specific time for the streaming step δt_{MD} has been defined that is distinguished from the collision step δt_C . The streaming step is in reality divided in many sub-steps each lasting δt_{MD} . The collision step takes place after that a sufficient number of sub-steps have been performed to reach δt_C . The δt_C time is an integer multiple of δt_{MD} . Actually this modification of the streaming step could also be needed in the collisional coupling scheme in the case that solute particles have to interact with each other or with the walls. Two simple examples of these ever present interactions could be the non-interpenetration interaction (two solutes do not have to have their center at less than the sum of their radius) or the electrostatic one. These aspects will be analyzed later.

The collisional coupling and the central force coupling will be briefly discussed in the following sections. It has been selected in this thesis for its simplicity and knowledge in the laboratory. The interaction used in the actual simulations will be reported in the result section of this chapter.

VI.2.d.ii CC - Collisional Coupling

The description of the solutes in the collisional coupling scheme is extremely simple. Practically the solutes are fluid SRD particles with a higher (not necessarily integer) mass M_j . In the streaming step their movement is ballistic just like fluid particles. In the collision step, the higher mass is considered when calculating the average speed of the cell. The solute contribution that adds to the fluid one weighted for its mass transforms the average speed of the cell to

$$V_{CC}^{cell} = \frac{\sum_{fluid\ particles} m_f * V_i + \sum_{solute\ particles} M_j * V_j}{\sum_{fluid\ particles} m_f + \sum_{solute\ particles} M_j} \quad (30)$$

The algorithm then continues without any other modification. Clearly the lighter the mass of the solute or the higher the number of fluid particles in a box the easier is for the fluid to accelerate or stop the solute particles. This scheme has, importantly, some approximations to be considered. The solute can be penetrated by the fluid particles thus it is not possible to describe fluid effects that could happen at the solute surface. Depletion forces, the force between two solids due to the reduced number of fluid molecules between them upon approach [37], cannot be adequately

described. It is not possible then to portray phenomena of reciprocal stick of solutes due to depletion force that could take place in real systems. In the same way lubrication forces, originating from the solvent particles that have to be displaced from a restricted space n [6], cannot at all be taken into account. The minimum size of the phenomena that could be described is the cell dimension. The description of the flow at the dimension of a single solute is then not valid. Various studies have been performed with this scheme analyzing in example the velocity autocorrelation function of a single solute particle or the diffusion coefficient for different values of the mean free path, of volume fraction and of mass [28] or particle density [38]. Some others have analyzed in example the sedimentation speed in function of the solute volume fraction [39] or the aggregation of charged colloids (Al_2O_3) in presence of shear in function of the pH (and thus the charge) and ionic strength [40] (upon addition of approximate potentials to describe lubrication and contact forces).

VI.2.d.iii CFC – central force coupling

In the CFC scheme the interaction between the solutes and the solvent particles is performed during the streaming step. As previously said many successive streaming sub-steps are performed before a collision step takes place. This is done because using rapidly varying potentials the translational motion of each sub-step has to be a little fraction of solute size in order to properly describe the interaction and not to pass through the solute in an unphysical manner. It is possible to change it independently from the streaming sub-step time δt_{MD} changing the temporal resolution of the interactions without modifying the collisional time δt_c (and then all the associated properties). In general the central force is described by a Lennard-Jones type repulsion potential (with σ_{cf} the solute diameter)

$$\varphi_{solute-fluid} = \begin{cases} 4 * \varepsilon_{cf} * \left[\left(\frac{\sigma_{cf}}{r} \right)^{24} - \left(\frac{\sigma_{cf}}{r} \right)^{12} + \frac{1}{4} \right] & \text{for } r < 2^{1/12} \sigma_{cf} \\ 0 & \text{for } r \geq 2^{1/12} \sigma_{cf} \end{cases} \quad (31)$$

This potential is always positive, and rather steep (this is why reduced δt_{MD} are needed not to penetrate too much in the solute walls). If more than a solute type is present, the potential for all of them ($\varphi_{solute1-fluid} \dots \varphi_{soluteN-fluid}$) has to be defined in function of the solute diameter ($\sigma_{cf1} \dots \sigma_{cfN}$). Because of this potential the volume inside the solutes cannot be accessed by the solvent. The description of the fluid flow around the solute is thus more precise than in the CC description allowing visualizing the flow around them. Therefore, the potential being central, it

doesn't modify the speed tangential to the solute thus non reproducing "stick" boundary conditions similarly to what done in the case of walls [31]. Bounce back and stochastic [39],[41] boundary condition can be used to solve this problem. Therefore, due to the excluded volume effect, the fluid particles per cell could be less than on average. Virtual particles have then to be introduced in the colloids in order to avoid slipping effects on the solute surface; the energy and momentum acquired by these particles is in this case transferred to the solute and is not destroyed. This momentum influences and contributes to the solute movement during the streaming step.

Various elements of interest arise when describing the simulations through this method. In example the description of depletion [6], [42], [43], that needs particular attention to avoid artifacts, is possible only with this method. The discussion of the CFC method is not continued because it has not been used during this thesis. To conclude, it has to be mentioned that the CFC method has been utilized four various applications involving sedimentation of colloidal particles [43] and clustering [42] where strong dependences on colloidal particles volume fraction has been inspected experimentally (which suggest that an explicit description of excluded volume effect should be taken into account).

VI.2.d.iv CFC-CC method comparisons

Only few examples of the same physical problems have been studied both with the CFC and CC methods [39], [44]. This makes a real confrontation between the methods difficult. However, some key elements can be extracted.

As described earlier the CC scheme allows describing hydrodynamics effects of a size larger than the solute particle and cannot take into account the effects due to the being solid of the solute particle. This is particularly important when the solute is a colloid, with dimension notably larger than fluid molecules, but can be somehow neglected in the case that the solute particles correspond to ions. The long range hydrodynamic interactions are indeed well described in the CC method too. Moreover, the representation of an ion with its excluded volume would need the knowledge of the short length potential with a higher degree of precision than in the simple CFC scheme because of the orientation and structuration effect of solvent molecules around ions. Ions could be described as complexes with the surrounding solvent layers in the CFC method, this would constitute an interesting development.

In the case of this thesis the considered solutes are small ions so the CC scheme is preferable.

Moreover the CC scheme has been demonstrated to better account for the hydrodynamic contribution of electric conductivity in respect of the CFC one [44] showing how it better describes collective transport phenomena that are of particular interest for this thesis.

VI.2.d.v Forces between solutes

In both CC and CFC descriptions, solutes particles interact with other ones. In this case a repulsion potential for this interaction to can be written

$$\varphi_{solute-solute} = \begin{cases} 4 * \varepsilon_{cf} * \left[\left(\frac{\sigma_{ss}}{r} \right)^{24} - \left(\frac{\sigma_{ss}}{r} \right)^{12} + \frac{1}{4} \right] & \text{for } r < 2^{1/12} \sigma_{ss} \\ 0 & \text{for } r \geq 2^{1/12} \sigma_{ss} \end{cases} \quad (32)$$

with σ_{ss} is the diameter of this interaction. If more than one type of solute is used (changing mass, radius or charge), all the possible pairs of potentials ($\varphi_{solute1-solute1} \dots \varphi_{soluteN-soluteN}$) have to be taken into account in function of their interaction diameters ($\sigma_{s1s1} \dots \sigma_{sNsN}$ which are the sum of the respective radii). When this kind of repulsive interaction is set between particles the simulation is said to have a WCA repulsion between solute particles (from the initial of the first authors using it [45]).

VI.2.d.vi Electrostatic interactions - Ewald summation

In a simulation involving charged particles, it is necessary to adequately describe the electrostatic interactions between them. The Coulomb law has a simple expression but the low scaling of the potential in respect of charge distance creates problems in small simulation boxes. The interactions with particles outside the simulation box (that are represented by their images) are indeed important and almost of the same order as the interactions between particles inside the box. The electrostatic interactions should then be written as

$$V(r_i) = k \sum_{j,n} \frac{q_j}{|r_{ij} + nL|} \quad (33)$$

where the sum is performed for all the charges j and all the n image cells (at the exception of the self-summation term for $i=j$ and $n=0$) and k is the electrostatic constant depending of the chosen units. In the performed simulations its value is 7.144. Common techniques involving the interactions with the nearest image charge and an explicit account of the energy deriving by them could constitute a first approximation. Unfortunately the summation is slowly convergent so a

high number of image cells should be considered seriously slowing down the calculation. The solution to this problem is to transform the given summation to the sum of other fast converging ones which can be calculated more easily.

In particular each charge is no more seen as a point charge but as the summation of a point charge surrounded by a screening Gaussian opposite charge distribution and a co-placed same charge Gaussian charge distribution. The two elements have fast converging summation and can be easily calculated. The surrounding charges are written as

$$Q_j = -q_j * \left(\frac{\alpha}{\pi}\right)^{\frac{3}{2}} e^{-\alpha r^2} \quad (34)$$

The point charges and their surrounding screening have zero net charge. This means that their long range interactions are negligible. This allows performing a real space summation with a low number of image cells to accurately describe the interaction due to this coupled structure in the whole space. The problem is still there for the same charge distribution that substituted the point ones for the long range initially non converging summations.

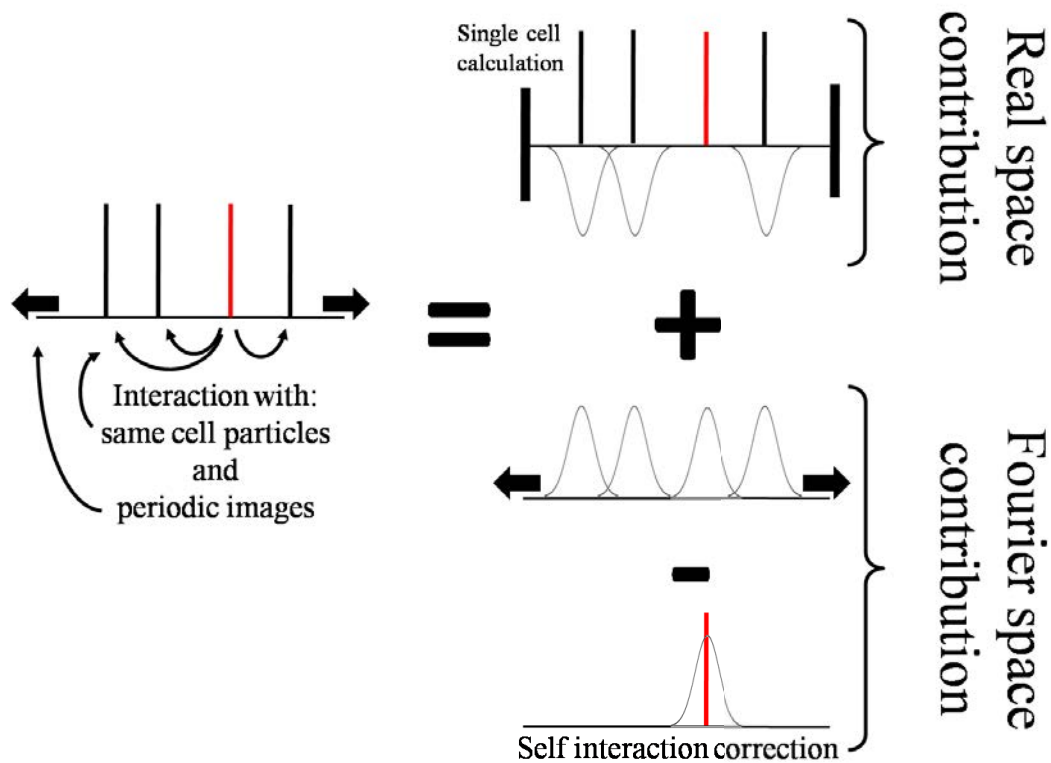


Figure.VI-6. Simple Scheme of the Ewald summation method. The electrostatic interaction between the point charges in the cell and their periodic images are split in two. Gaussian charge distributions of the opposite sign of the point charges surround them screening their interaction with the periodic images. Same charge distributions substitute them in the long range summation. The characteristic Gaussian function can be easily coupled to the Fourier method giving fast converging solutions in the reciprocal space. Upon subtraction of the considered particle (in red) with its corresponding charge and summation with the real space part exact values are obtained.

An easy solution to dodge this problem is to pass through the Fourier space thanks to the periodic boundary conditions of the system. A sum over all the image cells and particles is then substituted with a summation to all the reciprocal vectors and cell particles. This second summation converges much faster than the previous one. Taking care to subtract the self interaction term of the charge with its own image (in calculating the potential) and summing the previously calculated real space counterpart reasonable speed and accuracy can both be obtained. Being the algorithm rather long to explain the reader is invited to consult [46]. A simple scheme of the Ewald summation method is reported in Figure.VI-6.

It has here just to be stressed that the selected value of α ($\alpha=0.2$) had to be tested on the stationary state configuration of the charges. Its values have indeed considerably varied in function of the charged particles configuration. A screening involving the number of reciprocal vectors and the value of alpha has then to be performed in order to obtain stable and physical results.

VI.2.d.vii Ewald summation in slab geometry

Ewald summation has actually been developed to determine the Madelung constant of various crystal structures. Its algorithm is then conceived in a 3D space. The geometries considered in this thesis are actually periodic in 2 dimensions and of finite size in the third one. The images and interaction from the periodic cell in the 3rd dimension would then not be physical which means that the method, as it is, is not applicable. Adequate calculations that take into account 2D periodicity has been developed in the past years [47]–[51] but, unfortunately, the calculation speed in this configuration is significantly reduced because of particular features of the obtained equation. A second strategy, which was used during this thesis, is to consider a much larger unit cell in the non-periodic direction in order to increase the distance of interaction with the image cells and then reduce their interactions. An idea of this scheme is reported in Figure.VI-7. This scheme works reasonably well but a correction due to the dipolar long range interaction between planes has to be added to the already considered algorithm. The method has been tested reproducing the results presented for a 2D slab geometry for two oppositely charged planes as reported in [52], [53].

This and the other reported methods for the various contributions have been utilized in the simulations performed during this thesis. The results obtained during this thesis are reported in the next part of this chapter.

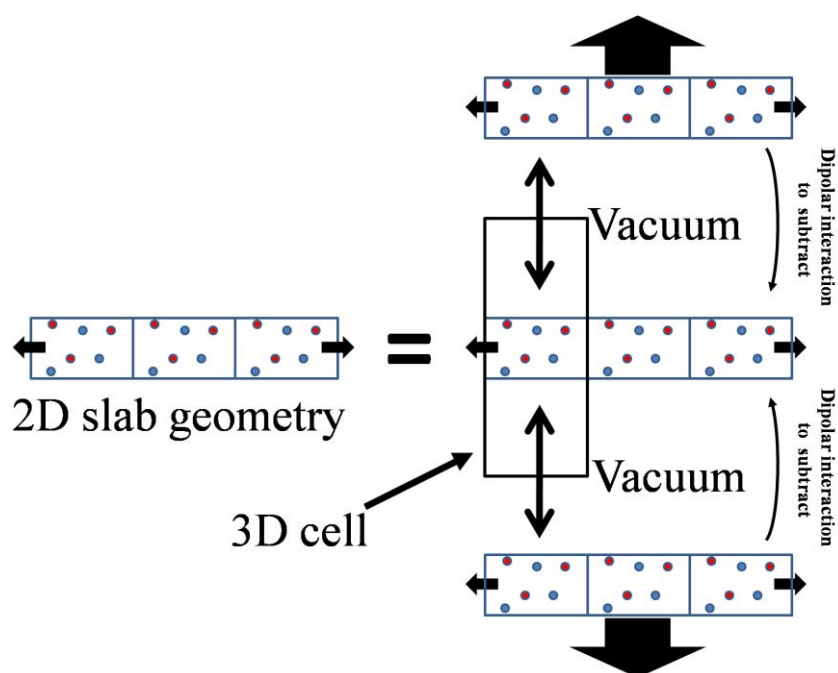


Figure.VI-7. Strategy utilized in this thesis to describe the electrostatic interactions. The interactions in the periodic cell 2D (black filled arrows for periodicity) scheme are taken into account considering a 3D periodic structure with a large space of vacuum between the created planed. This is easily realizable in the algorithm changing the box size in the Fourier transform. Dipolar interactions between from newly created planes have anyway to be corrected by the subtraction of an adjunctive easily calculable therm.

VI.3 : Simulation results

In the third part of this chapter the results obtained by the SRD simulation method are reported. The description of the electro-osmotic flow inside planar nanochannels has been the simulated system through SRD. Some preliminary results for the same phenomenon are also introduced for reduced size PPNs (the actual dimensions of the PPNs would have required a too high computational effort to obtain acceptably smooth curves).

The SRD method had never been used to describe electro-osmotic flow phenomena despite the fact the analytical solution is perfectly known under certain hypothesis. During this thesis the SRD method has been validated for the first time comparing it to the known results of electro-osmotic flow in planar nanochannels. The equivalence of the simulation and analytical ion charge and flow profiles under the said hypothesis constituted indeed an excellent proof on the validity of SRD for the description of electro-osmotic phenomena. This represents an important result because it demonstrates the applicability of the method to electrokinetic problems. The validation has to be performed considering points like charges and monovalent ions in order to use the same hypothesis of the known theories. Further results have been obtained out of the hypothesis of the analytical theory showing the utility of the method to explore the effect of non-considered parameters in the analytical description. The effect of ion size has then been studied. In the same way the effect of charge distribution on the planar nanochannels walls has been investigated. Interesting tendencies have been found that are not normally considered in used theories.

Some preliminary results regarding the electro-osmotic flow in reduced size PPN structures are also presented. The fluid patterns are analyzed and some initial results of charge distribution reported. The calculations are still running when this thesis is written and the obtained results will be more widely exposed in a subsequent scientific article.

In this study, the collisional coupling, CC scheme, has been used to describe the ions–solvent interactions and bounce back boundary condition with virtual particle and cell wise thermostat have been used to describe the flow.

Moreover WCA potential has been used when considering ion size and the 2D-Slab modified Ewald summation method, presented in the second section, utilized in order to take into account electrostatic interactions.

VI.3.a Validation of the SRD method

In order to validate the method it is necessary to make a confrontation with the known analytical theories. To do that a simple SRD model has to be built. Its parameters are described here; a simple scheme of it is reported in Figure.VI-8. The channel height is called L_{hyd} . The other two dimensions of the simulation box are not variables of the physical system. They are not cited in the scheme but are defined later. The fluid particles can stream in all the volume defined by L_{hyd} , the channel hydrodynamic height. In some cases, solute particles are not allowed to approach too much the channel walls and a bounce back condition is set for them too. The diameter for this interaction is called σ_w . The space accessible to solute particles is then defined by L_{el} , the electric charge accessible height, and is equal to the difference between the channel hydrodynamic height and the ion-wall interaction diameter $L_{hyd} - \sigma_w$. The electric field E pushes the monovalent positive ions in the forward direction.

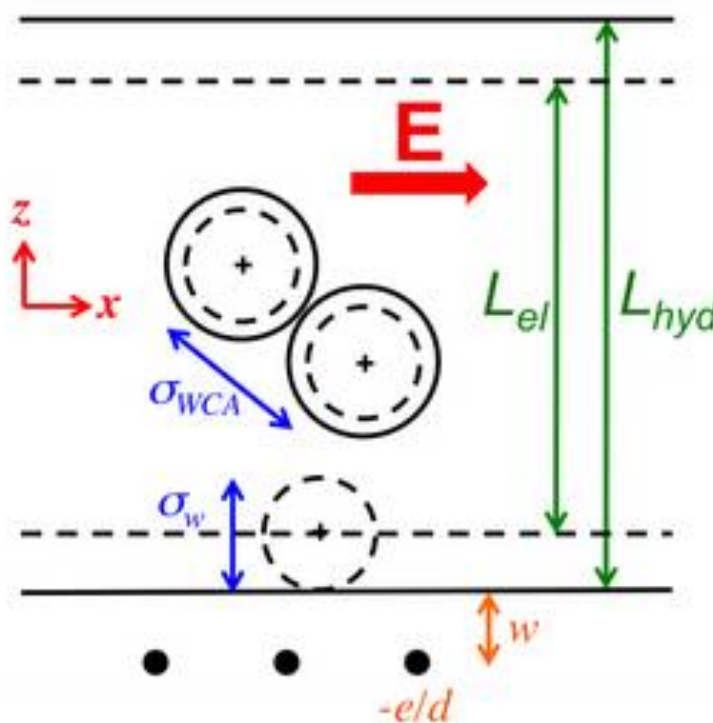


Figure.VI-8. System simulated with Stochastic Rotation Dynamics. Two parallel, infinite charged walls are separated by counterions in a solvent. An electric field E is applied along the surfaces. The solvent can explore the whole space between the walls, separated by a distance L_{hyd} , while an effective ion-wall diameter σ_w restricts the ion to a space of width $L_{el} = L_{hyd} - \sigma_w$. The average surface charge density σ is distributed over discrete size of charge $-e/d$ located at a depth w within the solid wall. The short-range repulsion between ions may be taken into account by a WCA potential, with diameter σ_{WCA} .

In some simulations, the ions interact through a WCA potential. Electrostatic interactions are taken into account through the Slab Ewald Summation algorithm previously described. Charges in

the wall stay at a distance w from the surface in order to avoid singularities in the simulation space. The charges are distributed with a value $-e^-/d$ with d an integer number. The number of the total charge on the surface is represented by the surface charge σ . Fixed charges can be split in d sub charges distributing more or less the surface charge. Theoretically a simulation without fixed charges could be performed but the dipolar term in the Slab Ewald Summation algorithm would be badly defined which causes uncontrolled effects on the simulation. Charges have always been explicitly described then.

VI.3.a.i Simulation box and boundary conditions

The simulation characteristic length a_0 has been set equal to 1 Ångström. A box of $36 \times 36 \times 45 a_0$ has been utilized in the XYZ direction with periodic boundary conditions in the X and Y directions and a “wall” in the Z one (so 3,6 nm in the X and Y directions and 4,5 nm in the Z direction defining the channel height L_{hyd}). In the Z direction, solvent particles experience a bounce-back if the wall is encountered in the streaming step and interact with virtual particles using the “virtual particles” method previously introduced [35]. The number of fluid particles per cell is set to $\gamma=5$, the rotation angle to $\alpha=130^\circ$ and the collisional time $\delta t_C=0.1*t_0$ defining the viscosity to $\eta_{SRD} = 4.045 m_f a_0^{-1} t_0^{-1}$. The value of l_{B-SRD} the Bjerrum length is equal to $7.14*a_0$. The unit of time is then equal to $t_0=8.09 fs$ (setting the viscosity equal to the one of water ($10^{-6} m^2.s^{-1}$)). The value of m_f can be deduced from a_0 and t_0 being $m_f=2.7*10^{-23} kg$ and the value of the ions equal to $M=5*m_f$ to enhance the hydrodynamic coupling as indicated in [28]. In all the simulations, the electric field intensity was set so that $e^-E=0.1 a_0^{-2} t_0^{-2}$ which gives for the Reynolds number a value of 0.03 using the previously defined typical speed $v_0 = \frac{e^-E}{2\pi\eta*l_B}$ and the Reynolds number definition $Re = u_0 L_{hyd} \gamma / \eta$. The regime is then laminar in the simulation too (as it is in the nanochannels due to their reduced dimensions). The value of the Mach number v_0/v_{sound} is also verified to be lower than 0.3 being the typical speed equal to $v_0 = 7.3*10^{-4} a_0/t_0$ and the speed of sound in the SRD fluid $v_{sound}= 1.29 a_0/t_0$. The surface charge are placed inside the wall at a depth w of $0.1 nm$ ($1 a_0$) and can assume values σ of $-0.2, -0.5, -1, -2$ and $-4 e^-nm^{-2}$. Moreover the unit charges in the walls have been in certain cases divided among d sites each having a value of charge e^-/d as already stated. Values of d have been varied between 1 and 26 decreasing progressively the depth of the potential wells in correspondence of the fixed charges. The distribution of these charges has been chosen randomly with the condition of minimum distance equal to $(\sigma/e^-)^{0.5}$. Different distances of minimum approach for the ion-wall interactions have also been defined setting L_{el} at 4.5 nm, 4.4 nm and 4.3 nm (corresponding to $\sigma_w = 0, 1, 2 a_0$

respectively). Not all the combinations of parameters have been performed. The list of the simulation made without considering the WCA potential between the ions is reported in Table.VI-1.

	$\sigma = -0.2 \text{ e}^- \text{nm}^{-2}$	$\sigma = -0.5 \text{ e}^- \text{nm}^{-2}$	$\sigma = -1 \text{ e}^- \text{nm}^{-2}$	$\sigma = -2 \text{ e}^- \text{nm}^{-2}$	$\sigma = -4 \text{ e}^- \text{nm}^{-2}$
$L_{el} = 4.3 \text{ nm}$	d=26,8,1	d = 8, 1	d = 4, 1	d = 1	d = 1
$L_{el} = 4.4 \text{ nm}$	d = 26, 13, 1	d = 8, 4, 2, 1	d = 4, 2, 1	d = 2, 1	d = 1
$L_{el} = 4.5 \text{ nm}$	d = 26, 6.5, 1	d = 8, 2, 1	d = 4, 2, 1	d = 2, 1	d = 1

Table.VI-1 Simulated systems. $-e/d$ is the charge of the sites within the solid walls, i.e. each elementary charge is divided into d sites on the wall, L_{el} is the width of the space available to the center of the counterions between the walls (in nm) and σ is the average charge density of the walls (in $\text{e}^- \text{nm}^{-2}$).

The total simulation time in each case was more than $10^{10} t_0$. In the case of simulations with WCA interactions only the cases with d equal to 1 and L_{el} equal to 4.4 nm were performed with a total simulation time of $4 \cdot 10^8 t_0$.

VI.3.a.ii Validation

After having described all the parameters of the performed simulations, the system whose properties are more similar to the hypothesis of the PNP (Poisson-Nernst-Planck) theory has to be confronted with the analytical laws. The hypothesis of having monovalent free ions is respected by all the systems. The lowest possible surface charge is selected in order to respect the hypothesis for the Poisson-Boltzmann distribution. It is noteworthy to say that with a charge of $-0.2 \text{ e}^- \text{nm}^{-2}$ four ions only are present in the simulation box. An even lower surface charge would have necessitated an increase of the simulation box size and then calculation time. With a too low number of ions, indeed, the ions interact mostly with their periodical images generating potentially unrealistic results. However the results obtained with this surface charge density were satisfying. There was indeed no need to further decrease it.

The charge distribution for $\sigma = -0.2 \text{ e}^- \text{nm}^{-2}$ and three values of σ_w (blue, red and green for $\sigma_w = 0, 1, 2 a_0$ respectively with blue, red and green as color code in this and the following figures) are reported in Figure.VI-9. In the three graph the calculated ion distribution for $d=1$, $d=26$ and from the Poisson Boltzmann theory (indicated as PNP to be uniform with the next results on fluid flow for the Poisson-Nernst-Planck theory) are reported. In the case of $\sigma_w=1$ the ion distribution in presence of a WCA potential between the ions is also shown.

As it is easily identifiable the effect of the surface charge distribution has an important role for $\sigma_w=0$ while in the other two cases the ion distribution doesn't change too much modifying the parameter.

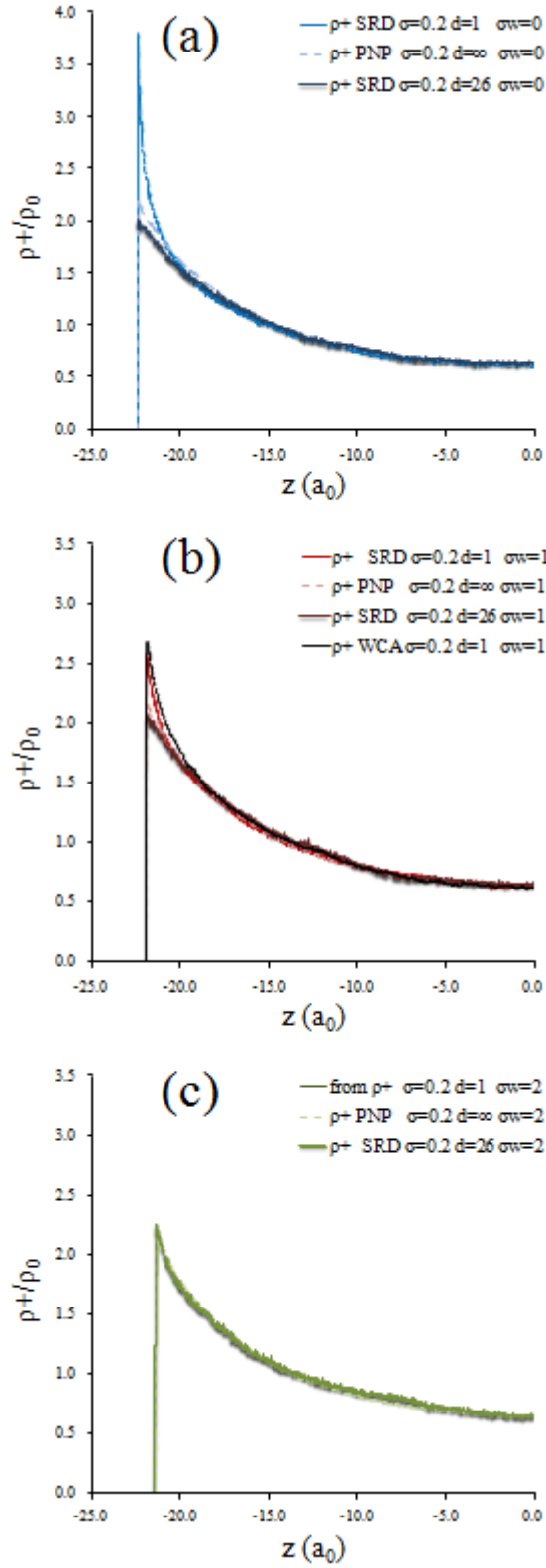


Figure.VI-9. Values of the ion distribution for three values of σ_w . Blue, red and green are code colors used in the next discussion for $\sigma_w = 0, 1, 2$ a_0 respectively. For $\sigma_w = 1$ the values obtained adding a WCA potential between the ions is also reported. These data have a black color.

Therefore, in the exception of the results for $\sigma_w=0$ and $d=1$, the ion distribution is remarkably near the one calculated from the Poisson-Boltzman theory (indicates with PNP for uniformity with the following results on fluid flow). This means that it is possible to make a proper confrontation between the values of osmotic flow obtained with the SRD method and the PNP theory at this surface charge value. This is also valid for the values obtained at $\sigma_w=1$, $d=1$ in presence of a WCA potential between the ions (Figure.VI-9b) which are indicated in black.

The ion distribution can be integrated twice, as indicated in Equation (3) in order to obtain a flow profile from the Nernst-Planck theory. The values of fluid velocities calculated in this way are indicated in the following figures as “from ρ^+ ”. The profiles indicated as “SRD” are the results obtained from the SRD simulations without WCA potential between the ions. “WCA” is instead the label for the flow values of simulations with a WCA potential between the ions.

In Figure.VI-10 it is possible to make a confrontation between the values and profile of the flow from the PNP theory, the values calculated with SRD in absence of WCA potential for $d=1$ and $d=26$ and with a WCA potential ($d=1$) for $\sigma_w=1$. The values obtained applying the Equation (3) to the ion charge distributions are also reported.

As can be inspected the profiles are rather similar. The fluid flow profiles obtained through SRD follow reasonably well the values calculated through the PNP theory (in brilliant red). An effect of the discretization parameter can also be observed. The flow speed is indeed increased for the higher value of d . This could be explained by the fact that for $d=1$ the ions could remain trapped in the potential wells created by the strong surface charge. WCA interactions between ions, on the contrary, seem to slow down the fluid flow. The origin of this effect has still to be investigated. The values obtained integrating the ion distributions are in all the cases extremely near the PNP theory. This is remarkable because it indicates that the effects of fastening or slowing down of the fluid flow cannot be attributed to the slight differences in ion distribution in the z direction found in Figure.VI-9. It has to be finally noticed that the noise inspected in these curves is due to the short calculation time and low number of particles. Distributions with more particles are indeed smoother.

From these results it can be said that the SRD method reproduces the expected results in the limits for which the analytical model gives the correct values. SRD can thus be considered adequate to describe the electro osmotic flow in nanochannels. The difference between PNP theory and SRD calculated fluid flow is always smaller than 10% in exception of the wall boundary layer where a slight slip is visible.

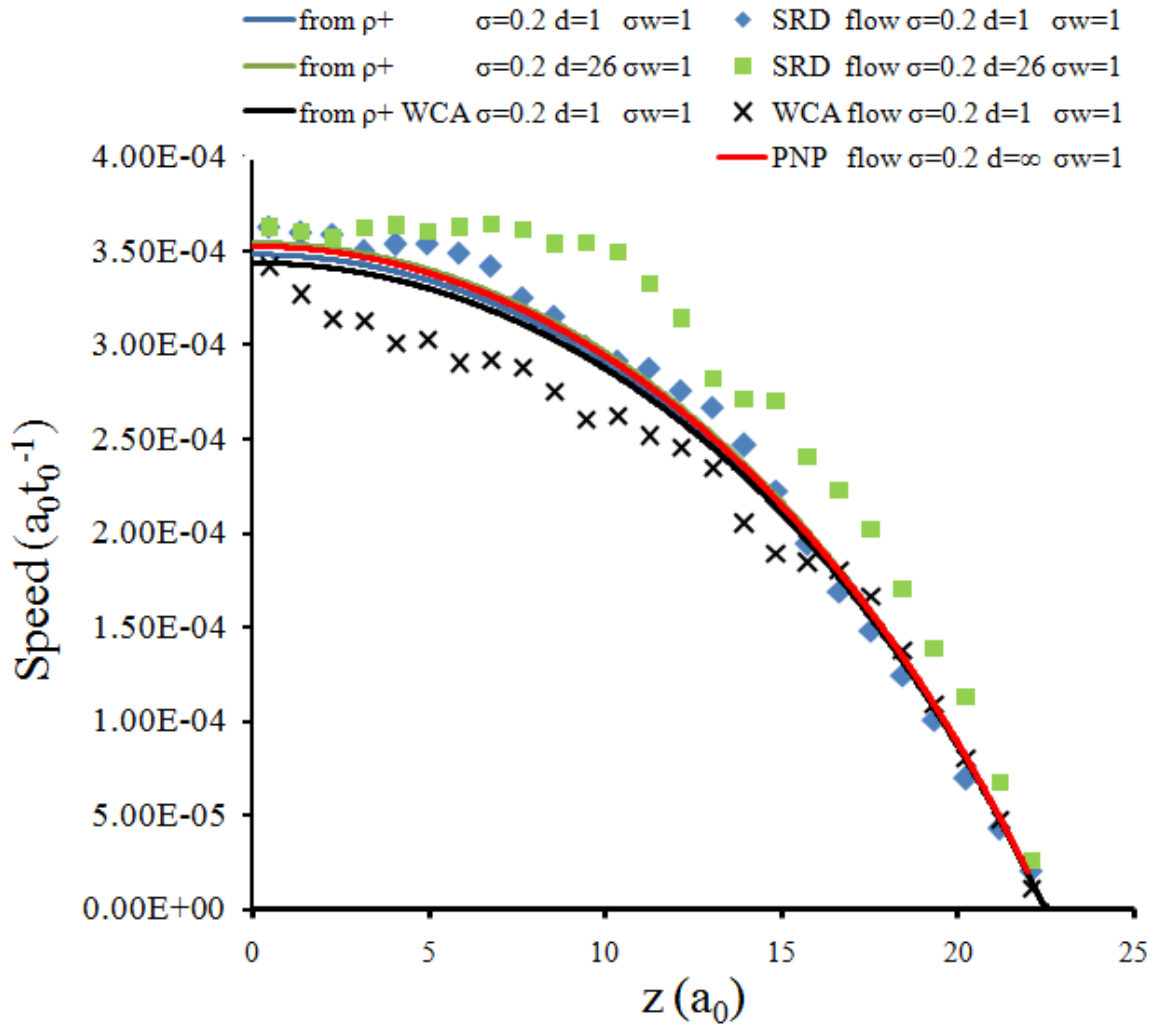


Figure.VI-10. Solvent velocity field $u_x(z)$ in the direction of the electric field, averaged in the x-y plane. PNP stands for Poisson-Nernst Planck theory. The SRD results are shown for two values of the discretization parameter d . For the SRD simulations, the profile obtained by integrating twice the counterions density $\rho(z)$ is also shown though the Nernst-Planck equation (these data are labeled “from ρ^+ ”).

VI.3.a.iii *Effect of σ_w and d for low surface charge values*

After having validated the SRD method for $\sigma_w=1$ it is interesting to investigate if for the other values of σ_w equivalent results are obtained. From the ion charge distribution no serious differences are expected in exception of the flow for $\sigma_w=0$ and $d=1$. The peak near the channel walls is indeed twice as high the one expected from the Poisson Boltzmann theory. In Figure.VI-11 and Figure.VI-12 are reported the results for $\sigma_w=0$ and $\sigma_w=2$ respectively with different values of d .

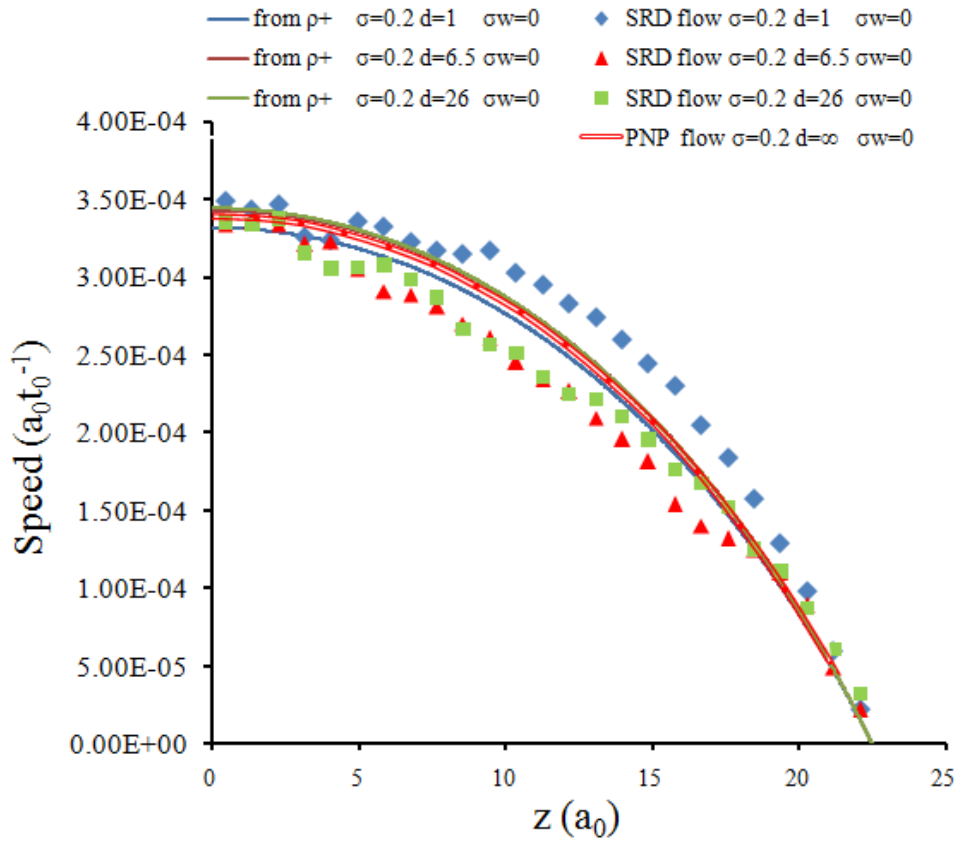


Figure.VI-11.Solvent velocity field $u_x(z)$ in the direction of the electric field, averaged in the x-y plane for $\sigma=0.2 \text{ e}^-.nm^{-1}$ and $\sigma_w=0 a_0$. The same code of Figure.VI-10has been used.

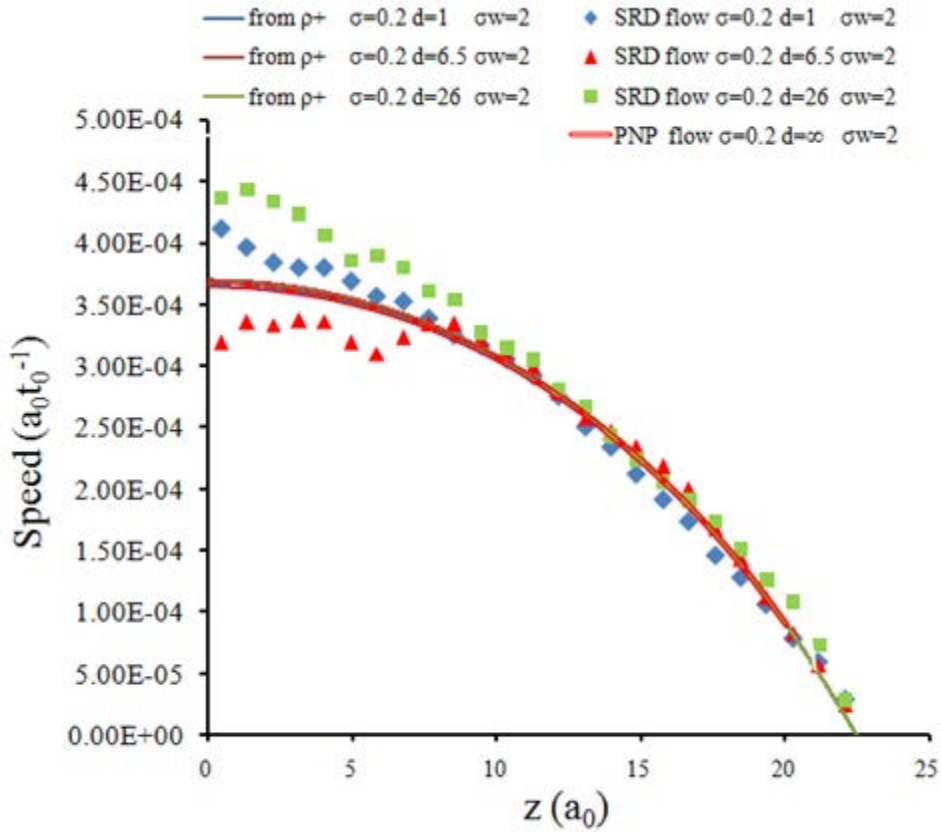


Figure.VI-12. Solvent velocity field $u_x(z)$ in the direction of the electric field, averaged in the x-y plane for $\sigma=0.2 \text{ e}^-.nm^{-1}$ and $\sigma_w=2 a_0$. The same code of Figure.VI-10has been used.

In all cases the obtained results follow rather well the PNP theory. Actually for the $\sigma_w=0$ and $d=1$ case a faster speed is obtained in respect of the cases with higher values of d . As will be shown this is the only case that contradicts the mentioned tendency of faster speed increasing the d value. This effect is then naturally attributed to the different charge distribution (higher peak next to the channel walls) reported in Figure.VI-9 in respect of the other cases. Nevertheless, as can be seen by confrontation of the fluid flow for various values of σ_w at constant d ($d=1$ in Figure.VI-13 and $d=26$ in Figure.VI-14), the fact to have a charge distribution nearer to the wall (Figure.VI-15) usually means a slower flow in both theory and simulation. If, indeed, the charge is more in the center of the channel the momentum transferred to the SRD or analytical fluid is transferred more in the center too. The gradient of velocity in the direction perpendicular to the flow results then to be lower at equal velocity which produces, as a consequence, a faster flow. A more precise investigation is then needed to understand the effect of acceleration for the $\sigma_w=0$ and $d=1$ case but it has not been realized during this thesis.

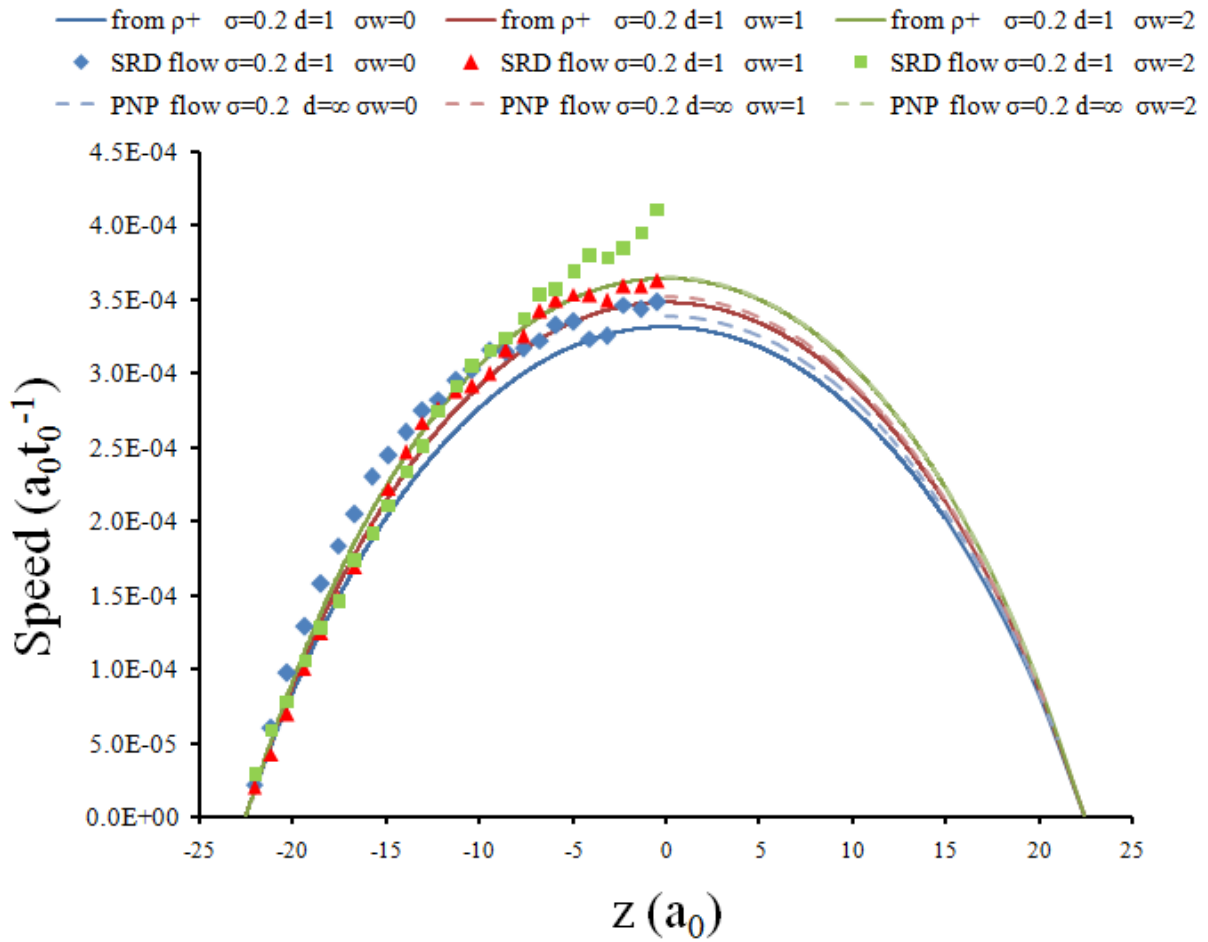


Figure.VI-13. . Solvent velocity field $u_x(z)$ in the direction of the electric field, averaged in the x - y plane for $\sigma=0.2 \text{ e}^-.\text{nm}^{-1}$ and $d=1$. PNP stands for Poisson-Nernst Planck theory. The SRD results are shown for three values of σ_w . For the SRD simulations, the profile obtained by integrating twice the counterions density $\rho(z)$ is also shown though the Nernst-Planck equation (these data are labeled “from ρ^+ ”).

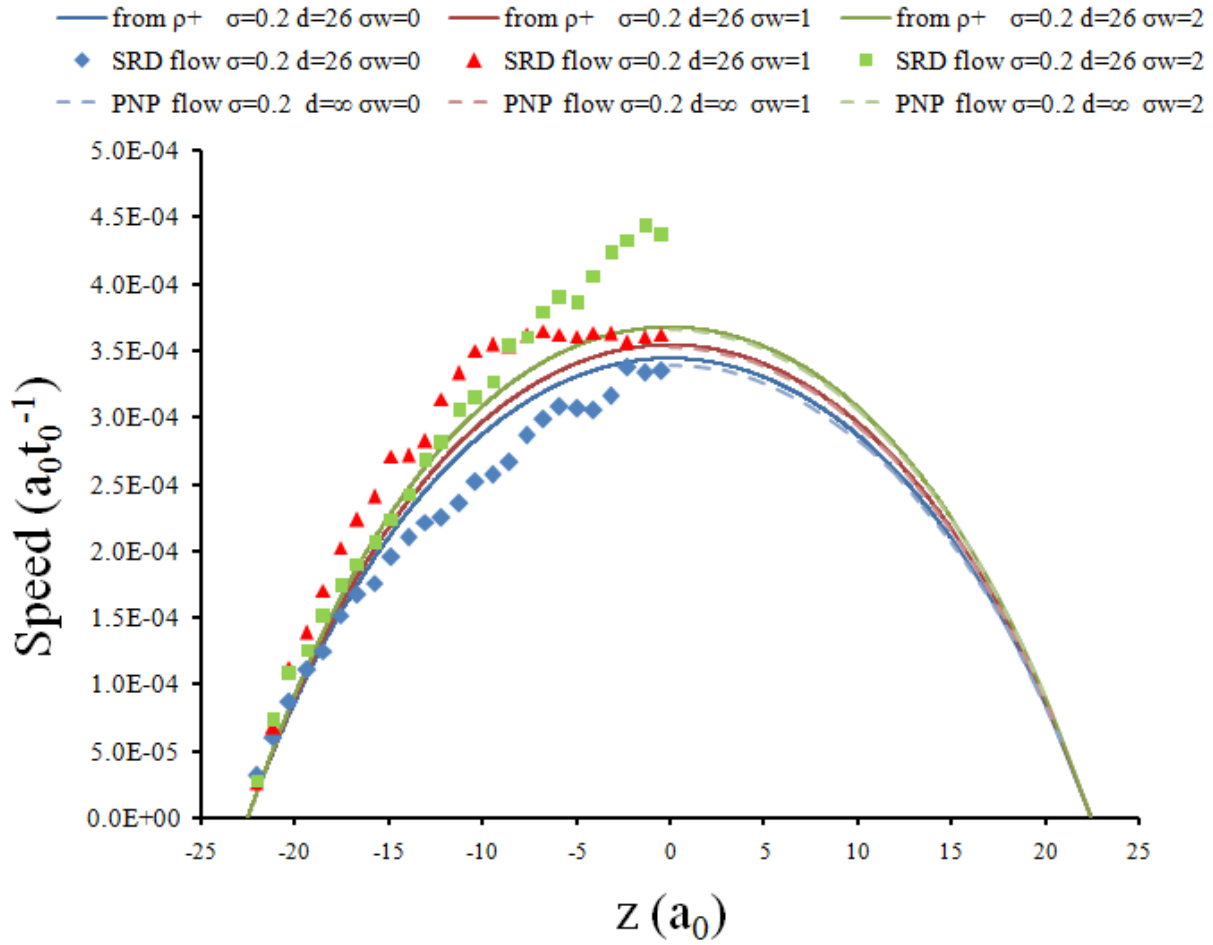


Figure.VI-14. . Solvent velocity field $u_s(z)$ in the direction of the electric field, averaged in the x - y plane for $\sigma=0.2 \text{ e}^-.\text{nm}^{-1}$ and $d=26$. The same code of Figure.VI-10 has been used.

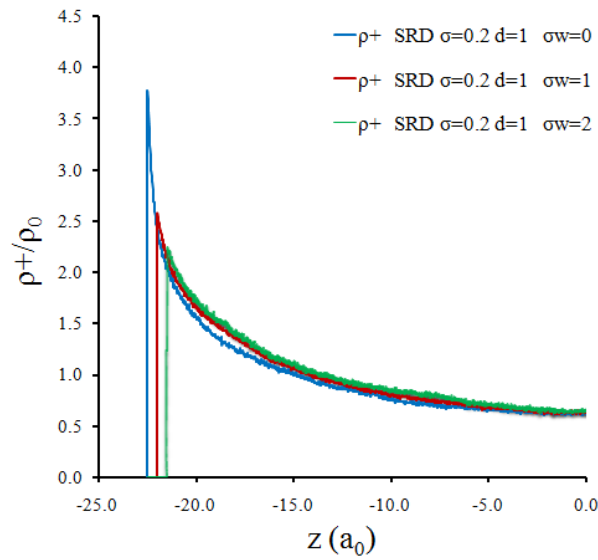


Figure.VI-15. Ion charge distribution in function of σ_w for $\sigma=0.2 \text{ e}^-.\text{nm}^{-1}$ and $d=1$. The same code of Figure.VI-10 has been used.

VI.3.b Non-ideal case: beyond the PNP hypothesis

Once that the SRD method is validated it can be utilized to detect the effects of simulation parameters in conditions that cannot be described analytically. It is in this way possible to study the electro-osmotic flow outside the field of validity of the hypothesis utilized to create the PNP model. In particular, as it is shown hereafter, it is the Poisson Boltzmann equation that doesn't adequately describe the ion charge distribution giving unrealistic flows for the PNP theory. In Figure.VI-16 are reported the ion distribution for $\sigma = 4 \text{ e}^- \cdot \text{nm}^{-2}$ $d=1$ and $\sigma_w = 0, 1, 2 \text{ } a_0$ respectively with blue, red and green as color code, for both the SRD simulation and the Poisson-Boltzmann theory. At a first sight the same features of the case at low surface charge seem to be present and no serious difference is evidenced. The peaks from PB value and SRD have indeed a difference similar to the one inspected for $\sigma = 0.2 \text{ e}^- \cdot \text{nm}^{-2}$. Nevertheless, analyzing directly the data for $\sigma = 4 \text{ e}^- \cdot \text{nm}^{-2}$, it is possible to see that in the central part of the channel the ion charge distribution calculated by PB can attain a value up to 2 times more elevated (Figure.VI-17a) than those obtained with SRD. This means that the PNP model strongly overestimates the charge in the middle of the channel in respect of the SRD values. For $\sigma = 0.2 \text{ e}^- \cdot \text{nm}^{-2}$ this error is not reported and the PNP theory follows the SRD results as shown in the previous chapter. This is illustrated in Figure.VI-17 where the $\rho^+_{\text{PNP}}/\rho^+_{\text{SRD}}$ ratio is reported.

Because the charge in the SRD simulation is at a shorter distance from the wall, the momentum acquired from the ion-electric field interaction is, in the SRD scheme, more readily destroyed by the viscous interactions with the wall than in PNP. It is then reasonable to think that the SRD results would give slower fluid speeds in respect of what expected from the PNP theory. Actually this is verified and reported in Figure.VI-18. The PNP theory gives speeds sensibly different from the one simulated with SRD due to the difference in ion charge distribution. This effect is more pronounced for $\sigma_w = 0$ and decreases going to $\sigma_w = 2$ consistently with the higher modification of the charge distribution reported in Figure.VI-17. This can be explained from the fact that for $\sigma_w = 0$, has already showed, the distribution in SRD simulation is particularly peaked near the walls leaving less charge in the middle of the channel in respect of the other values of σ_w . This causes

the ratio ρ_{+PNP}/ρ_{+SRD} to be higher for $\sigma_w=0$ with consequent increased error in the analytical evaluation of the fluid flow.

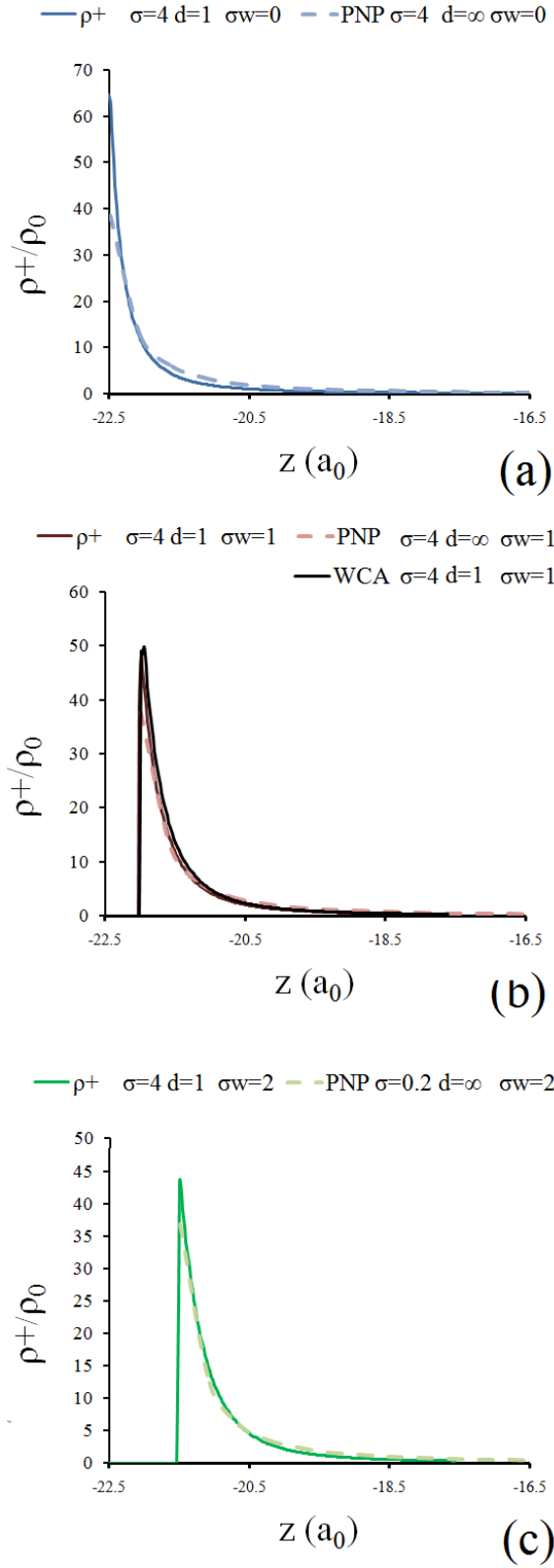


Figure.VI-16. Values of the ion distribution for three values of σ_w . Blue, red and green are code colors used in the next discussion for $\sigma_w = 0, 1, 2 a_0$ respectively. For $\sigma_w=1$ the values obtained adding a WCA potential between the ions is also reported. These data have a black color.

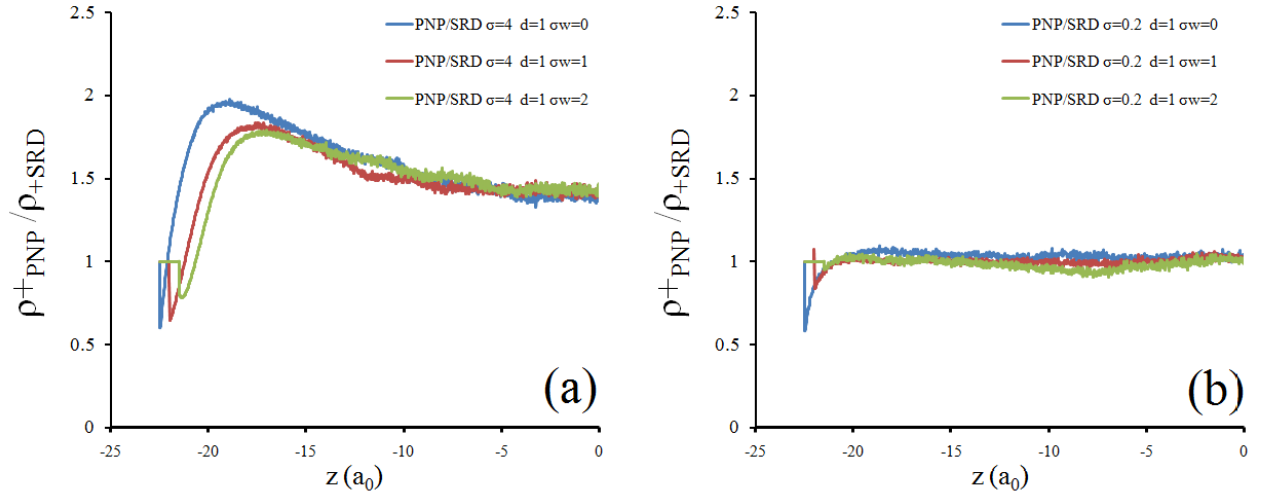


Figure.VI-17. Ratio between the ion charge distribution calculated though the Poisson-Boltzmann equation and the SRD simulated value for (a) $\sigma = 4 \text{ e}^*.\text{nm}^{-2}$ and (b) $\sigma = 0.2 \text{ e}^*.\text{nm}^{-2}$. The same code of Figure.VI-10 has been used.

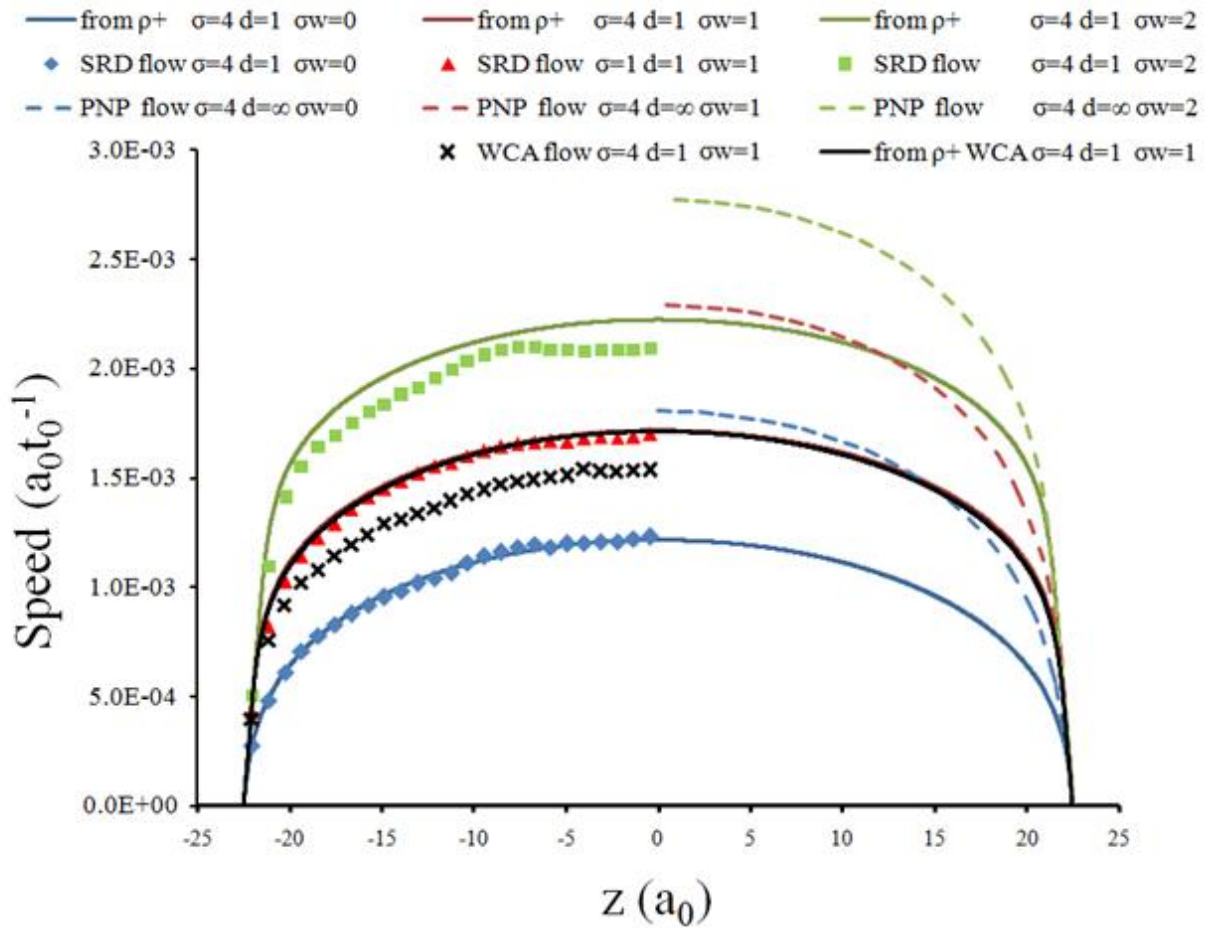


Figure.VI-18. Solvent velocity field $u_x(z)$ in the direction of the electric field, averaged in the x-y plane for $\sigma = 4 \text{ e}^*.\text{nm}^{-1}$ and $d = 1$. The same code of Figure.VI-10 has been used.

In Figure.VI-18 the values of the flow obtained integrating twice the SRD ion charge distribution are also reported with continuous lines being indicated as “from ρ^+ ”. These values follow, instead, reasonably well the actual SRD flow confirming that the difference in flow with the PNP theory is originated by the different ion distribution in the channel. The Nernst-Plank equation can then be still utilized even for higher surface charges and ion concentrations if the ions are considered not interacting with themselves. A slower actual SRD flow is indeed found for the case with a WCA potential between ions in respect of the “from ρ^+ ” curve as already reported for low values of surface charge (for the WCA case $\sigma_w=1$ and $d=1$). This effect will be discussed after introducing the equivalent results for the other values of surface charge simulated in this thesis.

VI.3.c From high to low surface charge

The fluid flow for $\sigma = 2 \text{ e}^- \cdot \text{nm}^{-2}$, $\sigma = 1 \text{ e}^- \cdot \text{nm}^{-2}$ and $\sigma = 0.5 \text{ e}^- \cdot \text{nm}^{-2}$ respectively at $d=1$ are reported in Figure.VI-19, Figure.VI-20 and Figure.VI-21. These results will be analyzed in three brief subsections.

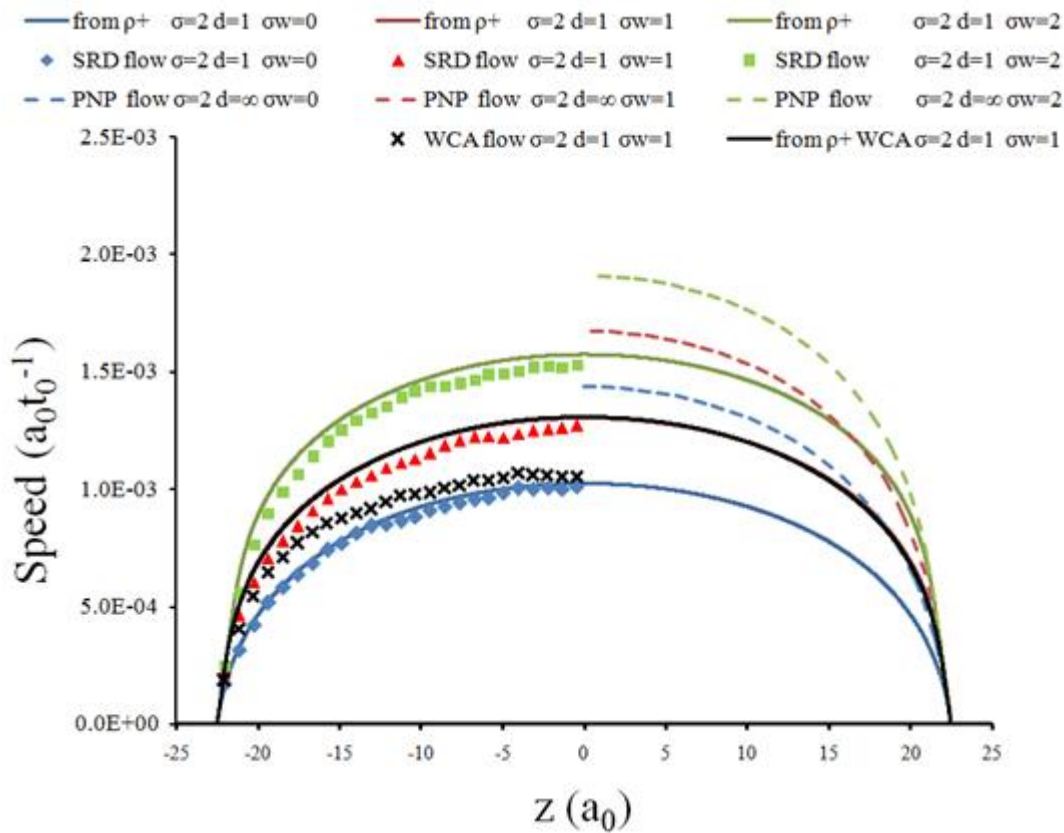


Figure.VI-19. Solvent velocity field $u_x(z)$ in the direction of the electric field, averaged in the x - y plane for $\sigma=2 \text{ e}^- \cdot \text{nm}^{-1}$ and $d=1$. The same code of Figure.VI-10 has been used.

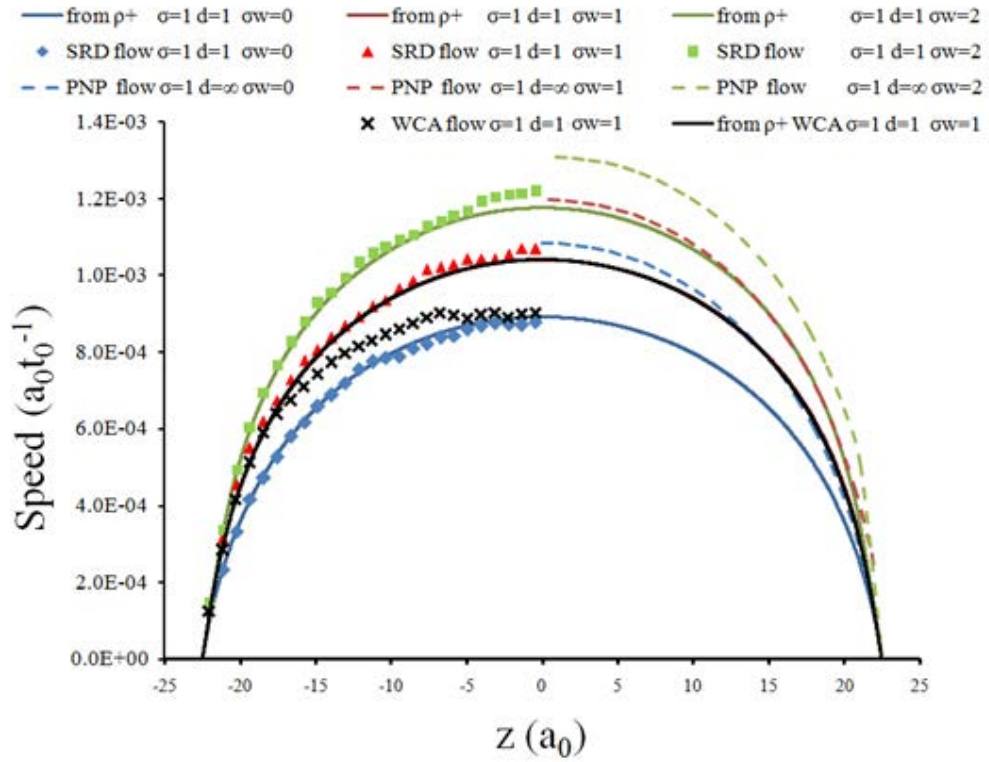


Figure.VI-20. Solvent velocity field $u_x(z)$ in the direction of the electric field, averaged in the x - y plane for $\sigma=1 \text{ e.nm}^{-1}$ and $d=1$. The same code of Figure.VI-10 has been used.

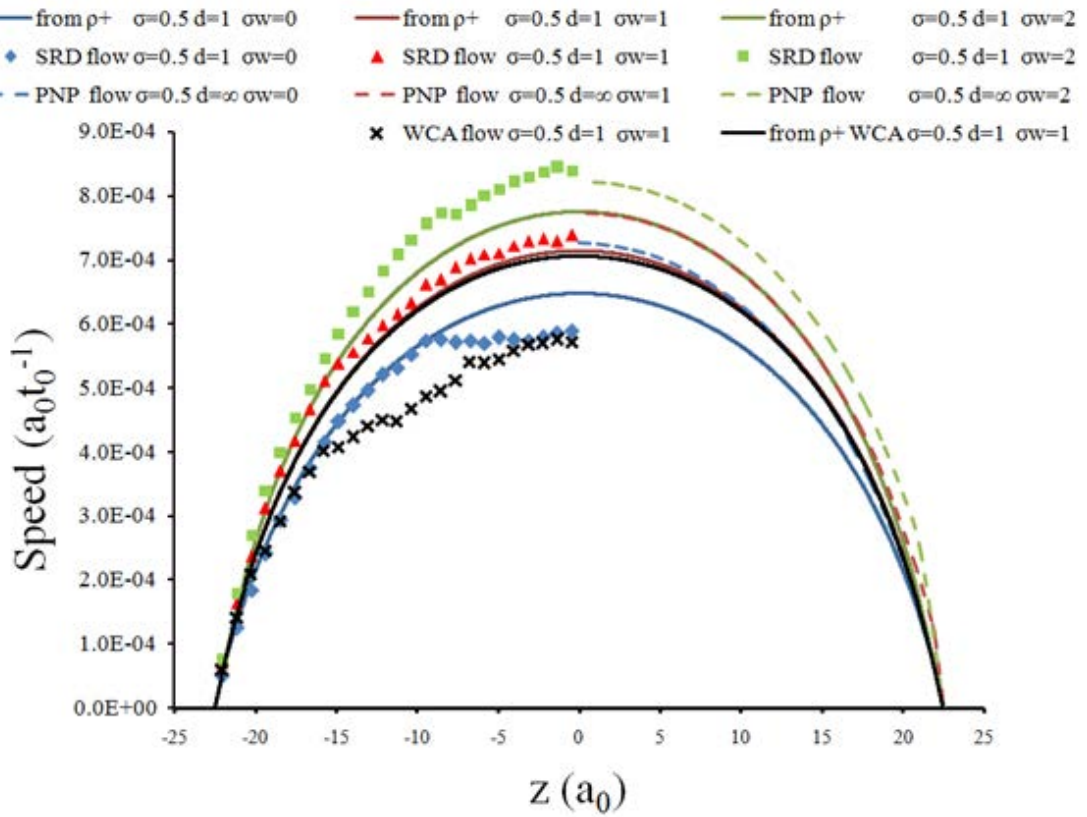


Figure.VI-21. Solvent velocity field $u_x(z)$ in the direction of the electric field, averaged in the x - y plane for $\sigma=0.5 \text{ e.nm}^{-1}$ and $d=1$. The same code of Figure.VI-10 has been used.

VI.3.c.i PNP-“from ρ^+ ”-SRD flow confrontation and WCA interactions effect

A diminution of the surface charge causes the simulated SRD to progressively approach the PNP expected values until match is obtained for $\sigma=0.2 \text{ e}^-.\text{nm}^{-2}$ (Figure.VI-13). The PB distribution indeed becomes more and more similar to the one found by SRD. The values obtained integrating the SRD ion charge distribution (“from ρ^+ ”) are in all case matching with the SRD simulated flow when no ion volume is considered demonstrating the applicability of the Nernst-Planck equation. On the other hand the addition of a WCA potential between the ions reduces the SRD flow leaving substantially unaltered the ion-distribution (for the WCA case $\sigma_w=1$ and $d=1$). This reduction of the SRD simulated flow is very similar in all the cases ($0.17 a_0.t_0^{-1}$, $0.22a_0.t_0^{-1}$, $0.165 a_0.t_0^{-1}$, $0.167 a_0.t_0^{-1}$ for $\sigma=4 \text{ e}^-.\text{nm}^{-2}$, $\sigma=2 \text{ e}^-.\text{nm}^{-2}$, $\sigma=1 \text{ e}^-.\text{nm}^{-2}$, $\sigma=0.5 \text{ e}^-.\text{nm}^{-2}$ respectively) which corresponds to a much higher relative effect in decreasing the surface charge (for $\sigma=0.2 \text{ e}^-.\text{nm}^{-2}$ the difference is smaller ($0.05 a_0.t_0^{-1}$)). The effect of the WCA potential is then stronger diminishing the ion concentration in the channel. This is somehow counterintuitive because volume effects should be greater at higher volume fractions. Further analysis should be performed to understand this tendency.

VI.3.c.ii Effect of σ_w

The effect of σ_w on the ion distribution has already be discussed for the $\sigma = -0.2 \text{ e}^-.\text{nm}^{-2}$ case. In the other configurations similar results are obtained with a similar distribution for $\sigma_w=1$ and $\sigma_w=2$ and a more peaked one for the SRD simulation in respect of the PB for $\sigma_w=0$ and $d=1$. What is here interesting to analyze is the effect on fluid flow. From the preceding figures it is possible to see that increasing the value of σ_w increases the fluid flow in a much higher extent for high value of surface charge than for low values. The effect of “centering” the charge becomes indeed more important if more charges are present in the channel speeding up the fluid flow. It is interesting to notice that this tendency is found also with the PNP analytical solution. The difference in fluid flow of $\sigma_w=0$ and $\sigma_w=1$ is furthermore identical for the SRD simulated and PNP flow indicating that the PNP takes into account this parameter properly.

VI.3.c.iii Effect of d

The effect of d has been already discussed for the $\sigma = -0.2 \text{ e}^-.\text{nm}^{-2}$ case. For the other values of surface charge too no substantial effect is found for $\sigma_w>0$. This can be seen in Figure.VI-22 for $\sigma = -1 \text{ e}^-.\text{nm}^{-2}$ and $\sigma_w=1$.

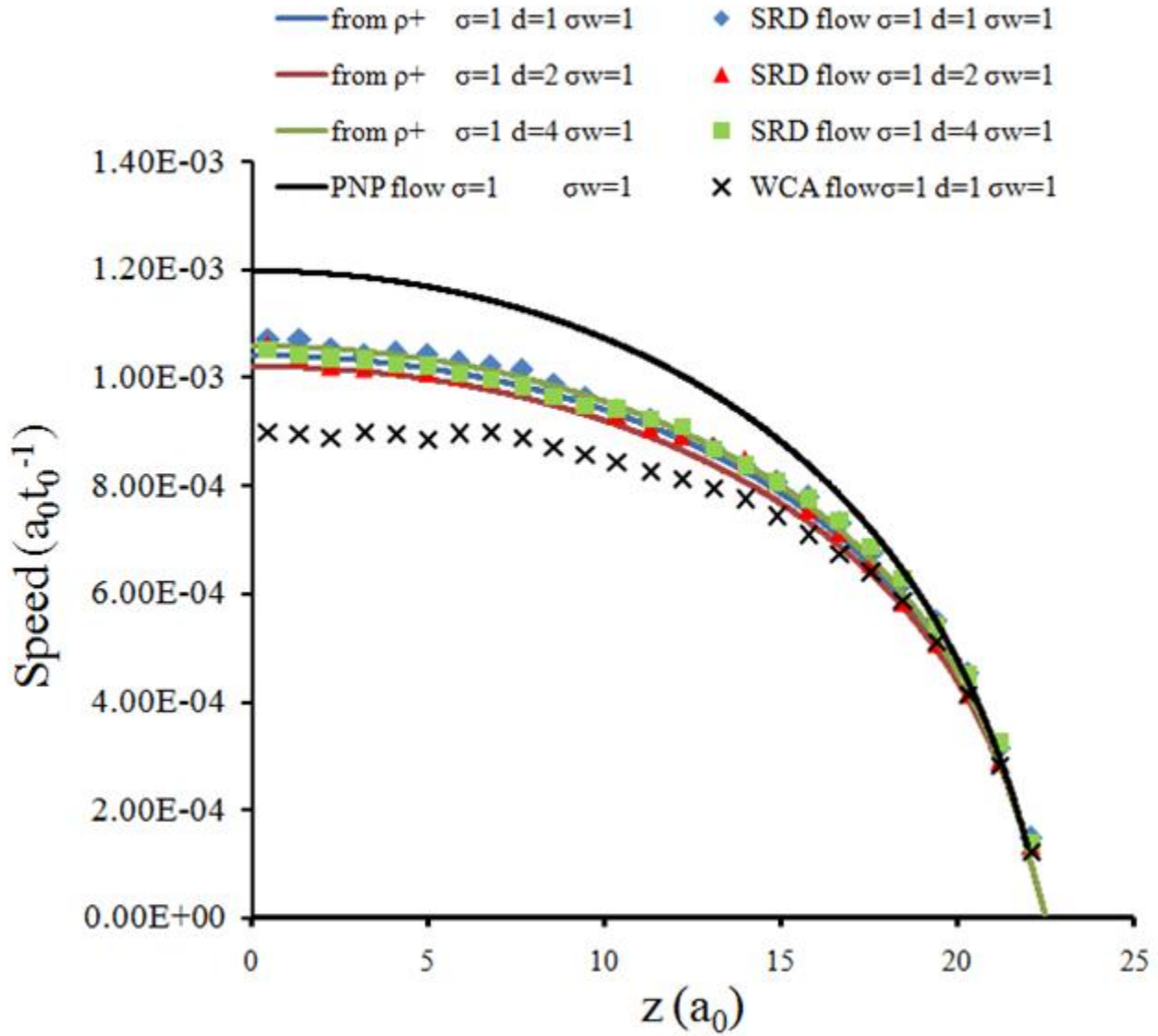


Figure.VI-22. Solvent velocity field $u_s(z)$ in the direction of the electric field, averaged in the x-y plane for $\sigma=1 \text{ e}^-. \text{nm}^{-1}$ and $\sigma_w=1 \text{ a}_0$. The same code of Figure.VI-10 has been used.

A difference can anyway be found for $\sigma_w=0$ with a stronger effect for low values of surface charge than for higher ones. This can be explained by the fact that for higher surface charge values the absolute number of charged spots is in any case high. This means that an ion interacting with a surface charge at $d=1$ “feels” anyway another charge on the surface and is less strongly captured in the electrostatic potential well of the nearest surface charge. The values for $\sigma_w=0$ with a surface charge of $\sigma = -0.5 \text{ e}^-. \text{nm}^{-2}$ and $\sigma = -1 \text{ e}^-. \text{nm}^{-2}$ are reported in Figure.VI-23 and Figure.VI-24 respectively.

This concludes the study of the effects of the various parameters on SRD simulations of simple planar nanochannels with counterions only. In the next section a salt (an equal number of positive and negative ions of the same size of the counterions) is added to the simulation.

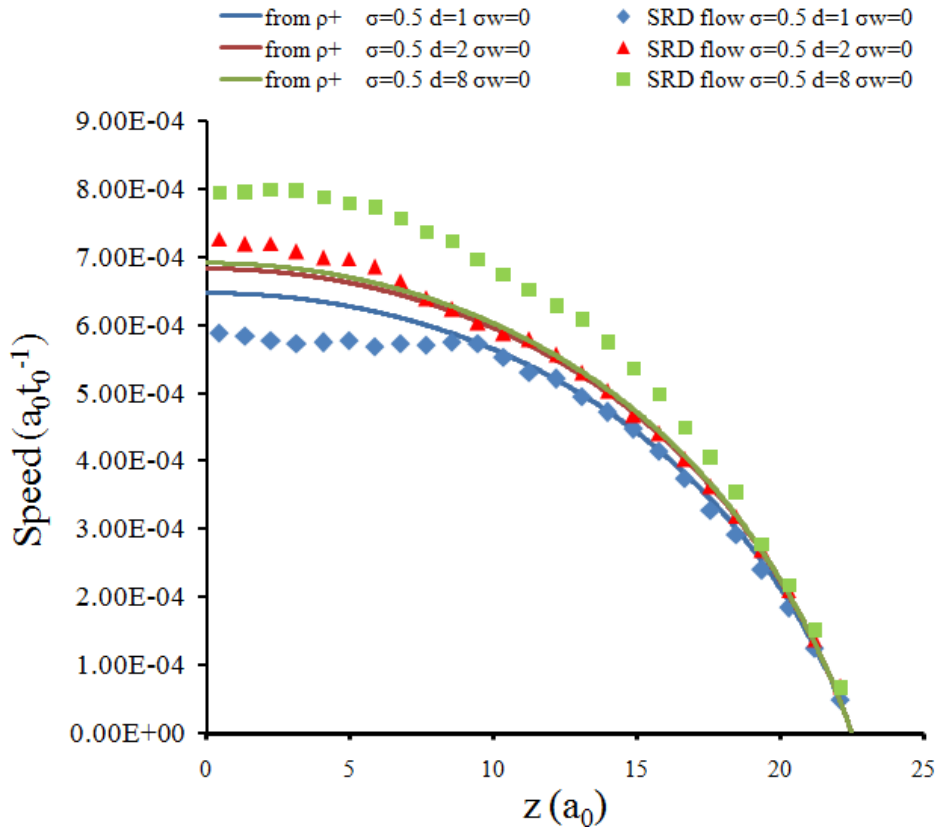


Figure.VI-23. Solvent velocity field $u_x(z)$ in the direction of the electric field, averaged in the x-y plane for $\sigma=0.5 \text{ e}^*.\text{nm}^{-1}$ and $\sigma_w=0 \text{ a}_0$. The same code of Figure.VI-10has been used.

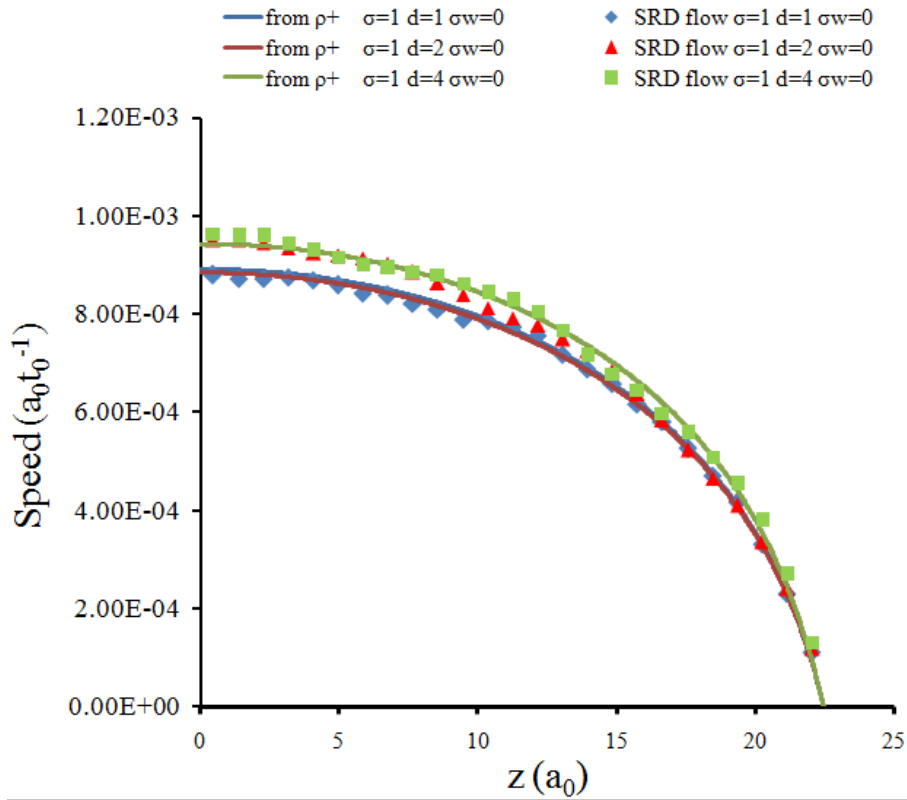


Figure.VI-24. Solvent velocity field $u_x(z)$ in the direction of the electric field, averaged in the x-y plane for $\sigma=1 \text{ e}^*.\text{nm}^{-1}$ and $\sigma_w=0 \text{ a}_0$. The same code of Figure.VI-10has been used.

VI.3.d Salt addition

After having validated the SRD method and having studied the effect of the various parameters on the SRD flow further simulations have been performed to obtain the flow in presence of an added salt concentration in the nanochannel. The PNP theory cannot be used anymore because the PB distribution described before doesn't take into account the presence of an added salt. However it could be possible to solve the PB differential equation in presence of salt in a given nanochannel numerically anyway. An analysis on SRD results only is then reported here.

Two cases have been studied adding to the simulation for $\sigma=1 \text{ e}^-.\text{nm}^{-1}$ (26 counterions in the box) 7 and 35 both positive and negative ions respectively. A WCA potential between the ions is then considered. The volume fraction of the ions in the simulation box is then increased and the electrostatic interactions modified by the ion charges. This can be seen indeed reporting the ion charge distribution of both positive and negative ions in Figure.VI-25 and Figure.VI-26 for 7 and 35 added ion couples. The negative ions are placed prevalently in the middle of the channel while the positive ones maintain a peak near the wall interface. Nevertheless the net positive charge, calculated by subtracting the negative charge distribution from the positive one (adequate weighting with the number of ions is considered), is sensibly reduced in the middle of the channel. Because of this the SRD flow is expected to be slower in presence of salts. This is particularly true for the case with 35 added ion couple where, as can be seen in Figure.VI-26b the net ion charge (black line) in the middle is almost zero.

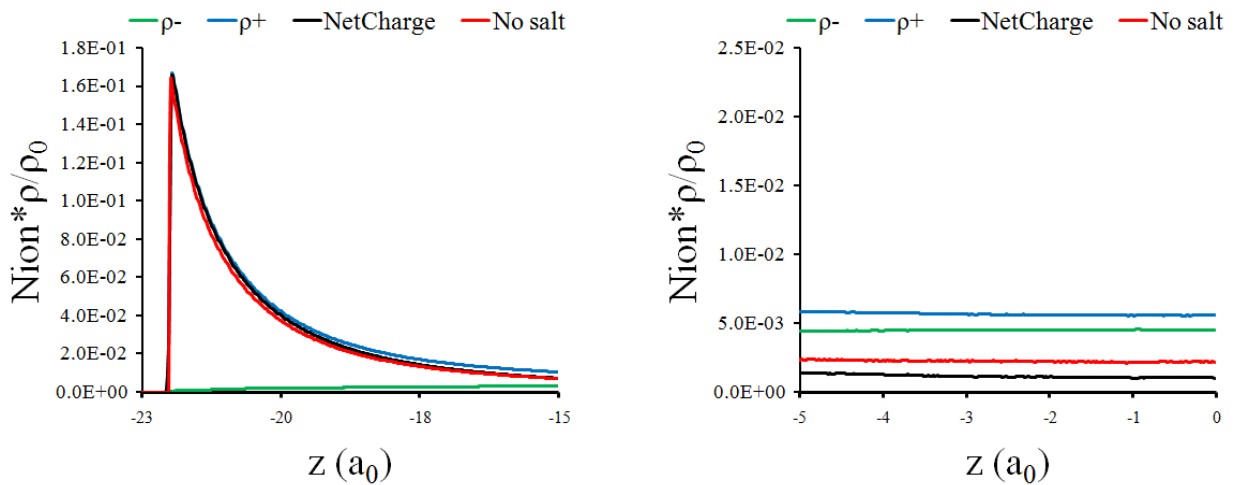


Figure.VI-25. Values of the ion distribution multiplied by the ion number for the case with 7 added ions of each sign. The distribution of the positive and negative charges is both reported. A subtraction is then made to obtain the final distribution of the excess charge (corresponding to the surface charge counterions). The data for the case without salt is reported for confrontation.

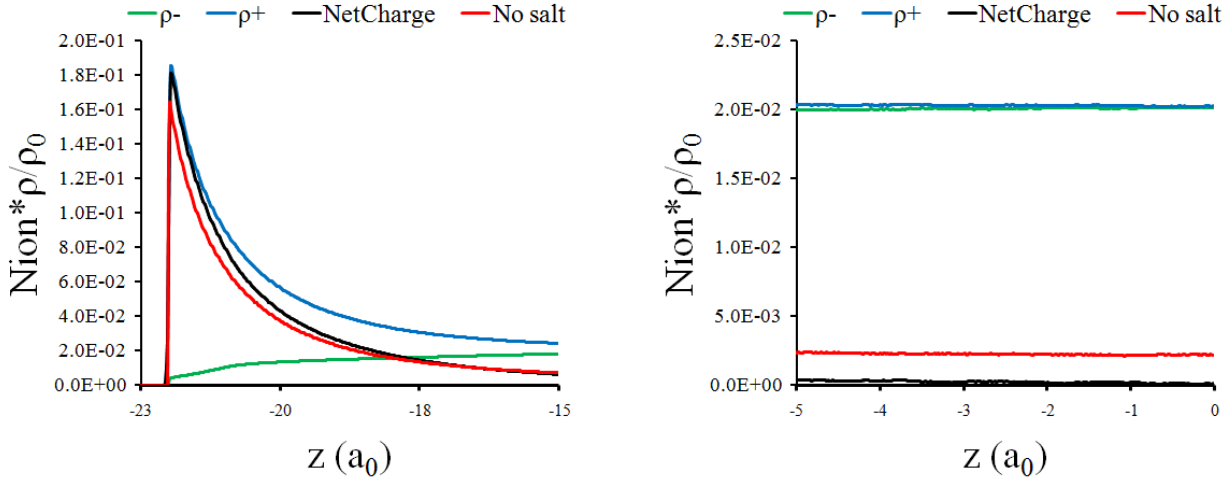


Figure.VI-26. Values of the ion distribution multiplied by the ion number for the case with 7 added ions of each sign. The distribution of the positive and negative charges is both reported. A subtraction is then made to obtain the final distribution of the excess charge (corresponding to the surface charge counterions). The data for the case without salt is reported for confrontation.

Furthermore, due to the change of the peak shape for 35 added salt couples a modification of the electro-osmotic profile is also expected. In Figure.VI-27 the simulated flow profiles for 0, 7 and 35 added ion couples are reported (the case 0 corresponds to the WCA flow reported in the discussion of the previous section). The flow profiles obtained from integration of the net charge distribution are also plotted. The Nernst-Planck equation seems in this case not to give results in strict accordance with the actual flow. Differently than in the previous case with the WCA interaction without salt the value obtained in the simulation is faster than the one obtained through the Nernst-Planck equation. Moreover, unexpectedly the fluid flow for 7 added ion couples is faster than the case without added salt even if the ion charge distribution plays towards a slowing down of the fluid flow. Added salts seem then to speed up the fluid flow with a mechanism that cannot be explained with the electrostatic interactions. The case with 35 added salt couples is anyway slower than the case without ions because the ion charge distribution difference becomes dominant. Hypothesis about this speeding effect are hard to make. The dynamics in the system is indeed much more complex in presence of salts. The negative ions create momentum in the opposite direction of the fluid flow and the positive charges create a much higher momentum in the right one; therefore the actual positive and negative charge in the middle of the channel is higher than in the salt free case and it is only the difference that approaches the zero. Moreover the wells of potential in correspondence of the walls become less important in presence of negative charges that can approach the trapped positive ones and steal them from the surface. The number of interactions in this system is so elevated that, at this point, maybe preferable not to make unfounded assumptions and continue the investigation in a future time.

A large statistic of ion collisions in proximity of the walls is needed to have a good comprehension of the actual phenomena. It is indeed the coupled effect of surface charges, salt ions and WCA potential in a many-body scheme that create these effects.

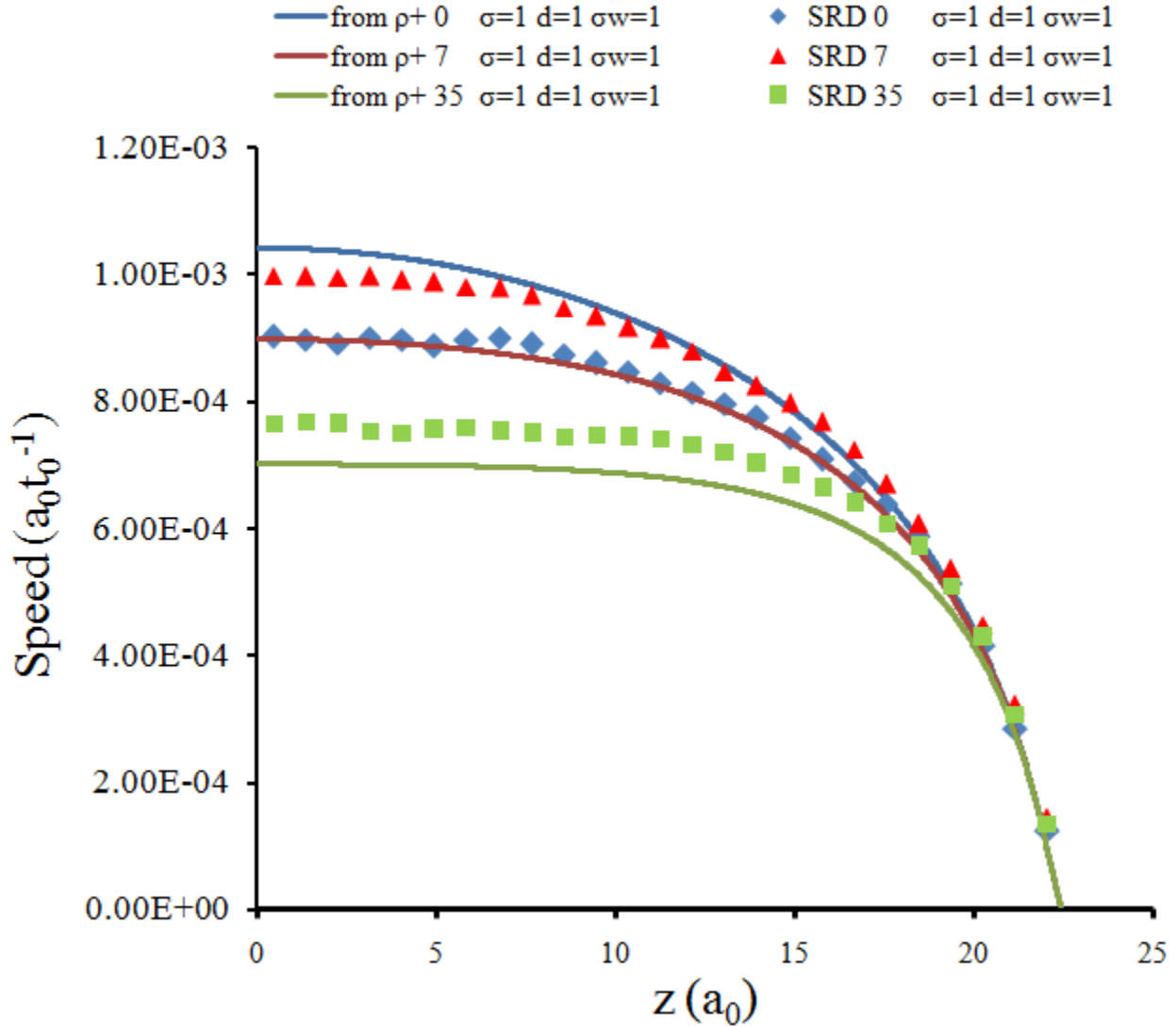


Figure.VI-27. Solvent velocity field $u_x(z)$ in the direction of the electric field, averaged in the x - y plane for $\sigma=1 \text{ e}^*.\text{nm}^{-1}$ and $\sigma_w=1 a_0$. The in function of the added ion couples number. The blue data are the original values without added salts. Red and green data corresponds to 7 and 35 ion couples added respectively.

To conclude, the effect of added salts produces unexpected results with an increasing speed contribution for low ion concentration. This demonstrates even more the utility of the SRD model to understand nanoscale phenomena involving electro-osmosis in planar channels or similar systems.

VI.3.e Electro-osmosis in PPNs

As introduced in the first part of this chapter, the SRD method has been extended to the description of more complex geometries. In particular the PPN structure with its high level of symmetry is an optimum candidate to perform SRD simulation. The same channel height has been used: $45 a_0$. The pillar center to pillar center distance has been set at $36 a_0$ and the pillar radius $R_{\text{cyl}}=8.6 a_0$.

In the simulations the surface charge has been set to be $\sigma=1 e^-.nm^{-1}$ and a WCA potential between ions always utilized. The ion-wall and ion-cylinder interaction are described by a WCA like potential with diameter $R_{\text{cyl}}+2\sigma_w$. σ_w is equal to 0.5 in these simulation. The unit cell (Figure.VI-28), has been extended in the y direction to $62 a_0$ in order to adequately reproduce the PPN structure with an x/y ratio of the cell size of $36/62$ which approximate reasonably well the $(1/3)^{0.5}$ ratio of the real cell size.

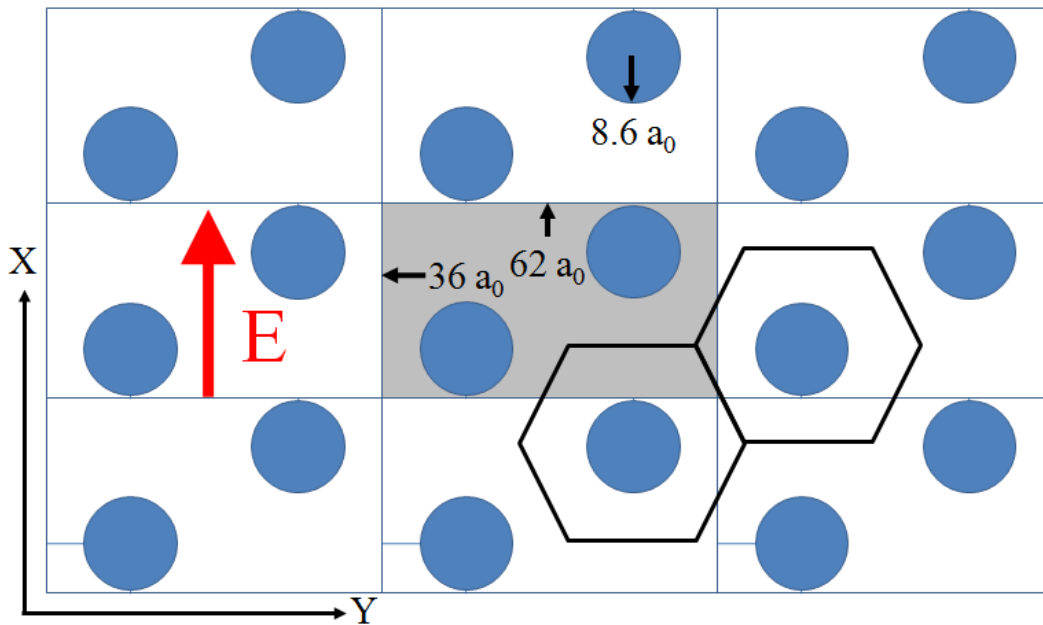


Figure.VI-28. Scheme representing the unit cell for the SRD simulation in the PPN structure.

The electric field is directed in the x direction. A hexagonal unit cell can be also defined. It will be used in the following discussion for the description of the fluid flow. Cylinder and flat surfaces have been considered separately and various tests have been performed. In one case both kinds of surfaces have been considered as charged (72 counterions – simulation called WALLS+CYL). Simulations for $d=1$ and $d=10$ have been performed. Other simulations have been done

considering as charged the cylindrical (28 counterions- simulation called CYL) or flat surfaces (44 counterions – simulation called WALLS) only (Figure.VI-29).

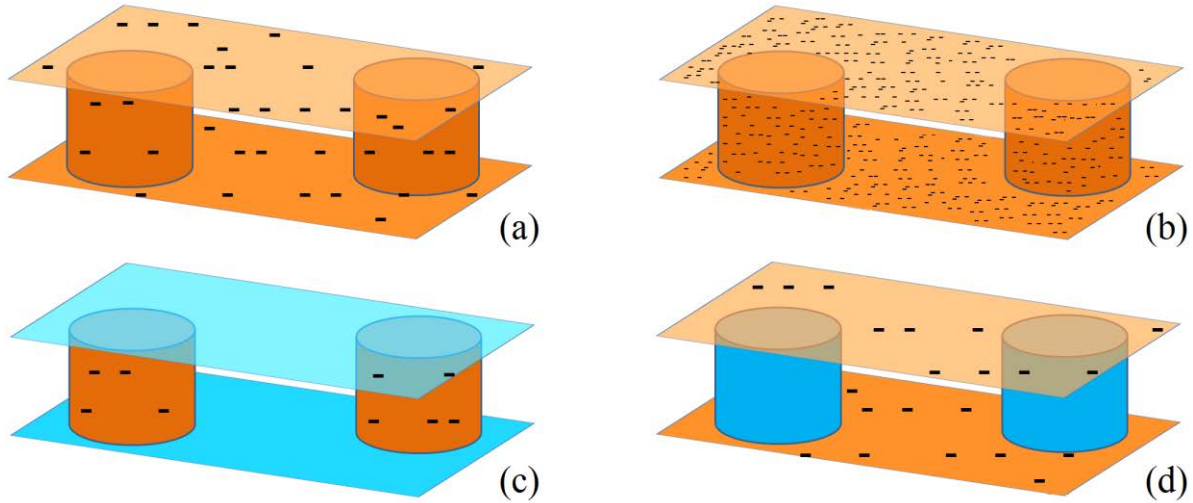


Figure.VI-29. The four schemes studied in the PPN configuration with SRD. (a) Charged walls and cylinder $d=1$ (CUL+WALLS $d=1$). (b) charged walls and cylinder $d=10$ (CYL+WALLS $d=10$). (c) charged cylinder only (CYL). (d) charged walls only (WALLS).

Fluid flow has been analyzed and a chart of residence time is currently being created to study the dynamics of ions in this system. The calculation is currently running and preliminary results only are now available. Unfortunately the statistics for the residence time is still insufficient; it will not then be presented in this thesis.

On the other hand the ion charged distribution integrated in the xy planes (as the ones presented in the precedent sections of this article) have already been obtained (Figure.VI-30). The ion distributions of the four cases are confronted with the case without cylinder.

The ion distribution with (WALLS) and without cylinder (WCA) with the charge on the walls is substantially the same. The ion concentration in the channel is indeed exactly the same and, even if the two cylinders create an excluded volume no serious modification in the equilibrium distribution is found. Things change when the charges are added on the cylinder (WALLS+CYL). Because of this it is more favorable for the ions to stay on its surface thus occupying the central part of the channel. This clearly decreases the peak size. Finally, in the case with the charge on the cylinder only (CYL), the ions stay mostly on the cylinder surface with an almost uniform distribution in the z direction.

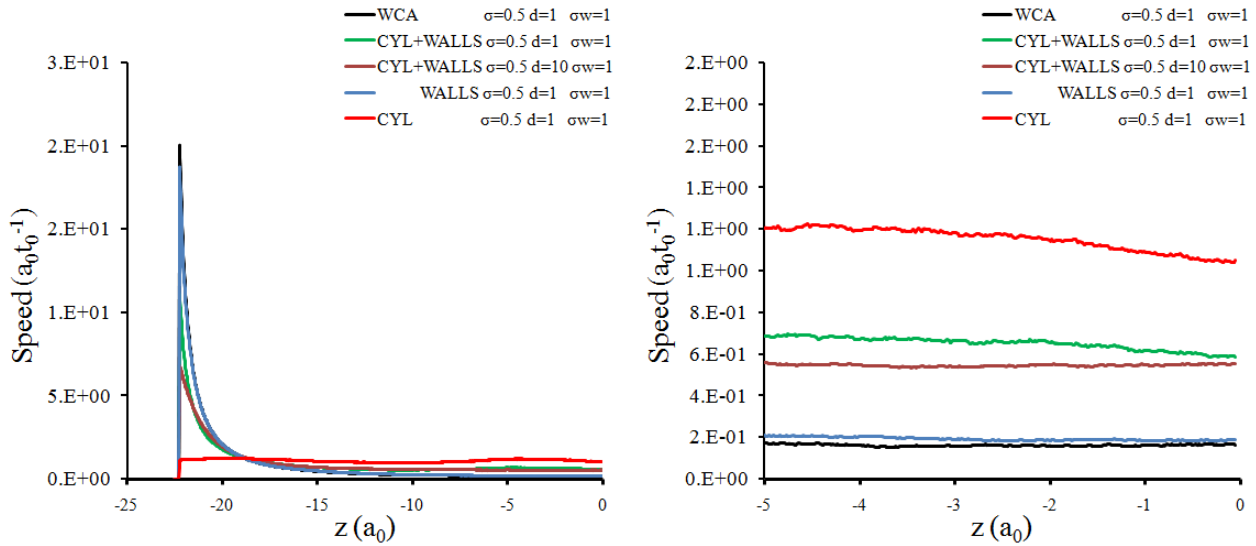


Figure.VI-30. Values of the ion distribution for the four simulation cases with pillars. WCA corresponds to a simulation without cylinders. The code is explained in Figure.VI-29.

However the previous reasoning about the effect of a higher charge quantity in the center of the channel that provokes a faster flow is no more valuable in presence of the cylinders. The cylinders indeed, with the bounce-back condition for the solvent, inhibit the fluid flow. This means that even if momentum is created by the ions interacting with the cylinder near the center of the channel the same momentum is immediately counterbalanced by the viscous stress generated by the cylinder presence. Actually the cylinders seriously slow down the flow. Eventual ions migrating toward the center of the channel due to a thermal fluctuation impact indeed with the cylinders and slow down instead of further accelerating. This is evident from Figure.VI-31 (the profiles are not yet smooth due to the short time of calculation). The flow without cylinders (WCA) is indeed much faster than the flow in presence of them (WALLS case). The slowest case is the one with neutral cylinder and charged walls. From this it can be understood that the hydrodynamic effect of the cylinder is substantial in diminishing the fluid flow creating a strong hydrodynamic resistance.

Given the presence of the cylinders in the unit cell, it is anyway advantageous to have a charge distribution more peaked in the middle. This can be understood considering the fact that for the CYL case the ion concentration in the channel is lower and that then the fluid flow is reduced due to the slower creation of momentum by the electric field (28 counterions in place of 44 for the WALL case and 72 for the CYL+WALLS ones). The fluid speed is indeed of the same order of the CYL+WALLS cases which have a more than double concentration of ions in the channel.

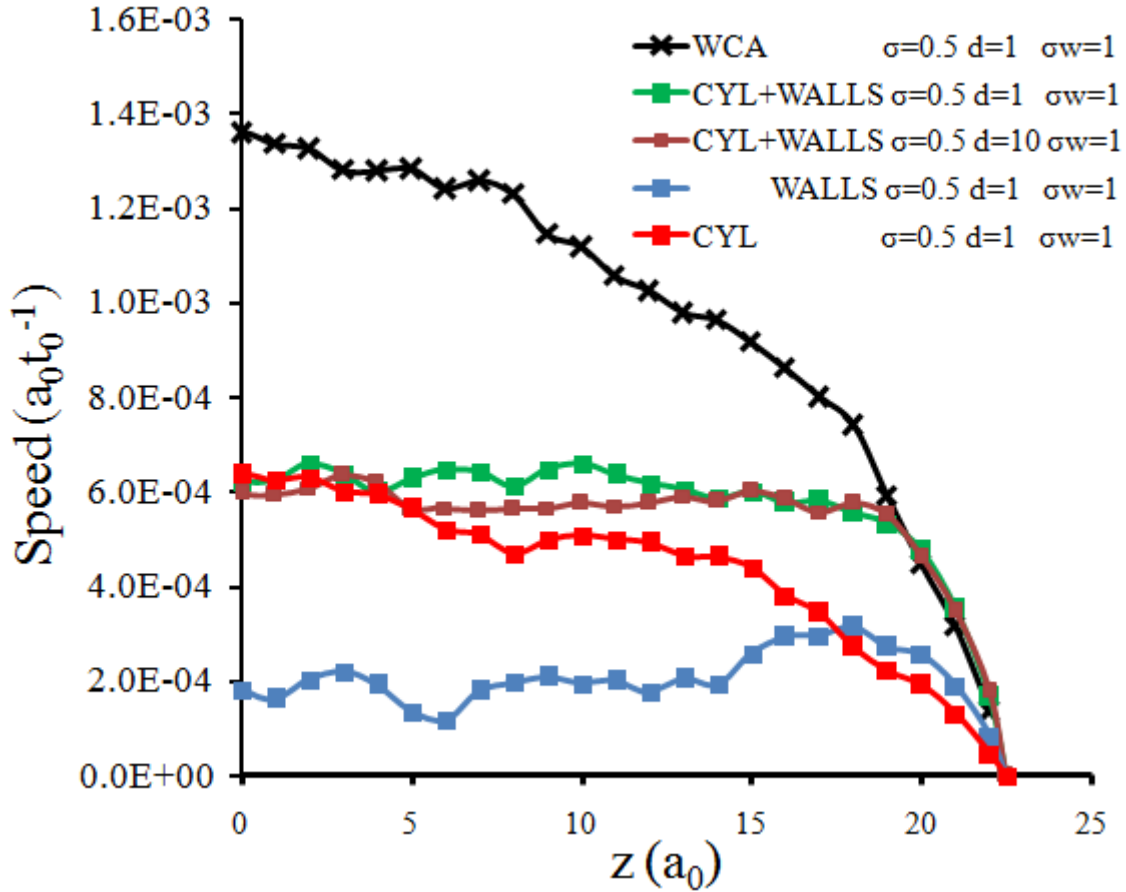


Figure.VI-31. Solvent velocity field $u_x(z)$ in the direction of the electric field, averaged in the x - y plane for $\sigma=1 \text{ e} \cdot \text{nm}^{-1}$ and $\sigma_w=0.5 a_0$ for the PPN geometry.

In the CYL case the momentum is created uniformly in the z direction. This corresponds somehow to the situation created by a gradient of pressure. It would then be interesting to make a comparison of the actual fluid flow chart for the electro-osmotic flow in these conditions with the corresponding chart for a pressure created one.

In the cases CYL+WALLS the ion distribution on the cylinder surface is lower than in the CYL case because of the stronger repulsion due to the counterions at the wall surfaces. Thus the fluid flow, that is anyway the fastest in presence of the cylinder due to the highest concentration of charge, is anyway slower than in the cylinder free (WCA) case.

To conclude it has here to be said that the simple WCA case is in this occasion faster for $\sigma_w=0.5$ than for the previously reported $\sigma_w=1$ with an inverse tendency of what previously reported for the simulation without WCA interaction between the ions. This seems to indicate that the role of the ion-ion WCA interaction make a serious difference in the interaction with the walls that has still to be understood.

VI.3.e.i Flow Charts

Because the PPNs structure loses the x-y symmetry the presented description in function of z only is rather partial. A hexagonal symmetry would exist in the system but in presence of the electric field it is lost too. A 3D description of the fluid flow is then preferable. In the case of this thesis two kinds of flow charts have been realized. Unfortunately the statistics is not yet large enough and the values of the flow in each voxel (element of volume in which the speed is averaged) are still rather noisy. It is then still impossible to discuss quantitative effects but some interesting qualitative ones can be presented.

The two charts strategies are reported in Figure.VI-32. The first one simply divides the simulation box in $18 \times 31 \times 24$ voxels in the xyz direction (voxel side of $2 a_0$ – two partially filled voxel layers describe the 0-0.5 and 44.5-45 z positions) with a squared dissection method. The second one instead uses the hexagonal symmetry of the system. A hexagon is drawn around the cylinder and is separated in $25 \times 12 \times 45$ in the r θ z direction of a cylindrical coordinate system.

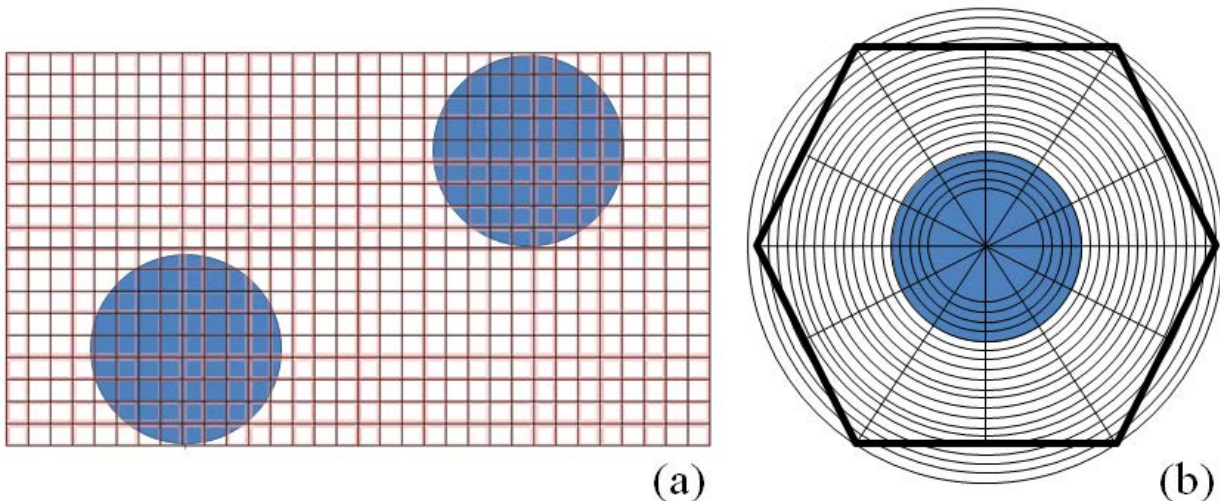


Figure.VI-32. Slice in the Z direction of the squared (a) and hexagonal (b) chart strategy.

It is then possible to visualize the flow profile of the SRD simulation and evaluate the local hydrodynamics. In example Figure.VI-33 a chart for the flow at $15 a_0$ from the ground is reported for the CYL+WALLS $d=10$ case. The flow around the cylinder is visualized in the arrow plot where the fluid direction is reported. The flow goes around the cylinders and tries to occupy all the space. However, as can be seen behind the cylinders some zone still has speeds in the negative x direction indicating that a sufficient statistic has not yet be attained (the regime is laminar so no inversion of velocity are expected). This can be better visualized in the color plot where positive values of the speed in the x direction are reported at increasing red intensity and negative value at increases green intensities.

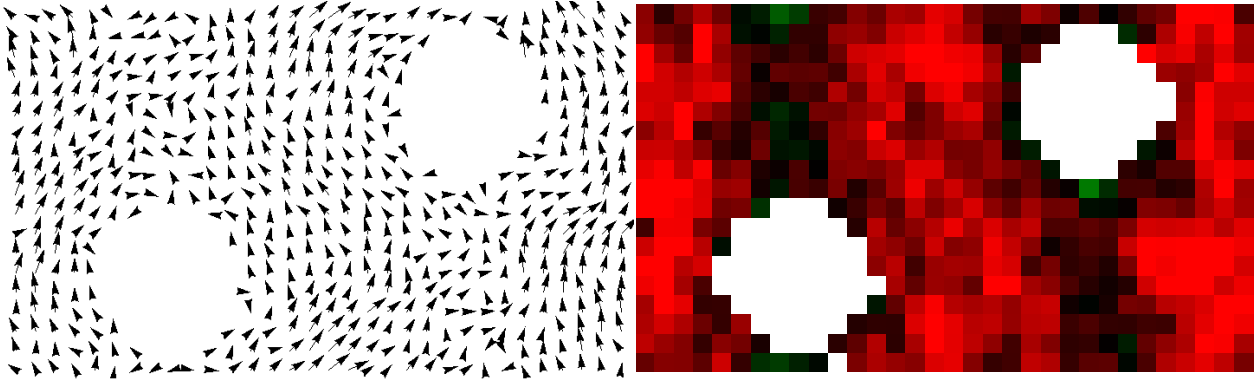


Figure.VI-33. Arrow and color plot of the slice at 15 a_0 from the floor for the CYL+WALLS $d=10$ case. The arrows indicate the fluid direction. The colors red and green indicate the fluid speed in the positive and negative x direction respectively.

Similar features are inspected in the WALLS case but, as already shown, the average speed is lower (as can be seen by the darker average red color and the presence of white spots corresponding to very low speed values). Thermal fluctuations are in this case strong enough to create large zones of negative speed in the x direction as can be seen from the color plot of Figure.VI-34. No clear streaming patterns are detectable because the momentum is principally created at the wall interfaces and spreads in the xy directions before reaching the considered z layer.

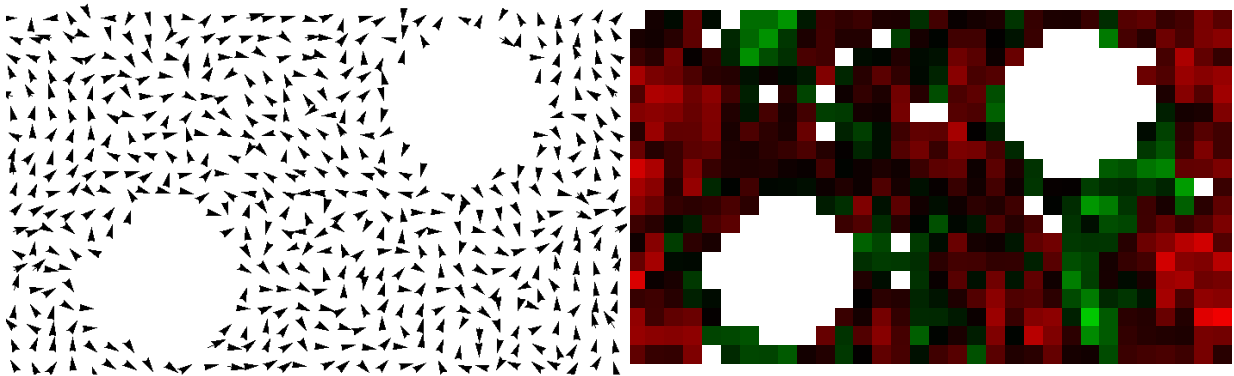


Figure.VI-34. Arrow and color plot of the slice at 15 a_0 from the floor for the WALLS case. The arrows indicate the fluid direction. The colors red and green indicate the fluid speed in the positive and negative x direction respectively.

This is not the case of the CYL simulation. The flow is much more directed in the x direction than in the preceding cases. The fluid particles in the center and at the left and right borders of the simulation box continue to flow in the x direction without really going around the cylinders. Ions create indeed the momentum locally which causes a much higher difference from zone of creation of the momentum (between the cylinders) and zones of its diffusion (behind the cylinders). Ions that create momentum then probably “fly” from a cylinder to the other moving in the x direction. This differentiates the reported flow from a pressure driven one. In that case indeed the

momentum is created behind the cylinders too but longer calculations have to be performed to obtain a chart with sufficient resolution to confirm this hypothesis.

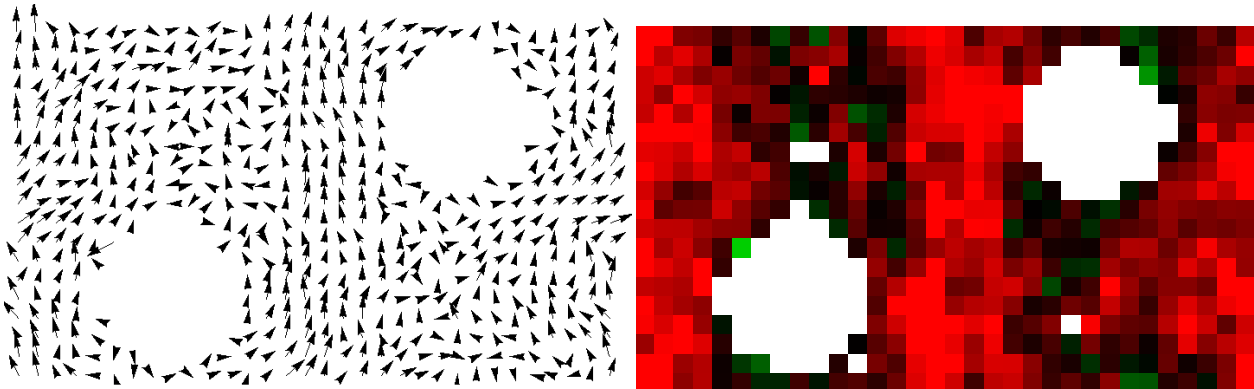


Figure.VI-35. Arrow and color plot of the slice at 15 a0 from the floor for the CYL case. The arrows indicate the fluid direction. The colors red and green indicate the fluid speed in the positive and negative x direction respectively.

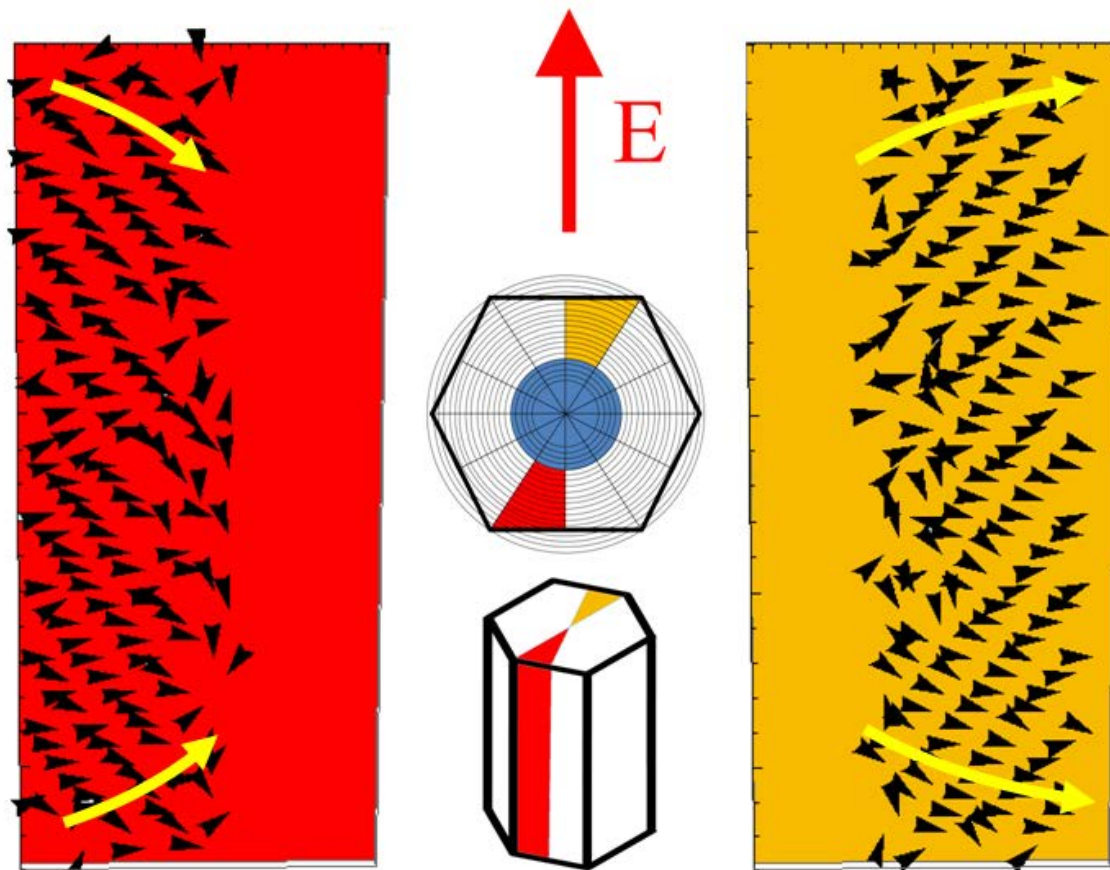


Figure.VI-36. Arrow plot of the indicated slices in the hexagonal speed chart for the CYL+WALLS d=1 case. The arrows indicate the fluid direction. The yellow arrows indicate the general tendency of the fluid to up to the cylinder upon encountering it and descending while leaving it.

To conclude an example of the hexagonal chart of fluid speed is reported. Two slices are selected around the pillar aligned with the fluid flow direction. As can be seen for the CYL+WALLS d=1 case a net flow going towards the center of the cylinder is found in approaching it while a contrary

flow towards the channel walls is generated when leaving it. Ions can then frequently interact at the cylinder center in this configuration and can more easily diffuse from a wall to the other in respect to cylinder-free simulations. They indeed do not need to wait for a particularly strong thermal fluctuation that detaches them from the wall surface. A similar flow is found for the WALLS case even if less clear. On the contrary the CYL one doesn't show it because the ions are not normally preferentially disposed next to the channel wall.

Upon refinement of the statistic further features could be investigated. Moreover a residence time chart is being calculated. This should allow evaluating the dynamics of ion diffusion directly.

VI.3.f Conclusion

In this chapter the SRD method has been validated to describe the electro-osmotic flow. Even if the analytical theory was known and easy confrontation with it could be made the work performed in this thesis is the first one to make a direct confrontation of the flow simulated by SRD and the known PNP theory (Poisson-Boltzmann-Nernst-Planck theory). The SRD conditions follow indeed perfectly the theory in its regime of validity which is low monovalent ion concentration without excluded volume interaction.

The SRD simulations have been then utilized to investigate the influence of various simulation parameters such as the minimum approach distance to the wall of the ion or the surface charge discretization which could not be taken into account the PNP theory being outside from its hypothesis.

The effect of excluded volume realized imposing a WCA interaction between the ions has also been investigated founding that it has a noticeable slowing-down effect of the electro-osmotic flow.

The electro-osmotic flow has also been simulated by SRD in presence of additional salt concentration. The effect of ion concentration has been evaluated to be complex because contrary tendencies of speeding-up and slowing-down are originated by the added salts. Further SRD studies are needed revealing the importance of the method.

Finally the electro-osmotic flow has also been simulated in more complex structures such as the already presented PPN. The simulation parameters have been discussed and the hydrodynamic and charge effects of the added cylinders/pillars have been discussed. Flow charts showing

interesting effects have also been reported but more statistical averaging is still needed to propose definitive conclusions.

SRD is then a valuable tool to study the nanofluidic phenomena. At the present time the matching between theory and experiment is extremely near. In the next few years it will be possible to study the same system with both methods and the SRD will reveal its absolute usefulness to have a better comprehension of the nanofluidic phenomena. On the other hand experimental results will allow to finely tuning the simulation conditions and approximations making them even more efficient.

VI.4 Appendix

I.1.a Adimensional numbers

VI.4.a.i Mach number

The Mach number is used to determine if the incompressibility approximation of the fluid is valid or, in general, to evaluate the compressibility phenomena effects in the fluid.

It is defined as

$$Ma = \frac{u}{v_{sound}} \quad (97)$$

with u speed of the fluid in respect of the boundaries and v_{sound} speed of the sound in the fluid. For values lower than 0.3 the fluid can be considered incompressible without serious errors.

If instead the mach number is superior to 0.3 compressibility cannot be neglected. In particular for high values of Ma shock-waves form with higher densities as the one reported in Figure.VI-37.

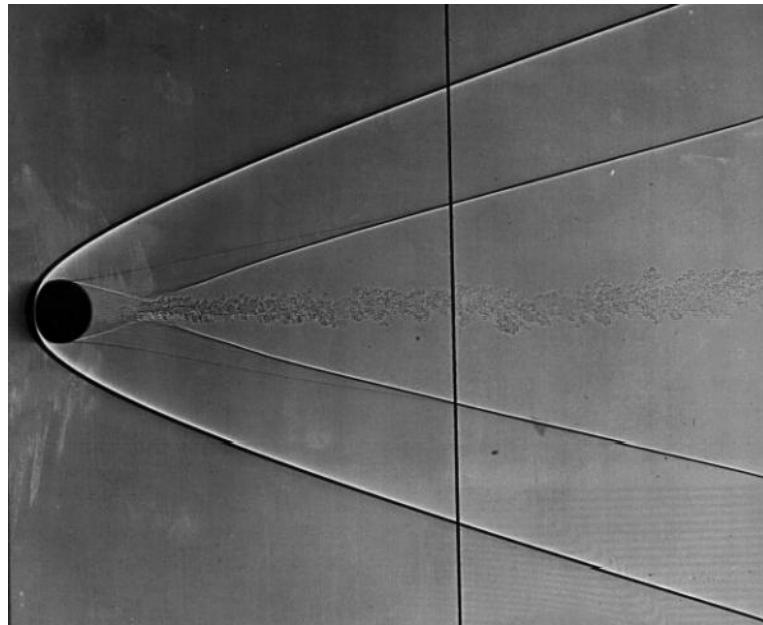


Figure.VI-37. Sphere at $M=4.01$ in atmospheric air. A separation takes place just behind the equator, accompanied by a weak shock wave, and formation of the N-wave that is heard as a double boom far away.

VI.4.a.ii Reynolds number

The Reynolds number gives an idea of the reciprocal intensity of inertial and viscous forces. For low values of the Reynolds number the system is viscosity dominated and the flow is laminar. For high values, on the contrary, turbulences can be found. It is defined as

$$Re = \frac{\rho * u * d}{\eta} \quad (98)$$

With ρ the density, d the typical dimension of the system and η the viscosity. For nanosystems the Reynolds number is generally extremely low because of the typical dimensions of the systems. Viscosity dominates the flow patterns. This is important when fluid flow inside nanochannels has to be described. Some images reporting the various regimes depending on its value are reported in the main text.

VI.4.a.iii Peclet Number

The Peclet number Pe measures the relative strength of convective transport to diffusive transport. For example for what concerns heat transport, for a fluid of thermal conductivity k and thermal capacitance C_p traveling at an average velocity v_0 in a channel of dimension L the Peclet number is defined as

$$Pe = \frac{\rho * C_p * L}{k} \quad (99)$$

The Peclet number can be interpreted as a ratio of a diffusive to a convective time scale of heat transfer. It is important for problems regarding the diffusion of heat through a diffusive or convective mechanism.

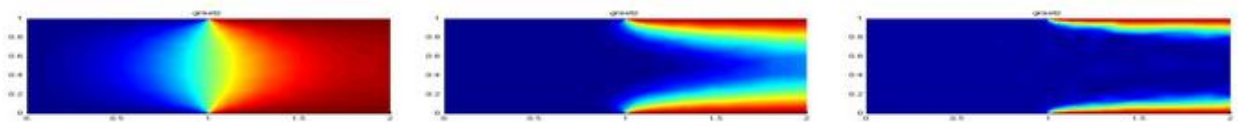


Figure.VI-38. An example of solution for a parameterized system. A classical heat transfer convection-conduction problem: "Graetz" flow with a parameterized Peclet number (represented at Peclet 0.1,1,99, respectively). The problem consists of the penetration of a cold liquid in a heated pipe. In the first case diffusion is faster than convection and the liquid heats up (higher temperatures in red. Increasing the Peclet number the fluid or moves faster or the diffusion is inhibited. This cause the liquid to exit the pipe still at a cold temperature.

A second Peclet number can be defined if mass transfer is instead considered. In this case

$$Pe = \frac{u * L}{D} \quad (100)$$

with u the fluid velocity and D the diffusion constant of the considered species (as in example a colloid). Similar patterns of the ones described in Figure.VI-38 can be found substituting temperature with the species concentration.

VI.4.a.iv Schmidt number

The Schmidt number

$$Sc = \frac{\eta}{\rho * D_{fluid}} \quad (101)$$

is important for characterizing a pure fluid. It expresses the rate of diffusive momentum transfer, measured by the kinematic viscosity, relative to the rate of diffusive mass transfer, measured by the fluid particle self-diffusion coefficient. For a gas, momentum transport is dominated by mass diffusion, so that Sc is of the order of 1, whereas for a liquid, momentum transport is dominated by interparticle collisions and Sc is much higher than 1.

VI.4.a.v Knudsen number

The Knudsen number is used to determine if the Navier-Stokes equations are still valid. A hypothesis of their use is the rapid interaction of fluid particles exchanging momentum. The mean free path should then be reduced (Knudsen number values under 0.1) to obtain normal Navier Stokes solutions. It is defined as

$$Kn = \frac{\lambda}{L} \quad (102)$$

Where λ is the mean free path of the fluid particle, that is the average distance between two collision, and L the typical dimension of the system. It is important for ultra-empty and space applications or gas-diffusion in nanometer scale porosity. In the last case, in particular, a variation of the diffusion coefficient of the gas increasing the Knudsen number can be inspected with higher diffusion rate at lower pressures.

VI.5 Bibliography

- [1] D. L. Ermak, “A computer simulation of charged particles in solution. I. Technique and equilibrium properties,” *J. Chem. Phys.*, vol. 62, no. 10, p. 4189, Sep. 1975.
- [2] T. J. Lane, D. Shukla, K. A. Beauchamp, and V. S. Pande, “To milliseconds and beyond: challenges in the simulation of protein folding,” *Curr. Opin. Struct. Biol.*, vol. 23, no. 1, pp. 58–65, Feb. 2013.
- [3] A. J. C. Ladd, “Hydrodynamic transport coefficients of random dispersions of hard spheres,” *J. Chem. Phys.*, vol. 93, no. 5, p. 3484, Sep. 1990.
- [4] J. P. Hernández-Ortiz, J. J. de Pablo, and M. D. Graham, “Fast Computation of Many-Particle Hydrodynamic and Electrostatic Interactions in a Confined Geometry,” *Phys. Rev. Lett.*, vol. 98, no. 14, p. 140602, Apr. 2007.
- [5] B. Cichocki, R. B. Jones, R. Kutteh, and E. Wajnryb, “Friction and mobility for colloidal spheres in Stokes flow near a boundary: The multipole method and applications,” *J. Chem. Phys.*, vol. 112, no. 5, p. 2548, Feb. 2000.
- [6] J. T. Padding and A. A. Louis, “Hydrodynamic interactions and Brownian forces in colloidal suspensions: Coarse-graining over time and length scales,” *Phys. Rev. E*, vol. 74, no. 3, p. 031402, Sep. 2006.
- [7] V. D. M., *An album of fluid motion*. Stanford California: Parabolic Press, 1982.
- [8] J. M. V. A. Koelman and P. J. Hoogerbrugge, “Dynamic Simulations of Hard-Sphere Suspensions Under Steady Shear,” *Europhys. Lett.*, vol. 21, no. 3, pp. 363–368, Jan. 1993.
- [9] P. J. Hoogerbrugge and J. M. V. A. Koelman, “Simulating Microscopic Hydrodynamic Phenomena with Dissipative Particle Dynamics,” *Europhys. Lett.*, vol. 19, no. 3, pp. 155–160, Jun. 1992.
- [10] E. MOEENDARBARY, T. Y. NG, and M. ZANGENEH, “DISSIPATIVE PARTICLE DYNAMICS: INTRODUCTION, METHODOLOGY AND COMPLEX FLUID APPLICATIONS — A REVIEW,” *Int. J. Appl. Mech.*, vol. 01, no. 04, pp. 737–763, Dec. 2009.
- [11] E. MOEENDARBARY, T. Y. NG, and M. ZANGENEH, “DISSIPATIVE PARTICLE DYNAMICS IN SOFT MATTER AND POLYMERIC APPLICATIONS — A REVIEW,” *Int. J. Appl. Mech.*, vol. 02, no. 01, pp. 161–190, Mar. 2010.
- [12] G. R. McNamara and G. Zanetti, “Use of the Boltzmann Equation to Simulate Lattice-Gas Automata,” *Phys. Rev. Lett.*, vol. 61, no. 20, pp. 2332–2335, Nov. 1988.

- [13] A. J. C. Ladd, “Short-time motion of colloidal particles: Numerical simulation via a fluctuating lattice-Boltzmann equation,” *Phys. Rev. Lett.*, vol. 70, no. 9, pp. 1339–1342, Mar. 1993.
- [14] F. Capuani, I. Pagonabarraga, and D. Frenkel, “Discrete solution of the electrokinetic equations,” *J. Chem. Phys.*, vol. 121, no. 2, pp. 973–86, Jul. 2004.
- [15] A. Obliger, M. Duvail, M. Jardat, D. Coelho, S. Békri, and B. Rotenberg, “Numerical homogenization of electrokinetic equations in porous media using lattice-Boltzmann simulations,” *Phys. Rev. E*, vol. 88, no. 1, p. 013019, Jul. 2013.
- [16] B. Rotenberg, I. Pagonabarraga, and D. Frenkel, “Coarse-grained simulations of charge, current and flow in heterogeneous media,” *Faraday Discuss.*, vol. 144, pp. 223–243, Oct. 2010.
- [17] B. Rotenberg, I. Pagonabarraga, and D. Frenkel, “Dispersion of charged tracers in charged porous media,” *EPL (Europhysics Lett.)*, vol. 83, no. 3, p. 34004, Aug. 2008.
- [18] S. H. Behrens and D. G. Grier, “The charge of glass and silica surfaces,” *J. Chem. Phys.*, vol. 115, no. 14, p. 6716, Oct. 2001.
- [19] W. J. V. I. Zarko, V. M. Gunko, L. S. Andiyko, E. V. Go, chaek, M. Matysek, E. Skwarek, “Influence of the nature of active surface sites of highly disperse oxides on adsorption of heavy metal ions,” in *Surface Chemistry in Biomedical and Environmental Science*, Springer Science & Business Media, 2006, p. 429.
- [20] Y. Wang, C. Bryan, H. Xu, and H. Gao, “Nanogeochemistry: Geochemical reactions and mass transfers in nanopores,” *Geology*, vol. 31, no. 5, pp. 387–390, May 2003.
- [21] Y. Wang, “Nanogeochemistry: Nanostructures, emergent properties and their control on geochemical reactions and mass transfers,” *Chem. Geol.*, vol. 378–379, pp. 1–23, Jun. 2014.
- [22] P. B. Warren, “Electroviscous Transport Problems via Lattice-Boltzmann,” *Int. J. Mod. Phys. C*, vol. 08, no. 04, pp. 889–898, Aug. 1997.
- [23] A. Malevanets and R. Kapral, “Mesoscopic model for solvent dynamics,” *J. Chem. Phys.*, vol. 110, no. 17, p. 8605, May 1999.
- [24] A Galilean-invariant mesoscopic model for fluid flow,” T. Ihle and D. M. Kroll, “Stochastic rotation dynamics: *Phys. Rev. E*, vol. 63, no. 2, p. 020201, Jan. 2001.
- [25] T. Ihle and D. M. Kroll, “Stochastic rotation dynamics. I. Formalism, Galilean invariance, and Green-Kubo relations,” *Phys. Rev. E*, vol. 67, no. 6, p. 066705, Jun. 2003.
- [26] T. Ihle, E. Tüzel, and D. M. Kroll, “Equilibrium calculation of transport coefficients for a fluid-particle model,” *Phys. Rev. E*, vol. 72, no. 4, p. 046707, Oct. 2005.
- [27] N. Kikuchi, C. M. Pooley, J. F. Ryder, and J. M. Yeomans, “Transport coefficients of a mesoscopic fluid dynamics model,” *J. Chem. Phys.*, vol. 119, no. 12, p. 6388, Sep. 2003.

- [28] M. Ripoll, K. Mussawisade, R. Winkler, and G. Gompper, “Dynamic regimes of fluids simulated by multiparticle-collision dynamics,” *Phys. Rev. E*, vol. 72, no. 1, p. 016701, Jul. 2005.
- [29] T. Ihle and D. M. Kroll, “Stochastic rotation dynamics. II. Transport coefficients, numerics, and long-time tails,” *Phys. Rev. E*, vol. 67, no. 6, p. 066706, Jun. 2003.
- [30] J. K. Whitmer and E. Luijten, “Fluid-solid boundary conditions for multiparticle collision dynamics,” *J. Phys. Condens. Matter*, vol. 22, no. 10, p. 104106, Mar. 2010.
- [31] J. T. Padding, A. Wysocki, H. Löwen, and A. A. Louis, “Stick boundary conditions and rotational velocity auto-correlation functions for colloidal particles in a coarse-grained representation of the solvent,” *J. Phys. Condens. Matter*, vol. 17, no. 45, pp. S3393–S3399, Nov. 2005.
- [32] H. C. Andersen, “Molecular dynamics simulations at constant pressure and/or temperature,” *J. Chem. Phys.*, vol. 72, no. 4, p. 2384, Jul. 1980.
- [33] G. Gompper, T. Ihle, D. M. Kroll, and R. G. Winkler, *Advanced Computer Simulation Approaches for Soft Matter Sciences III*. Berlin, Heidelberg: Springer Berlin Heidelberg, 2009.
- [34] J. K. Whitmer and E. Luijten, “Fluid-solid boundary conditions for multiparticle collision dynamics,” *J. Phys. Condens. Matter*, vol. 22, no. 10, p. 104106, Mar. 2010.
- [35] A. Lamura, G. Gompper, T. Ihle, and D. M. Kroll, “Multi-particle collision dynamics: Flow around a circular and a square cylinder,” *Europhys. Lett.*, vol. 56, no. 3, pp. 319–325, Nov. 2001.
- [36] D. Frenkel and B. Smit, *Understanding Molecular Simulation*. Elsevier, 2002.
- [37] Y. Mao, M. E. Cates, and H. N. W. Lekkerkerker, “Depletion force in colloidal systems,” *Phys. A Stat. Mech. its Appl.*, vol. 222, no. 1–4, pp. 10–24, Dec. 1995.
- [38] J. M. Lahtinen, I. Vattulainen, T. Ala-Nissila, and E. Falck, “Influence of hydrodynamics on many-particle diffusion in 2D colloidal suspensions,” *Eur. Phys. J. E - Soft Matter*, vol. 13, no. 3, pp. 267–275, Mar. 2004.
- [39] M. Hecht, J. Harting, T. Ihle, and H. J. Herrmann, “Simulation of claylike colloids,” *Phys. Rev. E*, vol. 72, no. 1, p. 011408, Jul. 2005.
- [40] M. Hecht, J. Harting, and H. J. Herrmann, “Stability diagram for dense suspensions of model colloidal Al₂O₃ particles in shear flow,” *Phys. Rev. E. Stat. Nonlin. Soft Matter Phys.*, vol. 75, no. 5 Pt 1, p. 051404, May 2007.
- [41] Y. Inoue, Y. Chen, and H. Ohashi, “Development of a Simulation Model for Solid Objects Suspended in a Fluctuating Fluid,” *J. Stat. Phys.*, vol. 107, no. 1–2, pp. 85–100.
- [42] S. H. Lee and R. Kapral, “Cluster structure and dynamics in a mesoscopic solvent,” *Phys. A Stat. Mech. its Appl.*, vol. 298, no. 1–2, pp. 56–68, Sep. 2001.

- [43] J. T. Padding and A. A. Louis, “Hydrodynamic and Brownian Fluctuations in Sedimenting Suspensions,” *Phys. Rev. Lett.*, vol. 93, no. 22, p. 220601, Nov. 2004.
- [44] G. Batôt, V. Dahirel, G. Mériguet, A. A. Louis, and M. Jardat, “Dynamics of solutes with hydrodynamic interactions: Comparison between Brownian dynamics and stochastic rotation dynamics simulations,” *Phys. Rev. E*, vol. 88, no. 4, p. 043304, Oct. 2013.
- [45] J. D. Weeks, “Role of Repulsive Forces in Determining the Equilibrium Structure of Simple Liquids,” *J. Chem. Phys.*, vol. 54, no. 12, p. 5237, Sep. 1971.
- [46] D. Frenkel and B. Smit, *Understanding Molecular Simulation*. Elsevier, 2002.
- [47] A. H. Widmann and D. B. Adolf, “A comparison of Ewald summation techniques for planar surfaces,” *Comput. Phys. Commun.*, vol. 107, no. 1–3, pp. 167–186, Dec. 1997.
- [48] A. Grzybowski, E. Gwóźdź, and A. Bródka, “Ewald summation of electrostatic interactions in molecular dynamics of a three-dimensional system with periodicity in two directions,” *Phys. Rev. B*, vol. 61, no. 10, pp. 6706–6712, Mar. 2000.
- [49] D. M. Heyes, M. Barber, and J. H. R. Clarke, “Molecular dynamics computer simulation of surface properties of crystalline potassium chloride,” *J. Chem. Soc. Faraday Trans. 2*, vol. 73, no. 7, p. 1485, Jan. 1977.
- [50] S. W. De Leeuw and J. W. Perram, “Electrostatic lattice sums for semi-infinite lattices,” *Mol. Phys.*, vol. 37, no. 4, pp. 1313–1322, Apr. 1979.
- [51] E. R. Smith, “Electrostatic potentials for simulations of thin layers,” *Mol. Phys.*, vol. 65, no. 5, pp. 1089–1104, Dec. 1988.
- [52] P. S. Crozier, R. L. Rowley, E. Spohr, and D. Henderson, “Comparison of charged sheets and corrected 3D Ewald calculations of long-range forces in slab geometry electrolyte systems with solvent molecules,” *J. Chem. Phys.*, vol. 112, no. 21, p. 9253, Jun. 2000.
- [53] I.-C. Yeh and M. L. Berkowitz, “Ewald summation for systems with slab geometry,” *J. Chem. Phys.*, vol. 111, no. 7, p. 3155, Aug. 1999.

Conclusion

In this thesis an alternative “bottom-up” approach for the fabrication of nanofluidic devices has been utilized in an effort to substitute or combine to the currently dominant “top-down” one. In particular, non-organized and organized sol-gel thin films were obtained and used for nanofluidic applications. The integration of these materials with microfluidic circuitry has been demonstrated too.

Advancements in the dip-coating deposition technique utilized to produce the nanoporous films have been reported. The so-called “accelerating mode” has been studied and utilized to create thin films with gradients in thickness. Patterned graded films have been used as molds to obtain graded PDMS microfluidic channels. In order to reduce the fabrication costs and scale up the sample production of nanostructured thin films the so called biphasic method” has been developed. It now constitutes a valuable tool for the deposition of expensive materials, such as the block copolymers, which are utilized to produce the presented Pillared Planar Nanochannels (referenced in “materialsviews.com”).

A set of thin films showing different porosities has then been produced exploiting the “Evaporation Induced Self Assembly” (EISA) mechanism. Pillared Planar Nanochannels have also been realized through a two step procedure involving the self-assembly of block copolymer thin films by solvent annealing and sol-gel replication of the adequately treated polymeric structure.

The prepared samples were utilized to study the infiltration of liquids in nanoporosities with different characteristics, revealing several interesting points. The critical role of bottle-necks has been identified in the determination of the capillary penetration speed. In particular, when bottle-necks and pores have the same size, capillary infiltration increases with the pore size. On the other hand, for a given small bottle-neck size, and thus a more closed porosity, the increase of pore size has been demonstrated to diminish the capillary filling speed. A mechanism of infiltration based on the successive evaporation and condensation of volatile solvents has been proposed as being responsible for these findings.

The infiltration of water has also been studied in the highly symmetrical PPN structure. Exploiting the symmetry, calculations with COMSOL finite element software) have been performed to determine the hydrodynamic resistance of the structure. The obtained values were employed to model the infiltration speed of water in PPN structures as a function of the structure geometry. Accordance of the experimental values with the model has been found if a material dependent multiplicative factor is added. The multiplicative factor is attributed to effects associated to the nanoscale on infiltration; the tunability of the PPN material composition was identified as an extremely useful feature to perform further fundamental studies.

The PPN structures have also been applied to perform some preliminary experiments into microfluidic-nanofluidic devices. Self-diffusion experiments and reactions experiments have been used to give an idea of the viability of the structure for future applications and real large-scale use.

In parallel to this experimental work, a theoretical-simulation one has been performed to study the electro-osmotic flow in flat and pillared nanochannels. A simulation method called Stochastic Rotational Dynamics (SRD) has been demonstrated to be suitable for describing the phenomenon and the values of the flow as a function of the simulated system parameters. The phenomenon will constitute a fundamental effect in the further development of nanofluidic applications and its deep knowledge could help to better ideate adequate and efficient devices.

The four challenges identified during this Ph.D. were:

1. The setting-up of a method that permits the preparation of nanochannels on large-scale production and the creation of different kinds of nanostructures for nanofluidic purposes.
2. The study of nanoscopic effects on nanofluidic phenomena in nanoporous structures and PPNs such as capillary infiltration.
3. The integration of bottom-up materials in nanofluidic devices for applications in nanoconfined separations and reaction
4. The understanding of nanofluidic phenomena through adequate models and simulations

They have been faced and some interesting results were obtained in dealing with each of them.

Starting from the given results many perspectives open for further development of the presented bottom-up nanofluidic devices. In particular further experiments in the range of applications such as DNA elongation or protein electrophoresis could constitute a good step to perform in the near future. A further development of the simulation methods used in this thesis would constitute an interesting advancement too. In particular the speed up of the algorithm could allow performing

more or more defined simulations to detect smaller scale effects or study larger dimension simulation boxes or slowly converging variable values.

The bottom-up approach constitutes, in my opinion, not only a valid alternative to the current fabrication methods but the only one that can be effectively extended to real large-scale applications. This is certainly due to the lower cost but also to the higher tunability of the systems due to the whole spectrum of sol-gel materials, among other factors. Moreover the fact that it is possible to realize many samples in short times permits to perform studies that are not performed nowadays. Researchers are currently not willing to waste (long production time) nanofluidic devices for experiments that potentially destroy them irreversibly (as a precipitation reaction in the nanochannels). These studies have still to be carried out in order to achieve an adequate statistic and a good knowledge of the nanofluidic phenomena

The role of simulations also plays a key role in increasing the understanding of the system. The present simulation techniques are indeed ready to describe nanofluidic phenomena at slightly smaller scale with respect to the currently used structures. Improving the algorithm will allow to describe a system of the adequate size and simulations could be utilized to support with extreme precision experimental research.

To conclude, much more work still needs to be done, but the bottom-up approach, not needing costly lithographic equipments like the top-down one, could spread more and more readily between laboratories. This work could be performed in few years by a large army of enthusiast scientists.

INTRODUCTION	1
I : STATE OF THE ART	I-5
I.1 NANOFLUIDICS	I-7
<i>I.1.a Nanofluidic applications</i>	<i>I-8</i>
I.1.a.i Biomedical applications	I-9
I.1.a.ii Energy applications: nanofluidic batteries	I-12
I.1.a.iii Desalinization – particle separation	I-13
I.1.a.iv Fundamental studies.	I-14
I.1.a.v Nanofluidic studies for chemical and material sciences	I-14
<i>I.1.b Fabrication of nanofluidic channels</i>	<i>I-15</i>
I.1.b.i Top-down fabricated channels	I-16
I.1.b.ii Bottom-up techniques	I-20
I.1.b.iii Pillared Planar Nanochannels	I-21
I.2 OBJECTIVES AND CHALLENGES	I-23
I.3 BIBLIOGRAPHY	I-25
II : ADVANCES IN DIP-COATING	II-35
II.1 INTRODUCTION	II-37
<i>II.1.a Withdrawal speed – thickness relation</i>	<i>II-39</i>
II.1.a.i General considerations	II-40
II.1.a.ii Model for the capillarity regime	II-43
II.1.a.iii Model for the draining regime	II-44
II.1.a.i Combining models to describe simultaneous both regimes:	II-45
II.2 FILM HOMOGENEITY	II-46
<i>II.2.a Draining and intermediate regime</i>	<i>II-46</i>
II.2.a.i Starting meniscus effect	II-46
II.2.a.ii Evaporation time effects.	II-46
II.2.a.iii Marangoni effects	II-49
II.2.a.iv Physical boundaries contributions	II-50
<i>II.2.b Capillary regime</i>	<i>II-52</i>
II.3 RESULTS	II-54
<i>II.3.a Bi-phasic dip-coating method</i>	<i>II-55</i>
II.3.a.i The “biphasic” method	II-56
II.3.a.ii Droplet method for single-face dip-coating	II-61
II.3.a.iii Conclusion	II-63

<i>II.3.b Dip-coating in acceleration mode</i>	II-64
II.3.b.i Dynamical variation of withdrawal speed	II-64
I.1.a.i.1 Effect of temperature, gradient intensity and concentration	II-65
II.3.b.ii Thickness programming	II-70
II.3.b.iii Applications	II-70
II.3.b.iii.1 Contact angle gradients	II-71
II.3.b.iii.2 Graded microfluidic channel	II-72
II.3.b.iv Conclusion	II-73
II.4 CONCLUSION	II-74
II.5 APPENDIX	II-75
II.5.a.i Draining regime (visco-capillary regime).	II-75
II.5.a.ii Visco-inertial regime.	II-77
II.5.a.iii Surfactant effect.	II-78
II.6 BIBLIOGRAPHY	II-82
III : MATERIALS SYNTHESIS	III-85
III.1 INTRODUCTION	III-87
III.1.a Sol-Gel chemistry	III-89
III.1.b Hybrid mesostructured materials	III-91
III.1.c Evaporation Induced Self Assembly	III-93
III.1.d Block copolymers self assembly	III-96
III.1.e Self-assembled block copolymer films	III-101
III.2 SYNTHESIZED MATERIALS	III-105
III.2.a Environmental-Ellipsometric-Porosimetry	III-106
III.2.b Non-organized porosities	III-108
III.2.c Pillared Planar Nanochannels	III-116
III.2.c.i Preparation of the nanoporous Polystyrene films	III-116
III.2.c.ii Sol-gel replica	III-119
III.2.c.iii PPN from PS-b-PLA analysis	III-120
III.2.c.iv PPN from PS-b-P2VP analysis	III-122
III.2.d Conclusion	III-123
III.3 BIBLIOGRAPHY	III-124
IV : CAPILLARY INFILTRATION	IV-133
IV.1 INTRODUCTION	IV-135
IV.1.a The Lucas-Washburn equation	IV-137

IV.1.b	Capillary filling in a plane channel-----	IV-138
IV.1.c	Liquid properties at the nanoscale-----	IV-141
IV.1.d	Examples of nanoscopic effects-----	IV-143
IV.1.d.i	Surface Tension and contact angle-----	IV-143
IV.1.d.ii	Viscosity-----	IV-146
IV.1.e	Capillary infiltration experiments in nanochannels-----	IV-149
IV.1.e.i	Experiments in nanosits -----	IV-149
IV.2	EXPERIMENTAL RESULTS -----	IV-153
IV.2.a	Critical effect of pore characteristics-----	IV-154
IV.2.a.i	Sample preparation and analysis -----	IV-154
IV.2.a.ii	Capillary ring experiment -----	IV-154
IV.2.a.ii.1	Capillary ring – solvent polarity influence -----	IV-155
IV.2.a.ii.2	Capillary ring – organic to inorganic precursor ration influence -----	IV-158
IV.2.a.iii	Dynamics of capillary infiltration-----	IV-161
IV.2.a.iii.1	Capillary infiltration speed and pore characteristics analysis-----	IV-161
IV.2.a.iii.2	Bottleneck – pore size dimensions influence on capillary filling speed. -----	IV-165
IV.2.a.iii.3	Size dependence of the transport mechanism. -----	IV-166
IV.2.a.iv	Conclusion -----	IV-170
IV.2.b	Capillary infiltration in PPNs -----	IV-171
IV.2.b.i	Description of the investigated PPNs structures. -----	IV-172
IV.2.b.ii	Dynamics of the capillary filling in PPN:-----	IV-173
IV.2.b.ii.1	The chemical nature of pillars has a strong influence on wicking -----	IV-174
IV.2.b.ii.2	The porosity of the pillars has a weak influence on wicking. -----	IV-174
IV.2.b.ii.3	The height of pillars matters only if it is small. -----	IV-175
IV.2.b.iii	Modeling the capillary filling in PPN: -----	IV-175
IV.2.b.iii.1	Computation of the hydrodynamic resistance of the PPN -----	IV-175
IV.2.b.iii.2	Evaluation of the pressure drop across the meniscus -----	IV-178
IV.2.b.iii.3	Computation of the Washburn transport coefficient-----	IV-178
IV.2.b.iii.4	Reproduction of the experimental results with a single fitting parameter-----	IV-180
IV.2.b.iii.5	The model helps understanding the influence of the PPN dimensions -----	IV-181
IV.2.b.iv	Conclusion -----	IV-182
IV.3	APPENDIX -----	IV-183
IV.4	BIBLIOGRAPHY -----	IV-185
V	: SELF-DIFFUSION AND REACTIONS -----	V-191
V.1	EXPERIMENTAL RESULTS -----	V-193
V.1.a	Patterning the PPN structure. -----	V-194
V.1.b	Coupling with microfluidics: self-diffusion -----	V-196
V.1.b.i	Self diffusion of charged chromophores -----	V-197

<i>V.1.c Coupling with microfluidics: reactions</i>	V-198
V.1.c.i Metallic silver nanoparticles	V-198
V.1.c.ii Multiple reactions: silver halides precipitation	V-205
<i>V.1.d Conclusions</i>	V-207
V.2 BIBLIOGRAPHY	V-209

VI : HYDRODYNAMIC SIMULATIONS-----**VI-211**

VI.1 INTRODUCTION	213
<i>VI.1.a Nanofluidic simulations</i>	<i>214</i>
<i>VI.1.b Hydrodynamic interactions</i>	<i>215</i>
VI.1.b.i Navier-Stokes equations and hydrodynamic regimes	215
VI.1.b.ii Hydrodynamics in presence of particles (moving boundary conditions)	218
<i>VI.1.c Electroosmotic flow – phenomenon</i>	<i>219</i>
VI.2 STOCHASTIC ROTATIONAL DYNAMICS.	223
<i>VI.2.a The algorithm</i>	<i>224</i>
<i>VI.2.b Adimensional numbers and time scales</i>	<i>227</i>
<i>VI.2.c Walls, thermostat and Poiseuille flow</i>	<i>229</i>
VI.2.c.i Fluid-walls interaction	229
VI.2.c.ii Thermostat	231
VI.2.c.iii Poiseuille flow between two planes	232
<i>VI.2.d Solutes in SRD</i>	<i>235</i>
VI.2.d.i Fluid interaction with the solutes and force description	235
VI.2.d.ii CC - Collisional Coupling	236
VI.2.d.iii CFC – central force coupling	237
VI.2.d.iv CFC-CC method comparisons	238
VI.2.d.v Forces between solutes	239
VI.2.d.vi Electrostatic interactions - Ewald summation	239
VI.2.d.vii Ewald summation in slab geometry	241
VI.3 : SIMULATION RESULTS	243
<i>VI.3.a Validation of the SRD method</i>	<i>244</i>
VI.3.a.i Simulation box and boundary conditions	245
VI.3.a.ii Validation	246
VI.3.a.iii Effect of σ_w and d for low surface charge values	249
<i>VI.3.b Non-ideal case: beyond the PNP hypothesis</i>	<i>253</i>
<i>VI.3.c From high to low surface charge</i>	<i>256</i>
VI.3.c.i PNP-“from p ⁺ ”-SRD flow confrontation and WCA interactions effect	258
VI.3.c.ii Effect of σ_w	258
VI.3.c.iii Effect of d	258

<i>VI.3.d Salt addition</i>	261
<i>VI.3.e Electro-osmosis in PPNs</i>	264
VI.3.e.i Flow Charts	268
<i>VI.3.f Conclusion</i>	271
VI.4 APPENDIX	273
<i>I.1.a Adimensional numbers</i>	273
VI.4.a.i Mach number	273
VI.4.a.ii Reynolds number	274
VI.4.a.iii Peclet Number	274
VI.4.a.iv Schmidt number	275
VI.4.a.v Knudsen number	275
VI.5 BIBLIOGRAPHY	276
CONCLUSION	281
RESUME EN FRANCAIS	291
ACKNOWLEDGEMENTS	309

COUCHES MINCES NANOPOREUSES COMME
PLATEFORME POUR APPLICATIONS
NANOFLUIDIQUES.

Résumé en français

Par Davide Raffaele Ceratti

Thèse de Doctorat de Chimie et Physico-Chimie des Matériaux

Dirigée par David Grosso

Soutenance prévue le 30 Septembre 2015

Sommaire

INTRODUCTION	293
CHAPITRE I : ÉTAT DE L'ART	293
CHAPITRE II: AVANCEMENTS DANS LA TECHNOLOGIE DU DIP-COATING.....	294
CHAPITRE III : SYNTHÈSE DE MATÉRIAUX	297
CHAPITRE IV : INFILTRATION CAPILLAIRE.....	299
CHAPITRE V : AUTODIFFUSION ET RÉACTIONS	302
CHAPITRE VI : SIMULATIONS HYDRODYNAMIQUES	303
CONCLUSIONS.....	308

Introduction

Le résumé de cette thèse parcourt brièvement tous les points importants du travail effectué. La structure suit celle de la thèse originale avec la même division par chapitres.

L'accent est posé sur la méthode « bottom-up » de fabrication des systèmes nanofluidiques en contraste avec la méthode courante dit « top-down ». La première méthode forme des systèmes par l'auto-assemblage des molécules au travers de procédés où l'organisation et la forme ne sont pas contrôlées directement de façon physique mais par des effets chimiques connus. La deuxième méthode, par contre, utilisant des techniques comme la lithographie à électrons (entre autres) crée des systèmes directement avec un procédé qui peut être dit similaire à l'écriture. Si cette deuxième méthode est plus précise, la première donne des avantages particulièrement importants en termes de réduction de coût, de réduction de temps de fabrication, d'augmentation de taille et surtout avec une meilleure flexibilité au niveau des structures et matériaux (réalisés par sol-gel) qui peuvent être utiles pour de nouvelles applications et pour augmenter, en général, la compréhension de plusieurs phénomènes nanofluidiques restant encore à explorer.

Chapitre I : État de l'art

Dans le premier chapitre de la thèse, l'état de l'art concernant les applications nanofluidique aussi bien que les méthodes de fabrication, est analysé.

La plupart des applications envisagées sont de type biomédical. En particulier les systèmes de concentration de biomolécules, de séparation et d'élongation de molécules d'ADN sont communs dans la littérature. Toutes ces applications exploitent les propriétés de l'échelle nano en utilisant la grande quantité de charge de surface par unité de volume (qui cause des effets de filtration sur les espèces chargées) ou la similarité de la taille des molécules d'ADN où d'autres biomolécules avec les dimensions typiques des canaux nanofluidiques.

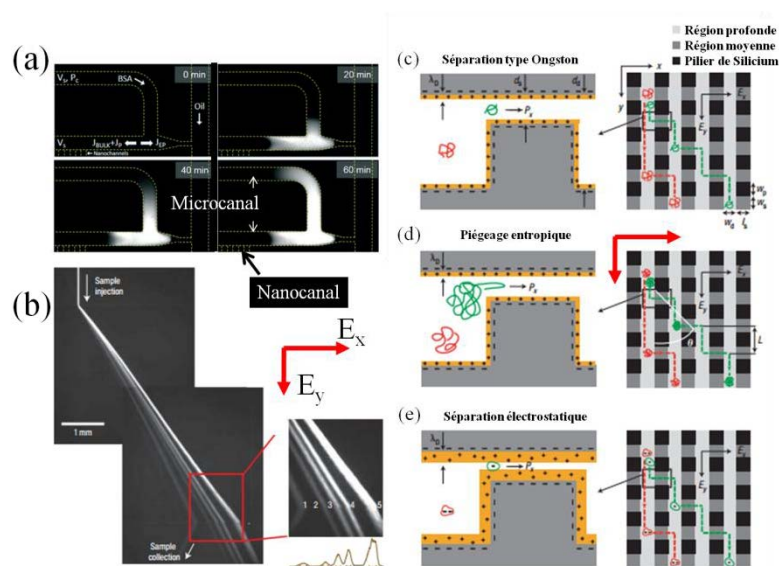


Figure. 1. (a) système pour la concentration de biomolécules. (b) système pour la séparation des molécules d'ADN de longueur différente. (c-e) Mécanismes de séparation des biomolécules.

Dans la figure.1 quelques applications de type biomédical sont reportées.

Des applications différentes sont aussi mentionnées dans la littérature. En particulier les caractéristiques des canaux nano-fluidiques peuvent être utilisées également pour les dites « batteries nano-fluidiques » qui transforment l'énergie chimique due au gradient de salinité, en énergie électrique. Les applications comme

la séparation des particules inorganiques ou la modification de la sélectivité des réactions ont aussi été prises brièvement en compte mais nécessitent encore plus d'efforts par la communauté scientifique.

Au niveau des techniques de fabrication, on compte les méthodes telles que la photolithographie conventionnelle (Conventional photolithography), la lithographie à interférence (Interference lithography), la lithographie à nano-impression (Nanoimprint lithography), la lithographie à faisceau d'électrons (Electron beam lithography) ou la lithographie à faisceau de l'ion ciblé (Focused Ion Beam lithography). Les informations les plus importantes sur ces méthodes sont résumées dans le tableau qui suit.

Méthode de fabrication	Dimension minimal du canal [nm]	Matériaux/substrats	Avantage/désavantage
Conventional photolithography	40–100 in one dimension	Photoresist polymère/silicium(vitre)	Facile et accessible, grande quantité / dessin simple seulement, basse résolution
Interference lithography	30 (avec traitement approprié)	Photoresist polymère/silicium(vitre)	Vat, sans masque, nanocanaux profonds / géométrie simple seulement
Nanoimprint lithography	6–40	Photoresist polymère/silicium(vitre)	Grande quantité/ problèmes de conservation de la forme , canaux pas profonds, fabrication de la matrice
Electron beam lithography	<5	Photoresist polymère/silicium(vitre)	Liberté de géométrie, haute résolution / relativement lent, chère
Focused Ion Beam Lithography	10 nm	Si/vitre/quartz/oxydes	Liberté de géométrie, haute résolution / très lent, chère

Certaines techniques bottom-up ont aussi été trouvées dans la littérature ; en particulier l'utilisation des cracks contrôlés comme nano-canaux a été présentée mais elle ne permet pas les grandes possibilités de la chimie sol-gel déjà mentionnées dans l'introduction et montrées ensuite dans le manuscrit. Elle ne permet pas en particulier de créer des structures telles que les PPNs ci-après décrits (chapitre III).

Chapitre II: Avancements dans la technologie du dip-coating

Dans le deuxième chapitre de cette thèse, les avancements obtenus concernant la technologie du dip-coating sont présentés après une introduction de la méthode et une description des inconvénients que la méthode peut comporter.

Le dip-coating est une méthode qui permet de créer des couches minces sur un substrat régulier. Il consiste en l'immersion d'un substrat dans un liquide et de son retrait. Après le retrait du substrat de la solution, le liquide déposé peut se solidifier ou, plus souvent, sécher laissant une couche mince solide sur le substrat. Les propriétés chimiques du solide formé sont déterminées principalement par la composition de la solution mais l'épaisseur est fortement influencée par la vitesse de retrait du substrat. En général, pour les cas considérés dans cette thèse deux régimes sont identifiables. Ils sont appelés régime de drainage et régime capillaire comme défini par Faustini *et al* (CIT). Dans le premier cas (avec une vitesse de retrait comprise entre 0,1 et 10 mm/s) l'épaisseur de la couche est déterminée par l'équilibre entre la force visqueuse, créée par le mouvement du substrat, et la force capillaire, due à la concavité du ménisque, l'une entraînant le liquide vers le haut et l'autre vers le bas à cause de la diminution de la pression au ménisque. Pour le régime de drainage il est possible de démontrer (appendice du chapitre) que l'épaisseur du film est proportionnelle aux deux tiers à la viscosité et à la vitesse de retrait et inversement proportionnelle à la sixième racine de la tension de surface de la solution. Pour des vitesses plus faibles (inférieures à 0,1 mm/s) l'épaisseur du film est déterminée par le dépôt du soluté sur le substrat en mouvement lent, dû à l'évaporation du solvant (phénomène du rond de café). La quantité de matière déposée étant constante dans le temps, l'épaisseur du film est inversement proportionnelle à la vitesse de retrait. La figure.2 reporte les équations et des résultats expérimentaux typiques pour les deux régimes.

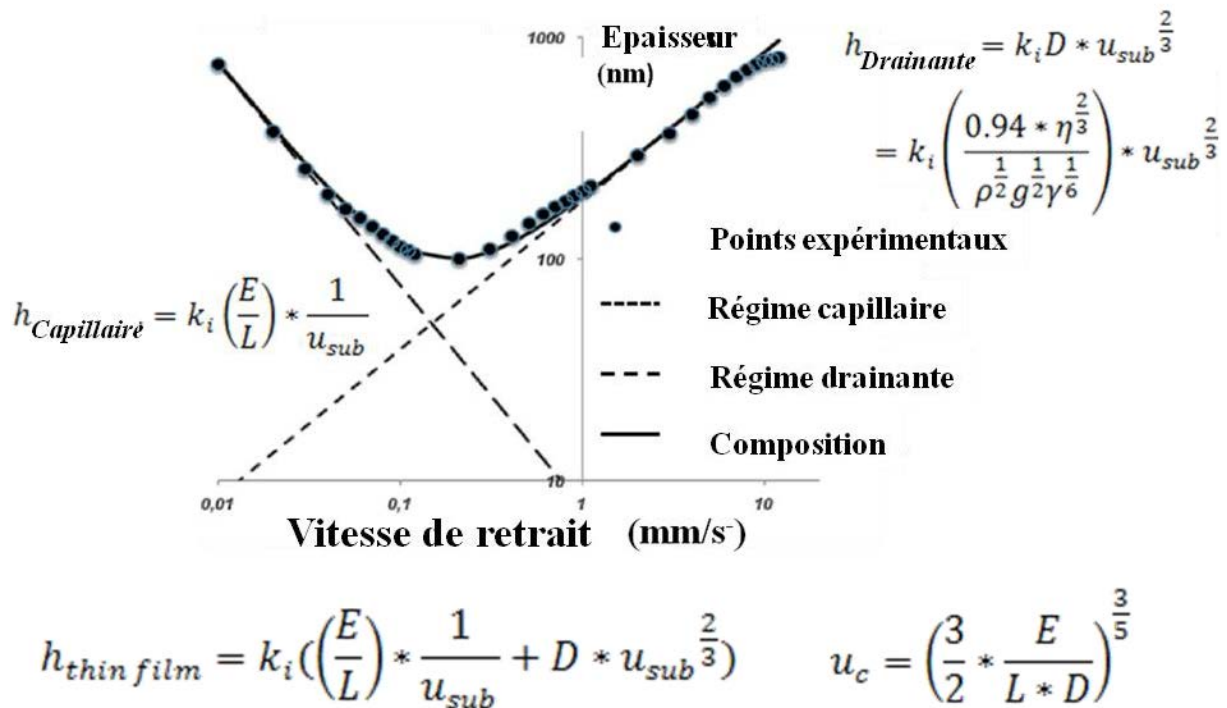


Figure.2. Equations et données typiques de l'évolution de l'épaisseur d'une couche mince avec la vitesse de retrait du substrat pour les deux différents régimes.

Malheureusement, dans certains cas, le dip-coating peut présenter des inconvénients qui peuvent empêcher l'obtention de films homogènes. Une brève analyse est accomplie en considérant les rôles du temps d'évaporation du film mince, des effets Marangoni et de l'influence de la forme du substrat et de la cuve dans laquelle est effectué le dip-coating. L'expertise acquise dans la résolution des problèmes d'homogénéité dus à ces effets est exposée, identifiant d'ailleurs le régime intermédiaire (autour de 0.1 mm/s) comme le plus adapté pour faire des couches minces homogènes. Si la vitesse doit être différente le contrôle de la température peut être aussi utile pour éliminer les problèmes liés à l'évaporation.

La méthode du dip-coating présente, à un niveau expérimental, un problème lié à la manière dont elle est conçue. Il est en effet nécessaire d'utiliser une grande quantité de liquide pour couvrir des substrats de la même taille comparé à d'autres méthodes de dépôt par voie liquide. Cela signifie que si une solution très onéreuse (à base de co-polymères à blocs ou de métaux précieux) doit être utilisée, l'investissement pour réaliser un seul film est bien plus élevé qu'en envisageant d'autres méthodes. D'autre part, à la différence d'autres méthodes, après avoir réalisé une couche mince, il est possible d'en faire plusieurs autres parce que la solution utilisée n'est pas perdue après le premier dépôt. Par exemple, si une confrontation est faite avec la méthode du spin-coating, si l'on veut couvrir un substrat de quelques centimètres carrés, il est nécessaire d'utiliser juste quelques gouttes pour le spin-coating mais plusieurs millilitres pour le dip-coating. D'autre part il est possible de réaliser des dizaines d'échantillons avec ces millilitres alors qu'un même nombre d'échantillons réalisés par spin-coating requiert des dizaines de millilitres. Une nouvelle méthode de dip-coating appelé « biphasique » est donc introduite et démontrée comme valable pour résoudre ces problèmes. La quantité de solution nécessaire pour faire une couche mince avec la méthode biphasique est équivalente à celle qui est nécessaire pour le spin-coating mais l'avantage de réutilisation de la solution est conservé. L'idée de la méthode est extrêmement simple : la plupart de la solution théoriquement coûteuse est substituée par un liquide lourd (qui reste au fond du réservoir) et inerte (tel qu'un perfluoré ou un métal liquide) qui ne se mélange pas avec la solution et ne s'accroche pas au substrat. La petite quantité de solution est donc placée sur le liquide inerte et le dépôt est effectué normalement en retirant le substrat. Sur la figure.3, l'idée de la méthode est reportée.

Méthode monophasique

Méthode biphasique

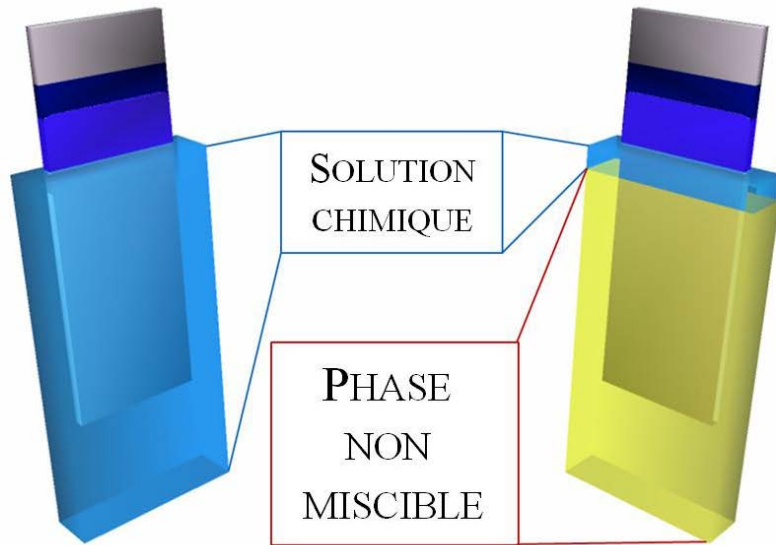


Figure.3. Schéma de la méthode biphasique. La phase non miscible (perfluorates ou métaux liquides) est utilisée pour substituer une grosse partie de la solution à déposer.

Une variation de la méthode permet d'éviter d'avoir un dépôt sur tous les faces du substrat, et donc d'avoir un dépôt sur un coté seulement ; ce qui peut être extrêmement important pour des applications en électronique ou en optique. Il suffit dans un premier temps d'immerger le substrat dans la phase inerte et dans un deuxième temps d'ajouter les gouttes de solution nécessaires au dépôt en faisant attention à ce que la solution ne mouille pas les côtés qui ne doivent pas être recouvert. L'équivalence entre les couches mince réalisées avec la méthode biphasique et avec la méthode classique a été démontrée. Ainsi la validité de la méthode biphasique a été prouvée. Sur la figure.4, l'épaisseur et l'indice de réfraction des couches minces de silice et titane réalisées avec les deux méthodes (avec des niveaux différents de liquide à déposer et liquides inertes) sont présentés. Il est apposé également une photo de trois films : deux de silice obtenus avec la méthode biphasique en utilisant comme liquide inerte du perfluorohexane puis du mercure et un de silice également obtenu avec la méthode de dip-coating classique.

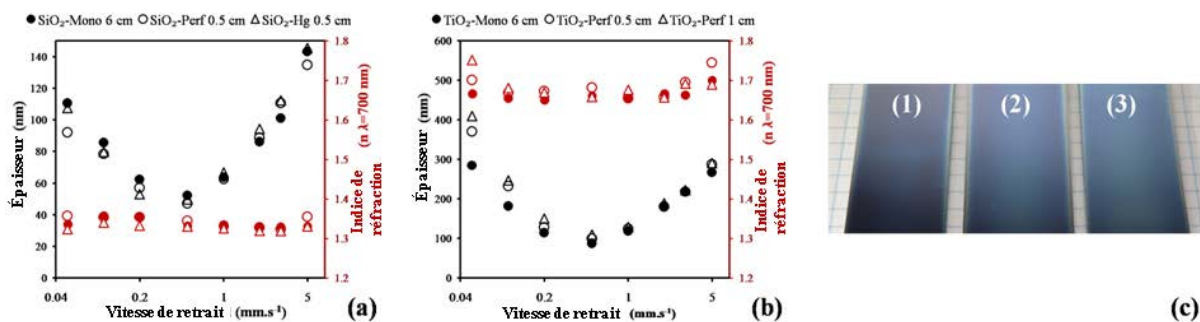


Figure.4. Épaisseur et indice de réfraction des couches minces de silice (a) et titane (b) en fonction de la vitesse de retrait pour les deux méthodes. (c) les couches minces (1) et (3) ont été réalisées avec la méthode biphasique avec comme liquide inerte du perfluorohexane et du mercure. La (2) avec la méthode monophasique.

Un deuxième avancement technologique effectué pendant cette thèse regarde la création de couches minces par dip-coating avec un gradient d'épaisseur. En faisant varier localement la vitesse de retrait du substrat selon les lois montrées précédemment, il est possible de varier localement l'épaisseur de la couche. Certaines limites ont été identifiées dans l'accélération possible et la concentration maximale possible pour obtenir des couches avec un profil désiré. En plus la température a été identifiée comme un paramètre additionnel pour favoriser l'évaporation et pousser un peu plus les limites identifiées précédemment. Il est

possible d'obtenir avec cette technique plusieurs profils comme ceux présentés en figure.5 avec plusieurs matériaux.

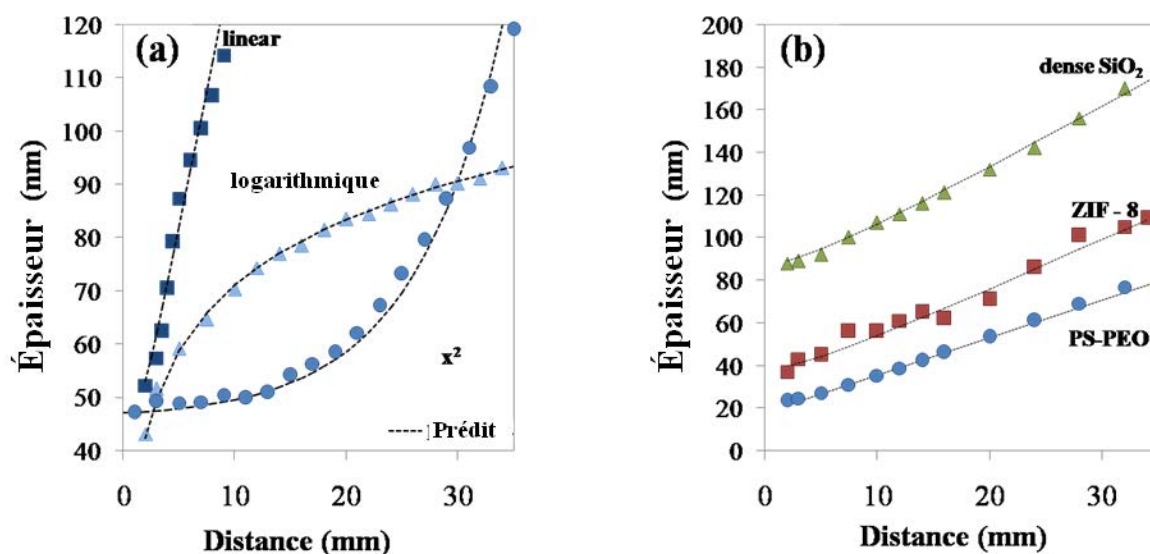


Figure.5. (a) profils obtenus avec la méthode en accélération pour du titane poreux. (b) gradients d'épaisseurs obtenus avec plusieurs matériaux.

Des applications ont été présentées en créant d'une part des couches minces à gradient d'angle de contact et d'autre part des canaux micro-fluidiques avec gradient de hauteur.

Chapitre III : Synthèse de matériaux

Dans le troisième chapitre, une description des stratégies adoptées pour réaliser des couches minces utilisées ensuite pour des expériences de nano-fluidique, est reportée.

Une première stratégie consiste à coupler la méthode de dip-coating du chapitre précédent avec la chimie sol-gel, pour laquelle un travail de littérature a été accompli concernant les concepts « auto assemblage induit par l'évaporation » ("Evaporation Induced Self-Assembly" (EISA)) et « assemblage des micelles induit par évaporation » (Evaporation Induced Micellar Assembly (EIMA)). Pour ces deux concepts, une solution sol-gel avec un surfactant ou un copolymère à block en-dessous (pour l'EISA) ou au-dessus (pour l'EIMA) de la cmc (concentration micellaire critique) est utilisée pour le dip-coating entraînant la formation de nanostructures induites par évaporation.

Une deuxième stratégie consiste à déposer une couche mince de copolymère à block (par dip-coating ou spin-coating) et à exploiter les propriétés d'auto-assemblage du polymère avec une exposition en température ou concentration du solvant élevé dans une chambre de post-traitement (annealing en anglais). Le copolymère est donc traité spécifiquement ; un des blocs du polymère éliminé ou déplacé laisse un espace vide et est ensuite rempli par un sol-gel.

Pour les deux stratégies, après calcination et destruction de la phase organique de la couche mince, une couche avec une certaine porosité reste et cette porosité est exploitable comme canal nano-fluidique plus ou moins organisé.

La porosité est analysable avec une méthode appelée en anglais Environmental Ellipsometric Porosimetry (EEP) ; avec cette méthode l'épaisseur du film et son indice de réfraction sont mesurés à différentes pressions de vapeurs. Parce que la condensation des liquides dans des pores à l'échelle nano a lieu à des humidités faibles quand les pores sont petits, il est possible utiliser le phénomène de condensation d'eau dans les pores, identifiable par une vive variation de l'indice de réfraction de la couche, pour déterminer la taille des pores dans la structure de la couche. En réalité si la porosité des couches minces est caractérisée

par des pores avec des goulots de diamètre réduit il est possible d'identifier aussi la taille de ces goulots en identifiant l'humidité pour laquelle la porosité se vide en diminuant la pression de vapeur d'eau.

Plusieurs couches minces réalisées avec les deux stratégies sont donc présentées. En changeant le type et la quantité du surfactant ou copolymère à blocs, il est possible de varier la quantité et la taille des pores dans les couches minces. Quatre exemples sont montrés sur la figure.6 où les tailles maximales des pores et les tailles de leurs goulots peuvent être presque égales, intermédiaires ou très différentes. Le volume relatif occupé par les pores peut aussi diminuer comme c'est possible de le voir sur la figure.6.d

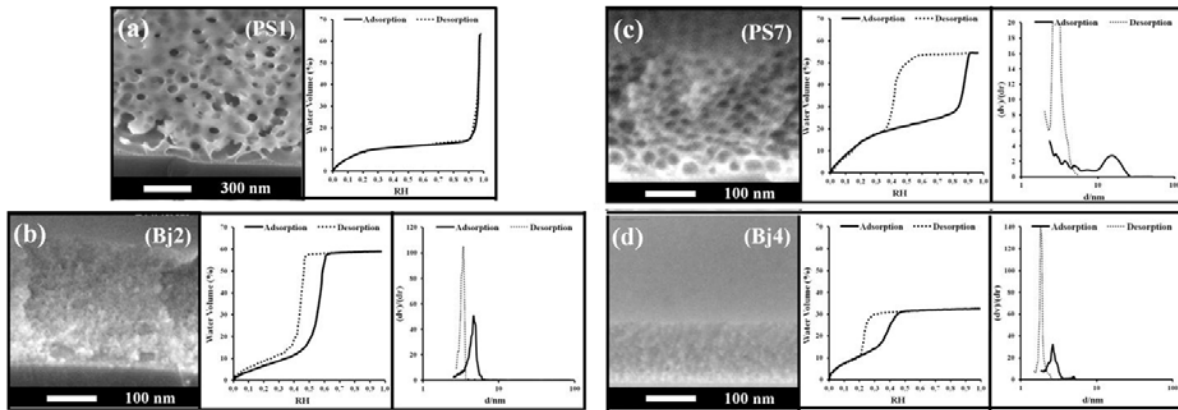


Figure.6. Couches minces avec tailles maximales des pores et les tailles de leurs goulots presque égales (a), intermédiaires (b) ou très différentes (c). (d) couche mince avec un volume de pores réduit.

Si la deuxième stratégie est utilisée, il est possible de réaliser des structures plus ordonnées comme les PPNs (Pillared Planar Nanochannels) « Nano-canaux Planaires soutenus par Piliers ». La stratégie est résumée brièvement sur la figure.7.

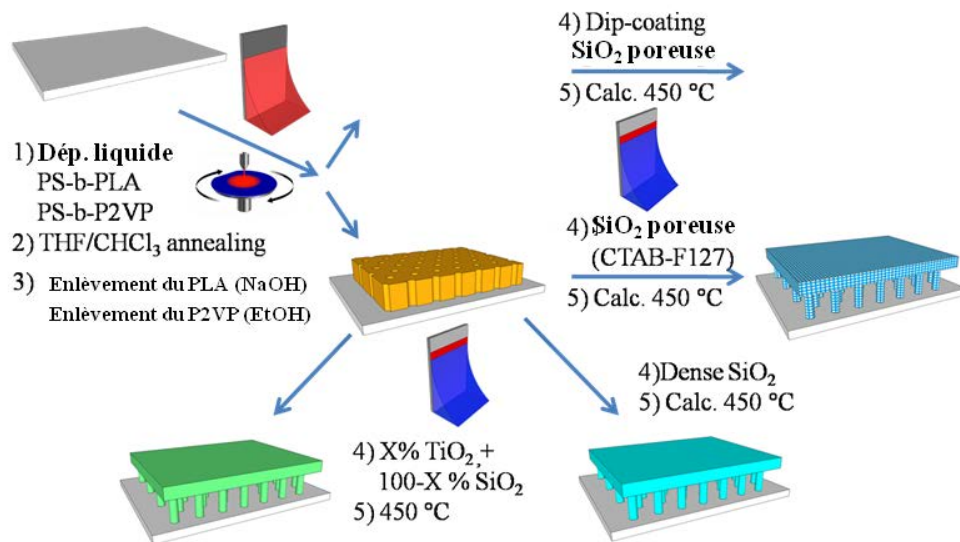


Figure.7. Stratégie de fabrication des PPNs.

Les piliers ont été réalisés en plusieurs formes et dimensions. Pour obtenir ces résultats il est simplement nécessaire de varier la hauteur de la première couche mince de copolymère à bloc, ou de varier le copolymère à bloc et donc sa périodicité, à la première étape du procédé. Le substrat initial peut également être varié comme le matériau sol-gel utilisé pour imprégner la porosité vide du copolymère traité dans la deuxième étape du procédé.

Sur la figure.8 on peut voir la modification possible de ces structures.

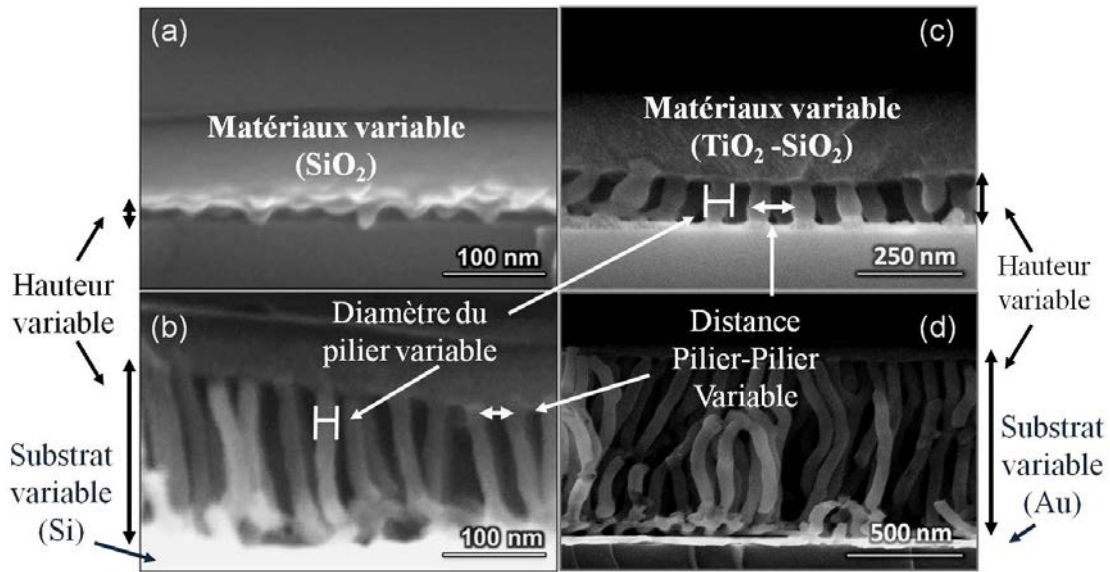


Figure.8. Eléments variables dans la fabrication des PPNs

Les couches minces réalisées avec les deux stratégies ont donc été utilisées pour des expériences nano-fluidiques reportées dans le chapitre suivant.

Chapitre IV : Infiltration Capillaire

Au sein du chapitre IV les couches minces introduites précédemment ont été utilisées pour des expériences d'infiltration capillaire. L'influence de la forme de la nanostructure à matériel constant et du matériel à structure constante ont été étudié en variant la composition de la phase organique dans des solutions sol-gel désorganisé ou de la phase inorganique sol-gel dans la production des PPNs.

L'infiltration unidimensionnelle des liquides dans des milieux poreux est gouverné par une loi de type diffusive avec le carré de la longueur parcourue l proportionnel au temps t selon une constante D dite de Washburn.

$$l^2 = D * t \quad (1)$$

Cette constante dépend de façon complexe de la structure mais elle est aussi proportionnelle à la tension de surface du liquide et à l'angle de contact entre le liquide et le solide. De la même façon elle est inversement proportionnelle à la viscosité. Au niveau nanométrique ces paramètres ont une valeur qui ne peut pas être pensée comme égale aux valeurs de niveau macroscopique. En plus il faut faire attention à la définition même des ces grandeurs qui est définie statistiquement à grande échelle et pas forcément au niveau nano où la statistique est plus petite et l'importance des fluctuations peut être plus grande. Ces modifications génèrent une variation inattendue de la constante D qui a souvent été étudiée dans la littérature et trouvée selon une valeur plus petite que la valeur que attendue même dans des cas simples de nano-canaux planaires.

Pour extraire la valeur de D de ces expériences de remplissage, il suffit de recouvrir une couche mince avec du PDMS pour éviter l'évaporation et filmer avec un microscope la position de l'eau, identifiable grâce au changement de couleur de la couche dû au changement d'indice de réfraction, en fonction du temps. Pour plus de clarté l'idée est présentée dans la figure.9.

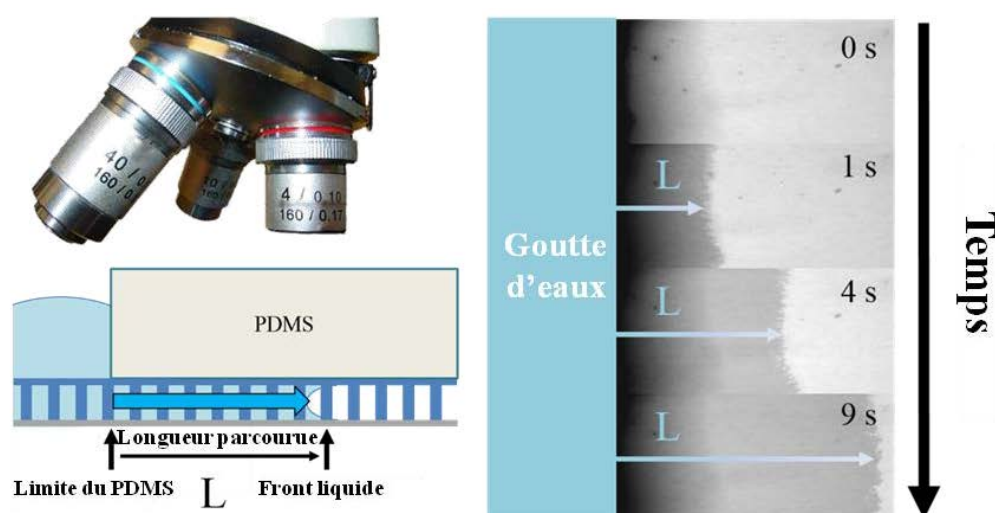


Figure.9. Stratégie pour la visualisation de l'infiltration capillaire.

En plus l'analyse de la vitesse de remplissage effectuée sur des échantillons de silice avec des pores et des goulots des pores de taille différente a permis d'identifier que dans certains cas le mécanisme d'avancement de l'eau à l'intérieur de la nano-porosit  peut d couler d'un m canisme fait d' vaporation et de condensation successives.

En g n ral il a  t  possible d'observer que, si les pores n'ont pas de goulots ou ont des goulots des pores d'une taille proche   la taille maximale des pores (diam tre du pore), la constante D est proportionnelle   la taille des pores. Par contre si les deux dimensions sont tr s diff rentes une tendance diverse est identifi e. En particulier, pour une dimension de goulots des pores constante, en augmentant la taille des pores, la constante D diminue de fa on exponentielle. Ce comportement est difficilement explicable si un m canisme d'avancement purement liquide est suppos . Sur la figure.10 les donn es obtenues exp rimentalement sont pr sent es. Dans le cas d'une porosit  avec une taille uniforme, une ligne droite a  t  dessin e pour aider   comprendre l'allure exp rimentale.

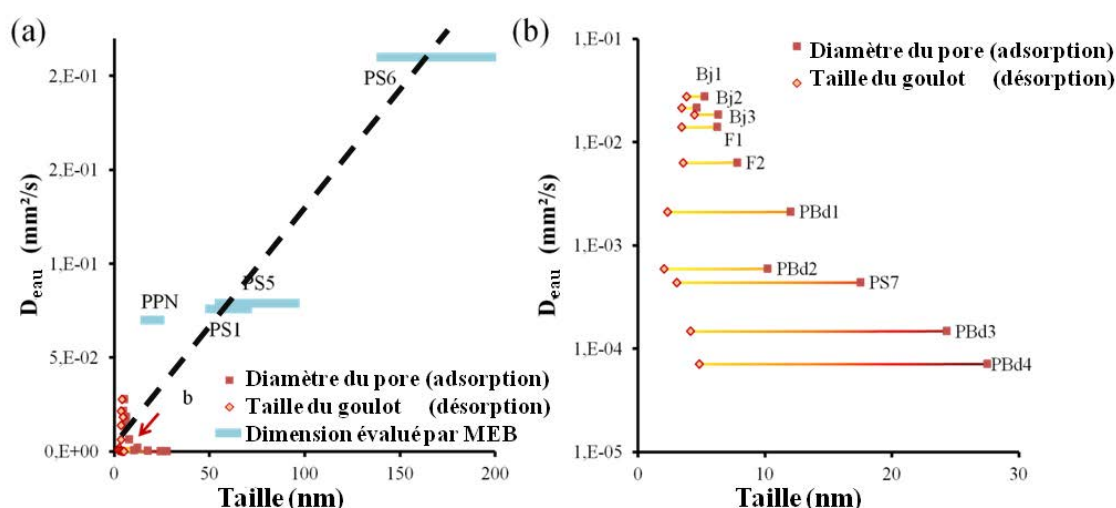


Figure.10. Donn es exp rimentales de la vitesse de remplissage de plusieurs couches minces avec l'eau. La figure (b) est le zoom du coin en bas   gauche de l'image (a)

Si la technique utilis e pour identifier la taille des pores a  t  le MEB (pour des grands pores qui ne peuvent pas  tre mesur s par EEP) la barre d'erreur est repr sent e par une barre bleue ciel. Sur le deuxi me graphique les valeurs pour des porosit s avec petit goulots sont montr es. La taille de goulot est   l'extr me gauche et la taille maximale du pore est   l'extr me droite de chaque ligne horizontale. Il faut

utiliser l'échelle logarithmique pour mettre en évidence l'allure exponentielle de D avec la taille des pores. Si des expériences de remplissage sont accomplies sur les même couches minces avec des liquide ioniques non volatiles, il est possible de voir que pour les porosités avec des goulots des pores plus petits le ratio entre la vitesse de remplissage purement liquide (liquide ionique) et celle de l'eau est beaucoup plus élevé que pour les échantillons où le goulots ne sont pas importants. Cela a permis de comprendre qu'en effet le mécanisme d'avancement de l'eau dans la porosité avec des petit goulots n'est pas purement liquide mais est amené par des pas successifs d'évaporation et condensation. Cet aspect peut être très important pour la compréhension des phénomènes et des applications liés à la géologie et à l'extraction du pétrole.

Les informations décrites sont résumées sur la figure.12

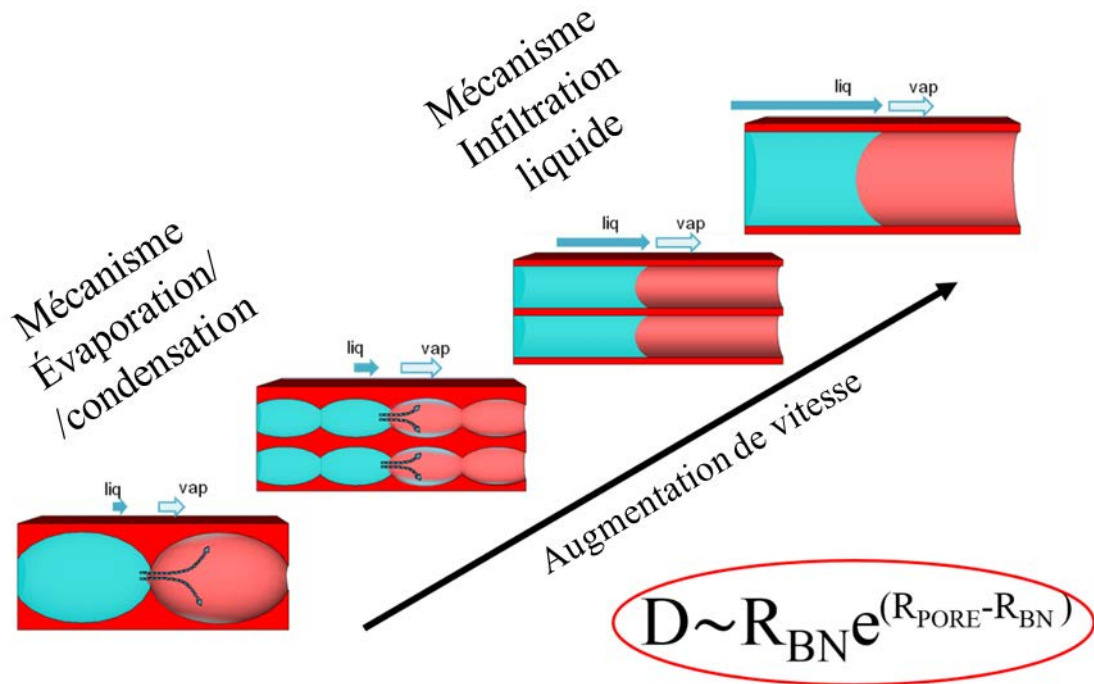


Figure.11. Mécanismes d'infiltration par l'eau en fonction de la géométrie des pores. La tendance est décrite par l'équation dans le coin en bas à droite.

Une deuxième étude a montré l'influence du matériau composant la nanostructure à géométrie donné. Pour réaliser cette étude, des échantillons de PPNs ont été réalisés en faisant varier la composition de la solution sol-gel utilisée pour générer la phase inorganique. Des PPNs de silice poreuse, de silice dense et d'un mélange de silice et de titane ont été utilisés. La hauteur des piliers a été variée également. Avec l'aide des valeurs de résistance hydrodynamiques obtenues par un logiciel à éléments finis (COMSOL), qui a pu être utilisé grâce à la haute symétrie du système, il a été possible déterminer les valeurs de la constante D selon des lois macroscopiques pour toutes les hauteurs de piliers. Selon ce calcul, la valeur de D pour la silice pure et pour le mélange silice-titane ne doit pas être plus différente que de 10%. D'autre part les valeurs expérimentales obtenues sont respectivement 3,5 et 1,5 plus petites que les valeurs attendues pour la silice et pour le mélange silice-titane mais la tendance en fonction de la hauteur est respectée si l'on considère cette constante multiplicative. Sur la figure.12, un exemple des simulations faites avec COMSOL, les données expérimentales (points) et la prévision avec la constante multiplicative sont confrontées.

Solution des équations de N-S

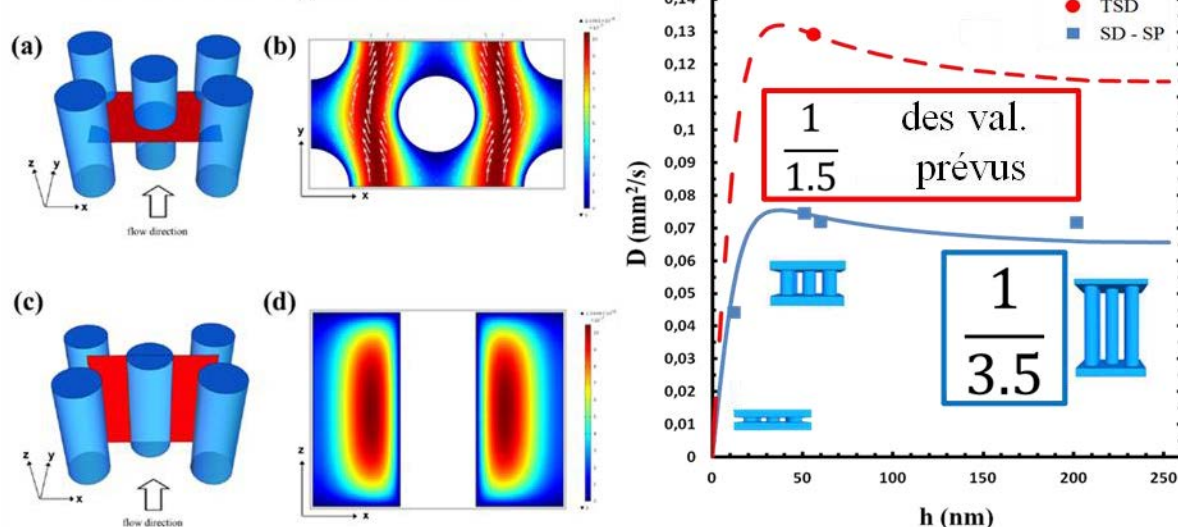


Figure.12. à gauche solution des équations de Navier-Stokes pour la géométrie des PPNs. A droite, tendances prévues par les lois macroscopiques multipliées par la constante indiquée. En bleu PPNs de silice et en rouge de mélange silice-titane.

La porosité de la matrice inorganique, beaucoup plus petite que la porosité entre les piliers, n'a pas d'influence sur la vitesse de remplissage. C'est d'ailleurs possible de déduire cela de ce qui a été dit précédemment. Une dépendance du matériau si élevée n'est pas prévue par la loi macroscopique; c'est une caractéristique de l'échelle nano. Les PPNs sont un très bon candidat pour étudier la dépendance du matériau sur la vitesse de remplissage à cause de la géométrie identique réalisable avec des matériaux différents. Cet aspect est encore plus important si l'on effectue une confrontation avec des expériences similaires réalisées avec la plus commune des technologies en ce moment, la technologie top-down, qui ne permet pas de réaliser des structures égales avec tous les matériaux et ne permet pas de contrôler la rugosité et la chimie de surface.

Le sol-gel et en particulier les PPNs ont donc été identifiés comme des parfaits candidats pour la compréhension des phénomènes nano-fluidiques, non seulement pour leur coût réduit déjà décrit dans le troisième chapitre mais aussi pour des motivations scientifiques additionnelles qui ne sont pas atteignables avec d'autres méthodes de fabrication de systèmes nano-fluidiques.

Chapitre V : Autodiffusion et réactions

Dans le chapitre V, les possibilités offertes par les PPNs ont été exploitées pour réaliser des séparations et des réactions en espace confiné afin d'explorer la mise en application de la chimie sol-gel et des PPNs pour créer des systèmes nano-fluidiques complexes.

Dans une première section, des techniques de structuration de surface par UV ont été présentées. Ces techniques peuvent être utiles pour l'intégration de systèmes nano-fluidiques dans un circuit micro-fluidique en créant des réseaux de PPNs avec une taille de quelques microns dans la direction horizontale pour, par exemple, créer plusieurs canaux nano-fluidiques parallèles.

L'intérêt de créer des systèmes nano-fluidiques est aussi des réaliser des séparations. Pour tester la séparation une solution contenant de la rhodamine B et de la carboxy-fluorescéine a été diffusée dans les PPNs. Le valeur de la constante d'autodiffusion pour ces deux molécules a été trouvée plus ou moins deux cent fois plus petite que dans l'eau pure. En plus la rhodamine B, qui dans l'eau pure est plus lente, est dans ce cas plus vite que la carboxy-fluorescéine.

Un deuxième test a été effectué en mélangeant deux solutions qui créent un précipité au milieu du réseau de PPNs. Pour faire cela un simple chip-micro-nano-fluidique a été réalisé. Une photo est montrée en figure.13. Des canaux microfluidique en PDMS amènent les réactants aux deux côtés. Les réactants ont été diffusés en même temps ou successivement afin d'obtenir des conditions différentes. En particulier si du nitrate d'argent a été mis en réaction avec de l'hydrazine, la formation de nanoparticules d'argent métalliques a été relevée par voie optique. Si l'un des réactants est introduit en premier, au moment de l'ajout du deuxième, la formation des nanoparticules commence du côté du canal de la deuxième injection. Si le canal du premier réactant est plus long, l'endroit où la précipitation survient bouge vers le centre de la zone entre les canaux et, quand un état stationnaire est atteint, une ligne est formée par la précipitation continue de l'argent au même endroit. La position de cette ligne dépend de l'ordre d'injection du réactant à cause de la différente interaction de ces derniers avec le matériau qui compose le PPN. De plus, la dynamique selon laquelle la précipitation se produit et selon laquelle la ligne est formée dépend des conditions et de l'ordre d'injection, ainsi que du matériau des PPNs.

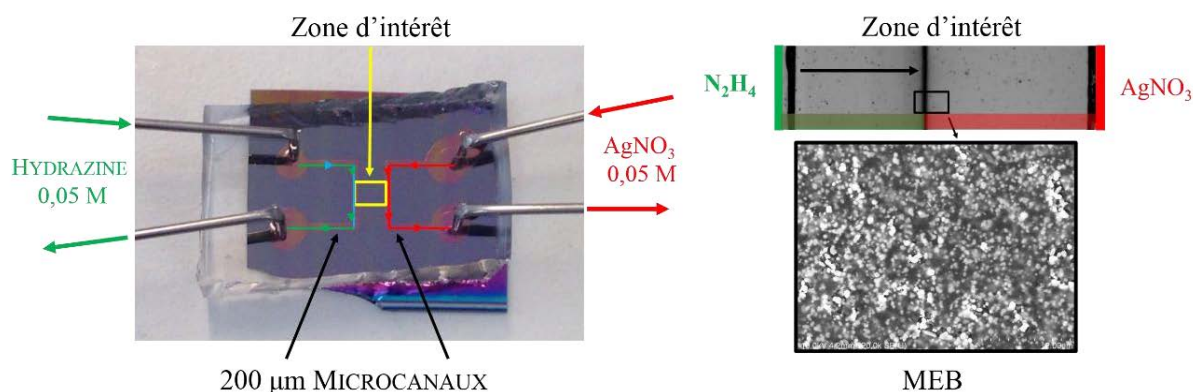


Figure.13. à gauche, système composé microfluidique et nanofluidique qui permet l'introduction des réactants des deux côtés. à droite zoom sur la zone d'intérêt après réaction et MEB de la ligne mise en évidence dans l'image optique.

Des tests similaires ont aussi été accomplis avec un mélange d'halogénures de potassium et une solution de nitrate d'argent. La précipitation successive des halogénures d'argent a formé plusieurs lignes et des formations dendrimerique différentes en fonction de l'halogénure qui précipitait.

La compréhension des phénomènes à l'intérieur de ce système est encore complexe. Plusieurs éléments doivent être étudiés séparément. Néanmoins il a été démontré que les PPNs, grâce à leur bas coût et leur facilité de création, peuvent donner à la Science les moyens d'étudier plus profondément les phénomènes mentionnés.

La partie expérimentale touche à sa fin ici. Une approche plus théorique a été utilisée dans le dernier chapitre afin de montrer qu'il est nécessaire également de travailler le côté théorique pour pouvoir comprendre les phénomènes nano-fluidiques.

Chapitre VI : Simulations hydrodynamiques

Dans le dernier chapitre, le chapitre VI, le point d'observation est transporté à l'échelle nano. Aucune expérimentation réelle n'a été accomplie mais le comportement des espèces chargées a été étudié à l'intérieur des structures nanométriques par l'intermédiaire d'une méthode de simulation appelé SRD (Stochastic Rotational Dynamics). Cette méthode décrit avec succès les interactions hydrodynamiques qui influencent le mouvement des espèces dans les milieux nanométrique. Sa force, comparée à d'autres méthodes de simulations des fluides, est qu'elle permet de considérer artificiellement des phénomènes qui se passent à des échelles de temps extrêmement différentes sans recourir à un très grand nombre d'étapes. Les temps typiques de l'agitation moléculaire comme de la relaxation des interactions hydrodynamique ou de la corrélation entre les molécules de solvants qui sont distribués sur 15 ordres de magnitudes sont compressés (avec une éventuelle redéfinition des interactions) sur 3 ordres de magnitudes. Des simulations

avec des milliers d'étapes peuvent donc considérer toutes les interactions alors qu'une simulation qui doit considérer les temps réels nécessite des millions de milliards d'étapes pour obtenir le même résultat.

La méthode a été principalement utilisée pour étudier de façon nouvelle le phénomène de l'électro-osmose. L'électro-osmose est un phénomène assez complexe : dans des espaces de dimensions nano la charge de surface assume un rôle important si un solvant est introduit dans la porosité. En particulier les contre-ions de la charge de surface sont dissolus dans le solvant et interagissent à un niveau hydrodynamique avec lui. Si un champ électrique est ajouté au système, une quantité de mouvement est transférée au liquide qui commence à couler. Plusieurs paramètres gouvernent l'écoulement comme la taille du système, la charge des contre-ions et, comme il a été démontré, la position et la distribution des charges de surface. Pour simuler de façon adéquate le système, il est nécessaire de définir plusieurs paramètres additionnels comme la distance d'approche minimale entre les ions, la distance d'approche entre les ions et les parois, la charge des ions et les distributions des charges de surface (qui peuvent être, à parité de charge totale, peu et très chargées ou être peu chargées et très nombreuses). Clairement l'intensité du champ électrique est aussi un paramètre fondamental. Sur la figure.14, le nom des paramètres et leur signification est simplement illustré.

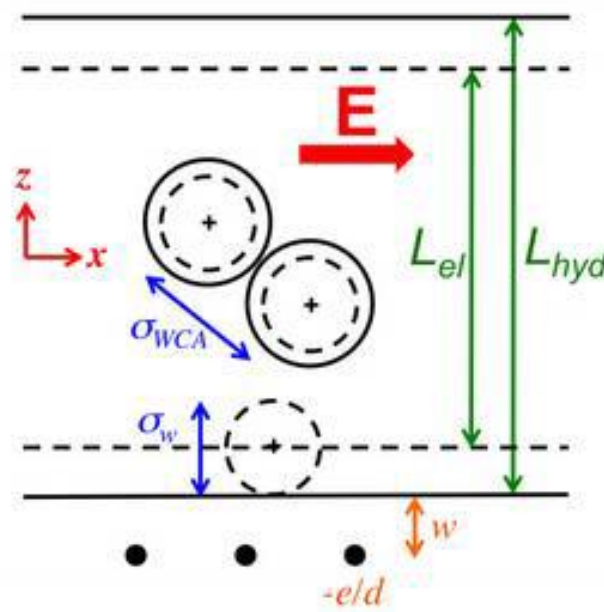


Figure.14. Schéma avec les paramètres utilisés dans les simulations SRD.

Pour calculer les interactions entre les parois et les ions à la distance σ_w , une interaction de type « bounce back » (égale à celle utilisée par le solvant qui prévoit un rebond de la particule impactant les parois en direction inverse à son mouvement original avec la même vitesse) a été établie ; dans certains cas une interaction répulsive de type WCA avec diamètre σ_{WCA} a été ajoutée à la toujours présente interaction électrostatique décrite par l'algorithme d'Ewald-Slab-2D entre les contre-ions et les charges de surface. Ces derniers peuvent avoir une charge unitaire ou être distribués sur d sites avec chacun une fraction $1/d$ de charge.

Plusieurs valeurs de charge de surface, degré de distribution et distance d'interaction avec les parois ont été testées et leur influence analysée. Les effets de l'interaction WCA entre les ions a été également analysée.

Cependant, il était nécessaire de valider la méthode SRD pour l'étude de l'électro-osmose. Cela a été accompli par une confrontation avec les résultats théoriques empruntant la théorie PNP (Poisson-Nernst-Planck) qui est valable pour une charge de surface faible et uniforme. Les résultats des simulations sont confrontés avec la théorie dans les conditions de validité de la théorie ($0,2$ charges e^- par nm^2 , $\sigma=0.2$). Etant possible dans chaque cas d'analyser la distribution des ions dans le canal et le profil de vitesse du solvant

dans le canal, dans ce résumé, seul le deuxième élément a été analysé. Sur la figure.15, sont montrés les profils de vitesse du fluide en variant la distribution de charge (paramètre d) avec les autres paramètres constants et en variant la distance d'approche des ions avec les parois (paramètre σ_w) avec les autres paramètres constants. Bien sûr, les résultats de simulations (indiqués comme « SRD flow ») suivent très bien la théorie (« PNP flow »).

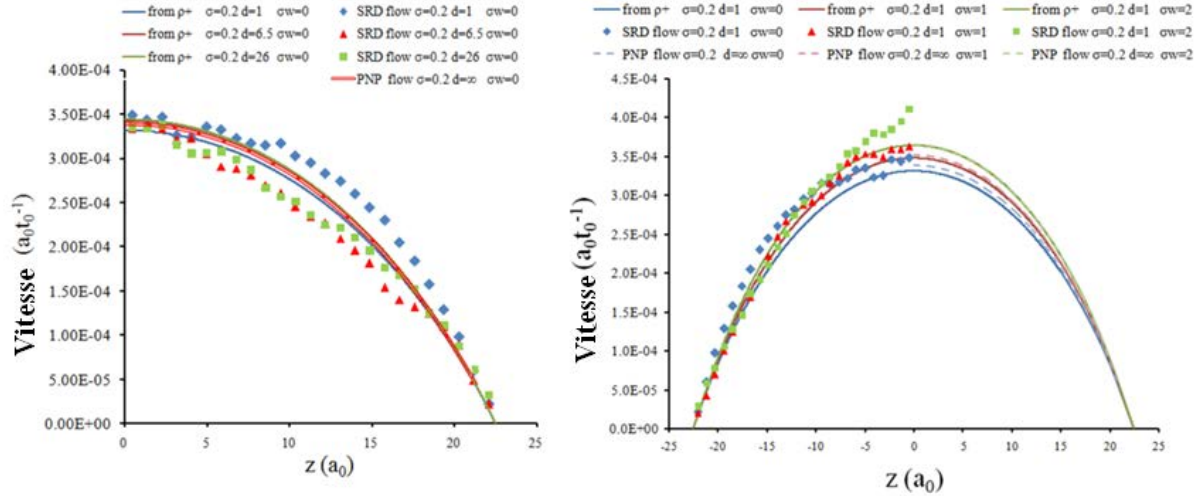


Figure.15. Profils des vitesses pour un flux électro-osmotique pour une basse charge de surface calculée par la théorie PNP et confrontés avec les valeurs de simulation pour différentes valeurs de la distribution des charges sur les parois (à gauche) et de distance minimale d'approche entre les ions et les parois (à droite).

Dans la réalité, la théorie PNP est séparée en deux parties : la première prévoit une distribution de charge dans le canal (selon la théorie de Poisson-Boltzmann) et la deuxième utilise cette distribution pour décrire le profil de vitesse selon l'équation suivante :

$$u_x(z) = u_x\left(\frac{L_{ch}}{2}\right) - \frac{e^{-E}}{\eta} \int_{\frac{L_{ch}}{2}}^z \int_0^{z'} \rho_+(z'') dz'' dz' \quad (2)$$

Le profil de vitesse obtenu en utilisant cette équation et la distribution de charge déterminée par SRD est indiqué comme « from ρ^+ ». Sur la figure, les valeurs calculées avec cette équation, respectant aussi les résultats de la théorie PNP, sont présentés.

La condition pour laquelle la théorie de Poisson-Boltzmann est validée, est telle que la charge de surface doit être petite. Ce n'est donc pas étonnant que, même si la méthode SRD a été validée, elle donne des valeurs différentes à celles données par la méthode PNP pour des plus grandes charges de surface (avec une différence qui augmente d'ailleurs avec cette dernière), comme il est possible de voir sur la figure.16.

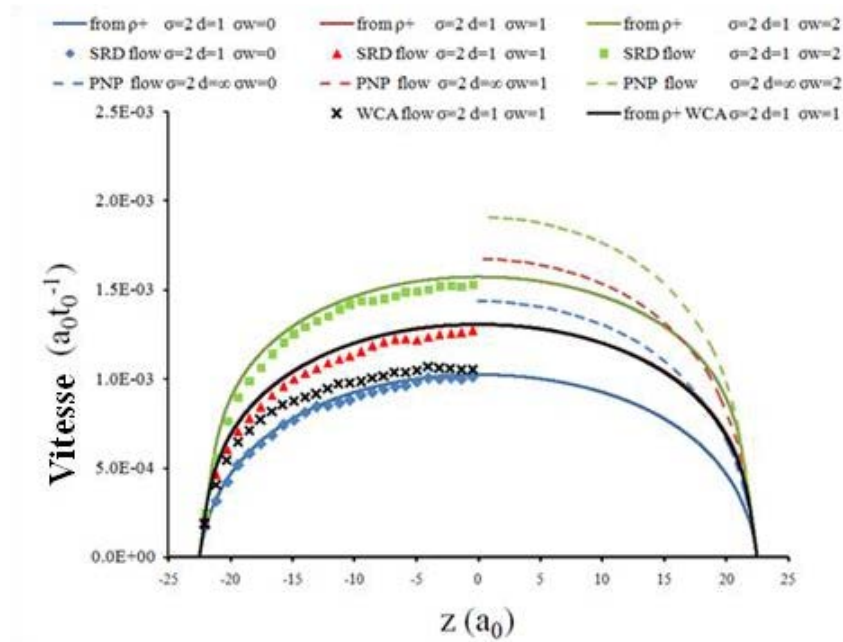


Figure.16. Profils des vitesses pour un flux électro-osmotique pour une haute charge de surface calculée par la théorie PNP et confrontés avec les valeurs de simulation pour différentes valeurs de distance minimale d'approche entre les ions et les parois.

La théorie PNP donne des vitesses plus élevées pour $\sigma=2$ que celles données par la théorie SRD. Par contre l'équation juste introduite est encore utilisable car le profil calculé (from p^+) suit les valeurs obtenues par la simulation (SRD).

Avec les figures précédentes il a été possible d'évaluer qu'en augmentant σ_w , la vitesse du fluide augmente. Ce comportement est explicable en notant que pour des valeurs élevées de σ_w , la charge qui produit le moment est plus éloignée des parois et donc la friction visqueuse est réduite. Par contre la variation du paramètre d sur la figure.15 semble ne pas trop changer la vitesse du fluide. En effet, l'influence du paramètre d est évidente pour $\sigma_w=0$ avec un effet qui diminue pour des charges de surfaces plus élevées.

Par contre l'ajout d'un potentiel WCA entre les ions, ayant pour effet de ralentir la vitesse d'écoulement (figure.16, crois noires), n'est pas idéalement pris en compte par l'équation 2 qui donc perd de validité.

Cet effet est encore plus marqué quand un nombre pair de co-ions et de contre-ions sont ajoutés au système. La charge nette distribuée dans la solution reste égale à la vitesse et le profil d'écoulement n'est pas réellement décrit par l'équation 2. Sur figure 17, il est montré le profil de vitesse d'écoulement pour une valeur de charge de surface $\sigma=1$ (26 charges e^-) avec un ajout de 0, 7, 35 couples de ions. L'effet de cet ajout est inattendu avec une augmentation de la vitesse d'écoulement pour peu de charges ajoutées et un fort ralentissement pour beaucoup de charges ajoutées. Un nombre plus conséquent de simulations est encore nécessaire pour avoir une meilleure compréhension de ce phénomène.

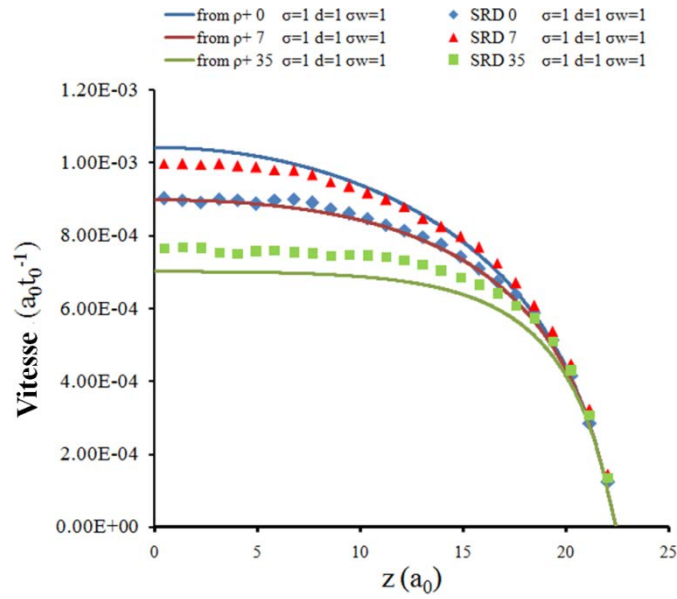


Figure.17. Profils des vitesses pour un flux électro-osmotique pour une haute charge de surface avec ajout des ions supplémentaires (0, 7, 35 couples pour la ligne bleue, rouge et verte) calculée avec l'équation.2 et confrontés avec les valeurs de simulation.

La méthode SRD a été également utilisée pour étudier l'écoulement électro-osmotique dans une structure de PPNs. Plusieurs cas ont été pris en compte en distribuant la charge de surface sur toutes les parois, seulement sur les piliers, ou seulement sur le « plafond » et le « sol ». Les différents cas sont représentés sur la figure.18.

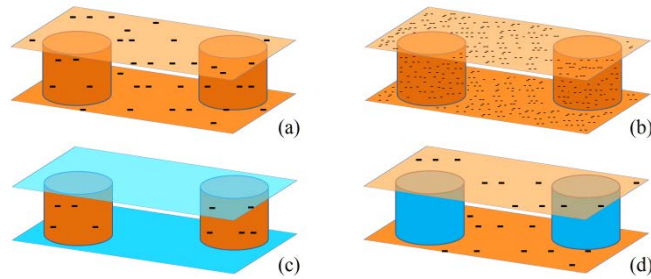


Figure.18. Différentes distributions de charge utilisées pour la simulations SRD d'électro-osmose dans la structure des PPNs.

Différents effets ont été démontrés avec une plus grande variation de la position verticale des ions pour les cas où les piliers sont chargés. De plus, une variation des trajectoires des ions a été trouvée au cas par cas selon les conditions. Sur la figure.20 il est possible de visualiser la carte des directions et des vitesses (couleur rouge plus foncée pour une vitesse supérieure) dans la direction verticale, pour le cas de la charge de surface distribuée sur toutes les parois (champ électrique en direction verticale, piliers vus en section).

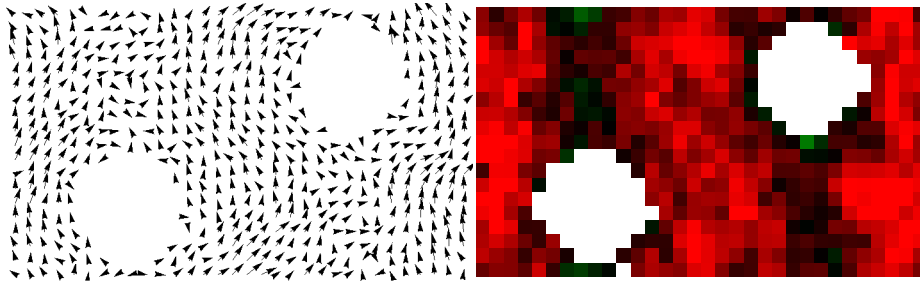


Figure.20. Carte des directions (à gauche) et des vitesses dans la direction verticale (à droite- rouge intensité maximale, vert minimale) de flux électro-osmotique dans une structure de PPNs avec toutes les parois chargées. Le champ électrique est dans la direction verticale et le plan représenté est une section horizontale de la boîte de simulation.

Les piliers causent en général un effet de ralentissement de la vitesse d'écoulement par rapport au cas sans piliers mais cet effet dépend de la position et de la quantité de charge de la surface. Une étude plus approfondie et une plus longue statistique sont actuellement en cours pour comprendre avec plus de précision l'effet mentionné.

En général la méthode SRD s'est montrée comme un moyen valable pour augmenter la compréhension des systèmes nano-fluidiques. Ce sera encore plus évident quand les méthodes expérimentales et de simulation pourront se rejoindre sur les mêmes systèmes ; une possibilité qui semble maintenant très proche.

Conclusions

Cette thèse a permis de valider l'idée de mettre en œuvre la voie « bottom-up » pour des applications de nanofluidique. Plusieurs routes ont été empruntées afin de pouvoir avancer autant sur le plan technologique/expérimental que sur le plan de la compréhension globale.

La méthode du dip-coating biphasique réduit encore plus l'investissement nécessaire à la réalisation de systèmes nano-fluidiques par voie « bottom-up » permettant ainsi une facilité de mise en application. En plus le dip-coating en accélération constitue une deuxième avancée technologique qui peut aider à réaliser des systèmes nano-fluidiques complexes.

La chimie sol-gel en particulier permet de réaliser des couches minces avec différents degrés d'ordre et de propriétés de surface qui peuvent être utilisées pour des applications et pour des études fondamentales afin de comprendre les phénomènes de fluidique à l'échelle nano. La structure des PPNs préparés avec leur haut niveau de symétrie, et exploitant la propriété d'auto assemblage de certains copolymères à blocs, a permis de rationaliser et de simuler le flux les traversant.

L'infiltration des liquides dans la nanoporosité a été sélectionnée comme élément à étudier. Les effets de la géométrie des pores et de la composition du matériau ont été mis en évidence. En particulier un mécanisme d'infiltration par l'eau au travers d'un mécanisme d'évaporation et condensation a été identifié pour les petites porosités. En plus l'influence de la composition des parois des nano-canaux sur la vitesse de remplissage a été démontrée en changeant cette composition avec différents échantillons des PPNs.

Finalement les PPNs ont aussi été couplés avec un simple circuit microfluidique afin de réaliser des séparations et des réactions à l'intérieur de leur structure. Avec ce couplage le système des PPNs a été montré comme adapté pour de vraies applications nanofluidiques qui actuellement ne pouvaient pas être envisagées à cause d'un coût très élevé et des défauts des méthodes de production courantes.

En parallèle, des études de simulation empruntant la méthode SRD ont été accomplies afin de vérifier la validité de la méthode et obtenir des informations préliminaires sur le phénomène de l'électro-osmose dans les systèmes réalisés ; Cela représente la prochaine étape également dans le domaine expérimental.

Pour conclure, les méthodes mises en œuvre dans cette thèse peuvent laisser présager d'un grand avenir pour la nanofluidique comparé à son échelle d'application actuelle amputée suite aux coûts élevés, aux équipements nécessaires et aux possibilités limitées des méthodes de fabrication actuelles.

ACKNOWLEDGEMENTS

Je tiens ici à remercier mon Professeur David Grosso. Il m'a toujours soutenu dans la vie de recherche et de chaque jour. C'est difficile d'imaginer un encadrement meilleur de ce que j'ai eu.

Merci aussi donc à Marco Faustini avec lequel j'ai pu toujours discuter, m'inspirer et me confronter. Et merci à Cédric Boissiere qui a été toujours prêt à donner des idées et son point de vue.

La mélange de liberté, confiance, incitation, participation dans laquelle j'ai vécu dans le groupe de recherche m'a permis d'obtenir tout ce que j'ai eu pendant cette thèse et de vivre ces trois années de ma vie que seront toujours souvenirs comme fantastiques.

Merci aussi à Vincent Dahirel et Marie Jardat qui m'ont supporté sur la partie modélisation de cette thèse et sont resté toujours patients avec moi.

Je tiens aussi à remercier mes trois amis et coéquipiers Benjamin Louis, Xavier Paquez et Mickael Boudot qui ont fait devenir amusant chaque jour de cette thèse.

Merci aux directeurs ancien et nouveau du laboratoire LCMCP, Clément Sanchez et Florence Babonneau, qui avec leur gestion ont fait développer un laboratoire exceptionnel à niveaux scientifique et aussi humain.

Merci au Labex Matisse pour le financement.

E grazie alla mia Famiglia, Mamma e Papà che sono sempre con me e alla mia Nonna che ha sempre voluto bene al suo « Davidone » fino all'ultimo giorno di questo dottorato.